Textile Fibre Composites in Civil Engineering

Edited by T. C. Triantafillou

Textile Fibre Composites in Civil Engineering

Related titles

Blast Protection of Civil Infrastructures and Vehicles Using Composites
(ISBN: 978-1-84569-399-2)

Fangueiro, Fibrous and Composite Materials for Civil Engineering Applications
(ISBN: 978-1-84569-558-3)

Textiles, Polymers and Composites for Buildings
(ISBN: 978-1-84569-397-8)

Woodhead Publishing Series in Civil and Structural Engineering: Number 60

Textile Fibre Composites in Civil Engineering

Edited by

Thanasis Triantafillou

AMSTERDAM • BOSTON • CAMBRIDGE • HEIDELBERG
LONDON • NEW YORK • OXFORD • PARIS • SAN DIEGO
SAN FRANCISCO • SINGAPORE • SYDNEY • TOKYO
Woodhead Publishing is an imprint of Elsevier

ELSEVIER

WP
WOODHEAD
PUBLISHING

Notices
Knowledge and best practice in this field are constantly changing. As new research and experience broaden our understanding, changes in research methods, professional practices, or medical treatment may become necessary.

Practitioners and researchers must always rely on their own experience and knowledge in evaluating and using any information, methods, compounds, or experiments described herein. In using such information or methods they should be mindful of their own safety and the safety of others, including parties for whom they have a professional responsibility.

To the fullest extent of the law, neither the Publisher nor the authors, contributors, or editors, assume any liability for any injury and/or damage to persons or property as a matter of products liability, negligence or otherwise, or from any use or operation of any methods, products, instructions, or ideas contained in the material herein.

For information on all Woodhead Publishing publications
visit our website at http://store.elsevier.com/

Working together
to grow libraries in
developing countries

www.elsevier.com • www.bookaid.org

Contents

List of contributors

L. Bisby University of Edinburgh, Edinburgh, UK

D. Bournas University of Nottingham, Nottingham, UK

W. Brameshuber RWTH Aachen University, Aachen, Germany

R. Chudoba RWTH Aachen University, Aachen, Germany

M. Curbach Technische Universität Dresden, Dresden, Germany

T. Gries Institut fuer Textiltechnik of RWTH Aachen University, Aachen, Germany

J. Hegger RWTH Aachen University, Aachen, Germany

V. Mechtcherine Technische Universität Dresden, Dresden, Germany

E. Müller Technische Universität Dresden, Dresden, Germany

B. Mobasher Arizona State University, Tempe, AZ, USA

C. Morales Cruz RWTH Aachen University, Aachen, Germany

A.E. Naaman University of Michigan, Ann Arbor, MI, USA

C.G. Papanicolaou University of Patras, Patras, Greece

I.C. Papantoniou University of Patras, Patras, Greece

A. Peled Ben Gurion University of the negev, Beersheba, Israel

T. Quadflieg Institut fuer Textiltechnik of RWTH Aachen University, Aachen, Germany

M. Raina Institut fuer Textiltechnik of RWTH Aachen University, Aachen, Germany

M. Raupach RWTH Aachen University, Aachen, Germany

S. Scheerer Technische Universität Dresden, Dresden, Germany

K. Schneider Technische Universität Dresden, Dresden, Germany

A. Scholzen RWTH Aachen University, Aachen, Germany

O. Stolyarov St. Petersburg State Polytechnical University, St. Petersburg, Russia

T. Triantafillou University of Patras, Patras, Greece

N. Will RWTH Aachen University, Aachen, Germany

Preface

The use of brittle materials with low tensile strength, such as concrete or masonry, has been known for thousands of years. The idea of embedding fibers in brittle materials, so that cracking does not lead to failure, is also not new. Thousands of years ago straw was added to clay bricks in order to make them tougher. Later on, techniques were devised to strengthen concrete that were based on the use of metallic reinforcement. In recent decades, various methods have been developed to replace the conventional steel reinforcement in concrete structures through the use of short fibers (e.g. steel, glass, or polymeric), with a recent development along these lines being the ultra-ductile concrete. Another development is the use of fiber reinforced polymers (FRP), which are typically made of long, continuous fibers (e.g. carbon, glass, aramid) in a polymeric matrix, which yield reinforcing elements such as bars, strips, and sheets, for the reinforcement, strengthening, or seismic retrofitting of new or existing concrete and masonry structures.

Considerations to combine continuous fibers with inorganic binders in the construction of new structures began in the 1980s, and the first research efforts were made in Germany in the 1990s, leading to the product known as textile reinforced concrete (TRC). This material consists of textiles made of long woven, knitted, or even unwoven fiber rovings in at least two directions, embedded in an inorganic fine-grained binder (typically—but not necessarily—cementitious).

In the early 2000s, the textile-based composites were used successfully in the field of strengthening and seismic retrofitting of concrete and masonry structures, in an attempt to solve problems associated with the use of polymeric resins in FRP products. At the beginning, these new "textile fiber composite" materials were given (in Europe) the name "textile reinforced concrete" (TRC) or "textile reinforced mortar" (TRM). Strictly speaking, the inorganic matrix is not classified as "concrete", due to the very small size of aggregates. More recently (in the USA), the materials were given the name "fabric reinforced cementitious matrix systems" (FRCM).

The introduction of textile fiber composites to the market have been accompanied with an extensive expansion of research on TRC or TRM or FRCMs. Many research units worldwide deal with topics relevant to new constructions, as well as to the retrofitting of existing ones. A wide variety of publications already demonstrate the worldwide interest in this innovative structural material, which is expected to grow rapidly.

The book provides a state-of-the-art review from leading experts in the field on the developments which have appeared over the last decade or so, on the use of textile fiber composites in structural engineering, with a focus on both new and existing concrete and masonry structures. The book reviews materials, production technologies,

fundamental properties, testing, design aspects, applications, and directions for future research and developments.

The book provides broad coverage of a wide range of topics and includes 18 contributions from leading experts in the field. The material is divided into four parts: Part one covers materials, production technologies, and manufacturing of textile fiber composites for structural engineering. Part two moves on to review testing, mechanical behavior, and durability aspects of textile fiber composites. Part three analyzes the structural behavior and design of textile reinforced concrete. This section includes a number of case studies providing thorough coverage of the topic. Finally, part four details the strengthening and seismic retrofitting of existing structures with textile-based composites. Chapters in this part investigate concrete and masonry structures, in addition to providing information on case studies and insight into future directions in the field.

Textile Fiber Composites in Civil Engineering is a key volume for researchers, academics, practitioners, and students working in civil and structural engineering and advanced construction materials, written by international experts and researchers in the field. Their great effort in providing excellent contributions is gratefully acknowledged.

Patras, Greece   Thanasis C. Triantafillou
September 2015

Woodhead Publishing Series in Civil and Structural Engineering

This page intentionally left blank

Part One

Materials, production technologies and manufacturing of textile fibre composites for structural and civil engineering

This page intentionally left blank

Manufacturing of textiles for civil engineering applications

<div align="right">**1**</div>

T. Gries*, M. Raina*, T. Quadflieg*, O. Stolyarov[†]
*Institut fuer Textiltechnik of RWTH Aachen University, Aachen, Germany, [†]St. Petersburg State Polytechnical University, St. Petersburg, Russia

1.1 Introduction

Over the last 100 years, steel has traditionally been used as reinforcement for concrete. Along with a set of important positive properties of concrete structures, such as strength and stiffness, their weight is very high, and steel reinforcement limits the size and shape of concrete products. Moreover, reinforcing steel bars are subject to corrosion, which can cause destruction of the concrete by reducing the effective cross-sectional area of the bars and consequently increasing the stresses in the structure. One of the alternatives to conventional steel reinforcement is the use of textile reinforcement, which results in increased durability and reliability of civil engineering construction.

High-strength textile materials are widely used in various fields of construction, including the construction of unique buildings and structures, road construction, hydraulic engineering, and others. Textile reinforcement for composites includes various hierarchical structural levels: fiber, yarn, and fabric (Hearle et al., 1972). Traditionally, the reinforcement of composites with chopped, short fibers has been used for the manufacture of structural composites. The use of continuous reinforcement in the form of textile reinforcing structures has gained popularity in the last two or three decades. The main advantages of using them consist of sufficient flexibility of textile manufacturing processes and the possibility of using a wide range of raw materials. Reinforcement with textiles offers many opportunities, including manufacturing very thin composite and concrete parts, no risk of corrosion of reinforcement materials, and the ability to manufacture structural parts with complex shapes and predetermined properties.

In general, textiles are associated with clothing or household applications; however, today the application of textiles is broader in various branches of industry. In the manufacture of high-strength reinforcing materials, mainly fibers such as glass, carbon, aramid, basalt, and others are used. These types of fibers have very high mechanical characteristics (strength, modulus, etc.) comparable to those possessed by metals and sometimes exceeding them. As a consequence, it is necessary to ensure satisfactory processing of high-strength fibers for textile machines because of their high stiffness. The raw materials for the production of reinforcing structures have a critical deformation stiffness. Therefore, it is necessary to place special demands

on textile technology. One of the main approaches is to provide a practical basis for processing these yarns on textile machines. Various textile structures in the form of yarns and fabrics are used as reinforcement. The yarn structures include cabled, friction-spun, and commingled yarns. The use of these yarn structures improves the bonding behavior of the concrete or polymer matrix compared to the results when using conventional filament yarns. The load-oriented yarns in the composite matrix may be realized in different geometrical orders. Textile fabric reinforcements come in the forms of woven, nonwoven, and knitted structures, which differ in their manufacturing processes (Peled and Bentur, 1998, 2003).

Processes for manufacturing textile materials allow making reinforcing structures with their reinforcing elements at a predetermined location. They may be in the form of either short fibers in the manufacture of nonwoven fabrics, or filaments with continuous length in the manufacture of woven and knitted fabrics. The form of reinforcing structures themselves may be either planar (two-dimensional (2D)) or spacer (three-dimensional (3D)). In the latter case, they are able to sustain loads not only in one or two directions within a plane but also within a volume, i.e., in the through-thickness direction of the reinforced structure. Three-dimensional structures may have the shape of the final composite part. This leads to a reduction of manpower within the production of structural composite parts (Hanisch et al., 2006). Depending on the direction of the externally applied load, textile fabrics can be produced with predetermined properties in order to sustain a certain load in any direction. This is possible because the properties of reinforcing fabrics can be readily adjusted, from isotropic to anisotropic, by introducing the necessary amount of reinforcing elements in the form of yarns with special characteristics per unit width.

1.2   Yarn structures

Yarns that are used for manufacturing technical textile products and designed primarily to meet a product's technical requirements are known as technical yarns (Chattopadhyay, 2010). Various types of yarns are used as reinforcing elements of textile structures. The yarns should have high mechanical properties in order to meet the requirements imposed on structural elements. Production of yarns with different structures is not fundamentally new. As mentioned above, high-strength and high-modulus filament tows and rovings are used for basic structural applications. The choice of raw material is made with regard to several factors, such as mechanical properties, resistance to various aggressive media, and cost. For example, in the manufacture of textile-reinforced concrete, alkali-resistant glass (AR-glass) fibers are used because of their good resistance to alkaline environments and low cost. Yarns used in reinforcing textiles for civil engineering applications can be manufactured by various techniques, including cabling, friction spinning, and commingling (Tyagi, 2010).

The original multifilament yarns produced at chemical fiber factories are smooth, continuous-filament yarns without twist, usually consisting of a few hundred or

thousand individual filaments of small diameter (on the order of 5–20 μm). Sometimes these yarns have quite unsatisfactory characteristics when interacting with the matrix in the composite. As a consequence, they need to be further processed to obtain the desired characteristics. This bonding behavior can be changed by using different yarn structures especially manufactured for use in concrete. Modification of the surface texture of the yarn can improve its outer bond to the matrix. For example, to improve the bonding of yarns with a concrete matrix, an additional spiral cable for smooth surface yarns can be used to form a profile similar to the conventional, periodic profile of steel bars (Hanisch et al., 2006). This form of yarn is extremely important to ensure the load-carrying capacity of structural elements. When using friction-spinning technology, reinforcing yarns are covered with fibers, creating a structure with core yarns. As core yarn, high-strength yarns are used to bear the load. As sheath yarn, short polymer fibers are used. This technology creates a loose surface that improves bonding with concrete. To improve the inner bonding between the core yarns and the sheath and between the outer filament yarns and the concrete, yarns may be subjected to further processing with polymers. Impregnated filament yarns have significantly greater strength compared to nonimpregnated yarns, owing to the larger number of active filaments in the former's cross-section. Technical yarns are further processed into preforms as woven, nonwoven, and knitted fabrics.

1.2.1 Cabled yarns

The manufacture of cabled yarn is an advanced technology used to produce new high-performance types of yarns having new combinations of unique properties. Cabled yarn consists of a straight core yarn and spiral-running cover yarn (BISFA, 2009). Unlike conventional textile yarns consisting of one fibrous material, these yarns consist of two or more components comprising a core and an outer layer that is distributed uniformly along the length of the core. The core is made of a continuous, high-strength filament yarn that carries the load. During processing, the core yarn is not given a twist and lies on the axis of the overall yarn. Metal wire can also be used as a starting material for the core. As for the outer layer, various filament yarns can be used, the main function of which is a modification of the surface texture. In addition, the outer layer serves a protective function, preventing the damage of fragile, high-strength yarns. Selection of various combinations of these components provides the necessary physical and mechanical properties.

In the cabling process, one or two yarns are twisted around each other in a single operation without the individual strands themselves being twisted (Hanisch et al., 2006). These yarns are produced by a cabling machine as shown in Figure 1.1. The core is an untwisted yarn that is unwound from a bobbin and led through a hollow tube. The hollow tube carries a bobbin with cover yarn. Cabling occurs due to the rotation of the spool of cover yarn around the tube through which the core yarn passes. The cover yarn is unwound from the bobbin on the hollow tube and is wrapped in a spiral around the core with a certain step distance. Reinforcing yarn with a ribbed surface is thus produced. This ensures better cohesion and therefore
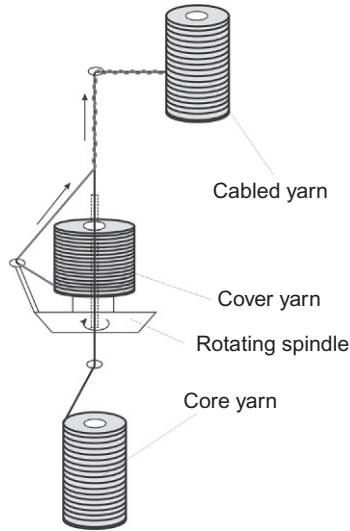
Figure 1.1 Cabling principle.
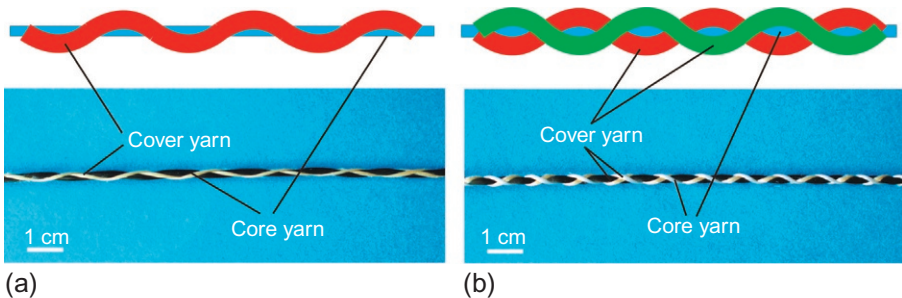
Figure 1.2 The cabling principle and yarn structures of a singly covered (a) and a doubly covered (b) yarn.

a better degree of fiber support. The yarn of the outer layer does not carry the axial load and does not directly increase the strength of cabled yarn; however, the axial compression caused by cover yarns may slightly increase the strength of the entire cabled yarn. The yarn structure obtained by a single-step cabling process is shown in Figure 1.2a. If the procedure is repeated on the yarn with the spindle rotation direction reversed, a yarn with opposite spiral directions can be produced as shown in Figure 1.2b. The twist density can be varied by different adjustments of the process parameters. This makes this structure interesting as a reinforcing material because, within the construction industry, the residual bearing capacity is of major importance. Abbott and Freischmidt (1985) have used this technology to produce cabled yarns in the reinforcement of composite materials.

1.2.2 Friction-spun yarns

In the process of friction spinning, the core yarn is covered with a sheath so that a yarn with a core-sheath structure is created. This method is based on coating the core yarn of the outer layer fibers. The yarn thus obtained consists of a core and an outer sheath, uniformly twisted around the core as shown in Figure 1.3. The resulting yarn has a fluffy surface that improves outer bonding with the composite matrix (Hanisch et al., 2006). Furthermore, this yarn can be used to generate a profiled strand, also capable of improving the bonding. In making profiled filaments, for example, by the partial melting of the thermoplastic component of the outer-layer filaments (if they are made of thermoplastic fibers such as polypropylene and polyamide) and using a knurling tool, a defined surface texture profile is formed. The mechanical properties of yarns manufactured by the friction-spinning process or by cabling are determined mainly by the properties of the core yarn. At the same time, the outer layer of the filament provides little radial compression of the core by increasing the strength of the entire yarn. The friction-spinning system may produce yarns from a wide range of different fibers for technical applications (Merati, 2010). The mechanical properties of a friction-spun yarn depend mainly on the core yarn. At the same time, the sheath fibers provide a transverse force, binding the individual filaments and resisting their slippage (Vigneswaran and Chandrasekaran, 2010; Hasan and Cherif, 2011; Yadav and Chattopadhyay, 2012).

1.2.3 Commingled yarns

Commingled yarns are hybrid structures in which two different materials in the form of fibers are mixed to form continuous-filament yarns. Commingling techniques use air jets to blend two types of filaments together at the filament level. In the commingling process, rapidly moving air in a jet is used to generate entanglements in and among the filaments of the supplied yarns (Alagirusamy and Ogale, 2005). Figure 1.4 shows a schematic with the most important components of a modern

1 mm
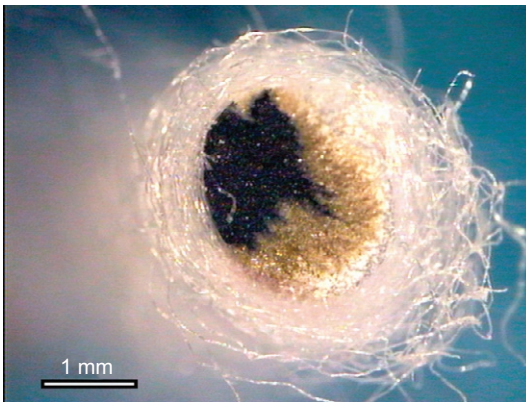
Figure 1.3 Friction-spun yarn.
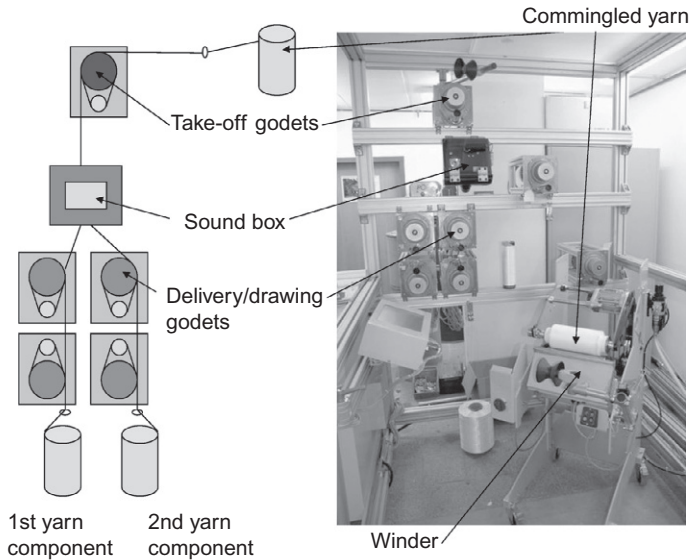
Figure 1.4 A commingling device.

commingling device. The yarn components are fed by means of separate godet pairs in order to adjust the speed of supply for the different process speed of the fibers. Usually, there is a slide overfeeding between the upper delivery godet (DG) and the take-off godet (TG). This means that the DG rotates faster than the TG. During the mingling process, the air stream impacts the yarn orthogonally, leading to the formation of open segments (at the position where the air jet acts) and of compact sections called nips (on either sides of the open segments). The factors that determine the structure of commingled yarns can be classified as follows: (a) process parameters such as air pressure, degree of overfeeding, and production speed; (b) nozzle design; and (c) raw material parameters (Kravaev et al., 2014).

Commingled yarns may be used as reinforcement in civil engineering applications. Janetzko et al. (2010) developed commingled yarns for concrete reinforcement consisting of reinforcing fibers (AR-glass fibers) and water-soluble polyvinyl acetate (PVA) filaments used as placeholders for the reinforcing fibers. After embedding the reinforcement structure in concrete, the PVA filaments should dissolve owing to the alkaline matrix. Thus, hollow spaces are generated between the glass filaments. The concrete matrix reinforced with this commingled yarn is able to flow into these cavities and to penetrate the internal filaments of the reinforcement. The PVA yarn is also used to enhance the penetration of the high-strength fiber by the concrete. Previous research has shown that the PVA component also improves the microstructure of the concrete matrix by intervening in the nucleation and the crystallization of the mineral components of the concrete (Kravaev et al., 2008).

1.3 Planar textile structures

In the manufacture of textile structures for reinforcement of structural composites, all types of textile processes are involved. Planar textile structures are fabrics in which the structural elements (fibers or yarns) are arranged in a plane and are able to sustain the load in one or more directions. Planar textile structures having yarn specifically oriented in the direction where forces arise are suitable as composite reinforcements. The number of these yarns may vary depending on the required level of tensile forces to be sustained (Wulfhorst, 1998). Properties of fabrics are defined by the following factors: the structure of constituent elements, their number per unit width, their mutual arrangement, and the bonding (for example, the force of friction) between them. The main advantage in the use of textile fabrics for composite reinforcement is the ability to control their properties over a variety of ranges. This is mainly achieved by the use of different manufacturing technologies. The main methods of production of textile fabrics include: weaving, knitting, and nonwoven technology. Until now, woven fabrics occupied a dominant position among all kinds of textile fabrics. This was mainly because of the established tradition in the manufacture of garments and other textile products, including reinforcing fabrics for composite materials; however, other textile technologies are now becoming more and more popular in the manufacture of reinforcing structures for composite materials.

1.3.1 Woven fabrics

Weaving is a process of forming fabric by interlacing two or more sets of yarns using a stable machine called a loom. Weaving is a method of fabric production in which two distinct sets of yarns or threads are interlaced at right angles to form a fabric or cloth.

Warp yarns are fed from large reels called creels or beams. Typically, these hold about 4500 separate pieces of yarns, each about 450 m long. The filling yarns are fed from bobbins, called quills, carried in shuttles (hollow projectiles). These shuttles move back and forth across the warp yarns, placing some of the weft over and some under. The shuttle is designed so that the yarn it carries can unwind freely as the shuttle moves. The yarn folds over itself at the end of each pick and forms another pick as the shuttle returns. Usually, the majority of textile products are produced by one of the three basic weaving techniques, namely a plain weave, satin weave, or twill. Figure 1.5 shows the movement of the shuttle in the weaving process.

For construction applications, woven fabrics are typically made of AR-glass, carbon, or event basalt. Applications are generally in the field of concrete or plaster reinforcement, geotextiles, and agrotextiles; however, for these applications, a special kind of fabric with a leno weave is normally used. For applications of these kinds of leno fabrics, a market with about a 20% growth is predicted over the next few years. The entire geotextiles market has grown by about 300% between 1985 and 2000, with a production of about 100 million m^2 per year.

Leno fabrics are open but stable fabrics with a grid structure. As compared to conventional fabrics, the leno weave has two sets of warp yarns that are twisted around a
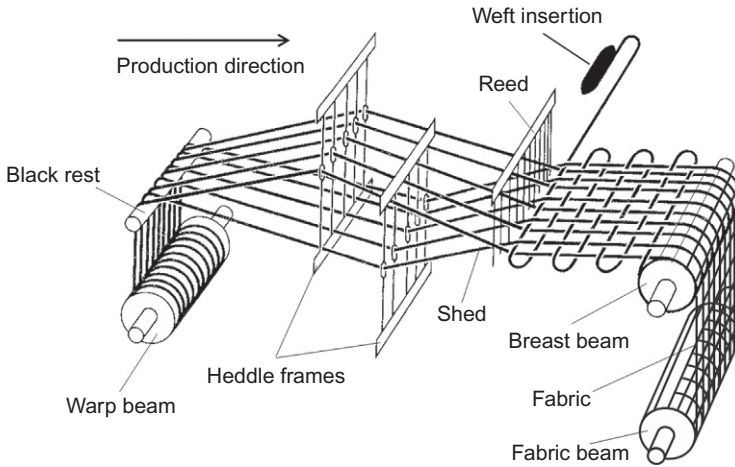
Figure 1.5 The weaving process.
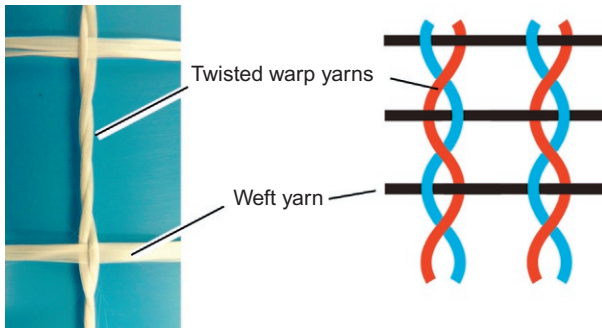
Figure 1.6 A leno weave with glass weft yarns (left); schematic diagram of a leno weave (right).

weft yarn, thus holding it stable within the fabric. The warp yarns crossing around the weft provide dimensional stability to the fabric (Figure 1.6). The advantages of the leno weave include:

- High dimensional stability
- Very low undulation of weft yarns
- Realization of open, grid-like structures

Leno weaves can be made on conventional weaving machines. Here the heald wires of the weaving machine need to be modified with leno heald wires and heald shafts (Figure 1.7). A production speed of up to 250 m/min can be achieved. This is, however, very low compared to the speeds of conventional weaving techniques.

A new leno weaving technique has been launched in the market using propeller leno technology. This leno weaving technology can help in the manufacture of grid structures at a speed of about 800 m/min. A schematic diagram of the new technology is seen in Figure 1.8.
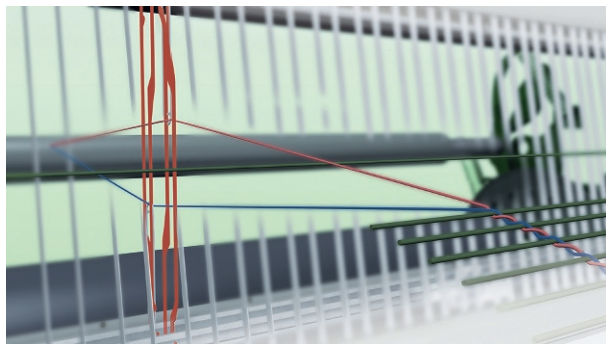
Figure 1.7 Conventional leno manufacturing technique.
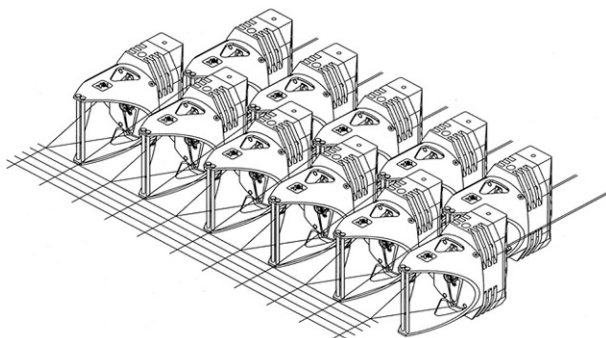
Figure 1.8 Propeller leno weaving technology.

Table 1.1 **Applications of leno weaving technology**

	Plaster reinforcement	**Flooring reinforcement**	**Concrete reinforcement**
Min. mesh size Max. mesh size Market relevance	3.0 mm × 2.5 mm 11.5 mm × 9.8 mm Very high	15.7 mm × 10.1 mm 40 mm × 20 mm High	5 mm × 5 mm 20 mm × 20 mm Very high

The conventional applications of the leno weaving technology along with the grid mesh size are mentioned in Table 1.1.

1.3.2 Knitted fabrics

Knitting technology is one of the most versatile and flexible methods of production for textile fabrics. Selection of traditional textile techniques, such as knitting, is currently of great interest because of the potential for producing net-shape/near-net-shape

fabrics with mass production, low fabrication cost, and the ability to conform to complicated contours (Leong et al., 1999; Huang and Ramakrishna, 2000). Knitted fabrics are produced by interlooping one or many yarns. The elements of the knitted structure include open and closed laps, floats, insertion weft, and warp yarns. Knitted fabrics are mainly divided according to their method of formation into two groups including weft- and warp-knitted fabrics (Spencer, 2001). In the weft-knitting process, knitting is performed in the transverse direction with one or more yarns, and in the warp-knitting process, knitting is performed in the longitudinal direction from a large number of parallel yarns. Weft-knitted and warp-knitted structures are shown in Figure 1.9a and b, respectively. Depending on the application, the knitted fabric can be manufactured as a continuous, closed fabric having a certain permeability, or as a material with an open-mesh structure with cells in a rectangular shape. Standard industrial knitting machines can produce almost any type of knitted fabric for composites.

Properties of knitted fabrics can be freely adjusted according to the specific application: from highly stretchable to almost inextensible, with fixed sizes; from thin, open structure to dense; from smoothly surfaced to nonplanar arrangements with textured or embossed surfaces. Varying the structural elements can improve strength or stiffness, reduce material consumption, etc. Depending on the application and the manufacturing process, different types of knitting patterns are used in the production of reinforcement structures.

1.3.2.1   Weft-knitted fabrics

Weft-knitted fabrics are generally used for the manufacture of clothing; however, they also serve in a number of applications for reinforcing composites (Ramakrishna et al., 1997; Leong et al., 1999; Huang and Ramakrishna, 2000; Khondker et al., 2004; De Araujo et al., 2009). In weft-knitting, yarn feeding and loop formation occur at each needle in succession across the needle bed during the same knitting cycle (Spencer, 2001). Weft-knitted fabrics are produced on flat and circular weft-knitting machines. Weft-knitted fabrics have undulated yarns in their structure and,

(a)   (b)
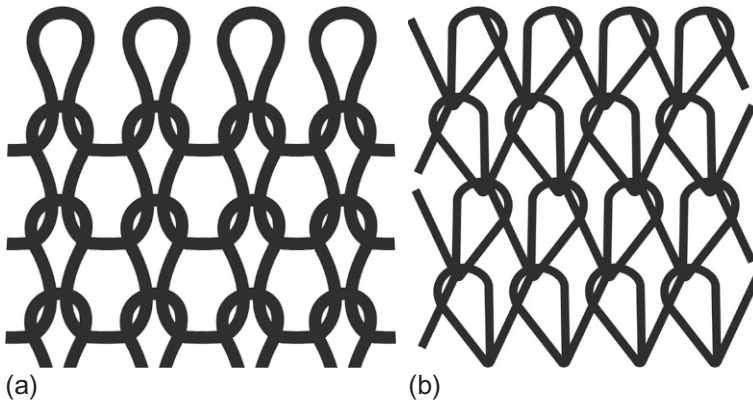
Figure 1.9 (a) Weft- and (b) warp-knitted structures.

consequently, have a much lower strength when compared with other types of textile fabric. In addition, during loop formation, the yarns are exposed to tensile and bending forces that can cause damage to the yarn and result in lower failure loads compared to the results of other production methods. The main problem is that high-strength yarns are very fragile and may be easily damaged during knitting. It should be noted that yarns with low knittability are better incorporated into the knitted structure in the form of straight, inlaid yarns in the lengthwise and crosswise directions. The main advantage of these structures is their good drapability, i.e., their ability to cover the surface of a complex shape without wrinkling.

1.3.2.2 Warp-knitted fabrics

In a warp-knitting process, simultaneous yarn-feeding and loop-forming actions occur at every needle in the needle bar during the same knitting cycle (Spencer, 2001). The main difference from weft-knitted structures consists of the fact that all working needles on warp-knitting machines move simultaneously and, consequently, the loops are formed in a row simultaneously. Loop structures are formed in the warp yarn system in the length direction of the fabric. Thus, during one revolution of the shaft of the warp machine, from a few tens up to thousands of loops are formed. Warp-knitting features substantially higher performance compared with weft-knitting. In contrast to weft-knitted fabrics, warp-knitted fabrics find widespread use in the reinforcement of various composite materials, including those for civil engineering applications. Manufacturing technology for warp-knitted fabrics combines the benefits of weaving and knitting. Similar to weaving, yarns are wound from warp beams, and are located in the fabric in two perpendicular directions. In the manufacture of technical fabrics, directly oriented warp- and weft-reinforcing, high-strength yarns are inserted to provide the necessary mechanical characteristics and dimensional stability of the fabric. The reinforcing yarns are then combined with warp-knitting yarns.

Warp-knitted fabrics manufactured for civil engineering applications have the following basic elements:

– 0° inlay yarns are straight yarns that are placed in the warp-knitted fabric in the machine's longitudinal (warp) direction
– 90° inlay yarns are the straight yarns that are placed in the warp-knitted fabric in the transverse (weft) direction
– Inlay yarns in the diagonal direction are the straight yarns that are placed in the warp-knitted fabric in the diagonal direction (e.g., ±45°)
– Warp-knitting yarns are the yarns that stitch-bond the fabric

It should be noted that inlay yarns do not participate in loop formation during the knitting process, but serve as reinforcing elements. As inlay yarns, high-strength rovings, hybrids, or multifilament yarns may be used. The loop length of the warp-knitting yarns influences both the inner friction of the straight reinforcing yarns and other properties such as, for example, concrete penetration ability (Hanisch et al., 2006). The linear density of the filaments and the inlaid reinforcing yarn's hinge structure usually differ in size by one or two orders of magnitude. The result of this manipulation is a structure with fundamentally new properties.

(a)   (b)

(c)
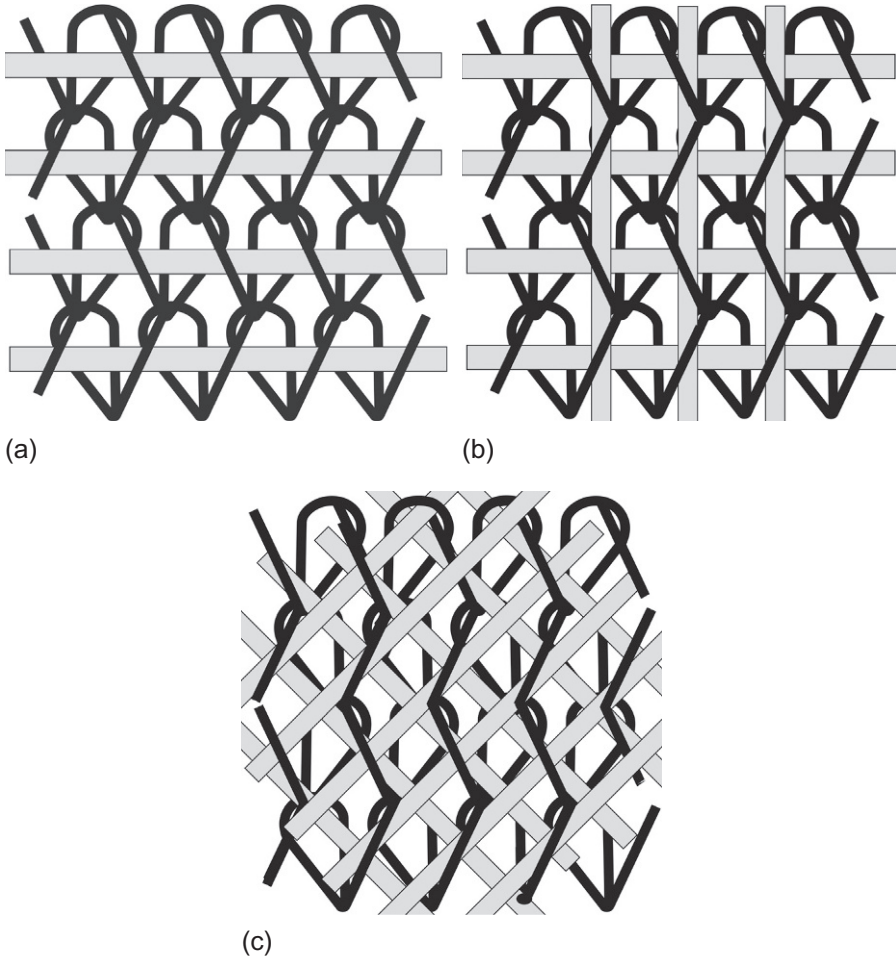
Figure 1.10 (a) Uniaxial, (b) biaxial, and (c) multiaxial warp-knitted structures.

Planar warp-knitted fabrics may be uniaxial, biaxial, or multiaxial. In uniaxial structures, the weft yarn is inserted across the width of the fabric (Padaki et al., 2006). This is also known as magazine weft insertion (Raz, 2000). Figure 1.10a illustrates warp knit with a weft inlay yarn. As a result, a unidirectional structure that can sustain a load only in one particular direction is produced. In comparison with woven fabrics, higher strength due to the straight arrangement of the weft yarn is achieved. In biaxial structures along with weft inlaid yarns, additional yarns are incorporated into the knitted structure in the machine direction as shown in Figure 1.10b. The resulting structure combines the advantages of knitted and woven fabrics (Godou et al., 1998), and can carry loads in two directions. In addition to horizontal and vertical reinforcing yarns, additional diagonal yarns may be introduced at various angles to the machine direction of the fabric. These fabrics are called multiaxial or noncrimp fabrics, i.e., the

reinforcing yarns are placed in the same plane but in different directions. Such structures may consist of several layers and have different orientations of their constituent yarns as shown in Figure 1.10c (Raz, 2000).

The properties of warp-knitted fabrics are affected by the knitting pattern. Although there are a variety of knitting stitches, only a limited number of them is used for the production of reinforcing fabrics. Typically two types of knitting stitches, namely pillar (Figure 1.11a) and tricot (Figure 1.11b) stitches, are used in the warp-knitting process. In the pillar stitch, the same guide always overlaps the same needle. In the tricot stitch, one thread crosses between wales respectively (Spencer, 2001).

Warp-knitted fabrics with a tricot stitch embed the yarns or rovings with a flat, ribbon-shaped cross-section into the textile structure. Due to the flat shape of the roving, the contact surface between the filaments and the concrete increases. Also, in comparison to a round-shaped filament bundle, the minimal penetration depth decreases by almost 50% (Janetzko et al., 2010). Thus, reinforcement structures are produced that can be easily penetrated by the concrete matrix, providing a good bond between the filaments and the concrete. Warp-knitted fabrics with a tricot pattern show higher load-bearing capacity than specimens reinforced with pillar-stitch textiles (Roye, 2007); however, the spacing width of the textiles between the individual rovings decreases due to the ribbon shape of the reinforcement yarn and the closed mesh of the knitting yarn (Figure 1.12a). For this reason, these reinforcement structures are further processed into structural parts mainly by lamination or spraying.

Warp-knitted fabrics with pillar stitches offer open-grid reinforcement structures as shown in Figure 1.12b. These grid textiles are very suitable for the production of concrete elements by using the casting process, where highly liquid concrete mixtures are used (Janetzko et al., 2010). Due to the openings within the fabric, the concrete mixture can flow through the fabric layers to fill the formwork; however, the contact surface between the concrete and the reinforcing roving is low owing to the circular shape of the roving (Roye, 2007).

Warp-knitted fabrics may also be produced with reinforced zones. Local reinforcement is created by locally applied yarns in reinforcement structures. The

(a)   (b)
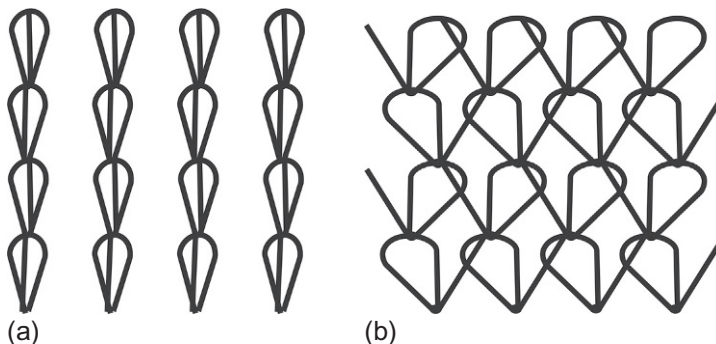
Figure 1.11 Different stitch types: (a) pillar and (b) tricot.

(a)   (b)
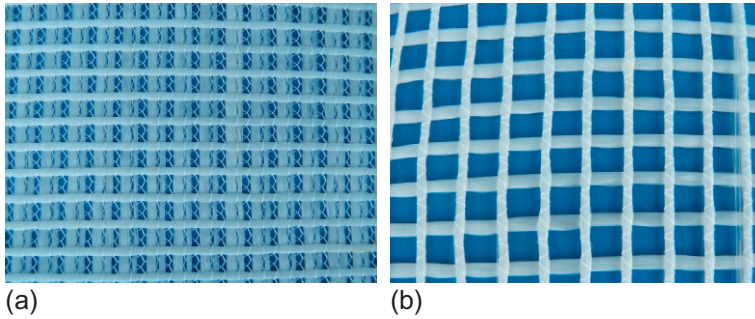
Figure 1.12 Warp-knitted biaxial fabrics with (a) tricot stitches and (b) pillar stitches for concrete reinforcement.

local reinforcements may be introduced directly during the manufacturing process or later in an additional process, e.g., with the help of sewing or embroidery techniques for tailored fiber placement (Kolkmann et al., 2005).

1.3.3   Nonwoven fabrics

Nonwoven fabrics consist of intermingled fibers that are consolidated either by means of chemical, mechanical, or thermal bonding. The relevant properties of nonwovens in the civil engineering field include their isotropic nature and porosity. Nonwoven fabrics have two important properties that make them applicable in civil engineering. They are generally used for:

- Drainage sheets for drainage of fluids from a system
- Distribution of fluids in a system
- Providing homogeneous concrete surfaces

1.4   Three-dimensional textile structures

A significant achievement over the last several decades in textile technology has been the development of 3D textile structures (3D textiles) that have new, unique properties compared to conventional, planar textile structures. The main impact of 3D textile development has been seen in the limited use of conventional planar textiles, mostly woven as reinforcing fabrics for particularly critical structural elements. Unlike planar textile reinforcements, 3D textile structures have the advantage that the yarn can be built-in in three directions in space, including the through-thickness direction. Development of textile fabrics with reinforcing elements in their structures, and having the shape of the reinforcing structure, is quite cost-effective technology. The use of such structures makes it possible to reduce labor costs related to the manufacture of composite materials owing to the creation of integrated systems of reinforcing elements (Gries and Roye, 2003; Roye and Gries, 2007).

Three-dimensional structures can be defined based on either the manufacturing process or the dimensionality of the internal structure. Thus, Buesgen (1993) defined three-dimensional textiles: "textiles or fabrics are three-dimensional textiles when they appear in a three-dimensional geometry without any transformation step and/or when they exist in at least three different layers of yarn systems which are oriented in all three directions (three-dimensional structure)." Roye et al. (2004) defined a 3D textile as a textile that has three directions in yarn architecture and/or textile architecture, regardless of whether it is made in a one-step process or multiple-step process. Thus, in general, a 3D textile is a structure having yarns oriented in three orthogonal directions.

Fabrication of 3D structures can be carried out in either one-step or multiple-step processes; however, production in multiple-step processes involves many additional operations such as cutting, laying, and joining. Therefore, the development of a one-step process for three-dimensional structures is currently a priority. All major textile technologies, including weaving, knitting, and nonwoven technology, are suitable for the production of three-dimensional textile structures.

1.4.1   3D-woven structures

Weaving technology can be used in the narrow-fabric form as well as in the broad-width-fabric form for the manufacture of 3D textiles. These textiles are suitable for an array of different applications, including:

*   High energy absorption
*   Low crack propagation
*   Good impact behavior
*   High tensile strength

These structures can be used for the manufacture of frameworks in building. These framework structures can be woven and directly extruded to be used in applications such as door and window frames.

1.4.2   3D-knitted structures

Knitting technology is widely used in the production of 3D structures. Three-dimensional-knitted structures can be manufactured by both weft-knitting and warp-knitting techniques; however, the warp-knitting technique is the most popular in manufacturing 3D structures for composite reinforcement. Warp-knitted spacer fabric is one of the special types of 3D textiles for use in structural applications. In forming 3D warp-knitted fabrics, two warp-knitted structures having the same or different structures are simultaneously and independently produced on each side of the machine. They are connected together during fabric production by another set of yarns, together forming a 3D structure (Roye and Gries, 2007).

Spacer fabrics show specific characteristics thanks to their special structures. Spacer fabric is a sandwich structure consisting of two outer surfaces and a connection layer, as illustrated in Figure 1.13. Spacer fabrics are produced on double-needle-bar Rachel machines. The upper and lower surfaces of spacer fabrics are produced on the
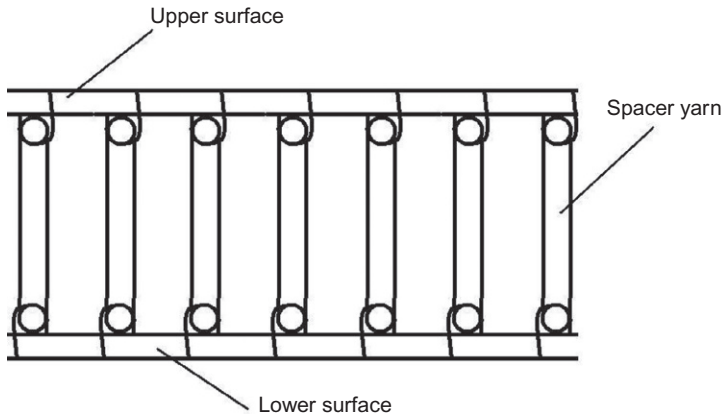
Figure 1.13 Spacer fabric components.

front and rear needle beds, respectively. The needle bars operate in alternation (Raz, 2000). The upper and lower surfaces of the spacer fabric consist of rovings laid at angles of 0° and 90° connected by warp-knitting yarn. In addition, there are spacer yarns located in the through-thickness direction that bind the two outer surfaces of the fabrics to each other.

Spacer fabrics may have open or closed structure or a gridded, mesh-like structure. Various mesh sizes can be obtained by regulating the distance between inlay yarns in two directions. Spacer fabrics with open structures find appropriate application for concrete reinforcement owing to better flow of the concrete mixture into the fabrics. The upper and lower surfaces of spacer fabrics can be produced from the same or different inlay yarns. As a spacer yarn, single, continuous yarns are used. Selection of different inlay yarns allows spacer fabric with different predetermined characteristics to be obtained. The length of spacer yarns between two surfaces can be varied up to 60 mm (Raz, 2000). With this range of length, different fabric thicknesses can be realized depending on composite geometry.

Along with high-strength textile yarn used as inlay yarn, metal wire may be used as a 3D warp-knitted textile for structural reinforcement in hybrid metal or plastic products (Janetzko et al., 2009). The main advantage of spacer fabrics for concrete applications is in the final shape of the component. The high-strength inlay yarns are located in the outer layers of spacer fabrics where the highest tensile and compressive forces occur. The two layers of the spacer fabric can be designed to have different forms, even allowing different distances between the layers, as shown in Figure 1.14. It is also possible to leave out free areas if the concrete element is designed with holes. A spacer fabric with open structure has been designed for façade elements, as shown in Figure 1.15 (Hanisch et al., 2006).

The factors affecting the properties of spacer fabrics include the thickness; the number of inlay yarns per width and the number of spacer yarns per unit area; the properties of inlay and spacer yarns; the spacer yarn laying angle; and the pattern of the warp-knitting yarn.
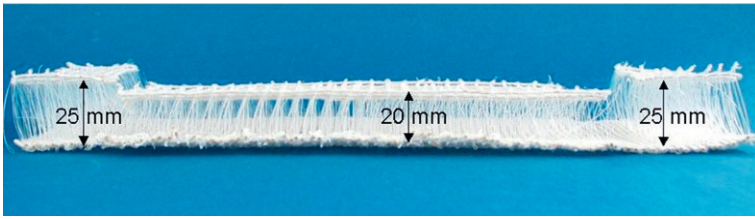
Figure 1.14 Warp-knitted spacer fabric with varying distances between outer layers.
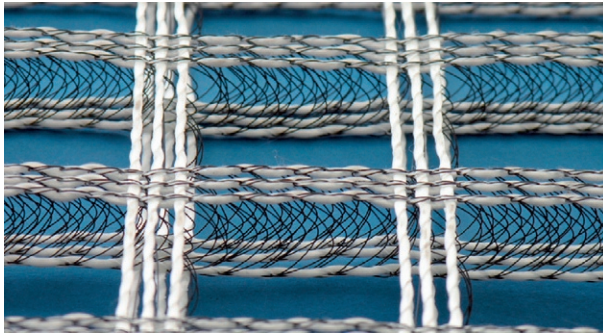
Figure 1.15 Warp-knitted spacer fabric with open structure.

1.5 Coating of textiles

The coating of textiles has the aim of stabilizing the inner structure and shaping and fixing the form of the textile. Furthermore, the tensile strength of a textile-reinforced component increases due to the activation of the roving's inner filaments. Usually the coating is applied to impregnate the whole roving. Figure 1.16 displays the effect of a coating on the stress distribution within the filaments.

Without impregnation, the concrete penetrates only the outer part of the roving, and only parts of the filaments are in direct contact with the surrounding concrete. In the
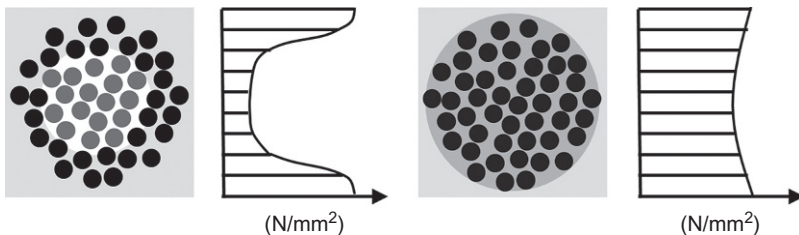
Figure 1.16 Roving cross-section without impregnation (left) and with impregnation (right) (Engler, 2008).

center of the roving is a zone without direct contact with the concrete, which has a lower stress-bearing level. This can partly cause pull-out failure of the roving. Only the load-bearing filaments are pulled, separating from the unloaded parts. With impregnation, the load can be transferred more homogeneously among the filaments. This leads to higher load-bearing capability and smoother component response to loads. The amount of surface area in contact with the concrete is determined by the polymer coating.

A coating line for impregnation of textiles used as reinforcement usually consists of a raw material depot, an impregnation part, a drying part, and a semifinished product depot.

Figures 1.17 and 1.18 illustrate the coating process with the use of a foulard; other coating methods are knife-blade coating, transfer coating, and kiss coating. Within the foulard, the dry fabric is conveyed through a bath of resin. Depending on the viscosity of the resin, squeezing rollers can be added to the bath to achieve full impregnation. Another pair of squeezing rollers above removes excess resin and sets the desired weight fraction; typical values are around 50% coating and 50% textile, by weight. Within the heating zone, the material is either dried (dispersion) or hardened. In a roll-to-roll process, the semifinished textile is wound into a roll. With stiff polymer coatings, the wet textile can also be shaped and cured to get near-net-shaped reinforcements.
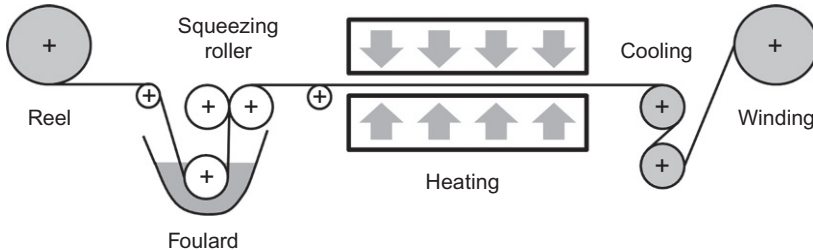
Figure 1.17 Schematic layout of the coating process.

Figure 1.18 Ongoing coating process with an opened foulard (left) and a squeezing roller (right).
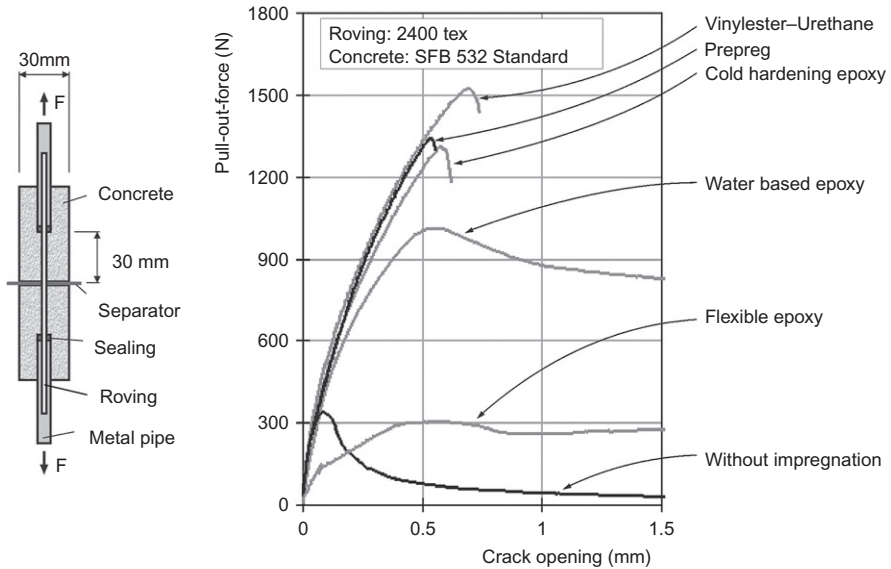
Figure 1.19 Stress diagram for different coatings (Schleser, 2008).

The influence of the coating on component behavior depends strongly on the coating material used. Polymers with a high Young's modulus increase the maximum force that can be sustained and decrease the ductility of the component. Figure 1.19 shows the crack opening under stress of different coatings.

The filaments of rovings without impregnation are pulled out separately during crack opening. The maximum load level is rather low compared to coated rovings, but the bearable deformation is much higher. Impregnated rovings cause a much stiffer member response and can sustain higher maximum loads. Still, failure of members reinforced with coated rovings occurs earlier. The effect of different polymer systems in terms of increasing strength was investigated in several works (Naik and Madhavan, 2000; Dilthey et al., 2006; Glowania et al., 2011). It was shown that, with high-modulus polymers such as epoxy resin, almost total activation of all the filaments in the load-bearing direction is achieved.

Another issue when using polymer coatings is their environment. Temperatures above 100 °C cause a loss in strength, and some polymers are not fireproof.

1.6 Conclusions and future trends

In this chapter, the basic modern processes for the manufacture of textiles for use in reinforcing structures were considered. It was shown that reinforcing textiles are used in various structural levels, from fiber to yarn to fabric. Manufacture of technical yarns such as cabled yarns, friction-spun yarns, and commingled yarns, and their basic

characteristics, were considered and analyzed. Textile fabrics for structural applications may take the form of either planar or spacer structures. In the manufacture of textile structures for reinforcement of structural composites, all types of textile processes are involved. Different methods of fabric formation in woven, knitting, and nonwoven processes for planar and spacer structures, characteristics of fabrics, and production process parameters were considered.

To date, these textile structures have found only limited use in architectural or structural applications. In the short term, textile reinforcing structures will be more and more in demand, especially in the field of construction. As a consequence, the need will arise for mass production of ready-made items in the form of reinforcing structures. The main trend in the manufacture of textile reinforcing structures is likely to be a high demand for knitting, because of the opportunity it provides for the production of directionally oriented structures with low material consumption under existing conditions. Particular attention will be paid to the development of hybrid textile structures, which contain two or more components of different materials.

References

Abbott, G.M., Freischmidt, G., 1985. Wrapped-yarn reinforced composites. II. Composite properties. Compos. Sci. Technol. 24, 147–158.

Alagirusamy, R., Ogale, V., 2005. Development and characterization of GF/PET, GF/Nylon, and GF/PP commingled yarns for thermoplastic composites. J. Thermoplast. Compos. Mater. 18, 269–285.

BISFA, 2009. Terminology of man-made fibres. The International Bureau for the Standardization of Man-Made Fibres, Brussels.

Buesgen, W.A., 1993. Neue Verfahren zur Herstellung von dreidimensionalen Textilien für den Einsatz in Faserverbundwerkstoffen. Aachen, Techn. Hochsch., Diss (in German).

Chattopadhyay, R., 2010. CBE Types of technical textile yarn. In: Technical Textile Yarns. Woodhead Publishing, Cambridge, pp. 3–55.

De Araujo, M., Fangueiro, R., Soutinho, F., 2009. Improving the stiffness of unidirectionally oriented weft-knitted structures for polymer matrix composite reinforcement. J. Text. Inst. 100, 715–721.

Dilthey, U., Schleser, M., Hanisch, V., Gries, T., 2006. Yarn tensile test of polymer-impregnated textiles for the reinforcement of concrete. Tech. Text. 49, 48–50.

Engler, T., 2008. Aktuelle Entwicklungen auf dem Gebiet textiler Bewehrungen für Beton, 47. Internationale Chemiefasertagung, Dornbirn, pp. 17–19.

Glowania, M., Gries, T., Schoene, J., Schleser, M., Reisgen, U., 2011. Innovative coating technology for textile reinforcements of concrete applications. Key Eng. Mater. 466, 167–173.

Godou, U., Diestel, O., Offermann, P., 1998. Biaxially reinforced multilayer knit fabrics for plastic reinforcement. Tech. Text. 41, 202–204.

Gries, T., Roye, A., 2003. Three dimensional structures for thin walled concrete elements. In: Curbach, M. (Ed.), Textile Reinforced Structures. Proceedings of the 2nd Colloqium on Textile Reinforforced Structures (CTRS2). Technische Universität Dresden, Dresden.

Hanisch, V., Kolkmann, A., Roye, A., Gries, T., 2006. Influence of machine settings on mechanical performance of yarns and textile structures. In: Proceedings of the 1st International RILEM Symposium (Textile Reinforced Concrete ICTRC) RILEM TC201-TRC, pp. 13–22.

Hasan, M.M.B., Cherif, C., 2011. Analysis of the influence of process parameters on the mechanical properties of carbon core friction spun hybrid yarns for composites. Fibres Text. East Eur. 87, 59–64.

Hearle, J.W.S., Konopasek, M., Newton, A., 1972. On some general features of a computer-based system for calculation of the mechanics of textile structures. Text. Res. J. 42, 613–626.

Huang, Z.M., Ramakrishna, S., 2000. Micromechanical modelling approaches for the stiffness and strength of knitted fabric composites: a review and comparative study. Compos. Part A 31A, 479–501.

Janetzko, S., Gries, T., Jacob, M., Bührig-Polaczek, M., 2009. Warp-knitted spacer fabrics—vitamin C for hybrid products. Kettenwirk-Praxis 4, 24–26.

Janetzko, S., Kravaev, P., Gries, T., et al., 2010. Textile reinforcement with spread and commingled yarn structures. In: International Conference on Material Science and 64th RILEM Annual Week in Aachen—MATSCI.

Khondker, O.A., Fukui, T., Inoda, M., et al., 2004. Fabrication and mechanical properties of aramid/nylon plain knitted composites. Compos. Part A 35, 1195–1205.

Kolkmann, A., Roye, A., Gries, T., 2005. Warp knitting technology for reinforcing fabrics in specific zones—the possibilities for 2D and 3D textiles. Kettenwirk-Praxis 4, 18.

Kravaev, P., Janetzko, S., Gries, T., et al., 2008. Innovative spread yarn structures for reinforcement of concrete structural elements. Tech. Text. 51 (4), 158–161.

Kravaev, P., Stolyarov, O., Seide, G., Gries, T., 2014. Influence of process parameters on filament distribution and blending quality in commingled yarns used for thermoplastic composites. J. Thermoplast. Compos. Mater. 27, 350–363.

Leong, K.H., Ramakrishna, S., Bibo, G.A., Huang, Z.M., 1999. The potential of knitting for engineering composites—a review. Compos. Part A 31, 197–220.

Merati, A.A., 2010. Friction spinning. In: Advances in Yarn Spinning Technology. Woodhead Publishing. pp. 274–314.

Naik, N.K., Madhavan, V., 2000. Twisted impregnated yarns: elastic properties. J. Strain Anal. Eng. Des. 35, 83–91.

Padaki, N.V., Alagirusamy, R., Sugun, B.S., 2006. Knitted preforms for composite applications. J. Ind. Text. 35, 295–321.

Peled, A., Bentur, A., 1998. Reinforcement of cementitious matrices by warp knitted fabrics materials and structures. Mater. Struct. 31, 543–550.

Peled, A., Bentur, A., 2003. Fabric structure and its reinforcing efficiency in textile reinforced cement composites. Compos. Part A 34, 107–118.

Ramakrishna, S., Cuong, N.K., Hamada, H., 1997. Tensile properties of plain weft knitted glass fiber fabric reinforced epoxy composites. J. Reinf. Plast. Compos. 16, 946–966.

Raz, S., 2000. The Karl Mayer Guide to Technical Textiles. Karl Mayer Textilmaschinenfabrik, Germany.

Roye, A., 2007. Hochleistungsdoppelraschelprozess für Textilbetonanwendungen. RWTH Dissertation, Shaker, Aachen.

Roye, A., Gries, T., 2007. 3-D textiles for advanced cement based matrix reinforcement. J. Ind. Text. 37, 163–173.

Roye, A., Gries, T., Peled, A., 2004. Spacer fabric for thin walled concrete elements. In: Fiber Reinforced Concrete—BEFIB, pro 39, RILEM, pp. 1505–1514.

Schleser, M., 2008. Einsatz polymerimprägnierter, alkaliresistenter Glastextilien zur Bewehrung zementgebundener matrices. Dissertation, RWTH University, Aachen.

Spencer, D.J., 2001. Knitting Technology. A Comprehensive Handbook and Practical Guide, 3rd ed. Woodhead Publishing, Cambridge.

Tyagi, G.K., 2010. Yarn structure and properties from different spinning techniques in the book. Advances in Yarn Spinning Technology. Woodhead Publishing, Cambridge, pp. 119–154.

Vigneswaran, C., Chandrasekaran, K., 2010. Tensile characteristics of dref-III friction core-spun yarns. J. Text. Inst. 101, 729–738.

Wulfhorst, B., 1998. Textile structures as reinforcements for concrete. Concr. Precast. Plant Technol. 64, 133–138.

Yadav, A., Chattopadhyay, S.K., 2012. Structure–property relationship of DREF-3000 friction spun yarn. J. Polym. Mater. 29, 115–126.

Mineral-based matrices for textile-reinforced concrete

2

V. Mechtcherine*, K. Schneider*, W. Brameshuber†
*Technische Universität Dresden, Dresden, Germany, †RWTH Aachen University, Aachen, Germany

2.1   Introduction

Textile reinforced concrete (TRC) is a composite material consisting of a cement-based matrix with typically small maximum aggregate grain sizes and high-performance, continuous multifilament yarns made of alkali-resistant (AR) glass, carbon, polymer, or other materials (Brameshuber, 2006). The major advantages of TRC are its high tensile strength and pseudoductile behavior, the latter characterized by large deformations arising out of its tolerance of multiple cracking, and its expected high durability due to the corrosion resistance of the reinforcement. With its excellent mechanical properties and durability, this material can be highly appropriate to many applications for new, light structures and for the strengthening or repair of old structural elements made of reinforced concrete or other traditional materials (Lieboldt et al., 2008; Weiland et al., 2008; Ehlig et al., 2012; Mechtcherine, 2013).

Today, one common application of TRC is in prefabricated façade panels. Figure 2.1a shows the construction of a lab building at the Technische Universität (TU) Dresden, where 30-mm thick TRC panels with dimensions of 1300–2000 mm were used. Reinforcement consisted of two textile layers made of AR glass yarns impregnated with styrol-butadien resin and interconnected by thin polymeric fibers acting as spacer.

While planar geometries have dominated thus far, more sophisticated prefabricated elements can be produced as well. The pavilion structure shown in Figure 2.1b was put together using eight identical shell elements. The last example given here is a hybrid pipe system with an inner polymer layer (see Figure 2.1c and d); it combines the advantages of polymer pipes, high chemical resistance, water and gas impermeability, and excellent hydraulic properties associated with the advantages of TRC, e.g., high stiffness, high ductility. Production of such new products requires new technologies both for straight pipes and arc elements using different wrapping techniques (Lieboldt et al., 2008).

Strengthening with TRC is another promising area of application for the new composite material. The first practical application in Germany was carried out in 2006 when retrofitting a reinforced concrete (RC) shell at the University of Applied Sciences in Schweinfurt (Ehlig et al., 2012). Altogether, three layers of carbon-yarn textile were placed using a lamination technique (see Figure 2.2a). The total thickness of the strengthening TRC layer was only approximately 15 mm. Such kinds of

Figure 2.1 Examples of TRC use in prefabrication: (a) façade panels; (b) light shell elements (Ehlig et al., 2012); (c) application of textile reinforced concrete on a thin polymeric pipe (Lieboldt et al., 2008); and (d) cross-section of the hybrid pipe wall (six layers of reinforcement) (Lieboldt et al., 2008).
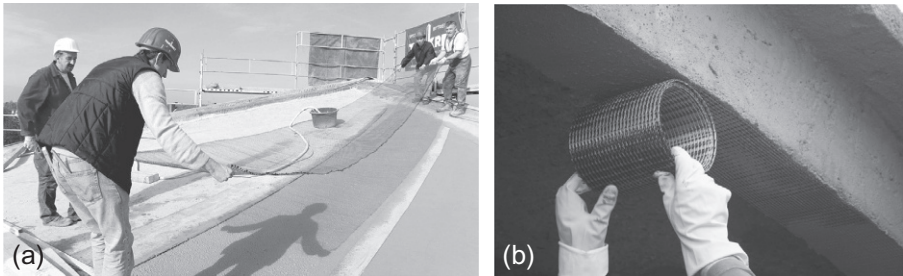
Figure 2.2 Strengthening with TRC—placing textile reinforcement on (a) the hypar-shell's cantilevered area (Ehlig et al., 2012); (b) lower end of the T-beam supporting a cross-section supporting a barrel-shaped roof (Weiland et al., 2008).

strengthening couple the advantages of a two-dimensional reinforcement layer with low dead weight. Taking advantage of these benefits, a large, barrel-shaped concrete roof on the historical school of engineering in Zwickau, Germany was strengthened. TRC lamination was the method of choice for refurbishment since it best complied with the requirements of historical preservation, fire resistance, and the design itself (Weiland et al., 2008).

While first applications are very promising, much work must be done before TRC can become widely accepted as a standard construction material. First of all, a solid

basis in the form of codes and guidelines for structural design and material specifications must be developed and introduced into the construction practice. This is not an easy task since on the one hand, there is both wide variability in the properties of existing TRC already being used and ongoing development of new types of textile reinforcement and matrix compositions. On the other hand, there is relatively little knowledge of and experience with the specific material behavior of TRC under various conditions of loading and exposure. The purpose of this chapter is to analyze the current state of development of matrices for TRC, identify actual problems and challenges related to the TRC production, and define the corresponding tasks to be addressed in further research.

2.2   Overview of matrix compositions for TRC

Various matrix compositions for the production of TRC have been developed with an eye to the requirements of workability, adequate bonding to the textile reinforcement, durability, etc. The fine-grained concrete most often used for TRC production has a water/binder (w/b) ratio of 0.3–0.4 with a binder content of 40–50% by volume. The high content of binder is essential for sufficient bonding between the fine concrete and the filaments of the textile reinforcement as well as for the workability of the fresh concrete. The maximum grain size of the aggregates typically ranges between 1 and 2 mm, depending on the distance between the yarns of the textile reinforcement, the spacing of the textile reinforcement layers and the dimensions of the structural element. Table 2.1 gives five representative fine-grained matrix compositions as developed and used for TRC within the framework of the Collaborative Research Centres 528 at the TU Dresden (see, e.g., Butler et al., 2009; Lieboldt, 2012) and the Collaborative Research Center 532 at RWTH Aachen (Brockmann, 2006; Hinzen, 2014).

Additional specific requirements are the result of particular application scenarios. For example, high productivity in the prefabrication of thin-walled, large-scale elements requires very free flowing and self-leveling capacities as well as the capacity to flow through fine-mesh reinforcing textiles, in some cases several layers, and the ability to envelop the individual yarns. The mixtures PZ-0899-01 and FA-1200-01 (see Table 2.1) fulfill these requirements to a large extent: they have slump flow diameters of 340 and 260 mm, respectively, measured with a small cone and funnel flow times of 7 and 5 s, respectively, measured with a small funnel. In addition to developing adequate, low-viscosity, self-leveling, robust compositions, special attention must be directed to adjusting the techniques for distributing, compacting, and curing the concrete. In doing this, the esthetic appearance of the surfaces must be considered for such applications as façade panels (see Figure 2.2). Some details on this topic are addressed in Section 2.5.

In contrast, the application of concrete matrix by spraying on inclined or vertical surfaces or overheads as used in the strengthening, repair, or production of complex geometries in prefabrication requires relatively high form stability after placement and good adhesion to the substrate. These requirements are met, for example, by compositions M1, M3, and M7 (see Table 2.1). All three mixtures exhibit table-flow

Table 2.1 **Representative matrix compositions for TRC**

Materials		Mineral-based matrices				
		PZ-0899-01 SFB 532	FA-1200-01 SFB 532	M1 SFB 528	M3 SFB 528	M7 SFB 528
Cement c	kg/m^3	490	210	539	549	839
Cement type	–	CEM I 52.5	CEM I 52.5	CEM III/B 32.5	CEM I 32.5 R	CEM I 32.5 R
Fly ash f	kg/m^3	175	455	243	246	–
Silica fume s		35	35	–	–	–
Silica slurry (w:s = 1:1)		–	–	53.9	54.6	–
Binder (c+f+s)		700	700	809	822	839
Plasticizer	% by mass of binder	1.0–1.5	0.9	2.1–2.2	2.3–2.4	2.1–2.2
Siliceous fines 0–0.125 mm	kg/m^3	500	470	–	–	–
Siliceous fine sand 0.2–0.6 mm		715	670	–	–	–
Sand 0–1 mm		–	–	1079	1092	1189
Water		280	280	242.7	245.6	279.7
w/c	–	0.57	1.33	0.45	0.45	0.33
w/b = w/(c+f+s)	–	0.40	0.40	0.30	0.30	0.33

spread after 15 strokes of 200–220 mm when measured with the small cone according to EN 1015–3 (1999).

The sketched approaches to adjusting the properties of matrices in their fresh and hardened states for TRC applications are still, generally speaking, too much of the framework of modern concrete technology as applicable to steel-reinforced concrete structures. With the development of newer, heavier reinforcing textiles with relatively large spaces between yarns, there is a tendency to use compositions with larger maximum aggregate sizes, which consequently become increasingly similar to "common" concrete mixes; however, the potential for novel approaches is immense.

Following the radical change from steel reinforcement to reinforcement made of carbon, AR glass, or basalt, the requirements of the concrete matrix should be reconsidered completely. For example, while in the case of RC, the high pH value of the pore solution is essential for corrosion protection of the steel reinforcement, in the case of textile reinforcement, the highly alkaline matrix constitutes a very aggressive environment for fibers made of glass or basalt and for polymer coatings of yarns made of carbon or other materials (Scheffler et al., 2009; Butler et al., 2010; Hempel et al., 2015). The change in these paradigms suggests a new generation of concrete. To be future-oriented, these new matrices must have—in addition to properties that satisfy the usual requirements, like high durability at various exposure conditions or optimal bonding to the reinforcement—a considerably improved energy and CO_2-release balance. Obviously, energy consumption and CO_2 release can be partly lowered by the conventional approach of partially replacing Portland cement clinker by latent-hydraulic and pozzolanic materials like slag, fly ash, or silica fume (SF). In the near future, calcined clays are likely to develop into a commercially available and worldwide producible alternative. While the trend to low clinker content is today one of the driving forces in concrete technology in general, it has specific benefits in combination with nonmetallic reinforcement: In contrast to steel reinforcement, which requires highly alkaline environments for corrosion protection, many types of textile reinforcements exhibit more favorable behavior in low-alkaline environments (Butler et al., 2010). These and other more radical approaches for improving the sustainability of TRC are presented in Section 2.5. So far there are few dry premix compositions commercially available as they are mainly developed for use in TRC application for strengthening and repair of concrete structures.

2.3 Testing properties of fresh TRC matrices

Some characteristics related to the workability of fresh matrices have been addressed in Section 2.2 already. Here more information is needed on the subject.

First, the testing methods common to characterizing the rheological behavior of fresh mortar may be applied to fine-grained TRC matrices, since the maximum aggregate grain size does not usually exceed 1 or 2 mm. Depending on the consistency of the matrix, techniques such as the slump-flow test (DIN EN, 12350–2, 2009) and the V-funnel test (DIN EN, 12350–9, 2010) (both suitable only for highly flowable concretes or mortars such as the mixtures PZ-0899-01 and FA-1200-01 in Table 2.1), or the spreading test on a shock table, suitable for less flowable mixtures (see, e.g.,

mixtures M1, M3, and M7 in Table 2.1), which are usually applied. It must be emphasized here that the consistency of fresh concrete is commonly tested with similar methods but with considerably larger dimensions of the testing equipment, that is, higher representative volumes of concrete, which also has different geometry. Therefore, some recalculation is necessary to estimate the consistency of TRC matrices in accordance with standards for concrete, but tested on "mortar geometries." Also the need for the corresponding standardization is obvious in respect to testing and classification of TRC matrices.

Second, the above-mentioned tests are single-point tests; as such, they are based on empirical approaches and provide very limited information on rheological properties of mixtures. For very flowable mixtures like self-compacting mortar or concrete, a combination of two tests—usually the slump-flow test and the V-funnel-funnel test—enables a sufficiently complete characterization of their rheological behavior. Here the slump-flow diameter has been proven to correlate with the yield stress of fresh concrete, while the flow time in V-funnel testing can be related to plastic viscosity. For less flowable mixtures, such separation cannot be made on the basis of purely empirical tests; thus, more advanced testing procedures using concrete rheometers or viscometers are applied (see, e.g., Mechtcherine et al., 2015).

The workability of matrices for TRC must be adjusted to the type and amount of textile reinforcement as well as the production process. In the case when rather stiff reinforcement textiles, for example, those impregnated with epoxy resin, are used, casting often is the only meaningful production method. The textile reinforcement is then placed in the formwork first, followed by the pouring of the concrete, preferably in an operational step. Here, the contemporary casting technology reaches its limits when the reinforcement structure is too dense. Even highly flowable mixtures cannot penetrate a fine-mesh reinforcement if the formwork has a complex geometry. Thus, at this stage, mostly flat, horizontally cast components can be produced using pouring. There is a need to deal with this problem in more detail in order to extend the range of producible geometries and increase the efficiency of production of TRC elements. One first step toward the estimation of the penetration behavior of fresh concrete through textile reinforcement is to test this feature on cut-outs of the reinforcing components. Figure 2.3 shows two examples of such tests (Brockmann, 2001).

(a)   (b)   Foto: Sebastian Wochner GmbH
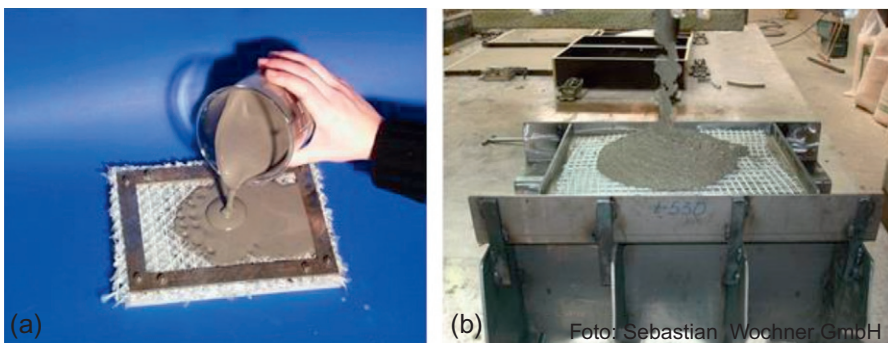
Figure 2.3 Testing penetration behavior of fresh concrete through textile reinforcement: (a) from Brockmann (2001); (b) courtesy of Sebastian Wochner GmbH.

2.4   Basic properties of hardened TRC matrices

Due to the small maximum aggregate size of usually no more than 4 mm and to TRCs being used for production of thin elements or strengthening layers, the properties of hardened fine concrete are, as a rule, tested according to the standard procedures for mortar rather those for ordinary concrete. The compressive and flexural strengths can be determined according to DIN EN 196–1 (2005) on standard prisms measuring 40 mm × 40 mm × 160 mm. The storage of the test specimen is generally carried out as specified in water at a temperature of 20 °C until testing; however, depending on the particular application of TRC, other curing regimes may be advisable. The compressive strength is determined on both fragments of the foregoing three-point bend test; however, if in the course of construction, the specification of the concrete compressive strength class is given according to DIN EN 206 (2014), the tests must be performed on cylinders (height 300 mm, diameter 150 mm) or cubes (edge length 150 mm) in accordance with this norm for structural concrete.

Compressive strength testing of TRC matrices yields values usually in the transitional range from ordinary concrete to high-strength concrete. This holds true as well for flexural strength as measured on plain matrices. Table 2.2 gives the corresponding values for several fine-grained TRC matrices developed in Aachen and Dresden (see also Table 2.1 for concrete compositions). Young's modulus is below the values estimated for the given compressive strengths according to fib MC2010 (2013). Clearly, this can be traced back to the lower maximum aggregate size and subsequently lower aggregate content and high fines content in TRC matrices in comparison to ordinary concrete. This has to be taken into account for the stress–strain diagrams used for design (Brockmann, 2006).

This is also one of the reasons for the relatively high shrinkage values (see Table 2.2). Another reason is the high water content of the mixtures, again in comparison to ordinary concrete. Due to small maximum aggregate size of TRC matrices and their use in typically thin-walled TRC structures, the shrinkage behavior of fine-grained concrete can be measured, for example, using prismatic specimens of

Table 2.2   Basic properties of hardened TRC matrices

Materials		Mineral-based matrices				
		PZ-0899-01 SFB 532	FA-1200-01 SFB 532	M1 SFB 528	M3 SFB 528	M7 SFB 528
Compressive strength 28d	MPa	74.0	32.0	53.7	63.5	72.3
Flexural strength 28d	MPa	7.6	5.1	7.5	8.6	11.2
Young's modulus 28d	GPa	33.0	24.8	21.0	25.5	30.8
Shrinkage 28d	mm/m	0.81	0.56	0.2	0.83	0.53
Shrinkage 360d	mm/m	1.01	–	0.85	1.27	–

dimensions $40\ mm \times 40\ mm \times 160\ mm$ according to the German Industrial Norm DIN EN 52450 (1985), as was done when determining the values in Table 2.2. Here, the total shrinkage values are given. The total shrinkage of concrete is comprised of drying shrinkage and autogenous shrinkage. With decreasing w/b ratios, the portion of autogenous shrinkage increases while the portion of drying shrinkage decreases. Due to the relatively low w/b of TRC matrices, they exhibit a relatively high autogenous shrinkage deformation. To measure shrinkage deformation, the prismatic specimens are usually wrapped in a vapor-tight foil. While in accordance with the concrete norms, this method has the evident disadvantage that the actual measurement cannot begin before demolding the prisms and wrapping them in the foil, which usually occurs at a concrete age of one or two days after casting. Up to this point, the autogenous deformations that have developed and can indeed be substantial, cannot be recorded when this procedure is followed. Therefore, the corrugated tube method is suggested as a more accurate testing alternative; this method enables taking measurements immediately after filling the tubes with concrete (Tian et al., 2008) (see also Figure 2.4a). Drying shrinkage is calculated by subtracting autogenous shrinkage from total shrinkage.

It should be mentioned here that thin-walled elements tend to arch due to the difference in drying shrinkage deformations on the upper surface (free, smoothed) and the lower surface (facing formwork) (see Figure 2.4b). The second, planar specimen in the image was cast with both surfaces facing the formwork. This example indicates that particular attention must be paid to the shrinkage behavior of TRC and elements made of it.

The tendencies described for the modulus of elasticity and shrinkage behavior are expected also with regard to creep deformations; they are higher in comparison to ordinary concrete.

Figure 2.4 (a) Setup for testing autogenous shrinkage; (b) effect of shrinkage on TRC specimen cast with both surfaces facing the formwork (left specimen) and just one surface facing the formwork (right specimen).

Little is known of the strength and deformation behavior of TRC matrices subject to sustained and cyclic tensile loading. This information is essential for the practical use of TRC, especially in the design of new and the strengthening of existing structural components. Also, the effects of temperature and moisture content on mechanical performance under such loading conditions must still be investigated.

The durability of the composite material TRC depends on the durability of its individual components: concrete matrix, fiber, and fiber-matrix interphase, thus the optimization of the system begs a holistic approach (see Mechtcherine, 2012). This subject is addressed in Chapter 8 of this book.

2.5 Alternative binder systems for TRC

2.5.1 Mineral additives

As indicated already in Section 2.2, TRC matrices must have a considerably improved energy and CO_2-release balance. An obvious option is to replace Portland cement clinker in part by latent-hydraulic and pozzolanic materials. This can be done by producing composite cements containing these materials or by mixing these materials as mineral additives into the concrete during production. Generally, in contrast to steel-reinforced concrete, there are no concerns in lowering the pH value of the matrix due to pozzolanic reactions, just the opposite: low alkalinity of the matrix is in most cases highly beneficial with regard to the durability of nonmetallic reinforcement. Therefore, a much higher pozzolana content can be used for TRC matrices in comparison to concrete used for production of RC elements. The limiting factor here is for the most part the durability of the matrix itself, specifically with regard to its freeze-thawing resistance. In the following paragraphs, various pozzolanic materials are briefly addressed and evaluated with respect to their actual or possible roles in matrices for TRC.

Microsilica (SF) is an artificial, highly reactive pozzolana having very small spherical particles with average sizes of about 100 nm (Taylor, 1997). When used in cement-based systems, it increases the packing density (micro-filler effect) of the matrix. Furthermore, it reacts with calcium hydroxide, one of the main products of cement hydration, which leads to further densification of the matrix and higher strength, and at early ages, but also to a considerable increase in durability, especially with respect to chemical attack. The last feature can be traced back primarily to the stability of the products of the pozzolanic reaction in comparison to that of calcium hydroxide. Furthermore, the denser microstructure of SF-modified matrices is beneficial for bonding between matrix and textile reinforcement. The very large specific surface area of SF, approximately 15–35 m^2/g, has a significant impact on the water demand and, as a consequence, on the workability of the matrices; however, at a low percentage of SF addition, the water demand of the binder system cement-SF decreases due to the micro-filler effect of SF. With additions exceeding approximately 5% by mass related to cement, this trend reverses; higher values of yield stress and plastic viscosity are measured with increasing SF content.

Fly ash is a residue of coal combustion in power plants and has an average particle size in the range of ordinary Portland cement, that is, 10–30 μm; however, in contrast

to cement, fly ash has predominantly spherical particles. Due to the low water demand of fly ash, replacing a portion of cement with fly ash improves the workability of concrete mixtures. While reacting more slowly in comparison to SF, the use of fly ash leads in the long term to a denser microstructure, which results in an improvement in mechanical performance and in better resistance to chemical attack; however, the development in the early-age strength is retarded in comparison to concrete without fly ash (Mobasher, 2011). As already indicated above, the pozzolanic reactions reduce the alkalinity of the pore solution in TRC matrices and thus increase the durability of AR glass or basalt reinforcement.

The substitution of a part of Portland cement clinker by *granulated blast-furnace slag* (GBFS) results in an improvement in the mechanical properties of concrete and its resistance to chemicals as well as to a decrease of the alkalinity of the pore solution. The latent-hydraulic nature of GBFS delays the development of early strength and reduces the hydration heat. In the long-term, concrete produced with GBFS has higher strength and higher chemical resistance than concrete made of Portland cement as the only binder; however, the freezing-thawing resistance decreases with increasing GBFS content. Similar to fly ash and SF, the availability of GBFS depends directly on the extent of industrial activities out of which these materials accrue as by-products. Presently, in many developed industrial countries, nearly all such by-products are used already in the production of concrete. Since the industries involved are not growing in those countries, no increase in use of their own by-products can be expected in the near future.

Metakaolin is a highly reactive pozzolana; it leads to higher compressive and flexural strengths, and a better bond between matrix and textile reinforcement. Similar to SF, its addition results in a denser material structure and an increase in the durability and reduction of the permeability of concrete. In addition, the use of metakaolin reduces shrinkage (Siddique, 2009).

Stone powders—first of all, *limestone powder*—are frequently used as inert mineral additives to reduce the content of energy-intensive reactive binders. It contributes to the stability of fresh concrete mixtures but also can lead, when the grading curve is properly chosen, to a higher packing density. Since limestone powder is inert, the replacement of a portion of the cement by this constituent results in a reduction in strength and durability indicators; however, due to the increase in packing density, this decrease can be partly compensated.

Higuchi et al. (2014) suggest using the *dicalcium silicate γ phase* and *fly ash* as a partial replacement for cement in combination with treatment with CO_2 emitted by a power plant. According to the authors, the amount of CO_2 emitted during preparation of the concrete was below zero. They showed the feasibility of the approach on concrete cylinders and suggested the use of this technology in producing nonreinforced concrete elements like bank protection blocks, since concrete produced in this manner has a pH value below 8 and thus does not provide any chemical protection for steel reinforcement. The application of this novel approach to TRC would be, however, even more beneficial for two reasons: (1) TRC elements are usually thin-walled, thus, the carbonation process can be achieved in the entire element in a relatively short time; (2) nonmetallic textiles do not require an alkaline environment; as explained above, an alkaline environment can often even lead to deterioration of the fiber and of the

polymers used for its impregnation. Matrices with pH values approaching neutrality would open a possibility for the use of alkali-sensitive, inexpensive textile made of E-glass or natural fiber won from sisal, jute, or coir plants. Using natural fiber would be another step toward highly sustainable, "green" TRC, provided that some of the durability problems of such fibers are solved.

2.5.2 Alternative cements

Since Portland cement is both ecologically troublesome and produces highly alkaline environments broadly harmful to textile reinforcement, alternative cements that do not have these disadvantages have been the focus of TRC research in the recent years.

Recently, the applicability of *high-alumina cements* (HACs) in the production of TRC has been studied. Due to their chemical composition based on lime and alumina components, this type of cement has fundamentally different hydration processes from the Portland or slag cements. Other special features, such as rapid solidifying capacity and high early-age strengths, may be interesting in the prefabrication of TRC elements, where minimal demolding times are required. After mixing with water, the alumina cements reach within 24 h up to 90% of their ultimate strength. This effect is used in practice already in the production of quick-setting cements, where faster setting times are achieved by adding small amounts of alumina cement. There is, however, very little research on using HAC for fine-grained concretes as the main binder. In particular, the use of conventional viscosity agents turned out to be troublesome; some of them cause extreme bleeding and retarding effects; while some do not exhibit any positive effect on workability. While studies have shown that the use of alumina cements in TRC is possible in principle, this option has not proven very practicable yet, since the mixing procedure is too complicated and the dosage of viscosity agent requires very high accuracy.

Calcium aluminate cement (CAC) was investigated within the German research project SFB 532 as another possible binder for TRC matrix (see, e.g., Brameshuber and Brockmann, 2001). Again, the investigations showed the suitability of CAC as a binder for TRC in principle, but the mixtures were difficult in their practicability due to a rather complex mixing procedure and high accuracy requirements with respect to the dosing of plasticizer and stabilizer. Nevertheless, some of the CAC-based mixtures showed improved durability in TRC made of AR glass, as demonstrated in the strand-in-cement (SIC) test (Van Itterbeeck et al., 2008). Furthermore, they exhibited high early-age strengths, desirable in industrial production processes; however, their rapid setting as well as their lack of highly flowable but stable consistencies were disadvantages in their practical use. Further research on CAC-based binder systems might lead to optimized matrix compositions that would be better suited for TRC applications.

Inorganic phosphate cements (IPCs) were recently developed as an alternative binder, especially in glass-fiber-reinforced concrete. These cements are generally acidic in their fresh state and pH-neutral after hardening. Also, under such conditions ordinary, non-AR E-glass fibers could be used as textile reinforcement. It should be noted that E-glass fiber is much cheaper than AR glass fiber (see, e.g., Orlowsky et al., 2005). IPCs are composed of a powder component and a liquid component.

The powder consists of calcium silicate, which reacts with the metal phosphates in the liquid component (Wastiels, 1999). Similar to HACs and CACs, a major disadvantage of IPCs is their particularly rapid hardening, which makes it difficult to use them in the conventional production of concrete elements and structures. Thus, their practical application is often reduced to the field of concrete repair. It is worthy to note that a special type of IPC with retarded hardening properties was developed without compromising its durability (Wastiels, 1999). It was also shown that concrete made of IPC has higher compressive strength than conventional concrete (Wagh et al., 1997). In addition, IPC is very heat- and corrosion-resistant (Trepalina et al., 2011).

Geopolymers are not cement materials as such, though they are inorganic; however, they are presented here, since they have begun to be used in civil engineering as a replacement for cements. Matrices made of geopolymers are chemically highly resistant, in particular to acidic environments, which are very aggressive in comparison to other types of concrete matrices (Lyon et al., 1997). Thus, TRC made of geopolymers could be used for repairs or as protective layers instead of polymeric resins. Furthermore, they exhibit low shrinkage deformations, high tensile strength, and high fire resistance. Menna et al. (2013) presented and discussed results of an experimental study on the suitability of a geopolymer system based on a combination of metakaolin and silica filler for an externally bonded composite system designed for flexural strengthening of RC beams. A field demonstration project dealing with strengthening and protecting concrete columns was described by Defazio et al. (2006). Here, a potassium aluminosilicate geopolymer was used with and without continuous fiber reinforcement. The report also provides also some positive results of long-term experiments in which geopolymer-coated surfaces were exposed to a number of snow storms, freeze–thaw cycles, deicing salts, and abrasion cycles by snow removal equipment. Still, there is a great need for research in the field of geopolymers, in particular with respect to their use as binder material in TRC applications.

2.5.3   Polymer-modified cement-based systems

By adding polymers to finely grained concrete mixtures, a controlled modification of the properties of the concrete and, in turn, of the properties of the composite TRC is possible. The polymers used in TRC matrices can be the same as those used for conventional polymer cement concrete, for example, in the case of repair mortar. These polymers meet the requirements for use in cement-based systems, for example, sufficient alkali resistance. In particular, the following examples can be given: aqueous dispersions and redispersible powders based on acrylate or styrene–butadiene, reactive resins such as water-based epoxy resin or silane–siloxane compounds. The modification polymers commercially available as concrete or mortar additives were developed and tested in the context of conventional concrete and mortar technology. Thus, additional requirements must be considered for TRC, and it seems likely that "tailor-made" polymers will be specifically developed for use in TRC.

Table 2.3 shows as examples some commercially available materials that have been proven in terms of their processability with fine-grained concrete and their

Table 2.3 Modifying substances for use in TRC and their properties (Büttner et al., 2009; Keil and Raupach, 2011)

	Units	PD1.8	EP3.1.2	EP3.2.2	HY4.3
Chemical base[a]	–	Copolimerisat methyl methacrylat+n-butylacrylat	Resin: bisphenol-A/F +reactive diluent Hardener: polyamine/ polyglycolic	Resin: bisphenol-A/F +reactive diluent Hardener: epoxy-amine adduct, slurry	Siloxane, powder, redispersible
Solid content/ active ingredient	%	50[a]	70.2	75.5	50[a]
MFT/T_G	°C	14/15[a]	–/55[c]	–/60[c]	n.s.
Particle diameter	μm	0.15[a]	0.05–0.3[d]	0.05–0.3[d]	n.d.
Density (liquid)	g/cm^3	1.05[a]	1.09	1.10	n.d.
pH	–	7.5[a]	n.d.	n.d.	6.0–9.0[a]
Tensile strength	MPa	5.0[a]	31±5.08[b,e] 20.0±1.55[b,f]	33±3.1[b,e] 10±1.3[b,f]	n.s.
Strain capacity	%	400[a]	n.s.	n.s.	n.s.
Young's modulus	MPa	0.56[b]	1150±97.60[b,e] 990±57.4[b,f]	1280±87.3[b,e] 870±95.8[b,f]	n.s.

n.d.: not determinable.
n.s.: not specified.
[a]Manufacturer's data.
[b]Test in accordance with DIN EN ISO 527, Young's modulus determined in the strain range between 0.5‰ and 2.5‰, test temperature: 23 °C.
[c]Measurement by DSC (Differential Scanning Calorimetry), determined in the second DSC-drive.
[d]Recording with transmission electron microscope (TP A3).
[e]Storage: 14d 23 °C/50% r.F.
[f]Storage: 1d 23 °C/95% r.F., 6d 23 °C/pore solution (pH 13.8), and 7d 23 °C/50% r.F.

satisfactory bond characteristics with respect to textile reinforcement. Further polymer materials and compositions can be found in Keil and Raupach (2011).

The main benefits of using polymer modifications of fine concretes are as follows:

- Increase in the durability of TRC. Due to the modification by the polymer, the water absorption of fine-grained concrete matrix is reduced, which increases the durability of TRC made with AR glass reinforcement (Büttner et al., 2009). The "sealing" of the pore microstructure in the matrix also enhances the chemical resistance (Hojczyk et al., 2011) as well as the frost resistance.
- Improvement of the mechanical properties of TRC. The use of polymers improves the bonds among the inner filaments in the case of uncoated rovings since the polymers can fill the spaces between filaments. This is the partial impregnation effect, in effect "gluing" inner filaments together better than is possible in purely cement-based matrices. As a result, the inner filaments are activated not only by friction with the outer filaments, but also as the bond enables an early stress transfer from the matrix through outer filaments to the inner filaments. Additionally, the bond between the matrix and rovings is improved. Finally, the tensile strength of the matrix is enhanced. Together, these increase the load-carrying capacity of TRC as shown, for example, by Keil and Raupach (2011).
- Reduction of early-age shrinkage and drying shrinkage.

2.6   Modification of TRC matrices by short fiber

Generally speaking, TRC exhibits very favorable stress–strain behavior, showing high load-carrying capacity and a certain ductility in relatively high inelastic deformations, which result from the formation and opening of a considerable number of fine cracks (Jesse, 2004). Such large deformations prior to material failure are crucial in respect of both structural safety and energy dissipation in the case of impact loading (Silva et al., 2011); however, there are at least three concerns related to the high stress levels being reached only at high deformations:

(1) For the service state where only small deformations are acceptable, the design load-bearing capacity of TRC must be much lower than its tensile strength
(2) In the case of strengthening of RC or masonry structures, TRC contributes little to their load-bearing capacity at small deformations
(3) For fair-face concrete applications like façade panels, the TRC must remain uncracked for esthetic reasons, that is, the first-crack stress of TRC is the crucial parameter for design of such elements

The shapes of the stress–strain curves of TRC under tensile loading can vary widely depending, first of all, on the quality and quantity of the respective textile reinforcement. With increasing content and fineness of yarns, the tensile strength of TRC increases while the strain capacity (strain at composite failure) decreases (Lieboldt, 2012). Certainly the material properties of the yarns themselves, including the effect of the various impregnation materials, play a major role as well; however, higher content of textile reinforcement does not enhance the first-crack stress of TRC. This parameter can be considerably improved by using short glass, carbon, or polymer fibers as dispersed reinforcement in the matrix (see, e.g., Barhum and Mechtcherine,

Figure 2.5 Effect of short dispersed and integral AR glass fibers on the stress–strain behavior of TRC plates subjected to tensile loading (Barhum and Mechtcherine, 2013).
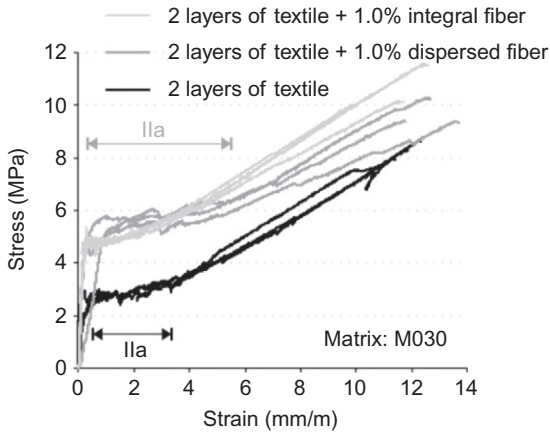
Region IIa represents the multiple-cracks formation region

2012, 2013; Hinzen, 2014; see also Figure 2.5). In this section, the effects of short fiber on this and other properties of TRC are presented and discussed.

The action mechanisms of short, fine, well distributed fibers in cement-based matrices have been fairly well studied and described; they bridge and arrest microcracks and, thus, limit their development. Therefore, the merging of microcracks is delayed by the presence of short fibers, and higher loads are needed to open and propagate these microcracks. Said differently, the tensile strength of the composite in the pre-cracking stage can be improved. Depending on the fibers' properties (type, aspect ratio, volume fraction, etc.) and the properties of the matrix, short fibers can bridge macrocracks as well. This leads to prevention of the brittle failure of concrete, and in some cases even to strain-hardening behavior (Mechtcherine, 2013).

Barhum and Mechtcherine investigated the effect of the addition of short AR glass fibers, both integral and dispersed (2013), as well as short dispersed carbon fibers (2012) and short polyvinyl-alcohol (PVA) fibers, on the stress–strain behavior of various TRCs composed of two different matrices and two or four layers of AR glass textile reinforcement. The results can be summarized as follows:

- First-crack stress in TRC specimens increased significantly, by more than double, due to the addition of 1.0% by volume of short PVA fibers or short integral glass fibers, and even more distinctly when short dispersed glass or carbon fibers were added. For lower percentages of short fibers, the increase in first-crack stress was less pronounced.
- Expansion of the strain region, where multiple cracks form, was observed for the stress–strain curves due to the addition of all types of short fibers (see also Figure 2.5). The visual inspection of the specimens' surfaces confirmed this finding and showed that a higher number of cracks, finer cracks, and finer crack patterns for given strain levels were formed when short fibers were added to TRC; in this respect, dispersed fibers were found to be more effective than integral fibers.
- In comparison to dispersed glass fibers, integral glass fibers had more pronounced positive effects on both the tensile strength and the work-to-fracture of the composite. While the

advantage of the addition of short dispersed fibers began to fade at relatively high strain levels (this holds true also for dispersed carbon fibers), integral fibers improved the load-bearing capacity of the TRC over the entire strain range, right up to failure.

- The addition of PVA fibers led to similar improvements in the mechanical performance of TRC, as in the case of integral AR glass fibers. The strain capacity of TRC increased, however, in comparison to TRC without short fibers. This can be traced back to the ductility of the PVA fibers and their lower stiffness in comparison to glass or carbon fibers.

- All types of short fibers under investigation improved the bond between multifilament yarns of the textile reinforcement and the surrounding matrix. Because of their relatively larger size, short integral fibers provided, by means of new adhesive cross-links, larger and stronger anchors into the surrounding matrix than those provided by short dispersed fibers.

Similar findings with regard to the effects of the addition of short fiber on the stress–strain behavior of TRC were made by Hinzen (2014). He found that the variation of first-crack stress due to different curing conditions became much less pronounced.

A number of further positive effects of the addition of short fibers to TRC should be considered for practical application, one being shrinkage crack control. Fine, short fibers are known to have a significant effect on plastic shrinkage and related early-age cracking of cement-based composites. Kronlöf et al. (1995) reported that the use of polypropylene fibers (1% by volume) reduced free plastic shrinkage by about 30%. Boshoff and Combrinck (2013) investigated the effects of three different microfiber types, namely polypropylene, fluorinated polypropylene, and polyester, all at a volume of 0.1%. A clear reduction, on average by more than 50%, of the crack area was observed.

Another positive effect of adding short fibers is the mitigation of delamination of textile reinforcement from the concrete matrix. The occurrence of such failure increases with increasing stiffness in the textile reinforcement, decreasing concrete cover, increasing deformation level, unfavorable loading modes (bending, shear), etc. First test series showed that due to the addition of short AR glass or carbon fibers, delamination could be considerably delayed or even obviated.

The addition of short fibers cause some loss in workability since fine fibers have relatively high water demand and at higher concentrations prevent the flowing of the matrix by forming a kind of lattice framework. This feature should be considered when planning the use of short fibers for TRC matrices.

2.7 Summary

The use of TRC opens new possibilities in the strengthening of existing concrete structures, the prefabrication of thin-walled concrete elements, and other applications. While the results of the first applications are very promising, much work must be done before TRC becomes widely accepted and used as a construction material. A solid basis for structural design and material specifications in the form of codes and guidelines must be developed and introduced into construction practice. To achieve this, purposeful research on various related issues is needed. This chapter provides an overview of the contemporary state of development mineral matrices for TRC and identifies actual problems and challenges related to the materials utilized in TRC

production. Some matrix compositions and binders have been proven over the years, but there is still a great need for further development. At this juncture, the main challenge is in reducing binder content, specifically the Portland cement clinker without compromising the processability, mechanical properties, and durability of the TRC. The goal is in particular to make TRC ecologically and economically attractive for the construction industry. Many of the challenges addressed in this chapter should be dealt with within the project Carbon Concrete Composites (C^3), sponsored by the German Ministry for Education and Research (BMBF) and coordinated by the TU Dresden.

Acknowledgments

References

Barhum, R., Mechtcherine, V., 2012. Effect of short, dispersed glass and carbon fibres on the behaviour of textile-reinforced concrete under tensile loading. Eng. Fract. Mech. 92, 56–71.

Barhum, R., Mechtcherine, V., 2013. Influence of short dispersed and short integral glass fibres on the mechanical behaviour of textile-reinforced concrete. Mater. Struct. 46, 557–572.

Boshoff, W.P., Combrinck, R., 2013. Modelling the severity of plastic shrinkage cracking in concrete. Cem. Concr. Res. 48, 34–39.

Brameshuber, W., Brockmann, T., 2001. Calcium aluminate cement as binder in textile reinforced concrete. Calcium Aluminate Cement 2001. © IOM Communications Ltd, Edinburgh, Scotland, pp. 659–666.

Brameshuber, W. (Ed.), 2006. Textile reinforced concrete: report no. 036 of the RILEM State-of-the-Art Report, RILEM Technical Committee 201-TRC.

Brockmann, T., 2001. Anforderungen und Eigenschaften zementgebundener Feinbetone. In: Tagungsband zum 1. Fachkolloquium der Sonderforschungsbereiche 528 und 532, Aachen, pp. 82–98.

Brockmann, T., 2006. Mechanical and fracture mechanical properties of fine grained concrete for textile reinforced composites. In: Schriftenreihe Aachener Beiträge zur Bauforschung, Institut für Bauforschung der RWTH Aachen, Nr. 13; ISBN 3-86130-631-X.

Büttner, T., Keil, A., Orlowsky, J., Raupach, M., 2009. Einsatz von Polymeren in Textilbeton—Entwicklung polymermodifizierter Betone und Einflüsse auf die Dauerhaftigkeit. In: 4th Colloquium on Textile Reinforced Structures (CTRS4), pp. 197–211.

Butler, M., Mechtcherine, V., Hempel, S., 2009. Experimental investigations on the durability of fibre–matrix interfaces in textile-reinforced concrete. Cem. Concr. Compos. 31, 221–231.

Butler, M., Mechtcherine, V., Hempel, S., 2010. Durability of textile-reinforced concrete made with AR glass fibre—effect of the matrix composition. Mater. Struct. 43, 1351–1368.

Defazio, C., Arafa, M.D., Balaguru, P.N., 2006. Geopolymer Column Wrapping. Rutgers University Center for Advanced Infrastructure and Transportation, New Brunswick.

DIN EN 196–1, 2005. Methods of Testing Cement Part 1: Determination of Strength.

DIN EN 206, 2014. Concrete—Specification, Performance, Production and Conformity.

DIN EN 1015–3, 2007–05. Methods of Test for Mortar for Masonry—Part 3: Determination of Consistence of Fresh Mortar (by flow table); German version EN 1015-3:1999+A1:2004 +A2:2006.

DIN EN 12350–2, 2009. Testing Fresh Concrete—Part 2: Slump-Test.

DIN EN 12350–9, 2010. Testing Fresh Concrete—Part 9: Self-Compacting Concrete— V-Funnel Test.

DIN EN 52450, 1985. Testing of Inorganic Non-Metallic Building Materials; Determination of Shrinkage and Expansion on Small Specimens.

Ehlig, D., Schladitz, F., Frenzel, M., Curbach, M., 2012. Textilbeton—Ausgeführte Projekte im Überblick. Beton Stahlbetonbau 107, 777–785.

fib Model Code for Concrete Structures 2010, 2013. Ernst & Sohn, Berlin.

Hempel, S., Butler, M., Mechtcherine, V., 2015. Bond behaviour and durability of basalt fibres in cementitious matrices. In: Brameshuber, W. (Ed.), RILEM Proceedings PRO 98. RILEM Publications S.A.R.L, pp. 225–234.

Higuchi, T., Morioka, M., Yoshioka, I., Yokozeki, K., 2014. Development of a new cological concrete with CO_2 emissions below zero. Constr. Build. Mater. 67, 338–343.

Hinzen, M., 2014. Einfluss von Kurzfasern auf die Frisch- und Festbetoneigenschaften sowie das Tragverhalten von Textilbeton. In: Schriftenreihe Aachener Beiträge zur Bauforschung, Institut für Bauforschung der RWTH Aachen, Nr. 20; ISBN 3-86073-938-7.

Hojczyk, M., Weichold, O., Walther, A., Möller, M., 2011. Korrelation der makroskopischen Alterung mit nanoskaligen Veränderungen in hybriden Polymer/Zement-Oberflächenaktivierungen für Glasfaserrovings in Textilbeton. In: Curbach, M., Ortlepp, R. (Eds.), Textilbeton Theor. Parx, pp. 201–215. Berlin.

Jesse, F., 2004. Tragverhalten von Filamentgarnen in zementgebundener Matrix. Dissertation, Technische Universität Dresden.

Keil, A., Raupach, M., 2011. Polymermodifizierte Feinbetone—Untersuchungen zum Feuchtetransport. In: Curbach, M., Ortlepp, R. (Eds.), Textilbeton Theor. Prax, pp. 215–226. Berlin.

Kronlöf, A., Leivo, M., Sipari, P., 1995. Experimental study on the basic phenomena of shrinkage and cracking of fresh mortar. Cem. Concr. Res. 25, 747–1754.

Lieboldt, M., Butler, M., Mechtcherine, V., 2008. Application of textile reinforced concrete (TRC) in prefabrication. In: Gettu, R. (Ed.), Seventh International RILEM Symposium on Fibre Reinforced Concrete: Design and Applications. RILEM Publications S.A.R.L, pp. 253–262.

Lieboldt, M., 2012. Transport von Flüssigkeiten und Gasen im Textilbeton. Doctoral Thesis, Schriftenreiche des Instituts für Baustoffe, Heft 2012/1, TU Dresden.

Lyon, R.E., Foden, B.A., Sorathia, U., Davidovits, J., Davidovics, M., 1997. Fire resistant aluminosilicate composites. Fire Mater. 21, 13.

Mechtcherine, V., 2012. Towards a durability framework for structural elements and structures made of or strengthened with high-performance fibre-reinforced composites. Constr. Build. Mater. 31, 94–104.

Mechtcherine, V., 2013. Novel cement-based composites for the strengthening and repair of concrete structures. Constr. Build. Mater. 41, 365–373.

Mechtcherine, V., Secrieru, E., Schröfl, C., 2015. Effect of superabsorbent polymers (SAPs) on rheological properties of fresh cement-based mortars—development of yield stress and plastic viscosity over time. Cem. Concr. Res. 67, 52–65.

Menna, C., Asprone, D., Ferone, C., Colangelo, F., Balsamo, A., Prota, A., 2013. Use of geopolymers for composite external reinforcement of RC members. Compos. B Eng. 45, 1667–1676.

Mobasher, B., 2011. Mechanics of fiber and textile reinforced cement composites. CRC Press, Boca Raton, Florida, pp. 33–34.

Orlowsky, J., Raupach, M., Cuypers, H., Wastiels, J., 2005. Durability modelling of glass fibre reinforcement in cementitious environment. Mater. Struct. 38, 155–162.

Scheffler, C., Gao, S.L., Plonka, R., Mäder, E., Hempel, S., Butler, M., Mechtcherine, V., 2009. Interphase modification of alkali-resistant glass fibres and carbon fibres for textile reinforced concrete I: fibre properties and durability. Compos. Sci. Technol. 69, 531–538.

Siddique, R., 2009. Influence of metakaolin on the properties of mortar and concrete: a review. Appl. Clay Sci, 392–400.

Silva, F.A., Butler, M., Mechtcherine, V., Zhu, D., Mobasher, B., 2011. Strain rate effect on the tensile behaviour of textile-reinforced concrete under static and dynamic loading. Mater. Sci. Eng. A 528, 1727–1734.

Taylor, H.F.W., 1997. Cement chemistry. Thomas Telford Publishing, London.

Tian, Q., Jensen, O.M., Sun, W., Van Bruegel, K., Miao, C., Ye, G., Chen, H., 2008. Measuring autogenous strain of concrete with corrugated moulds. In: Microstructure Related Durability of Cementitious Composites, RILEM Proceedings pro061. RILEM Publications S.A.R.L, pp. 1501–1511.

Trepalina, Y.N., Doroganov, V.A., Evtushenko, E.I., 2011. High-alumina composite concretes and coatings based on modified phosphate binder suspensions. Refract. Ind. Ceram. 52, 291–293.

Van Itterbeeck, P., Cuypers, H., Orlowsky, J., Wastiels, J., 2008. Evaluation of the strand in cement (SIC) test for GRCs with improved durability. Mater. Struct., 1109–1116.

Wagh, A.S., Jeong, S.-Y., Singh, D., 1997. High Strength Phosphate Cement Using Industrial Byproduct Ashes. Energy Technology Division, Argonne National Laboratory, pp. 542–553.

Wastiels, J., 1999. Sandwich panels in construction with HPFRCC-faces: new possibilities and adequate modelling. In: 3rd International Workshop on HPFRCC, RILEM Proceedings 6, pp. 143–152.

Weiland, S., Ortlepp, R., Hauptenbuchner, B., Curbach, M., 2008. Textile reinforced concrete for flexural strengthening of RC-structures—Part 2: application on a concrete shell. In: ACI SP-251-3, Design & Applications of Textile-Reinforced Concrete, pp. 41–58.

This page intentionally left blank

Manufacturing methods for textile-reinforced concrete

3

W. Brameshuber
RWTH Aachen University, Aachen, Germany

3.1   Introduction

When a new building material is established, applications are important to prove that it is suitable for practical use; however, application projects can only be put into practice using manufacturing methods that meet the practical requirements of the building material textile-reinforced concrete (TRC). In the State-of-the-Art Report of the RILEM Technical Committee 201-TRC (Brameshuber and RILEM, 2006), production techniques of TRC were already described. There, building components are mostly manufactured applying the casting, laminating or spraying technique. Slabs can, however, also be produced, for example, using pultrusion (Peled and Mobasher, 2008). During the pultrusion process, the textile reinforcement is pulled through a cement suspension. A connected system of rollers forms the slab and the target thickness is produced.

The laminating, casting and spraying techniques have already been successfully applied in the manufacturing of test specimens and demonstrators as well as in pilot projects, for example, a diamond-shaped framework was manufactured in the casting technique and a barrel shell in the spraying technique. These three techniques as well as the spinning technique were developed further for the serial batch production of building elements made of TRC (Brameshuber et al., 2007, 2008). It was the aim to produce three-dimensional (3D) building components with a sharp-edged cross-section and an exact positioning of the textile reinforcement. The spraying technique was applied to produce a sealing system made of TRC (Mott and Brameshuber, 2007). Also for producing *in situ* strengthening strips on ceilings and walls the spraying technique in combination with the laminating method has been developed and applied in practice (Mechtcherine, 2013; Schladitz et al., 2009; Weiland et al., 2008).

Following are four possible manufacturing methods for TRC components. These methods all have in common the batch production that, besides a number of advantages, also exhibits the disadvantage that the respective number of molds must be available when large quantities will be produced. In this context, continual processes feature the advantage that the workflow is mostly less complicated and even more economical.

3.2   Casting

In the casting technique, the textile reinforcement can either be clamped into the formwork or alternately inserted loosely, and afterwards the concrete is cast in one

work step. Two-dimensional (2D) fabrics combined with spacers as well as 3D fabrics are applied. The fine-grained concrete mix should feature a very flowable consistency.

The following figures (Figures 3.1–3.4) illustrate the manufacturing process of a diamond-shaped building element made of TRC applying the casting technique.

At first, a diamond-shaped inner formwork was made. The fabrics were clamped around this formwork element. Sleeves were used as spacers between the fabric layers. These sleeves were pushed over the anchoring elements that had been placed in all four corners of the diamond. For the deflection of the fabric, additional perforated plates were installed at the anchoring elements (see Figure 3.1).

Upon completion of the mold, the fine-grained concrete was cast into the mold (see Figure 3.2).

Figure 3.3 illustrates the demolding process. First, the four corners of the diamond were stripped from the formwork. Afterwards, the outer side walls could be removed followed by the inner formwork elements. Figure 3.4 displays the finished diamond-shaped element made of TRC.
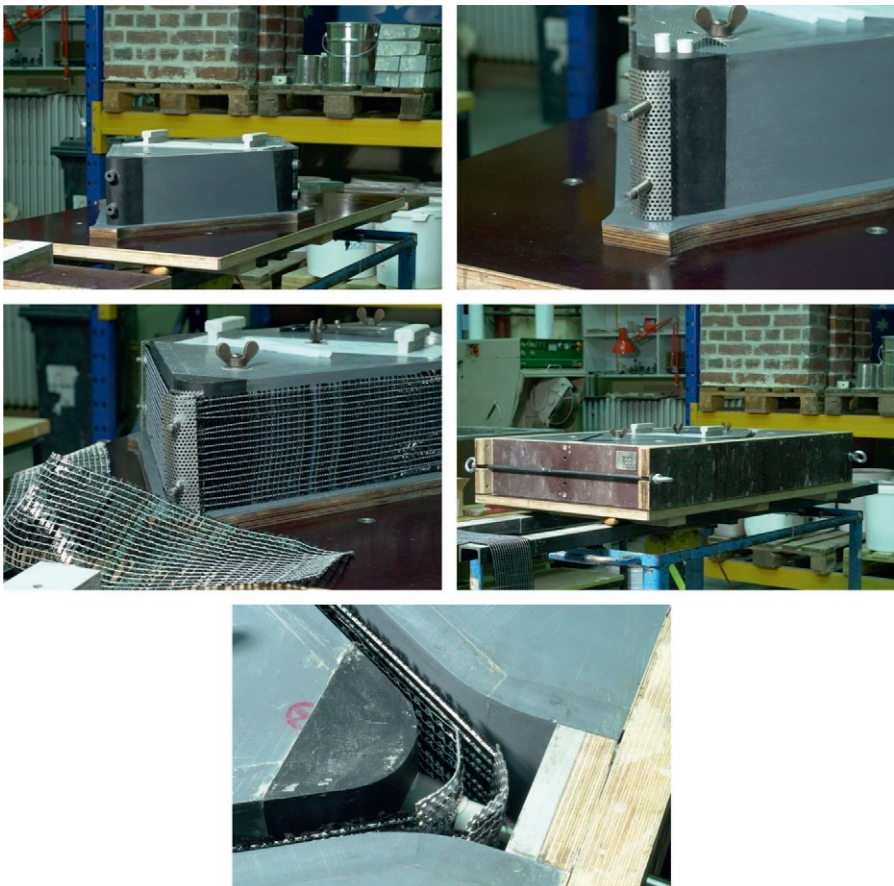
Figure 3.1 Manufacturing the mold and placing the textile reinforcement.

Figure 3.2 Casting the diamond-shaped element made of textile-reinforced concrete.

Figure 3.3 Demolding the diamond-shaped element made of textile-reinforced concrete.
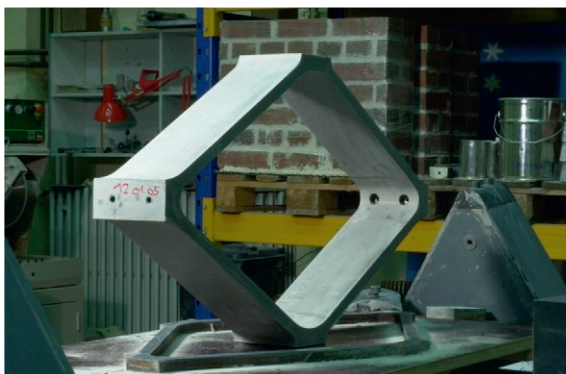
Figure 3.4 Diamond-shaped element made of textile-reinforced concrete.
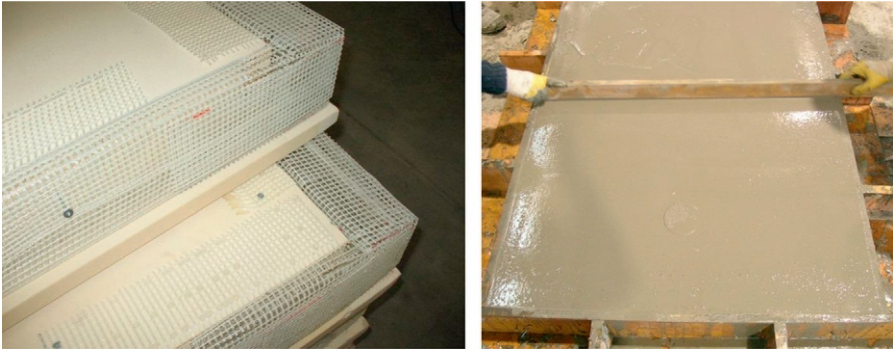
Figure 3.5 Reinforcement cage and cast sandwich element.

The casting method reaches its limits when the reinforcement structure becomes too dense at a horizontal production or when it has an insufficient stiffness at a vertical production. A reinforcement structure that is too dense, for example, several closely placed layers of fabric, cannot be penetrated by the fine-grained concrete even when a high compaction energy is applied. At an insufficient stiffness, a stable position of the reinforcement cannot be ensured during compaction due to the pressure exerted by the concrete. When spacers are used, a minimum thickness of the spacers of 4 mm should be kept in order to ensure a good penetration.

The casting method is suited for the manufacturing of 2D slabs and of simple 3D building elements. Presently, the production of large-size building elements is mostly only possible when considerable effort is involved in the manufacturing and fixation of the fabrics. Figure 3.5 illustrates a reinforcement cage as well as a completely cast sandwich element.

3.3   Laminating

When TRC elements are laminated, the fine-grained concrete and the fabric are alternately inserted into the formwork layer by layer until the component thickness is reached (Figure 3.6).

In this case, a sun protection plate with at least a 3-m span length has been produced for a hospital building. Figure 3.6 shows the steps for production of the first prototype: the concrete layer compaction (Figure 3.6a); the insertion of one textile (Figure 3.6b) and the bottom side view of the first element (Figure 3.6c). The fabrics used are 2D fabrics that should be uncoated and consist of rovings with a flat structure so that they can be smoothly inserted and rolled into the concrete. Coated fabrics that are subsequently rolled for transportation or storage purposes mostly show a permanent deformation when being unrolled, which interferes with the laminating process because of the bending stiffness of the finished fabric.
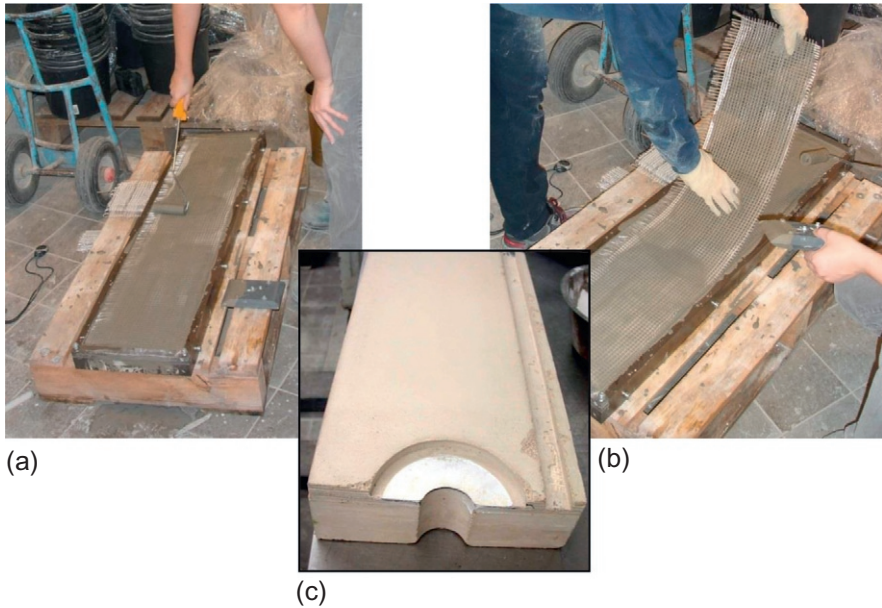
Figure 3.6 Laminating technique: (a) concrete layer compaction, (b) insertion of one textile, and (c) bottom side view of the first element.

The fine-grained concretes can feature high flowability up to rather stiff consistencies. At a high flowability, the fine-grained concrete can easily be distributed in the formwork and the yarns of the fabric can be well penetrated by the concrete in order to ensure a good bond between fine-grained concrete and fabric. The rolling of the fabrics into the fine-grained concrete with a roller additionally improve the penetration and thus the bond; however, it turned out that the waviness of the fabric in the building element increases as compared to cast samples with lightly prestressed fabrics. Hence, the maximum load-bearing capacity of the laminated samples is lower. On the basis of the current knowledge, this difference is caused by the different fabric stresses of both methods.

The laminating method is suited for the manufacturing of 2D and simple 3D slabs as well as of simple shell structures. The reinforcement ratio can be controlled almost arbitrarily. The thickness of the concrete layer between the individual layers of fabric should, however, amount to no less than 3 mm. Figure 3.7 shows the manufacturing of a large façade element applying the laminating technique.

The dimensions of a slab produced in the laminating technique are only limited by the self-weight, the stripping and the transportation. Slabs for façade with the dimensions of 5.0×2.5 m are technically feasible. Also, sandwich elements for façades may be produced in the same manner (Hegger et al., 2012).

Figure 3.7 Manufacturing a façade element.

3.4   Spraying/shotcreting

The spraying of fine-grained concrete is based on a low-pressure system with a pressure of up to 8 bar as it is also used, for example, for spraying plaster. The procedure is very similar to that of laminating. Also here, the fine-grained concrete and the fabric are alternatingly applied in layers.

The requirements on the fabric are the same as for the laminating technique. The rovings must have a flat structure. Therefore, very often the same uncoated 2D fabrics are used as in the laminating method. Also textiles coated with styrol-butadien-acrylate, which are soft polymeric materials, may be used to increase the load-carrying capacity of the yarns in the textile. Also here, the fabric should be rolled into the fine-grained concrete using a roller in order to ensure a good penetration and good bond behavior.
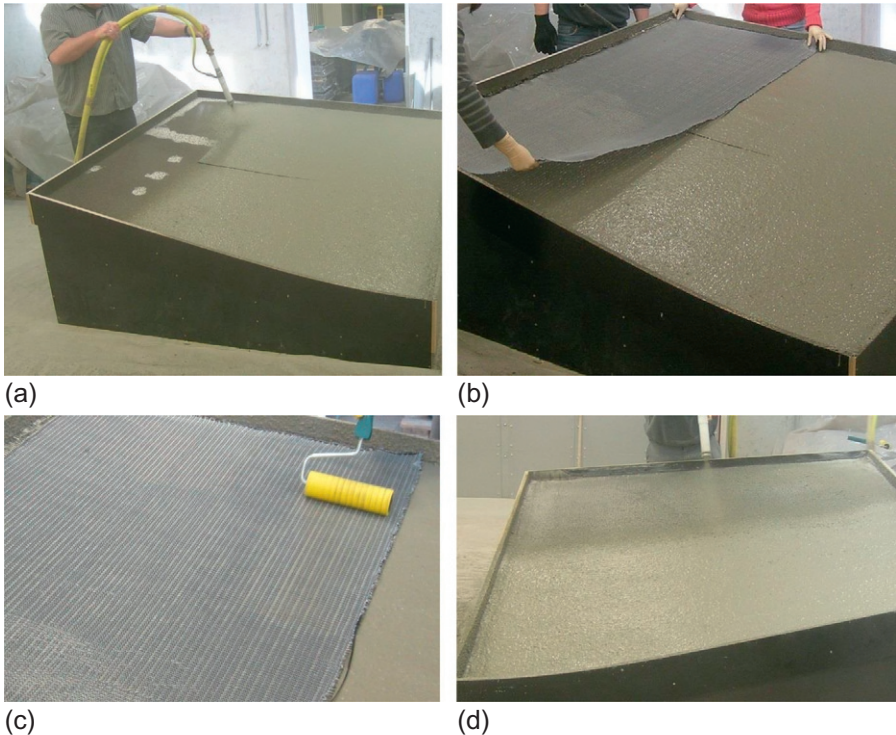
Figure 3.8 (a) and (d) Applying the fine-grained concrete in the spaying method, (b) inserting the fabric, and (c) rolling it into the concrete.

Figure 3.8 displays the sequence of the spraying method. First, a layer of fine-grained concrete is applied in the formwork. Afterwards the fabric is inserted and rolled into the concrete using a roller. This is followed by spraying another layer of fine-grained concrete. In a last step, the surface of the building element can be trowelled.

When vertical surfaces will also be sprayed, the spraying method places different requirements on the fine-grained concrete mix in contrast to the laminating method. Generally, the spraying technique requires a mix that is pumpable and sprayable. Thus, to adhere even to vertical surfaces, the mix must feature a higher viscosity and tack.

The spraying method enables the production of building elements in a horizontal as well as vertical alignment with a defined position of the fabrics in the component. Therefore, this method is suited for the manufacturing of single or multicurved shells and where vertical surfaces will be produced. Sprayed building components can have a high reinforcement ratio just as in the laminating technique.

When producing building elements in a horizontal position, the spraying method can also be applied as an alternative to casting/laminating. With this technique, even
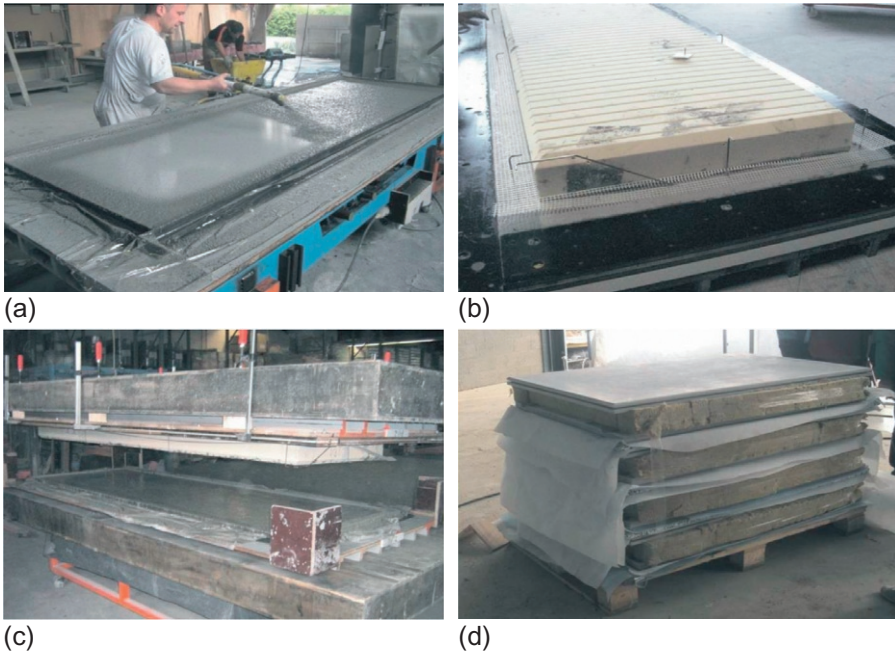
Figure 3.9 Manufacturing a sandwich element: (a) spraying of the outer face sheet made of concrete, (b) core of a sandwich element with an already finished outer concrete layer, (c) assembling a sandwich element, and (d) finished sandwich elements.

larger surfaces can be cast quickly. Using turning devices in precast plants, sandwich structures, for example, can also be manufactured (see Figure 3.9).

Applications of the spraying method that have already been put into practice are, for example, the production of barrel shells as well as double curved shells as demonstrators for the Collaborative Research Centre 532 in Germany (Schneider et al., 2013). Depending on the respective geometry, several square meters can be produced in one work step, applying the spraying technique. The arbitrary geometry of the building component is an advantage of this method so that even multicurved elements can be manufactured.

Existing buildings often have to be maintained by strengthening for higher bending moments and/or shear forces. Very often, this strengthening is carried out by bonding steel or fiber reinforced polymer (FRP) composites on the surface of the structure. Both systems require additional protection against fire. Cementitious materials combined with carbon textiles improve the fire resistance of the strengthening structure (Mechtcherine, 2013; Schladitz et al., 2009). The concrete is applied on site with the spraying method using the laminating techniques, see Figure 3.10.

(a)   (b)
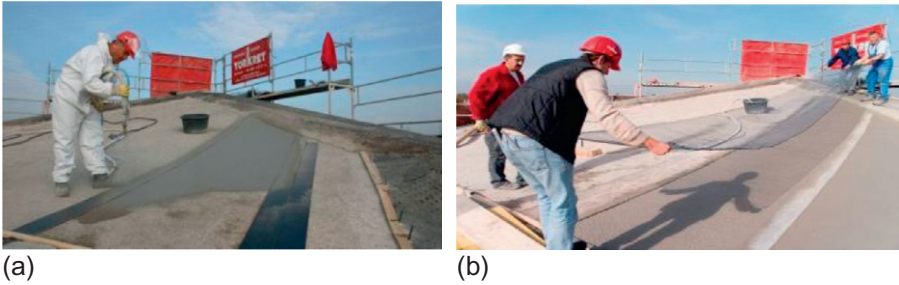
Figure 3.10 Strengthening a concrete shell with textile-reinforced concrete: (a) spraying the first layer and (b) application of textile.
Source: TU Dresden, Curbach, M.

3.5 Spinning

The spinning method is a procedure where the concrete is compacted by fast rotation around the axis in the formwork. Mainly tubes, poles and columns are manufactured applying this method.

In early studies, a turning lathe was used for the spinning of the tubes. Thus it was possible to axially clamp the tubes and to spin them evenly without any unbalance (Figure 3.11).

Mixes without and with short fibers can be used as a fine-grained concrete mix. They should feature a flowable consistency as well as a low water-to-binder (w/b) ratio.

For the spinning of the fine-grained concrete mix without short fibers uncoated as well as coated, 2D fabrics can be used. Since uncoated 2D fabrics can, however, not keep their position when the tubes are produced in one work step, to insert these fabrics, the spinning process must be interrupted at each insertion. That way, an even arrangement of the fabrics in the cross-section of the tube is possible and a high

Figure 3.11 Clamped tube during the spinning process.

reinforcement ratio can be achieved. However, this manufacturing process is very time-consuming. Figure 3.10 illustrates a spun concrete tube with four layers of textile reinforcement. The concrete thickness between the individual layers can be further minimized. A wall thickness of 16 mm has already been accomplished.

To be able to conduct the manufacturing process in one work step, the 2D fabrics must be stiffer, that is, coated and provided with spacers. The coating of the fabrics must have a sufficient flexibility for an exact insertion of the fabrics into the form-work. Uniform grit consisting of oven-dried sand grains is very well suited as a spacer because it is a regular component of a concrete mix. The grit is distributed over the coated fabrics and afterwards, the fabric is hardened under the action of heat (Figure 3.11). Thus, the grit adheres to the fabric and ensures an invariable distance to the formwork during the casting process. The grain diameter of the grit depends on the required distance between the individual fabrics and between fabric and form-work, respectively; it should, however, not fall below 4 mm. This ensures that the fine-grained concrete can penetrate the fabrics (Figures 3.12 and 3.13).

Supplementary tests showed that the short fiber matrix could be spun easily. The use of additional coated textile reinforcement had to be restricted to one layer at the

Figure 3.12 Spun tube with four layers of textile reinforcement.
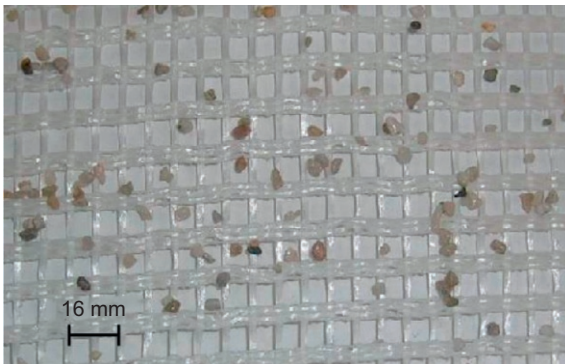
Figure 3.13 Coated 2D fabric with grit (4 mm).

spinning in one work step because a denser arrangement of the reinforcement cannot be completely penetrated by the rheological, significantly different short fiber mix.

In the spinning technique, circular, textile-reinforced hollow profiles with a defined positioning of the layers can be manufactured, containing a high reinforcement ratio. The wall thickness of, for example, poles and thus their self-weight can be considerably reduced as compared to steel-reinforced concrete. By means of prefabricated reinforcement cages, sections of arbitrary lengths with the different diameters can be produced.

3.6   Extruding

A continual production of building components entails the advantage of low manufacturing costs due to an automated production. Apart from the application of (serial) batch production methods, this type of producing textile-reinforced building components is a necessary precondition for a complete implementation of this composite material in the practical application on site.

Presently, the extrusion of TRC is a subject of research. The extrusion method is a production technique in which viscous, hardenable materials are pressed under high pressure and temperature through an extrusion die or a nozzle in a continuous process. The extrudate is compacted by an extruder (screw compressor) and the required cross-section is determined by the shape of the nozzle or the die.

By means of the extrusion technique, the manufacturing of bar-shaped hollow profiles, such as standard I-beams or channel sections, is feasible. The production of such profiles could not yet be implemented because the bar-shaped building components could only be designed in a laminar way and not as hollow profiles due to the missing production method. Further cross-sections that can be extruded are, for example, honeycomb slabs, which can be used as formwork elements or hollow core slabs.

Instead of mixing and dispersing, another option may be chosen to prepare the concrete mix for extrusion. As an alternative, the high-speed intensive mixing equipment has been chosen. An Eirich intensive mixer is a good alternative to the traditional mixing procedure as, for example, used for clay products. Two basic mixes have been designed for the first steps of investigating the rheological properties for concretes suitability for the extrusion process. They are given in Table 3.1.

Mixture 1 is a consequent development of mixture 2, which is the basic mixture for TRCs developed at Aachen University (Brameshuber and RILEM, 2006). Both mixes contain methylcellulose to improve the possibility of extrusion, but for normal cast concretes, superplasticizers have to be added.

In Figure 3.14, different mixing methods have been tested: B1 and B5 with a nearly constant revolution time of 500/min for dry mixing and wet mixing; and B4 and B8 with a revolution time of 500/min within the first 1.5 min (dry mixing) and 800/min after a short interruption for adding water, respectively. The difference between both mixtures B1 and B5 and mixtures B4 and B8 is the type of cement, which is CEM I 42.5 for B1 and B4 and CEM I 52.5 for B5 and B8, respectively. All mixes are based on mixture type 1 (see Table 3.1).

Table 3.1 Mix design of basic mixtures

Raw material	Unit	Mixture type 1	Mixture type 2
1	2	3	4
CEM I 52.5 or CEM I 42.5 (c)	kg/m^3	700	781
Fly ash HKV (f1)		–	167
Fly ash SWF (f2)		210	–
Silica fume (s)		70	167
Quarzitic aggregate 0–0.6 mm		970	671
Water (w)		256	314
Methyl cellulose	% by mass of c	1.5	1.5
w/c	–	0.37	0.40
$w/c_{eq} = w/(c+0.4f+s)$		0.30	0.31
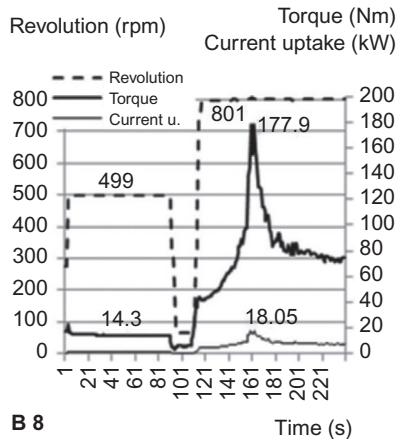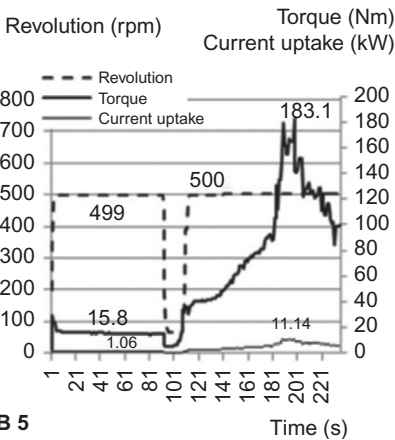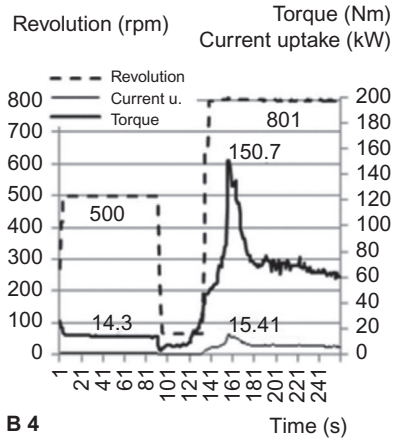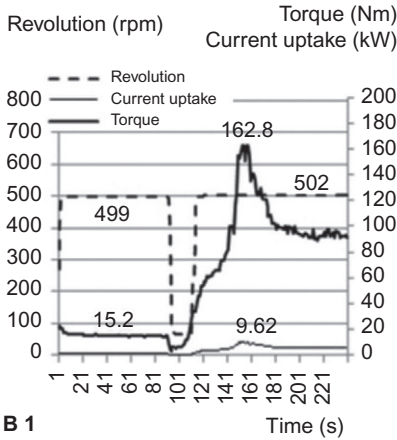
Figure 3.14 Influence of cement type and mixing method on the flow parameter of concretes for extrusion.

Figure 3.15 Extrusion with feeding device for textiles.

In this example, the revolution of the mixing device clearly dominates the torque as well as the current uptake. Indirectly, these parameters are an indication of the flow parameters of the concrete. Due to the high consistency of concretes for extrusion, no direct method to measure the viscosity and the limit of flow exist. Some methods as penetration needles or slab viscosity measurement devices had been tested but found to be inapplicable. Absolutely the torque is higher for a revolution of 800/min instead of 500/min, but the maximum is quite earlier (What exactly do you mean here? This is not so clear). An increase of torque is similar to a decrease of the concrete viscosity. A constant revolution means that the dispersion is finished. A lot of mixture designs with varying contents of methylcellulose have been tested for finding the optimal mix in connection with the dispersing procedure in the extrusion process but cannot be described within this contribution; however, the mix design suitable for the extrusion process has to be found for the specific equipment of mixing and extruding on a case-by-case basis.

The major item for embedding textiles during the extrusion process is to control the concrete flow. Figure 3.15 shows the extension of the pressure head with the textile feed channel. In comparison to pure concrete or fiber-reinforced matrices, the flow of the concrete before this feed element has to be changed by narrowing elements. Otherwise the concrete, which has to flow through the meshes of the textiles, is too slow.

At the moment, coated textiles compared to noncoated textiles have given the best results. In this case, the coating consisted of styrol-butadien-acrylate. Tests using epoxy-resin-coated textiles are scheduled for the near future. The chosen feeding device for the textiles does not allow the use of uncoated types.

3.7   Summary

Applying the manufacturing methods casting, laminating, spraying, spinning and extrusion, different building components can be made of TRC. While the casting and laminating techniques are better suited for laminar components, using the spraying method, curved shapes can also be produced, and in the spinning technique, for example, even tubes can be manufactured. Table 3.2 gives a survey of the application areas of the different manufacturing methods.

Table 3.2 Application areas of the different manufacturing methods

Manufacturing method	Component geometry		Fabric				Reinforcement ratio	Building component
	2D	3D	2D	3D	Uncoated	Coated		
Casting	++	O	++	++	++	++	Reinforcement ratio limited by the density of the structure Spacers required in most cases	Façades, formwork elements, sandwich elements, structural elements (e.g., diamonds)
Laminating	++	O	++	−−	++	o (+)	Reinforcement ratio can be controlled almost arbitrarily	Façades, slabs
Spraying	++	++	++	−−	++	o (+)	Reinforcement ratio can be controlled almost arbitrarily	Slabs in horizontal and vertical alignment, shells
Spinning	−−	++[a]	++	+ (o)	++	++	Reinforcement ratio can be controlled almost arbitrarily	Tubes, poles, columns
Extrusion	++	++	Yet unknown					Bar-shaped profiles, honeycomb slabs, formwork elements, hollow core slabs

++, very well suited or very easily producible; +, well suited or easily producible; o, suited or possible; −, suited to a limited extent or possible to a limited extent; −−, not suited or not producible.
[a]Circular hollow profiles.

References

Brameshuber, W., RILEM, 2006. RILEM TC 201-TRC: textile reinforced concrete. State-of-the-art report of RILEM Technical Committee 201-TRC. Bagneux, RILEM. Report 36. ISBN 2-912143-99-3.

Brameshuber, W., Hegger, J., Gries, T., Dilger, K., Böhm, S., Mott, R., Voss, S., Barlé, M., Hartung, I., 2007. Serielle Einzelfertigung (Stückfertigung) von Bauteilen aus textilbewehrtem Beton. AiF-Forschungsbericht Nr. F882. Aachen, Institut für Bauforschung, Institut für Massivbau, Institut für Textiltechnik (alle RWTH Aachen), Institut für Füge- und Schweißtechnik (TU Braunschweig).

Brameshuber, W., Mott, R., Hegger, J., Voss, S., Gries, T., Barle, M., Böhm, S., Hartung, I., 2008. Serielle Stückfertigung von Bauteilen aus textilbewehrtem Beton (Serial Batch Production of Building Members Made of Textile Reinforced Concrete). Beton- und Stahlbetonbau 103 (2), 64–72.

Hegger, J., Kulas, C., Horstmann, M., 2012. Spatial textile reinforcement structures for ventilated and sandwich facade elements. Adv. Struct. Eng. 15 (4), 665–676.

Mechtcherine, M., 2013. Novel cement-based composites for the strengthening and repair of concrete structures. Constr. Build. Mater. 41, 365–373.

Mott, R., Brameshuber, W., 2007. Subsequently applied waterproof basements made of textile reinforced concrete using the spraying method (Nachträglich ausgeführte wasserundurchlässige Keller aus Textilbeton hergestellt im Spritzverfahren). Farmington Hill: American Concrete Institute, ACI SP-251, 2008. In: Aldea, C.-M. (Ed.), Design and Applications of Textile Reinforced Concrete, ACI Fall Convention 2007, Fajardo, Puerto Rico, 14.-18.10.2007. 14 Seiten.

Peled, A., Mobasher, B., 2008. Effect of processing on mechanical properties of textile-reinforced concrete. Farmington Hills, Mich. American Concrete Institute, ACI SP-250. In: Dubey, A. (Ed.), Textile-Reinforced Concrete. ACI Fall 2005 Convention, Kansas City. 14 Seiten.

Schladitz, F., Lorenz, E., Jesse, F., Curbach, M., 2009. Strengthening of a barrel-shaped roof using textile reinforced concrete. In: Proceedings of 33rd symposium of the IABSE, 2009 September 9–11, Bangkok, Thailand, pp. 416–417.

Schneider, M., Scholzen, A., Chudoba, R., 2013. Filigrane Schalenkonstruktion aus Textilbeton In [Textilbeton—in Theorie und Praxis: 5. Anwendertagung Textilbeton; 24./25. September 2013, Friedrichshafen]. TUDALIT. Leichter bauen—Zukunft formen. Dresden: TUDALIT. 5 (2013) 9, S./Art.: 8–8.

Weiland, S., Ortlepp, R., Hauptenbuchner, B., Curbach, M., 2008. Textile reinforced concrete flexural strengthening of RC-structures—part 2: application on a concrete shell. Farmington Hill: American Concrete Institute, ACI SP-251. In: Aldea, C.-M. (Ed.), Design and Applications of Textile Reinforced Concrete, ACI Fall Convention 2007, Fajardo, Puerto Rico, 14–18 October 2007. 18 Seiten.

This page intentionally left blank

Part Two

Testing, mechanical behaviour and durability aspects of textile fibre composites used in structural and civil engineering

This page intentionally left blank

Bonds in textile-reinforced concrete composites

4

A. Peled
Ben Gurion University of the Negev, Beersheba, Israel

4.1 Introduction

Textile-reinforced concrete (TRC) composite is made of a cement-based matrix (paste, or fine-grained concrete, also known as mortar) reinforced with textile fabric. The properties of TRC composite are dependent on the properties of the textiles, including material types and geometries, the cement-based matrix properties and the bonds developed between them. The textile–matrix bond strongly influences the entire behaviour of the composite, its strength, ductility and toughness (Brameshuber, 2006). In general, strong bonding usually leads to the fracture of the reinforcement, providing a high-strength composite with low ductility and relatively brittle behaviour; whereas weak bonding leads to fibre pullout, providing a more ductile composite with lower strength. In regard to the material type, beyond the fibre's chemical characteristics, one dominant parameter (that influences the bond between the fibre and the cement matrix) is the modulus of elasticity (Stang, 1996; Peled and Bentur, 2000, 2003). Increasing the modulus of elasticity of the fibre enhances the bond strength (Figure 4.1), due to the higher clamping stresses that develop around the fibres, caused by the autogenous shrinkage of the matrix (Stang, 1996). Such differences in bonding affect the mechanical behaviours of these cement composites. The use of high-strength, high-modulus fibres will usually increase the strength and toughness of the cement composites by enhancing strain-hardening behaviour; whereas low-modulus fibres usually increase the ductility of the cement composites, but not their strength, resulting in a strain-softening or elastic–plastic behaviour.

Modern textile technology offers a wide variety of fabrics with great design flexibility and various fibre geometries. Variables in such fabrics include their geometries and distributions of the fibres in two and three dimensions. They can be produced by different methods, such as weaving, knitting or breading or be nonwoven. They differ in the way that the yarns (the basic reinforcing unit in the fabric) are connected to each other at the junction points (Figure 4.2). The interlacing of the yarns to form a fabric affects not only the geometry of the fabric itself, but also the geometry of the individual yarns (which make up the fabric), whether they are nonstraight, such as crimp, or a more complex structure (Figure 4.2). When polymer matrices were reinforced with fabrics in which the yarns did not maintain a straight geometry, a reduction in the reinforcing effectiveness was reported (Zeweben, 1989). Therefore, in polymer matrix composites, the reinforcing fabrics should contain as many straight yarns as possible. The prediction of the reinforcement efficiency of the fabric usually takes into account
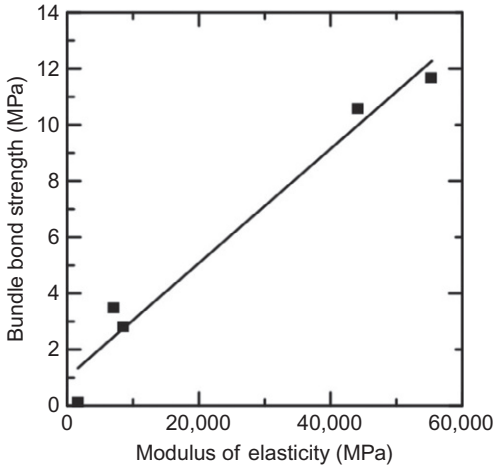
Figure 4.1 Effect of modulus of elasticity of the yarn on bond strength in a cement matrix (Peled and Bentur, 2003).
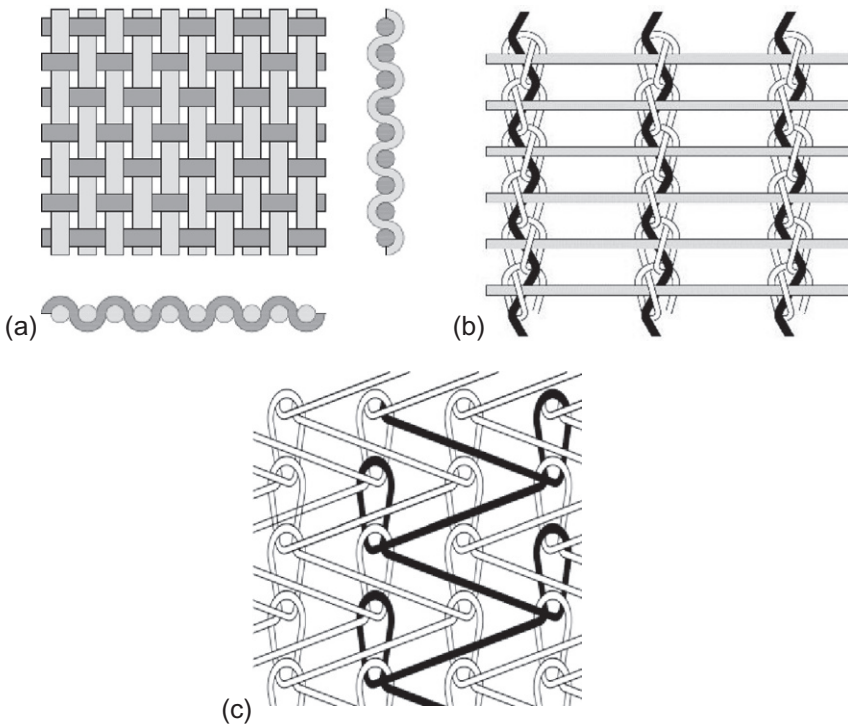
Figure 4.2 Different fabric structures and their individual yarn geometries: (a) woven (severe crimping); (b) weft-insertion, warp-knitted (light crimping of the warp yarns) and (c) short-weft, warp-knitted (zigzag).

only the longitudinal yarns in the fabric, which are in the loading direction. The perpendicular yarns are treated as 'non-structural'; their purpose is to provide a mechanism to hold the longitudinal yarns in place during the production of the composite. In regard to cement composites, this concept is inadequate, as the nature of the interactions between the cement matrix, the fabric and its individual yarns is more complex, because the interfacial shear bond is rather small. This may be attributed to the particulate nature of the matrix, which is quite different than the more continuous microstructure of the polymer matrix. Therefore, in fabric cement-based composites, the fabric geometries and the special geometries of the yarns have significant effects on bonding with the cement matrix, where the anchoring of the fabric and the yarns in the cement matrix is the dominant mechanism (Figure 4.3) (Peled et al., 1997, 1998b, 1999; Peled and Bentur, 1998, 2000).

Furthermore, textile fabrics are produced from yarns that have two main forms: monofilament or multifilament; the latter is composed of hundreds or thousands of filaments (Figure 4.4). Monofilament yarns are mainly made of low-property fibre materials, such as polypropylene (PP) or low-density polyethylene (PE). Conversely, most high-performance fibres are in the form of multifilament bundle yarns (roving); however, low-performance fibres may also be composed in a multifilament form.

(a)   (b)

(c)
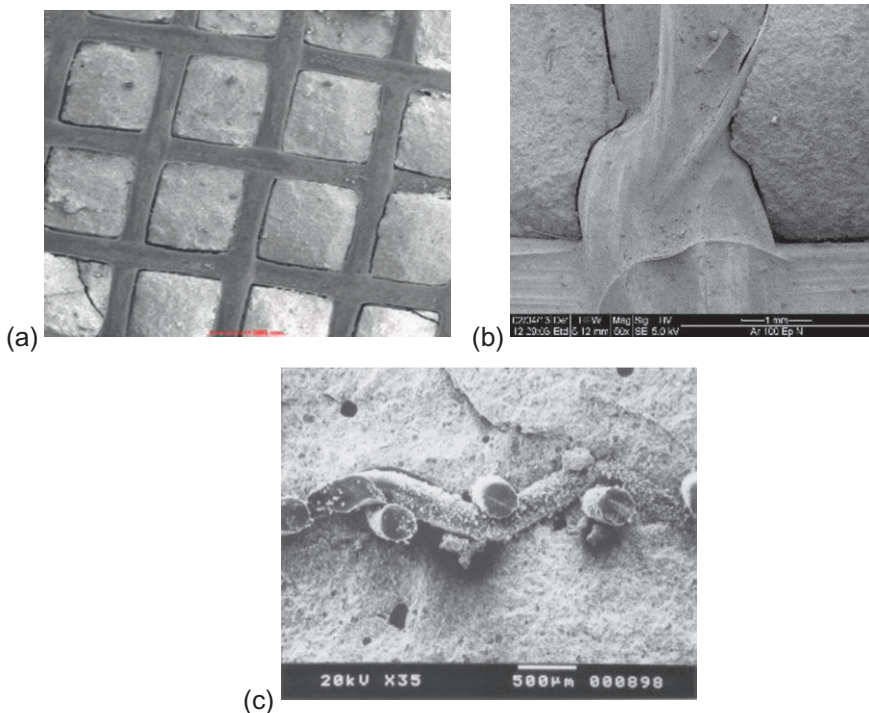
Figure 4.3 Anchoring in the cement matrix of: (a) the entire fabric structure (Peled and Mobasher, 2005); (b) an individual yarn in a knit fabric (Sasi and Peled, 2015) and (c) an individual yarn in a woven fabric (Peled et al., 1998b).

(a)   (b)
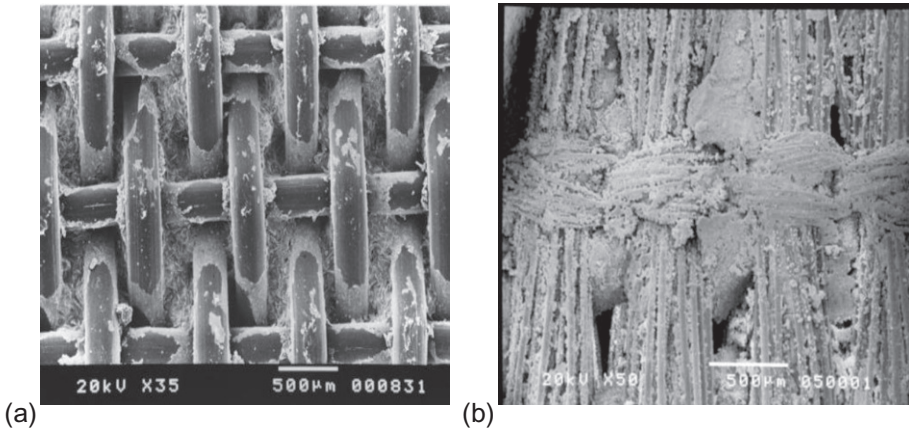
Figure 4.4 (a) Woven fabric made of monofilament yarns (Peled et al., 1999) and (b) weft insertion warp-knitted fabric made of multifilament yarns (Peled and Mobasher, 2006) embedded in cement matrix.

In relation to textile reinforcement, the bonding mechanism and the microstructure in the vicinity of the yarn/fabric, that is, at the yarn (fabric)–matrix interface, can be rather different. This depends on: the form of the yarn (mono- or multifilament), the fabric and its yarn geometry, as well as the composition of the yarn (fibre) material.

A significant number of experimental and analytical investigations have characterized the bond between the fibre and the cement matrix. These investigations have explored different types of single fibres of high- and low-modulus with different geometries. The bonding of fabric reinforcement is much more complicated, due to the function of the yarns transverse to the load direction and the complex geometries of the individual reinforcing yarns making up the fabric, which provide anchorage, as well as the mono- or multifilament nature of the yarn. This chapter will discuss the main bonding mechanisms and the various parameters influencing them: multifilament yarns, including yarn coating and filling; yarn geometry and fabric geometry. First, the main concepts of bond characterization and bond modelling of fabrics in cement-based composites are introduced.

4.2   Characterization and modelling of bonding

4.2.1   ACK model

In cement-based composites, the ultimate strain in the tension of the cement matrix is considerably smaller than that of the fibres; therefore, the matrix fails long before the full potential of the fibre is actualized (i.e. before the fibre reaches its peak tensile stress). Thus, fibre reinforcement becomes effective mainly after the matrix has cracked and the fibres are bridging over the crack, carrying the additional load

imposed on them. With the increase in the tensile force, the load is gradually transferred from the fibre to the matrix; once the stress in the matrix reaches its peak, a new crack appears. These distributed transverse cracks form gradually as the composite is loaded beyond the initial cracking stages, until the entire composite length is completely cracked, with an average crack spacing equal to a critical length in between the upper and lower bounds of x and $2x$. The average stress transfer length (i.e. the distance between the developing cracks) is mainly controlled by the bond that develops across the fibre–matrix interface, namely, 'bond strength'. The higher the bond strength is, the smaller the average crack spacing is. By measuring the spacing between the cracks that develop during a tensile test, it is possible to characterize the bond strength between the matrix and the reinforcement. By using the crack-spacing measurement, the bond between the fabric and the cement matrix may be calculated by the ACK model (Aveston, Cooper & Kelly) (Aveston et al., 1971; Aveston and Kelly, 1973). This model is presented by Equation (4.1).

$$\tau_{fu} = \left(\frac{V_m}{V_f}\right) \times \frac{\sigma_{mu} r}{2x} \tag{4.1}$$

where τ_{fu} is the bond strength; V_m and V_f are the volume fraction of matrix and fibre (reinforcing yarns), respectively; σ_{mu} is the matrix tensile strength; r is the fibre/yarn radius; and x is the average distance between the cracks.

Figure 4.5 presents the stress–strain curves of two different cement composites, reinforced with glass fabrics, along with the spacings that developed between their cracks – one with high bond strength (ARG-P900) and the other with poorer bond strength (ARG P100). The greater bond is observed where there is denser crack spacing during the entire loading process. More detailed information on cement composite tensile behaviour and crack spacing can be found in Chapter 11.
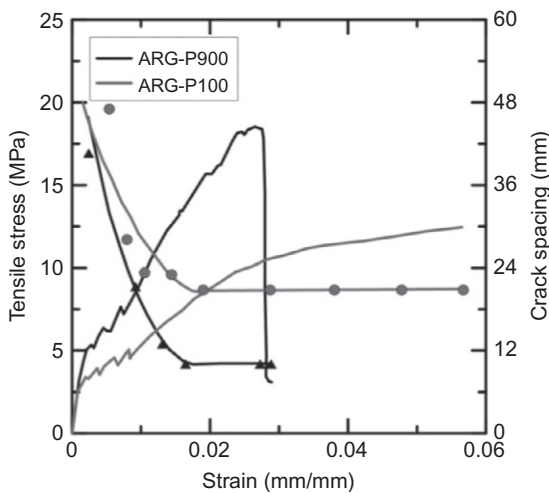
Figure 4.5 Stress–strain responses of two different cement composites reinforced with glass fabrics along with the spacing developed between the cracks during loading, with high (ARG-P900) and low bonding (ARG-P100) (Peled and Mobasher, 2005).

4.2.2 Pullout behaviour

4.2.2.1 Introduction

Many analytical models have been developed to predict the pullout load versus the slip relationship for a straight, smooth fibre from a cement matrix (Cox, 1952; Lawrence, 1972; Bartos, 1984; Gray, 1984; Alwan et al., 1991; Naaman et al., 1991a,b). These models distinguish between two stages: the elastic stage (adhesion) and the slip stage (friction). Figure 4.6a presents a typical pullout scheme for testing and modelling. A force P is applied to the tip of a fibre embedded in a cementitious matrix over a length l_e. The assumed relationships, between the interfacial shear stress and the relative fibre slip, in such models are shown in Figure 4.6b. The initial portion of the curve is modelled as linear elastic, up to the point at which the adhesional bond strength is reached (τ_{au}). Beyond the peak stress, the behaviour is assumed to be purely frictional, with a constant frictional shear stress, τ_{fu}, over the whole slip range. Several researchers (Lawrence, 1972; Bartos, 1984; Naaman et al., 1991a) developed correlations between the bond shear stress and slip, like the one presented in Figure 4.6b, and, based on that, predicted the whole pullout curve (pullout load vs. slip).

For composites containing fibres that are not in a straight form, the bond with the cement matrix is also affected by the geometry of the fibres. Modelling of the pullout behaviour of crimped and deformed yarns was developed by Mallikarjuna and Banthia (1991) and Alwan et al. (1999). Mallikarjuna et al. applied finite element analysis using a three-dimensional element to model the pullout behaviour of crimped yarns. They assumed that the relationship presented in Figure 4.6b is also applicable to crimped yarns. Alwan et al. (1991) investigated deformed steel fibres. They observed, from their tests, that the pullout behaviour of deformed fibre is similar to that of smooth fibre up to a complete interfacial debonding of the fibre. The assumptions they made are the same as for smooth fibre up to this stage. Peled and Bentur (2003) investigated the respective pullout behaviours and bond strengths, τ_{au} and τ_{fu}, of straight and crimped PE yarns, showing a marked increase in both types of bonding mechanisms with the increase in yarn crimp density, due to enhanced mechanical anchoring. Banholzer et al. (2005) simulated the behaviour of multifilament yarns (roving), for the case in which the roving consists of bundled filaments with N-piecewise linear bond stress versus a slip relation with no limitation of N.

In fabric-reinforced cement-based matrices, the bonding situation is much more complex than in single fibres/yarns, due to the presence of yarns transverse to the load
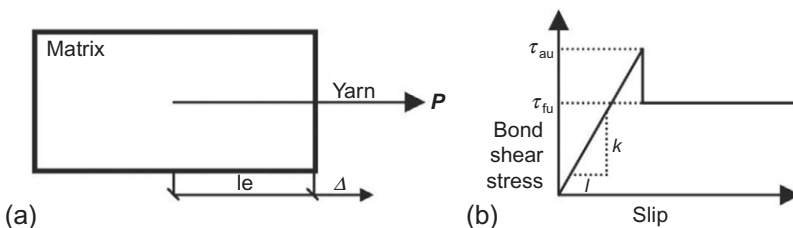
Figure 4.6 (a) Schematic presentation of typical pullout test configuration and (b) shear bond stress at different slip values assumed for the modelling of pullout behaviour.
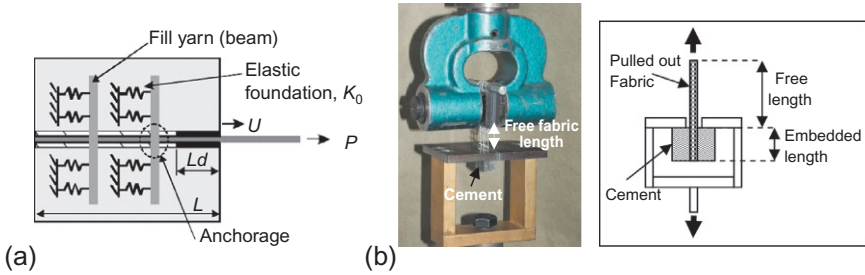
Figure 4.7 (a) Fabric pullout model across a matrix crack (Mobasher, 2012) and (b) actual fabric pullout setup (Peled et al., 2006; Sueki et al., 2007).

direction and the nonstraight shape of the individual yarns comprising the fabric. The yarns perpendicular to the pullout direction and the curved shapes of the reinforcing, pulled-out yarns must be taken into consideration, as they provide anchorage points. Peled et al. (2006) and Sueki et al. (2007) modified Naaman's model (Naaman et al., 1991a,b) to simulate the pullout responses of different fabric-reinforced cement matrices. The model considered the anchoring effect of the transverse yarns at the fabric junctions caused by periodic arrangement of linear springs (Figure 4.7a) and the anchorage caused by the curvature of the yarn within the fabric (most significant in woven fabrics). The basic pullout mechanism of a fabric embedded in a cement matrix is shown in Figure 4.7a, and the actual pullout setup is presented in Figure 4.7b. An analytical model is presented in the following sections (also see Chapter 11).

4.2.2.2 Mathematical derivation

The presented model is based on earlier work by Naaman et al. (1991a,b) and work done by Sueki et al. (2007). In this model, the fabric, except for the pulled yarn, is treated as a continuum matrix. The interface between the pulled yarn and remaining yarns (hereafter: 'the matrix') is defined by a shear strength diagram, as shown by the inset in Figure 4.8. Figure 4.8 also shows a simplified pullout load versus slip response, obtained by pulling one yarn out of the fabric. The response seen in the graph may be divided into two stages according to the shear stress distribution at the contact surface of the yarns. Initially, the curve shows a linear response corresponding to the uncrimping of the pulled yarn (stage I). When the loading reaches the peak load, the yarn starts to translate (stage II). The shear strength mechanism, force distribution and derivations for each stage are explained in the following.

Static equilibrium requires that the tensile force (F) in the yarn be transferred to the matrix (M) by means of bonding along the embedded length. This relationship is expressed in the differential form as:

$$\frac{dF}{dx} = -\frac{dM}{dx} = \psi\tau \tag{4.2}$$
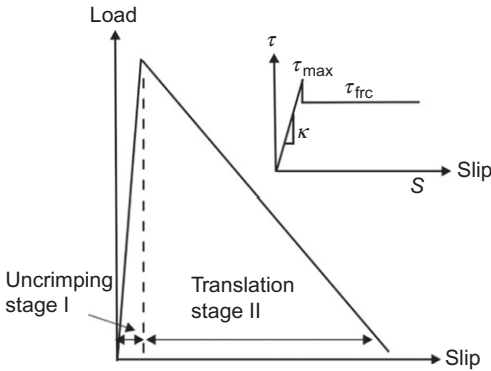
where ψ is the equivalent circumference of the yarn and τ is the shear stress at the interface. For small loads, local shear stress behaves linearly as a function of slip, with slope, κ, defined by the shear strength diagram. The slip, S, is defined by the difference in the elongation of the yarn, δ_y, and the shortening of the matrix, δ_m, over a finite length, dx:

$$\tau = \kappa S = \kappa(\delta_y - \delta_m) = \kappa \int_0^x \left[\varepsilon_y(x) - \varepsilon_m(x)\right] dx \tag{4.3}$$

where $\varepsilon_y = \frac{F}{A_y E_y}$, $\varepsilon_m = -\frac{F}{A_m E_m}$, A is the cross-section area, E is the Young's modulus and subscripts 'y' and 'm' refer to the yarn and the matrix, respectively. Substituting Equation (4.3) into Equation (4.2), and taking the derivative with respect to x, results in a differential equation for the yarn pullout force given as Equation (4.4):

$$\frac{d^2 F}{dx^2} - \beta^2 F = 0 \tag{4.4}$$

where $\beta^2 = \psi \kappa Q$ and $Q = \frac{1}{A_y E_y} + \frac{1}{A_m E_m}$. The general solution of the second differential equation has the following form:

$$F(x) = C_1 e^{\beta x} + C_2 e^{-\beta x} \tag{4.5}$$

The yarn force distribution is obtained by applying force boundary conditions $F(0) = 0$ and $F(L) = P$ in Equation (4.5). By taking the derivative, with respect to x and divided by ψ, the shear stress distribution is obtained as follows:

$$F(x) = P \frac{\sinh(\beta x)}{\sinh(\beta L)} \tag{4.6}$$

$$\tau(x) = \frac{P\beta}{\psi} \frac{\cosh(\beta x)}{\sinh(\beta L)} \tag{4.7}$$

Stage I: Uncrimping

When loaded, the yarn first starts to straighten, and the shear stress immediately exceeds the maximum shear strength, τ_{max}, due to the flexibility of the fabric. This leads to uncrimping for a length d (see Figure 4.9a), while the pulled yarn is still in the original configuration for the $(L-d)$ portion. The shear stress distribution is governed by a constant frictional strength, τ_{frc}, along the uncrimping zone, in addition to the maximum strength value, τ_{max}, at the transition point between the uncrimping and the crimping zones. The modelling algorithm is based on incrementally imposing the uncrimping length, d, and calculating the applied force from the shear stress distribution along the embedded length. Resistance to the pullout load in stage I, P_1, is calculated by the summation of the two forces – the uncrimping-resistant force, $P_{u,max}$, and the translation-resistant force, P_t.

$$P_1 = P_t + P_{u,max} = \tau_{frc}\psi d + \frac{\tau_{max}\psi}{\beta}\tanh\left(\beta(L-d)\right) \tag{4.8}$$

where $P_{u,max} = \dfrac{\tau_{max}\psi}{\beta}\tanh\left(\beta(L-d)\right)$. The force boundary conditions for stage I are: $F(0)=0$, $F(L-d)=P_{u,max}$, and $F(L)=P_1$. By applying these boundary conditions to Equation (4.5), one may obtain force distributions for the uncrimping and translation zones.

$$\begin{aligned} F_u(x) &= P_{u,max}\frac{\sinh\left(\beta x\right)}{\sinh\left(\beta(L-d)\right)}, & 0 \leq x \leq L-d \\ F_t(x) &= P_{u,max} + \tau_{frc}\psi(x-L+d), & L-d \leq x \leq L \end{aligned} \tag{4.9}$$

Slip at the end of the yarn is obtained from these two separate regions.

$$\begin{aligned} S(L)_1 &= \int_0^{L-d}\left[\frac{F_u(x)}{A_yE_y} + \frac{F_u(x)}{A_mE_m}\right]dx + \int_{L-d}^L\left[\frac{F_t(x)}{A_yE_y} + \frac{F_t(x)}{A_mE_m}\right]dx \\ &= \frac{P_{u,max}Q\left[\cosh\left(\beta(L-d)\right)-1\right]}{\beta\,\sinh\left(\beta(L-d)\right)} + \frac{1}{2}Qd\left(\tau_{frc}\psi d + 2P_{u,max}\right) \end{aligned} \tag{4.10}$$
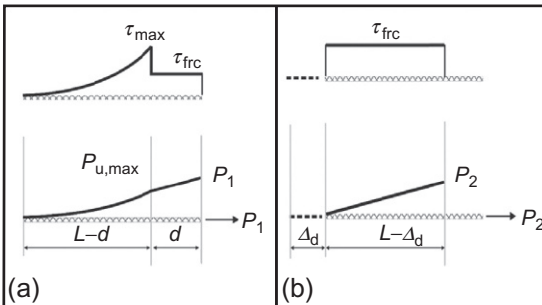
Figure 4.9 Shear strength and force distribution along yarn: (a) stage I (uncrimping) and (b) stage II (translation) (Sueki et al., 2007).

Stage II: Translation

Stage II is defined as a translation response (Figure 4.9b). It is assumed that, at this stage, the yarn is completely uncrimped and starts to translate ($\Delta_d > 0$). Shear resistance remains constant at τ_{frc} throughout the process, while the embedded length reduces to ($L - \Delta_d$) as the pullout progresses. The pullout force at the end of the yarn is:

$$P_2 = \tau_{frc} \psi (L - \Delta_d) \tag{4.11}$$

From Figure 4.9b and static equilibrium, it is possible to write the force distribution as:

$$F(x) = P_2 + \tau_{frc} \psi (x - L + \Delta_d) = \tau_{frc} \psi x, \quad 0 \le x \le L - \Delta_d \tag{4.12}$$

The slip at the end of the yarn is calculated in a same way as in Equation (4.9):

$$S(L)_2 = \int_0^{L-\Delta_d} \left[\frac{F(x)}{A_f E_f} + \frac{F(x)}{A_m E_m} \right] dx = \frac{\tau_{frc} \psi Q}{2} (L - \Delta_d)^2 \tag{4.13}$$

The total slip at the end of the yarn, measured during translation stage, is derived from the slip at the end of stage I, $S(L)_1$, and the translation in stage II, $S(L)_2$:

$$S_{total}(L)_2 = S(L)_1 + S(L)_2 \tag{4.14}$$

Note that the measured, experimental sliding displacement in stage II, $D_{measured}(L)_2$, consists of the total slip given by Equation (4.14) and the rigid body displacement, Δ_d:

$$D_{measured}(L)_2 = S(L)_1 + S(L)_2 + \Delta_d \tag{4.15}$$

The analytical model described above may be used to simulate the experimental pullout responses obtained as follows: (1) during uncrimping (stage I), incrementally imposing the uncrimping length, d, and calculating the corresponding load, P_1, and slip, $S(L)_1$, by means of Equations (4.8) and (4.10). It is assumed that stage I ends, and the translation stage begins when the computed slip, $S(L)_1$, starts to decrease; (2) during translation (stage II), the load and total slip, P_2, and $S(L)_2$ are calculated by Equations (4.11) and (4.13). The total displacement in this simulation, including both slip and translational displacement is calculated via Equation (4.15).

4.2.2.3   Contacts between pulled yarn and fill yarns

Due to the undulated nature of the fabric, the contact area between the pulled yarn and fill yarns is not constant during pullout. It is assumed here that the contact area at each crossover joint is one half of the circumference of the pulled yarn (warp) for a stationary unit length (C_1, as shown in Figure 4.10). As the yarn is displaced, the pre-existing undulations become out of phase with the undulation imposed by the weave. When the phase shift reaches the point at which the imposed undulation is exactly opposite the
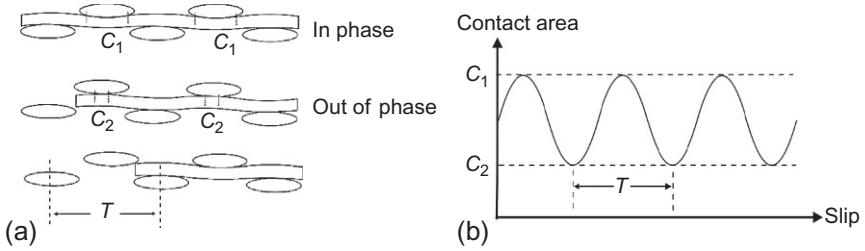
Figure 4.10 Contact area during yarn translation: (a) contact area at different stages and (b) sinusoidal function describing the contact area change during pullout with maximum and minimum values, C_1 and C_2, respectively (Mobasher, 2012).
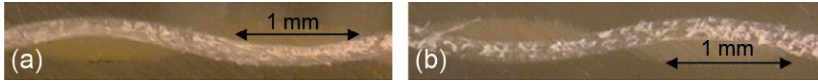
Figure 4.11 Cross-sectional micro-image of: (a) warp yarn and (b) fill yarn in aramid fabric without any loading (Bansal, 2007).

set undulation, that is, after the slipping yarn has slipped a distance equal to the spacing of the fill yarns (T), the contact area is minimum (C_2, as shown in Figure 4.10).

Figure 4.11 shows the crossing-sections of warp yarn and fill yarn in aramid fabric without any loading obtained by optical microscopy (Bansal, 2007). After image analysis, the cross-section of the warp yarn may be approximated as an ellipse with a semi-major axis of 0.655 mm and a semi-minor axis of 0.085 mm. The circumference of the warp yarn is given as:

$$C \approx \pi \left[3(a+b) - \sqrt{(3a+b)(a+3b)} \right] \tag{4.16}$$

The cross-section area of the warp yarn is calculated by:

$$A_y = \pi ab \tag{4.17}$$

where a is the semi-major axis and b is the semi-minor axis of the ellipse. As the contact area periodically changes between C_1 and C_2 during pullout, it is assumed that the contact area follows a sinusoidal function with a period of oscillation equal to the distance between the two adjacent peaks of the force–displacement curve. In order to simulate the oscillation behaviour after peak load, the effective contact area, C_{ef}, at stage II (translation) is defined as:

$$C_{ef} = \frac{C}{2} + C_0 \left[\sin\left(\frac{2\pi}{T} S\right) - 1 \right] \tag{4.18}$$

where C is the circumference of the warp yarn; C_0 is the amplitude of sinusoidal function; T is the period of oscillation; and S is the slip distance. The value of C_{ef} is between C_1 and C_2, or $C/2 - 2C_0 < C_{ef} < C/2$.

4.2.2.4   Analytical model simulation: Results and discussion

The response of each test is simulated and the shear parameters (τ_{max} and τ_{frc}) are found by fitting the simulation response to the experimental results. This model has demonstrated the ability to fit various representative curves (averaged responses) of different fabrics, matrices, embedded lengths, levels of transverse force and processing methods (also see Chapter 11).

Figure 4.12a–d compares test data with the simulation results for typical tests using 50 mm, 65 mm and 90 mm specimens with 100 N nominal transverse force, as well as a 90 mm specimen, also with 400 N nominal transverse force. The model shows a relatively close prediction, except that the post-peak portion drops linearly in the
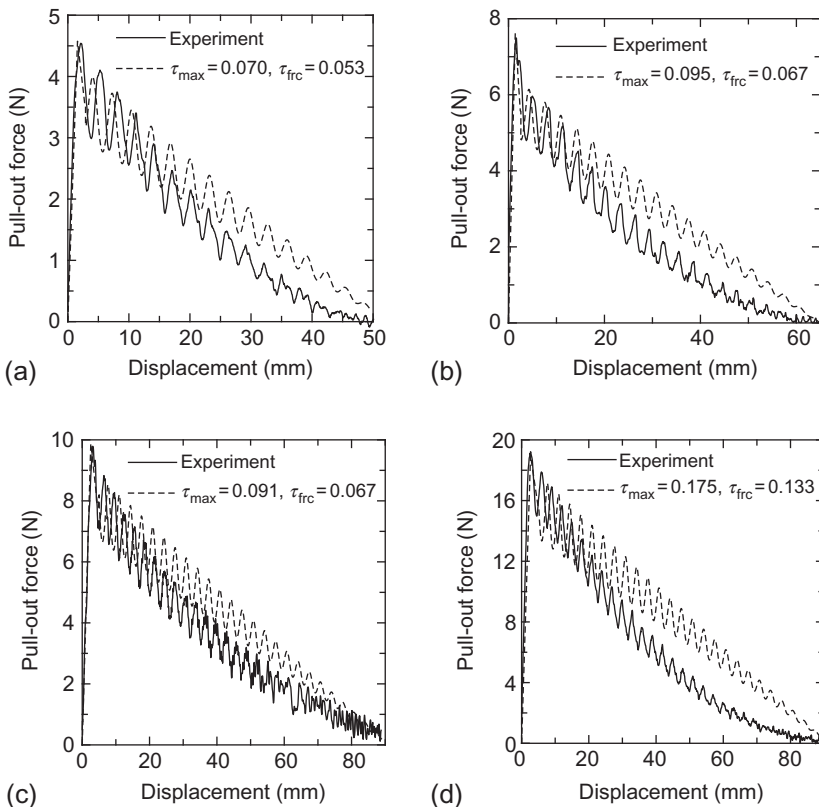
Figure 4.12 Comparison of experimental data and simulation: (a) 50 mm, (b) 65 mm, (c) 90 mm specimens with 100 N nominal transverse force and (d) 90 mm specimen with 400 N nominal transverse force. τ_{max} and τ_{frc} are in MPa.

simulations, while the experimental data shows nonlinear behaviour. This may be explained because that frictional shear strength is assumed to be constant along the embedded yarn throughout the pullout process. In addition to the shear strength diagram, a single value of nominal shear stress, τ_{nom}, is used as another measure to quantify the friction between the contact area, defined as:

$$\tau_{nom} = \frac{F_{max}}{\pi \phi L} = \frac{2F_{max}}{CL} \qquad (4.19)$$

where F_{max} is the maximum pullout force; ϕ is the effective diameter of a single yarn; L is the total pullout length of a single yarn and C is the circumference of the warp yarn.

More detailed test and simulation results are presented in Chapter 11.

4.3 Multifilament yarns

4.3.1 Microstructure

In many cases, fabrics are made of multifilament yarns (rovings) that are composed of hundreds or thousands of fine-diameter filaments. This form of yarn offers numerous advantages as reinforcement, making it applicable to the development of advanced cementitious composites. However, the use of multifilament reinforcements for cements is challenging, due to the particulate nature of the cementitious matrix. This consists of relatively large particles ($\sim$5–70 µm particles) – larger than the spaces between the filaments of the strand (having internal spaces of less than $\sim$5 µm). As such, the cement particles cannot fully penetrate the spaces between the inner filaments of the strand spacing. This results in a unique microstructure, in which the external filaments (sleeve) are in direct contact with the hydration products (thanks to good cement grain penetrability), whereas the internal filaments (core) remain relatively free (due to the limited cement penetrability or even the absence of the cement matrix in between the core filaments) (Bartos, 1987; Zhu and Bartos, 1997; Banholzer, 2004; Brameshuber et al., 2006; Bentur and Mindess, 2007). In such a microstructure, the reinforcing unit is not a single filament completely embedded in a matrix, but rather a multifilament strand with inner gaps between filaments, surrounded by a particulate matrix (Figure 4.13).

Zhu and Bartos (1997) confirmed the presence of gradient cement particle penetrability within a bundle embedded in a cementitious matrix by means of a push-in test. The microstructure and micro-strength at the interfacial zone were investigated for selected individual filaments within a strand. They demonstrated differences in filament-sliding resistance at different locations, with relation to the bundle perimeter; much greater resistance was measured for the outer 'sleeve' filaments than for the inner 'core' filaments. Peled et al. (2008) identified different atomic components at different strand locations using an atomic force microscope (AFM) and X-ray electron dispersive microscopy (XEDS) at the cement bulk. In the external filaments, calcium
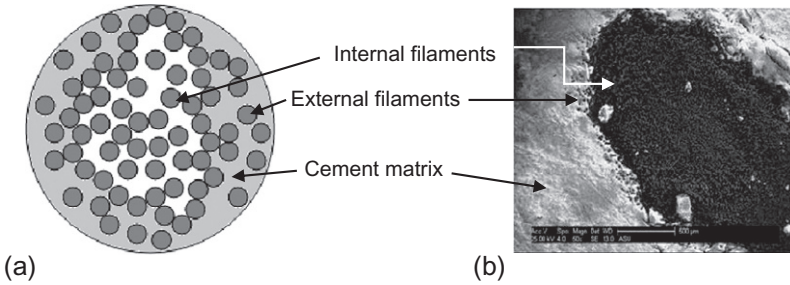
Figure 4.13 Cross-section of a bundle embedded in cement matrix: (a) scheme and (b) actual carbon bundle in cement matrix (Zhu et al., 2013).

silicate hydrates (CSH) were recorded; in the inner filaments, mainly calcium hydroxide was identified. However, in the bundle core, no hydration products were found, indicating different phases at the fibre–matrix interface. Dolatabadi et al. (2011) demonstrated the physical limitations of cement particle penetrability into fibre bundles by a simple model evaluating the quantity of cement grain penetration into the bundle. They did this in accordance with the cement particle size distribution and the geometry of the bundle – namely, fibre diameters, packing density and the titer of the bundle, while assuming a hexagonal arrangement of the fibres in the cross-section. They showed, empirically and numerically, that low packing density corresponds to higher cement grain penetration, whereas dense packing density limits cement grain penetrability to less than 10%.

4.3.2   Bonding mechanism: Telescopic pullout

This unique type of partial cement penetration (above) produces special bonding mechanisms, in which the external filaments (sleeve filaments) are in direct contact with the cement matrix and are well-bonded to the matrix. Thus, they become fractured during loading, providing high first-crack stress. After the external filaments fail, a telescopic type of pullout is generated, whereby the internal (core) filaments slip against the external (sleeve) filaments. They then interact and transfer stresses only through surface contacts between them (Figure 4.14) (Bartos, 1987; Banholzer, 2004; Brameshuber et al., 2006). Therefore, the core filaments are not effectively utilized for the stress transfer and may be considered as 'wasted'. The inefficient use of the internal filaments is evident when comparing the tensile behaviour of cement composites reinforced with carbon fabric to that of the fabric itself (not embedded in a cement matrix) (Figure 4.15) (Zhu et al., 2013). Significantly lower tensile strength of the cement composite is observed compared to that of the fabric alone, due to low cement penetrability (Figure 4.13b). Moreover, the composite exhibited greater strain compared to the strain obtained in the solo fabric, due to the pullout of the core filaments from the composite bundle; indeed, the composite filaments, lacking direct contact with the matrix, were free to slide.
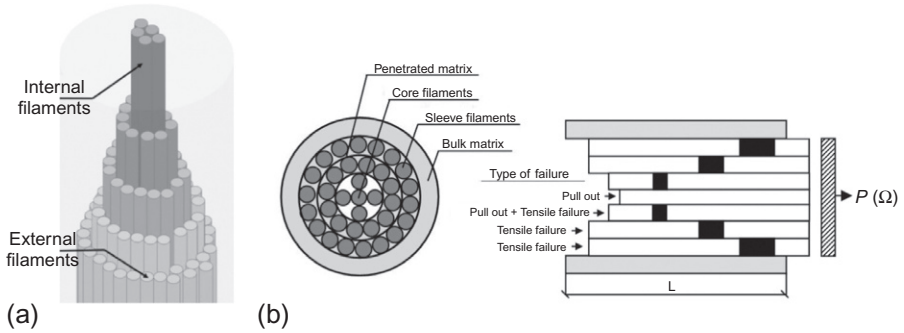
Figure 4.14 The telescopic pullout behaviour of a bundle embedded in a cement matrix: (a) after the pullout process, three-dimensional scheme (Cohen and Peled, 2010) and (b) two-dimensional scheme, including the fractured filaments (Banholzer, 2006).
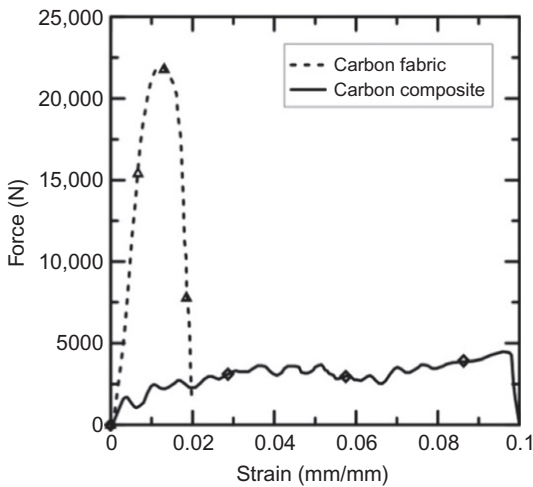
Figure 4.15 Comparison of tensile responses of the carbon composite and of the carbon fabric itself (not embedded in the cement matrix) (Zhu et al., 2013).

The telescopic mode of failure has been extensively described for glass strands (Banholzer, 2004, 2006; Brameshuber, 2006) and was visualized using the FILT (Failure Investigation using Light Transmission) test developed by Banholzer et al. (2006). This test is applied to a pullout cross-section of a strand embedded in the cement matrix. It is exposed on one side to a light source; the light is transferred through the glass filaments, detected by a camera on the opposite side and then converted to binary images (black and white pixels). These images are recorded simultaneously with the load–slip curves of the pullout test. The tested strand may be distinguished from the surrounding matrix due to its exposure and, therefore, bright appearance. Once the filament has failed during the pullout test, it is no longer able to transfer light and no longer appears on recorded images. Figure 4.16 shows examples of images obtained by this method, along with the load–slip diagram, $P(\Omega)$, at different stages of the pullout
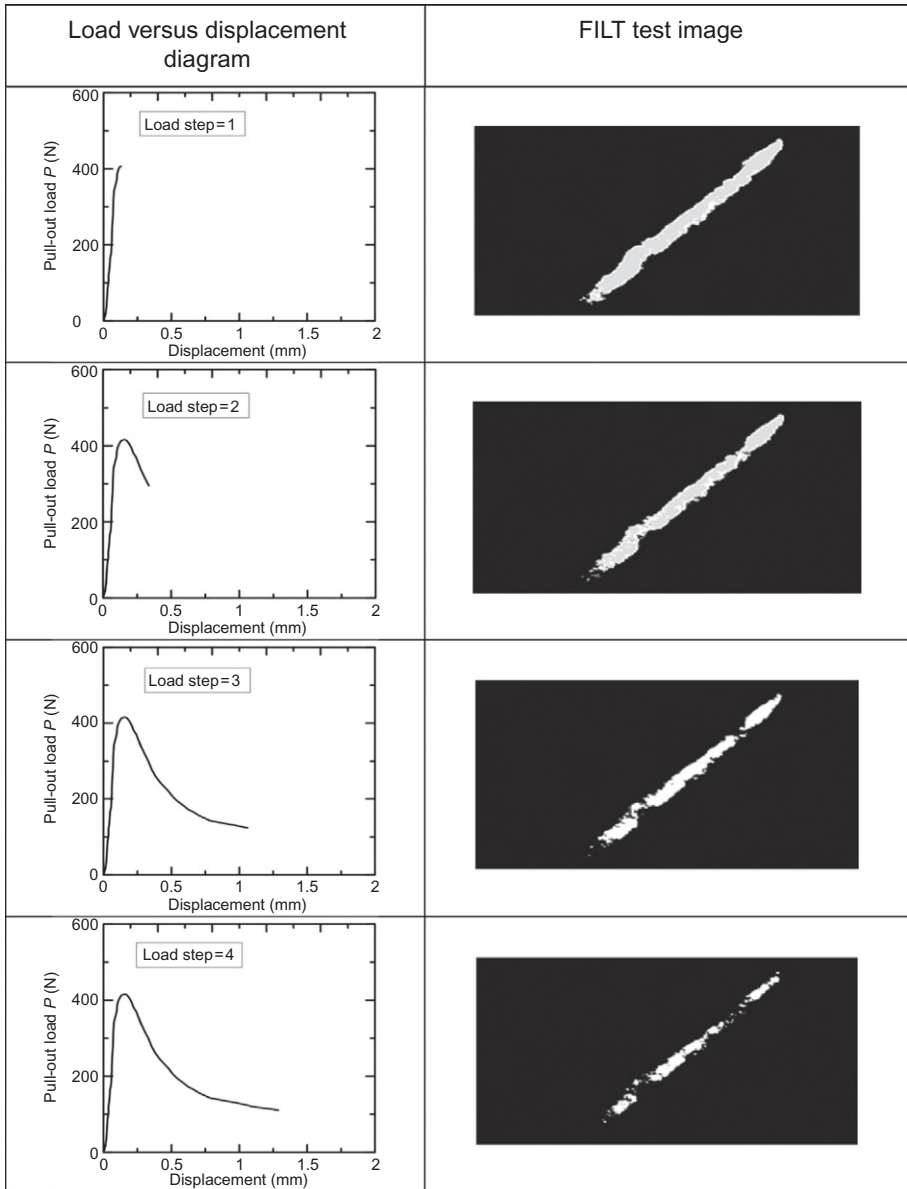
Figure 4.16 Failure process of a glass strand embedded in cement-based matrix during pullout loading. Load–slip curves at several stages and images of intact filaments (FILT tests) (Banholzer, 2006).
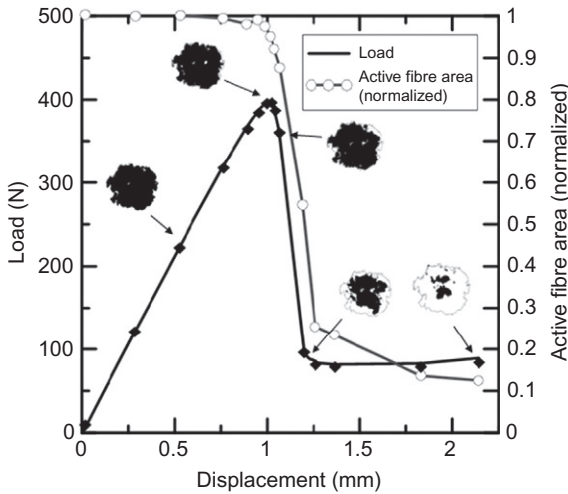
Figure 4.17 Load versus displacement curve during a pullout test (using the FILT test method developed by Banholzer et al. (2006)) and images of active filaments at different stages of pullout loading (Bentur et al., 2010).

process. The remaining, intact filaments, that is, activated filaments (those that still transfer the light) observed in the figure as white pixels versus displacement. Clearly, with increasing pullout displacement, the amount of intact filaments decreases. Furthermore, the external filaments break first, while the internal filaments do not fail and remain complete (without breakage) until the end of testing, as shown by Bentur et al. (2010) in Figure 4.17, via the FILT test. These results may also be evaluated with respect to the number of remaining, intact filaments, that is, activated filaments, and their location within the strand during the pullout process (Figure 4.17). Such results support the telescopic mode of failure, in which pullout behaviour is controlled by the strong bonding between the external filaments in the strand and the matrix. It is also controlled by the slip of the inner filaments that successively break down the layers of the bundle, from the sleeve to the core filaments (Figure 4.14).

Moreover, due to inner gaps between the filaments, the nature of the bonds change during the lifetime of a composite, by the slow and gradual process of deposition of hydration products in between the filaments (Zhu and Bartos, 1997; Bentur and Mindess, 2007). This means that bonding changes over time, as do the composite properties and durability. Zhu and Bartos (1997) clearly revealed this behaviour using the push-in test method on glass strands embedded in cementitious matrices. They measured the micro-strength of individual filaments at different locations within the strand after accelerated ageing. The resistance to filament sliding increased significantly due to ageing, while composite embrittlement was accompanied by a substantial increase in filament micro-strength at the core of the strand during the ageing process. In other words, composite ageing produces stronger bonds, which is a favourable effect. However, this effect may also lead to embrittlement, mainly when brittle fibres, such as glass, are used (Banholzer, 2004; Bentur and Mindess, 2007; Bentur et al., 2010; Cohen and Peled, 2010). In the case of glass roving, due to its sensitivity to the alkali environment of cement paste, the diffusion process of cement products between the filaments of the bundle over time may lead to intensive

corrosion. This may happen by means of a chemical attack on the filaments, when they are surrounded by cement hydrates (Zhu and Bartos, 1997; Raupach et al., 2006a), because more fibres are in direct contact with the hydrate products in the cement paste matrix. This can cause a severe reduction of the overall behaviour, toughness and strength of glass fibre composites. In carbon bundles, due to their high resistance within a cement matrix environment, such changes in bonding over time result not only in greater composite strength but also in improved toughness (Zamir et al., 2014).

4.3.3   Bond improvement

4.3.3.1   General concept

Based on the above, in order to get high composite performance, it is necessary to ensure efficient composite action by the transfer of forces from the matrix to the entire filament bundle. In other words, this is necessary to improve the stress transfer between the inner filaments and the cement matrix. Furthermore, mainly for glass bundles, one must also keep the filaments away from the cement matrix to improve composite performance during ageing.

Thus, the spaces between the bundle's filaments must be filled to facilitate better stress transfer between the filaments and greater loadbearing capacities for most or all of the filaments.

4.3.3.2   Coating and fillers

Improved composite performance is commonly achieved by filling the spaces between the filaments in a strand and coating it with polymers. Many studies have been dedicated to the positive effects of coating the bundles and filling-in bundle gaps with polymers (Krüger et al., 2003; Schorn et al., 2003; Gao et al., 2004; Butler et al., 2006; Raupach et al., 2006b; Schleser, 2008; Glowania and Gries, 2010; Weichold, 2010; Hartig et al., 2012). Stress transfer is found to be dependent on whether the bundle is coated or non-coated. Krüger et al. (2002) and Xu et al. (2004) concluded, for example, that fabrics with epoxy-impregnated bundles exhibit stiff and improved bond resistance in cement-based composites, as compared to non-coated bundles (Figure 4.18). This was reported for carbon, alkali resistance (AR) glass and aramid rovings. Following epoxy impregnation, the prestressing of the roving leads to enhanced bond strength and stiffness. Increased bond strength, due to coating, is supported by SEM images of the bundle embedded in the cement matrix, showing good filling of the spaces between the bundle filaments throughout the entire bundle cross-section; this, in turn, leads to the enhancement of reinforcing efficiency of the core filaments. Recall that non-coated bundle filaments provide poor cement penetrability, such that a portion of the roving does not take part in the force transfer between the concrete and the reinforcing bundle. The pullout behaviour observed in this experimental study has also been confirmed by a numerical study using a nonlinear finite element code proposed by Ožbolt et al. (2002) and modified for textile reinforcement (Krüger et al., 2002). Note that in this model, no distinction was made between the bonds of the inner and outer filaments; however good agreement was obtained in the pullout test results (Xu et al., 2004).
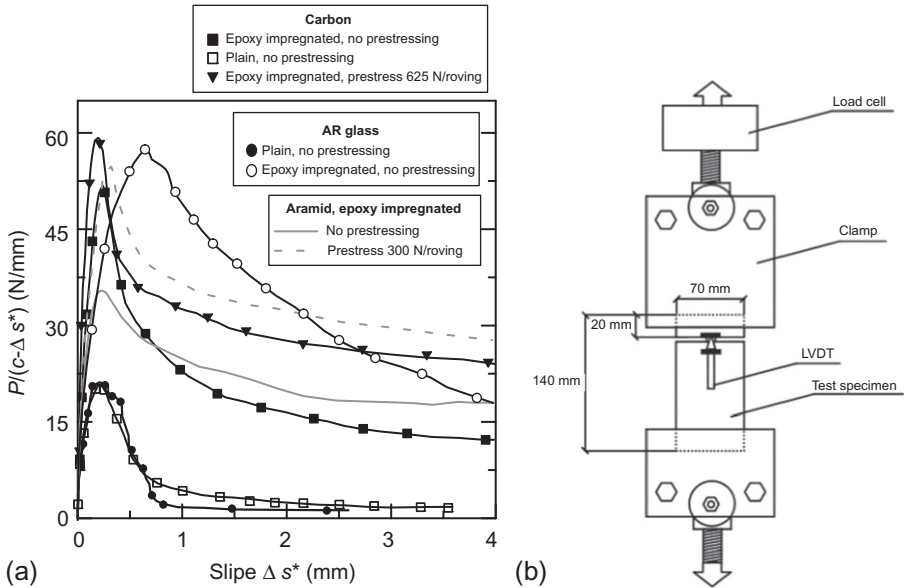
Figure 4.18 (a) Shear force per unit length versus slip of carbon, aramid and alkali resistant (AR) glass textiles (20 °C, 65% relative for 40 days) and (b) the test setup used to obtain the results (two-sided pullout arrangement with 20 mm initial bonding length) (Xu et al., 2004).

Hegger et al. (2006) observed improved composite performance (tensile), due to improved bonding by impregnating AR glass fabric with epoxy resin, as compared to same fabric impregnated in acrylate. Evidence of this improved bonding is seen in the denser crack-spacing pattern and the finer cracks in the epoxy composite. Improvements in composite load-bearing capacity by means of polymer coating were also reported for carbon fabrics (Koeckritz et al., 2010). Greater bond improvements in carbon fabrics and cement matrices were reported by Li and Xu (2011), attained by spreading sand on the polymer coating to promote stronger mechanical anchoring of the carbon textile within the cement matrix. The addition of nanoparticles to the coating was also found to improve composite performance, due to the development of hydration products at the yarn–matrix interface and the corresponding enhancement of interface stiffness in the composites (Scheffler et al., 2009).

One limitation of polymer coating, however, is its relatively low bonding with the cement matrix, due to their opposed chemical characteristics, resulting in composite delamination (Li and Xu, 2011), as evident in Figure 4.19 for an epoxy-impregnated carbon-fabric composite (Zamir et al., 2014). Furthermore, polymer-based fillers are sensitive to high temperatures, which may be problematic during the practical use of such cement-fabric composites.

Therefore, on one hand, it is necessary to overcome these limitations, while maximizing the efficiency of the reinforcement, by filling in the spaces in the filament bundles.
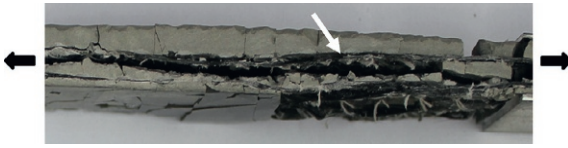
Figure 4.19 Delamination of a cement composite reinforced with carbon fabric impregnated with epoxy, indicated by the arrow (Zamir et al., 2014).

Yet, on the other hand, it is essential to limit the deposition of hydration products between the filaments within the strand during ageing, to preserve the composite's telescopic mechanism and, thus, maintain its ductility (mainly for glass). In order to accomplish both of the above, the spaces between the filaments were filled with nanoparticles, rather than polymers. Mineral nanoparticles (fillers) have been studied and compared to polymer-based coating (Bentur et al., 2010, 2013; Cohen and Peled, 2010, 2012) for AR glass and various aged carbon fabrics made of multifilament yarns. In addition, hybrid fillers, combining polymers and mineral nanoparticles in one bundle, were investigated (Zamir et al., 2014). Good filling (Figure 4.20) and significant improvement in tensile

(a)   (b)

(c)
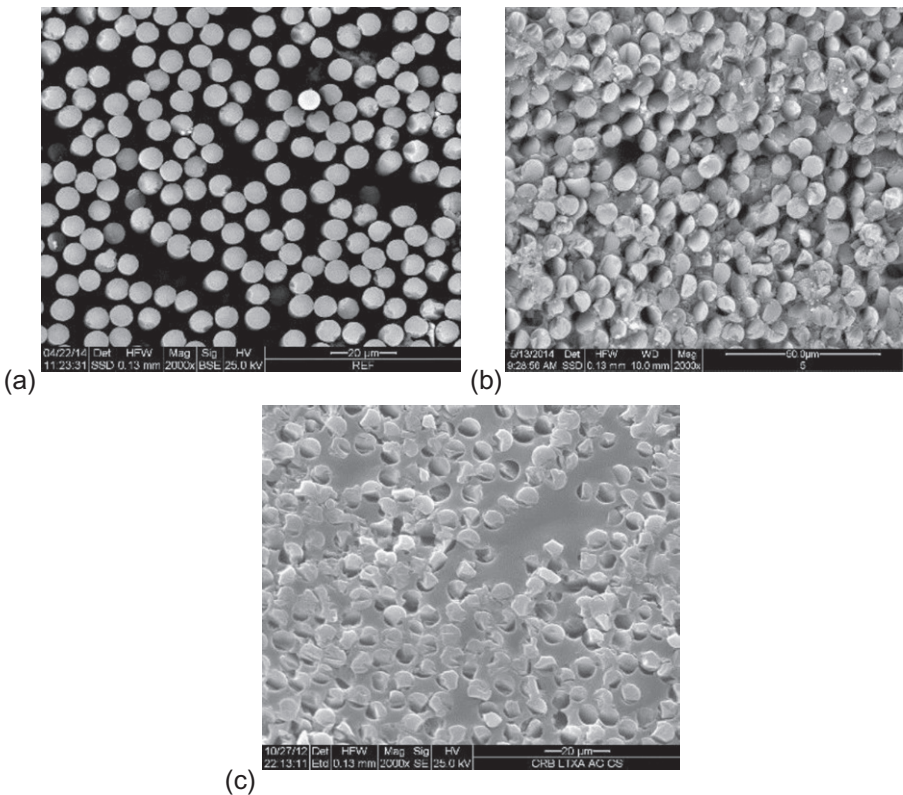
Figure 4.20 SEM micrographs of the cross-sections of a composite reinforced with carbon bundles: (a) with no filler, (b) filled with silica fume and (c) filled with epoxy (Zamir et al., 2014).

strength and toughness were observed in the filled carbon-fabric composites, relative to the reference (with no filler), both at early ages and over time (Figure 4.21).

In carbon fabrics, polymer filler composites exhibited the best mechanical performances (Figures 4.21 and 4.22) and good penetrability in between the bundle filaments (Figure 4.20c). However, they also exhibited low bonding with the cement matrices and critical delamination (Figure 4.19), due to their hydrophobic characteristics, as opposed to the hydrophilic properties of the cement matrices. However, good bundle filling (Figure 4.20b) and strong bonding, with no delamination, was observed for the mineral filler composites (silica fume fillers) with improved tensile properties, relative to the reference composite (Figures 4.21 and 4.22). The poor bonding between the polymer-filled fabric and the matrix was evident in the large crack spacing (Figure 4.22b). In contrast, composites containing mineral fillers exhibited denser cracking patterns (Figure 4.22b), explained by the pozzolanic reaction of the filler
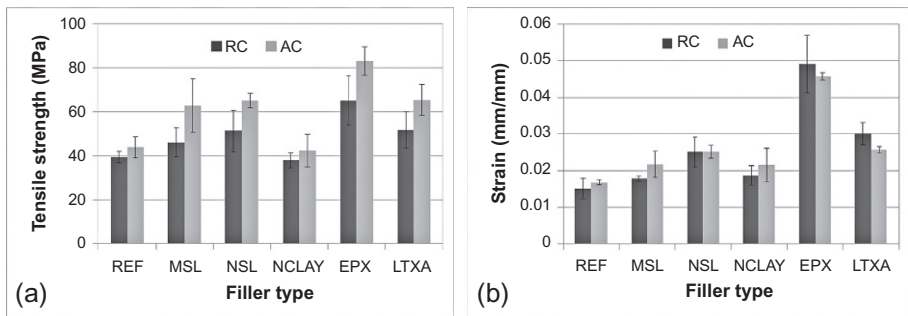
Figure 4.21 Average tensile properties of carbon-fabric composites filled with silica fume with different particle sizes (MSL and NSL) or with polymer (EPX and LTXA) relative to non-impregnated fabric (REF) under regular curing (RC) and accelerated curing (AC): (a) tensile strength and (b) toughness (Zamir et al., 2014).
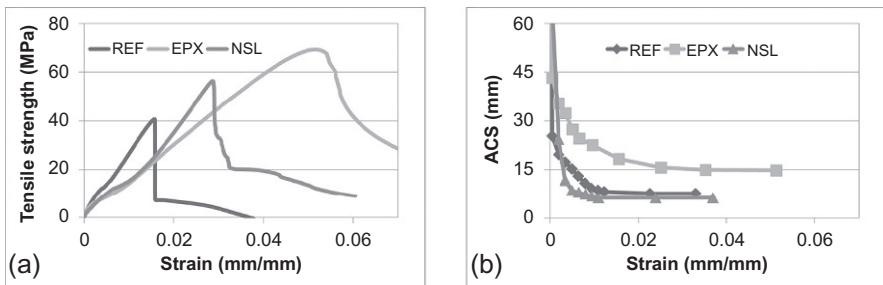
Figure 4.22 (a) Stress–strain curves of three selected composites: REF (unmodified); epoxy-impregnated (EPX); and micron-sized silica fume (MSL) composites and (b) average crack spacing (ACS) versus strain curves of the three composites (cured under regular conditions) (Dvorkin, 2014).
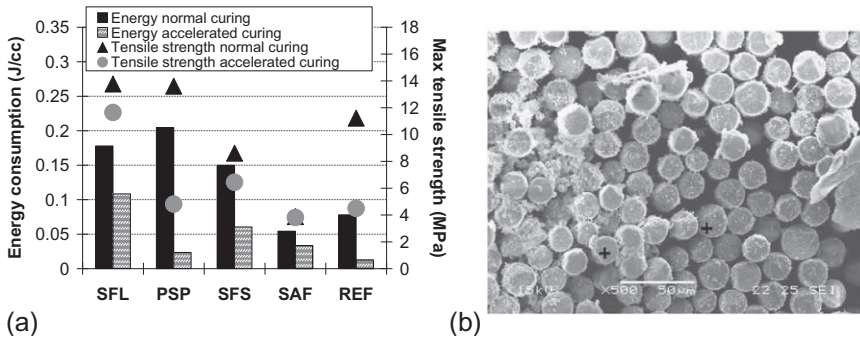
Figure 4.23 (a) Tensile strength and energy consumption of the different composites with various fillers, before and after accelerated ageing; (b) glass bundle embedded in a cement matrix after accelerated ageing, showing some irregularity in filament cross-section shape (two are labelled within the figure), which may imply an alkaline attack (Cohen and Peled, 2010).

with the cement matrix products at the bundle–matrix interface. This promoted greater bonding and improved tensile behaviour (Dvorkin, 2014).

In the glass-fabric composites (Cohen and Peled, 2010, 2012; Bentur et al., 2013), most of the fillers showed improved composite performance before ageing, compared to the reference (without fillers); however, even they could not completely prevent composite embrittlement after ageing (Figure 4.23a). It was the composite with mineral silica fume filler and relatively large particles (200 nm, silica fume large (SFL)) that obtained the best performance, with respect to its initial properties and the retention of strength and energy after ageing, compared to both the smaller silica fume filler (SFL) composite and the polymer (polystyrene) filler composite (polystyrene particle (PSP)). The polymer particles of the PSP filler could not prevent the transition of cement products into the bundle during ageing, nor the consequent chemical attack of the filaments within the bundle (Figure 4.23b). This caused the most drastic reduction in composite properties after accelerated ageing (a more than 60% reduction in strength and a 90% reduction in energy consumption). These results were even worse than those obtained with the aged REF composite, although the PSP filler could highly improve the stress transfer within the bundle to provide high performance at an early age. It was concluded that glass-fabric composites favour filler systems that moderate the penetrability of cement hydrates between the bundle filaments over time. These keep the telescopic pullout mode and composite ductility and, at the same time, protect the core filaments from chemical attack, thus retaining their high performance and the overall tensile strength of the composite.

Bundles may also be treated with detergent, in order to improve their chemical affinity for bonding to the cement matrix; this is especially effective when hydrophobic fibre bundles are considered, for example, PP. Treatment by a surface-active agent was studied on a PP bundle surface, to improve surface wetting and bonding with the cement matrix (Peled et al., 2008). A non-ionic detergent, Triton X100, was used for that purpose and the bond was measured by pullout tests. This treatment changes the

surface properties of the PP fibre and helps fibre–matrix affinity. The maximum pull-out load of the treated bundle was reported to be almost two times greater than that of a non-treated bundle. The improved average bond strength of the treated bundle was about three-fold.

4.3.3.3 Influence of processing

Another parameter that may influence the bonding between fabrics and cement matrices is the composite production method and processing, which affects the efficiency of the bundle's filaments within a cement composite (Vilkner, 2003; Reinhardt and Krüger, 2004; Xu et al., 2004; Peled and Mobasher, 2005, 2006, 2007; Peled et al., 2006).

   The interaction between the processing and the interfacial bond development of woven and knitted fabrics was investigated using two different processing methods: pultrusion and conventional laminated casting. Pullout and tensile tests were conducted (Peled and Mobasher, 2005; Peled et al., 2006). In the pultrusion process, the fabric first passes through a slurry infiltration chamber and is then pulled through a set of rollers to squeeze the paste in between the fabric and the bundle openings. Finally, fabric-cement composite laminate sheets are formed. The advantages of the pultrusion technique, compared to the conventional hand lay-up casting process, have been clearly demonstrated. Pultrusion enhances composite tensile behaviour (Figure 4.24a) by improving the bonding of PP fabric composites, as indicated by the resulting: high pullout resistance (Figure 4.24c), dense crack spacing and fine crack width over the entire loading process (Figure 4.24a). This improvement is explained by the good penetrability of the cement matrix in between the bundle filaments (Figure 4.25a) during the aggressive impregnation process in the pultrusion procedure. Such enhanced composite performance was mainly observed in composites made of knitted fabrics with multifilament yarns and open junction points (Peled and Mobasher, 2005; 2006; 2007; Mobasher et al., 2006; Peled et al., 2006). In knitted fabrics, intensive shear forces are needed during processing to open up the spaces between the filaments and ensure that they are filled with the matrix. The pultrusion process does so effectively, resulting in a stronger bond and the more efficient use of the filaments. The mobilization of the filaments during the pultrusion process causes strain hardening in the composite, even when the yarn modulus is relatively low, as demonstrated by tensile tests of PP fabrics (Figure 4.24a). However, in fabrics with precoated, polymer-filled bundle yarn (Figure 4.25b), the pultrusion process does not offer any advantage from a mechanical point of view. This is because no fibre interstitial spaces are available for impregnation; as such, both casting and pultrusion produce similar composite tensile behaviour (Figure 4.24b) and pullout resistance (Figure 4.24d). Additional pressure applied on top of the laminated composite (immediately after the pultrusion process, while the composite is still fresh) further improves its tensile strength by approximately 40%. It also reduces its ductility by more intensively pushing the matrix into the spaces between the bundle's filaments and the fabric openings (Peled and Mobasher, 2005, 2006). This improved fabric–matrix bonding is evident by the denser crack spacing. In addition, extending the duration of the applied
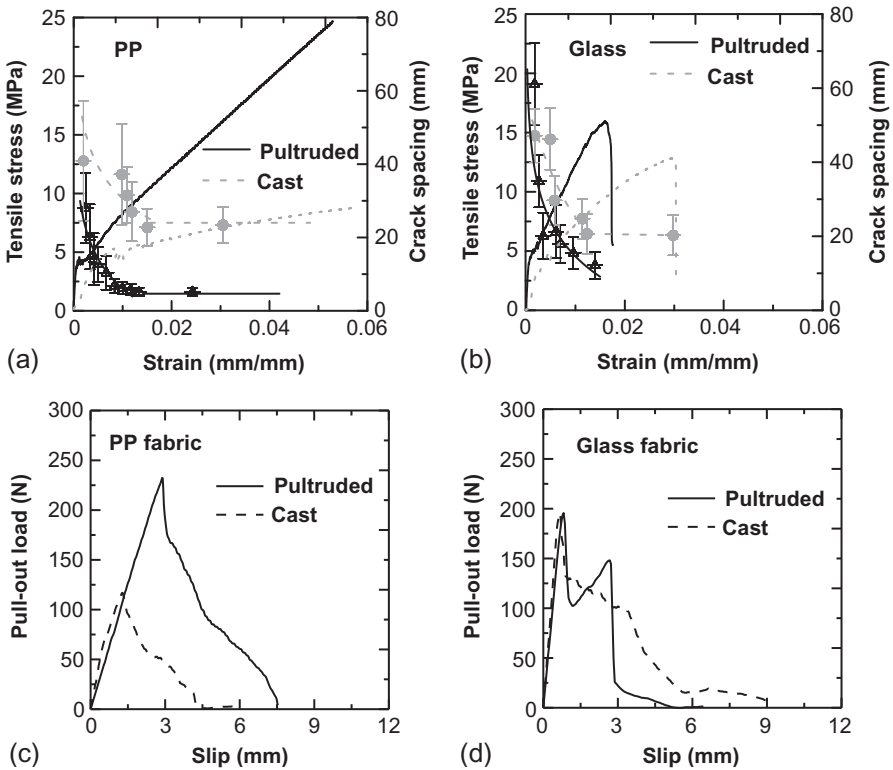
Figure 4.24 Influence of composite production method, cast and pultrusion: (a) and (b) tensile response of composites reinforced with (a) PP and (b) glass fabrics, along with their crack-spacing development (Peled and Mobasher, 2007); (c) and (d) pullout responses of (c) PP and (d) glass fabrics (Sueki et al., 2007).

load was also found to slightly improve composite mechanical behaviour (Peled and Mobasher, 2005) (also see Chapter 11).

Another way of improving fabric–matrix bonding and enhancing the associated composite mechanical performance is by fabric pre-tensioning during composite production via the conventional casting process (Vilkner, 2003; Krüger, 2004; Reinhardt and Krueger, 2004; Xu et al., 2004; Mobasher et al., 2007; Peled, 2007). Pre-tensioning can promote yarn alignment in the loading direction (Mobasher et al., 2007) and, when applied at a high level, it may also improve bonding and composite mechanical performance (Reinhardt and Krueger, 2004; Xu et al., 2004; Peled, 2007). Improvements in bonding may be caused by the development of compression and friction forces between the fabric and the surrounding matrix, due to the release of lateral extension of the yarns after pre-tension. At that time, the fabric shifts back and, therefore, typically exhibits fine cracks in a denser crack pattern (Reinhardt and Krueger, 2004; Xu et al., 2004).
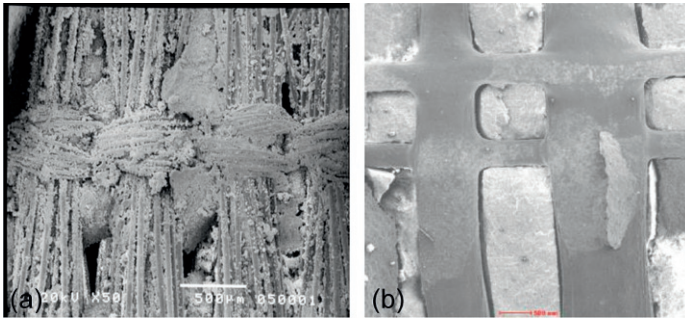
Figure 4.25 Influence of composite production method, cast and pultrusion on cement penetrability in between the yarn and fabric opening: (a) PP and (b) glass fabrics (Peled and Mobasher, 2007; Sueki et al., 2007).

4.3.4 Modelling

The special microstructure of multifilament bundles in a cement matrix and the telescopic mode of failure lead to different bonding mechanisms of the inner and outer filaments. These mechanisms cannot be simply simulated by 'conventional' models, so alternative ones have been developed for this purpose. In general, bundled yarn is characterized by a layered filament structure, in which the bundled filaments are not uniformly bonded; the bond decreases from the external to the internal filaments, and the stress distribution over a roving section is non-uniform. Such non-uniform bonding leads to the successive failure of the filaments, starting from the external towards the internal filaments.

The bond–slip relation in each layer may be described by a smeared bond relation, in which the bond is effective along the entire length of the filament with decreasing quality from the outer filaments towards the inner ones (bond layer model) (Hegger et al., 2004, 2006).

Another approach was taken, in which cement products were present in between the filaments in a discontinuous manner. The filaments were completely embedded in the outer layers and there was a gradual decrease towards the inner filaments (Figure 4.26) (Banholzer, 2006).

The developed models are based on a simple, two-layer structure with a sleeve and a core; or a multilayered structure with a varying number of layers. A simple, two-ring model, containing a sleeve and core system, having two border layers: a 'filament–matrix interface' and a 'filament–filament interface' was introduced by Ohno and Hannant (1994). Their model assumes that there is constant bond stress between the different 'rings', without any consideration of the filaments' tensile failure. A similar concept developed by Hegger et al. (2004, 2006) is a two-layer sleeve-and-core model with a smeared bond between the filaments, in which the bond lessens towards the inner core filaments (bond layer model). That is, this model takes into account the deterioration of the bond with the increasing distance between the
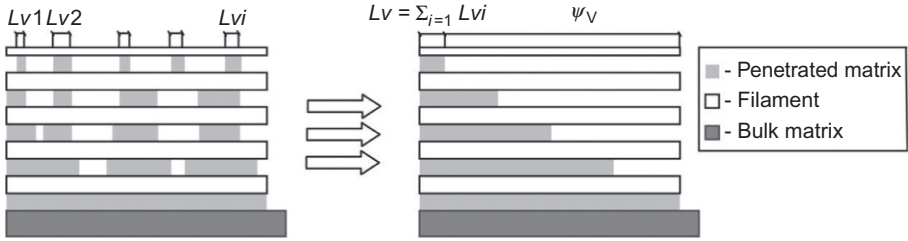
Figure 4.26 The bonding around filaments within a bundle embedded in cement matrix. All individual embedded lengths $L_{v,i}$ of a specific layer are summed up to the entire embedded length, L_v (bonded fraction), and the entire filament-free length, ψ_v (free fraction) (Banholzer, 2004, 2006).

filament and the matrix. The calibrated parameters are the bond quality distribution function and the effective tension strength of the filaments. Hegger et al. (2006) verified this model by means of experimental pullout and tensile tests.

Banholzer et al. (2006) introduced an analytical model based on a multilayer structure with a varying number of layers (not only sleeve and core), as seen in Figure 4.26. This model was based on a ring-layered structure (Figure 4.27) consisting of m layers with $o(v)$ filaments per layer (for $1 \leq v \leq m$), where each layer, v, carries an average pullout load of $p_v(\Omega)$. In this model, the outer layer of filaments fails first, followed by the successive failure of the adjacent layers, until the core filaments are finally pulled out. If the pullout response, $P(\omega)$, of every single filament, i, for $1 \leq i \leq N_{F,m}$ at every single load step is known, then the resulting load displacement relationship and, hence, the overall response of the yarn, $P(\Omega)$, may be calculated by a simple summation procedure. In this procedure, $N_{F,m}$ corresponds to the number of filaments per yarn and Ω to the displacement measured during the yarn pullout test. The above model was justified by the FILT test and was also able to simulate the reduction in the active filaments (those that didn't failed) versus load relationship $N_F(\Omega)$
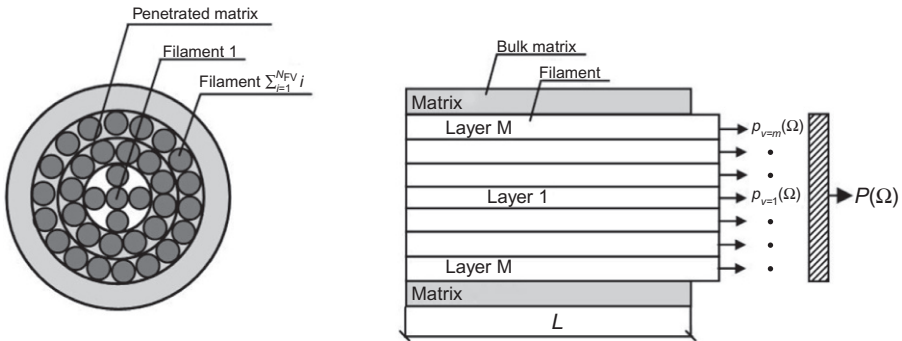
Figure 4.27 Modelling of the failure mechanism of a strand embedded in a cement-based matrix under a pullout load (Banholzer, 2004, 2006).
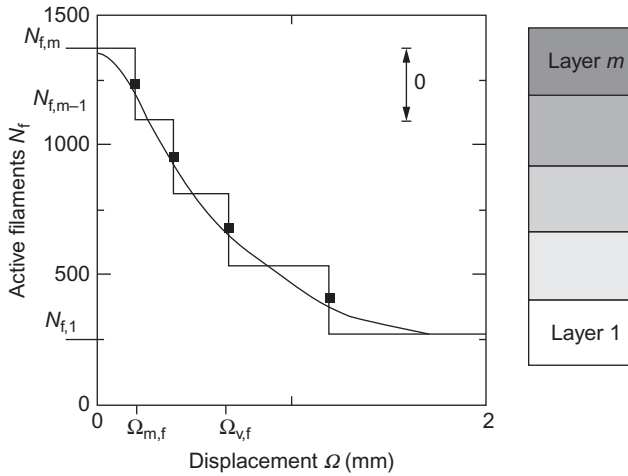
Figure 4.28 Active filaments versus displacement relation, $N_{F(\Omega)}$, obtained during a pullout test (Banholzer, 2004, 2006).

(Figure 4.28) by means of a step-wise calculation. This model is based on several assumptions:

- the filaments carry only normal loads,
- the matrix that penetrated in between the filaments carries only shear,
- the bond law between the bonded single filaments and the matrix is bond stress versus slip relations (BSR) $\tau(s)$, and
- the BSR $\tau(s)$ is identical for all the filaments in the different bundle layers.

An analytical description of the pullout behaviour of a yarn in a cement-based matrix under a pullout load is presented in Equation (4.20), assuming that:

- the average pullout force, p_v, of a layer, v, is governed only in the embedded region of the filament, L_v (only the portion of the filament embedded in the matrix, see Figure 4.26);
- the corresponding displacement, Ω, of a layer, v, consists of two components:
  - (I) the slip, ω, of the filaments;
  - (II) the elongation, Δ, resulting from the deformation of the filaments over the free length, Ψ_v, (see Figure 4.26):

$$P(\Omega) = \sum_{v=1}^{m} P_v(\Omega = \omega + \Delta) \equiv \sum_{v=1}^{m} P_v(\omega) \times o, \quad \Delta = \frac{P_v(\omega)}{E_f A_f} \frac{(\Omega_{v,f} - \omega_{v,f}) \times E_F}{f_{v,t}} \tag{4.20}$$

where the average pullout response, $p_v(\Omega)$, of layer, v, is equivalent to o times the response, $P_v(\omega)$, of a filament in a single filament pullout test; E_F is the Young's modulus of the filament and A_F is the filament's cross-sectional area; $f_{v,t}$ is the tensile strength of the filaments (it may be layer-dependent); and $\omega_{v,f}$ is the corresponding pullout displacement.

This model has demonstrated the ability to fit various pullout curves, $P(\Omega)$, for different numbers of layers, and is supported by experimental results.

An adhesive, cross-linkage model was introduced by Schorn (2003, 2004) and Lepenies et al. (2007). This model was also based on a discontinuous (random) distribution of the hydration products in between the bundle filaments. These discrete cement products act as adhesive cross-linkages between the filaments and are responsible for the bonds between adjacent filaments. The amount of adhesive cross-linkages was assumed to decrease from the peripheries to the centre of the bundle.

For the purpose of modelling, these distributed cross-linkages were grouped together into continuous solid regions, while leaving various unbonded free lengths, $l_v(r)$ (Figure 4.29a); l_{max}, is the free length portion of the external filament, l_R. Thus, the individual filaments are differently restrained, according to their relative positions within the bundle, causing higher stresses in the external filaments (σ_{max}) at the bundle periphery (sleeve filaments), and decreasing towards the core filaments (Figure 4.29a). The filaments with the fewest free lengths fail first when the matrix cracked, because the stress build-up in them is higher than in the core, while the remaining filaments carry the loads (Figure 4.29b). Any further increase in crack width causes successive tensile failures of the filaments, as they reach their rupture elongation (according to their effective free length). As such, the total tensile strength of a bundle, $F(w)$, may be calculated at different loading stages (i.e. different crack openings):

$$F(w) = \int \sigma(r)\mathrm{d}A = \int_{r=0}^{R} E \frac{w}{l_w(r)} \mathrm{d}A \qquad (4.21)$$

where E is the Young's modulus of the filament; w is the half-crack width; R is the circular yarn radius; $l_w(r)$ is the free length profile; A is the cross-section of the yarn (for circular cross-sections, $\mathrm{d}A = 2\pi r \mathrm{d}r$); and $\sigma(r)$ is the individual filament stress relative to its position within the bundle.

This model distinguishes between brittle and quasi-ductile roving failure, depending on the extent of hydration-product impregnation within the roving. It was confirmed by means of finite element analyses, using either a continuous, smeared (effective) interface parameter (Zastrau et al., 2003; Richter, 2005;
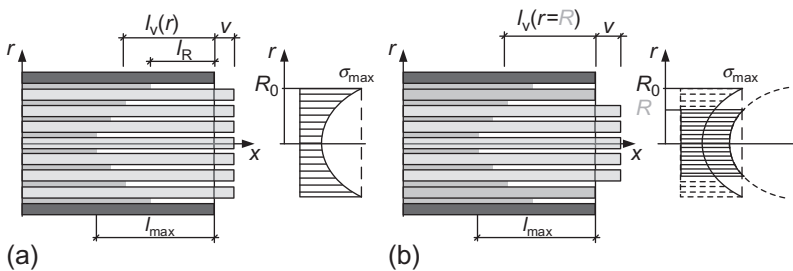
Figure 4.29 Free length zones within a bundle and related stress distributions: (a) before loading (non-broken filaments) and (b) after failure of the external filaments (Lepenies et al., 2007).
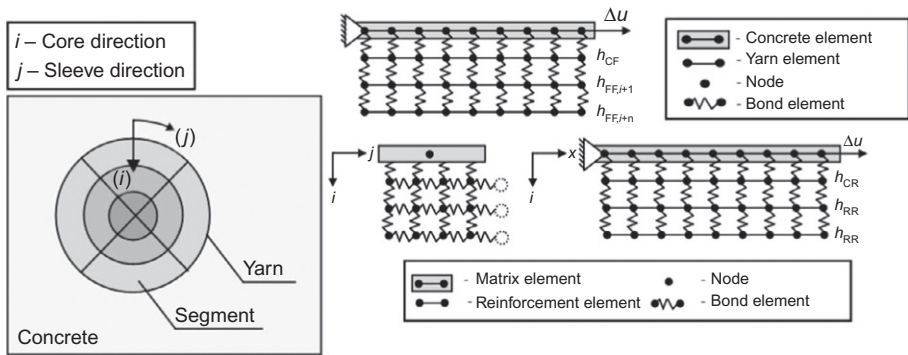
Figure 4.30 Multilayered, finite-element model based on bundle yarn segmentation (Haussler-Combe and Hartig, 2007; Hartig et al., 2008).

Richter and Zastrau, 2006; Richter et al., 2002; Zastrau et al., 2008) or a discontinuous bond model with randomly distributed adhesive cross-linkages.

Haussler-Combe and Hartig (2007) and Hartig et al. (2008) developed analytical models based on multilayered structures with smeared bonds, as shown in Figure 4.30.

Their basic assessment was that a yarn in a fabric cannot be homogeneous over its cross-section; thus, it is divided into either one or several segments, according to the number of filaments composing the yarn. In some cases, a group of filaments may be treated together as one segment, if the whole group is homogeneous over its cross-section, as well as throughout the concrete. Such segmentation in the sleeve (tangential) and the core (radial) directions, arranged schematically like a matrix, is shown in Figure 4.30. Note that the bond elements connect the concrete and the yarn segments at the nodes. Here, two types of bond laws were introduced: $h_{CF}(s)$ for concrete–filament interaction and $h_{FF}(s)$ for filament–filament interaction, where s is the slip between a segment and its neighbours. Based on this model, the influence of several bond properties on composite tensile behaviour has been investigated by a parametric study using finite-element analysis to determine the stress distribution, as well as the ultimate mean stresses and mean strains of uniaxial tensile specimens.

4.4 Bonding in a fabric

The influence of fabric-textile structures on bonding with cement matrices and their consequential influence on the control of the mechanical performance of cement composites was studied by Bentur et al. (1997), Peled et al. (1997, 1998a,b, 1999) and Peled and Bentur (2000, 2003). Geometric characteristics were investigated, taking into consideration the nature of the basic reinforcing unit in the fabric (yarn) and the various geometries by which these yarns are combined together in the fabric. Bonding was evaluated by pullout tests (similar to those presented in Figure 4.7b) performed on the individual yarns used to produce the fabrics and on the fabrics

themselves. Warp-knit, short-weft and weft-insertion fabrics were compared to woven fabrics in a plain weave with various fills (transverse yarns) and differing densities – parameters that change the crimp geometry of the individual yarn within the woven fabric. The woven and short-weft knitted fabrics were made of low modulus ($E = 260$ MPa) monofilament PE yarns. The warp-knitted, weft-insertion fabrics were made of multifilament yarns of low modulus ($E = 500$ MPa) PP and high modulus ($E = 1960$ MPa) PE. The geometry of a given fabric might enhance the bonding and achieve strain-hardening behaviour from low modulus yarn fabrics, due to the special shape of the yarn induced by the fabric. The bond strength values obtained in this work are presented in Table 4.1.

Note that the bonding behaviour of single yarns is correlated with the mechanical properties of the fibres; the yarns with a higher modulus exhibit higher bond strength, as expected (Stang, 1996) (also see Figure 4.1). However, in the actual fabric, no clear correlation between the bond and the modulus of elasticity is observed. High-modulus fabric exhibits relatively low bond strength, as compared with the bond strength of low-modulus fabric. These differences are attributed to the differences in the geometrical characteristics of the yarns within the fabric. The crimped shape in the woven fabric tends to increase the bonding, while the multifilament nature of weft-insertion, knitted fabrics tends to decrease bonding, due to the limited penetration of the matrix.

The effect of the crimp shape of the individual yarns within the woven fabric (yarns unravelled from the woven fabric) was further investigated, taking into account two parameters: the wave amplitude and the wave length. The maximum pullout resistance was greater for the crimped yarn with the larger amplitude, that is, for the yarn with the 0.13 mm amplitude (Figure 4.31a), indicating that wave amplitude makes a major contribution to bonding. A linear correlation may be established when plotting the

Table 4.1 **Bond characteristics of single straight yarn and yarn in the fabric (Peled and Bentur, 2003)**

Yarn type	Modulus of elasticity (MPa)	Number of filaments in a bundle	Bond per unit external bundle surface (MPa)		Bond of yarn in a fabric relative to the bond of a straight yarn[a] (%)
			Single straight yarn	Fabric	
PE (woven)	1760	1	0.17	1.2	700
7 yarns/cm[b]					
5 yarns/cm[b]				0.73	430
PP (knit)	6900	100	3.5	2.8	80
HDPE (knit)	55,000	900	11.5	1.8	15

Note that the knit fabrics are weft insertion type.
[a]Calculated per single filament.
[b]Density of yarn perpendicular to reinforcing direction.
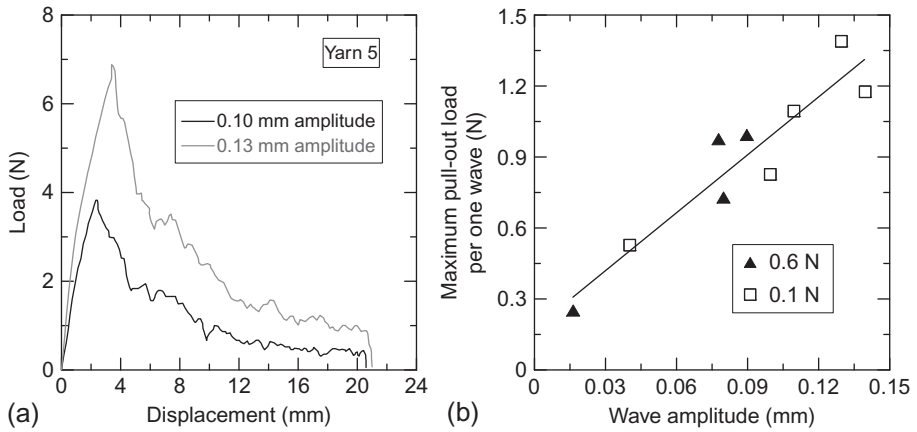
Figure 4.31 Effects of wave amplitude on the pullout resistance of untied crimped yarns: (a) load-displacement response of crimped yarns with different wave amplitudes and (b) maximum pullout load per one wave versus wave amplitude of different crimped yarns (Peled and Bentur, 2003).

pullout resistance per one wave versus the wave amplitude of the different crimped yarns (Figure 4.31b) (Peled et al., 1997; Peled and Bentur, 2003).

The linear regression ($R = 0.88$) obtained from the data presented in Figure 4.31b is as follows:

$$p = 8Amp + 0.18 \tag{4.22}$$

where p is the pullout resistance per one wave (N); Amp is the crimped yarn amplitude (mm); and 0.18 is the constant that reflects the contribution of the straight yarn per unit length.

Based on this relation, the maximum pullout resistance, P_{max}, per unit length was calculated by multiplying the pullout resistance per one wave in Equation (4.23) by the number of waves per unit length:

$$P_{max} = p\frac{l_e}{\lambda} = (8Amp + 0.18)\left(\frac{l_e}{\lambda}\right) \tag{4.23}$$

where P_{max} is the total pullout resistance (N); l_e is the embedded length (mm) and l is the wave length (mm).

A comparison of the calculated P_{max}, based on Equation (4.23) and the experimental pullout values, shows an excellent agreement for two embedded lengths, 10 and 20 mm (Figure 4.32a).

The same empirical approach was applied to calculate the contribution of the crimped yarns to the overall bonding in the woven fabric (Figure 4.32b), suggesting that most of the pullout resistance in the woven fabric may be attributed to the crimped geometries of its individual yarns, due to a strong anchoring effect. Because the

(a)

(b)
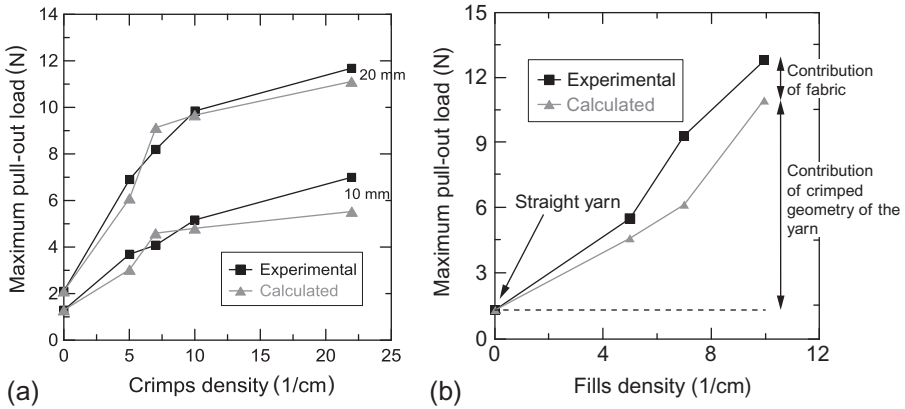
Figure 4.32 Comparison between the calculated maximum pullout resistance values and the experimental results of: (a) untied crimped yarns and (b) woven fabrics (Peled et al., 1998b).

calculated values are only slightly lower than the experimental results and only a small contribution may be related to the fabric structure, perhaps some anchoring is provided by the perpendicular yarns.

Differences in the bonding that may be attributed to the overall fabric structure and to the shapes of the individual yarns are reflected in the flexural properties of the entire cement composite (Figure 4.33). They demonstrate opposing influences – the improved performance of woven and short-weft, knitted fabrics (compared to that of straight-yarn fabrics; Figure 4.33a and b) and the drastic reduction in the performance of

(a)

(b)
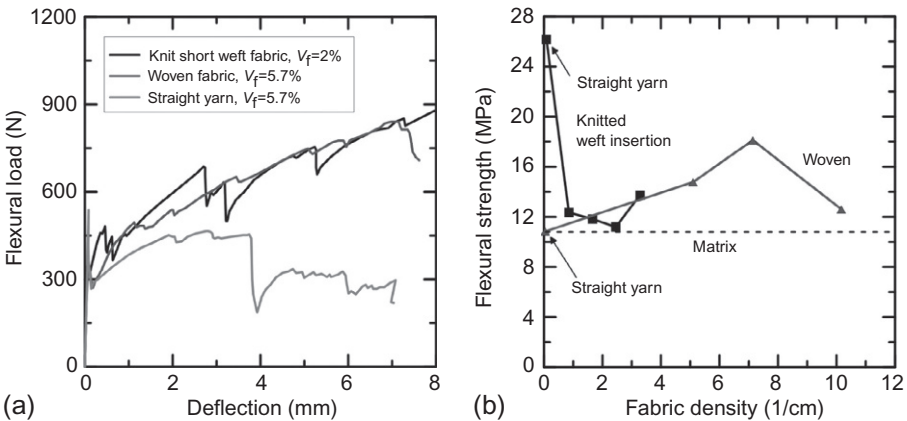
Figure 4.33 Flexural properties of cement composites reinforced with various fabric structures: (a) flexural behaviours of woven fabric (with 7 fills per cm), short-weft knitted fabric and straight-yarn composites and (b) effects of the densities of yarns perpendicular to the load direction on the flexural strength of knitted, weft-insertion fabrics made of HDPE yarns and woven fabrics made of PE yarns. (The results for composites with straight yarns = 0.) (Peled and Bentur, 2003).

weft-insertion, knitted fabrics (also compared to that of straight-yarn fabrics; Figure 4.33b). This is explained by the differences in the shapes and natures of the individual yarns that affect bonding in the different fabrics. Remember that weft-insertion, knitted fabrics have bundled yarns and a straight geometry, providing low bonding; whereas woven and short-weft, knitted fabrics are monofilamental and do not maintain a straight geometry. Rather, they have crimp geometry in woven fabrics (Figure 4.2a) and have relatively complex 'zigzag' geometries in short-weft, knitted fabrics (Figure 4.2c), which are characterized by strong mechanical anchoring and high bonding. In the short-weft fabric, the reinforcing yarn shape is more complex than the crimping geometry of the yarn in the woven fabric. Moreover, these yarns are also held tightly by the knitted-fabric structure, which apparently induces extremely strong anchoring effects. In the weft-insertion knitted fabrics, the yarns are bundled and straight, as well as being connected at the joint points by stitches. This leads to poor penetration of the matrix between the filaments, partially due to the presence of the bulky stitches themselves, in addition to their tightening effect. This strongly holds the filaments in the bundle and prevents spaces from being opened between them. Thus, high-density PE (HDPE) knitted fabrics show poor performance relative to the superior properties of their yarns and, as such, are no better than low modulus PE fabrics (Peled and Bentur, 2003). It was concluded that the geometry of a fabric has a marked effect on the properties of its composites. At one extreme, the fabric geometry may enhance bonding and bring about strain-hardening behaviour in low-modulus yarn composites. At the other extreme, it may drastically reduce the efficiency of high-performance bundled yarns that are very effective as reinforcement, when they are not a part of the fabric.

4.5   Summary

A significant number of experimental and analytical investigations have characterized the bond between fibre and the cement matrix, exploring different types of single fibres of high and low modulus with different geometries. However, the bonding of fabric reinforcement is much more complicated, due to the function of the yarns transverse to the load direction and the complex geometries of the individual reinforcing yarns that make up the fabric. These yarns provide anchorage, as well as the mono- or multifilament nature of the yarn. The bonding mechanism and the microstructure in the vicinity of the yarn/fabric, that is, at the yarn (fabric)–matrix interface can be rather different, depending on: the form of the yarn (mono- or multifilament), the fabric and its yarn geometry, the composition of the yarn (fibre) material and yarn coating and filling.

References

Alwan, J.M., Naaman, A.E., Hansen, W., 1991. Pull-out work of steel fibers from cementitious composites: analytical investigation. Cem. Concr. Compos. 13, 247–255.
Alwan, J.M., Naaman, A.E., Guerrero, P., 1999. Effect of mechanical clamping on the pull-out response of hooked steel fibers embedded in cement matrices. Concr. Sci. Eng. J. 1, 15–25.

Aveston, J., Kelly, A., 1973. Theory of multiple fracture of fibrous composites. J. Mater. Sci. 8, 352–362.

Aveston, J., Cooper, G.A., Kelly, A., 1971. Single and multiple fracture. In: The Properties of Fibre Composites: Conference Proceedings – National Physical Laboratory. IPC Science and Technology Press, Guilford, pp. 15–24.

Banholzer, B., 2004. Bond behavior of a multifilament yarn embedded in a cementious matrix. Ph.D. Dissertation, Rheinisch-Westfälische Technische Hochschule, Aachen.

Banholzer, B., 2006. Bond of a strand in a cementitious matrix. Mater. Struct. 39, 1015–1028.

Banholzer, B., Brameshuber, W., Jung, W., 2005. Analytical simulation of pull-out tests: the direct problem. Cem. Concr. Compos. 27, 93–101.

Banholzer, B., Brockmann, T., Brameshuber, W., 2006. Material and bonding characteristics for dimensioning and modelling of textile reinforced concrete (TRC) elements. Mater. Struct. 39, 749–763.

Bansal, S.K., 2007. The development of micro-mechanical model of kevlar fabrics used in engine containment system of aircrafts. M.Sc. Dissertation, Arizona State University, Phoenix.

Bartos, P., 1984. Analysis of the pull-out tests on fiber embedded in brittle matrices. J. Mater. Sci. 19, 1680–1691.

Bartos, P., 1987. Brittle matrix composites reinforced with bundles of fibres. In: From Material Science to Construction Materials: Proceedings of the RILEM Symposium. Chapman & Hall, London, pp. 539–546.

Bentur, A., Mindess, S., 2007. Fiber Reinforced Cementitious Composites, second ed. Taylor & Francis, New York.

Bentur, A., Peled, A., Yankelevsky, D., 1997. Enhanced bonding of low modulus polymer fibers–cement matrix by means of crimped geometry. Cem. Concr. Res. 27 (7), 1099–1111.

Bentur, A., Tirosh, R., Yardimci, M., Puterman, M., Peled, A., 2010. Bonding and microstructure in textile reinforced concrete. In: Textile Reinforced Concretes: Proceedings of the International RILEM Conference on Material Science (MatSci), vol. 1. RILEM Publications, Aachen, pp. 23–33.

Bentur, A., Yardimci, M.Y., Tirosh, R., 2013. Preservation of telescopic bonding upon aging of bundled glass filaments by treatments with nano-particles. Cem. Concr. Res. 47, 69–77.

Brameshuber, W. (Ed.), 2006. Textile Reinforced Concrete: State of the Art Report (RILEM TC-201-TRC, Report 36). RILEM Publications, Aachen.

Brameshuber, W., Brockmann, T., Banholzer, B., 2006. Material and bonding characteristics for dimensioning and modeling of textile reinforced concrete (TRC) elements. Mater. Struct. 39, 749–763.

Butler, M., Hempel, R., Schorn, H., 2006. Bond behavior of polymer impregnated AR-glass textile reinforcement in concrete. In: Proceedings of the International Symposium – Polymers in Concrete (ISPIC). University of Minho, Guimaraes, pp. 173–183.

Cohen, Z., Peled, A., 2010. Controlled telescopic reinforcement system of fabric-cement composites: durability concerns. Cem. Concr. Res. 40, 1495–1506.

Cohen, Z., Peled, A., 2012. Effect of nanofillers and production methods to control the interfacial characteristics of glass bundles in textile fabric cement-based composites. Composites A 43, 962–972.

Cox, H.L., 1952. The elasticity and strength of paper and other fibrous materials. Br. J. Appl. Phys. 3, 72–79.

Dolatabadi, M.K., Janetzko, S., Gries, T., Sander, A., Kang, B.G., 2011. Permeability of AR-glass fibers roving embedded in a cementitious matrix. Mater. Struct. 44 (1), 245–251.

Dvorkin, D., 2014. Telescopic pull-out failure mechanism in textile reinforced cement-based composites. M.Sc. Dissertation, Ben-Gurion University of the Negev, Beer-Sheva.

Gao, S.L., Mäder, E., Plonka, R., 2004. Coatings for glass fibers in a cementitious matrix. Acta Mater. 52, 4745–4755.

Glowania, M., Gries, T., 2010. Coating of high-performance fibers and textiles for textile reinforced concrete. In: 8th International fib PhD Symposium in Civil Engineering. Technical University of Denmark (DTU), Kongens Lyngby, pp. 79–89.

Gray, R.J., 1984. Analysis of the effect of embedded fiber length on fiber debonding and pull-out from elastic matrix. Part 1: review of theories. J. Mater. Sci. 19, 861–870.

Hartig, J., Hausller-Combe, U., Schicktanz, K., 2008. Influence of bond properties on the tensile behavior of textile-reinforced concrete, cement and concrete composites. Cem. Concr. Compos. 30, 898–906.

Hartig, J., Jesse, F., Schicktanz, K., Haussler-Combe, U., 2012. Influence of experimental setups on the apparent uniaxial tensile load-bearing capacity of textile reinforced concrete specimens. Mater. Struct. 45, 433–446. http://dx.doi.org/10.1617/s11527-011-9775-0.

Haussler-Combe, U., Hartig, J., 2007. Bond failure mechanisms of textile reinforced concrete (TRC) under uniaxial tensile loading. Cem. Concr. Compos. 29, 279–289.

Hegger, J., Bruckermann, O., Chudoba, R., 2004. A smeared bond–slip relation for multi-filament yarns embedded in fine concrete. In: 6th RILEM Symposium on Fibre Reinforced Concrete (FRC)-BEFIB. RILEM Publications, Varenna, pp. 1453–1462.

Hegger, J., Will, N., Bruckermann, O., Voss, S., 2006. Load–bearing behaviour and simulation of textile reinforced concrete. Mater. Struct. 39, 765–776.

Koeckritz, U., Cherif, C., Weiland, S., Curbach, M., 2010. In situ polymer coating of open grid warp knitted fabrics for textile reinforced concrete application. J. Ind. Text. 40 (2), 157–169.

Krüger, M., 2004. Prestressed textile reinforced concrete. Ph.D. Dissertation, Institute of Construction Materials, University of Stuttgart, Stuttgart (in German).

Krüger, M., Ožbolt, J., Reinhardt, H.-W., 2002. A discrete bond model for 3D analysis of textile reinforced and prestressed concrete elements. Otto-Graf J. 13, 111–128.

Krüger, M., Ožbolt, J., Reinhardt, H.-W., 2003. A new 3D discrete bond model to study the influence of bond on the structural performance of thin reinforced and prestressed concrete plates. In: Fourth International Workshop on High Performance Fiber Reinforced Cement Composites (HPFRCC-4). RILEM Publications, Ann Arbor, pp. 49–63.

Lawrence, P., 1972. Some theoretical considerations of fiber pull-out from an elastic matrix. J. Mater. Sci. 7, 1–6.

Lepenies, I., Meyer, C., Schorn, H., Zastrau, B., 2007. Modeling of load transfer behavior of AR glass rovings in textile reinforced concrete. Am. Concr. Inst. SP 244 (7), 109–124.

Li, Q., Xu, S., 2011. Experimental research on mechanical performance of hybrid fiber reinforced cementitious composites with polyvinyl alcohol short fiber and carbon textile. J. Compos. Mater. 45 (1), 5–28.

Mallikarjuna, M., Banthia, N., 1991. Macromechanics modeling of steel fiber pull-out from cementitious matrices. In: Proceedings of the 3rd International Symposium on Brittle Matrix Composites. Elsevier Science Publishers, London, pp. 173–183.

Mobasher, B., 2012. Mechanics of Fiber and Textile Reinforced Cement Composites. CRC Press, Boca Raton.

Mobasher, B., Jain, N., Aldea, C.M., Soranakom, C., 2007. Mechanical properties of alkali resistant glass fabric composites for retrofitting unreinforced masonry walls. Am. Concr. Inst. SP 244 (8), 124–140.

Mobasher, B., Pahilajani, J., Peled, A., 2006. Analytical simulation of tensile response of fabric reinforced cement based composites. Cem. Concr. Compos. 28, 77–89.

Naaman, E.A., Namur, G.G., Alwan, J.M., Najm, H.S., 1991a. Fiber pullout and bond slip I: analytical study. J. Struct. Eng. 117 (9), 2769–2790.

Naaman, E.A., Namur, G.G., Alwan, J.M., Najm, H.S., 1991b. Fiber pullout and bond slip II: experimental validation. J. Struct. Eng. 117 (9), 2791–2800.

Ohno, S., Hannant, D.J., 1994. Modelling the stress–strain response of continuous fibre reinforced cement composites. Am. Concr. Inst. Mater. J. 91 (3), 306–312.

Ožbolt, J., Lettow, S., Kožar, I., 2002. Discrete bond element for 3D FE analysis of reinforced concrete structures. In: Beiträge aus der Befestigungstechnik und dem Stahlbetonbau. Ibidem-Verlag, Stuttgart, pp. 239–258.

Peled, A., 2007. Pre-tensioning of fabrics in cement-based composites. Cem. Concr. Res. J. 37 (5), 805–813.

Peled, A., Bentur, A., 1998. Reinforcement of cementitious matrices by warp knitted fabrics. Mater. Struct. 31, 543–550.

Peled, A., Bentur, A., 2000. Geometrical characteristics and efficiency of textile fabrics for reinforcing composites. Cem. Concr. Res. 30, 781–790.

Peled, A., Bentur, A., 2003. Fabric structure and its reinforcing efficiency in textile reinforced cement composites. Composites A 34, 107–118.

Peled, A., Mobasher, B., 2005. Pultruded fabric-cement composites. Am. Concr. Inst. Mater. J. 102 (1), 15–23.

Peled, A., Mobasher, B., 2006. Properties of fabric-cement composites made by pultrusion. Mater. Struct. 39, 787–797.

Peled, A., Mobasher, B., 2007. Tensile behavior of fabric cement-based composites: pultruded and cast. J. Mater. Civil Eng. 19 (4), 340–348.

Peled, A., Yankelevsky, D., Bentur, A., 1997. Microstructural characteristic of cementitious composites reinforced with woven fabrics. Adv. Cem. Res. J. 9 (36), 149–155.

Peled, A., Bentur, A., Yankelevsky, D., 1998a. Effect of woven fabric geometry on the bonding performance of cementitious composites: mechanical performance. Adv. Cem. Based Mater. J. 7 (1), 20–27.

Peled, A., Bentur, A., Yankelevsky, D., 1998b. The nature of bonding between monofilament polyethylene yarns and cement matrices. Cem. Concr. Compos. J. 20 (4), 319–328.

Peled, A., Bentur, A., Yankelevsky, D., 1999. Flexural performance of cementitious composites reinforced with woven fabrics. J. Mater. Civil Eng. 11 (4), 325–330.

Peled, A., Sueki, S., Mobasher, B., 2006. Bonding in fabric-cement systems: effects of fabrication methods. J. Cem. Concr. Res. 36 (9), 1661–1671.

Peled, A., Zaguri, E., Marom, G., 2008. Bonding characteristics of multifilament polymer yarns and cement matrices. Composites A 39 (6), 930–939.

Raupach, M., Orlowski, J., De Bolster, E., Van Itterbeeck, P., Wastiels, J., Cuypers, H., 2006a. Durability of glass fibre reinforced composites experimental methods and results. Compos. A Appl. Sci. Manuf. 37, 207–215.

Raupach, M., Orlowski, J., Büttner, T., Dilthey, U., Schleser, M., 2006b. Epoxy-impregnated textiles in concrete: load bearing capacity and durability. In: Proceedings of the 1st International RILEM Conference on Textile Reinforced Concrete. RILEM Publications, Aachen, pp. 77–88.

Reinhardt, H.W., Krueger, M., 2004. Prestressed concrete plates with high strength fabrics. In: PRO 39: 6th International RILEM Symposium on Fibre-Reinforced Concretes (FRC) – (BEFIB'2004). RILEM Publications, Aachen, pp. 187–196.

Richter, M., 2005. Development of mechanical models to describe material properties of textile reinforced fine-grained concrete. Ph.D. Dissertation, Technische Universität Dresden, Dresden (in German).

Richter, M., Zastrau, B.W., 2006. On the nonlinear elastic properties of textile reinforced concrete under tensile loading including damage and cracking. Mater. Sci. Eng. A: Struct. Mater. 422, 278–284.

Richter, M., Lepenies, I., Zastrau, B., 2002. On the influence of the bond behavior between fiber and matrix on the materials properties of textile reinforced concrete. In: Proceedings of the International Symposium 'Anisotropic Behaviour of Damaged Materials' (ABDM'2002). ABDM, Krakow, pp. 1–24.

Sasi, E.A., Peled, A., 2015. 3D fabrics as reinforcement for cement-based composites. Composites A 74, 153–165.

Scheffler, C., Gao, S.L., Plonka, R., Mader, E., Hempel, S., Butler, M., Mechtcherine, V., 2009. Interphase modification of alkali-resistant glass fibres and carbon fibres for textile reinforced concrete II: water adsorption and composite interphases. Compos. Sci. Technol. 69, 905–912.

Schleser, M., 2008. Einsatz polymerimprägnierter, alkaliresistenter Glastextilien zur bewehrung zementgebundener matrices. Ph.D. Dissertation, Institut für Schweißtechnikund Fügetechnik der RWTH Aachen University, Aachen (in German).

Schorn, H., 2003. Ein Verbundmodell für Glasfaserbewehrungen im Beton. Bautechnik 80 (3), 174–180 (in German).

Schorn, H., 2004. An adhesive cross-linkage model for textile reinforcement in concrete. In: 2nd International Conference on Structural Engineering, Mechanics and Computation (SEMC). SEMC, Cape Town, pp. 1563–1567.

Schorn, H., Hempel, R., Butler, M., 2003. Mechanismen des Verbundes von textilbewehrtem Beton. In: Tagungsband 15. Internationalen Baustofftagung ibausil, vol. 2. Bauhaus-Universität, Weimar, pp. 247–270 (in German).

Stang, H., 1996. Significance of shrinkage-induced clamping pressure in fiber–matrix bonding in cementitious composite materials. Adv. Cem. Based Mater. 4, 106–115.

Sueki, S., Soranakom, C., Mobasher, B., Peled, A., 2007. Pullout-slip response of fabrics embedded in cement paste matrix. J. Mater. Civil Eng. 19 (9), 718–727.

Vilkner, G., 2003. Glass concrete thin sheets reinforced with prestressed aramid fabrics. Ph.D. Dissertation, Columbia University, New York.

Weichold, O., 2010. Preparation and properties of hybrid cement-in-polymer coatings used for the improvement of fiber–matrix adhesion in textile reinforced concrete. J. Appl. Polym. Sci. 116, 3303–3309.

Xu, S., Krüger, M., Reinhardt, H.W., Ožbolt, J., 2004. Bond characteristics of carbon, alkali resistant glass and aramid textiles in mortar. J. Mater. Civil Eng. 16 (4), 356–364.

Zamir, M., Dvorkin, D., Peled, A., 2014. Fabric cement-based composites with nanoparticles filler, interfacial characteristics. In: 3rd International RILEM Conference on Strain Hardening Cementitious Composites (SHCC-3). RILEM Publishers, Dordrecht, pp. 171–178.

Zastrau, B., Richter, M., Lepenies, I., 2003. On the analytical solution of pullout phenomena in textile reinforced concrete. J. Eng. Mater. Technol. 125, 38–43.

Zastrau, B., Lepenies, I., Richter, M., 2008. The multi-scale modeling of textile reinforced concrete. Tech. Mech. 28 (1), 53–63.

Zeweben, C., 1989. Mechanical behavior and properties of composite materials. Delaware Composites Design Encyclopedia 1, Technomic Publishing Company, Lancaster, pp. 3–45.

Zhu, W., Bartos, P., 1997. Assessment of interfacial microstructure and bond properties in aged GRC using novel microindentation method. Cem. Concr. Res. 27 (11), 1701–1711.

Zhu, D., Mobasher, B., Peled, A., 2013. Experimental study of dynamic behavior of cement-based composites. J. Sustain. Cem. Based Mater. 2 (1), 1–12.

This page intentionally left blank

Textile fiber composites: Testing and mechanical behavior

5

B. Mobasher
Arizona State University, Tempe, AZ, USA

5.1   Introduction

In order to develop structural applications for textile fiber composite materials, fundamental approaches for analysis and design for tensile, shear, and flexural design are needed. This chapter addresses methods to conduct experiments and translate the results to design-based properties. Mechanical tests are conducted to measure the entire load-deformation properties, and results are interpreted and analyzed using analytical models to obtain fundamental material properties. These material properties must be interrelated to explain the role of matrix, textile, and interface under various loading conditions such as tension, flexural, shear, impact and high-speed situations, and the constitutive properties obtained such that they are compatible with standard analytical models such as finite-element program or structural analysis models of moment–rotation or nonlinear stress–strain. These models are then applicable for analysis and design of various structural systems including structural panels, impact- and blast-resistance structures, repair and retrofit, earthquake remediation, strengthening of unreinforced masonry, and beam-column connections.

A fundamental understanding in the tensile stress–strain response and crack formation mechanisms is important for design aspects. The chapter investigates the cracking mechanisms and the strain-hardening behavior in textile-reinforced concrete (TRC) composites that can be obtained when there are adequate reinforcements by the long aligned fibers within the textile. The multiple cracking behavior under direct tension is due to the high stiffness in the postmatrix cracking region, which is offered by the fibers that intersect the matrix crack. A single strength parameter is therefore not meaningful and the entire tension stress–strain curve is used as the fundamental material property. Tension-hardening behavior has been shown to exist when long aligned fibers are employed in steel, glass, polymeric, and even natural fibers such as sisal (Mobasher et al., 2006; Peled et al., 2004).

Experimental procedures are used to monitor and analyze the distributed cracking phenomenon and determine the crack spacing during tensile tests. Photographs of the crack formation taken during the test and post-processed by image-analysis techniques such as the digital image correlation (DIC) allow quantitative measurements. The crack spacing can be correlated with the applied stress as well as stiffness at different strains. Microstructural evaluations correlating the fiber–matrix interface with the composite's mechanical response can also indicate the efficiency of textile structure's type and reinforcement.

5.2   Tension tests

Direct tensile tests are routinely conducted using a servo-hydraulic testing machine as shown in Figure 5.1. Static tensile tests are controlled by the cross-head at a constant rate of displacement (such as 0.1 mm/min) or by means of transducers mounted on the specimens. Specimen sizes are generally rectangular, although dog-bone samples are also used despite the extra labor involved in their preparation. Typical size of specimens is in the range of 150–400 mm in length, 24–50 mm in width, and 6–12 mm in thickness. A gage length of 150–300 mm can be used depending on the size of the textile and sufficient representation of the textile yarns throughout the specimen width; however, longer gage lengths are preferable since they permit a more uniform measurement of crack spacing. Both fixed-fixed boundary conditions as well as pinned-boundary conditions for the grips have been used, and the effects have been well documented in terms of the specimen rotation versus fixed displacement, especially during the initial loading stages. The use of two parallel displacement sensors allows for characterization of sample rotation during the initial loading and crack propagation stages. In many cases, however, the rotation effects are diminished in the multiple cracking region and a uniform tensile stress is applied throughout. The hydraulic grips pressure should be adjusted in order to minimize stress concentration and reduce the potential for crushing and damage. Thin aluminum sheets can also be glued on both ends of the specimen to redistribute the pressure due to clamping. The tensile load, cross-head displacement, and strain are
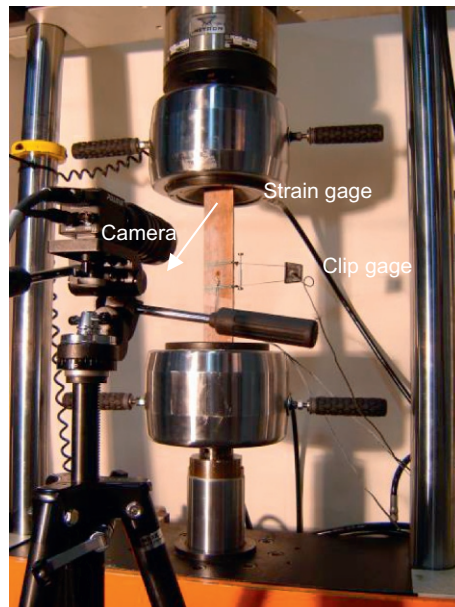
Figure 5.1 Tension test setup in a servo-hydraulic testing machine 500 kN.
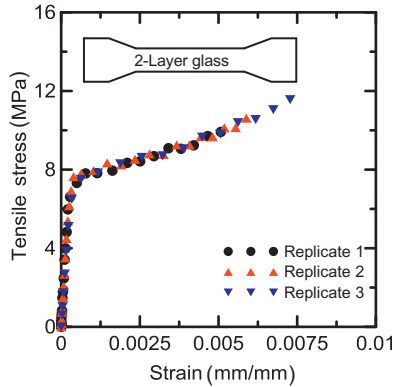
Figure 5.2 Tensile stress–strain response of a two layer TRC using AR-glass fibers.

routinely recorded. The tensile strains are also measured by resistance-type strain gage glued on the specimen that provide a perspective of the local state of strain compared to use of a clip gages with a gage length of 10–25 mm, or the global stroke displacement, which inherently includes spurious deformations.

Figure 5.2 represents a typical tensile stress–strain response of alkali-resistant (AR)-glass fabric-reinforced cement composite. The tensile response shows a linear behavior up to about 5 MPa; beyond this level, the stress–strain response becomes nonlinear, while a major change in the stiffness of the sample occurs at bend-over point (BOP) around 7.5 MPa, which is characterized by a knee in the stress–strain curve. The specimen continues to carry load at a significantly lower stiffness up to an ultimate strain level of 7.5%. In the region between the BOP and ultimate strength, crack activity is the formation of distributed crack and later on as the crack widens. The experimental data consist of a range of parameters in terms of the initial stiffness, stress (initial and final levels of BOP state of stress and strain), post-BOP stiffness, ultimate strength capacity, crack spacing toughness (Mobasher et al., 2006), and pullout stiffness.

The first step in the analysis of this type of data is to focus on the specific regions of the response and isolate the main contributors. The data chosen for this type of analysis are based on a sisal fiber composite with high tensile/bending strength and toughness for structural applications. The fabric was obtained by stitching the single filament fibers laid side by side in a unidirectional manner and used as a reinforcement in a multilayer compression-molded composite. Figure 5.3a shows a typical tensile stress–strain response of the sisal TRC composite system. Two measures of strain are used; the localized strain measure from the electrical resistance gage, and the nominal strain defined by the cross-head stroke displacement divided by the specimen length. These two responses are used to discuss the various stages of loading corresponding to initiation, propagation, distribution, opening, and localization of a crack system in the specimen.

The initial aspect of analysis is the distinction between crack initiation and propagation. In a lightly reinforced system, these two events normally occur in an
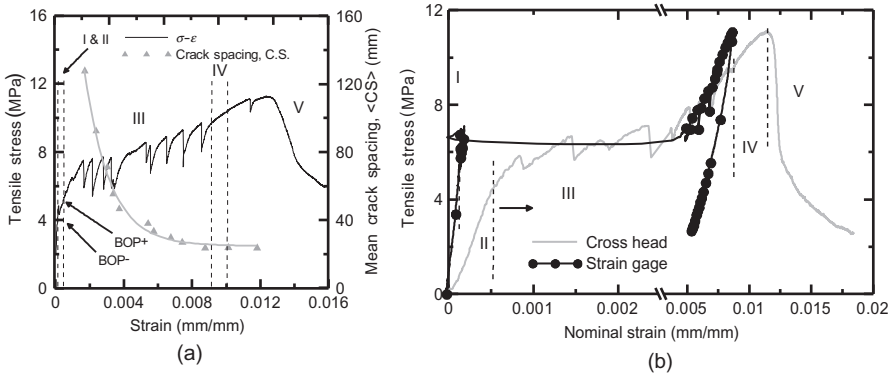
Figure 5.3 Tensile response (a) tensile stress and crack spacing vs. strain and (b) comparison of tensile stress vs. strain from strain gage measurements and cross-head displacement.

indistinguishable manner; however, they are differentiated in a heavily reinforced section. The initial stress–strain response is linear elastic as the specimen exhibits a high stiffness with the first-crack strain capacity that is quite low. From a macro perspective, the BOP corresponds to the formation of matrix cracking and its propagation across the width of the specimen. Five distinct zones are identified using Roman numerals with two zones prior to and three zones after the BOP. Figure 5.3b shows both the initial and the overall response of the stress–strain curve using a multiscale axis representation. Figure 5.4 shows the relationship between the strain gage and the strain measured by the stroke transducer. These two gages differentiate the ranges. Zone I corresponds to the elastic-linear range where both matrix and the fiber behave linearly. Due to low volume fraction of fibers (<10%), this zone is limited to strain measures of up to 150–175 μstr as shown by the insert of Figure 5.4, and the stiffness is dominated by matrix properties. The sensitivity of the stroke displacement in this range is within the instrumentation error, therefore, the strain gage response is the only reliable measurement. Zone I is terminated by initial crack formation in the matrix phase
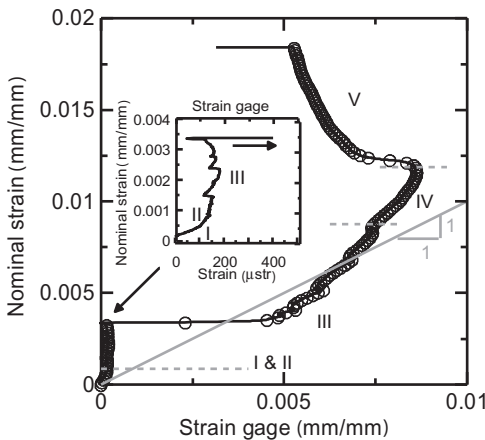
Figure 5.4 Relationship between the strain gage and strain measured by the stroke.

(reported from experiments as $\sigma_{\text{BOP}-}$) as shown in Figure 5.3a; however, the load-carrying capacity does not vanish as the cracks are bridged by the longitudinal fibers.

Immediately after the initiation of first matrix crack, other matrix cracks also initiate throughout the specimen at regular intervals and they all begin to propagate across the width of the specimen. The strain gage in this range remains within a constant level as several cracks that initiate and propagate across the width of the specimen. The term defined as BOP^+ corresponds to the first matrix crack that completely propagates across the width of the specimen, thus the strain range within Zone II is associated with formation of matrix cracks, while no single crack has traversed the entire length of the specimen. As indicated in the experimental results shown in Figure 5.3a and b, the linear behavior terminates at the $\sigma_{\text{BOP}-} = 4.0$–$4.5$ MPa. The BOP ranges from the beginning of nonlinearity at 4.50 MPa to a point where the slope drastically decreases ($\sigma_{\text{BOP}+} = 5.0$–$5.2$ MPa). Zone II is therefore defined as the stable cracking range between the two stress levels of $\sigma_{\text{BOP}-}$ and $\sigma_{\text{BOP}+}$.

Formation of distributed cracking in Zone III occurs right after the BOP stage and represents a homogenization phase. As the applied strain increases, more cracks form and the spacing decreases in an exponential manner. The strain measured by the strain gage initially remains constant, while several cracks form in the overall section. The two strain measures approach a relatively single value as shown in Figure 5.3b. Figure 5.3a also shows that at a strain of up to 0.004 mm/mm (Zone III), crack spacing drastically decreases from an initial value of 130 to 45 mm.

During the multiple crack formation, the crack spacing decreases up to Zone IV where it becomes constant at 23 mm. Zone IV corresponds to completion of cracking phase and initiation of debonding. The strain gage recording fails to increase at the same rate as the overall strain and no additional cracks are formed as cracking saturates. Zone IV is dominated by progressive damage and characterized by a crack widening stage ultimately leading to fiber failure. The postpeak response occurs in Zone V where a residual strength of approximately 2 MPa is observed.

Considerable differences exist between the initial and postcrack modulus from cross-head displacement data and strain gages. The discrepancy is attributed to the spurious deformation, slipping, and localized damage at the grips, indicating that initial stiffness computation from the cross-head displacement may be significantly erroneous.

From the crack spacing measurements shown in Figure 5.3a a general decrease is observed in the spacing during loading until the curves reach a steady state and remain constant at the end of Zone II and Zone IV. This constant level of crack spacing is defined as saturation crack spacing, beyond which reduction in crack spacing is not observed. Since no new cracks are forming, additional imposed strain results in widening of the existing cracks. The final mechanism of failure is due to fiber debonding and pullout.

5.3 Role of microstructure

Figure 5.5 shows environmental scanning electron microscope (ESEM) micrographs of samples extracted from specimens tested under tensile stress where Figure 5.5a is a lateral view and Figure 5.5b a cross-sectional view. The contribution of the sisal fibers
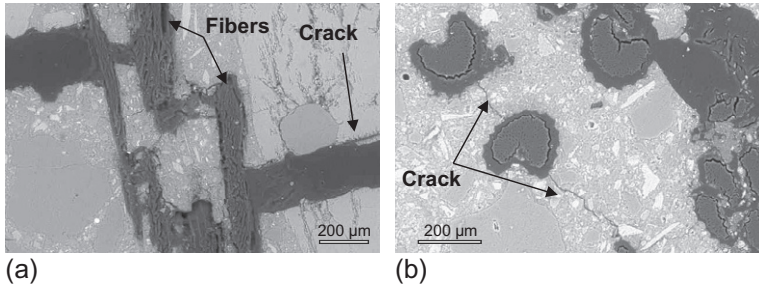
Figure 5.5 ESEM micrographs: (a) Lateral and (b) cross-section views.
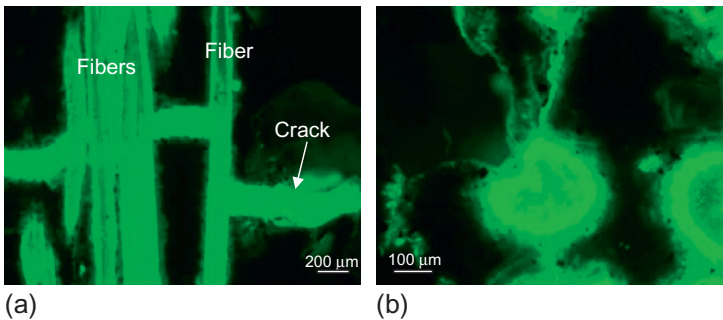
Figure 5.6 Optical fluorescent micrographs: (a) lateral and (b) cross-section views.

to crack arrest and bridging mechanisms is observed. The crack propagates through the thickness of the specimen from one fiber layer to the next (Figure 5.5a and b), hence, crack arresting and bridging mechanisms that lead to a ductile composite are observed. Similar micrographs are shown using the optical microscope with fluorescent excitation as shown in Figure 5.6a (lateral view) and 5.6b (cross-section view). Crack arrest and crack bridging was observed.

5.3.1   Parameters of distributed cracking

From a modeling point of view, the interaction of distributed cracking and the stress–strain response of the matrix, fabric, and the composite are shown in Figure 5.7. Four distinct zones up to the peak load are identified using Roman numerals with two zones prior to BOP and two zones after the BOP range. The strain softening that was due to localization and identified previously is not addressed. Zone I corresponds to the elastic-linear range where both matrix and the fabric behave linearly, and is modeled using composite laminate theory to relate the properties of fabric and matrix to the composite response. This zone is terminated by initial crack formation in the matrix phase at a point labeled "A" and designated as σ_{t1} at the strain level ε_{t1} (Agarwal and Broutman, 1990) (reported as of σ_{BOP^-} from experiments).
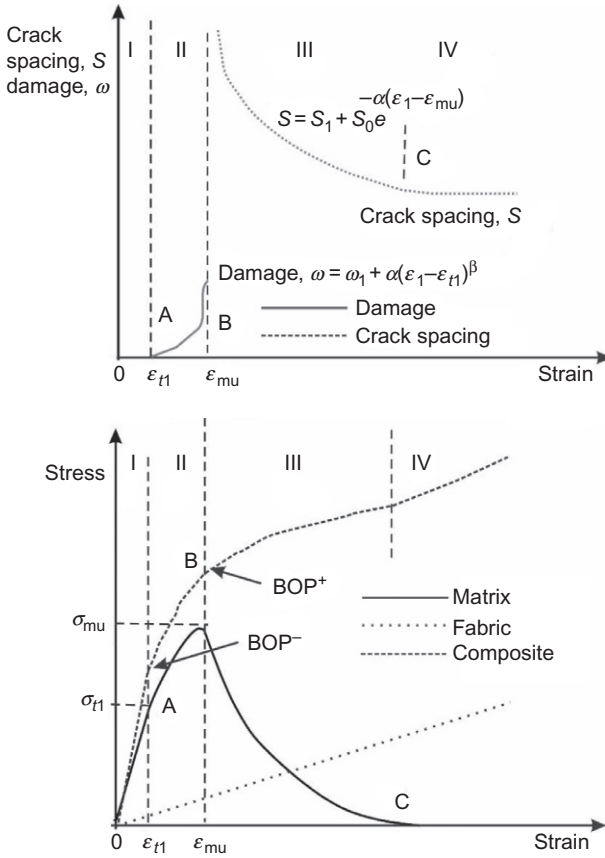
After the initiation of matrix cracks, and initiation of bridging by the longitudinal yarns, Zone II occurs between two stress levels of σ_{BOP^-} and σ_{BOP^+} as matrix cracks propagate across until the first complete crack across the cross-section between points "A" and "B" are formed. Zone II terminates at a damage level corresponding to the stress (σ_{BOP^+}) level, which is also the ultimate strength of matrix in the presence of fibers σ_{mu}. The BOP strain level (ε_{mu}) may theoretically be obtained using the Aveston–Cooper–Kelly (ACK) approach (Aveston et al., 1971a) or other methods (Mobasher and Li, 1996) that predict the strain capacity of the matrix in the presence of fibers as shown in Equation (5.1),

$$\varepsilon_{mu} = \left[\frac{12\tau\gamma_m E_f V_f^2}{E_c E_m^2 r V_m} \right]^{1/3} \tag{5.1}$$

where τ is the shear strength of the matrix; γ_m is the fracture toughness of the matrix; E_c is the composite modulus; r is the fiber radius and V_m is the volume fraction of the matrix. This equation is applicable for the cement-based materials by showing that the

strength of the matrix is increased in the presence of fibers (Mobasher and Shah, 1990). The experimentally obtained values for ε_{mu} correspond to the values reported as $\varepsilon_{BOP(+)}$ and reported to be higher than the first-cracking strain. The correlation between experimental and theoretical simulations of the stress and strain at BOP level can be used to obtain material parameters for the various fabric-cement systems used (Mobasher et al., 2004). The stiffness degradation up to the BOP^+ level takes place by an increasing number of dilute microcracks and techniques such as acoustic emission and holography that have been used to monitor the damage evolution in this phase of response. The major reduction in stiffness is associated with the formation of parallel cracks to reach the characteristic crack spacing level. The experimental results of average crack spacing as a function of applied strain have been modeled using an exponentially decay function:

$$S(\varepsilon_i) = S_1 + S_0 e^{-\alpha(\varepsilon_i - \varepsilon_{mu})} \quad \varepsilon_i > \varepsilon_{mu} \tag{5.2}$$

where S is average crack spacing; S_1 is a parameter describing saturation crack spacing; S_0 and α are parameters describing the decay rate; ε_i is strain at which the spacing is computed; ε_{mu} is strain at the BOP(+) level. The function representing crack spacing is also plotted in Figure 5.8, along with the stress–strain response and discussed in detail in Mobasher et al. (2004).

5.3.2   Crack spacing and its measurements

By evaluating cracking patterns at regular time intervals, the crack development throughout the loading cycle of tensile and bending tests is recorded. A two-step process for quantitative measurement for crack spacing is discussed in Peled and Mobasher (2005) and Peled et al. (2004). During the first step, newly formed cracks
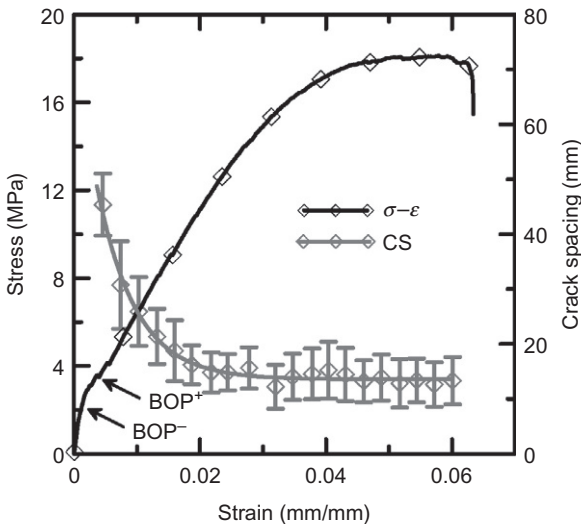
Figure 5.8 The crack spacing and stress as a function of applied strain for the AR-glass fabric-reinforced cement-based composite.

Table 5.1 **Average crack spacing and stiffness degradation parameters for various TRC systems (Mobasher et al., 2004)**

	Stiffness degradation			Crack spacing equation			
	$X_1 + X_2 * \exp(-X_3 * \varepsilon)$			$S_1 + S_0 * \exp(-a * (x - \varepsilon_1))$			
Specimen	X_1	X_2	X_3	S_1	S_0	a	ε_1, µstr
ARG-P100	132	2411.7	283.9	21.07	497.9	451	−1156
ARG-P900	501	3154.2	438.9	8.74	168.8	190	−10,800
ARG-SP0.2	317	2783.0	361.4	39.71	136.0	92	−658
ARG-FA	395	2429.1	586.0	39.30	133.0	153	7510
ARG-SF10	309	1921.6	319.2	17.30	339.2	27	−6990
PE-Plain	24	2203.8	239.2	5.56	485.3	143	−12,293
PE-SF5	153	1773.7	197.0	16.46	325.4	117	−18,101
PE-SF10	−73	2058.8	246.0				

of each image are traced and added to data from previous loading increment. In the second step, the crack spacing is measured using an automated procedure for segment length distributions and their statistical parameters.

The typical stress–strain curve shown in Figure 5.7 is compared with the crack spacing evolution. An inverse relationship between crack spacing and damage functions form with applied strain. In the pre-BOP range, the damage level increases; however, in the post-BOP stage, the crack spacing decreases with applied strain until a constant level referred to as the crack saturation density (CSD) is reached. The CSD is indicated by the flattening of the crack spacing curve since no more new cracks are formed. The CSD level as shown in Figure 5.8 is at about 12 mm and depends on the strength, toughness of matrix, stiffness, bond, and volume fraction of fibers. Beyond this point, reduction in crack spacing is not observed, as further increase in the strain causes textile debonding, pullout, and widening of existing cracks.

The formation of distributed cracking in post-BOP stage, Zone III, can be represented by parameters S_0, S_1, α, and ε_{mu} (Equation 5.2) as shown in Table 5.1 for various TRC systems. The stiffness of the fabric-cement system is sufficiently high to keep the newly formed cracks from widening and thus promoting additional cracking. This stiffness affects the rate of reduction of crack spacing, or α parameter (Mobasher et al., 2004).

5.4 Interface characterization

5.4.1 Single-fiber pullout

The stiffness of fiber-interface-matrix system directly affects the toughening mechanisms. In brittle matrix composites, if the ultimate strain capacity of the fibers exceeds that of the matrix, fibers will bridge matrix cracks. The force transferred due to the bridging reduces the stress concentration at the matrix crack. The constitutive

response of the debonding phase depends on the length of cylindrical shear micro-cracks that form at the interface, and the ability of the interface to transmit the traction across a matrix crack. For properly designed systems, matrix's tolerance to the crack propagation and thus composite strength may increase significantly as shown by Aveston et al. (1971b) and Stang et al. (1990). As fibers bridge across the matrix cracks, processes of debonding and pullout lead to toughening and energy dissipation.

Many fiber pullout models have been used to characterize bond properties of single fibers with a cementitious matrix. A variety of analytical solutions (Stang et al., 1990; Naaman et al., 1991a; Sujivorakul et al., 2000) assume that while fiber and interface behave elastically in bonded regions, a constant residual shear strength is in the debonded region. Bond strength models for rebars also address the pre- and postpeak response (Abrishami and Mitchell, 1996; Focacci et al., 2000); however, the more detailed the bond strength model, the more complex the analytical solution. Currently, most bond properties of the textile structure are obtained from straight fiber pullout that treat textile (grid reinforcement) as an equivalent smooth longitudinal fiber. The mode of load transfer in textile composites, however, is much more complicated due to the function of transverse yarns, which provide anchorage. Equivalent bond properties based on a one-dimensional (1D) bond pullout model are relatively high and include the anchorage effect due to transverse yarns.

5.4.2 Textile pullout tests

Pullout experiments measure the effect of fabric type, mixture design, and processing methods such as pultrusion, vacuum casting, or rheology modification (Sueki et al., 2007a). Using an assemblage of up to eight yarns, sections of a textile embedded in the cement matrix were tested at a cross-head rate of 0.25 mm/s. The test setup is presented in Figure 5.9a and b. Since it was not possible to hold the textile in the grip at exactly its exit point from the matrix, the compliance of the free sample length in between the edge and the grip was taken into account (Sueki, 2003).
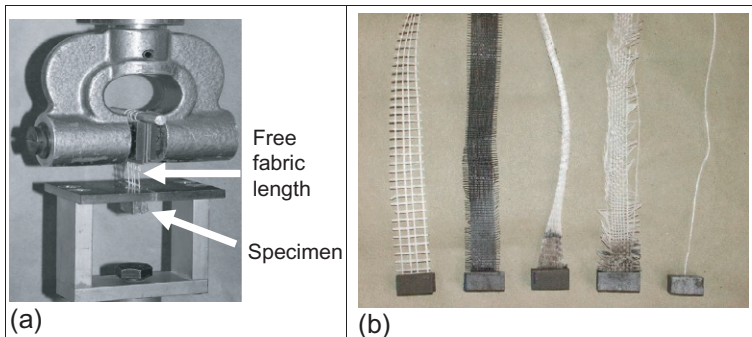
Figure 5.9 Schematics of pullout experiments on fabric-reinforced systems: (a) sample in a loading grip and (b) various TRC pullout samples.
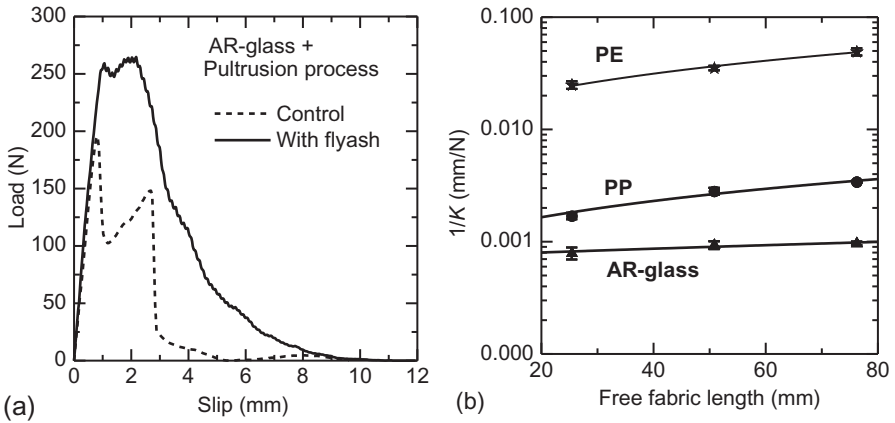
Figure 5.10 (a) Pullout response of an AR-glass fabric using control and fly ash blended matrix; (b) the effective stiffness of the interface transition zone obtained from the pullout experiments.

The effect of matrix type (shown in Figure 5.10a) indicates the glass fabric exhibits the best bond when high content of fly ash is used. The dual peak in the response is associated with the failure of the junction bonds and transfer of the load down the fiber length. The effective stiffness of interface transition zone is shown in Figure 5.10b, providing a comparative evaluation of the bond stiffness parameter for various fabric systems. There is an order of magnitude difference between the bonding characteristics of different systems. The most basic measure of interfacial failure response is by calculation of nominal shear strength, defined as the averaged shear strength along the embedded length. This measure assumes a constant frictional mechanism along the embedded length, but does not take into account the interaction due to the transverse yarns. The nominal shear strength defined as the strength per fiber surface area is:

$$\tau_{nom} = \frac{P_{ult}}{n\pi\phi L} \tag{5.3}$$

where P_{ult} is the ultimate load attained, n is the number of fibers resisting the load, ϕ is the nominal diameter of the fiber and L is the embedded length. The average values and standard deviation of strength parameters show that shear strength values can reach as high as 4 MPa due to the inclusion of anchorage effects in the shear strength results of an equivalent yarn model. Furthermore, the pultrusion technique increases bond strength where noncoated multifilament was used (polypropylene [PP] and polyvinyl acetate [PVA]) while the vacuum technique increases bond strength in AR-glass but is ineffective with PP.

The simplest expression for pullout model parameters is defined by four variables: initial stiffness of the pullout curve; ultimate load; slip at ultimate; and the toughness evaluated up to ultimate load. The initial stiffness is obtained from the slope of the linear portion of the curve. The pullout response sometimes shows several peak loads

(a)   Slip (mm)

(b)   Slip (mm)
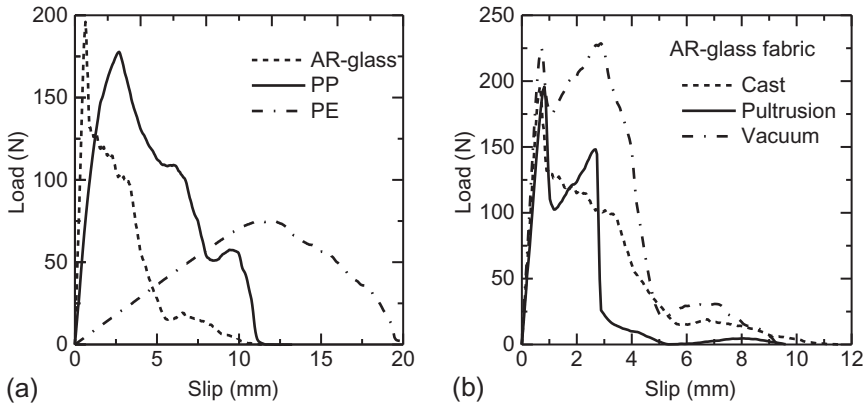
Figure 5.11 The response of the nonlinear textile debonding model. (a) Comparison of pullout-slip response of AR-Glass, PP, and PE textiles. (b) Effect of processing parameters of casting vs. pultrusion and vacuum processing on the pullout response.

in the case of textile materials. Toughness is defined by the area under the pullout-slip. These parameters, however, and not material properties, depend on the fiber length, diameter, and testing conditions.

Some of the features of the experimental data are evident as the responses are plotted. Figure 5.11a shows the comparison of three fabric systems of AR-glass, PP, and polyethylene (PE). Note that the glass system is the stiffest and strongest system, whereas the PP-woven fabrics result in the highest energy absorption. Figure 5.11b compares the results of three processing methods of cast, pultrusion, and vacuum of the paste used on the same AR-glass and shows both the vacuum and pultrusion processing result in higher strength and energy absorption during pullout.

As an alternative to parameter estimation, one can back-calculate the material properties using the experimental data as input parameters (Sueki et al., 2007a). The model fits various representative curves of different fabrics, matrices, embedded length and processing methods. Internal interface parameters (κ, τ_{max}, τ_{frc}, τ_{dyn}, and stiffness efficiency factor η) are calculated by back-calculation.

The responses and model simulations of the control test series (cast with and without fly ash using AR-glass, PP, PE, and PVA) show that parameters such as shear strength abrupt changes in the postpeak responses are due to the sudden change of shear strength from τ_{frc} to τ_{dyn}. The averaged response of the control test series (G105, PP105, PE105, and PVA105) as shown in Figure 5.11 were selected to demonstrate the fit of the model and the experiments by determination of the internal parameters (κ, τ_{max}, and τ_{frc}).

Main factors of fiber type, matrix type, embedded length, and processing methods have a sizable effect on the bond strength and efficiency of the textile-cement composite. Results reveal that bond strength of the textile ranked from the highest to the lowest is AR-glass, PVA, PP, and PE, respectively. Fly ash replacement of up to 40% by volume increases bond strength for AR-glass in all except PVA textiles. The bond strength obtained from specimen with shorter embedded length yield slightly higher value with larger scatter. The processing methods indicate that the pultrusion

technique increases bond strength in PP and PVA textile, but not in AR-glass while the vacuum technique increases in AR-glass, but not in PP.

In general, the highest bond strength is observed in glass textile systems, whereas the PE, PP, and PVA show the lower strengths. Bonding of the glass textile is due to the high modulus of elasticity of fibers, adhesion of glass to cementitious matrix, and the nature of the interlock in bonded textile. The low bond of the PVA textiles was attributed to the relatively large diameter of the bundle due to the high number of filaments that led to a dense textile structure and poor paste penetration between the filaments in a yarn. Addition of fly ash to the glass system improves the durability of the glass textile as much as 35% (Mobasher et al., 2004). Variations in embedded length do not significantly influence the shear strength values for PP nor for PVA textiles. Use of the pultrusion manufacturing increases bond strength in PP roughly by 72% and PVA by 85%, but not in the AR-glass ($\approx 10\%$). Improvement in bonding by the pultrusion of the PP system and PVA is by better penetration of the cement matrix between the filaments of the bundle (Mobasher et al., 2014). In contrast, vacuum technique increases bond strength in AR-glass, but decreases in PP system by 38%. The higher viscosity and poor penetrability of vacuumed paste within the fine grid and small filament spacing of PP textile was noted in comparison to the coarse grid AR-glass textile that performs much better with the vacuum paste.

5.4.3 Single-yarn pullout testing with lateral load

Even when the yarns in longitudinal and transverse directions are not connected by means of knitting or bonding, stresses in a direction will result in increased frictional bonding and transfers the load to the other direction. The connection between orthogonal yarns are shown in Figure 5.12a and b. A series of experiments addressed the effect of transverse loads on the woven fabrics on the pullout characteristics of the single-fiber yarns under lateral load (Zhu et al., 2011a). The effect of fiber geometrical change during the pullout was measured under a biaxial stress.
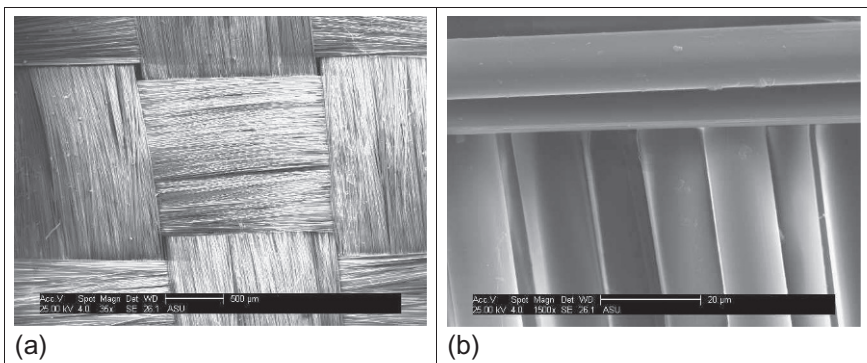
Figure 5.12 Scanning Electron Microscopy (SEM) micrographs showing: (a) woven fabric; (b) individual filaments within a yarn.

An analytical model for the force–displacement response of the yarn slipping and its subsequent sliding frictional pullout was developed. Maximum bond and frictional shear strength depend on the specimen size and the level of transverse preload. In addition to analytical approaches, 3D finite element (FE) models were also used to simulate the single-yarn pullout behavior and the effect of friction and transverse loads on the pullout force. The friction between yarns and transverse direction (fill yarns) influence the pullout force significantly (Stahlecker et al., 2009).

Figure 5.13 shows a test setup with an edge-clamped fabric holding fixture and a pneumatic grip that is used to clamp and subject the yarn to pulled out. Two load cells measure the pullout force and transverse preload applied by the sliding edge clamp. Figure 5.14a shows the schematic of the yarn loading process (Kirkwood et al., 2004). Figure 5.14b shows the corresponding pullout force versus displacement and the variations in the preapplied transverse force. During uncrimping, the yarn progressively straightens and locally disturbs the nominal woven architecture (Figure 5.14a), however the force–displacement curve is nearly linear as shown in Figure 5.14b (Shockey et al., 2004; Bazhenov, 1997). After the peak load, the entire yarn translates within the fabric swath and the force gradually decreases. Oscillations in the force–displacement curve correspond to the sliding yarn passing by fill yarns as shown in Figure 5.14a and b. Test results for single-yarn pullout test of plain weave Kevlar® 49 fabric for a sample of 90 mm length is shown in Figure 5.14b and used to validate the analytical model discussed in the next section. Maximum pullout force and energy associated with it depend on the specimen length and transverse force. It is clear that the preapplied transverse force does not remain constant during the test as it reaches a maximum level when the force reaches the maximum load, and then gradually drops until the end of test. The final transverse force is slightly lower than the initial preapplied value since the fill yarns straighten and relax as the yarn is pulled out. It also shows that the oscillations after peak load of both curves are in phase with each other.

Figure 5.15 shows the dependence of the peak pullout force and pullout energy on the transverse forces for three specimen lengths (50, 65, and 90 mm). Increasing the
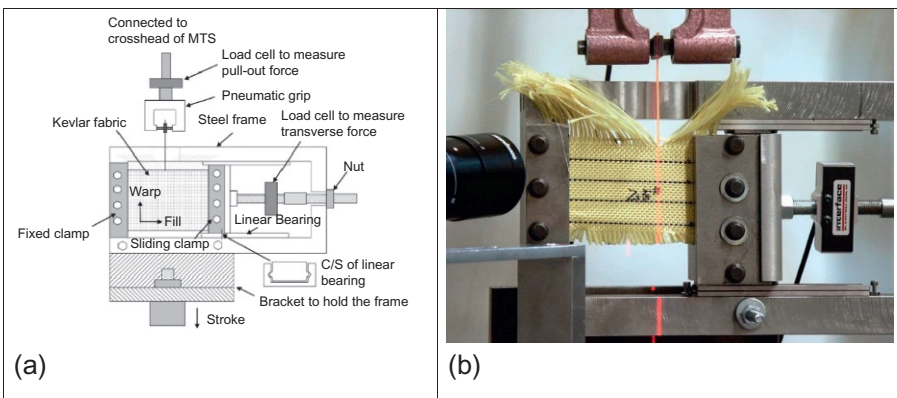
Figure 5.13 Yarn pullout test: (a) schematic; (b) experimental setup.

(a)

(b)
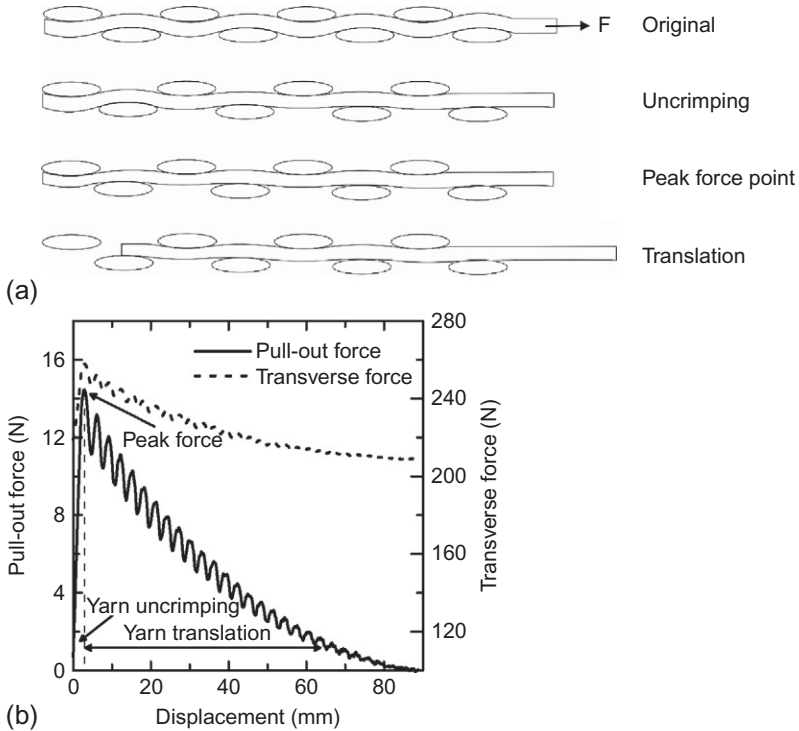
Figure 5.14 (a) Schematic of yarn behavior during pullout; (b) typical single-yarn pullout force and corresponding preapplied transverse force vs. displacement curves of a 90-mm specimen.
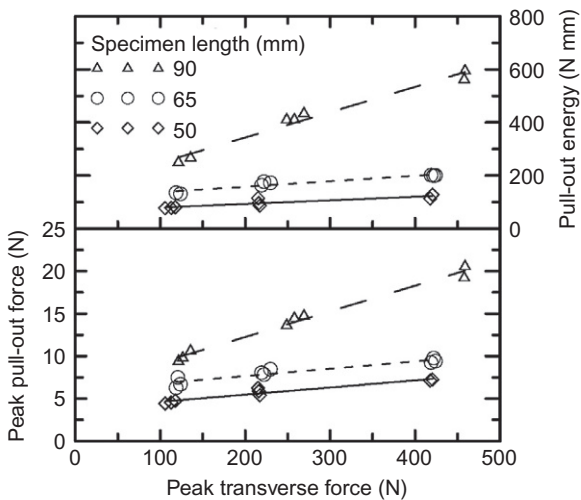
Figure 5.15 Peak pullout force and pullout energy vs. peak transverse force.

transverse force proportionally increases the peak pullout force and yarn pullout energy. Increasing the tension on the transverse yarns increases the normal force between yarns as well as the frictional resistance to pullout (Kirkwood et al., 2004). There is no clear relation between the preapplied transverse force and displacement at peak pullout force for each specimen length.

5.4.4 Analytical model for interfacial parameters

A model based on the earlier work by Naaman et al. (1991b,c) and Sueki et al. (2007a) was used to simulate the pullout behavior of fabric from cement paste matrix. The basic model is shown in Figure 5.16. The fabric is treated as a continuum, and the interface between the debonded and intact yarns are defined by the shear strength diagram as shown by the insert in Figure 5.16 that shows a simplified pullout load versus slip response of a single yarn. The response is divided into two stages according to shear stress distribution at the contact surface. Initially, the curve shows a linear response up to initiation of debonding (stage I). When the load reaches the peak load, the yarn starts to translate (stage II). The mechanism of shear strength, force distribution, and derivations for each stage are obtained.

Pullout response in elastic stage (I) continues as long as the shear stress at interface is less than the maximum shear strength τ_{max}, yarn and matrix are fully bonded, and the applied load is less than the maximum bonded load. This is shown in the various modes of Figure 5.17. In this case, the standard shear lag solutions apply. Pullout response in nonlinear stage (II) as shown in Figure 5.17b occurs after loading beyond the elastic limit, debonding at the right end starts and extends by a distance d, with a frictional shear strength τ_{frc} while on the left portion (L–d), the two materials are still perfectly bonded. The criteria for the growth of debonding is specified as a shear strength with a constant frictional stress along the debonded zone, in addition to a shear lag model terminating with τ_{max} at the debonding junction. Pullout response in dynamic stage (III) shown in Figure 5.17c1 and c2 consists of two conditions: initial stage up to complete debonding and rigid body motion. It is assumed that until
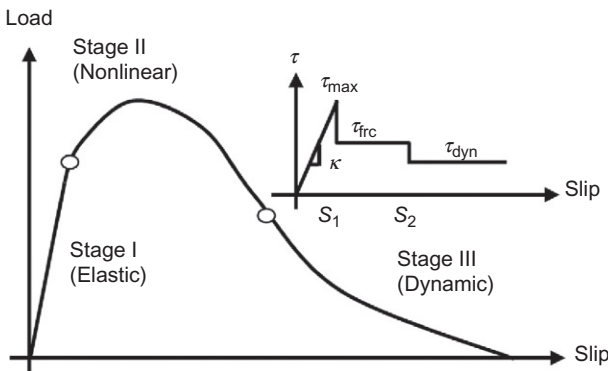
Figure 5.16 Pullout-slip response and shear strength diagram.
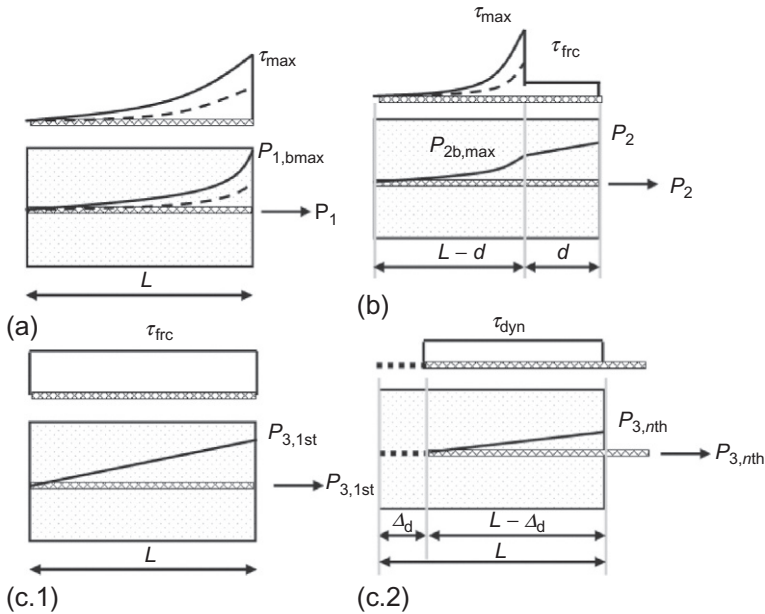
Figure 5.17 Shear stress and force distribution along the yarn: (a) stage I (elastic response); (b) debonding, (c.1) frictional pullout; (c.2) sliding mode.

complete debonding, the shear resistance still remains τ_{frc}, and no sliding occurs ($\Delta_d = 0$) until the yarn begins rigid body sliding motion shown in Figures 5.14a and 5.17.

The analytical model is also used to address the effect of single-yarn pullout under the action of transverse load. Response of each test is simulated and the shear parameters (τ_{max} and τ_{frc}) defined for the fiber-to-fiber interaction are also found by fitting the simulation response to the experimental results of transverse fiber pullout. Model predictions are shown in Figure 5.18 in terms of the initial and extended debonding, as well as frictional pullout demonstrated for various fiber systems. Due to the interface transition zone and the bundle effect in many filament-based fiber systems, an inefficient contact area exists. A parameter representing the efficiency of the yarn stiffness ($\eta < 1$) is introduced to reduce the nominal contact stiffness to account for the bonding inefficiency, since exact estimation of the stiffness of a yarn ($A_y E_y$) overestimates the experimental values significantly. Contributing factors include the variations in bond of interface zone, inefficiency due to the sleeve effect, lack of uniform strain in all the yarns during the test, the initial curvature in the yarns, and lack of bonding of 100% of filaments due to imperfections and porosity. By representing the percentage of filaments actively contributing to the apparent axial stiffness ($\eta A_f E_f$) of the yarn, one can verify the observations of sleeve filaments bonded to the matrix, which contribute to axial stiffness while the core filaments provide marginal stiffness in multifilament yarns (Banholzer, 2004).
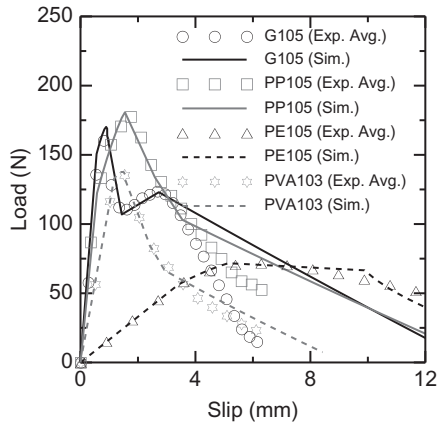
Figure 5.18 Simulation of representative pullout curve of control test series: G, PP, PE, and PVA.
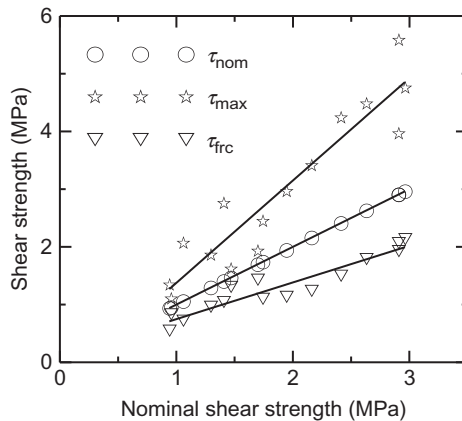
Figure 5.19 Correlation of nominal (τ_{nom}), maximum (τ_{max}), and frictional shear strength (τ_{frc}).

The maximum bond τ_{max} and frictional shear strength τ_{frc} correlate well with the nominal shear strength τ_{nom}. These results are compared in Figure 5.19 and show that all three stress measures are much higher than the tensile strength of the cement matrix phase, since mechanical bond mechanisms are included in the bond parameters. Nominal shear strength, defined as the average strength at maximum load, lies in between τ_{max} and τ_{frc} as shown in Figure 5.19. As the nominal shear strength increases, both the maximum and frictional shear strength values increase for a range of specimens regardless of conditioning or fabric types.

The model is also applied to the study of the effect of lateral stress on the pullout of yarns. Figure 5.20 shows the effect of specimen length on the maximum and frictional shear strengths at three levels of transverse force for the biaxial textile pullout tests.
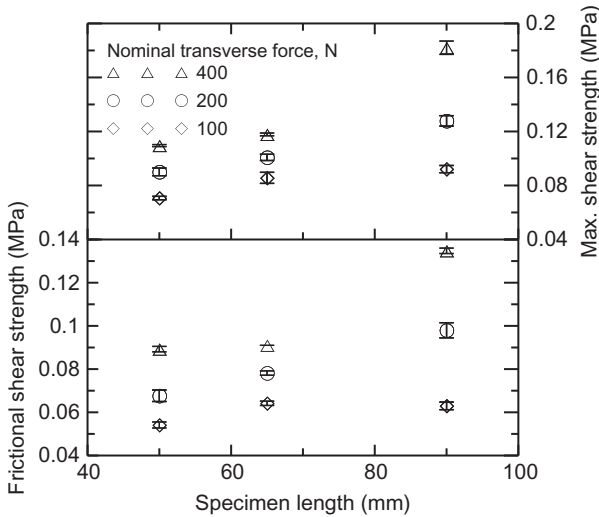
Figure 5.20 Frictional and maximum shear strength as a function of sample length and lateral force.

Both shear strength parameters increase with specimen length and transverse force. For the nominal transverse force of 100 N, the maximum shear strength increases from 0.072 to 0.092 MPa and frictional shear strength increases from 0.054 to 0.065 MPa when the length of specimen increases from 50 to 90 mm. It is noted that when the nominal transverse force is high at 400 N, the maximum and frictional shear strengths increase exponentially with specimen length.

5.4.5 Development of 3D FE model and simulation results

The analytical model discussed in previous sections has its own limitation due to the continuum assumption. One has to extend the modeling to use an FE model suitable for an implicit FE analysis to directly capture the fabric mesostructure; in this study, this was done using LS-DYNA. This method, used by Stang et al. (1990), Mobasher et al. (2014), Zhu et al. (2011a), Ng et al. (1998), Boisse et al. (2001), among others, has the advantage of capturing the yarn interactions and providing a detailed description of the mechanisms of fabric deformation at the mesostructural level. The purpose of the 3D FE model is to obtain a more detailed pullout analysis results to investigate the effect of friction and preload in transverse direction (fill yarns) on the pullout behavior.

Images of the cross-sections of the fabric were used to quantify the shape, size, and profile of the yarns for the FE model. The warp and fill yarns as elliptical cross-sections that follow a sinusoidal shape. The measurement of the geometric parameters associated with the fabric warp and fill yarns using 3D solid (continuum) elements are discussed in detail in an earlier publication (Zhu et al., 2012). A small FE model compared to the experiment was chosen. The 3D model contains 10×10 yarns (instead of 30–56 yarns in the experiments) and is shown in Figure 5.21 using 36,300 nodes in 20,000 eight-noded solid elements.
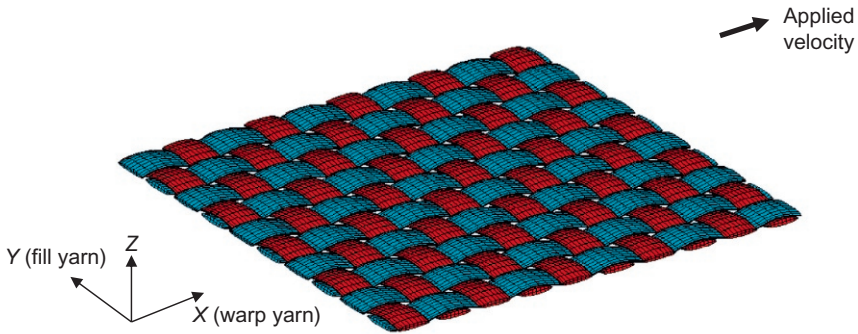
Figure 5.21 3D FE model of the fabric.

The yarns that make up the plain-woven fabric have strongly directional material properties. The axial stiffness is considerably greater than the transverse stiffness. A crimped yarn can only weakly resist tensile deformation until it straightens out. The orthotropic elastic continuum was used with the shear moduli G_{12}, G_{13}, G_{23} and Poisson's ratios ν_{12}, ν_{13}, ν_{23} specified as very small. In addition, the transverse elastic moduli E_{22} and E_{33} are also quite small compared to the longitudinal elastic modulus E_{11} (Gasser et al., 2000). Material Type 2 (orthotropic elastic material) in LS-DYNA allows definition of independent elastic moduli, Poisson's ratios, and shear moduli in each of the three orthogonal orientations (LSTC, 2007). Since yarns in the plain-woven fabric are crimped and the longitudinal elastic modulus E_{11} is defined along fiber direction, it is necessary to define local coordinate system for each FE that is permanently linked to the element's position during deformation. Table 5.2 lists the nine orthotropic elastic material data for the yarn continuum model.

Verification of the FE model was first carried out using the model of a single crimped yarn subjected to a tensile force. Results showed that the material data and the model were able to describe the crimped yarn's behavior.

Two types of boundary conditions are applied on the fabric. The first is two opposite edges clamped (all the six degrees of freedom are constrained for nodes located on the two edges) and a constant velocity applied to one yarn along the direction of clamped edges in the central area of the fabric (see Figure 5.21); the second is the

Table 5.2 Orthotropic linear-elastic material data (GPa) for yarn continuum

E_{11}	E_{22}	E_{33}	G_{12}	G_{13}	G_{23}	ν_{12}	ν_{13}	ν_{23}
72	3.6	3.6	3.6	3.6	3.6	0	0	0

two opposite edges preloaded with certain force and a constant velocity applied to the pulled yarn. The contact between the warp and fill yarns is defined by automatic surface-to-surface contact in LS-DYNA. The coefficient of friction is assumed to be dependent on the relative velocity v_{rel} of the surfaces in contact according to the relationship given by (Zhu et al., 2012)

$$\mu_c = \mu_d + (\mu_s - \mu_d)e^{-\zeta|v_{rel}|} \tag{5.4}$$

where μ_s is the static coefficient of friction; μ_d is the dynamic coefficient of friction; and ζ is the exponential decay coefficient.

Considering the numerical stability and computational time, the simulation pullout velocity is much faster than actual experimental parameters. In order to examine the effects of the friction, cases are modeled where only the frictional coefficient μ_c is varied. The computational time of each simulation is approximately 36 h. Figure 5.22 shows the various stages of yarn pullout from the textile. Results have been documented to show the interaction of transverse load, as well as the degree of slack and fiber shape on the overall yarn pullout.
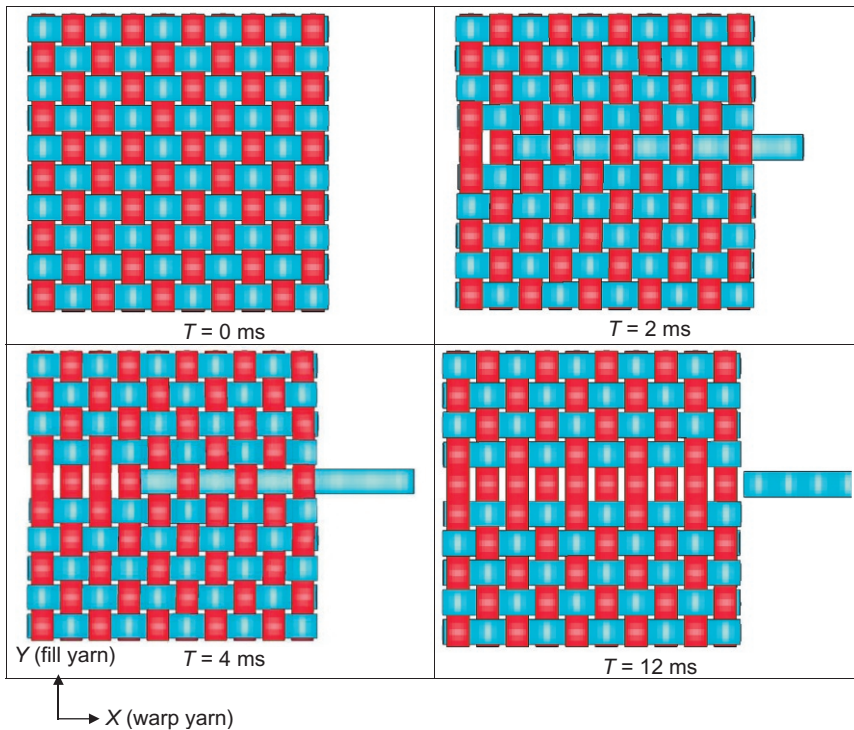
Figure 5.22 Top view of the pulled yarn and fabric for the case with two edges clamped without any preload and $\mu = 0.2$.
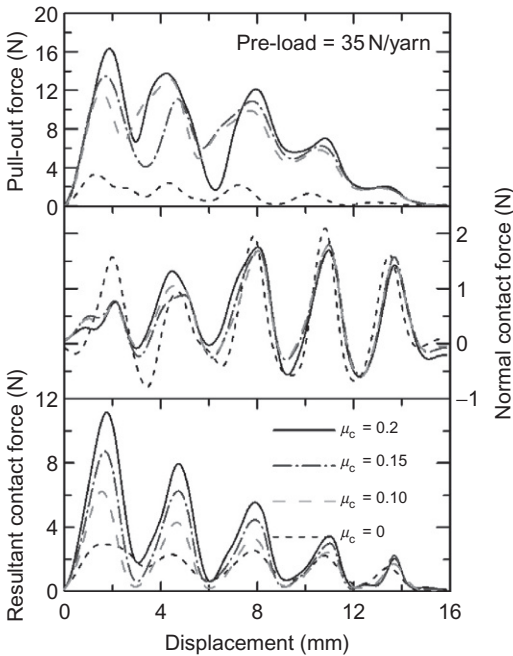
Figure 5.23 Comparison of the pullout force, normal force, and resultant contact force vs. displacement when two edges preloaded with 35 N/yarn and different frictional coefficients.

5.4.6 Comparison between the FE simulations and experimental data

The apparent discrepancy in the pullout force between the 3D FE model and the experiment is shown in Figure 5.23. For example, the peak pullout force of 50 mm specimen with 99 N initial transverse preload in the experiment is 4.42 N, while the peak pullout force obtained by the 3D FE model is 14.66 and 11.41 N when μ_c is 0.2 and 0.1, respectively (see Figure 5.23). It should be noted that the size of specimen in the FE model is even smaller than that in the experiment and there is also no preload applied in these two simulations. The overprediction of the pullout force is due to the fact that the actual yarns are not solid, actually consisting of hundreds of filaments that compact and slide with each other during deformation and resulting in much lower overall stiffness than the nominal value used in the FE model. Despite the discrepancy, the FE simulation results show that the frictional coefficient and transverse preload play a big role in the single-yarn pullout behavior.

5.5 Correlation of tensile and flexural properties

5.5.1 Simplified strain—softening and hardening composite model

The tensile behavior of TRC has been simplified by a constitutive model of a trilinear strain-hardening tensile, and an elastic-perfectly-plastic compression model as derived by Soranakom and Mobasher (2008a, 2009). By normalizing all parameters
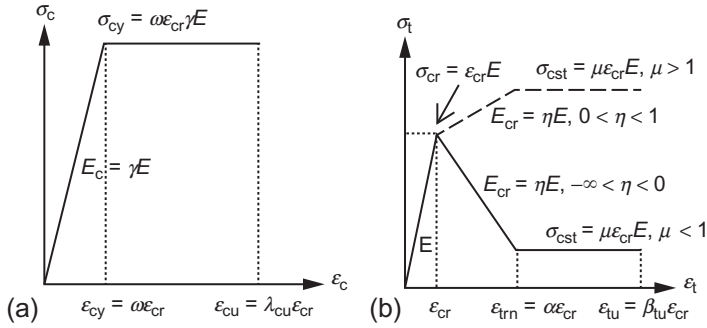
Figure 5.24 Material models for both strain-hardening and strain-softening FRC: (a) compression model; (b) tension model (Naaman et al., 1991b,c).

with respect to a minimal number of variables, closed-form derivations are obtained. Material parameters as shown in Figure 5.24 are summarized as tensile stiffness E, first-crack tensile strain ε_{cr}, cracking tensile strength $\sigma_{cr} = E\varepsilon_{cr}$, and postcracking modulus E_{cr}, which is assigned a negative or positive value in order to simulate either strain softening or hardening materials. Constant tensile strength at the end of tension model $\sigma_{cst} = \mu E\varepsilon_{c}$ and an ultimate tensile capacity ε_{tu} are defined in the postcrack region. For a TRC with an idealized trilinear response in tension where the multiple cracking region is treated as a two-step process with the initial part occurring at a constant stress, one has to integrate both steps into a single parameter η, which represents the average postcrack stiffness as shown in Figure 5.24.

The elastic-perfectly-plastic compressive stress–strain is characterized by a linear response that is terminates at yield point $(\varepsilon_{cy}, \sigma_{cy})$. This is followed by a plateau phase in the stress–strain response at constant compressive yield stress $\sigma_{cy} = \omega\varepsilon_{cr}\gamma E$ until reaching the ultimate compressive strain ε_{cu} as shown in Figure 5.24b. Applied tensile and compressive strains at bottom and top fibers, β and λ are also defined as model variables. Using the first-crack tensile strain and modulus as intrinsic material parameters, ε_{cr} and E, seven normalized variables are defined as listed in Equation (5.7) for different fiber-reinforced materials. Parameter γ represents the ratio of tensile to compression modulus of elasticity (Naaman et al., 1992). Normalized stress–strain responses and toughness G_f are expressed as:

$$\frac{\sigma_c(\lambda)}{E\varepsilon_{cr}} = \begin{cases} \gamma\lambda & 0 \le \lambda \le \omega \\ \gamma\omega & \omega < \lambda \le \lambda_{cu} \\ 0 & \lambda_{cu} < \lambda \end{cases}, \quad \frac{\sigma_t(\beta)}{E\varepsilon_{cr}} = \begin{cases} \beta & 0 \le \beta \le 1 \\ 1 + \eta(\beta - 1) & 1 < \beta \le \alpha \\ \mu & \alpha < \beta \le \beta_{tu} \\ 0 & \beta_{tu} \le \beta \end{cases} \tag{5.5}$$

$$G_f = E\varepsilon_{cr}^2 \left[\left(\frac{\alpha - \mu - \mu\alpha}{2} \right) + \mu\beta_{tu} \right] \tag{5.6}$$

Back-calculation model parameters, normalized tensile strain α, constant postpeak stress level, μ, postcrack modulus η, compressive yield strain, ω, tensile and

compressive strain at the bottom and top fiber, β, λ are defined in Equation (5.3) (Naaman et al., 1991b,c).

$$\alpha = \frac{\varepsilon_{trn}}{\varepsilon_{cr}}, \ \mu = \frac{\sigma_{cst}}{E\varepsilon_{cr}}, \ \eta = \frac{E_{cr}}{E}, \ \omega = \frac{\varepsilon_{cy}}{\varepsilon_{cr}}, \ \beta = \frac{\varepsilon_t}{\varepsilon_{cr}}, \ \lambda = \frac{\varepsilon_c}{\varepsilon_{cr}} \tag{5.7}$$

Material parameters, α and β_{tu} are scalar multipliers that apply to the first-crack strain, ε_{cr}. Parameters γ and η are multipliers that apply to the modulus E. Parameter μ is a scalar multiplier that applies to the first-crack tensile strength, σ_{cr}. Simulated flexural response is therefore generated by changing these trilinear tensile model parameters using an approach to fit the elastic modulus, E, followed by cracking strain parameter, ε_{cr}, which determines the start of elastic–plastic phase. Postcracking modulus, η, is obtained from the postcracking slope, and the transition phase is terminated by strain capacity α. Finally, the residual strength parameter, μ, is used to simulate the constant stress region. By assuming linear strain distribution across the depth and ignoring shear deformations, stress distribution across the cross-section at three stages of imposed tensile strain: $0 \leq \beta \leq 1$, $1 < \beta \leq \alpha$, and $\alpha < \beta \leq \beta_{tu}$ is obtained in closed form and shown in Figure 5.25 (Soranakom and Mobasher, 2008a). The normalized maximum tensile strain, β, and maximum compressive strain λ are linearly related through the neutral axis parameter, k as in Equation (5.1).

$$\lambda = \frac{k}{1-k}\beta \tag{5.8}$$
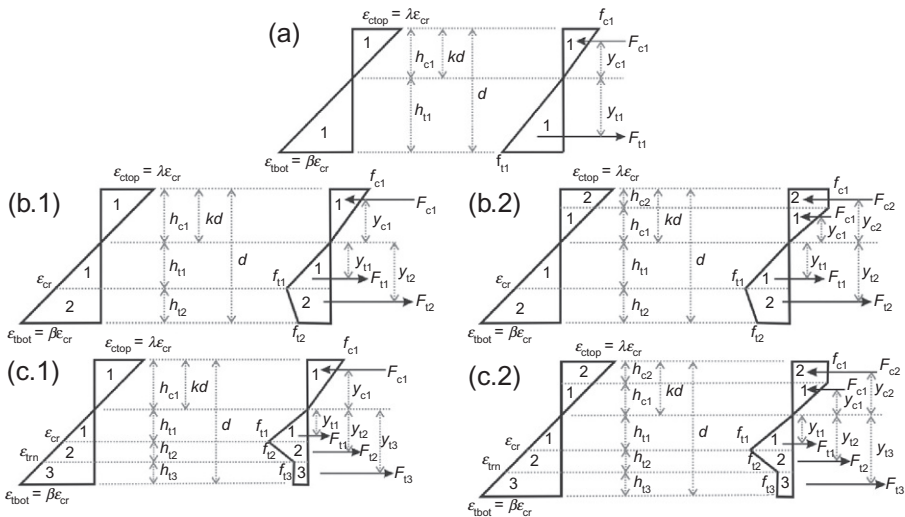
Figure 5.25 Stages in strain distribution across a cross-section: (Stage 1, (a)): $0 < \beta \leq 1$ and $0 < \lambda \leq \omega$; (Stage 2.1, (b.1)): $1 < \beta \leq \alpha$ and $0 < \lambda \leq \omega$; (Stage 2.2, (b.2)): $1 < \beta \leq \alpha$ and $\omega < \lambda \leq \lambda_{cu}$; (Stage 3.1, (c.1)): $\alpha < \beta \leq \beta_{tu}$ and $0 < \lambda \leq \omega$; (Stage 3.2, (c.2)): $\alpha < \beta \leq \beta_{tu}$ and $\omega < \lambda \leq \lambda_{cu}$.

During Stage 1, elastic tensile and compressive stresses represent a linear moment curvature with stiffness *EI*. As shown in Figure 5.25, the elastic Stage 1 ends by the tensile cracking, and the neutral axis moves toward the elastic compression zone denoted as Stage 2.1 (tension cracking-elastic compression). The condition in Stage 2.1 ends under two potential alternatives of entering either a tension-softening Stage 3.1 or Stage 2.2 (tension cracking-plastic compression), depending on the compression zone in elastic ($0 < \lambda \leq \omega$) or plastic range ($\omega < \lambda \leq \lambda_{cu}$). If the compression zone has already entered the plastic range (2.2) then the next step would be tension softening-plastic compression or Stage 3.2. Depending on the relationship among material parameters, any of the Stages 2.1 and 2.2, or 3.1 and 3.2 are potentially possible in succession. In typical strain-hardening fiber-reinforced concrete (FRC), with compressive strength higher than tensile strength, the flexural capacity is controlled by the tension component. The ratio of compressive and tensile modulus, parameter γ, has a negligible effect on the ultimate moment capacity and was assumed as unity (Sueki et al., 2007b).

Moment capacity of a beam section according to the imposed tensile strain at the bottom fiber ($\varepsilon_t = \beta \varepsilon_{cr}$) is derived based on the force components and the centroidal distance to the neutral axis. For a rectangular cross-section with a width "*b*" and depth "*d*," the Kirchhoff hypothesis is applied. The location of neutral axis k, moment M', and curvature ϕ', for a given tensile strain level β is provided in Table 5.3 and represents all potential combinations of interaction of tensile and compressive material models. The moment M_i and curvature ϕ_i at each stage i (corresponding to input β) are normalized with respect to the values at cracking M_{cr} and ϕ_{cr}.

$$M_i = M' M_{cr}; \quad M_{cr} = \frac{1}{6} b d^2 E \varepsilon_{cr} \tag{5.9}$$

$$\phi_i = \phi_i' \phi_{cr}; \quad \phi_{cr} = \frac{2 \varepsilon_{cr}}{d} \tag{5.10}$$

The load–deflection response of a beam can be obtained by moment distribution and moment-curvature relationship using crack localization rules. The mid-span deflection is obtained directly using the double integration of curvature distribution, or by closed form solution of bilinear moment curvature response. A set of equations for calculating the mid-span deflection δ of four-point and three-point bending at the first cracking (δ_{cr}) and at ultimate (δ_u) under the condition of $\mu > \mu_{crit}$ is presented in Table 5.4.

5.5.2 Experimental verification

Tensile properties can be back-calculated from the flexural tests using an inverse analysis algorithm. The design-oriented model based on the inverse analysis can be adopted as a design algorithm as well. There are two ways to accomplish the curve fitting: forward calculation using tension data, and back-calculation of the flexural data. Only the back-calculation approach is used, since it uses multiple attempts of the forward calculation procedure. Applicability of this model to TRC composites

Table 5.3 **Neutral axis parameter k, normalized moment m, and curvature ϕ for each stage of tensile strain at bottom fiber (β)**

Stage	Parameters	k	$m = M/M_{\mathrm{cr}}$	$\phi = \Phi/\Phi_{\mathrm{cr}}$
1	$0 < \beta \leq 1$	$k_1 = \begin{cases} \dfrac{1}{2} & \text{for } \gamma = 1 \\ \dfrac{-1+\sqrt{\gamma}}{-1+\gamma} & \text{for } \gamma \neq 1 \end{cases}$	$m_1 = \dfrac{2\beta\left[(\gamma-1)k_1{}^3 + 3k_1{}^2 - 3k_1 + 1\right]}{1-k_1}$	$\phi'_1 = \dfrac{\beta}{2(1-k_1)}$
2.1	$1 < \beta \leq \alpha$ $0 < \lambda \leq \omega$	$k_{21} = \dfrac{D_{21} - \sqrt{D_{21}\gamma\beta^2}}{D_{21} - \gamma\beta^2}$ $D_{21} = \eta\left(\beta^2 - 2\beta + 1\right) + 2\beta - 1$	$M'_{21} = \dfrac{(2\gamma\beta^3 - C_{21})k_{21}{}^3 + 3C_{21}k_{21}{}^2 - 3C_{21}k_{21} + C_{21}}{1 - k_{21}}$ $C_{21} = \dfrac{(2\beta^3 - 3\beta^2 + 1)\eta + 3\beta^2 - 1}{\beta^2}$	$\phi'_{21} = \dfrac{\beta}{2(1-k_{21})}$
2.2	$1 < \beta \leq \alpha$ $\omega < \lambda \leq \lambda_{\mathrm{cu}}$	$k_{22} = \dfrac{D_{22}}{D_{22} + 2\omega\gamma\beta}, \ D_{22} = D_{21} + \gamma\omega^2$	$M'_{22} = \left(3\gamma\omega\beta^2 + C_{22}\right)k_{22}{}^2 - 2C_{22}k_{22} + C_{22},$ $C_{22} = C_{21} - \dfrac{\gamma\omega^3}{\beta^2}$	$\phi'_{22} = \dfrac{\beta}{2(1-k_{22})}$
3.1	$\alpha < \beta \leq \beta_{\mathrm{tu}}$ $0 < \lambda \leq \omega$	$k_{31} = \dfrac{D_{31} - \sqrt{D_{31}\gamma\beta^2}}{D_{31} - \gamma\beta^2}$ $D_{31} = \eta\left(\alpha^2 - 2\alpha + 1\right) + 2\mu(\beta - \alpha) + 2\alpha - 1$	$M'_{31} = \dfrac{(2\gamma\beta^3 - C_{31})k_{31}{}^3 + 3C_{31}k_{31}{}^2 - 3C_{31}k_{31} + C_{31}}{1 - k_{31}}$ $C_{31} = \dfrac{(2\alpha^3 - 3\alpha^2 + 1)\eta - 3\mu(\alpha^2 - \beta^2) + 3\alpha^2 - 1}{\beta^2}$	$\phi'_{31} = \dfrac{\beta}{2(1-k_{31})}$
3.2	$\alpha < \beta \leq \beta_{\mathrm{tu}}$ $\omega < \lambda \leq \lambda_{\mathrm{cu}}$	$k_{32} = \dfrac{D_{32}}{D_{32} + 2\omega\gamma\beta}, \ D_{32} = D_{31} + \gamma\omega^2$	$M'_{32} = \left(3\gamma\omega\beta^2 + C_{32}\right)k_{32}{}^2 - 2C_{32}k_{32} + C_{32},$ $C_{32} = C_{31} - \dfrac{\gamma\omega^3}{\beta^2}$	$\phi'_{32} = \dfrac{\beta}{2(1-k_{32})}$

Table 5.4 Equations for calculating deflection at mid-span

Deflection	Four-point bending	Three-point bending
Elastic region	$\delta_{cr} = \frac{23}{216}L^2\varphi_{cr}$	$\delta_{cr} = \frac{1}{12}L^2\varphi_{cr}$
$\mu > \mu_{crit}$ Deflection hardening	$\delta_u = \frac{L^2}{216}[a_1\varphi_u + a_2\varphi_{cr}]$ $b = \frac{M_{cr}}{M_u}$, $a_1 = 23 - 4b - 4b^2$, $a_2 = 4 + 4b$	$\delta_u = \frac{L^2}{24}[a_1\varphi_u + a_2\varphi_{cr}]$ $b = \frac{M_{cr}}{M_u}$, $a_1 = 2 - b - b^2$, $a_2 = 4 + b$
$\mu < \mu_{crit}$ Deflection hardening or softening	$\delta_u = \frac{5L^2\varphi_u}{72} + \frac{M_uL^2\varphi_{cr}}{27M_{cr}}$	$\delta_u = \frac{\varphi_u L_p}{8}(2L - L_p) + \frac{M_u\varphi_{cr}L}{12M_{cr}}(L - 2L_p)$

was verified by analyzing a series of data from a variety of composites. Tensile response of PE textile-reinforced composite (Mobasher et al., 2004, 2006, 2014; Peled and Mobasher, 2005; Peled et al., 2006), glass and carbon fiber cementitious laminates (Krauss and Mobasher, 2011) were studied. Simulation of experimental data is shown in Figure 5.26. Modeling parameters introduced in Equations (5.5)–(5.7), (5.9), (5.10) and Table 5.5 were used to calibrate the experimental tensile response as reported in Table 5.4. The values for the simulation of results are shown
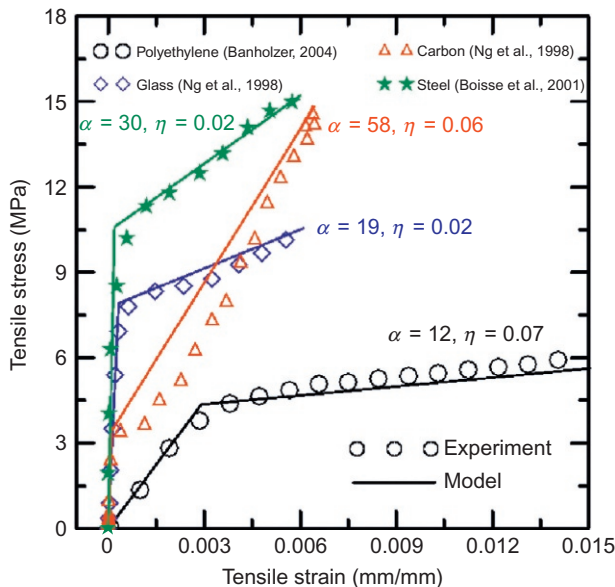
Figure 5.26 Simulation of reference tensile response of textile-reinforced concrete (TRC) (Banholzer, 2004; Ng et al., 1998), steel fiber-reinforced concrete (Boisse et al., 2001).

Table 5.5 Model parameters used to simulate tensile response of reference data (Peled and Mobasher, 2005; Peled et al., 2004; Mobasher et al., 2004)

Ref. data	E (MPa)	ε_{cr} (µstr)	α	γ	H	μ	β_{tu}
Polyethylene TRC	1500	2900	12	1	0.070	0.80	14
Glass TRC	24,000	330	19	1	0.019	0.16	20
Carbon TRC	31,000	111	58	1	0.058	0.90	58
Steel FRC	53,000	200	30	1	0.015	0.65	75

in Table 5.5. The analytical approach is capable of predicting the tensile properties of different TRC composites with a reasonable degree of accuracy as shown in the figure.

Curve fitting of flexural results by varying the input tensile data was accomplished for the TRC composites with the individual fabrics with aramid (100A), carbon (100C), glass (100G), and PP (100P) and the resulting final tensile model was compared with the experimental tension data. The key parameters α, η, and μ were changed to fit the experimental load–deflection and predict tensile stress–strain curves.

Figure 5.27 shows the experimental and predicted responses of aramid fabric composites (100A). Solid lines represent the simulated response for both flexural and tensile response, obtained from the constitutive model. Experimental flexural data is represented by symbols only, whereas experimental tensile responses are presented as shaded bands. Figure 5.27a shows the flexural load–deflection, and Figure 5.27b shows the tensile stress–strain responses of the aramid composites. The load-versus-deflection response based on the simulated fit of the data matches the experimental response as shown in Figure 5.27a. The overall predictions are well established, and the discrepancies could be attributed to the variation between the individual test
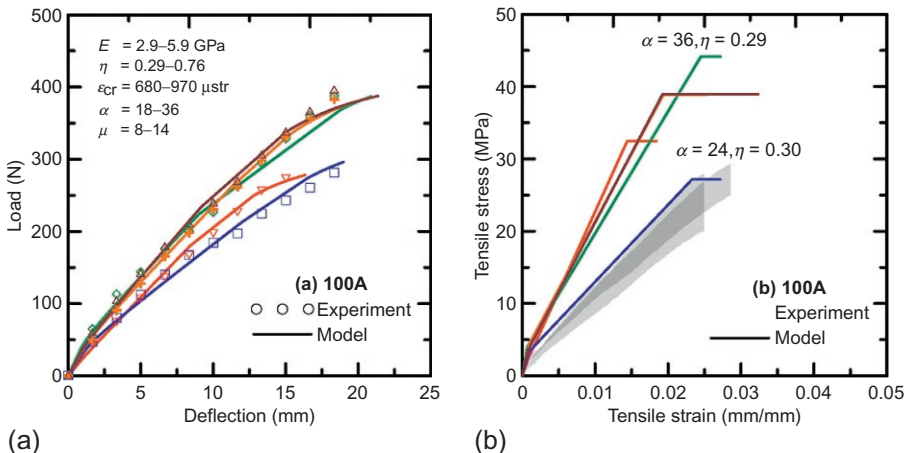
Figure 5.27 100% aramid: (a) flexural; (b) tension responses.

results. Representative properties for the simulation of upper- and lower-bound values obtained from the 100% aramid specimens were: $E=2.9$–5.9 GPa, $\alpha=18$–36, $\mu=8$–14, $\eta=0.29$–0.76, $\varepsilon_{cr}=680$–970 µstr. In all these fits, the parameters for the ratio of compressive to tensile stiffness and strength were held constant at $\gamma=1$, and $\omega=11$. The strain limits were set at $\beta_{tu}=23$–42 and $\lambda_{cu}=71$. As evident, direct correlation among samples shows lower flexural strength associated with lower values for the fit parameters.

Tensile stress–strain responses are shown in Figure 5.27b and compare the experimentally obtained and back-calculated response from the flexural data. Note that the initial linear portion of the curve is not well captured, since the recording of the first-crack strain was based on deflection measurements from the actuator, which over-estimated the real deformation in the test coupon. This affects estimation of the real deflection/strain in the specimen under the imposed loading. While the model is quite accurate in fitting the flexural data, the tensile parameters obtained from back-calculation do not correlate very well in terms of the overall postcrack stiffness, stress, and strain capacity.

The majority of the back-calculated tensile results overpredict the experimental tension data. This is attributed to the definition of axial strain based on the cross-head displacement, which leads to inclusion of spurious and excessive deformations. The size effect is apparent as the tensile results are generally lower than the values predicted from the flexural tests, and that is expected, as the tension test has a much larger tensile region compared to a flexural test.

Response of different fabric systems are shown in Figure 5.28a and b. As evident, the carbon system shows an exceedingly high tensile strength and postpeak modulus, which can be evaluated using model parameter, η; however, its flexural stiffness and deflection capacity are comparable to the glass composites. Peak load strain capacity, characterized by parameter α, is moderately higher for glass composites compared to carbon. The aramid system shows intermediate tensile/flexural strength and postcrack
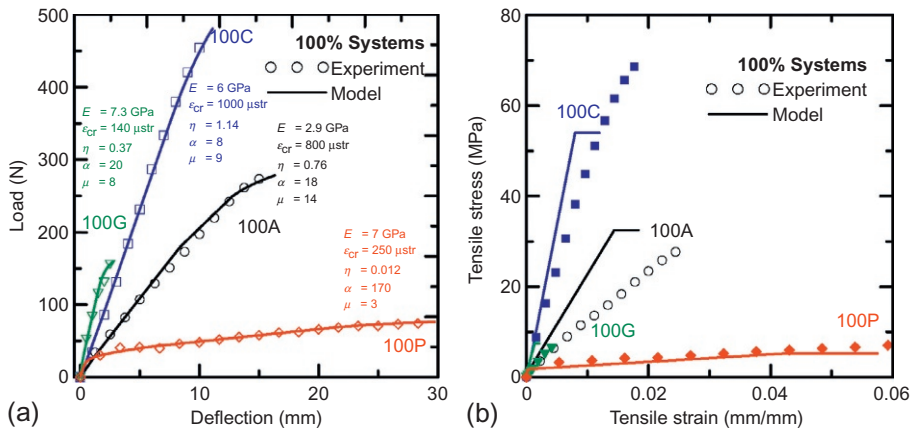
Figure 5.28 Comparison between carbon (100C), AR-glass (100G), polypropylene (100P), and aramid (100A) systems: (a) flexural; (b) tension responses.

modulus, and has strain capacity similar to glass system. The PP system exhibits the lowest load carrying, but highest deflection capacity. Strain capacity of PP composites is an order of magnitude higher than the other textile systems. First-cracking strain capacity of glass and polypropylene systems are similar and much smaller than carbon and aramid composites. A comparison of tension-simulated and experimental results in Figure 5.28b indicates that while the back-calculation approach manages to simulate the tensile strength of aramid and glass systems reasonably well, however postcracking stiffness is overpredicted. On the contrary, while the simulated tensile strength of carbon and PP composites are overpredicted, the initial and postcracking stiffness values are similar to the experimental responses.

5.6   High-speed tensile tests

5.6.1   Testing methods

Characterization of dynamic tensile properties of materials is challenging, as the failure process is affected by the mode and manner of testing. Problems appear at high rate loading due to inertial effect, nonuniform loading, and reliability of measuring mechanical properties. Lack of general agreement about the standards and methodology used to conduct dynamic tensile tests further complicates the merging of the databases (Xiao, 2008). Mechanical response of cement-based materials depends on the strain rate (Xu et al., 2004; Zhang et al., 2005; Bharatkumar and Shah, 2004; Silva et al., 2010). Most of the available literature on the dynamic tensile behavior of concrete are based on plain concrete in compression, and only limited data support an increase in tensile strength due to strain rate effects (Candoni et al., 2001; Xiao et al., 2008). Dynamic tensile data on fiber and fabric-reinforced concrete are even more limited.

A number of experimental techniques are used to investigate high strain rate material properties, which includes: split Hopkinson pressure bar (SHPB), falling weight devices, flywheel facilities, hydraulic machine, etc. (Meyers, 1994; Nicholas, 1981; Kenneth, 1966; Zabotkin et al., 2003). Most of the experimental studies under high strain rates (above 1 s^{-1}) have been performed using split Hopkinson bar (SHB) tests. Use of servo-hydraulic machines in medium strain rate tensile testing was reported for metals (Bastias et al., 1996; Bruce et al., 2004), plastics (Xiao, 2008; Hill and Sjöblom, 1998), composite materials (Fitoussi et al., 2005), and woven fabrics (Zhu et al., 2008a,b).

The dynamic tensile tests for TRC materials conducted using an MTS® high-speed servo-hydraulic testing machine are presented in Figure 5.29a and b (Yao, 2013). The speed of the actuator was controlled by the servo-valve, and the nominal strain rate was measured from the stroke rate and sample gage length. Full-size pictures that recorded the cracking and failure of samples were captured at a rate of 10,000 fps.

Depending on the methodology used in the measurement of sample displacement, strain rate values may significantly depend on the test setup. Several dynamic tensile test results have used the linear variable differential transformer (LVDT) of the
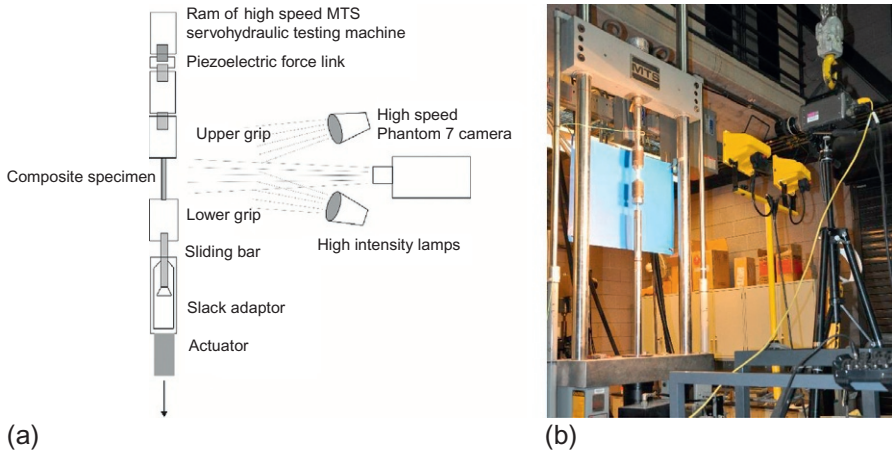
Figure 5.29 (a) Schematic drawing; (b) setup of the testing system with high-speed camera.

actuator in the servo-hydraulic high-rate testing machine (Silva et al., 2011). The accuracy of the measurement is affected by the compliance and inertial effects of the testing fixtures, and may differ from testing machine to machine.

5.6.2 Digital image correlation

Digital image correlation (DIC) is a noncontacting optical full-field deformation measurement approach that addresses the complex behavior of TRC materials. Developed by Sutton et al. (1983) and Bruck et al. (1989), this method has been widely applied for composites and reinforced concrete sections (Destrebecq et al., 2011; Koerber et al., 2010; Gao et al., 2015). In order to perform DIC, an area of interest (AOI) is manually specified and divided into an evenly spaced virtual grid as shown in Figure 5.30a. The displacements are computed at each point of the virtual grids to obtain full-field deformation. The imposed red square is the subset (a set of pixels) for tracking the movement of its center point $P(x, y)$ from the reference image (before deformation) to deformed images $P'(x', y')$ (Figure 5.30b). The tracking of subset is conducted using selected correlation functions such as cross-correlation (CC) or normalized cross-correlation (NCC) (Pan et al., 2009). Subsequently, the strain fields can be derived by smoothing and differentiating the displacement fields.

5.6.3 Discussion of results

Silva et al. (2010) performed high-speed tensile tests in sisal fiber-reinforced cement composites at $\dot{\varepsilon} = 24.6 \text{ s}^{-1}$ as shown in Figure 5.31. The oscillations in load represent the dynamic ringing effect. Two different displacement measuring approaches are shown, which include the cross-head displacement as well as the image analysis using the DIC approach. Pronounced strain rate dependence was noted for toughness and failure strain due to the pullout behavior. Mechanics of rate sensitivity under pullout
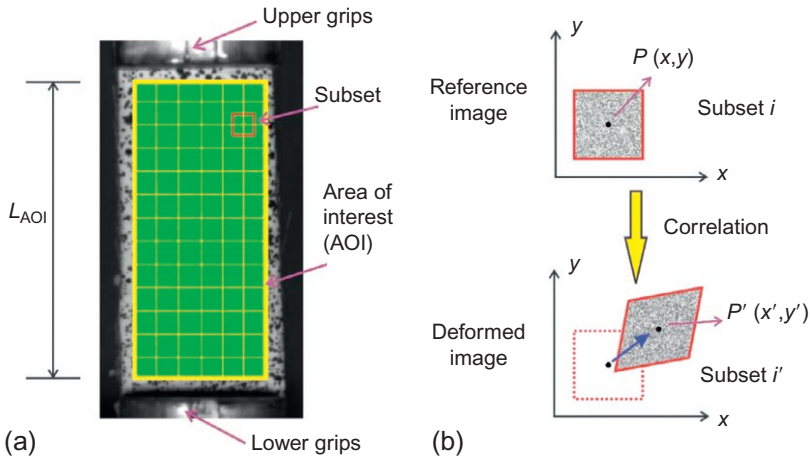
Figure 5.30 (a) Area of interest (AOI) and subset in a reference image; (b) schematic presentation of a reference subset before deformation and the corresponding target subset after deformation.
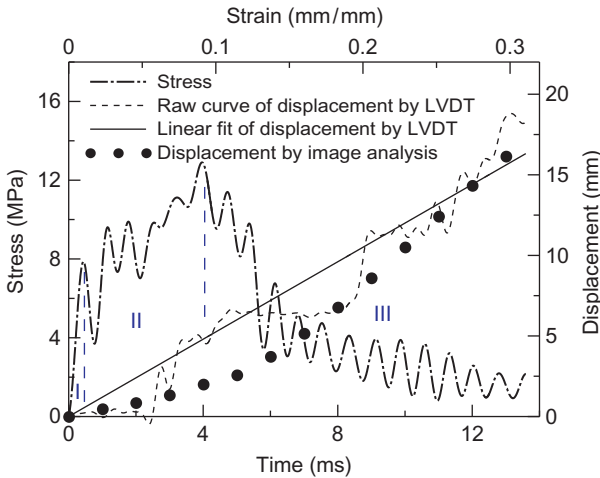
Figure 5.31 Stress–strain and displacement–time curves of sisal fiber cement composite obtained by the LVDT and the image analysis (DIC).

were the dominant mechanisms affecting the response. High-speed tensile test results of Silva et al. (2010) in sisal fiber-reinforced cement composites at $\dot{\varepsilon} = 24.6$ s^{-1} show a pronounced dependence for ultimate strain (average value of 10%) due to the pullout fracture of fibers.

5.6.4 Hybrid systems—short fibers with TRC

The influence of matrix modifications by the addition of short fibers on the quasistatic tensile response of TRC was investigated in several studies (Silva et al., 2011; Hinzen and Brameshuber, 2009; Barhum and Mechtcherine, 2010). Silva et al. (2011)
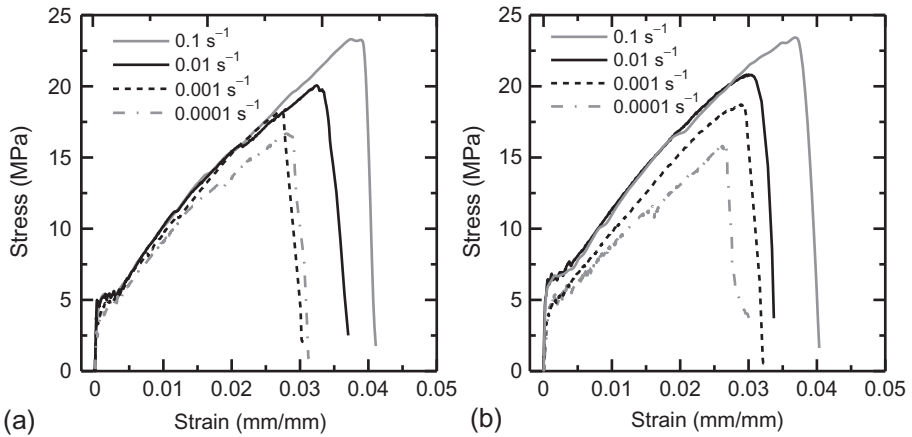
Figure 5.32 Effect of strain rate on the tensile stress–strain response of (a) TRC and (b) TRC with short glass fibers for rates up to 0.1 s^{-1}.

subjected TRC with and without short glass fibers in the matrix to tensile loading ranging from 1×10^{-4} to 50 s^{-1}. An increase in tensile strength, strain capacity, and work-to-fracture was observed with increasing strain rates up to 0.1 s^{-1}.

Figure 5.32 shows the representative stress–strain curves for TRC specimens tested at different low strain rates, i.e., 0.1 s^{-1} and below, with and without the addition of short fibers. TRC, with and without short fibers, displayed an increase in tensile strength, work-to-fracture, and strain capacity (see Figure 5.32a and b). The average tensile strength of TRC with plain matrix increased from 16.1 to 23.6 MPa, work-to-fracture rose from 18.5 to 33.5 J, and strain capacity increased from 3.08% to 3.92%. For TRC with the addition of short glass fibers tensile strength rose from 17.1 to 23.2 MPa, work-to-fracture from 16.1 to 31.7 J, and strain capacity from 2.65% to 3.58%. The σ_{BOP^+}, i.e., the stress where the first crack is formed, showed an increase with increasing strain rate for both materials under study, but with superior values for TRC with short fibers. Young's modulus showed a general tendency to increase; however, the scatter of the results was too high to draw firm conclusions.

Figure 5.33a and b shows typical stress–strain curves obtained at high strain rates ($\geq 5 \text{ s}^{-1}$) on TRC specimens with and without short fibers, respectively. The shapes of the curves differ significantly to those obtained for lower strain rates; however, there was a similar multiple cracking pattern in combination with strain-hardening behavior. Oscillations of the system at its natural frequency are observed for specimens tested at 5 and 20 s^{-1}. These oscillations seem to decrease as the strain rate increased. Composites tested at high strain rates showed an increase in tensile strength, work-to-fracture, and first-crack strength, but a decrease in the strain capacity with increasing strain rate. The decrease in the strain capacity corresponds to the increase in the stiffness of the composite (measured as the slope of the stress versus strain curve from the first-crack strength up to the ultimate strength) when increasing the strain rate after the first crack formation.
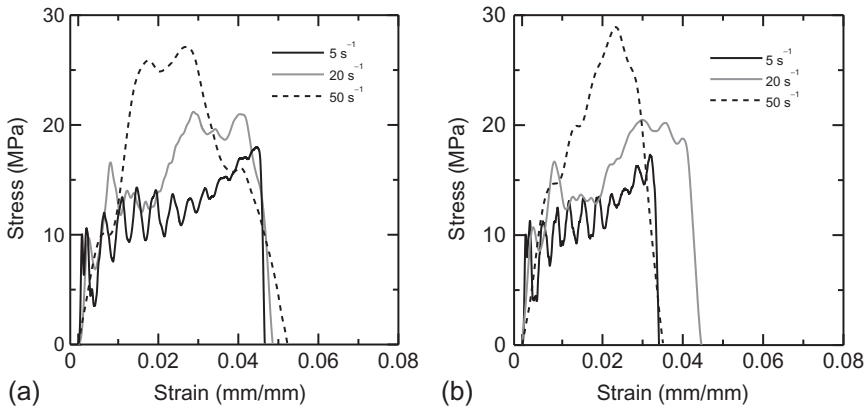
Figure 5.33 Effect of strain rate on tensile stress–strain response of (a) TRC and (b) TRC with short glass fibers for rates ranging from 5 to 50 s^{-1}.
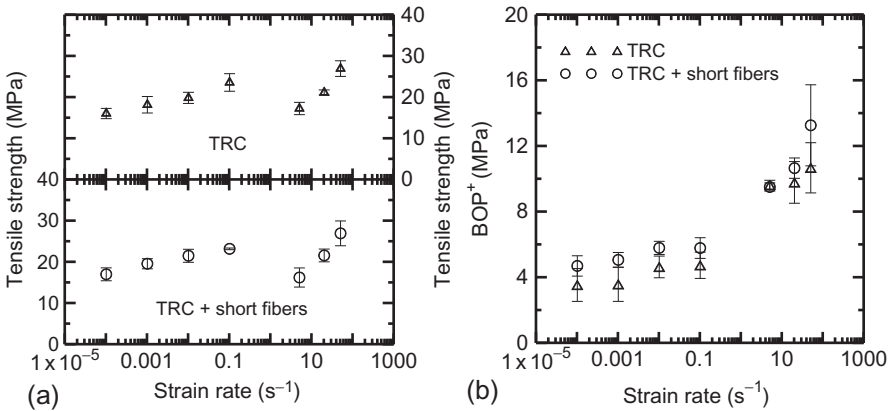
Figure 5.34 Effect of strain rate on (a) tensile strength and (b) on bend-over point (BOP$^+$) of TRC and TRC with short fibers.

For strain rates above 5 s^{-1}, increase in the tensile strength and work-to-fracture was observed with a decrease in the strain capacity. High loading rate tests as shown in Figure 5.34 indicate a pronounced effect of the strain rate on the mechanical properties—with increasing rate, the tensile strength increased significantly. The overall effect of strain rate on the tensile strength and first-crack strength response of the samples with and without short fibers are shown.

Yao et al. (2015) studied the multiple cracking mechanisms in TRC samples tested under high-speed tensile loads and varying temperatures. Three types of textiles were used: (1) laminated AR-glass that is coated with sizing and referred to as SG; (2) warp-knitted AR-glass without sizing and referred to as

GL; and (3) warp-knitted PP-glass hybrid referred to as PP. Figure 5.35 compared the force–strain responses of various TRC specimens tested under different temperatures. Multiple cracking and textile pullout phenomenon was observed both for GL-TRC and SG-TRC in Figure 5.35a and b, respectively. Unlike the AR-glass TRCs, failure mode of the PP-TRCs is dominated by the fiber fracture due to the low tensile strength of PP as shown in Figure 5.35c. The highest tensile strength of 38.1 MPa and work-to-fracture of 46.6 J were observed in the GL-TRC specimens at $-30\ °C$. Composites with strength ranging from 10.8 to 14.3 MPa under varying temperatures were obtained from PP-TRCs.
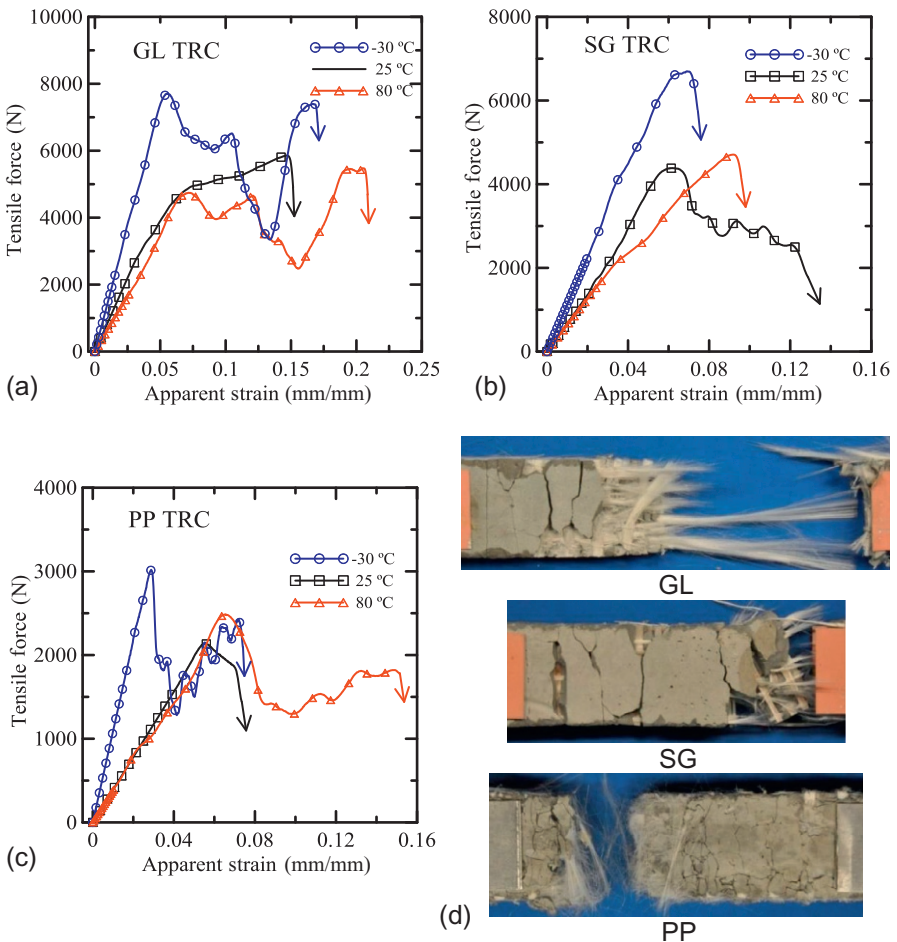
Figure 5.35 Representative force–strain responses at varying temperatures for: (a) GL-TRC; (b) SG-TRC; (c) PP-TRC; (d) tested specimens.

5.6.5   Analysis of distributed cracking and damage using DIC

5.6.5.1   Detection of cracks and measurement of crack width

Figure 5.36a shows the contour of longitudinal displacement of a TRC sample tested at 25 s^{-1} after cracking. The sequential formation of five individual cracks is indicated in Figure 5.36b. The distribution of the displacement field is shown in Figure 5.36b for various stress levels with the cracks identified as the discontinuities in the displacement. The location and width (ω) of a certain crack is represented by the x-coordinate and the vertical amplitude of the discontinuity. Figure 5.36c shows the evolution of cracks and the mean response versus time up to failure. The stress-versus-time history is also plotted, indicating the loading level. The mean crack widths obtained by DIC was correlated with the stress responses of representative samples, as shown in Figure 5.36d. The linear elastic stage is represented by a vertical line and extends to the BOP as the first-cracking strength, from 2.9 to 4.2 MPa. Pronounced strain-hardening effect was observed after cracking, as the tensile stresses increased with a reduced stiffness.
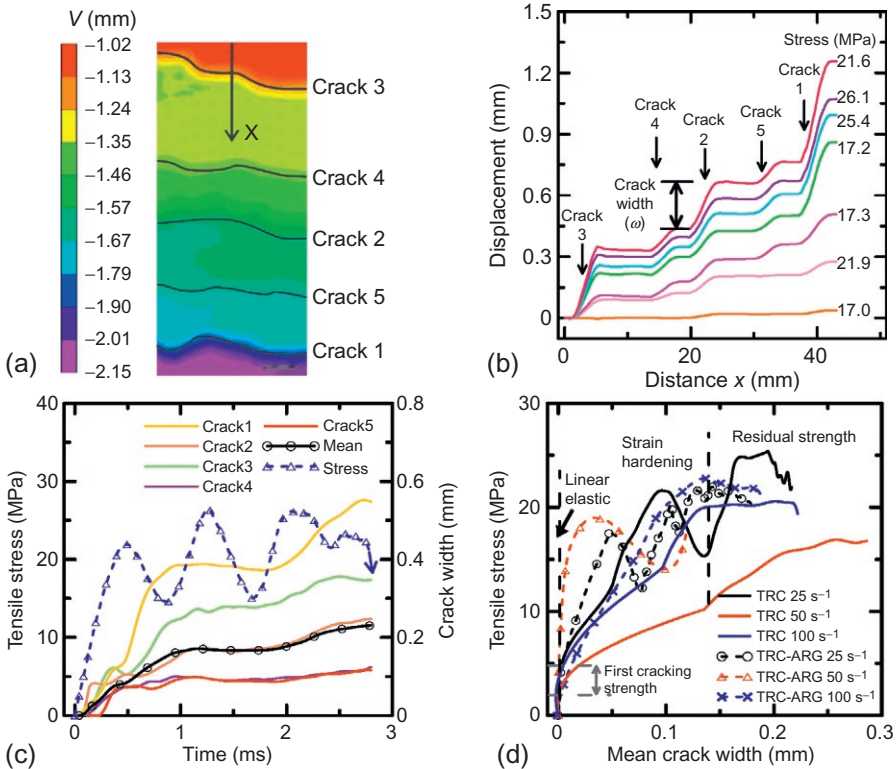
Figure 5.36 (a) Longitudinal displacement contour of a TRC specimen tested at 25 s^{-1}; (b) distribution of displacement at seven loading stages; (c) crack width and tensile stress vs. time histories; (d) stress-crack width responses of representative specimens.

5.6.5.2 Quantification of the strain fields

The longitudinal strain (ε_{yy}) fields of ARG-TRC specimens tested at 25 s^{-1} are shown in Figure 5.37a using a color code, with purple representing the lowest strain value and red at 5.0% strain. Saturation of transverses cracks was coincident with maximum tensile stress ($\sigma = 21.6$ MPa) as shown in Figure 5.37b with three identified zones as: (A) the localization zone in red that contains the transverse crack with the majority of the load carried by the textile phase; (B) the shear lag zone in green/blue, where the slip between fiber and matrix cannot be ignored and the bond stress follows a shear lag pattern; (C) the uniform zone where no crack is formed, composite is behaving linearly, and slip is negligible. The variation of fiber stress along the length reaches a maximum level in the bridge zone (A) and minimum at the "perfectly bonded" zone (C).

The three distinct zones identified by DIC observations are shown in Figure 5.37b. The distance is normalized with respect to the length of AOI, and zones are separated by
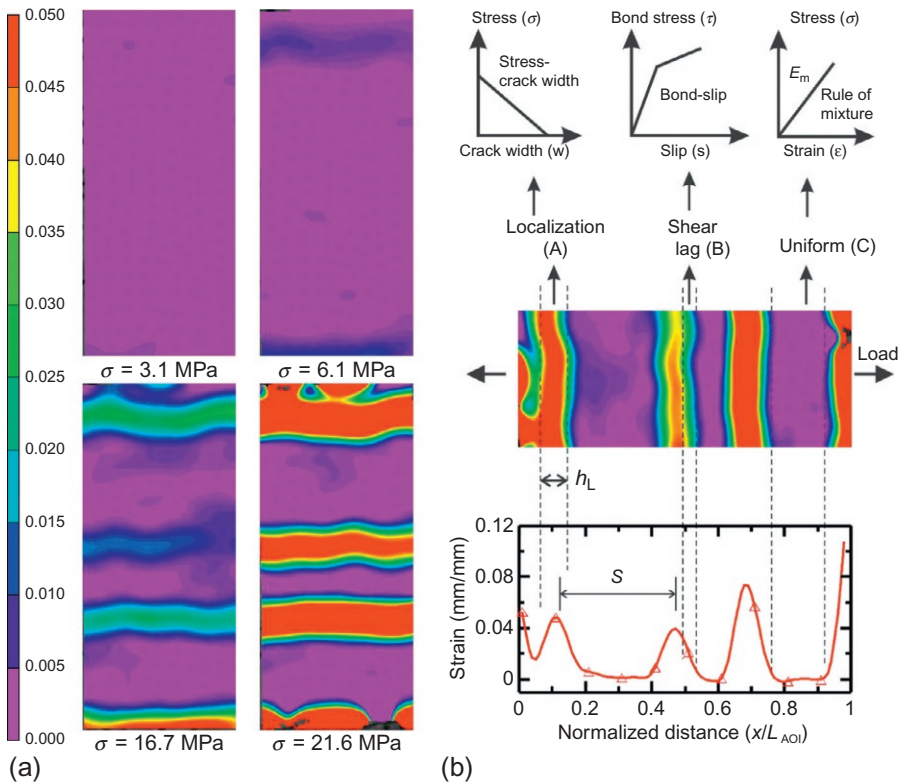
Figure 5.37 (a) Strain fields (ε_{yy}) obtained by DIC for TRC-ARG specimen tested at the strain rate of 25 s^{-1}; (b) identification of three zones: localization, shear lag, and uniform strain and corresponding modeling approaches.

the dashed lines. The behaviors at zones can be modeled as different points an σ–ω relationship, nonlinear bond stress–slip relationship, and with a linear stress–strain relationship, respectively.

5.6.6 Tension-stiffening model

A finite difference method developed by Soranakom and Mobasher (2008b) was used to model the tension-hardening behavior in TRC. A tension specimen is idealized as a series of 1D segments consisting of fiber, matrix, and interface elements. The matrix is treated as brittle with no strain-softening response. An iterative solution algorithm is used to enforce material constitutive laws and obtain load deformation. The pattern and distribution of slip and fiber stress in cracked segments are schematically shown in Figure 5.38a, where the fiber slip occurs in cracking regions indicated by the bold lines. Figure 5.38b shows the model of a cracked specimen. Figure 5.38c presents the cracking criterion by four distinct and competing mechanisms: matrix cracking criterion; interface bond-slip characteristics; tensile stress–strain of the longitudinal yarn; and mechanical anchorage provided by cross-yarn junctions.

Transverse yarns are simulated as spring elements attached to the nodes at cross-yarn junctions and provide additional resistance to pullout force. Due to the inefficiency of the bond, a postcrack stiffness efficiency factor η for textile was introduced to account for the reduction of the elastic stiffness of plain textile to its apparent stiffness as observed in the experiments. Experimental stress–strain responses are compared with the numerical simulations in Figure 5.39. The crack spacing measured from high-speed images was verified using the DIC. It is noted that the PP composites have the largest number of cracks and smallest average crack spacing, while SG composites have the largest crack spacing but fewer cracks than PP.

5.7 Flexural impact

5.7.1 Introduction

Low-velocity impact applications are an attractive area where the use of TRC materials can be justified. Various impact tests include: Charpy, Izod, drop-weight, uniaxial tension, and ballistic tests, and may be instrumented or heuristically based. The resistance can be measured based on fracture energy, damage accumulation, and/or measurement of the number of drops to achieve a desired damage or stress level. Bindiganavile and Banthia (2001a,b) showed that flexural strength of FRC is higher under impact loading in comparison to quasistatic loading. Polymeric FRC showed an improvement in energy absorption under impact loading. Manolis et al. (1997) also showed that fibrillated PP fibers significantly improve the impact resistance of concrete slabs. Wang et al. (1996) addressed fiber fracture and fiber pullout as two different damage mechanisms for FRC under drop-weight impact. Zhu et al. (2009) studied the impact behavior of AR-glass TRC. Maximum flexural stress and absorbed energy of beam specimen increased with the number of textile layers. Impact properties of PE TRC were compared to AR-glass TRC by Gencoglu and Mobasher (2007a).
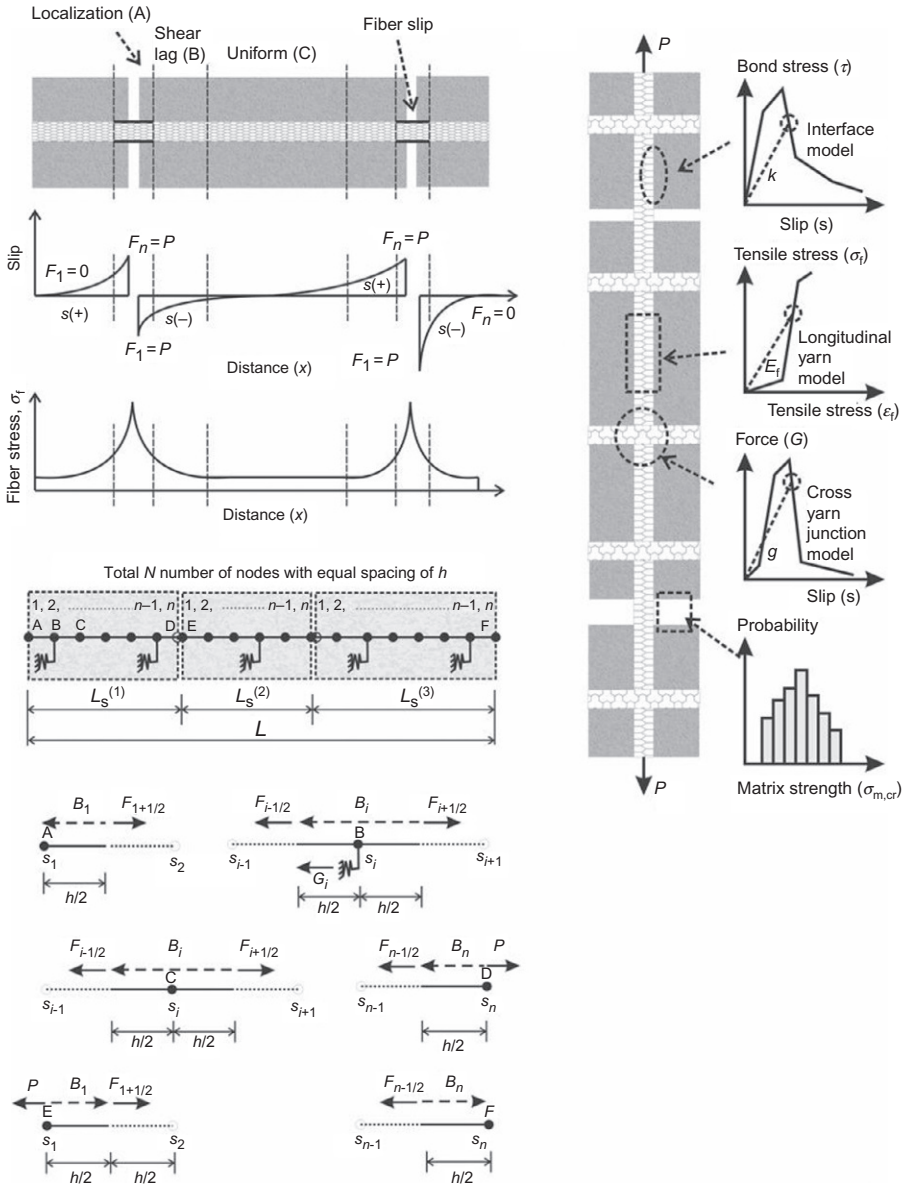
Figure 5.38 Finite difference model: (a) three distinct zones with corresponding distribution of fiber stress and slip; (b) discretized fabric pullout model and free-body diagram of six representative nodes; (c) mechanical behavior of a cracked TRC specimen.
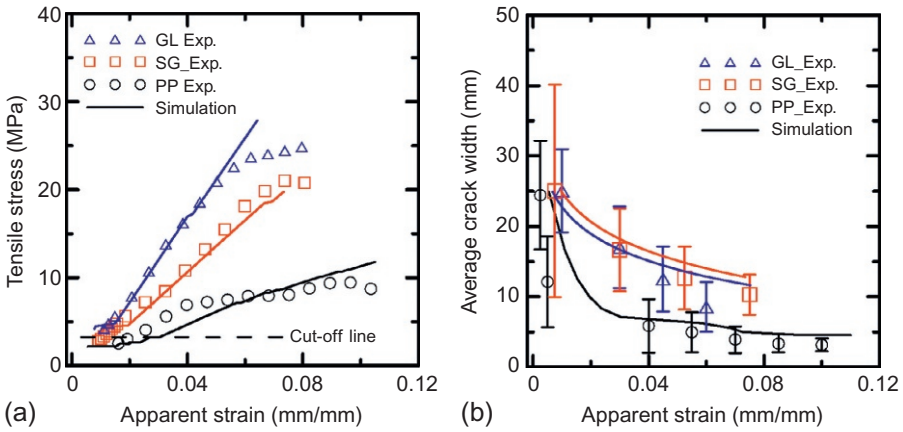
Figure 5.39 Simulations of experimental (a) tensile stress–strain responses and (b) average crack spacing-strain.

The PE textile composites showed higher load-carrying capacity at large deflections and hence more ductile than AR-glass textile composites.

5.7.2 Test setup

Schematics of the testing setup are shown in Figure 5.40. The hammer weighing 14 kg is released from a predefined drop height by means of a mechanical trigger, and the force of impact is measured by a 90 kN capacity strain-gage-based load-cell mounted in between the hammer and blunt-shaped impact head. An LVDT with a range of ±10 mm measured the deflection by means of a lever arm. An accelerometer with a capacity of ±500 g m/s^2 attached to the bottom of the specimen is used to measure
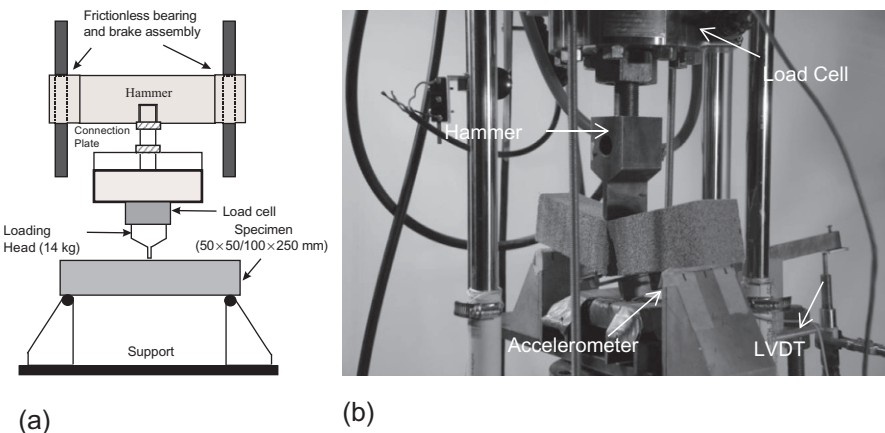
Figure 5.40 Impact test setup (a) schematic diagram and (b) actual setup.

acceleration-time history and act as a trigger for the data acquisition system, which operated at a sampling rate of 20 kHz for 0.2 s. A digital filter with a pass through frequency of 2000 Hz is used to remove the high-frequency noise data (Cain, 1987). Test results were analyzed to determine the load–displacement history, velocity of impact, strain rate, and absorbed energy (Zhu et al., 2009).

5.7.3   Results and discussion

5.7.3.1   Impact response of TRC

TRC composites developed using the pultrusion production process (Peled and Mobasher, 2005) with AR-glass and PE textiles exhibit strain-hardening behavior, tensile strength in the range of 20–25 MPa, and strain capacity of the order of 2–5%. Their impact properties were investigated under three-point bending conditions using the instrumented drop-weight system and variables that include specimen orientation and drop height. The mix design for cement paste of fabric-reinforced cement-based composites was 42% cement, 5% silica fume, 0.1% superplasticizer, and 50% water by volume as the water/cement ratio by weight was 0.4. The AR-glass fibers were with tensile strength of 1270–2450 MPa, elasticity modulus of 78,000 MPa and filament diameter of 13.5 μm. The PE fibers had a tensile strength of 260 MPa, 1760 MPa modulus of elasticity and 0.25 mm diameter. Each composite was made with six layers of fabrics, resulting in reinforcement content of about 4.0% and 8.0% by volume of AR-glass fibers and PE fibers, respectively (Gencoglu and Mobasher, 2007b; Zhu et al., 2011b).

Figure 5.41a and b represents a time-history of load, deflection, and acceleration response of a PE and AR-glass reinforced fabric composites subjected to low-impact velocity. Both the acceleration and deceleration response of the hammer and specimen indicate an initial acceleration as high as 50 g, and the load experienced as high as 2700 N. The phase lag in the deflection signal due to the loading of the specimen indicates that the maximum deflection is achieved as the load decreases and the specimen decelerates to come to rest after the event. The load and strain signals stabilize after the impact event; however, permanent deflection and postfailure oscillations after the impact event are noted. The impact event takes longer for the PE composites than the glass composites, which may be attributed to the distributed cracking and oscillations in the accelerometer signals. The superior energy absorption of TRC can be clearly observed, especially if these data are compared to the plain concrete specimens.

The effect of fabric type as evaluated in Figure 5.42a and b indicates that at each drop height level, the composites with AR-glass textile are stronger, but more brittle than composites with PE TRC. The PE TRC exhibit more load-carrying capacity at large deflections than the AR TRC. The ductility effect is more pronounced after the peak stress when data at the same drop heights are compared. The processing may also contribute to the differences in the results. Due to the size of the opening in the PE fabric, even with the use of pultrusion process, the cement paste may not
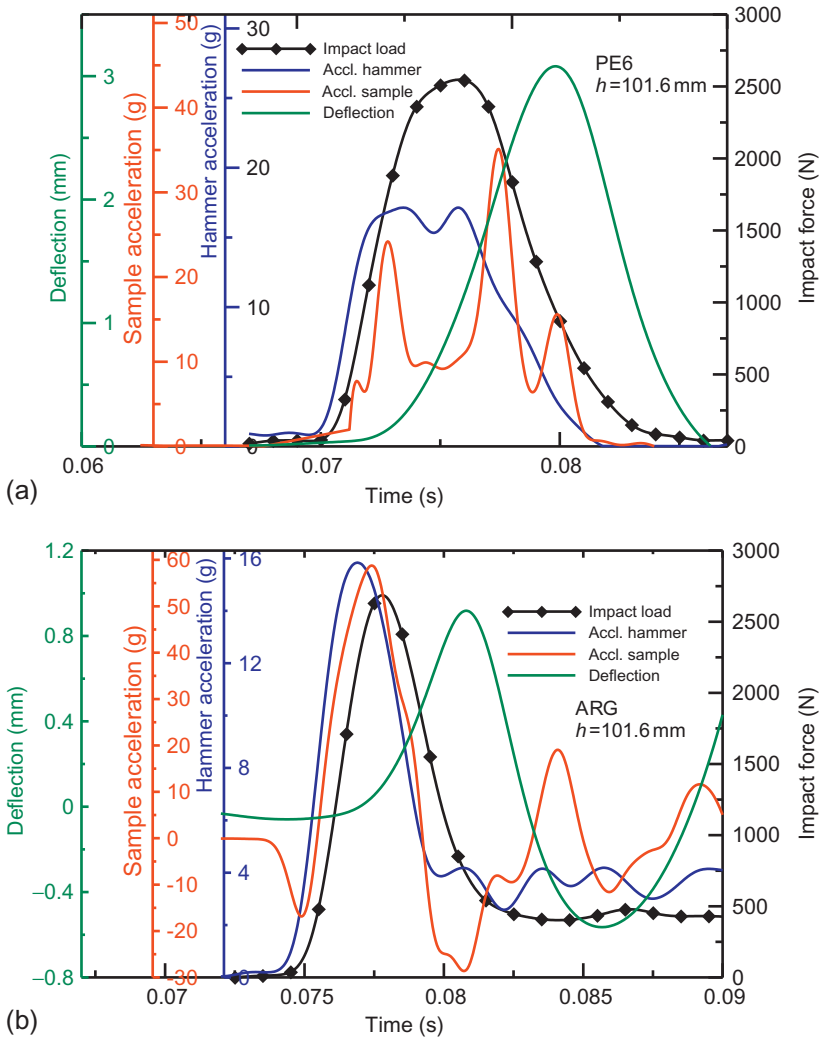
Figure 5.41 Time-history of load, deflection, and acceleration of a fabric-reinforced composite subjected to low-impact velocity: (a) polyethylene fabric; (b) AR-glass fabric.

sufficiently penetrate between the yarns as well as AR-glass fabric. Although the impact load-carrying capacity of PE composites is almost equal to those with AR-glass for same drop height, the impact flexural stress of composites with AR-glass is higher due to the thickness differences between the two systems. It was observed that AR-glass fabrics maintained the bond far better than the PE composites, which exhibited signs of delamination after the impact load indicating that AR-glass TRC have stronger interlaminar bonding than PE TRC.
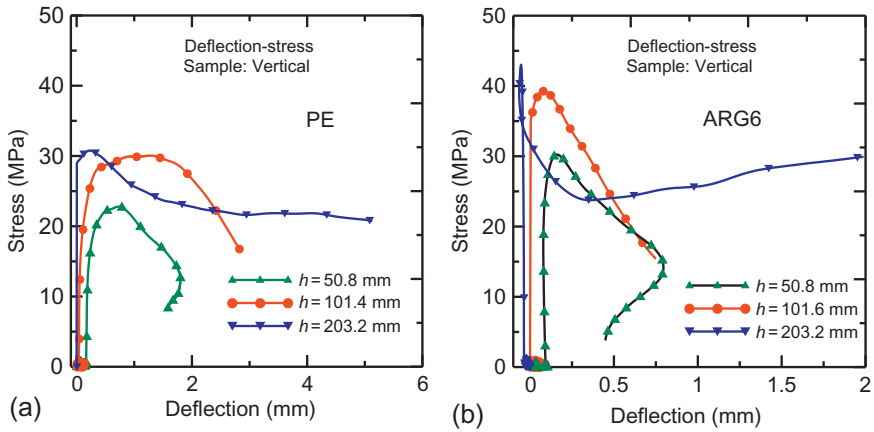
Figure 5.42 Stress vs. deflection of (a) PE and (b) ARG TRC at different drop heights.

5.7.4 Impact response of 3D TRC

TRC composites developed using 3D warp-knitted fabric structures were studied under impact. The 3D fabrics were developed and produced by ITA, RWTH Aachen, and consisted of two sets of independent 2D knitted fabrics, and connected together with a third set of yarns along the thickness direction (referred as spacer yarns). The yarns in the X and Y directions were made from AR-glass bundles of 1200 tex with tensile strength of 1325 MPa and 67 GPa modulus of elasticity. The reinforcing yarns were connected together by stitches (loops) made of fine polyester. The volume content, V_f, of AR-glass reinforcement yarns was of ~1% at the composite plain at both directions. The spacer yarns in the Z direction were used mainly for stabilization of the 3D fabric.

Two 3D fabric composites were prepared: one with cement paste (3DGPC); and the other with replacement of 20% by volume of cement by fly ash (3DGFA). Both mixtures had a 0.4 water/cement ratio and vacuum was applied during casting to allow for matrix penetrability into the opening of the 3D fabric. Samples were demolded after 24 h and cured in 100% relative humidity for 7 days and then at room environment until testing at 28 days after casting. Specimens with dimensions of $200 \times 50 \times 25$ mm of length, width, and thickness were tested.

Two loading arrangements of parallel (vertical) to fabric layers, and perpendicular (horizontal) arrangements were carried out (Figure 5.43a and b, respectively). In the horizontal arrangement, the two faces of the 3D fabric are located at the top and bottom of the specimen relative to the drop direction of the hammer, where the spacer yarns are passing through the thickness from top to bottom. In the vertical arrangement, the two faces of the 3D fabric are located at the sides of the specimen relative to the drop of the hammer, and the spacer yarns are passing through the width of the composite between the two sides of the composite.

A comparison of the typical curves of each system is presented in Figure 5.44a and b, showing the impact stresses versus deflection versus time. The rebound
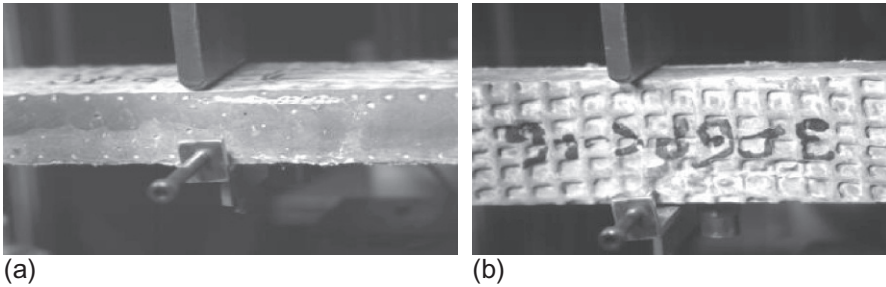
Figure 5.43 3D fabric structure and composite testing arrangements: (a) horizontal; (b) vertical.
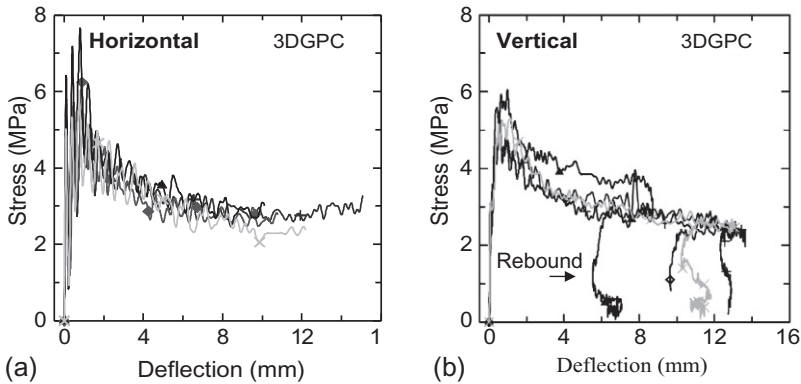
Figure 5.44 Impact behavior of 3D fabric composites at (a) horizontal and (b) vertical arrangements.

mechanism is obvious for the vertically tested system. On the other hand, no such rebound, i.e., shifting back behavior, is seen for the composites tested at horizontal arrangement. Due to this rebound behavior, the entire duration of the test is about twice greater than the composite tested vertically. The toughness of the vertical system is also much greater than that of the horizontal system, providing much better energy absorption of the vertically tested composite; however, the horizontal system exhibits greater maximum stress as compared to the vertical system.

5.7.5 Impact response of sandwich composites

One of the main areas of opportunity for lightweight construction is in the development of sandwich composites. Sandwich composites with AR-glass textile-reinforced cementitious skin were studied in depth with autoclaved aerated concrete (AAC) and fiber-reinforced aerated concrete (FRAC) core material. Quasistatic and low-velocity flexural tests were conducted on two specimen dimensions, and significant improvements in flexural and energy-absorption capacity were reported (Dey et al., 2015). Low-velocity impact response of AAC was investigated by Dey et al. (2013, 2015)
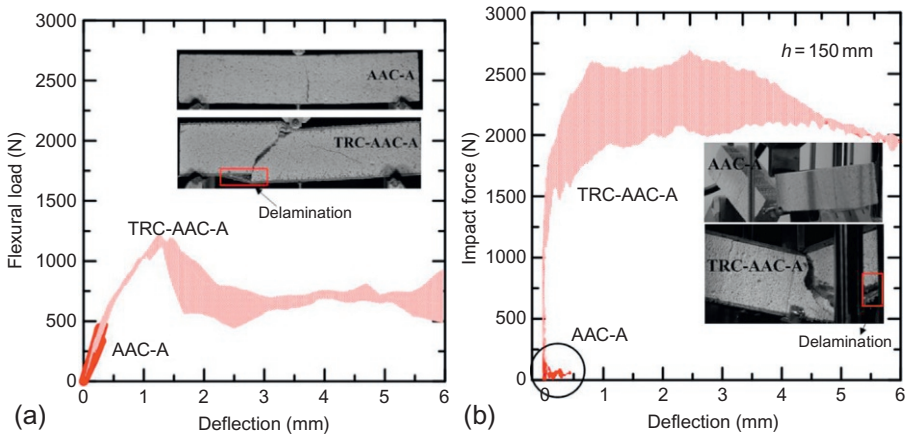
Figure 5.45 Effect of textile reinforcement on AAC under (a) static loading and (b) impact loading.

and Serrano-Perez et al. (2007), and the load-carrying capacity was stated to be limited due to the brittle nature.

Figure 5.45 compares the flexural response of the AAC core alone, as well as core plus TRC skin in the context of sandwich composites for nominal specimen depth of 50 mm (AAC-A vs. TRC-AAC-A). In both quasistatic and impact-loading cases, the plain AAC undergoes a predominantly brittle failure with a single crack in the mid-span. In the presence of the skin layer, however, a ductile behavior with multiple flexural cracks in the tension skin and diagonal tension cracks in the core element are evident in Figure 5.46a and b. This is followed by textile delamination within the skin layer (Figure 5.46b) especially in the region near the supports. Subsequent debonding between the interface of the TRC skin and core is also evident, especially for TRC-AAC composites at higher deflection levels and strain rates. Interfacial delamination as shown in Figure 5.46a–c is mainly caused at higher strain rates,
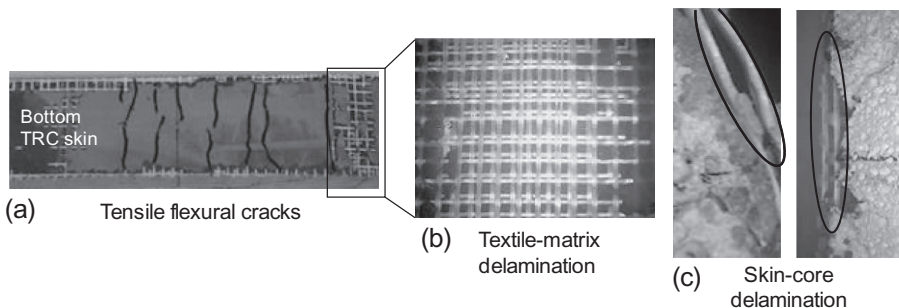
Figure 5.46 Damage mechanisms evident in TRC skin layer subjected to typical flexural loading. (a) Delamination of the skin layer at the edge of the sample, (b) magnified view of delamination, and (c) the delamination between the skin and core fibers within a bonded yarn.

possibly due to the bending-stiffness mismatch between the layers and is related to the delamination fracture toughness (Hong and Liu, 1988; Pozuelo et al., 2006).

Since widening of the major flexural cracks along the depth is restricted by the skin layers, additional flexural cracks form, which further enhance energy-absorption capacity. Toughening mechanisms by the skin layer is by improving the energy-absorption capacity, and residual strength, especially at higher strain rates, thus delaying of the ultimate failure of the core element. The increase of flexural strength of TRC-AAC under both static and impact loading is by factors of 2 and 4 when compared to the plain core.

Figure 5.47a and b compares the behavior of sandwich composites with FRAC and AAC as core elements, under static and impact loading at a drop height of 150 mm. Apparent flexural strength was calculated using the classical bending equation for beams subject to midpoint loading (Dey et al., 2015). Under static loading, flexural strength of TRC-FRAC-A is 3.7 ($\pm$0.1) MPa, which is about 55% higher than TRC-AAC-A. Initial stiffness of TRC-FRAC-A of 1.98 ($\pm$0.31) kN/mm is comparable to TRC-AAC-A at 1.74 ($\pm$0.34) kN/mm. Energy-absorption capacity (toughness), measured as the area enclosed in the load–deflection response for TRC-AAC-A is 1.95 ($\pm$0.25) J at a deflection limit of 2.5 mm is, however, 30% lower than TRC-FRAC-A. Under static loading, the apparent flexural strength of TRC-FRAC-A is higher due to comparatively larger extent of distributed cracking. This is attributed to better interfacial bonding between the skin and FRAC core compared to the AAC core. Thus, beyond the peak load, the load-carrying capacity drops significantly for TRC-AAC-A beam as the brittle AAC core does not offer much resistance to crack propagation. In the advent of a weak core–skin interface, postpeak performance of the composite depends predominantly on the residual load-carrying capacity of the core material.
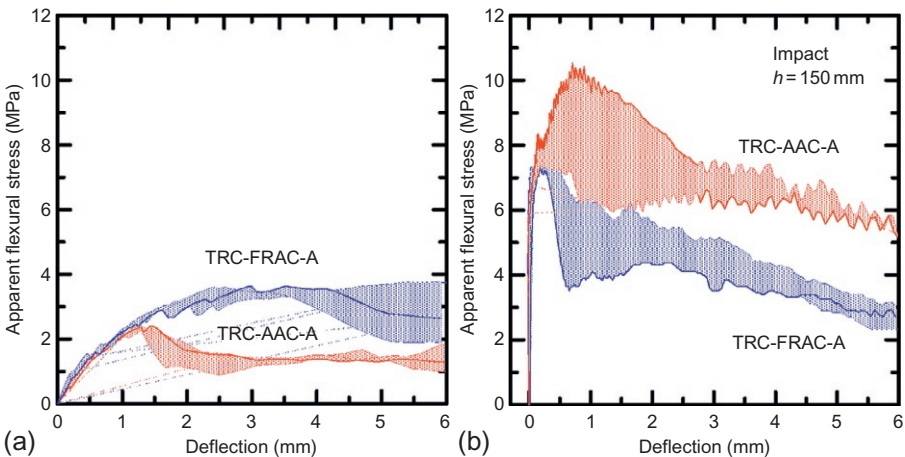
Figure 5.47 Flexural response of sandwich composites under (a) static and (b) impact loading.

References

Abrishami, H.H., Mitchell, D., 1996. Analysis of bond stress distributions in pull-out specimens. J. Struct. Eng. 122 (3), 255–261.

Agarwal, B.D., Broutman, L.J., 1990. Analysis and Performance of Fiber Composites, second ed. Wiley, New York.

Aveston, J., Cooper, G.A., Kelly, A., 1971a. The properties of fiber composites. In: Conference Proceedings, National Physical Laboratory (IPC Science and Technology Press Ltd), Paper 1, p. 15.

Aveston, J., Cooper, G.A., Kelly, A., 1971b. Single and multiple fracture. The Properties of Fiber Composites. PC Science and Technology Press, Guildford, UK. pp. 15–26.

Banholzer, B., 2004. Bond behaviour of a multi-filament yarn embedded in a cementitious matrix. Ph.D. Dissertation, Aachen University.

Barhum, R., Mechtcherine, V., 2010. Effect of short fibers on fracture behaviour of textile reinforced concrete. In: Oh, B.H., et al. (Ed.), Fracture Mechanics of Concrete and Concrete Structures. Korea Concrete Institute, Seoul, pp. 1498–1503.

Bastias, P.C., Kulkarni, S.M., Kim, K.Y., Gargas, J., 1996. Non-contacting strain measurements during tensile tests. Exp. Mech. 36 (1), 78–83.

Bazhenov, S., 1997. Dissipation of energy by bulletproof aramid fabric. J. Mater. Sci. 32 (15), 4167–4173.

Bharatkumar, B.H., Shah, S.P., 2004. Impact resistance of hybrid fiber reinforced mortar. In: Kovler, K.K., Marchand, J., Mindess, S., Weiss, J. (Eds.), International RILEM Symposium on Concrete Science and Engineering: A Tribute to Arnon Bentur e-ISBN: 2912143926, Evanston, Illinois.

Bindiganavile, V., Banthia, N., 2001a. Polymer and steel fiber-reinforced cementitious composites under impact loading. Part 1: bond-slip response. ACI Mater. J. 98 (1), 17–24.

Bindiganavile, V., Banthia, N., 2001b. Polymer and steel fiber-reinforced cementitious composites under impact loading. Part 2: flexural toughness. ACI Mater. J. 98 (1), 17–24.

Boisse, P., Buet, K., Gasser, A., Launary, J., 2001. Meso/macro-mechanical behavior of textile reinforcements for thin composites. Compos. Sci. Technol. 61 (3), 395–401.

Bruce, D.M., Matlock, D.K., Speer, J.G., De, A.K., 2004. Assessment of the strain-rate dependent tensile properties of automotive sheet steels. SAE Technical Paper Series. Society of Automotive Engineers Inc, Troy, MI. 0507.

Bruck, H.A., McNeil, S.R., Sutton, M.A., Peters, W.H., 1989. Digital image correlation using Newton–Raphson method of partial differential correction. Exp. Mech. 29 (3), 261–267. http://dx.doi.org/10.1007/BF02321405.

Cain, P.J., 1987. Digital filtering of impact data. In: Kessler, S.I., et al. (Ed.), Instrumented Impact Testing of Plastic and Composite Materials. ASTM, Philadelphia, p. 963.

Candoni, E., Labibes, K., Albertini, C., Berra, M., Giangrasso, M., 2001. Strain-rate effect on the tensile behaviour of concrete at different relative humidity levels. Mater. Struct. 34 (1), 21–26.

Destrebecq, J.-F., Toussaint, E., Ferrier, E., 2011. Analysis of cracks and deformations in a full scale reinforced concrete beam using a digital image correlation technique. Exp. Mech. 51 (6), 879–890.

Dey, V., Bonakdar, A., Mobasher, B., 2013. Low-velocity flexural impact response of fiber reinforced aerated concrete. Cem. Concr. Compos. 49, 100–110.

Dey, V., Zani, G., Colombo, M., Di Prisco, M., Mobasher, B., 2015. Flexural impact response of textile-reinforced aerated concrete sandwich panels. J. Mater. Des. 86, 187–197. http://dx.doi.org/10.1016/j.matdes.2015.07.004.

Fitoussi, J., Meraghni, F., Jendli, Z., Hug, G., Baptiste, D., 2005. Experimental methodology for high strain rates tensile behavior analysis of polymer matrix composites. Compos. Sci. Technol. 65 (14), 2174–2188.

Focacci, F., Nanni, A., Bakis, C.E., 2000. Local bond slip relationship for FRP reinforcement in concrete. J. Compos. Constr. 4 (1), 24–32.

Gao, G., Huang, S., Xia, K., Li, Z., 2015. Application of digital image correlation (DIC) in dynamic notched semi-circular bend (NSCB) tests. Exp. Mech. 55, 95–104. http://dx.doi.org/10.1007/s11340-014-9863-5.

Gasser, A., Boisse, P., Hanklar, S., 2000. Mechanical behavior of dry fabric reinforcement. 3D simulations versus biaxial tests. Comput. Mater. Sci. 17 (1), 7–20.

Gencoglu, M., Mobasher, B., 2007a. Static and impact behavior of fabric-reinforced cement composites in flexure. In: High-Performance Fiber-Reinforced Cement Composites (HPFRCC5), RILEM Proceedings, pp. 463–470.

Gencoglu, M., Mobasher, B., 2007b. Static and impact behavior of fabric reinforced cement composites in flexure. In: Reinhardt, H.W., Naaman, A.E. (Eds.), High Performance Fiber Reinforced Cement Composites—HPFRCC 5, RILEM Proceedings, Pro. 53, S.A.R.L., Cachan, France, pp. 463–470.

Hill, S., Sjöblom, P., 1998. Practical considerations in determining high strain rate material properties. SAE Technical Paper 981136.

Hinzen, M., Brameshuber, W., 2009. Improvement of serviceability and strength of textile reinforced concrete by using short fibres. In: Curbach, M., Jesse, F. (Eds.), Textilbeton Theorie und Praxis, 4th Colloquium on Textile Reinforced Structures (CSTR4), pp. 261–272.

Hong, S., Liu, D., 1988. On the relationship between impact energy and delamination area. Exp. Mech. 29, 115–120.

Kenneth, G.H., 1966. Influence of strain rate on mechanical properties of 6061.T6 aluminum under uniaxial and biaxial states of stress. Exp. Mech. 6 (4), 204–211.

Kirkwood, M.K., Kirkwood, J.E., Lee, Y.S., Egres, R.G., Wagner, N.J., 2004. Yarn pull-out as a mechanism for dissipation of ballistic impact energy in Kevlar® KM-2 fabric. Part I: Quasi-static characterization of yarn pull-out. Text. Res. J. 74 (10), 920–928.

Koerber, H., Xavier, J., Camanho, P.P., 2010. High strain rate characterisation of unidirectional carbon-epoxy IM7-8552 in transverse compression and in-plane shear using digital image correlation. Mech. Mater. 42, 1004–1019. http://dx.doi.org/10.1016/j.mechmat.2010.09.003.

Krauss, S., Mobasher, B., 2011. Tensile Testing of Textile Reinforced Concrete—A Round Robin Program (A report to RILEM Committee). Arizona State University.

Livermore Software Technology Corporation (LSTC), 2007. LS-DYNA Keyword User's Manual, Version 971.

Manolis, G.D., et al., 1997. Dynamic properties of polypropylene fiber-reinforced concrete slabs. Cem. Concr. Compos. 19, 341–349.

Meyers, M.A., 1994. Dynamic Behavior of Materials. John Wiley & Sons, New York.

Mobasher, B., Li, C.Y., 1996. Effect of interfacial properties on the crack propagation in cementitious composites. J. Adv. Cem. Based Mater. 4 (3), 93–106.

Mobasher, B., Shah, S.P., 1990. Interaction between Fibers and the Cement Matrix in Glass Fiber Reinforced Concrete. Am. Concr. Inst., SP 124, 137–156.

Mobasher, B., Peled, A., Pahilajani, J., 2004. Pultrusion of fabric reinforced high fly ash blended cement composites. In: di Prisco, M., Felicetti, R., Plizzari, G.A. (Eds.), Proceedings in Fibre-Reinforced Concretes, BEFIB 2004, RILEM Proceedings PRO 39, pp. 1473–1482.

Mobasher, B., Peled, A., Pahilajani, J., 2006. Distributed cracking and stiffness degradation in fabric–cement composites. Mater. Struct. 39 (3), 317–331.

Mobasher, B., Dey, V., Cohen, Z., Peled, A., 2014. Correlation of constitutive response of hybrid textile reinforced concrete from tensile and flexural tests. Cem. Concr. Compos. 53, 148–161.

Naaman, A.E., Namur, G.G., Alwan, J.M., Najm, H.S., 1991a. Fiber pull-out and bond slip. I: Analytical study. II: Experimental validation. J. Struct. Eng. 117 (9), 2769–2800.

Naaman, E.A., Namur, G.G., Alwan, J.M., Najm, H.S., 1991b. Fiber pullout and bond slip. I: Analytical study. J. Struct. Eng. 117 (9), 2769–2790.

Naaman, E.A., Namur, G.G., Alwan, J.M., Najm, H.S., 1991c. Fiber pullout and bond slip. II: Experimental validation. J. Struct. Eng. 117 (9), 2791–2800.

Naaman, A.E., Duane, O., Husamuddin, N., 1992. Elastic modulus of SIFCON in tension and compression. ACI Mater. J. 88 (6), 603–613.

Ng, S., Tse, P., Lau, K., 1998. Numerical and experimental determination of the in-plane elastic properties of 2/2 twill weave fabric composites. Compos. Part B 29B, 735–744.

Nicholas, T., 1981. Tensile testing of material at high rates of strain. Exp. Mech. 21 (5), 177–185.

Pan, B., Qian, K., Xie, H., Asundi, A., 2009. Two-dimensional digital image correlation for in-plane displacement and strain measurement: a review. Meas. Sci. Technol. 20, 062001, 17 pp. http://dx.doi.org/10.1088/0957-0233/20/6/062001

Peled, A., Mobasher, B., 2005. Pultruded fabric–cement composites. ACI Mater. J. 102 (1), 15–23.

Peled, A., Mobasher, B., Sueki, S., 2004. "Technology methods in textile cement-based composites" concrete science and engineering: a tribute to Arnon Bentur. In: Kovler, K., Marchand, J., Mindess, S., Weiss, J. (Eds.), RILEM Proceedings PRO 36, pp. 187–202.

Peled, A., Sueki, S., Mobasher, B., 2006. Bonding in fabric–cement systems: effects of fabrication methods. Cem. Concr. Res. 36, 1661–1671.

Pozuelo, M., Carreno, F., Ruano, O.A., 2006. Delamination effect on the impact toughness of an ultrahigh carbon-mild steel laminate composite. Compos. Sci. Technol. 66, 2671–2676.

Serrano-Perez, J.C., Vaidya, U.K., Uddin, N., 2007. Low velocity impact response of autoclaved aerated concrete/CFRP sandwich plates. Compos. Struct. 80, 621–630.

Shockey, D., Simons, J., Erlich, D., 2004. Explicit Finite Element Modeling of Multi-layer Composite Fabric for Gas Turbine Engine Containment Systems. Part 3: Model Development and Simulation of Experiments. Final Rep. No. DOT/FAA/AR-04/40/P3, Washington, DC.

Silva, F.A., Zhu, D., Soranakom, C., Mobasher, B., Toledo Filho, R.D., 2010. High Speed Tensile Behavior of Sisal Fiber Cement Composites. Mater. Sci. Eng. A 527 (3), 544–552.

Silva, F.A., Butler, M., Mechtcherine, V., Zhu, D., Mobasher, B., 2011. Strain rate effect on the tensile behaviour of textile-reinforced concrete under static and dynamic loading. Mater. Sci. Eng. A 528 (3), 1727–1734.

Soranakom, C., Mobasher, B., 2008a. Correlation of tensile and flexural response of strain softening and strain hardening cement composites. Cem. Concr. Compos. 30, 465–477.

Soranakom, C., Mobasher, B., 2008b. Geometrical and mechanical aspects of fabric bonding and pullout in cement composites. Mater. Struct. 42, 765–777.

Soranakom, C., Mobasher, B., 2009. Flexural analysis and design of textile reinforced concrete. In: 4th Colloquium on Textile Reinforced Structures (CTRS4), Dresden, Germany, June 3–5, pp. 273–288.

Stahlecker, Z., Mobasher, B., Rajan, S.D., Pereira, J.M., 2009. Development of reliable modeling methodologies for fan blade-out containment analysis. Part II: Finite element analysis. Int. J. Impact Eng. 36 (3), 447–459.

Stang, H., Li, Z., Shah, S.P., 1990. Pullout problem: stress versus fracture mechanical approach. J. Eng. Mech. 116 (10), 2136–2149.

Sueki, S., 2003. An analytical and experimental study of fabric-reinforced, cement-based laminated composites. MS Thesis, Arizona State University.

Sueki, S., Soranakom, C., Peled, A., Mobasher, B., 2007a. Pullout-slip response of fabrics embedded in a cement paste matrix. ASCE J. Mater. Eng. 19, 9.

Sueki, S., Soranakom, C., Peled, A., Mobasher, B., 2007b. Pullout-slip response of fabrics embedded in a cement paste matrix. J. Mater. Civ. Eng. 19, 718–727.

Sujivorakul, C., Waas, M., Naaman, A.E., 2000. Pullout response of a smooth fiber with an end anchorage. J. Eng. Mech. 126 (9), 986–993.

Sutton, M.A., Wolters, W.J., Peters, W.H., Ranson, W.F., McNeil, S.R., 1983. Determination of displacements using an improved digital correlation method. Image Vis. Comput. 1 (3), 133–139. http://dx.doi.org/10.1016/0262-8856(83)90064-1.

Wang, N.Z., Sidney, M., Keith, K., 1996. Fiber reinforced concrete beams under impact loading. Cem. Concr. Res. 26 (3), 363–376.

Xiao, X.R., 2008. Dynamic tensile testing of plastic materials. Polym. Test. 27 (2), 164–178.

Xiao, S., Li, H., Lin, G., 2008. Dynamic behaviour and constitutive model of concrete at different strain rates. Mag. Concr. Res. 60 (4), 271–278.

Xu, H., Mindess, S., Duca, I.J., 2004. Performance of plain and fiber reinforced concrete panels subjected to low velocity impact loading. In: di Frisco, M., Felicetti, R., Plizzari, G.A. (Eds.), Proceedings of RILEM Conference on Fiber Reinforced Concrete, BEFIB, Varenna, Italy, pp. 1257–1268.

Yao, Y., 2013. Application of 2-D Digital Image Correlation (DIC) method to damage characterization of cementitious composites under dynamic tensile loads. M.S. Thesis, Arizona State University.

Yao, Y., Bonakdar, A., Faber, J., Gries, T., Mobasher, B., 2015. Distributed cracking mechanisms in textile-reinforced concrete under high speed tensile tests. Mater. Struct. http://dx.doi.org/10.1617/s11527-015-0685-4.

Zabotkin, K., O'Toole, B., Trabia, M., 2003. Identification of the dynamic properties of materials under moderate strain rates. In: 16th ASCE Engineering Mechanics Conference, Seattle, Washington.

Zhang, J., Maalej, M., Quek, S.T., Teo, Y.Y., 2005. Drop weight impact on hybrid-fiber ECC blast/shelter panels. In: Banthia, N., Uomoto, T., Bentur, A., Shah, S.P. (Eds.), Proceedings of Third International Conference on Construction Materials: Performance, Innovation and Structural Applications, Vancouver, Canada.

Zhu, D., Mobasher, B., Rajan, S.D., 2008a. High strain rate testing of Kevlar 49 fabric. In: Society for Experimental Mechanics, 11th International Congress and Exhibition on Experimental and Applied Mechanics, vol.1, pp. 34–35.

Zhu, D., Mobasher, B., Rajan, S.D., 2008b. Image analysis of Kevlar 49 fabric at high strain rate. In: Society for Experimental Mechanics, 11th International Congress and Exhibition on Experimental and Applied Mechanics, vol.2, pp. 986–991.

Zhu, D., Gencoglu, M., Moabsher, B., 2009. Low velocity flexural impact behaviour of AR glass fabric reinforced cement composites. Cem. Concr. Compos. 31 (6), 379–387.

Zhu, D., Soranakom, C., Mobasher, B., Rajan, S.D., 2011a. Experimental study and modeling of single yarn pull-out behavior of kevlar$^{\circledR}$ 49 fabric. Compos. A: Appl. Sci. Manuf. 42 (7), 868–879.

Zhu, D., Peled, A., Mobasher, B., 2011b. Dynamic tensile testing of fabric–cement composites. Constr. Build. Mater. 25 (1), 385–395.

Zhu, D., Mobasher, B., Erni, J., Bansal, S., Rajan, S.D., 2012. Strain rate and gage length effects on tensile behavior of Kevlar 49 single yarn. Compos. Part A 43, 2021–2029.

Durability of structures made of or strengthened using textile-reinforced concrete

<div style="text-align:right">**6**</div>

V. Mechtcherine
Technische Universität Dresden, Dresden, Germany

6.1   Introduction

Textile-reinforced concrete (TRC) is a composite construction material in which textile reinforcement consisting of polymer, glass, carbon or basalt fibres is embedded into a fine concrete matrix. Since textile reinforcement generally needs no minimum concrete cover as a protection against corrosion, it is possible to manufacture thin-walled construction components and layers. The fibre material can be exploited very effectively by adjusting the volume proportion and orientation of the long fibres in the direction of tensile stress. TRC can be employed in the manufacture of thin-walled façade elements, load-bearing integrated formwork, tunnel linings or in the strengthening of existing structures, for example, reinforced concrete (Brameshuber, 2006; Butler et al., 2010a).

Most current applications of TRC are nonstructural. Textile reinforcement is primarily used in controlling shrinkage cracks as well as cracks induced by temperature changes. Furthermore, in TRC elements the control of cracks due to overloading during transport and mounting is an accomplished fact. As well, considerable laboratory research has been performed in the last few years on the behaviour of structural members made of TRC, and there are also a number of examples of the successful use of TRC for building new pedestrian bridges and strengthening existing structures. Based on these first insights, some major tendencies may be deduced already.

In some instances, textile reinforcement is combined with conventional steel reinforcement such as in the strengthening or repair of RC members by means of TRC. Figure 6.1 illustrates the case where a TRC layer is used to build an integrated formwork. In other instances, a combination of textile reinforcement positioned near the surface of a structural member and steel reinforcement (also pre-stressed) positioned deeper inside may be used to achieve optimal solutions in new construction with respect to load-carrying capacity, durability, serviceability and aesthetics. Thus, the protection of steel from corrosion must be considered with regard to the durability of such structures as well.

As an example, a practical application for the strengthening of existing structures using TRC is presented here briefly. This measure was carried out in 2006 for the retrofitting of an RC roof shell at the University of Applied Sciences in Schweinfurt,
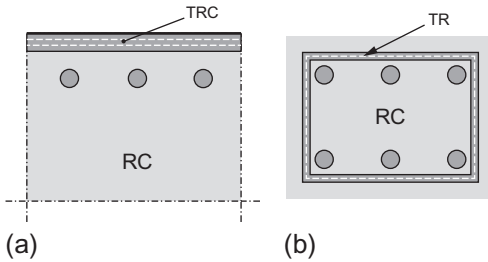
Figure 6.1 TRC as (a) strengthening layer or integrated formwork for RC structure and (b) structural member with hybrid reinforcement.

Figure 6.2 (a) Damaged steel-reinforced concrete hypar-shell at the FH Schweinfurt (Germany) and (b) strengthening with TRC (Weiland et al., 2008).

Germany. The project was carried out with the technical support of the Collaborative Research Centre SFB 528 "Textile Reinforcement for Structural Strengthening and Retrofitting" of the TU Dresden. The 80-mm thick RC hypar-shell has a lateral length of approximately 27 m and a maximum span of approximately 39 m (Figure 6.2). Large deformations (up to 200 mm drop) in the shell's cantilevered wings had been measured; the design tensile stress levels in the upper steel reinforcement layer of the shell had been exceeded significantly, such that strengthening measures were absolutely necessary. A TRC layer 15 mm thick, containing three layers of textile sheets made of carbon fibre was applied to these particular areas in order to increase the load-carrying capacity and prevent further increases in deformation (Weiland et al., 2008). A few questions arise with regard to this strengthening measure. How durable is the strengthening layer? Or, how well will this layer protect the reinforcement in the hypar-shell from corrosion?

Depending on the target applications, the durability requirements for different structures made of TRC may vary significantly. To meet these requirements best, the material composition of TRC may in turn vary considerably as well. This implies that a general framework for dealing with the problem of durability of such structural elements and structures is needed. This chapter is an attempt to provide such a framework.

6.2 Characteristic loads and exposures

The wide variety of potential applications for TRC means that the range of mechanical and environmental loads, as well as their possible combinations, may be very broad. Particular performance requirements may vary even for different parts of one structural member, for example (Inaguma et al., 2006).

In considering structural durability, the mechanical loads are of particular interest with regard to cracking since cracks dramatically increase the transport of fluids and gases in concrete. A consequence of this is the accelerated corrosion process. Apart from the mode of loading, for example, tension, shear and/or bending, all of which affect the cracks' pattern and width, the loading type should be considered since, for instance, single overloading, fatigue loading, or sustained high loads can affect the cracking behaviour of TRC in respect to crack width and distribution.

Crack formation and propagation, however, often begin before any crack-inducing mechanical loads are applied. Cracks resulting from thermal deformations, restrained drying shrinkage or autogenous shrinkage can eventually be exacerbated by fatigue loading, for instance. These load combinations for TRC or RC/TRC structures are generally the same as for steel-reinforced concrete structures.

In most cases, cracking is inevitable in concrete structures and is generally essential for the effective use of both steel bar and textile reinforcement. A great advantage of TRC is that this material group yields well controlled crack widths, which are very small in comparison to conventionally reinforced structures. This enables, at least theoretically, the full decoupling of the steel reinforcement from crack control if used in combination with textile reinforcement. Steel reinforcement is used only to ensure adequate load capacity, while TRC controls cracking behaviour. Obviously, TRC can be simultaneously used for both purposes, increasing the load-carrying capacity of structural members and crack control. These constellations open new opportunities for structural design, thereby allowing the very effective use of such hybrid reinforcements.

6.3 Basics of durability estimation and design

6.3.1 General remarks

While discussing the basics of durability design for structures with textile or hybrid reinforcement (steel and textile), reference is made to existing durability design rules for steel-reinforced concrete structures. The prescriptive design rules of current standards are unlikely to be suitable for taking full advantage of the new class of materials presented in this book. A performance-based durability design approach will likely be much more appropriate. While such an approach exists for crack-free ordinary concrete (OC) (DuraCrete Final Technical Report, 2000; fib bulletin 34, 2006; Schießl and Gehlen, 2005), significant efforts will be required to develop a similar approach suitable for cracked and crack-free TRC and RC/TRC structures.

Recently Altmann et al. (2012) and Altmann and Mechtcherine (2013) took a first step towards such a design concept by developing a fuzzy-probabilistic approach to

forecast chloride ingress into another novel cementitious material, so-called strain-hardening cement-based composite (SHCC). This approach allows the quantification of parameters based on limited data and expert knowledge. The same approach can be followed with regard to the durability of TRC as well as RC structures strengthened by TRC.

In order to ensure structural durability, the durability of the applied materials should first be assured. Since we are also considering a combination of steel reinforcement and TRC here, the following requirements arise with regard to the durability of individual system components and consequently of the system as a whole:

(1) Protection of the steel reinforcement from corrosion
(2) Durability of the TRC matrix
(3) Durability of fibre and polymer yarn coating
(4) Durability of the fibre–matrix bond properties

6.3.2   Protection of steel reinforcement from corrosion

Ordinary steel reinforcement requires anticorrosion protection, which the alkaline environment of the cementitious matrix provides. If aggressive agents such as chloride or carbon dioxide penetrate the matrix and reach the reinforcement, however, the steel may corrode. In established codes and regulations (e.g. Eurocode 2), three measures are demanded to protect steel reinforcement: limitation of the maximum crack width; sufficient concrete cover; and appropriate concrete quality as defined by corresponding threshold values, that is, minimum compression strength, maximum water-to-cement ratio and minimum cement content. In principle, these requirements also hold true for RC structures with a repair or strengthening layer made of TRC as well as for structures with hybrid reinforcement (steel bars and textile); however, the weighting and the thresholds values change accordingly.

Li and Stang (2004) suggested that tight crack-width control of high-performance fibre-reinforced materials, that is, $<100\ \mu m$, delays the penetration of aggressive agents in their movement towards the steel reinforcement. According to Mechtcherine and Lieboldt (2011), crack widths in TRC specimens under tension remain clearly below $100\ \mu m$ in the operating strain range up to 0.5% at least.

Comparing this consideration with existing codes, the following observations can be made:

–   Intrinsically small crack widths in TRC or RC/TRC structures are much smaller than the threshold values allowed by codes for RC structures. The question arises as to whether or not adjustments should be made regarding the other two protection measures of the steel reinforcement, namely the thickness of the concrete cover and concrete quality.
–   The requirement of a particular minimum value of concrete cover is based on numerous considerations, including the carbonation of concrete, the transport of aggressive agents through the concrete layer to steel reinforcement and resistance of the concrete to spalling. For OC spalling resistance increases with increasing thickness of the concrete layer (Müller et al., 2003). In the case of RC/TRC, a much higher spalling resistance other than that of OC can be achieved with only a very thin TRC overlay.

–   The lack of coarse aggregates means there are no large aggregate-matrix interfaces, which might serve as paths for the transport of fluids and gases, with higher porosity than aggregate-free, hardened cement paste; however, due to their higher binder content, the overall porosity of TRC may be more elevated than that of OC. Certainly, this depends on the mix's water-to-binder ratio, which is usually relatively low for TRC. Furthermore, it has been shown that multifilament yarns promote water transport actively for TRC (Mechtcherine and Lieboldt, 2011).
–   TRC usually possesses higher binder content than OC. The associated higher ability to bind aggressive substances such as chlorides and carbon dioxide is advantageous with regard to preventing steel corrosion.

In conclusion, it can be stated that for the same exposure classes (e.g. XC carbonation, XD de-icing salt or XS seawater according to CEN EN 206-1), the threshold values for TRC would probably differ significantly from the corresponding values for OC, if the established approach for durability design were to be applied to RC/TRC structures.

6.3.3   Durability of the matrix

Frost attacks, chemical attacks by aggressive substances, and, in some cases abrasion must all be considered regarding the durability of the TRC matrix. The basic effects of matrix composition on concrete resistance to such exposure are reasonably well known for OC; however, they cannot simply be extrapolated to predict the behaviour of TRC because of its very particular mixture composition, that is, the absence of coarse aggregates, the high binder content and the presence of fibres. Relatively fine textiles, especially used in combination with short fibre (see, e.g. Barhum and Mechtcherine, 2013), might hinder the deterioration of the composite to some extent, even if the matrix is severely loaded. The first results on the durability of TRC subject to the freeze–thaw exposure showed tendencies basically known for OC; for example, the frost resistance of TRC decreases with increasing substitution of Portland cement by fly ash and, particularly, blast furnace cement.

A chemical attack might very well affect the mechanical properties of the matrix, which would then lead to a change in TRC strength and especially in their ductility. A substantial amount of research is still required to investigate the behaviour of these materials under various exposures and to confirm the observed characteristic material performance statistically.

Other issues are the ageing process and the associated hydration, which alters TRC's mechanical performance by changing the composition of the hardened binder paste phases, and the microstructure and the properties of the bond between matrix and fibres (Section 6.3.5).

6.3.4   Durability of fibre and polymer coating

Alkali-resistant (AR) glass fibre and carbon fibre are materials used most often in the manufacture of TRC. There is also some research on the use of polymer, basalt and natural fibre for this purpose; however, there is little published information on the durability of such fibres when used as reinforcement in concrete. Carbon fibre is well

known for its high chemical resistance; no degradation of properties could be observed in the usual chemical environments. The situation with fibre made of AR-glass or basalt is, however, much more complex and should be addressed here in more detail.

Standard AR-glass contains 16–20% zirconium dioxide by mass and thus shows significantly enhanced resistance in highly alkaline environments compared to conventional glasses. The corrosive damage of AR-fibre occurs nonuniformly due to different element concentrations near the filament surface. This deterioration increases with increasing pH value of the pore solution and with temperature (Yilmaz and Glasser, 1991). Organic polymer sizes applied to filament surfaces during the production of the glass yarns can delay such corrosion significantly. Scheffler et al. (2009a) showed that the corrosion of AR-fibres in a cement solution in accelerated tests is characterised by the formation of holes of different size and depth (cf. Figure 6.3). According to Butler et al. (2009b) flaws in the size, inconsistencies in the composition of the bulk glass, and high pH values of the pore solution are necessary prerequisites for local damage to fibre made of AR-glass. Corrosion of glass filaments embedded in fine-grained concrete could be observed only as rare exceptions. The authors conclude that stress corrosion (delayed failure) at nanoscopic defects on the filament surface becomes an important mechanism for damage if, at least on some areas of the filament surface, the size is widely removed; however, in the multifilament yarns used in TRC, the failure of individual filaments due to corrosion can likely be compensated by the redistribution of the load to neighbouring filaments. This means that the failure of a few filaments cannot affect the load-bearing capacity of the multifilament yarn significantly (Butler et al., 2009b). Hence, other mechanisms seem to be additionally responsible for pronounced ageing behaviour of TRC made with AR-glass.

Basalt fibre has been considered an alternative to fibres made of AR-glass (Wei et al., 2010). Its good temperature resistance, wide availability worldwide and relatively low costs make basalt fibres suitable for a wide range of applications (Förster, 2014; Sim et al., 2005). During the fabrication of basalt fibres, due to the melting of basalt and the rapid subsequent cooling, the crystalline properties of the raw material vanish.
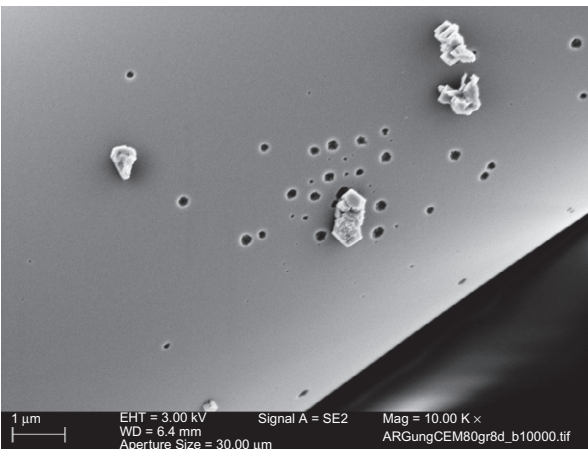
Figure 6.3 Formation of holes on the surface of an AR-glass fibre after 8-days' storage in cement solution at 80 °C (Scheffler et al., 2009a).

Hence, the microstructure of basalt fibres is primarily amorphous and therefore similar to that of a glass network. This leads to a decrease in the resistance of the material to alkaline environment, which has often as its consequence damage to the fibres, thus resulting in a decrease in their load-bearing capacity (Scheffler et al., 2009a). The alkali resistance of basalt fibres and their other properties strongly depend on their chemical composition. The main difference of basalt fibre to glass fibre is the relatively high content of Fe_xO_y of 7–15% of the former's (Förster, 2014). With an increase in the CaO/Fe_xO_y ratio, basalt fibre becomes less AR (Förster, 2014). Furthermore, it was found that the morphology of the corrosion products depended on the alkalinity of basalt raw material (rock), which had been used for the production of basalt fibre. The morphology of the corrosion products in its turn can considerably affect the rate of fibre dissolution due to their more or less pronounced barrier function (Förster, 2014). Generally, basalt fibres exhibit low alkali resistance in comparison to AR-glass fibre, but a higher resistance in comparison to E-glass fibre (Förster, 2014). The alkali resistance of basalt fibre can, however, be considerably improved by the addition of zirconia (Rybin et al., 2013).

6.3.5 Fibre–matrix bond durability

For TRC with textiles made of AR-glass, it was found (Butler et al., 2010b) that the extent of the observed performance losses with increasing age depends primarily on the matrix's alkalinity, which influences the formation of solid phases in the fibre–matrix interface and on the filament surface. The thickness and brittleness of these shell-like crusts increase with increasing potential for portlandite formation in the matrices. Also amplified precipitation of $Ca(OH)_2$ between the filaments can be observed with increasing alkalinity of the matrix (cf. Figure 6.4a). These filament

(a)   (b)
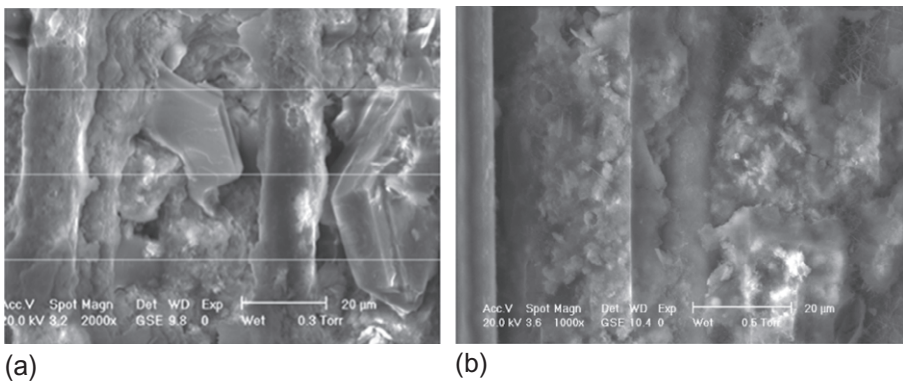
Figure 6.4 Environmental scanning electron microscope (ESEM) images of AR-glass filaments in matrix made of (a) Portland cement (here after 28 days of accelerated ageing) and (b) blast furnace cement and pozzolana (here after 360 days of accelerated ageing) (Butler et al., 2010b).

incrustations reduce the slip of filaments in the vicinity of the cracks, so that failure strain of filaments is reached at smaller crack widths. Furthermore, straining the filaments causes local spalling in and on the shells as well as the splitting of the $Ca(OH)_2$ crystals. The resulting singularities and lateral pressure caused by the wedged crystals act as notches, leading to premature failure of the filaments; however, when the Portland cement clinker content of the binder is low and pozzolanic additives are used (low alkalinity), a stratum of thin C–S–H phases leading to good bonding characteristics dominates the fibre–matrix interface (cf. Figure 6.4b). Such thin-walled coatings of the outer filaments enable good, flawless bonding with the matrix. In the vicinity of matrix cracks, partial debonding and filament slip is possible, leading to ductile overall behaviour of the crack-bridging yarn (Butler et al., 2010b).

Furthermore, during continued hydration and ageing, a slow and gradual process of deposition of hydration products between the filaments may change the nature of bonding by increasing the sleeve/core ratio (Cohen and Peled, 2010). This results in a stronger bond, which is a favourable effect, but may also lead to embrittlement, mainly when brittle fibres such as glass are used (Zhu and Bartos, 1997; Bentur and Diamond, 1987). This means that the bonding changes over time as do the composite properties and durability as well.

Cohen and Peled (2010) described two degradation mechanisms observed during ageing, both due to matrix penetrability into the bundle: (i) changing the telescopic pullout determined by cement penetrability as more fibres fracture after ageing, leading to more brittle behaviour and (ii) chemical deterioration of the glass fibres themselves as more fibres are in direct contact with the cement matrix, reducing composite strength. The authors found that favoured filler systems are those that moderate cement hydrates' penetrability between the bundle filaments over time. This upholds the telescopic pullout mode and the composite ductility, at the same time protecting the core filaments from chemical attack. This maintains their high performance and the overall tensile strength of the composite.

In contrast to AR-glass reinforcement, carbon fibres are inert (Ohama, 1989; Langlois et al., 2007). Some functionalization of the fibre surface can, however, be expected as a result of the sizing of individual fibres and coating of the yarns. The experiments by Butler et al. (2009a) demonstrated that independent of the type of cement and addition of pozzolanic materials and independent of the duration of accelerated ageing, the interphase to carbon yarns consisted of fine calcium–silicate–hydrate (C–S–H) formations while no $Ca(OH)_2$ crystals could be observed. The reason for this phenomenon is still to be investigated; however, it may be suggested that in the case of carbon fibres the morphology of the interphase is determined to a greater extent by the surface properties of carbon fibres and to a much smaller extent by the type of binder used (Butler et al., 2009a; Scheffler et al., 2009b). In all experiments performed by Butler et al. (2009a), an increase in tensile strength and strain capacity was observed after storing TRC made of carbon fibre in a fog chamber (temperature 40 °C, relative humidity of 99%) for a period of up to 1 year, thus showing contrary behaviour in comparison to TRC made of AR-glass fibre. A similar tendency was observed by Langlois et al. (2007) for bending and pullout tests performed at various concrete ages.

Hempel et al. (2015) investigated different types of basalt fibres for textile reinforcement with and without additional coating. They showed that accelerated ageing in a fog chamber led in the case of the specimens with the uncoated basalt fibres to a dramatic decrease in mechanical performance due to the inadequate resistance of both the sizing and the basalt fibres to the alkaline attack. This resulted in progressive fibre damage and the fibres' failure at relatively low force levels. The styrolbutadien coating applied to basalt yarns improved the strength of the basalt yarns and the bond behaviour distinctly; however, with the ongoing ageing caused by storage in the fog chamber, the decrease in mechanical performance was pronounced. The damage to the basalt fibres could be slowed by the coating but in the long term not prevented. The authors concluded that in order to improve basalt multifilament yarns with respect to their application in concrete structures and to protect the fibres in the alkaline matrix sufficiently, the development of suitable sizings and coatings designed specifically for this material is necessary.

The results of the investigations as presented above illustrate the diversity and complexity of the mainly unknown mechanisms with respect to the primary properties of the interphase and to their long-term development. General predictions on the time-dependent development of such material compositions cannot be derived based on the current state of research. Thus, experimental investigation of new fibre–matrix combinations remain indispensable. The uncertainty in the prediction of the material behaviour of TRC with uncoated yarns underlines the importance of using subsequent coatings that can ensure certain mechanical material characteristics.

6.4 Characteristic material properties to predict long-term durability and service life

6.4.1 General remarks

Based on the considerations regarding the durability of individual components outlined in Section 6.3, the following characteristic properties of the composite material seem to be decisive with regard to long-term durability and service life of TRC and RC/TRC structures:

– Transport properties of TRC in non-cracked and cracked states
– Effects on tensile strength and strain capacity of TRC
– Resistance of TRC in aggressive environments

On the material level, these issues are addressed in previous sections. The following sections provide a brief overview as well as special considerations for elements and structures made of TRC.

6.4.2 Transport properties

The key question is what effect a considerable number of fine, well distributed cracks have on the transport properties of TRC. Average crack width has been used routinely as a reference parameter; however, for materials with multiple cracks of self-limiting width, other approaches seem to be more appropriate, for example, using the

cumulative crack length (Mechtcherine et al., 2007) or crack density functions with specific consideration of larger cracks (DIN EN 13396, 2004). Where this is not practical, average strain may serve as a useful surrogate; however, it can be assumed that fine reinforcement in combination with a fine-grain matrix also affect the condition of crack profiles and the continuity of the entire crack system, which of course influences the transport of fluids and gases through the material. There is significant need for research into reliable and practical methods to describe the crack system in TRC both in laboratory as well as in field applications.

6.4.2.1   Air permeability

There is very little information available on the air permeability of TRC. The coefficient of oxygen permeability in crack-free TRC specimens was found to be influenced clearly by the polymer coating of the textile, but was only marginally dependent on the fineness of multifilament yarns in the textile (Mechtcherine and Lieboldt, 2011). The corresponding permeation coefficients were reduced by up to 65% if coated textiles were embedded into the composite instead of uncoated textile.

In situ permeation tests on cracked TRC subjected to uniaxial tensile loading revealed a pronounced non-linear increase in the transport rates of oxygen through the TRC (perpendicular to the composite surface) with increasing strain, corresponding to larger crack widths (Mechtcherine and Lieboldt, 2011). A higher degree of fineness in the textile reinforcement, that is, a higher degree of reinforcement, and the polymer coating of the multifilament yarns led to a larger number of cracks in the TRC specimens at given strain levels, but these cracks were considerably finer. As a result, the permeability for oxygen through the TRC made with such reinforcement was lower. This effect was distinctly apparent at strain levels above 0.2%.

6.4.2.2   Water-transport properties

Mechtcherine and Lieboldt (2011) reported that if measured parallel to the reinforcing textile layers, water absorption in TRC increases with increasing fineness of the multifilament yarns and decreases with an increasing amount of polymer used in coating the yarns. Both these observations can be traced back mainly to differences in the capillary system formed in multifilament yarns. For water permeability, dependencies between the crack system and the volume of transported media were found to be similar to those described above for oxygen permeability. It was also shown that the influence of imposed strain on the permeation of water through cracked TRC could be described by a simple model based on Hagen-Poiseuille's law; however, the model should be refined in future investigations in order to enable a more realistic description of the transport mechanisms in TRC.

Pourasee et al. (2011) described a series of experiments in which fluid transport was measured using X-ray radiography in cracked cement paste samples that were reinforced with different commercially available fabrics made with monofilament and multifilament yarns, both coated and uncoated. Results showed that fabrics made of multifilament yarns without coating may be problematic from a durability point of view; however, when multifilament yarns were coated, the fabric behaved as a

monofilament system. The transport behaviour was observed to be highly dependent on the quality of the coating. The authors concluded that this should be considered in addition to mechanical performance in assessing the type of fabrics that should be used for a specific application.

Lieboldt and Mechtcherine (2013) investigated the transport mechanisms of water in and through composite concrete specimens made of a cracked OC as a substrate and TRC as a cover layer for its strengthening and repair. The TRC cover layer was assessed with regards to its efficiency as a protective layer against the ingress of water. Since in real applications such TRC layers may actually be or presumed to be cracked, thereby activating the load-carrying function of the textile reinforcement, the TRC layer was cracked for purposes of this study. The water transport in the OC specimens without a TRC layer was used as reference. Neutron radiography served as the main testing technique. In OC, quick and deep ingress of water through relatively wide macro-cracks (100–200 μm), followed by transport through the capillary pore system, caused saturation of large areas in a rather short time (see Figure 6.5a). TRC applied to the OC surface reduced the ingress of water to a large extent. Its small crack widths of approximately 20 μm modified the suction behaviour fundamentally. In the cracked substrate of OC, capillary suction was obviated, and transport through the pore system of the matrix became the prevailing transport mechanism based on the suction force characteristic of capillary pores. Not only was the mechanism altered, but the transport of water deep into inner regions was significantly retarded as well (see Figure 6.5b).
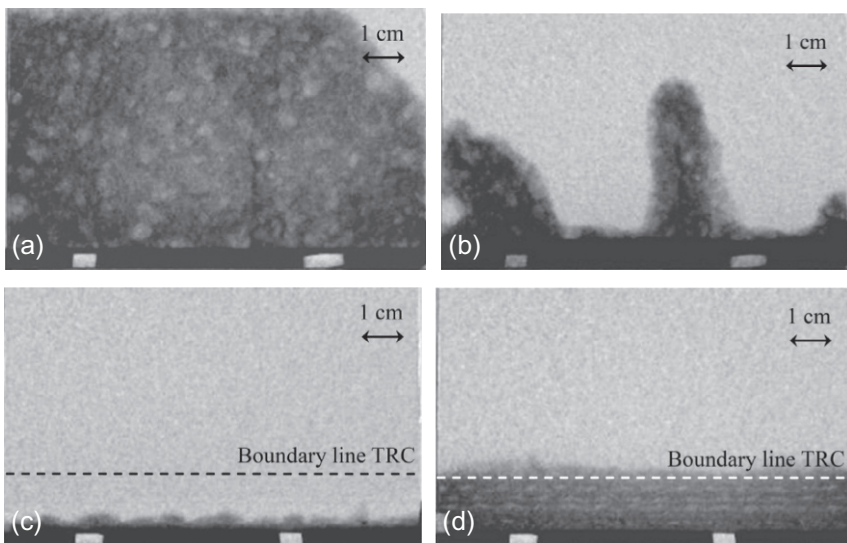
Figure 6.5 Water distribution in a cracked specimen made of ordinary concrete (a) 30 min and (b) 23 h after the beginning of the capillary suction; water distribution in a composite specimen consisting of cracked ordinary concrete substrate and a crack-free layer of TRC with carbon textile (c) 30 min and (d) 23 h after the beginning of the capillary suction (Lieboldt and Mechtcherine, 2013).

6.4.2.3   Chloride migration

So far, very little information has been made available on the chloride permeability of TRC. The observed higher resistance of both cracked and uncracked TRC against the ingress of chloride ions can be attributed to their higher cementitious material content, low w/c-ratio, self-limiting crack width and, as a result, self-healing of the cracks. While this is promising, more research is required.

The transport mechanisms of chloride ions dissolved in water—capillary suction, permeation and diffusion—are very complex and occur usually in parallel, both within the pore system of the cement matrix and through cracks. The transport rates for these mechanisms differ by about an order of magnitude. Lieboldt (2012) conducted chloride diffusion tests in order to assess the chloride migration rates for cracked and crack-free specimens consisting of a TRC layer placed on an OC substrate. The specimens were stored in a 3% sodium chloride solution, according to DIN EN 13396 (2004). After storing particular specimens for 28 days, 12 weeks and 6 months, qualitative tests with silver nitrate and quantitative chloride concentration tests were performed. It could be shown that the barrier effect of the TRC layer decreased the penetration of chloride ions into the adjacent OC. For certain exposure durations, the ingress of chlorides could be reduced by two-thirds in the cracked members by applying a 12-mm thick TRC layer. The results obtained, however, are valid only for the specific material and experimental combination as described by Lieboldt (2012). To enable a prediction of the protective behaviour of TRC in this respect, systematic studies on composite specimens with varying layer thicknesses, matrix materials, and different textile reinforcements must be performed while taking into account crack patterns and the various transport mechanisms. Furthermore, with respect to practical exposures, accumulation of water-dissolved, harmful chloride ions in TRC layers due to cyclic capillary suction process should be investigated.

6.4.2.4   Other transport properties

For sound OC numerous correlations were experimentally and in part also theoretically derived among different transport mechanisms, that is, diffusion, permeation, absorption, and for different transport media, for example, water, air and CO_2 (Hilsdorf et al., 1997; Lawrence, 1986). For cracked concrete, however, such comparisons have not yet been carried out, as is the case for TRC. The knowledge of possible correlations is essential for the prediction of the durability of structures made of or strengthened with TRC, even if it is based on the results of just one or two particular test methods. There is a great need for research in this area.

6.4.3   Strain capacity of TRC

6.4.3.1   Long-term strain capacity and ageing behaviour

Since high-strain capacity is a decisive property with regard to the durability of TRC, these materials as well as members or structures made of them can only be considered as truly durable if their strain capacities do not change negatively at a substantial rate over time.
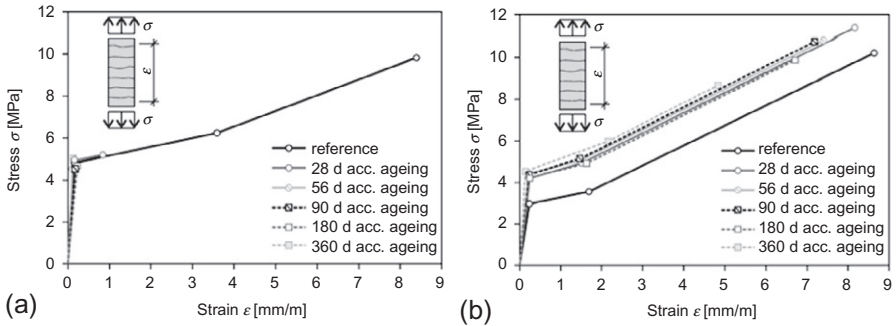
Figure 6.6 Tri-linear representations of stress–strain curves for TRC made with (a) Portland cement matrix and (b) blast furnace cement matrix with addition of pozzolana; after demoulding all specimens were stored for 6 days in water (20 °C); subsequently, the reference specimens were subjected to storage at 20 °C/65% RH until the testing at the age of 28 days; the other part of the specimens was subjected to accelerated ageing in a fog room (40 °C/99% RH); the respective durations of fog room storage were 28, 56, 90, 180 and 360 days (Butler et al., 2010b).

Butler et al. (2010b) investigated the effect of matrix composition by varying the hydration kinetics and alkalinity of the binder mix on the ageing of TRC. The results of tensile tests on specimens made of TRC subjected to conditions of accelerated ageing showed a pronounced decrease in the tensile strength and strain capacity for that TRC whose matrix was most alkaline; Portland cement was used exclusively as the binder in this composition (see Figure 6.6a). The performance of TRC made with a modified, reduced alkaline matrix composition was to a great extent unaffected by exposure to accelerated ageing (cf. Figure 6.6b). The authors showed that reductions in the toughness of TRC could be attributed mainly to the disadvantageous new formation of solid phases observed in the fibre–matrix interface (cf. also Section 6.3.5).

6.4.3.2 Behaviour under sustained loads

There are currently no sufficient, reliable data available to provide a suitable framework for long-term evaluation of TRC behaviour under sustained loading. Obviously, in addition to the mechanisms leading to deformations and crack formations under quasi-static loading, creep is a major factor to consider. Creep of TRC in total results from the creep of the matrix and the time-dependent crack development, accompanied by gradual delamination of fibres from the matrix and, eventually, fibre pullout. In this, the creep behaviour of the polymer yarn coatings plays a considerable role, especially at elevated temperatures and high relative humidity. Freitag et al. (2006) performed tensile creep experiments on cracked TRC specimens with AR-glass fibre. They concluded that deformations increased and time-to-failure decreased with increasing stress levels. More research is needed to be able to quantify the effects of sustained loads on TRC with various types of textiles.

6.4.4 Self-healing of cracks

The self-healing of cracks in cement-based materials is a well-known phenomenon. The main causes of such self-healing are twofold. On the one hand, nonhydrated binder particles (cement or pozzolana) can hydrate further on if the material comes in contact with water again. The newly formed C–S–H phases can effectively bridge fine cracks. On the other hand, calcium hydroxide (CH) can be deposited inside the cracks and can be converted to calcium carbonate as a result of carbonation (or, if pozzolanic materials are involved, to C–S–H phases). CH and calcium carbonate are rather weak from a mechanical point of view, making the crack bridging less effective, but they can and do fill and seal cracks.

In OC the crack widths are rather large, the water/cement ratio is relatively high, and the deposit of CH and calcite dominates the self-healing process. Larger cracks cannot be sealed completely. In contrast, TRC exhibits very small crack widths because of its tendency to multiple cracking. For these kinds of cementitious composites, the complete sealing of cracks and even a partial restoration of stiffness seem attainable to a great extent. The restoration of stiffness is due to the bridging of fine cracks by the newly developed C–S–H phases.

In order to investigate the effect of self-healing on the transport properties of TRC, water permeation measurements were carried out by Mechtcherine and Lieboldt (2011) in the unloaded, saturated state of TRC specimens at time intervals of 7 days. Figure 6.7 shows the time-dependent reduction of the transport rates of samples with different reinforcement textiles. After storing the cracked specimens in water for 14 days, the flow rate was reduced to less than 50% of the value obtained on the same specimen before storing in water. No measurable volume flow occurred after continued water exposure of 21–35 days, the particular duration depending on the type of the textile reinforcement used. The samples containing uncoated AR-glass yarns with low yarn fineness (1280 tex) needed longer until a negligible volume flow was reached, which can be traced back to the initially wider cracks in these specimens.
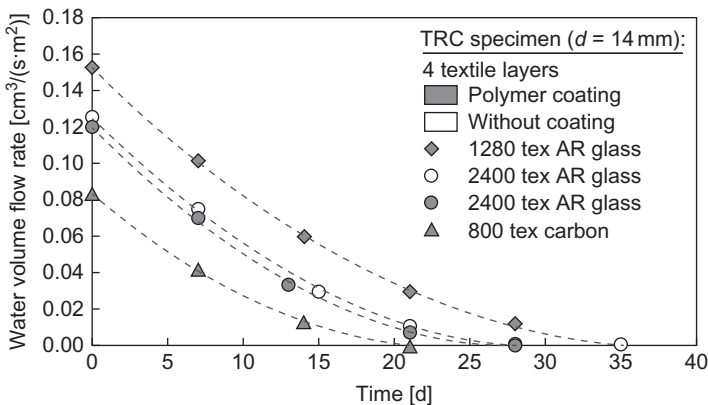
Figure 6.7 Time-dependent reduction of the water transport trough cracked TRC in unloaded state (Mechtcherine and Lieboldt, 2011).
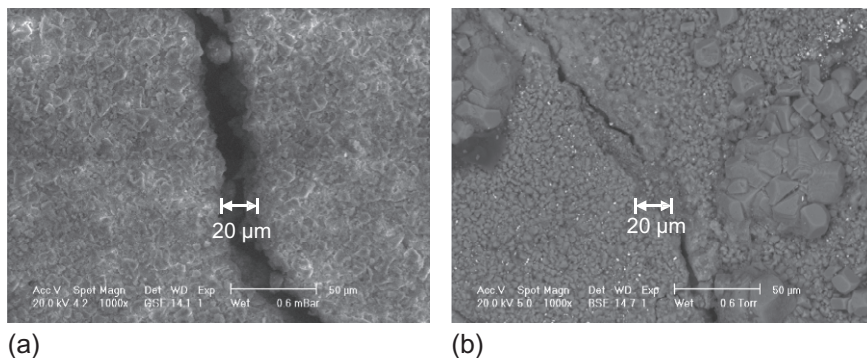
Figure 6.8 Self-healing effect in TRC: (a) crack before and (b) after exposure to water (Mechtcherine and Lieboldt, 2011); both images show the same specimen.

The specimens containing coated carbon textile layers showed the fastest self-healing, which could be expected since they had the finest cracks.

Using an environmental scanning electron microscope (ESEM), additional investigations of cracks before and after exposure to water revealed the formation of new crystal structures, which closed the cracks to transport (cf. Figure 6.8). Figure 6.8a shows the original crack with a width of 20 μm before water contact. Figure 6.8b illustrates the condition of a similar crack after the water permeability tests with duration of 21–35 days, indeed largely closed by deposits of calcium carbonate (calcite) (Mechtcherine and Lieboldt, 2011).

6.5 Summary

There is great potential for the application of TRC in structural elements and structures exposed to severe mechanical or environmental loading. Present knowledge indicates that TRC can yield high, long-term performance and favourable transport properties in the cracked state. Beyond that, TRC might show in many instances superior resistance to aggressive environments when compared to OC; however, with the exception of exposure to alternating freezing and thawing, there is no information available on the effects of aggressive environments on the mechanical properties of the materials.

Since TRC is a new material, there is no information available on the long-term field performance of elements and structures made of or strengthened with TRC; however, first field applications indicate that the superior performance in a laboratory environment, as summarised above, does indeed translate to superior field performance.

There is significant research needed to understand the long-term behaviour of TRC and RC/TRC elements under complex combined loads as encountered in the field. To be able to utilise the superior qualities of this new material fully, it will be necessary to develop a realistic, reliable, performance-based durability design concept for such structures.

Acknowledgments

References

Altmann, F., Mechtcherine, V., 2013. Durability design strategies for new cementitious materials. Cem. Concr. Res. 54, 114–125.

Altmann, F., Sickert, J.-U., Mechtcherine, V., Kaliske, M., 2012. A fuzzy-probabilistic durability concept for strain-hardening cement-based composites (SHCCs) exposed to chlorides: Part 1: Concept development. Cem. Concr. Compos. 34, 754–762.

Barhum, R., Mechtcherine, V., 2013. Influence of short dispersed and short integral glass fibres on the mechanical behaviour of textile-reinforced concrete. Mater. Struct. 46, 557–572.

Bentur, A., Diamond, S., 1987. Aging and microstructure of glass fiber cement composites reinforced with different types of glass fibers. Durability Build. Mater. 4, 201–226.

Brameshuber, W. (Ed.), 2006. Textile Reinforced Concrete: Report no. 036 of the RILEM State-of-the-Art Report. RILEM Technical Committee 201-TRC.

Butler, M., Hempel, S., Mechtcherine, V., 2009a. Zeitliche Entwicklung des Verbundes von AR-Glas- und Kohlenstofffaser-Multifilamentgarnen in zementgebundenen Matrices. In: Curbach, M., Jesse, F. (Eds.), Proc. 4th Colloquium on Textile Reinforced Structures (CTRS4), Dresden, pp. 213–226.

Butler, M., Mechtcherine, V., Hempel, S., 2009b. Experimental investigations on the durability of fibre–matrix interfaces in textile-reinforced concrete. Cem. Concr. Compos. 31 (4), 221–231.

Butler, M., Lieboldt, M., Mechtcherine, V., 2010a. Application of textile-reinforced concrete (TRC) for structural strengthening and in prefabrication. In: Advances in Cement-Based Materials. Taylor & Francis Group, London, pp. 127–136.

Butler, M., Mechtcherine, V., Hempel, S., 2010b. Durability of textile-reinforced concrete made with AR glass fibre—effect of the matrix composition. Mater. Struct. 43, 1351–1368.

Cohen, Z., Peled, A., 2010. Controlled telescopic reinforcement system of fabric-cement composites—durability concerns. Cem. Concr. Res. 40, 1495–1506.

DIN EN 13396, 2004. Products and systems for the protection and repair of concrete structures—test methods—measurement of chloride ion ingress.

European Brite-Euram Programm, 2000. Probabilistic performance based durability design of concrete structures. Report no. BE95-1347/R17 of the DuraCrete Final Technical Report.

Förster, T., 2014. Einfluss der chemischen Zusammensetzung und der Oberflächenmodifizierung auf die Eigenschaften von Basaltfasern, Doctoral thesis, Technische Universität Dresden.

Freitag, S., Beer, M., Jesse, F., Weiland, S., 2006. Experimental investigation and prediction of long-term behavior of textile reinforced concrete for strengthening. In: Hegger, J., Brameshuber, W., Will, N. (Eds.), Textile Reinforced Concrete—Proceedings of the 1st International RILEM Conference. RILEM, Aachen, pp. 121–130.

fib bulletin 34, 2006. Model Code for Service Life Design. International Federation for Structural Concrete (fib), Lausanne.

Hempel, S., Butler, M., Mechtcherine, V., 2015. Bond behaviour and durability of basalt fibres in cementitious matrices. In: Proc. of Ferrocement 11, Aachen.

Hilsdorf, H.K., Schönlin, K., Tauscher, F., 1997. Dauerhaftigkeit von Betonen. Beton-Verlag GmbH, Düsseldorf (in German).

Inaguma, H., Seki, M., Suda, K., Rokugo, K., 2006. Experimental study on crack-bridging ability of ECC for repair under train loading. In: Proceedings PRO 49 of International RILEM Workshop on HPFRCC in Structural Applications. RILEM Publications S.A.R.L., Honolulu, US, pp. 499–508.

Langlois, V., Fiorio, B., Beaucour, A., Cabrillac, R., Gouvenot, D., 2007. Experimental study of the mechanical behavior of continuous glass and carbon yarn-reinforced mortars. Constr. Build. Mater. 21, 198–210.

Lawrence, C.D., 1986. Measurements of permeability. In: Proceedings of 8th International Congress on the Chemistry of Cement, Rio de Janeiro, Brazil. FINEP, vol. V, pp. 29–34.

Li, V.C., Stang, H., 2004. Elevating FRC material ductility to infrastructure durability. In: Proceedings PRO 39 of BEFIB. RILEM Publications S.A.R.L., Varenna, Italy, pp. 171–186.

Lieboldt, M., 2012. Transport of liquids and gases in textile reinforced concrete. Doctoral thesis, Technische Universität Dresden, Schriftenreihe des Instituts für Baustoffe, Heft 2012/1 (in German).

Lieboldt, M., Mechtcherine, V., 2013. Capillary transport of water through textile-reinforced concrete applied in repairing and/or strengthening cracked RC structures. Cem. Concr. Res. 52, 53–62.

Mechtcherine, V., Lieboldt, M., 2011. Permeation of water and gases through cracked textile reinforced concrete. Cem. Concr. Comp. 33, 725–734.

Mechtcherine, V., Lieboldt, M., Altmann, F., 2007. Preliminary tests on air-permeability and water absorption of cracked and uncracked strain hardening cement-based composites. In: Proceedings of the International RILEM Workshop on Transport Mechanisms in Cracked Concrete. RILEM Publications S.A.R.L., Ghent, Belgium, pp. 55–66.

Müller, H.S., Mechtcherine, V., Geis, M., Hewener, A., 2003. Concrete degradation due to corrosion of steel reinforcement—numerical investigations. In: Proceedings of 15th International Conference on Building Materials Research (ibausil). F. A. Finger-Institut für Baustoffkunde, Bauhaus-Universität Weimar, Weimar, Germany, pp. 1457–1467.

Ohama, Y., 1989. Carbon–cement composites. Carbon 27, 729–737.

Pourasee, A., Peled, A., Weiss, J., 2011. Fluid transport in cracked fabric-reinforced-cement-based composites. J. Mater. Civil Eng. 23 (8), 1227–1238.

Rybin, V.A., Utkin, A.V., Baklanova, N.I., 2013. Alkali resistance, microstructural and mechanical performance of zirconia-coated basalt fibers. Cem. Concr. Res. 53, 1–8.

Scheffler, C., Förster, C., Mäder, E., Heinrich, G., Hempel, S., Mechtcherine, V., 2009a. Aging of alkali-resistant glass and basalt fibres in alkaline solutions: evaluation of the failure stress by Weibull distribution function. J. Non-Cryst. Solids 355 (52–54), 2588–2595.

Scheffler, C., Gao, S.L., Plonka, R., Mäder, E., Hempel, S., Butler, M., Mechtcherine, V., 2009b. Interphase modification of alkali-resistant glass fibres and carbon fibres for textile reinforced concrete I: fibre properties and durability. Comp. Sci. Technol. 69, 531–538.

Schießl, P., Gehlen, Ch., 2005. New approach to service life design of concrete structure. In: Proceedings of an International Workshop on Combined Mechanical and Climatic Loads (CMCL). Aedificatio Publishers, Qindao, China, pp. 3–14.

Sim, J., Park, Ch., Moon, D.Y., 2005. Characteristics of basalt fiber as a strengthening material for concrete structures. Compos. Part B 26, 504–512.

Wei, B., Cao, H., Song, S., 2010. Environmental resistance and mechanical performance of basalt and glass fibers. Mater. Sci. Eng. 527, 4708–5715.

Weiland, S., Ortlepp, R., Hauptenbuchner, B., Curbach, M., 2008. Textile reinforced concrete for flexural strengthening of RC-structures—Part 2: Application on a concrete shell. In: Design & Applications of Textile-Reinforced Concrete, ACI SP-251-3, pp. 41–58.

Yilmaz, V., Glasser, F., 1991. Reaction of alkali-resistant glass fibres with cement. Part 2: Durability in cement matrices conditioned with silica fume. Glass Technol. 32 (4), 38–47.

Zhu, W., Bartos, P., 1997. Assessment of interfacial microstructure and bond properties in aged GRC using novel microindentation method. Cem. Concr. Res. 27 (11), 1701–1711.

Fire resistance of textile fiber composites used in civil engineering

7

L. Bisby
University of Edinburgh, Edinburgh, UK

7.1 Introduction

Textile-reinforced mortar (TRM) systems have, in recent decades, emerged as novel structural systems and as means of strengthening damaged or deficient masonry or reinforced concrete structures (Brameshuber, 2006; Triantafillou and Papanicolaou, 2006). These systems generally consist of open-weave, high-strength and stiffness fiber fabrics (textiles), which are applied to the surfaces of structural elements using specialized inorganic mortars; typically these are cement-based. The open-weave fabrics for these systems normally consist of alkali-resistant (AR) glass, carbon, or aramid fibers (Brameshuber, 2006), which in some cases may lead to comparatively poor utilization of the fibers due to fiber pullout at relatively low load levels. This issue has been partly addressed by the development of novel fiber fabrics and textiles that provide anchorage using the weft fibers to anchor the warp fibers. Novel systems termed alternatively as fiber-reinforced cementitious matrix (FRCM) systems have also emerged in the last decade; these are generally based on non-woven fiber rovings such as polybenzoxozole (PBO) (Fallis, 2009). The unique chemical structure of the PBO fibers allows them to bond directly to cementitious mortar matrices, thus eliminating the need for an epoxy resin to bond the fibers to an inorganic substrate (Fallis, 2009).

TRM and FRCM materials and systems have several advantages over alternative systems, such as externally bonded or near-surface mounted fiber-reinforced polymer (FRP) systems; many of these are discussed in the other chapters of this book. This includes their breathability and potentially superior performance in fire (in particular their non-combustibility). However, research on their high-temperature performance remains scarce.

This chapter provides an overview of the available knowledge on the fire and high-temperature performance of TRM and FRCM materials used in civil engineering applications. The discussion in the current chapter focuses on TRM component materials and structural elements, as well as on TRM and FRCM structural strengthening systems for reinforced concrete or masonry structural elements.

7.2   Fire resistance

A critical issue to protect and preserve life safety in the design of structural elements in buildings is their mechanical and thermal performance during fire. Two types of performance against fire are important (Tanano et al., 1999): performance against initial fire; and performance in the *post-flashover* stage. Performance against initial fire includes: flammability, which affects the spread of fire (non-combustibility and flame retardancy); and smoke- and gas-generating properties, which affect the ability to safely evacuate a building. The performance against fire in the post-flashover stage includes: heat-insulating, flame-resisting, and smoke-barrier properties of separating members, such as floors or walls, and structural safety (or load-bearing capability) of framing members, such as columns and beams. Both aspects are discussed in this section; however the focus is on structural 'fire resistances' (Section 7.2.2).

7.2.1   Reaction-to-fire properties

In the context of performance in fire or elevated temperature service environments, it is noteworthy that a key advantage of many TRM and FRCM systems, being based on inorganic matrix materials such as specialized cement mortars (Bisby et al., 2013) or geopolymers (Kurtz and Balaguru, 2001), is their inherent non-combustibility (e.g, Istituto Giordano, 2008).

Previous research on FRP materials and strengthening systems in fire has shown that loss of the strengthening systems' mechanical performance during fire, whilst rapid and severe in most cases, due to physical deterioration and chemical degradation of the polymer matrix, may not be critical provided that sensible loading limits are imposed during design (ACI, 2008). However structural performance in fire is only one of a host of concerns that must be addressed when considering application of a novel structural material in a building. Fire ignition, severity, flame spread, heat release, smoke generation, and toxicity cannot be ignored in most cases—since these issues are critical to preserving tenable conditions and to allowing safe evacuation of a building's occupants in the early stages of a fire.

Unprotected FRP materials and strengthening systems, all of which incorporate polymer adhesives/matrices, will burn if directly exposed to fire, and will contribute fuel, increase flame spread, and generate toxic smoke (Bisby, 2003). FRP materials and strengthening systems, therefore, typically require protection by flame-spread coatings in interior applications in buildings to meet stringent life-safety objectives. TRM and FRCM systems, on the other hand, bonded with inorganic mortars, are typically inherently non-combustible and can therefore be used unprotected; this considerably reduces their material and installation costs and improves esthetics, particularly in structural strengthening applications in buildings.

Reaction-to-fire properties are normally defined based on compliance with regulatory requirements and test methods listed in national building and fire-testing codes. In Europe for instance, a wide range of tests is potentially applicable in different applications and jurisdictions, including, e.g., ISO 5658-2 lateral flame spread on

building/rail products in vertical configuration (ISO, 2006a); ISO 5660-1 cone calorimeter for measuring the rate of heat release of products (ISO, 2002a); ISO 5660-2 reaction-to-fire tests—heat release, smoke production and mass loss rate—Part 2: smoke production rate (dynamic measurement) (ISO, 2002b); ISO 4589-2 determination of burning behavior by oxygen index (ISO, 2015); ISO 5659-2 smoke generation (ISO, 2006b); ISO 4589-3: Annex A temperature index/flammability temperature test (ISO, 1996); ISO 11925-2 ignitability (ISO, 2010a); ISO 13823 single burning item (ISO, 2002c), EN ISO 1182 non-combustibility (2010b); and so on.

As previously noted, most TRM and FRCM materials and systems should perform very well in most of the above test methods, when compared with combustible/organic structural and strengthening materials such as FRPs. Local guidance should be sought to determine which reaction-to-fire compliance testing and certifications are needed in a given application.

7.2.2 Structural fire resistance

In all fire-regulated jurisdictions globally, structural design for fire safety is based on the principle that all structural and building elements should have a *fire resistance*—which is defined as "the ability of a structure or structural element to resist collapse, prevent fire spread, or some other failure mechanism"—that is greater that the *fire severity*—which is "a measure of the destructive impact of a fire, or of the temperatures or forces which could cause collapse or other failures as a result of fire" (Buchanan, 2001). From a building and fire code compliance perspective, *fire resistance* is typically defined in the time domain, such that structures and structural elements must be able to resist a certain prescribed duration of exposure to the applicable *standard temperature versus time curve* without experiencing *failure* when tested within a fire-testing furnace. It is important to note that fire resistance should be applied only to structures or elements of structures, rather than to specific materials or combinations of materials.

Fire resistance ratings are generally assigned in 30- or 60-min intervals based on the results of standard fire tests performed in accordance with national or international testing standards, such as ASTM E119 (2010), ISO 834 (1999), etc. The typical procedure by which standard fire tests are undertaken is that: (1) test specimens (structural elements) are constructed so as to accurately represent the as-built construction; (2) the specimen is placed with in a loading frame; (3) the loading frame and specimen are positioned inside, next to, or over a standard testing furnace (depending on the type of structural member—wall, floor, beam, column, etc); (4) the likely (mean nominal) service load is applied to the specimen in as realistic a fashion as possible; (5) the service load is maintained constant and the element is subjected to the standard time–temperature curve; (6) the test is continued until a *failure criterion* is reached; and (7) the test is stopped once failure is observed and a *fire resistance* rating is obtained (typically by rounding down to the nearest 30-min interval) (Buchanan, 2001).

For building applications, most fire codes and standards prescribe similar temperature versus time curves that rise to about 600 °C in 5 min, 900 °C in 30 min, and 1000 °C in 90 min; however, other standardized fire curves are available for other
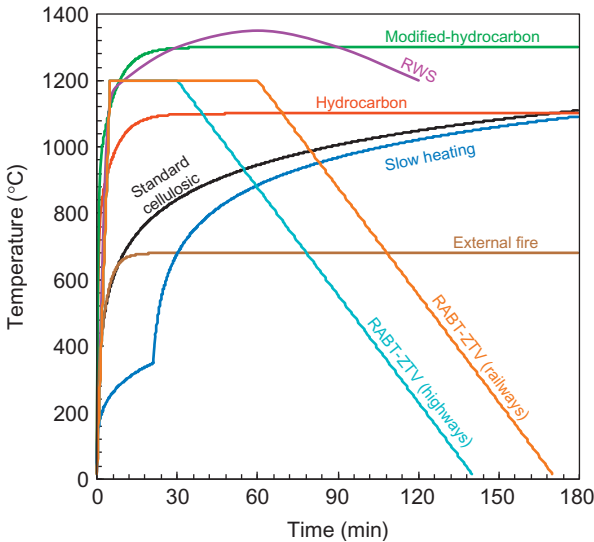
Figure 7.1 Various standard fire curves that may be used to assess the fire resistance of structural elements internationally (after Maluk, 2014).

applications (refer to Figure 7.1). Failure during testing is typically defined as one of: (1) loss of stability, meaning that the element collapses (or deflects too much or too quickly); (2) loss of integrity, meaning that it allows excessive passage of flame or hot gases; or (3) loss of insulation, meaning that it allows excessive heat transfer to the unexposed surface (for walls, doors, and floors). Of course, not all criteria apply to all types of members (e.g., columns must only meet the stability criterion).

Finally, it is noteworthy that in certain cases, expert opinion can be used in lieu of a standard furnace test; these expert opinions are typically based on accepted and validated rules for assessing fire resistance, or less commonly on detailed computational modeling and analysis. This requires a detailed understanding of materials response at elevated temperature, as described below for TRM systems.

The properties of TRM and FRCM materials at high temperature have not been extensively studied in the literature, and what little data are available are not readily applicable to the wide range of specific TRM or FRCM materials that might be used in civil engineering applications. Before detailed numerical studies on the structural fire resistance of TRM/FRCM systems can be conducted with confidence, a more complete understanding of the thermomechanical properties of these materials is essential. The following sections outline the results of the few studies performed to date to investigate these issues, with a focus on mechanical, rather than thermal, properties.

The thermal response of TRM materials can be reasonably assumed to be similar to that of concrete in most cases, as it is unlikely that the presence of fiber textiles will have a significant influence on their thermal response. Interested readers should refer to available guidance on the thermal response of different types of cement-based concretes, for example as given in Eurocode 2 for Concrete—EN 1992-1-2 (CEN, 2004).

7.3 Fiber response to elevated temperatures

The four most commonly used fiber types have significantly different thermomechanical properties at high temperature. Figure 7.2a–d shows the reductions in tensile strength of fibers of various types with temperature, based primarily on a database of available literature complied by Bisby (2003), with subsequent updating based on more recently presented data.

Aside from a tendency to oxidize at temperatures above 400–500 °C, some carbon fibers have shown negligible strength loss up to temperatures of 1000 °C. This is clear in Figure 7.2a, where the filled data markers that do show considerable reductions in tensile strength, likely due to interactions with a coating polymer (Ehlig et al., 2010)
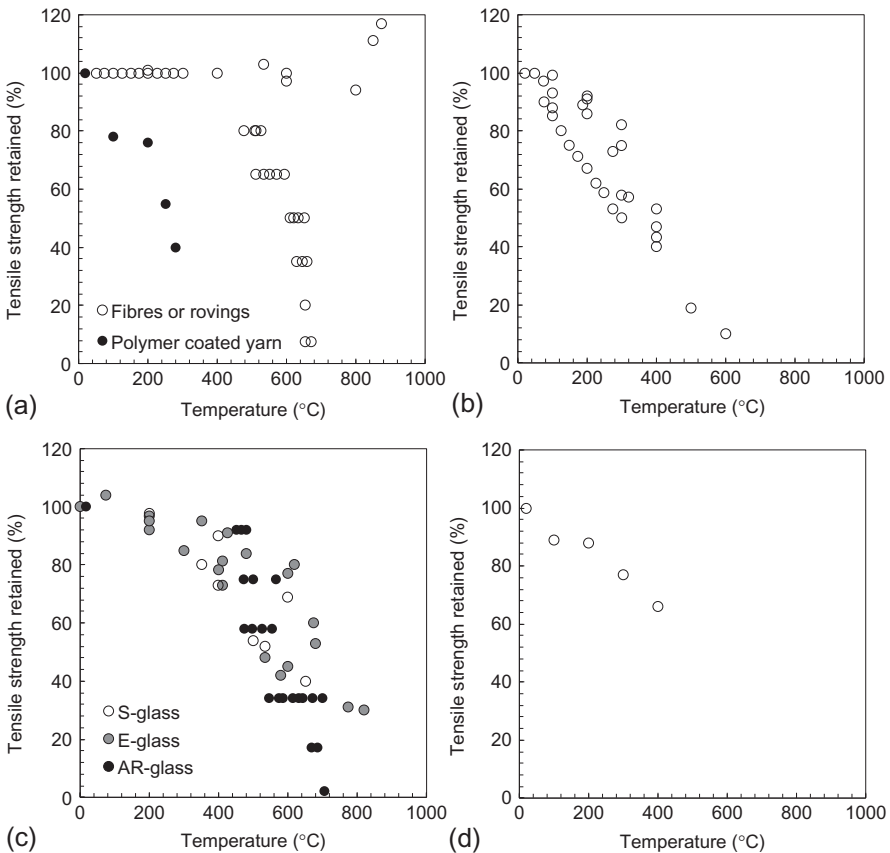
Figure 7.2 Reductions in short-term tensile strength of various types of fibers commonly used in TRM and FRM applications in civil engineering: (a) carbon; (b) aramid; (c) glass; (d) PBO (Bisby, 2003; Liu and Yu, 2006; Kulas et al., 2011; Antons et al., 2012).

are for polymer-coated carbon yarns rather than "bare" carbon fibers. The scatter in the unfilled data markers is likely the result of fibers being tested in both oxidizing and non-oxidizing environments, although this is not clear from the source publications, and additional research may be warranted to determine the response of carbon fibers used specifically in TRM applications. Aramid fibers have a high thermal stability, but oxidation limits their use above about 150 °C as shown in Figure 7.2b. Glass fibers will not oxidize, but tend to soften at temperatures in the range of 600–800 °C (Bakis, 1993), as shown in Figure 7.2c.

Sen et al. (1993) performed tests on a variety of different glass fiber types at high temperature and concluded that the strength reduction was independent of the type of glass fiber being used. More recently, Antons et al. (2012) and Kulas et al. (2011) have performed tests on specific AR-glass and carbon fibers of the types now used in many TRM materials. Again, there is no obvious difference in the sensitivity of AR-glass fibers as compared with S-glass or E-glass. PBO fibers, for which very little data was available in the literature until recently (Figure 7.2d), are similarly sensitive as aramid and glass fibers.

It is evident from Figure 7.2 that while all fibers are adversely affected by elevated temperatures, aramid is the most severely affected, with tensile strength reductions of more than 50% at 500 °C, and carbon is the least with reductions of less than 5% at the same temperature in some cases.

7.4   Matrix response to elevated temperatures

The wide variety of available matrix materials and additives for TRM and FRCM materials (discussed elsewhere in this book) make it difficult to provide useful generalizations with respect to their high temperature mechanical or bond behavior. Since most TRM matrix materials are based on Portland cement mortars (with various additives and fibers in most cases), and since many can be classified as high-strength or high-performance fine-grained concretes, it is expected that changes in their thermal and mechanical properties at elevated temperature will be similar to those suggested by Eurocode 2—EN 1992-1-2 for concrete (CEN, 2004). Figure 7.3a shows the reduction of compressive strength at elevated temperature for concretes of various types according to the Eurocodes; interested readers should consult the source documents (CEN, 2004) for additional information on this topic.

Kulas et al. (2011) and Antons et al. (2012) have presented the results of compressive strength testing at high temperatures on a specific fine-grained concrete mixture, with a characteristic compressive strength of 70 MPa, developed specifically for AR-glass TRM systems. The results of their testing are provided in Figure 7.3b, along with an idealized strength reduction curve that they proposed for use in design. The correlation of the test data in Figure 7.3b with available guidance for high-strength concrete given in Figure 7.3a is reasonable.

In suggesting the idealized curve in Figure 7.3b, Kulas et al. (2011) assume that a portion of the strength loss is due to the weight reduction (presumably dehydration), and is accounted for by a reduction to 0.75 between temperatures of 50 and 100 °C
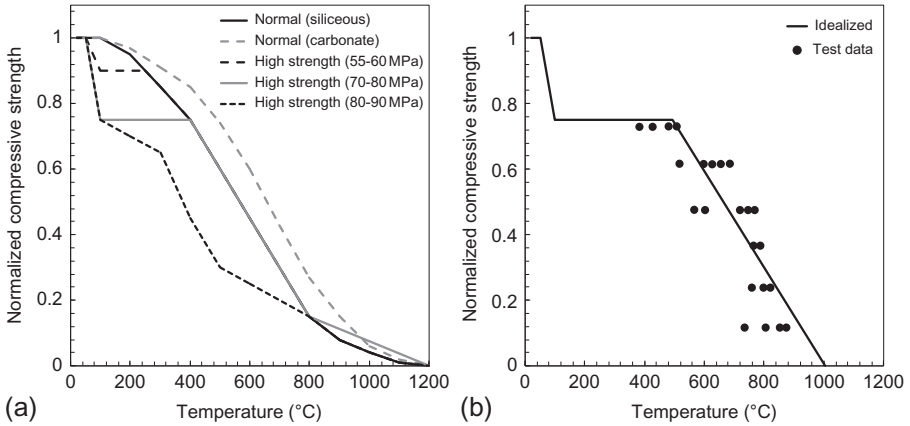
Figure 7.3 Reductions in the compressive strength of (a) concrete, according to BS EN 1992-1-2 (CEN, 2004); (b) fine-grained concrete mortar specifically developed for TRM applications with AR-glass textile reinforcement, according to Kulas et al. (2011).

(quoting the work of Schneider (1982) on conventional concrete mixes). From 100 to 488 °C, the reduction factor is assumed to remain constant, up to about 500 °C. A quartz inversion at temperatures in the range of 573 °C is assumed to result in strength losses, which are then linearly fitted up to the assumed ultimate temperature of 1005 °C.

The effects of heating on the shear strength, tensile strength, fracture energy and crack propagation of concretes is not well known for the possible matrix materials used in TRM and FRCM applications, and this issue requires additional research attention before conclusive statements can be made.

7.5 Textile-fiber composite response to elevated temperatures

Studies undertaken to interrogate and understand the specific mechanical response of TRM material systems at elevated temperature are extremely limited. Only the direct tensile response of thin TRM materials has been investigated in any detail, both at elevated temperature (Ehlig et al., 2009, 2010) and at ambient temperature *after* exposure to elevated temperature (Colombo et al., 2011).

Ehlig et al. (2009) present a series of tension tests on TRM coupons made from uncoated and polymer-coated AR-glass and carbon fiber textiles within a fine-grained cementitious matrix. They observed explosive spalling of the cementitious mortar after 4–5 min of exposure to the ISO 834 standard fire (ISO, 1999). Failure of the specimens occurred quickly during fire exposure, occurring between 45 s and 17 min from the start of heating, depending on the sustained load level and the type

of fiber reinforcement; unsurprisingly, carbon fibers and lower load levels led to the longest failure times.

Heat-induced explosive spalling is a serious concern for all cementitious materials and structural elements under severe heating, particularly high-strength and high-performance mixes as might be used in TRM materials and systems. Spalling remains poorly understood within the research community, but is widely considered to result from a combination of differential in-depth thermal stresses within the concrete during heating, combined with pore pressure build-up associated with the mass transport of water vapor within the concrete, the formation of a moisture clog, and build up of internal pore pressures promoting tensile rupture (Maluk, 2014). A wide range of factors is known to influence spalling, including the aggregate type(s), applied loads, concrete strength, restraining conditions, moisture content, addition of various types of supplementary supplanting materials and fibers, etc. A full description of spalling phenomena is avoided here, although an exhaustive summary of the relevant issues is given by Maluk (2014).

It is noteworthy that, while the mechanism of their action remains unknown and disputed within the research community, adding a low dose (2–2.5 kg/m^3) of polypropylene (PP) anti-spalling fibers to the concrete mix during casting appears to be the best available means to mitigate heat-induced spalling of concrete during fire exposure (Maluk, 2014). This was partly confirmed for TRM materials by Ehlig et al. (2009) through testing, where the addition of PP fibers to TRM materials prevented spalling; however, the failure time of the tensile coupons was only marginally improved.

Ehlig et al. (2010) present subsequent tests on TRM tensile coupons, again fabricated from a fine-grained cementitious mortar, but in this case reinforced with a stitch-bonded textile of polymer-coated carbon filament yarns. The tensile coupons were tested under sustained loads ranging between 25% and 75% of their room-temperature ultimate strength, whilst being heated using radiant heaters at a rate of either 2 or 10 °C/min. In all cases, failure was due to fiber pullout/rupture within the heated region, initiating at a tensile crack in the cementitious mortar. A trend of decreasing failure temperature with increasing sustained load was observed; however, the effect was relatively minor, which indicates that failure is likely to occur under any significant loading level once a critical temperature is exceeded; this critical temperature is likely linked to oxidation of the carbon fibers at temperatures in the range of 400–500 °C. Samples heated at higher rates generally displayed longer failure times due to self-insulation and the development of steep thermal gradients in the samples. The results of Ehlig et al.'s (2010) experiments are shown in Figure 7.4.

Colombo et al. (2011) present the results of post-high temperature exposure *residual* tests (i.e., tests at room temperature) to evaluate thermal damage to a specific TRM material consisting of AR-glass fibers in a cementitious mortar. They show that exposure to temperatures of 200 °C has only a small detrimental effect on the residual tensile strength of TRM coupons, but that for coupons exposed to temperatures exceeding 400 °C the mortar deteriorates and fiber sliding occurs, with subsequent significant reductions in tensile strength of the specific TRM system used in their studies.
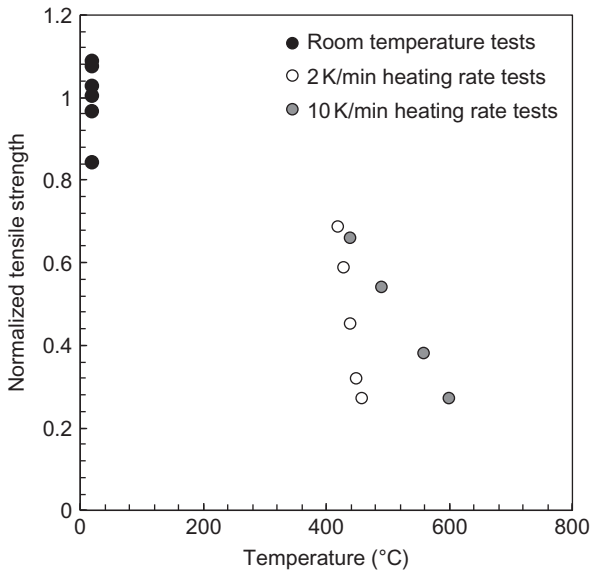
Figure 7.4 Variation of tensile strength of a specific carbon fiber/cementitious matrix TRM system reported by Ehlig et al. (2010) (at different heating rates).

7.6 Fire resistance of TRC structures

As is the case for the performance of TRM materials at elevated temperature, very few studies are available in the literature on the performance at high temperature of TRM structural elements. The author is aware of only two studies that have been published to date, and both of these were performed by Aachen University, Germany, in one case in partnership with Stuttgart University, Germany.

Krüger and Reinhardt (2006), Büttner et al. (2007) and Reinhardt et al. (2008) all report on the same series of standard cellulosic fire tests performed on TRM beams under sustained static loads. The beams were thin-walled and I-shaped in cross-section, with a depth of 120 mm, a flange width of 110 mm, and flange and web thicknesses of approximately 18 mm; they were reinforced internally with either carbon or AR-glass textile reinforcement. The beams were tested in four-point bending under sustained loads of 33% or 50% of their ambient flexural capacity. While the overall length of the beams was 1000 mm and the tested unsupported span was 900 mm, it is critically important to note that during fire testing, the beams were subjected to fire over a length of only 560 mm centered on midspan, thus ensuring cold anchorage of the textile reinforcement in the cooler end regions of the beams. It is also noteworthy that the top chords of the beams were thermally protected with mineral wool during fire testing.

These tests clearly demonstrated the superior performance of carbon-fiber textiles at high temperature as compared with AR-glass fibers. The beams reinforced with carbon-fiber textiles were able to achieve higher fire resistance durations (by as much as 600%), up to 90 min even under sustained loads at 50% of the ambient flexural failure load. This is expected based on the data provided previously in Figure 7.2, particularly in the case

that cold anchorage of the textiles is provided outside the heated region. Concrete spalling was observed in only one of the six tests performed; however, the reasons for this discrepancy are not known or commented on by the authors.

Interesting and significant differences in the time history of flexural deformation of the beams reinforced with either AR-glass or carbon-fiber textiles are also noted by the authors; these are thought to result from the fact that carbon fibers have a very small (or even negative) coefficient of thermal expansion, whereas glass fibers have a positive coefficient of thermal expansion that is similar to that of concrete (Bisby, 2003). This could theoretically lead to stress increases in carbon-fiber textiles under sustained load during fires, which could also potentially lead to carbon-fiber rupture in extreme cases. Additional research is needed in this area.

Büttner et al. (2007) suggest that the fire resistance of TRM structural elements, which appears to be comparatively poor based on their research, particularly when using AR-glass fibers, may be improved by: (1) increasing the concrete cover; (2) using carbon fibers or possibly combining carbon and AR-glass fibers; (3) applying fire-protective intumescent coatings; or (4) changing the micro-concrete. Only (1) and (2) are realistic options at present, and both present considerable disadvantages in terms of reduced structural efficiency and/or increased cost.

Antons et al. (2012) present the results of small-scale flexural tests on heated TRM prisms with dimensions of $40 \times 40 \times 200$ mm. The prisms were fabricated from the fine-grained cementitious mortar, for which the reduction in compressive strength with elevated temperature was given above in Figure 7.3b, and reinforced with AR-glass fibers, for which the reductions in tensile strength with elevated temperature are given in Figure 7.2c. The prisms were loaded in four-point bending, with a textile reinforcement anchorage length of 40 mm outside the loaded span, up to 30%, 50%, and 80% of the ambient temperature flexural capacity. The prisms were then heated at 5 °C/min until failure.

Based on these tests and on research by the same authors presented in Sections 7.3 and 7.4, Antons et al. (2012) conclude that below 300 °C, there is no obvious impact of temperature at the load levels considered, that there is an increasing negative influence of temperature with higher load levels between 300 and 600 °C, and that beyond about 620 °C, melting of the AR-glass fibers dominates response leading to rapid failure under any load level. The authors also suggest that the use of polymer impregnated textile rovings is preferable to uncoated textiles, though additional research is clearly needed before confident conclusions can be drawn.

7.7 Fire resistance of textile-reinforced strengthening systems for concrete and masonry

Strengthening reinforced concrete or masonry structures with externally bonded materials—e.g., FRP, TRM, FRCM systems—is widely recognized for its effectiveness and ease of application (Bisby et al., 2008, 2013). FRP, TRM or FRCM materials can all be bonded to the exterior faces of reinforced concrete or masonry elements, using ambient-cure epoxy adhesives (in the case of FRPs) or cementitious (or other)

inorganic mortars (in the case of TRMs or FRCMs). In these applications, the goal is to provide well-anchored tensile reinforcement to a reinforced concrete or masonry substrate. Such systems can be used to provide shear or flexural strengthening for reinforced concrete or masonry members (Triantafillou and Papanicolaou, 2006; Fallis, 2009) or for confinement and axial load enhancement of RC columns (e.g., Bournas et al., 2007), as described elsewhere in this book.

Fire-rated, insulated, externally bonded FRP strengthening systems have been tested and are available for use (e.g., Kodur et al., 2006), although current design guidelines conservatively suggest that the structural effectiveness of FRP strengthening systems should be ignored during fire (ACI, 2008); unless it can be shown (which has not yet been done for any currently available FRP system) that they would remain effective at the temperatures to be expected during a serious fire. Hence, applications of FRPs for strengthening concrete buildings, parking garages and certain industrial structures with elevated service temperatures are hindered by a lack of knowledge regarding the ability of FRP systems to maintain structural effectiveness under service loads at high temperatures.

Notwithstanding the comments above, and assuming that the reaction-to-fire properties of an externally bonded strengthening system are appropriately considered (see Section 7.2.1), the structural response of an externally bonded strengthening system in fire depends primarily on the temperatures it experiences. Traditional concepts of *fire resistance* or *critical temperature* are problematic for evaluating the performance of an externally bonded strengthening system, as these concepts should only be applied to structural *elements* rather than specific materials (Kodur et al., 2006). The specific performance of the strengthening system is thus not the critical issue for fire resistance design; rather it must be demonstrated only that the strengthened structural element can resist failure under the strengthened (i.e., increased) service loads for the required duration of fire exposure. This general design philosophy, illustrated schematically in Figure 7.5, assumes a standard fire exposure for simplicity, was first outlined by Kodur et al. (2006) for FRP strengthening systems, and is suggested by ACI 440 (ACI, 2008) and TR55 (Concrete Society, 2012) for structural strengthening applications with externally bonded systems.

Figure 7.5 shows that loss of structural effectiveness of a strengthening system need not mean failure when defining the fire resistance of the structural element. For example, if a reinforced concrete slab is strengthened with an externally bonded TRM system to carry increased service loads, it is entirely possible that the slab may be able to carry the increased service loads for the required duration of fire exposure, even if the effectiveness of the TRM is lost and no supplemental fire protection is applied. It is noteworthy that this would need to be demonstrated through full scale fire testing or by using advanced calculations (see BS EN 1992-2-1 [CEN, 2004], for instance), and that this would only be the case if the pre-existing structural element was originally *over-designed* with respect to its required fire resistance—as many members are, particularly in reinforced concrete buildings.

If the pre-existing member does not have sufficient capacity to meet the criterion described above, it would be necessary to provide supplemental fire insulation to the exterior of the strengthening system (as demonstrated by Kodur et al. (2006) for an
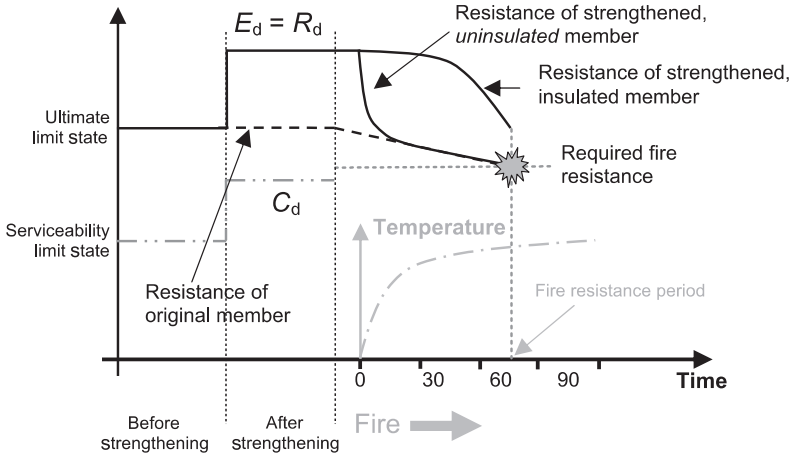
Figure 7.5 Schematic showing the need (or lack thereof) for maintaining the structural "effectiveness" of an FRP, TRM, or FRCM during fire to prevent collapse (after Bisby and Stratford, 2013).

externally bonded FRP strengthening system, for instance) such that the load-carrying capacity of the pre-existing member is preserved during fire even if the TRM system rendered ineffective. Considerable evidence is available for FRP systems, whether experimental (e.g., Bisby et al., 2005a; Williams et al., 2008) or computational (e.g., Bisby et al., 2005b; Chowdhury et al., 2011), to demonstrate the legitimacy of this approach.

There has been considerable debate within the externally bonded structural strengthening community as to how (or if) it can be shown that a given externally bonded strengthening system remains *active* during fire, such that strengthening systems might be applied as so-called *primary* reinforcement (i.e., the strengthening system remains load bearing under service loads during fire). It has been suggested (e.g., Fallis, 2009) that TRM or FRCM systems may outperform FRP strengthening systems at elevated temperatures or during fire, due to their inherent non-combustibility and possibly to superior strength retention at elevated temperatures. Only very limited studies on the performance in fire of specific TRM and FRCM systems for strengthening concrete are available in the literature.

Ehlig et al. (2009) present a series of fire tests on TRM strengthened reinforced concrete beams exposed to fire over a limited area in their midspan regions. Using either carbon or AR-glass fiber textiles, these TRM strengthened concrete beams were able to resist fire exposure according to ISO 834 (ISO, 1999) while being subjected to sustained loads equalling 66% of the presumed "working load" for more than 60 min. At 125% of the working load, however, failure of the TRM occurred after 45 min, in the case of AR-glass fibers, and 70 min, for carbon fibers. No spalling of the TRM was observed. The remaining load bearing capacities (post-fire residual strengths) after 60 min of fire exposure were 47% and 88% of the ambient temperature collapse loads for the AR-glass and carbon-fiber textiles, respectively.

Ehlig and Hothan (2011) present the results of a series of follow-on standard fire tests on seven one-way spanning reinforced concrete slabs; two of these were ambient temperature reference slabs and the other five were strengthened with a carbon fiber TRM strengthening system. The slabs were heated for durations of 30 or 60 min in accordance with ISO (1999), with sustained test loads varying between 0% and 65% of the ambient temperature ultimate load—representing working loads between 0% and 135% assuming a notional working load that is 50% of the ultimate load at room temperature. In cases where the slabs survived the fire tests, residual strength tests were undertaken. Again no spalling was observed during fire exposure. Hence, in addition to providing structural strengthening, the TRM systems also provided supplemental fire insulation to the pre-existing structural members.

Failure occurred by tensile rupture of the TRM system after 55 min of fire exposure for a working load of 100% (i.e., 50% of the ultimate ambient temperature strength) and after 30 min for a working load of 130%. Slabs tested after fire exposure displayed post-fire residual capacities of 65% and 70% of the ambient temperature ultimate load after 30 min of fire exposure, or 50% of the ambient temperature ultimate load after 60 min of fire exposure. Ehlig and Hothan (2011) note that the interactions between the TRM and internal steel reinforcement, as well as the failure modes during fire, require additional research attention.

Bisby et al. (2013) report on the results of a series of non-standard fire tests to compare the fire performance of specific commercially available FRP, TRM, and FRCM systems for flexural strengthening of reinforced concrete beams. Tests are presented on small-scale reinforced concrete beams at both ambient and elevated temperatures. Importantly, the tests presented presume that a "cool" anchorage zone is provided for the strengthening systems, such that the strengthening is not bond-critical—(i.e., failure by debonding in a heated anchorage zone is prevented through non-exposure, insulation, or by mechanical means). A comparison against a commercially available externally bonded carbon/epoxy FRP strengthening system is also presented.

Bisby et al. (2013) note that it is difficult in practice (using standard furnace tests) to observe the temperature or time of fire exposure when an externally bonded strengthening system loses mechanical strength or interaction (i.e., bond) with the substrate structural element. They address this problem using propane-fired radiant panels, rather than a standard fire-testing furnace, to apply severe heating to the surface of the test specimens.

Fourteen reinforced concrete beams were tested in total, either to failure at ambient temperature or under sustained load while being exposed to severe (but non-standard) heating over their midspan regions. Three different strengthening systems were used—including a unidirectional carbon fiber/epoxy FRP system, a basalt fire textile/cementitious TRM system, and a PBO fiber/cementitious mortar FRCM system—and post-fire residual strength tests were also performed on those beams that survived fire exposure. During fire testing, the beams were subjected to load levels between the unstrengthened ultimate strength and the ultimate strengthened strength, so as to interrogate loss of effectiveness of the respective structural strengthening systems.

Bisby et al. (2013) found that depending on the level of sustained stress in the strengthening system, the well anchored FRP, TRM, and FRCM strengthening systems were all able to withstand exposure to temperatures of at least 464 °C (i.e., they were able to remain structurally active at these temperatures). Thus, one approach to providing fire-rated structural strengthening systems could be to insulate only the anchorage zones. Clearly, additional testing is needed to better quantify the level of insulation that would be needed in such applications and to accurately define the temperature dependency of failure stress for the respective systems. Furthermore, in addition to being non-combustible and non-toxic under fire exposure, TRM and FRCM structural strengthening systems, bonded to the existing structural elements using an inorganic mortar, had the added advantage of providing additional concrete cover to the internal steel reinforcement, thus enhancing the pre-existing fire performance of reinforced concrete elements even in cases where the strengthening system was rendered structurally ineffective during fire—thus corroborating statements made by Ehlig and Hothan (2011). Bisby et al. (2013) conclude by warning that all the beams tested in their study, regardless of the strengthening system used, would be likely to fail within a few minutes of heating if the anchorage zones had been directly exposed to heating, and that their findings hold only in cases where cool anchorage regions can be assured.

Michels et al. (2014) report the results of a single furnace test performed on a reinforced concrete one-way spanning slab strengthened with a shotcrete layer including a carbon and glass fiber composite mesh (carbon in the warp and glass in the weft) as tensile reinforcement. The slab was tested under a constant service load and exposed to a standard fire (ISO, 1999) for 2 h, albeit only over its midspan region such that the textile's anchorage zones remained cool. This single fire test again demonstrated that a TRM-strengthened slab was able to carry a "significant" static load for 2 h of standard fire exposure without collapsing; however, future investigations are needed to study possible bond degradation between the composite mesh and the surrounding shotcrete at high temperature.

Despite the research discussed above, readers are cautioned to be wary of the use of externally bonded strengthening systems as primary reinforcement in structures, since in such cases, failure of the strengthening system could lead to collapse of the structural element under service loads. In any case, good practice in structural engineering and typical strengthening limits suggested in design codes for externally bonded FRP strengthening systems (for instance ACI 440.2 R-08 [ACI, 2008]), are equally applicable to TRM and FRCM systems and are not so restrictive as to prevent strength enhancements at levels that are likely in real projects.

7.8   Summary, knowledge gaps and research recommendations

It is clear from the information in this chapter that TRM and FRCM materials and strengthening systems offer significant potential advantages with regard to their performance in fire. In addition to being largely non-combustible and non-toxic, under

certain conditions—particularly when cold anchorage can be assured and when carbon-fiber textiles are used—TRM and FRCM materials and systems may offer superior high-temperature mechanical performance and compared with conventional FRP strengthening systems; however, considerable additional research is needed before the potential structural advantages of TRM and FRCM systems in fire can be used to advantage on real projects. Potential areas for future research attention include:

- development and characterization of fire-resistant geopolymer matrix TRM materials and systems;
- testing to elucidate mechanisms and means of mitigating heat-induced and mechanically induced splitting and spalling of TRM matrix materials at elevated temperatures and in fires;
- confident determination of anchorage lengths and bond properties for various types of fibers and textile geometries/weights at various elevated temperatures;
- developing a more complete understanding of the adhesion between TRMs and FRCMs and concrete or masonry substrates at elevated temperatures and in fire and the factors influencing this;
- determination of thermal and mechanical properties of inorganic mortars and fine-grained concretes used in TRM and FRM applications under exposure to a range of elevated temperatures, and when loaded in compression, tension and shear; and
- characterization of the post-heating residual mechanical response of TRM and FRCM materials and systems after exposure to elevated temperatures or fires.

References

ACI, 2008. 440.2R-08 Guide for the Design and Construction of Externally Bonded FRP Systems for Strengthening Concrete Structures. American Concrete Institute, USA.

Antons, U., Raupach, M., Kulas, C., Hegger, J., 2012. High temperature tests on concrete specimens reinforced with alkali-resistant glass rovings under bending loads. In: International Conference on FRP Composites in Civil Engineering, Rome, Italy.

ASTM, 2010. ASTME119-10b: Standard Test Methods for Fire Tests of Building Construction and Materials. American Society for Testing and Materials, New York.

Bakis, C.E., 1993. FRP reinforcement: materials and manufacturing. In: Nanni, A. (Ed.), Fibre-Reinforced-Plastic (FRP) Reinforcements for Concrete Structures: Properties and Applications. Elsevier Science Publishers B.V., Amsterdam, pp. 13–58.

Bisby, L.A., 2003. Fire behaviour of FRP-reinforced concrete (Ph.D. Thesis). Civil Engineering, Queen's University, Kingston, Canada.

Bisby, L.A., Stratford, T.J., 2013. Design for fire of concrete elements strengthened or reinforced with fibre-reinforced polymer: state of the art and opportunities from performance-based approaches. Can. J. Civ. Eng. 40, 1–10.

Bisby, L.A., Green, M.F., Kodur, V.K.R., 2005a. Fire endurance of fiber-reinforced polymer-confined concrete columns. ACI Struct. J. 102 (6), 883–891.

Bisby, L.A., Green, M.F., Kodur, V.K.R., 2005b. Modeling the behavior of fiber reinforced polymer-confined concrete columns exposed to fire. J. Compos. Constr. 9 (1), 15–24.

Bisby, L.A., Burke, P.J., Green, M.F., 2008. Comparative performance of externally-bonded and near surface mounted FRP strengthening systems at high temperatures. In: 5th International Conference on Advanced Composite Materials in Bridges and Structures (ACMBS-V), Winnipeg, Canada.

Bisby, L.A., Stratford, T.J., Hart, C., Farren, S., 2013. Fire performance of well-anchored TRM, FRCM and FRP flexural strengthening systems. Advanced Composites in Construction 2013. Network Group for Composites in Construction, Belfast, UK.

Bournas, D.A., Lontou, P.V., Papanicolaou, C.G., Triantafillou, T., 2007. Textile-reinforced mortar versus fiber-reinforced polymer confinement in reinforced concrete columns. ACI Struct. J. 104 (6), 740–748.

Brameshuber, W., 2006. State-of-the-Art Report of RILEM TC 201-TRC: Textile Reinforced Concrete. RILEM Publications S.A.R.L., Bagneaux, France.

Buchanan, A.H., 2001. Fire Resistance Design of Structures. Wiley, USA.

Büttner, T., Orlowsky, J., Raupach, M., 2007. Fire resistance tests of textile reinforced concrete under static loading—results and future developments. In: Fifth International Workshop on High Performance Fiber Reinforced Cement Composites (HPFRCC 5), Mainz, Germany.

CEN, 2004. BS EN 1992-1-2: 2004: Eurocode 2: Design of Concrete Structures—Part 1–2: General Rules—Structural Fire Design. European Committee for Standardization, Brussels.

Chowdhury, E.U., Bisby, L.A., Green, M.F., Benichou, N., Kodur, V.K.R., 2011. Heat Transfer and structural response modelling of FRP confined rectangular concrete columns in fire. Constr. Build. Mater. 25 (12), 1–28.

Colombo, I., Colombo, M., Magri, A., Zani, G., di Prisco, M., 2011. Textile reinforced mortar at high temperatures. Appl. Mech. Mater. 82, 202–207.

Concrete Society, 2012. Technical Report 55: Design Guidance for Strengthening Concrete Structures Using Fibre Composite Materials, 3/e. The Concrete Society, Camberley, UK.

Ehlig, D., Hothan, S., 2011. Reinforced concrete slabs strengthened with textile reinforced concrete subjected to fire. In: Second International RILEM Workshop on Concrete Spalling due to Fire Exposure, Delft, The Netherlands.

Ehlig, D., Jesse, F., Curbach, M., 2009. Textile reinforced concrete (TRC) under fire loading. In: 9th International Symposium on Ferrocement and Thin Reinforced Cement Composites (Ferro-9), Bali, Indonesia.

Ehlig, D., Jesse, F., Curbach, M., 2010. High temperature tests on textile reinforced concrete (TRC) strain specimens. In: International RILEM Conference on Material Science—MATSCI, Aachen, Germany.

Fallis, G.J., 2009. Innovation for renovation: cementitious matrix is used to bond high-strength polymeric mesh to concrete and masonry. Concr. Int. 31 (4), 62–64.

ISO, 1996. ISO 4589-3:1996 Plastics—Determination of Burning Behaviour by Oxygen Index—Part 3: Elevated-Temperature Test. International Standards Organization, Geneva, Switzerland.

ISO, 1999. ISO 834-1:1999: Fire-Resistance Tests—Elements of Building Construction—Part 1: General Requirements. International Standards Organization, Geneva, Switzerland.

ISO, 2002a. ISO 5660-1:2002 Reaction-to-Fire Tests—Heat Release, Smoke Production and Mass Loss Rate—Part 1: Heat Release Rate (Cone Calorimeter Method). International Standards Organization, Geneva, Switzerland.

ISO, 2002b. ISO 5660-2:2002 Reaction-to-Fire Tests—Heat Release, Smoke Production and Mass Loss Rate—Part 2: Smoke Production Rate (Dynamic Measurement). International Standards Organization, Geneva, Switzerland.

ISO, 2002c. BS EN 13823:2002 Reaction to Fire Tests for Building Products. Building Products Excluding Floorings Exposed to the Thermal Attack by a Single Burning Item. International Standards Organization, Geneva, Switzerland.

ISO, 2006a. ISO 5658-2:2006 Reaction to Fire Tests—Spread of Flame—Part 2: Lateral Spread on Building and Transport Products in Vertical Configuration. International Standards Organization, Geneva, Switzerland.

ISO, 2006b. ISO 5659-2:2006 Plastics—Smoke Generation—Part 2: Determination of Optical Density by a Single-Chamber Test. International Standards Organization, Geneva, Switzerland.

ISO, 2010a. ISO 11925-2:2010 Reaction to Fire Tests—Ignitability of Products Subjected to Direct Impingement of Flame—Part 2: Single-Flame Source Test. International Standards Organization, Geneva, Switzerland.

ISO, 2010b. ISO 1182:2010 Reaction to Fire Tests for Products—Non-combustibility Test. International Standards Organization, Geneva, Switzerland.

ISO, 2015. ISO/CD 4589-2 Plastics—Determination of Burning Behaviour by Oxygen Index—Part 2: Ambient-Temperature Test. International Standards Organization, Geneva, Switzerland.

Istituto Giordano, 2008. Classification Report No. 237540: Classification of Reaction to Fire of Construction Products in Accordance with UNI EN 13501-1:2007. Istituto Giordano, Bellarina, Italy.

Kodur, V.K.R., Bisby, L.A., Green, M.F., 2006. FRP retrofitted concrete under fire conditions. Concr. Int. 28 (12), 37–44.

Krüger, M., Reinhardt, H.W., 2006. Composite materials—6.4. Fire resistance. Textile Reinforced Concrete—State-of-the-Art Report of RILEM TC 201-TRC. RILEM Publications S.A.R.L., Bagneaux, France.

Kulas, C., Hegger, J., Raupach, M., Antons, U., 2011. High-temperature behavior of textile reinforced concrete. In: International RILEM Conference on Advances in Construction Materials Through Science and Engineering. Hong Kong, China.

Kurtz, S., Balaguru, P., 2001. Comparison of inorganic and organic matrices for strengthening of RC beams with carbon sheets. J. Struct. Eng. 127 (1), 35–42.

Liu, X., Yu, W., 2006. Degradation of PBO fiber by heat and light. Res. J. Text. Appar. 10 (1), 26–32.

Maluk, C., 2014. Development and application of a novel test method for studying the fire behavior of CFRP prestressed concrete structural elements (Ph.D. Thesis). School of Engineering, The University of Edinburgh, Edinburgh, UK.

Michels, J., Zwicky, D., Scherer, J., Harmanci, Y.E., Motavalli, M., 2014. Structural strengthening of concrete with fiber reinforced cementitious matrix (FRCM) at ambient and elevated temperature—recent investigations in Switzerland. Adv. Struct. Eng. 17 (12), 1785–1799.

Reinhardt, H.W., Krüger, M., Raupach, M., Orlowsky, J., 2008. Behavior of Textile-Reinforced Concrete in Fire. American Concrete Institute, USA. ACI Special Publication 250.

Schneider, U., 1982. Behaviour of concrete at high temperature. Deutscher Ausschuss für Stahlbeton, Heft 337. Ernst & Sohn Verlag, Berlin, Germany.

Sen, R., Mariscal, D., Shahawy, M., 1993. Durability of fiberglass prestensioned beams. ACI Struct. J. 90 (5), 525–533.

Tanano, H., Masuda, Y., Tomosawa, F., 1999. Characteristics and performance evaluation methods of continuous fibre bars—state of the art studies on fire properties and durability of continuous fibre reinforced concrete in Japan. Fibre Reinforced Polymer Reinforcement for Reinforced Concrete Structures. American Concrete Institute, USA.

Triantafillou, T.C., Papanicolaou, C.G., 2006. Shear strengthening of reinforced concrete members with textile reinforced mortar (TRM) jackets. Mater. Struct. 39 (1), 93–103.

Williams, B.K., Kodur, V.K.R., Green, M.F., Bisby, L.A., 2008. Fire endurance of FRP strengthened concrete T-beams. ACI Struct. J. 105 (1), 60–67.

This page intentionally left blank

Part Three

Textile reinforced concrete: Structural behaviour, design and case studies

This page intentionally left blank

Textile-reinforced concrete: Design models

8

J. Hegger, N. Will
RWTH Aachen University, Aachen, Germany

8.1 Introduction

Textile-reinforced concrete (TRC) has a high potential for construction of light-weight, load-bearing structures. Due to its noncorrosive textile reinforcement, made of alkali-resistant (AR) glass or carbon fibers, a minimum concrete cover is necessary. The possible application field of TRC ranges from façade panels (Hegger et al., 2011a; Rempel et al., 2015a), sandwich elements (Shams et al., 2014a,b), slender pedestrian bridges (Hegger et al., 2011b) to thin-walled shell structures (Scholzen et al., 2015a,b) (Figure 8.1). Depending on the demands of the specific application, in other words, the manufacturing method and the geometric boundary conditions, the material characteristics of the composite vary on a broad scale depending on the applied textile fabrics and fine-grained concrete mixture. The present chapter gives an overview of the major dependencies between material properties, fields of applications and available dimensioning approaches based on the previous work of the authors (Hegger et al., 2015; Rempel et al., 2015b; Scholzen et al., 2015c).

The textile reinforcement, especially the type of impregnation, has a major influence on the material characteristics of the composite and affects the choice of an applicable dimensioning approach for the ultimate limit state (ULS). In Section 8.2, available types of textile reinforcement are classified based on their material behavior. In Section 8.3, approaches to dimensioning of TRC structures are discussed, starting with simply supported beam and slab elements. Subsequently, a more general dimensioning approach applicable for freeform shell structures accounting for complex geometries, loading scenarios, and interaction between normal forces and bending moments is introduced. The described dimensioning procedures are exemplified for two realized application examples, including TRC façade panels as well as a double-curved shell structure.

8.2 Factors to consider in the dimensioning methods

The available types of textiles exhibit a wide range of mechanical properties depending on their fiber material, roving size, and binding type. The range of properties is even broader for epoxy- or polymer-impregnated yarns. As a consequence, specific mechanical behavior of TRC structures reinforced with impregnated and nonimpregnated fabrics calls for different approaches to dimensioning and ULS assessment. Besides the mechanical characteristics, also technological properties of

(a)   (b)

(c)
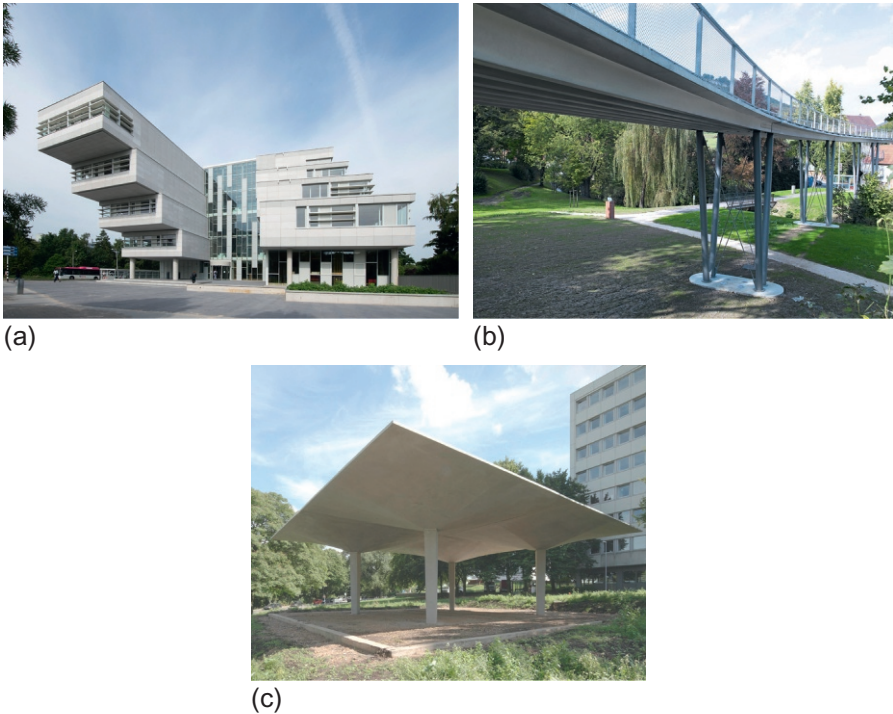
Figure 8.1 Application examples of lightweight TRC structures: (a) ventilated façade panels (photo: Ben Vulkers, *LIAG Architecten*); (b) pedestrian bridge (picture: *solidian*); and (c) hypar shell structure.

a particular type of fabrics (e.g., form stability) need to be considered in view of the feasibility of the manufacturing process (e.g., casting, spraying, and lamination). This section provides a brief summary of the main aspects relevant for the design and construction of TRC structures.

8.2.1   Characterization of the textile reinforcement

The mechanical behavior of TRC is primarily affected by the characteristics of the textile fabrics, in particular by the fiber material, cross-sectional area of the rovings (quantified by the unite "tex" describing the weight of the yarn in grams per kilometer length, i.e., (tex = g/km)), binding type of the warp-knitted fabrics (e.g., tricot, plain stitch bond) and, eventually, by the type of the applied impregnation material (e.g., epoxy-resin or styrene-butadiene). Impregnation of the fabrics leads to a homogenization of the stress profile within the multifilament yarn cross-section, resulting in a better activation of the inner filaments compared to nonimpregnated yarns and, thus, leads to a higher strength and reduction of the necessary anchorage length. Furthermore, yarn impregnation can be used to achieve form stability required for structural components using casting as production technique. At the same time, an impregnation of the textile fabrics reduces

**Table 8.1** **Characteristics of the textile fabrics depending on different impregnation types**

	Fabrics impregnated with epoxy-resin	Fabrics impregnated with styrene-butadiene	Nonimpregnated fabrics
Efficiency	High *Fineness-independent*	Medium *Fineness-dependent*	Medium/low *Fineness-dependent*
Anchorage length	Short *Fineness-independent*	Medium *Fineness-dependent*	Medium/long *Fineness-dependent*
Form stability	High *Applicable for preformed reinforcement elements*	Medium *Applicable for preformed reinforcement elements*	Low *Not applicable for preformed reinforcement elements*
Possible geometries	Straight, planar *Beams, slabs*	Curved, spatial *Shells*	

form flexibility needed for curved geometries. The material characteristics of different types of textile reinforcement are qualitatively summarized in Table 8.1.

8.2.1.1   Strength characteristics

In order to provide a qualitative orientation within the design space of TRC structures, let us compare the achievable strength of different fabric types with respect to fineness, binding type, and impregnation treatment. For example, for 3300 tex carbon yarns with an impregnation of epoxy-resin (Figure 8.2a), the maximum textile stress reached in composite tensile tests evaluates up to 3000 MPa (Rempel et al., 2015b). This stress level corresponds to the material strength of carbon fibers, reflecting an almost complete material activation of the yarn, including the inner filaments without direct contact to the concrete matrix. In comparison, a 3300 tex carbon yarns with impregnation of styrene-butadiene rubber (SBR) (Figure 8.2b) reaches lower textile stresses in composite of approximately 2000 MPa (Lorenz et al., 2015). The lower yarn efficiency for the SBR impregnation is due to lower bond properties, leading to a reduced activation of the inner filaments resulting in a longer anchorage length within the composite and a partial pullout of the inner filaments.

For nonimpregnated carbon fabrics, a still acceptable strength value of up to 1500 MPa can be achieved only with small yarn fineness and flat and open yarn cross-sections, as is the case for, e.g., 800 tex carbon yarns and warp-knitted fabrics with plain-stitch bond (Figure 8.2c). Larger cross-sections, especially with other binding types, lead to a significant decrease of the achievable textile stresses in the composite due to the insufficient activation of the inner filaments without direct contact to the surrounding concrete.
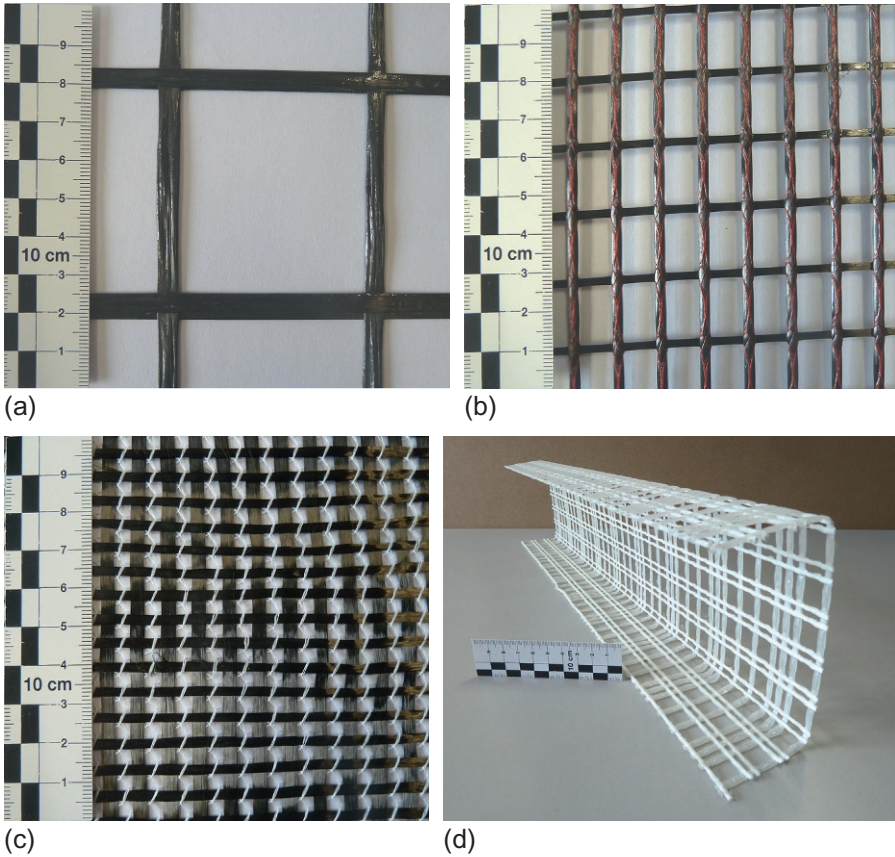
Figure 8.2 Examples of textile reinforcements: (a) planar carbon fabric impregnated with epoxy-resin; (b) carbon fabric impregnated with styrene-butadiene; (c) nonimpregnated carbon fabric; and (d) profiled reinforcement (AR-glass fabrics impregnated with epoxy-resin).

8.2.1.2 Form flexibility

Besides the strength of the fabrics, the type of impregnation also significantly affects their form flexibility. For applications in straight, rectangular structural components such as façade panels (Figure 8.1a) manufactured by casting of fresh concrete into the mold, a high-form stability of the fabrics is desired as it facilitates the production process, for example, the placing of the textile grids and control of its position in the formwork. An impregnation with epoxy-resin also makes it possible to produce form-stable reinforcement elements (Figure 8.2d) as has been done, for example, for the web reinforcement of the pedestrian bridge shown in Figure 8.1b; however, TRC structures with curved geometries such as the hypar-shell structure shown in Figure 8.1c require high form flexibility in order to follow the complex

double-curved shell geometry. In this case, the application of stiff epoxy-resin-impregnated textile fabrics is no longer feasible. For the depicted hypar-shell in Figure 8.1c, therefore, nonimpregnated fabrics were used in combination with the manufacturing technique of shotcrete and layer-wise laminating of the flexible fabrics. Another approach for the construction of curved TRC shell structure is described in Ehlig et al. (2012), where the precast shell elements were reinforced with SBR-impregnated fabrics. As fabrics with an SBR-impregnation retain certain form flexibility, curved geometries are possible, but require a closed formwork in combination with suitable spacers.

The mentioned application examples demonstrate the diversity of the design space available for existing versions of TRC. This fact can be seen as a challenge and chance at the same time. The material properties of the applied textile fabrics and fine-grained concrete need to be tailored for the specific field of application and applied manufacturing technique. Table 8.1 summarizes the main material characteristics of textile fabrics used in applications realized so far.

8.2.2 Evaluation of the cross-sectional strength characteristics

The availability of cross-sectional strength characteristics of frequently used fabric types in combination with frequently used cross-sectional shapes and reinforcement layouts is the key requirement for a wide application of TRC in engineering practice. As indicated in Section 8.2.1, a systematic approach to evaluation of strength characteristics has to consider the phenomenological differences in the material behavior of different reinforcement types. While impregnated yarns exhibit only a low effect of matrix cracking on the fabric strength, nonimpregnated yarns show a strong interaction of the cracking process and the effective fabric strength achievable in the composite (Rypl et al., 2013; Li et al., 2015).

As a result, for impregnated yarns, the ultimate tensile and bending strength can be derived from the material behavior of the composite components (i.e., the stress–strain curves of the yarn and fine-grained concrete) (Rempel et al., 2015b) using the equilibrium condition of normal forces and bending moments at the critical cross-section. If further validation tests are provided for particular material combinations, dimensioning tools such as ω-tables (with $\omega =$ mechanical reinforcement ratio) in analogy to steel-reinforced concrete can be envisioned in the future.

For nonimpregnated textile fabrics, the prediction of the cross-sectional strength based on the composite components using the equilibrium conditions is no longer possible. The reason for that is the interaction of the bond behavior with the matrix cracking leading to different yarn strength for different reinforcement ratios and/or cross-sectional layouts (Rypl et al., 2013; Li et al., 2015). As a consequence, the cross-sectional strength characteristics for TRC structures reinforced with nonimpregnated fabrics must be determined experimentally on specimens with the same cross-sectional layout as applied in the structural design at hand. Approaches to the experimental evaluation of the composite tensile and bending strength needed for

Table 8.2 Evaluation of the cross-sectional strength characteristics for different impregnation types of the textile fabrics

	Fabrics impregnated with epoxy-resin	Fabrics impregnated with styrene-butadiene	Nonimpregnated fabrics
Influence of matrix cracking on yarn strength	Low	Moderate	High
Cross-sectional strength characteristics	Derived from the material laws of the components *Yarn (tension), concrete (compression)*	Experimentally determined composite strength for given layout *Tensile and bending tests*	
Explicit cross-sectional dimensioning	ω-Tables *Based on yarn/concrete components*	Not possible	
Cross-sectional strength envelope for ULS design	n–m interaction diagram *Based on composite strength*		

the construction of *n–m* interaction diagrams are presented in Scholzen et al. (2015b). Table 8.2 gives an overview of the different approaches to the evaluation of cross-sectional strength characteristics depending on the type of impregnation.

8.2.3   Classification of approaches to ULS assessment

As the impregnated fabrics are mostly used for straight beam or slab elements, it is possible to formulate a ULS assessment based on the concept of the *a priori* known critical cross-section (e.g., at the midspan of a simply supported beam or the middle support of a two-span beam) (Rempel et al., 2015b). A description of the cross-sectional idealization is given in Section 8.3.1.

On the other hand, for shell structures with complex loading cases, the critical cross-section cannot be identified *a priori*. Therefore, the dimensioning approach must identify the critical cross-sectional accounting for interaction of normal forces and bending moments. Moreover, the anisotropy of the composite strength of a TRC cross-section due to the nonaligned direction of principal stresses and fabric orientation must be considered. Due to the higher complexity of the assessment procedure, a computer-aided ULS assessment is necessary (Scholzen et al., 2015b). The proposed dimensioning approach is exemplified for a hypar-shell depicted in Figure 8.1c in Section 8.3.2. To summarize, the discussed correspondence between the design options and the approaches to ULS assessment is given in Table 8.3.

Table 8.3 Classification of approaches to ULS assessment

	Beams	Slabs and shells
Interaction of normal force and bending moment	No *Mostly predominant bending*	Yes *Combined loading scenarios*
Critical cross section known *a priori*	Yes *Location of maximum bending moment*	No *Depends on interaction and material anisotropy*
ULS assessment	Check critical cross-section only	Check utilization ratio for entire structure

8.3 Dimensioning approach considering normal force and bending

8.3.1 Beam and slab elements with impregnated fabrics

As a high application potential of TRC is given for slender façade panels, the dimensioning of those structural components is frequently addressed in engineering practice. The thickness of TRC panels ranges between 20 and 40 mm depending on the span of the panels. As has been discussed in Section 8.2.1, straight, rectangular elements such as façade panels are in most cases reinforced with impregnated textile fabrics as they exhibit higher strength and facilitate the manufacturing process. Let us review the key issues of the approach with reference to a realized façade (Hegger et al., 2011a).

8.3.1.1 Application example: Large-sized façade panels

Figure 8.3a shows a façade with large-sized TRC panels ($A = 14.3$ m^2) with dimensions of $b/h = 3.20$ m/4.50 m and a thickness of 30 mm. As textile reinforcement, a single layer of carbon fabric made of 3300 tex rovings impregnated with epoxy-resin has been used (Figure 8.2a). The distance between the rovings amounts to 60 mm for the 0-degree direction and 62 mm for the 90-degree direction of the fabric, that is, $s_{\text{tex},0}$ and $s_{\text{tex},0}$, respectively. The free spaces between the rovings and the high form stability of the reinforcement are well suited for the precast manufacturing; the first layer of fresh concrete is poured into the formwork. After that, the textile reinforcement is placed in its position and the second concrete layer is applied.

The façade panels are fixed to the load-bearing structure of the building at two stiffening ribs with an increased thickness of 10 cm (Figure 8.3b). Horizontal wind loads are carried by the slabs only unidirectionally between the ribs. Thus, the dimensioning can be performed using a simply supported beam with rectangular cross-section of unit width.

(a)   (b)
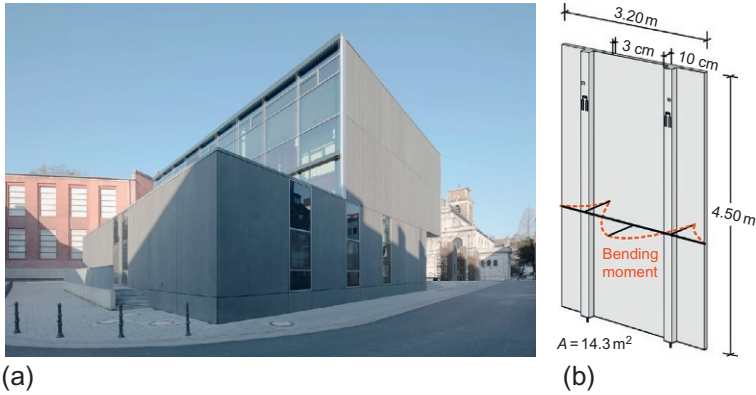
Figure 8.3 Large-sized TRC façade panels: (a) photo of the façade of the St. Leonhard school in Aachen, Germany (picture: Robert Mehl) and (b) backside of one TRC panel with supporting lines.

8.3.1.2 Prediction of the ultimate bending moment

As stated in Section 8.2.2, an explicit cross-sectional dimensioning of simple supported beam and slab elements reinforced with impregnated fabrics is possible based on the material behavior of reinforcement and concrete in analogy to conventional steel-reinforced concrete cross-sections. The cross-sectional model for TRC beam elements is schematically described in Figure 8.4 for the case of pure bending. Similar approach to assessment of retrofitted steel-reinforced structures is described in
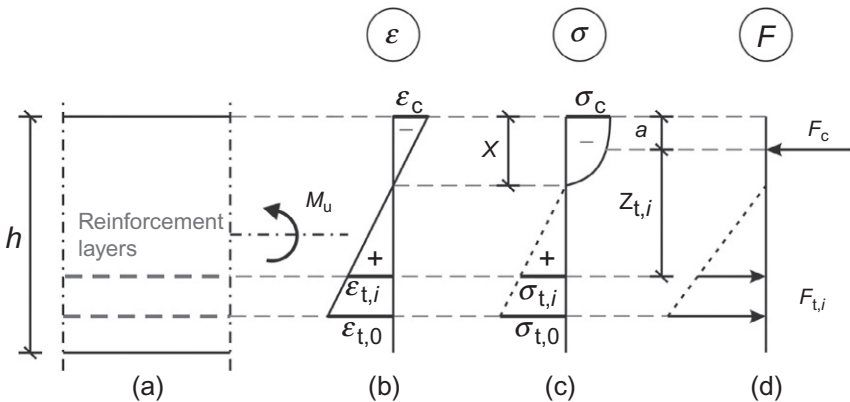
Figure 8.4 Calculation of the ultimate bending capacity of a TRC cross-section based on the material laws of concrete and yarn: (a) cross-sectional layout; (b) strain profile; (c) stress profile; and (d) internal forces.

Schladitz et al. (2012). Another related example of a cross-section-based design model including the effect of short fibers was presented in Mobasher (2011).

In order to predict the ultimate bending capacity M_u for a given cross-sectional layout, the material laws of concrete and textile reinforcement need to be *a priori* known, that is, they have to have been determined experimentally in compression tests and yarn tensile tests, respectively (Figure 8.5).

For the iterative calculation of the cross-sectional bending capacity of a given TRC cross-section (Figure 8.4a), a linear strain distribution over the cross-sectional height is assumed in analogy to Mobasher (2011). At the top of the cross-section, the strain evaluates to ε_c and for the lowest reinforcement layer to $\varepsilon_{t,0}$ (Figure 8.4b). For the calculation of the bending capacity M_u, the tensile strain $\varepsilon_{t,0}$ is limited to the rupture strain $\varepsilon_{t,u}$ as measured in the yarn tests, assuming a reinforcement failure of the composite cross-section:

$$\varepsilon_{t,0} \le \varepsilon_{t,u} \tag{8.1}$$

The value of the compressive strain ε_c at the top of the TRC cross-section needs to be determined iteratively by adaptation of the strain profile such that the equilibrium of internal normal forces is fulfilled. Therefore, as a first step in the calculation process, the stress distribution resulting from the assumed strain profile is evaluated based on the material laws for concrete and yarn determined in the material tests (Figure 8.4c). By integration of the compressive stresses σ_c over the compressive zone x, the resulting compressive force F_c is obtained (Figure 8.4d):

$$F_c = \int_0^{\varepsilon_c} \sigma_c(\varepsilon)\,d\varepsilon \tag{8.2}$$

The resulting tensile forces $F_{t,i}$ at each reinforcement layer i (Figure 8.4d) is obtained as:

$$F_{t,i} = A_{\text{tex},i} \cdot \sigma_{t,i} \cdot \varepsilon_{t,i} \tag{8.3}$$
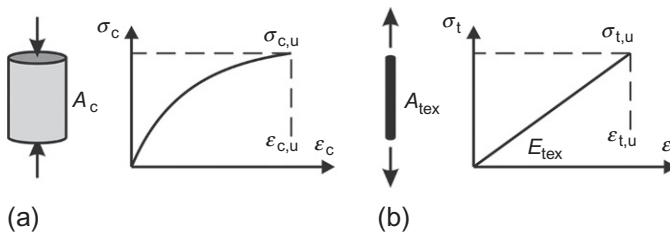
Figure 8.5 Schematic representation of the material laws of the composite components: (a) material law of the concrete for compression and (b) material law of the impregnated yarn for tension.

The compressive strain is determined iteratively requiring the equilibrium of internal normal forces:

$$F_c - \sum_i F_{t,i} = 0 \tag{8.4}$$

The ultimate bending capacity M_u can be obtained by multiplying the internal tensile forces $F_{t,i}$ with the corresponding lever arms z_i related to the compressive force F_c:

$$M_u = \sum_i F_{t,i} \cdot z_i \tag{8.5}$$

The parameter a represents the distance between the compressive force F_c and the top surface of the TRC cross-section.

8.3.1.3 *Validation of the cross-sectional model using bending tests*

In order to validate the described model specimens with different cross-sectional shapes, that is, rectangular slabs and profiled I-beams as shown in Figure 8.6, were tested in four-point bending tests (Rempel et al., 2015b). The specimens with rectangular cross-section were reinforced with one or with two layers of epoxy-resin-impregnated fabrics so that the influence of varying reinforcement ratios is also
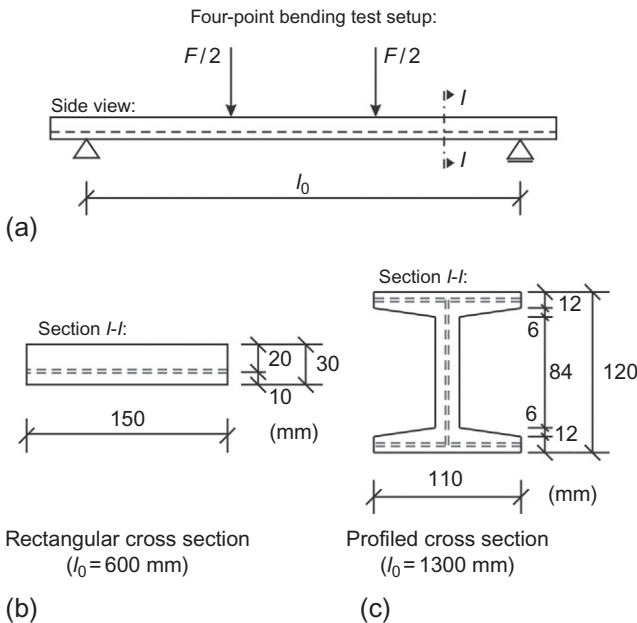
Figure 8.6 Conducted bending tests: (a) schematic test setup; (b) rectangular cross section; and (c) profiled cross-section.

included in the test series. The span of the bending test was chosen to $l_0 = 600\,\text{mm}$ for the slabs and $l_0 = 1300\,\text{mm}$ for the I-beams, respectively.

Both material components, that is, concrete and textile reinforcement, used for the investigated bending specimens corresponded to the application example of the TRC façade elements shown in Figure 8.3. The corresponding stress–strain laws for the textile fabric as well as the concrete matrix as determined experimentally in yarn tensile tests and compression tests, respectively, are shown in Figure 8.7.

The maximum grain size of the concrete was 5 mm and its compression strength evaluated to $f_{\text{cm,cyl}} = 87\,\text{MPa}$ ($f_{\text{cm,cube}} = 100\,\text{MPa}$) (Rempel et al., 2015b). The stress–strain curve measured in compression tests with cylindrical specimens ($D/h = 150\,\text{mm}/300\,\text{mm}$) is depicted in Figure 8.5 (solid line). According to DIN EN 1992-1-1 (Eurocode 2, 2011) the material law for a high-strength concrete can be approximated by Equation (9.6) (dashed line in Figure 8.7a):

$$\sigma_c(\varepsilon_c) = 87 \cdot \frac{1.3 \cdot \dfrac{\varepsilon_c}{2.4} - \left(\dfrac{\varepsilon_c}{2.4}\right)^2}{1 - 0.7 \cdot \left(\dfrac{\varepsilon_c}{2.4}\right)} \tag{8.6}$$

The tensile strength and rupture strain of the applied epoxy-resin-impregnated carbon fabric have been determined in yarn test with rovings extracted from the textile. The test results for five repetitions (gray lines) and the resulting average response (black line) are depicted in Figure 8.7.

A comparison of the calculated bending strength according to Equation (9.5) and the experimentally obtained bending capacity is shown in Figure 8.8a for the slab tests with rectangular cross-section and in Figure 8.8b for the beams with profiled cross-sectional shape, respectively. The evaluation shows a good agreement of the experimentally obtained values with the predicted values according to Equation (9.5) within a reasonable scatter of approximately 5%.
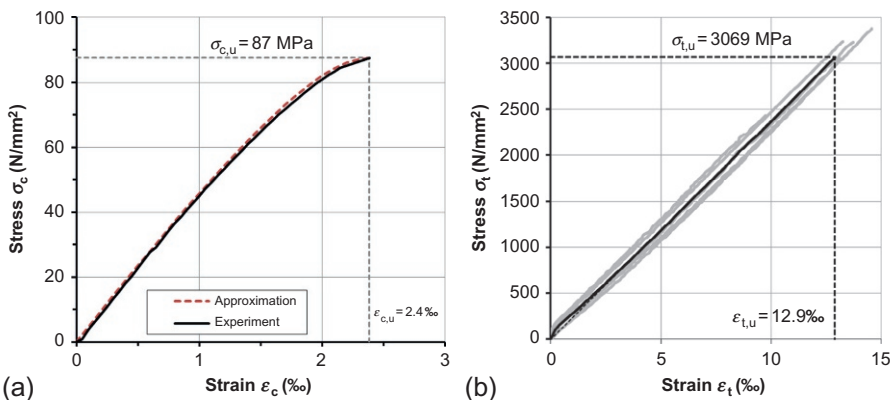
Figure 8.7 Experimentally determined material laws for: (a) concrete (compression) and (b) carbon yarn impregnated with epoxy-resin (tension).
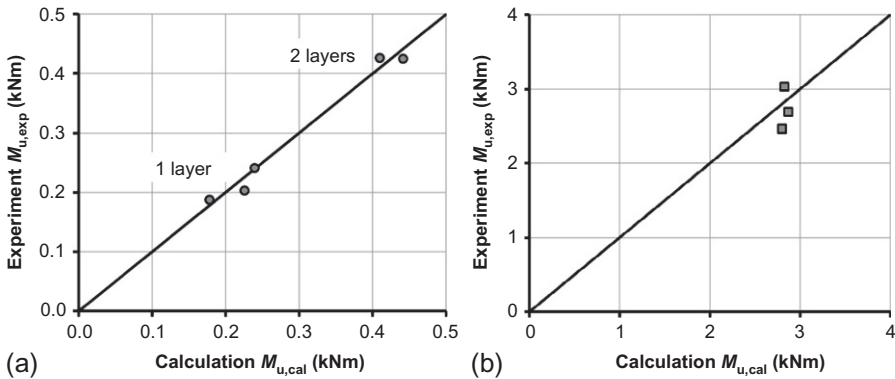
Figure 8.8 Comparison of the experimentally determined bending strength and the calculated bending capacity according to Equation (9.5): (a) for the specimens with rectangular cross-section and (b) for the specimen with profiled cross-section.

8.3.1.4 Conclusions

The experimental results document the fact that for impregnated textiles, a calculation of the bending capacity is well approximated based on the described cross-sectional model, for slab elements with varying reinforcement ratios as well as for profiled cross-sectional shapes. The input parameters for the iterative calculation of the ultimate bending moment are the material laws of the used concrete and textile fabric, which have to be determined experimentally. Based on the described cross-sectional model, standardized dimensioning tools for engineers similarly to the ones known in the steel-reinforced concrete practice (e.g., ω-tables) can be employed in the future, at least for certain combinations of material components.

8.3.2 Shells reinforced with nonimpregnated fabrics

In the case of spatial TRC structures with complex loading scenarios, two additional important effects need to be considered in the dimensioning approach:

(i) simultaneous action of normal forces and bending moments of a TRC shell cross-section;
(ii) strength reduction due to nonaligned loading with respect to the orientation of the textile fabrics.

The dimensioning procedure will be demonstrated with reference to a shell structure described in detail in Scholzen et al. (2015a).

8.3.2.1 Application example: TRC hypar-shell

As application example for thin-walled TRC shell structure led us to discuss the double-curved hypar-shell structure shown in Figure 8.1c, which has been constructed at RWTH Aachen University. The load-bearing structure is composed of four
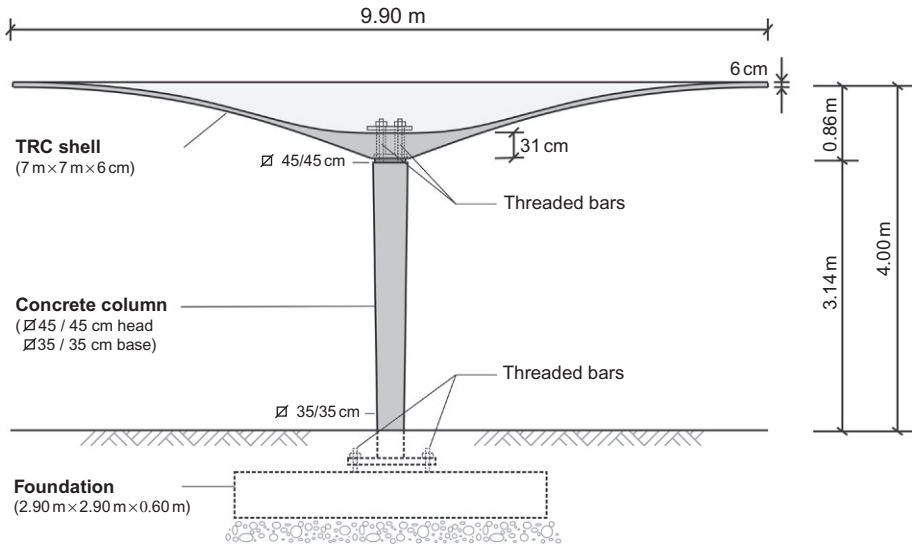
Figure 8.9 Diagonal cut of the load-bearing structure consisting of TRC shell, steel-reinforced concrete column and foundation.

large-sized TRC roof elements, each of which is supported at its center by a steel-reinforced concrete column (Figure 8.9). In projection, each shell has a base area of 7 m × 7 m and a thickness of 60 mm. At the shell center, the thickness increases to 31 cm in order to ensure a sufficient cross-sectional capacity for transferring the loads from the shell to the reinforced concrete column (Scholzen et al., 2015a). The architectural design by the Institute of Building Construction of RWTH Aachen University (Schätzke et al., 2011) uses umbrella-like shells as basic elements, each of which consists of an addition of four double-curved surfaces, known as hyperbolic paraboloids (hypar surfaces). Many variations on this type of shell structures have been constructed in the 1960s and 1970s by the Spanish architect Félix Candela (Cassinello et al., 2010); however, these structures have almost completely vanished from the awareness of the designers nowadays due to the corrosion problem of the steel reinforcement in combination with the thin-walled shell characteristics. Here, TRC offers new possibilities to realize concrete shells efficiently again today (Tysmans et al., 2009).

8.3.2.2 Utilization ratio for combined normal and bending loads

With reference to the design codes for steel-reinforced concrete structures, it can be stated that the absolute values of the composite strength characteristics provide an efficient means for ULS assessment of shell cross-sections exposed simultaneously to normal forces and bending moments. In analogy to the design codes for steel-reinforced concrete, a simplified n–m interaction diagram for TRC cross-section is proposed as depicted in Figure 8.10a using the absolute values of the experimentally
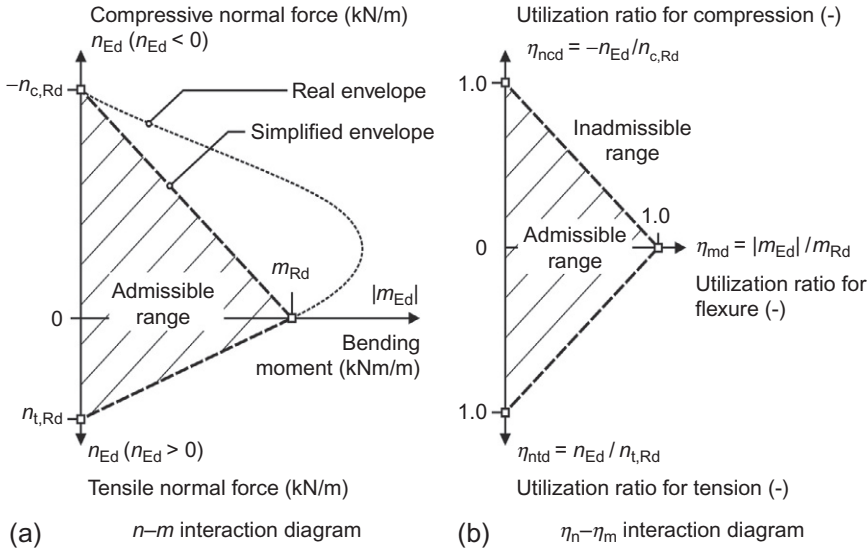
Figure 8.10 Dimensioning approach for TRC shell structures: (a) simplified n–m interaction diagram based on the composite strength characteristics and (b) interaction diagram with normalized stress resultants.

obtained composite strength for uniaxial tension $n_{t,Rd}$ (kN/m), uniaxial compression $n_{c,Rd}$ (kN/m) and pure bending m_{Rd} (kNm/m), assuming a linear interaction of the cross-sectional normal and bending strength (Scholzen et al., 2015b). For compressive normal forces, the composite strength for combined loading scenarios is underestimated and lies on the safe side. For tensile normal forces and simultaneous acting-bending moments, the real material behavior of TRC cross-sections is quite well captured as numerical studies and validation tests show.

For convenience, the linear n–m interaction diagram has been transformed into a normalized form as shown in Figure 8.10b, introducing the normalized stress resultants:

$$\eta_{ntd} = \frac{n_{Ed}}{n_{t,Rd}} \quad \eta_{ncd} = \frac{n_{Ed}}{n_{c,Rd}} \quad \eta_{md} = \frac{|m_{Ed}|}{m_{Rd}} \tag{8.7}$$

The normalized stress resultants represent the utilization ratio of the cross-section with respect to the design values of the strength characteristics for tension ($n_{t,Rd}$), compression ($n_{c,Rd}$), and bending (m_{Rd}). Considering the fact that the values of the strength characteristics are all positive, the normalized stress resultants attain their ultimate strength values for $\eta_{(.)} = 1.0$. For a combined loading of a cross-section with normal force and bending moment, the total utilization ratio η_{nmd} is defined as:

$$\eta_{nmd} = \max\left(\eta_{ntd}, \eta_{ncd}\right) + \eta_{md} \tag{8.8}$$

The ULS assessment of a TRC shell must prove that for all load case combinations, the total utilization ratio η_{nmd} lies within the admissible range in any cross-section of the shell (dashed area in Figure 8.10b):

$$\eta_{nmd} < 1.0 \tag{8.9}$$

In the described dimensioning procedure so far, we have tacitly assumed isotropic material properties with cross-sectional strength characteristics independent of the loading direction; however, a TRC shell cross-section, especially with a pronounced orthotropic reinforcement structure, exhibits anisotropic material behavior due to the misfit between the direction of the principal tensile stresses and the orientation of the fabrics. The deviation of the flexible textile reinforcement leads to an increased stress concentration in the outer filaments of the roving at the crack edges, thereby reducing the total load-bearing capacity. This can be taken into account introducing the reduction factor k_α depending on the deviation angle α (Hegger and Voss, 2008). Since the design values of the composite strength depend on the orientation of the textile fabrics, it is not possible to identify *a priori* the critical shell cross-sections relevant for the ULS assessment. While for each load-case combination, the cross-section with maximum principal tensile stresses can be determined, this cross-section does not necessarily become decisive for the dimensioning, because the largest deviation of the fabric orientation may occur at some other location of the shell. As a consequence, the design values of the stress resultants must be evaluated for all possible load-case combinations constructed in accordance with DIN EN 1990 (Eurocode 0, 2010) and for all locations of the TRC shell, taking into account the directional-dependency of the strength values.

8.3.2.3 Determination of the cross-sectional strength characteristics

In order to provide a direct comparison between the cross-sectional strength characteristics of the constructed TRC shell shown in Figure 8.9, the specimens of the conduced tensile and bending tests exhibited a thickness of $t = 60$ mm and were reinforced with 12 layers of carbon textiles equally spaced over the cross-sectional height (Scholzen et al., 2015a). As reinforcement, a nonimpregnated carbon warp-knitted fabric was selected (Figure 8.2c) that has been developed at the Institute for Textile Technology (ITA) of RWTH Aachen University. The nonimpregnated fabrics exhibit high-form flexibility necessary to follow the double-curved shell geometry of the hypar shell. The rovings of the carbon fabric had a linear density of 800 tex, and their spacing in the longitudinal direction (0-degree direction) amounted to 8.3 mm and in the transverse direction (90-degree direction) 7.7 mm. For the warp-knitted fabrics, a plain-stitch bond (Schnabel and Griess, 2011) was used, leading to an especially flat and open yarn structure. For this type of fabric, a much better penetration of the cementitious matrix into the interstitial spaces between the filaments of a yarns could be archived, leading to significantly higher bond strength as compared to the more common pillar and tricot stitch types.

The cross-sectional layout requires an appropriate production procedure allowing for a simple insertion of the thin concrete layers one by one. An obvious choice is the shotcrete technology. Hence, the fresh concrete properties of the fine concrete were optimized for shotcrete production of the shells. The concrete mixture developed by the Institute for Building Research (ibac) of RWTH Aachen University therefore has largest grain diameter of only 0.8 mm and contains short fibers of AR-glass with a diameter of 14 μm, a length of 6 mm and a volume fraction of 0.5% and was used in order to optimize the properties of the fresh concrete for the chosen manufacturing process.

While the composite-bending strength can be determined quite simply in a conventional three-point bending test, in the given case with specimen sizes $b/L/t = 20$ cm/125 cm/6 cm and a span of $l_0 = 115$ cm, the measurement of the composite tensile strength is nontrivial. As a consequence, several types of test setups have been developed with a different focus as summarized in Hartig et al. (2012). Recent test improvements for adjustable anchorage length and thick cross-sections were recently presented in Contamine et al. (2011) and Scholzen et al. (2015b,c). The standardization of tensile test is the current aim of the RILEM Technical Committee (RILEM, 2015).

The composite strength for tension and bending directly depends on the used textile reinforcement. Therefore, the strength characteristics need to be evaluated both for the 0-degree and 90-degree orientation of the textile fabrics. For the considered carbon fabric, the spacing of the rovings and therefore the resulting strength characteristics were almost identical in both directions so that only the smaller values obtained for the 0-degree direction were considered in the ULS assessment for the sake of simplicity. In the given test series, the average measured composite tensile strength amounted to $\sigma_{t,0} = 16.8$ MPa. The compressive strength of the TRC shell cross-section is mainly determined by the compressive strength of the fine-grained concrete. In the given case, the average compressive strength evaluated to $f_{cm, cube, dry} = 89$ MPa. Based on the conducted test results, the characteristic strength values (5% quantiles) were obtained using the statistical evaluation of the measured ultimate loads in accordance with EN 1990 leading to a reduction factor due to scatter. Taking into account a partial safety factor of $\gamma = 1.5$, the design values of the cross-sectional strength characteristics for tension, compression and bending evaluated to:

$$
\begin{aligned}
n_{t, Rd} &= 996 \, \text{kN/m} \\
n_{c, Rd} &= 2200 \, \text{kN/m} \\
m_{Rd} &= 8.3 \, \text{kN/m}
\end{aligned}
\tag{8.10}
$$

8.3.2.4 Computer-based ULS assessment

Based on the determined cross-sectional strength characteristics, the numerical ULS assessment of the TRC hypar-shell has been performed. Therefore, the cross-sectional utilization ratio has been calculated for all elements of the underlying finite element
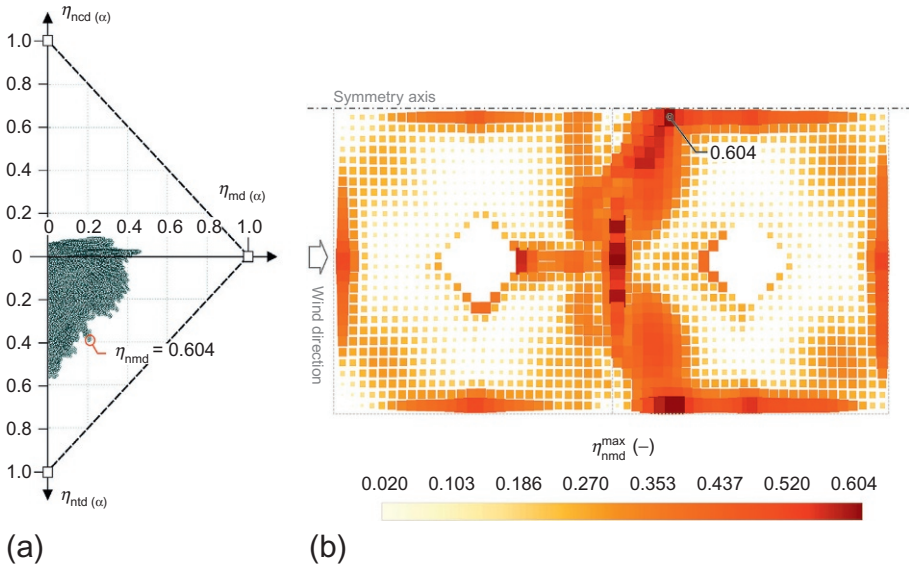
Figure 8.11 Computer-based ULS assessment of the TRC hypar-shell structure evaluating the utilization ratios of all elements of the finite element (FE) discretization and all load-case combinations: (a) normed interaction diagram and (b) spatial distribution of the maximum utilization ration for all loading cases (top view).

(FE)-analysis of the shell structure and all load case combinations according to DIN EN 1990 (Eurocode 0, 2010). The obtained results are depicted in Figure 8.11a in the normalized interaction diagram. As can be seen, all utilization ratios lie within the admissible limits given by Equation (9.9).

In order to provide a connection between the utilization ratios and its location within the shell structure, Figure 8.11b depicts the maximum utilization ratio obtained in all loading case combinations.

8.3.2.5   Conclusions

The application example demonstrates the proposed dimensioning approach for TRC shell structures accounting for interaction between normal forces and bending moments. The formulation allows for an efficient and straightforward ULS assessment of complex TRC structures. In order to take into account all load-case combinations and, at the same time, the direction of the stress resultants with respect to the orientation of the reinforcing fabrics, a computer-based assessment is necessary. A more detailed description of effects leading to material anisotropy as well as how strength reductions due to butt joints of the fabric layers can be added to the assessment procedure may be found in Scholzen et al. (2015b).

8.4 Summary

In order to provide a systematic approach to the dimensioning and assessment of TRC structures, a classification of possible cross-sectional designs is necessary. In particular, phenomenological different mechanical behavior of the composite is achieved depending on the choice of the fabrics types. At the same time, constraints on manufacturing procedures and achievable forms of components affect the choice of material. Despite the large range and complexity of the design space of TRC structures, dimensioning and assessment methods for TRC need to retain transparency and simplicity. The present chapter illuminates the elementary correspondences between the choice of material components, manufacturing procedures, possible geometrical shapes and loading conditions of TRC structural components. The different characteristics are summarized and the proposed dimensioning approaches exemplified for two selected application examples.

References

Cassinello, P., Schlaich, M., Torroja, J.A., 2010. Félix Candela. In memorian (1910–1997). From thin concrete shells to the 21st century light weight structures. Inf. Constr. 62, 5–26.

Contamine, R., Si Larbi, A., Hamelin, P., 2011. Contribution to direct tensile testing of textile reinforced concrete (TRC) composites. Mater. Sci. Eng. A 528, 8589–8598.

Ehlig, D., Schladitz, F., Frenzel, M., Curbach, M., 2012. Textile reinforced concrete—overview of realized projects (in German: Textilbeton—Ausgeführte Projekte im Überblick). Beton Stahlbetonbau 107, 777–785.

Eurocode 0, 2010. DIN EN 1990:2010-12: Basis for Structural Design. DIN (Deutsches Institut für Normung), Beuth Verlag GmbH, Berlin.

Eurocode 2, 2011. DIN EN 1992-1-1:2011-01: Design of Concrete Structures—Part 1-1: General Rules and Rules for Buildings. DIN (Deutsches Institut für Normung), Beuth Verlag GmbH, Berlin.

Hartig, J., Jesse, F., Schicktanz, K., Häußler-Combe, U., 2012. Influence of experimental setups on the apparent uniaxial tensile load-bearing capacity of textile reinforced concrete specimens. Mater. Struct. 45, 433–446.

Hegger, J., Voss, S., 2008. Investigation of the bearing behaviour and application potential of textile reinforced concrete. Eng. Struct. 30, 2050–2056.

Hegger, J., Kulas, C., Horstmann, M., 2011a. Realization of TRC façades with impregnated AR-glass textiles. Key Eng. Mater. 466, 121–130.

Hegger, J., Kulas, C., Raupach, M., Büttner, T., 2011b. Load-bearing behavior and durability of a slender textile reinforced concrete bridge (in German: Tragverhalten und Dauerhaftigkeit einer schlanken Textilbetonbrücke). Beton Stahlbetonbau 106, 72–80.

Hegger, J., Will, N., Chudoba, R., Scholzen, A., 2015. Classification of approaches to dimensioning and assessment of lightweight TRC structures. In: Brameshuber, W. (Ed.), 11th International Symposium on Ferrocement (FERRO-11) and 3rd international Conference on Textile Reinforced Concrete (ICTRC-3), Aachen, Germany, 7–10 June 2015, pp. 45–52.

Li, Y., Chudoba, R., Sadílek, V., Rypl, R., Vořechovský, M., 2015. Analysis of the tensile response of textile reinforced concrete using digital image correlation technique combined with multi-scale stochastic modelling. In: Brameshuber, W. (Ed.), 11th International

Symposium on Ferrocement (FERRO-11) and 3rd International Conference on Textile Reinforced Concrete (ICTRC-3), Aachen, Germany, 7–10 June 2015, pp. 141–148.

Lorenz, E., Schütze, E., Weiland, S., 2015. Textile reinforced concrete: properties of the composite material (in German: Textilbeton—Eigenschaften des Verbundwerkstoffs). Beton Stahlbetonbau, 29–41. Special Publication.

Mobasher, B., 2011. Development of design procedures for flexural applications of textile composite systems based on tension stiffening models. In: Curbach, M. (Ed.), 6th Colloquium on Textile Reinforced Structures (CTRS6), Berlin, Germany, 19–20 September 2011, pp. 297–313.

Rempel, S., Kulas, C., Hegger, J., 2015a. Slender façade structures made of textile-reinforced high performance concrete. In: Brameshuber, W. (Ed.), 11th International Symposium on Ferrocement (FERRO-11) and 3rd International Conference on Textile Reinforced Concrete (ICTRC-3), Aachen, Germany, 7–10 June 2015, pp. 337–345.

Rempel, S., Kulas, C., Hegger, J., 2015b. Bearing behavior of impregnated textile reinforcement. In: Brameshuber, W. (Ed.), 11th International Symposium on Ferrocement (FERRO-11) and 3rd International Conference on Textile Reinforced Concrete (ICTRC-3), Aachen, Germany, 7–10 June 2015, pp. 71–77.

RILEM TC 232-TDT (2011), 2015. Uniaxial tensile test—test method to determine the load bearing behaviour of tensile specimens made of textile reinforced concrete (draft).

Rypl, R., Chudoba, R., Scholzen, A., Vořechovský, M., 2013. Brittle matrix composites with heterogeneous reinforcement: multi-scale model of a crack bridge with rigid matrix. Compos. Sci. Technol. 89, 98–109.

Shams, A., Horstmann, M., Hegger, J., 2014a. Experimental investigations on textile-reinforced concrete (TRC) sandwich sections. Compos. Struct. 118, 643–653.

Shams, A., Horstmann, M., Hegger, J., 2014b. An analytical model for sandwich panels made of textile-reinforced concrete. Constr. Build. Mater. 64, 451–459.

Schätzke, C., Schneider, H.N., Joachim, T., Feldmann, M., Pak, D., Geßler, A., Hegger, J., Scholzen, A., 2011. Double curved shells and grid shells made of textile reinforced concrete (in German: Doppelt gekrümmte Schalen und Gitterschalen aus Textilbeton). In: Curbach, M., Ortlepp, R. (Eds.), Proceedings of the 6th Colloquium on Textile Reinforced Structures, Berlin, Germany, 19–20 September 2011, pp. 315–328.

Schladitz, F., Frenzel, M., Ehlig, D., Curbach, M., 2012. Bending load capacity of reinforced concrete slabs strengthened with textile reinforced concrete. Eng. Struct. 40, 317–326.

Schnabel, A., Griess, T., 2011. Production of non-crimp fabrics for composites. In: Lomov, S.V. (Ed.), Non-Crimp Fabric Composites: Manufacturing, Properties and Applications. In: Woodhead Publishing Series in Composites Science and Engineering, No. 35, Woodhead, Oxford.

Scholzen, A., Chudoba, R., Hegger, J., 2015a. Thin-walled shell structure made of textile reinforced concrete—Part I: structural design and construction. Struct. Concr. 16, 106–114.

Scholzen, A., Chudoba, R., Hegger, J., 2015b. Thin-walled shell structure made of textile reinforced concrete—Part II: experimental characterization, ultimate limit state assessment and numerical simulation. Struct. Concr. 16, 115–124.

Scholzen, A., Chudoba, R., Hegger, J., 2015c. Ultimate limit state assessment of TRC structures with combined normal and bending loading. In: Brameshuber, W. (Ed.), 11th International Symposium on Ferrocement (FERRO-11) and 3rd International Conference on Textile Reinforced Concrete (ICTRC-3), Aachen, Germany, 7–10 June 2015, pp. 159–166.

Tysmans, T., Adriaenssens, S., Cuypers, H., Wastiels, J., 2009. Structural analysis of small span textile reinforced concrete shells with double curvature. Compos. Sci. Technol. 69, 1790–1796.

This page intentionally left blank

Textile-reinforced concrete: Structural behavior

9

R. Chudoba, A. Scholzen
RWTH Aachen University, Aachen, Germany

9.1 Introduction

The question on structural behavior of textile-reinforced concrete (TRC) can be translated into the question, what is the effect of the local material behavior on the global response of a particular structural configuration in connection with an applied load. Due to the large number of combinations of structural topologies and geometries and loading conditions, a generally valid, simple answer to this question is not possible: however, it is possible to identify structural effects that can appear for common classes of structural geometries and loading conditions.

The starting point for the discussion of the structural behavior in any type of application is the material behavior of a general material point or, more specifically, of a cross-section, in response to elementary loading conditions, e.g., tension, compression, and shear. These types of loading induce disintegration effects in the material structure leading to nonlinear, inelastic material response. In the case of tensile loading, the dominant disintegration effects include matrix cracking and debonding of the fabrics from the matrix. The corresponding, macroscopically observed material response shown in Figure 9.1a in terms of the stress–strain curve $\sigma^{\text{sh}}(\varepsilon)$ is referred to as strain-hardening. Such type of inelastic material behavior possesses the desired property of ductility, providing large stiffness in the initial elastic stage and large deformation capacity as the stress level approaches the composite strength.

The particular shape of the strain-hardening curve $\sigma^{\text{sh}}(\varepsilon)$ can be affected by the design of the material structure. The identification of harmonizing properties of matrix and textile fabrics in combination with short-fiber reinforcement has been a subject of intensive research during the last decade (Barhum and Mechtcherine, 2012; Hinzen and Brameshuber, 2012). Besides experimental research (Contamine et al., 2011; Hartig et al., 2012; Colombo et al., 2013; Scholzen et al., 2015c), several modeling approaches aiming at targeted identification of suitable combinations of materials, fabric geometries, short-fiber volume fractions and lengths have been developed (Cuypers and Wastiels, 2006; Mobasher et al., 2006; Richter and Zastrau, 2006; Larrinaga et al., 2013; Rypl et al., 2013; Li et al., 2015). The models taking into account the material structure of the composite significantly contribute to the understanding of local damage processes and elementary failure mechanisms.

As indicated in Figure 9.1, the material design and structural design can be seen as two sides of the same coin. Both these design areas affect the resulting behavior of the

Material behavior   Structural behavior

(a)   (b)
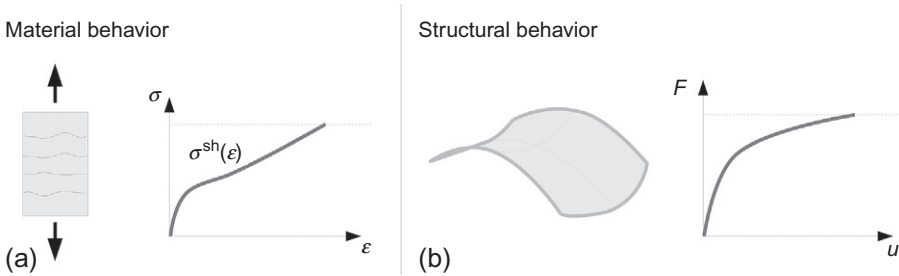
Figure 9.1 Interacting levels of design: (a) material and (b) structure.

structure in a nontrivial way. In structural design, for example, the inherent material ductility can be exploited by suitable geometry to increase the overall performance in terms of ultimate load and structural ductility visualized as force–displacement curve $F(u)$ in Figure 9.1b. Therefore, it is important to understand the interaction between both levels in order to exploit the maximum of the potential provided by the material components to be able to design highly efficient, competitive products.

This chapter attempts to shed light onto the complex interaction of the material and structural behavior, starting with an elementary analysis of the stress redistribution phenomenon in Section 9.2. In Section 9.3, a nonlinear finite element analysis is used to evaluate the structural reserves involved in the design of a large-scale TRC hyparshell. An experimental study of structural behavior is then presented and discussed in Section 9.4 for a barrel-vault shell element. All these studies are discussed in light of the assessment approach formulated in the previous chapter with the goal of providing an additional insight needed for the formulation of reliable structural design guidelines and assessment rules.

9.2 Effect of strain-hardening behavior on structural response

9.2.1 Elementary example

The key question addressed in this section is how does the locally observed strain-hardening response influence the global behavior of common types of TRC structures in response to particular loading conditions. The discussed situation is exemplified on a shell shown in Figure 9.2. The depicted tensile zone of a barrel-vault shell exhibits a nonuniform distribution of tensile strains in a direction perpendicularly to the edge. In combination with strain-hardening behavior $\sigma^{sh}(\varepsilon)$, the shown tensile zone exhibits inelastic stress redistributions that significantly influence the overall response of the structure. As will be documented later, such cases appear frequently in thin-walled shell structures. Similar strain profiles can also appear in the tensile zone of a bending element reinforced with several layers of textile fabrics. Therefore, it is worth analyzing
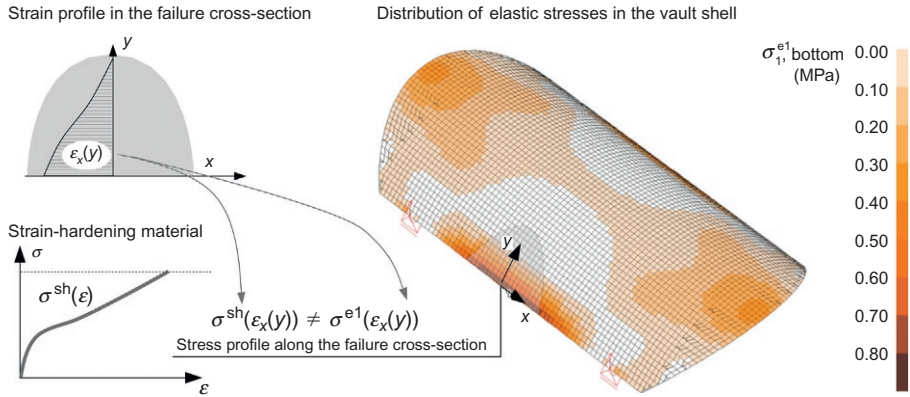
Figure 9.2 Tensile zone of a shell with smooth-strain gradient indicating the mismatch of inelastic and elastic stresses in the failure cross-section.

the elementary interaction effect between strain-hardening and nonuniform strain profiles in order to provide an insight into general principles of structural behavior of TRC structures.

In order to analyze the stress redistribution effects analytically, a simple structural configuration consisting of two discrete tensile members of different length with non-homogeneous strains is introduced in Figure 9.3b. The tensile members are fixed using rigid clamps on both sides, ensuring the same control displacement u at the ends of
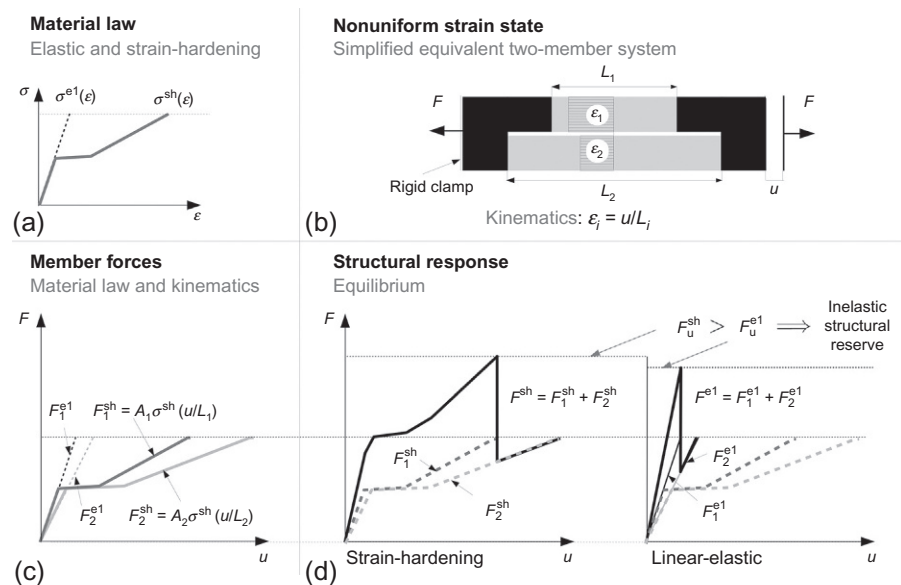
Figure 9.3 Sources of structural reserves exemplified for a two-member parallel system.

both members. This discrete structure can be regarded in analogy to the continuum tensile zone exemplified in Figure 9.2. It lends itself to simple graphical evaluation of structural response assuming elastic and inelastic behaviors shown in Figure 9.3a. The inelastic behavior is governed by the strain-hardening law $\sigma^{\mathrm{sh}}(\varepsilon)$ directly measured in the tensile test on TRC specimens (see Chapter 5). The linear-elastic material law $\sigma^{\mathrm{el}}(\varepsilon)$ is constructed by considering only the initial stiffness of the composite and measured material strength. Note that exactly this type of simplified elastic material behavior was used in the dimensioning approach described in Chapter 8.

The structural response for both considered cases of material behavior can be evaluated graphically as follows: the two tensile members with the lengths L_1, L_2 are exposed to the same control displacement u, inducing the strains $\varepsilon_1, \varepsilon_2$. Then, the force in each member is obtained by substituting the kinematic mapping $\varepsilon_i = u/L_i$ into the material law $\sigma(\varepsilon)$. Assuming equal cross-section of both members $A_1 = A_2$, this substitution induces simple scaling of the material laws in horizontal direction as depicted in Figure 9.3c both for elastic and strain-hardening cases. The overall structural response is then obtained as a sum of the member force contributions graphically shown for both types of material behavior in Figure 9.3d.

Comparison of the maximum achieved forces reveals that the ultimate force obtained for inelastic case is larger than the one obtained for elastic material law, i.e., $F_{\mathrm{u}}^{\mathrm{sh}} > F_{\mathrm{u}}^{\mathrm{el}}$. This structural effect can be seen in analogy with other ductile and quasiductile materials, e.g., steel-reinforced concrete. The process of stress redistribution can activate additional material zones or structural members during the load transmission process. The conclusion is that, similarly to other types of ductile materials, inelastic stress redistributions can significantly enhance the both the load-bearing and deformation capacities of the structure compared to purely elastic material behavior. Even though this might seem obvious, we consider it worth emphasizing, since the quasiductility is achieved using purely brittle material components by design—both at the level of composite material and, as documented here, at the level of the structural design.

The discussed structural effects can be observed both experimentally and numerically on large-scale structures. In the sequel to this chapter, we provide two case studies performed for realized TRC shell structures. In Section 9.3, numerical evaluation of structural reserves is performed using an anisotropic damage model of strain-hardening behavior. Later in Section 9.4, experimental measurement of structural reserves obtained on a large-scale shell test is compared with the elastic structural response predicted by simplified linear-elastic model used for ultimate state assessment.

9.2.2 Discussion

The idealization applied for the demonstration of the structural effect used a discrete parallel system of members, providing the possibility of simple explicit calculation of the overall response. This approach can be effectively used to analyze the limiting cases of material behavior and to gain deeper insight into the possible categories of structural response. It was used, for example, for categorization of the possible tensile
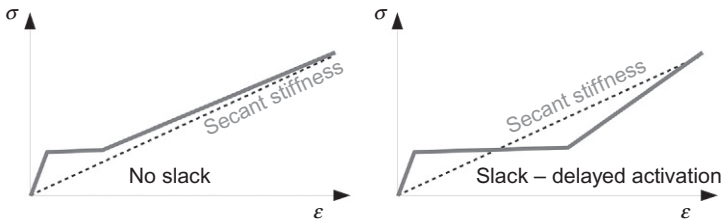
Figure 9.4 Material response of TRC in tension without and with slack due to yarn waviness and delayed activation of filaments.

response of yarn structures in Chudoba et al. (2006). As demonstrated there, further structural effects like slack can be easily studied using this approach.

In cases where the textile fabrics exhibit a high amount of slack due to waviness of reinforcement (Peled and Bentur, 2004; Steinigen et al., 2012) as qualitatively indicated on the stress–strain response shown in Figure 9.4, the positive effect on structural response described before is not provided. Indeed, the applied two-member idealization can be used to show that elastic analysis then overestimates the true level of ultimate load. Therefore, such cases should be considered with care in the formulation of the design rules, as the dimensioning based on linear-elastic model might result in an unsafe design.

The shown calculation of the ultimate failure load was performed by evaluating the maximum force achieved during the whole loading history. This type of evaluation defines the failure as a loss of global structural integrity. Such definition of ultimate failure accepts a local failure in one or more members. In the considered case of the two-member system, such a situation might be achieved by increasing the cross-sectional area of the longer member $A_2 > A_1$; however, in our opinion, this concept of ultimate failure definition is not applicable to TRC structures as it would admit designs with the rupture of fabrics. Such a scenario, however, is considered unsafe and, in most cases, beyond the serviceability limit. Therefore, the ultimate failure for TRC structures is defined as the local loss of integrity. In particular, a structure is considered unsafe once the fabric strength is achieved in some cross-section of the structure. This type of failure criterion was used in the approach to ultimate limit state (ULS) assessment described in Chapter 8. In the two-member system used here primarily for the explanation of the correspondence between the material law and structural response, the local and global failure criteria are equivalent.

9.3   Case study: Hypar-shell

9.3.1   Linear structural analysis

The ULS assessment presented in Chapter 8 "Design models" was based on stress resultants obtained using linear finite element analysis. As explained there, the choice of linear-elastic material behavior is justified by the need to consider many

load-case combinations of a real-world structure in the ULS design. Consequently, the linearity is required to preserve the possibility of superposition of multiple stress states.

The crucial issue to be addressed in this context is, how does the assumption of linearity underlying the design model correspond with the real behavior of TRC structures. On the one hand, the assessment must be safe and implicitly underestimate the real load-bearing capacity. At the same time, structural redundancy should not be unnecessarily large to avoid noneconomic use of a high-performance composite material.

Let us illuminate the tradeoff between safety and economic efficiency of the assessment procedure described previously in Chapter 8 reusing the example of the hypar-shell structure (Scholzen et al., 2015a). We study the response of a single shell exposed to vertical loading and compare the results evaluated using linear and nonlinear analysis. In particular, the chosen load-case combination consists of permanent loads, including self-weight (material density $\rho = 0.224\,\text{kN/m}^3$), additional surface loads on top of the shell (distributed load $g_k = 0.20\,\text{kN/m}^3$) and vertical line loads induced by the attached façade (line load $g_k = 0.35\,\text{kN/m}^3$).

The result of the performed linear-elastic analysis is shown in Figure 9.5. As we primarily focus on tensile failure, only the first principal tensile stresses are shown in color. Regions with dominating compressive stress remain white. The maximum stress value of 1.4 MPa obtained at the edge of the shell corresponds to the utilization ratio $\eta_{\text{nmd}} = 0.27$ evaluated using the assessment procedure described in Chapter 8 (Scholzen et al., 2015b).

Figure 9.5 shows the maximum tensile stresses develop along the shell edge and diminish toward the center of the shell. Thus, the failure cross-section can be expected
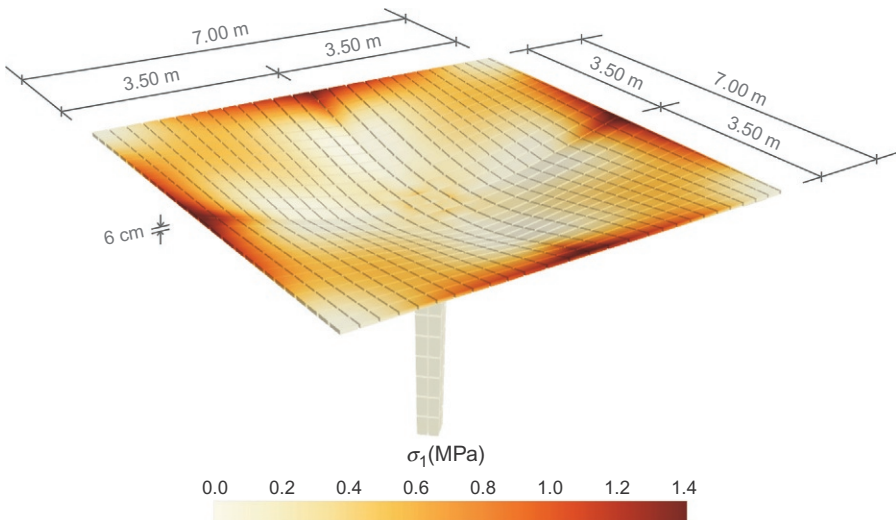
Figure 9.5 Linear-elastic stress in the hypar-shell structure.

to start at the middle of the shell edge and propagate toward the shell center. Based on the theoretical considerations given in the previous section, such failure cross-sections should exhibit the stress redistribution effect due to the strain-hardening behavior of the material. As a consequence, the real length of the failure cross-section should be larger than predicted by the linear structural analysis, so some amount of structural strength reserve should be provided.

9.3.2 Nonlinear structural analysis

In order to reflect the inelastic stress redistribution within the shell, a numerical simulation using an anisotropic damage model for TRC shell structures was performed for selected vertical load cases. The developed anisotropic material model is able to reflect damage-induced anisotropy as well as the characteristic strain-hardening behavior of TRC in the inplane direction of the shell. It belongs to the category of microplane models (Jirásek, 1999; Carol et al., 2001). The evolution of finely distributed, oriented cracks is captured in the form of direction-dependent damage variables. The model explicitly distinguishes between inplane and out-of-plane strain and stress components. Damage representing the cracking process can occur only in the inplane direction of the shell surface. This kind of damage representation was chosen in order to reflect the fact that cracks develop primarily over the whole height of the thin shell cross-section, i.e., perpendicularly to the textile fabrics. Details of the model formulation and its numerical implementation are described in detail in (Scholzen et al., 2010; Sharei et al., 2015). The formulated model represents the damage process within the shell surface phenomenologically without resolving the material structure into the individual components. This choice turns out to be advantageous in terms of computational efficiency due of the fact that TRC does not exhibit any softening, thus, no strain and damage localization. Therefore, the convergence is fast and no discretization bias is provided. An alternative approach to the macroscopic simulation of TRC structures with layer-wise resolved material components was presented in Möller et al. (2005).

The parameters of the material model were identified using tensile tests with the cross-sectional reinforcement layout equal to that of the studied shell. The calibration of the model is done by identifying the shape of the damage function (Figure 9.6a) in an incremental procedure requiring perfect fit of the numerical calculation with the experimentally determined stress–strain curve measured in the tensile tests (Figure 9.6b). For details on the calibration algorithm and model validation, the reader is referred to Scholzen et al. (2011) and Sharei et al. (2014).

The same load case as described in Section 3.1 is used in the nonlinear analysis. Its magnitude is controlled by the load factor λ. The reference load factor $\lambda_{ref} = 1.0$ corresponds to the level of design loads (i.e., self-weight with material density $\rho = 0.224 \, \text{kN/m}^3$, distributed load $g_k = 0.20 \, \text{kN/m}^2$, line load $g_k = 0.35 \, \text{kN/m}$) that induced the utilization ratio $\eta_{nmd} = 0.27$.

Figure 9.7 shows the dependency between the increasing load factor λ and the corner deflection ω obtained from the nonlinear simulation. Ultimate failure was
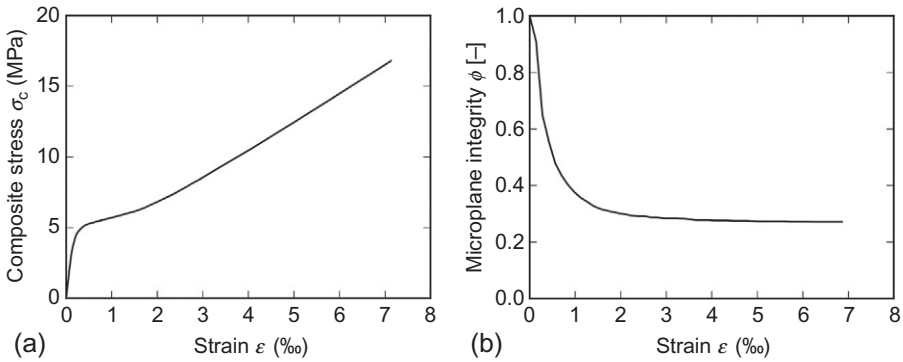
Figure 9.6 (a) Stress–strain curve obtained in tensile test and (b) corresponding calibrated damage function.
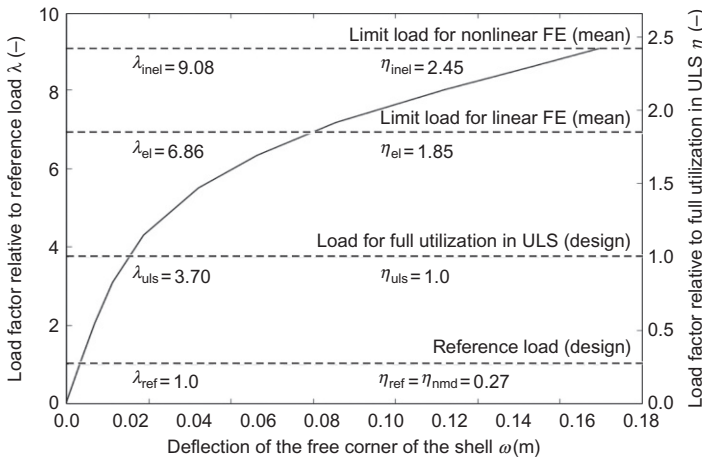
Figure 9.7 Structural reserves due to inelastic response.

triggered by the model once the first cross-section of the shell reported the fiber failure, i.e., exceeded the ultimate strain of the composite measured in the tensile tests. This was the case at the load level $\lambda_{inel} = 9.08$.

9.3.3 Comparison of elastic and inelastic response

Before comparing the linear and nonlinear calculations, we have to consider the fact that they were performed using different types of material parameters. As mentioned above, the parameters of the anisotropic damage model were identified based on the conducted tensile tests and, therefore, reflect the material behavior corresponding to the mean values of the cross-sectional strength characteristics. On the other hand,

the linear analysis was performed for design values of strength. This fact is considered in the comparison provided in Figure 9.7 indicating four values of load factor λ.

As stated in Section 3.1, the load factor $\lambda_{ref} = 1.0$ corresponds to the utilization ratio $\eta_{nmd} = 0.27$ induced by the design loads. Correspondingly, the full utilization of the critical cross-section would appear at the load level $\lambda_{uls} = 1/\eta_{nmd} = 1/0.27 = 3.7$; however, this load level corresponds to the design strength of material, considering the partial safety factor $\gamma_{tex} = 1.5$ and the coefficient $\chi = 0.81$ reflecting the scatter of the test results. In particular, given a characteristic/mean strength of the composite cross-section $\sigma_{comp,u}$, the design strength is given as $\sigma_{cd} = \chi/\gamma_{tex} \cdot \sigma_{comp,u}$. Thus, for linear behavior, the load factor corresponding to the structural failure at mean strength can be obtained directly as

$$\lambda_{el} = \gamma_{tex}/\chi \cdot \lambda_{uls} = 1.5/0.81 \cdot 3.7 = 6.85.$$

Comparing this load factor with the prediction obtained using the nonlinear model ($\lambda_{inel} = 9.08$), the structural reserves due to stress redistribution within the shell can be evaluated as $\lambda_{inel}/\lambda_{el} = 9.08/6.85 = 1.32$ for the considered load case.

Figure 9.8 depicts the spatial distribution of damage calculated using the nonlinear simulation for the discussed load levels λ_{ref}, λ_{uls}, λ_{el}, and λ_{inel} in Figure 9.7. The distribution of the maximum value of the microplane damage, i.e., $\max(\omega)$, on the top and bottom surfaces of the shell is depicted for each introduced load level. The analysis shows the propagation of damage, i.e., matrix cracking, starts in the middle of the shell edges and propagates along the ring of principal tensile stresses indicated already in the linear finite element analysis (Figure 9.5). Most importantly, the failure cross-section starting at the edge of the shell and running to its middle gets relatively long, which indicates the activation of a large zone of the shell in the transmission of tensile stresses in the failure cross-section and, thus, high amount of stress redistribution during the loading process. These redistributions, not reflected in the linear-elastic design, are the source of the load-bearing reserves identified using the nonlinear simulation.
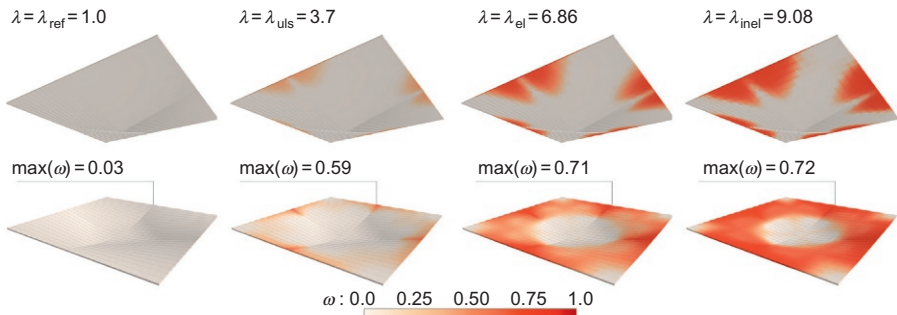
Figure 9.8 Damage evolution in the hypar-shell for load levels specified in Figure 9.7.

9.3.4   Discussion

The performed nonlinear analysis evaluates a 32% higher ultimate load as compared to the linear analysis underlying the design approach described in Chapter 8. This result is certainly only approximate. Even though the most significant damage effects are well captured in the nonlinear simulation, there are still relevant effects such as geometrical imperfections, discontinuities in the reinforcement layers due to butt joints, etc. Nevertheless, the existence of structural reserves can be documented plausibly by the numerical simulation and agrees well with the theoretical considerations made in Section 9.2. Both indicate that the real load-carrying capacity of a shell structure made of strain-hardening material is higher than the prediction assumed in the design model. In order to enforce these conclusions suggested by the numerical analyses, the next section presents an experimental case study of a full-sized TRC barrel-vault shell, allowing for a direct comparison of the experimentally observed structural behavior with the ultimate state assessment based on linear-elastic analysis.

9.4   Case study: Barrel-vault shell

9.4.1   Experimental analysis of structural behavior

The experimental study was performed in the framework of an applied research project focused on examination and verification of the developed design, manufacturing and construction methods on a real-world structure, a roof over a bicycle stand consisting of five TRC barrel-vault shells depicted in Figure 9.9. As shown in Figure 9.10, the shells with the thickness of 2 cm cover the area of $4.40 \times 2.14\,\mathrm{m}^2$. Figure 9.11 shows the step-wise cut through the composite cross-section containing six layers of carbon warp-knitted textile fabrics.
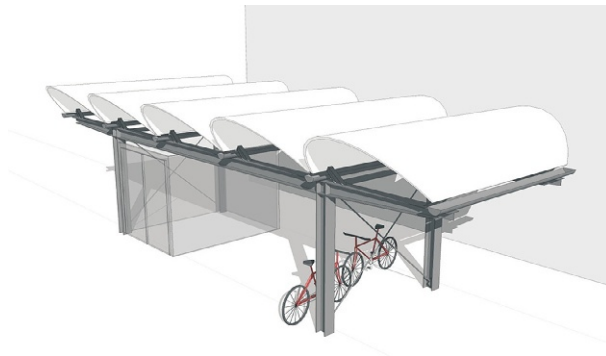
Figure 9.9 Architectural design of a bicycle stand using five TRC barrel-vault shells (animation: CARPUS & Partner, Aachen, Germany).
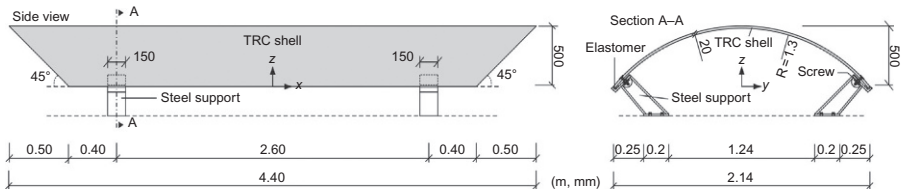
Figure 9.10 Dimensions of a single shell.
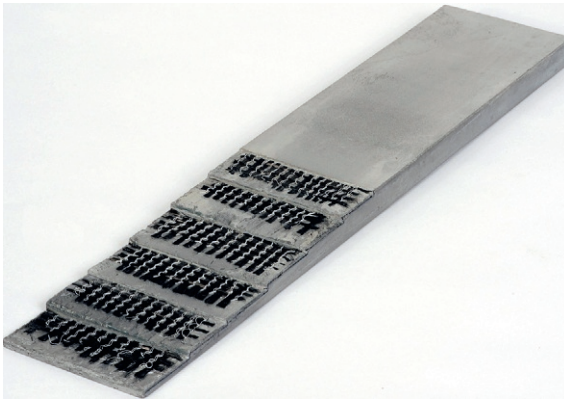
Figure 9.11 Step-wise cut through the shell cross-section.

Prior to the actual production and construction of the bicycle roof, three full-sized prototypes of the shells were produced in order to evaluate the feasibility of the manufacturing process and to validate the assumed load-bearing capacity of the shells. The test setup was designed with the goal of demonstrating the high ductility of the structure, stemming from the interplay between the strain-hardening material behavior and the stress redistribution over large zones of the shell. Therefore, it was important to avoid local failure of a cross-section. In particular, high local bending moments or local shear failure near the supports were undesirable, as they would induce early failure without sufficient amount of information about the overall structural behavior.

Keeping those considerations in mind, the test setup has been designed as follows: the TRC barrel-vault shell was supported at four points located near the corners of the shell, consistent with the actual structural design of the roof structure as depicted in Figure 9.12. In order to avoid a punctual introduction of load, a thin metal sheet strip was laid over the middle section of the shell depicted in Figure 9.13a and connected to hydraulic cylinders fixed to the ground as shown in Figure 9.13b. This kind of loading device introduces smooth stress gradients within the shell without dominating local stress peaks. In order to minimize the friction between the metal sheet strip and the shell surface, two additional greased steel sheets were laid in between. Using this load device, the tension load S introduced by the hydraulic cylinders was transparently transformed into a constant radial line load q in the middle section of the shell as indicated at the top of Figure 9.12 following the analytical formula $q = S/R$ with R denoting the vault radius.

η_{nm} (−)

0.00   0.0006   0.00113   0.00170   0.00226
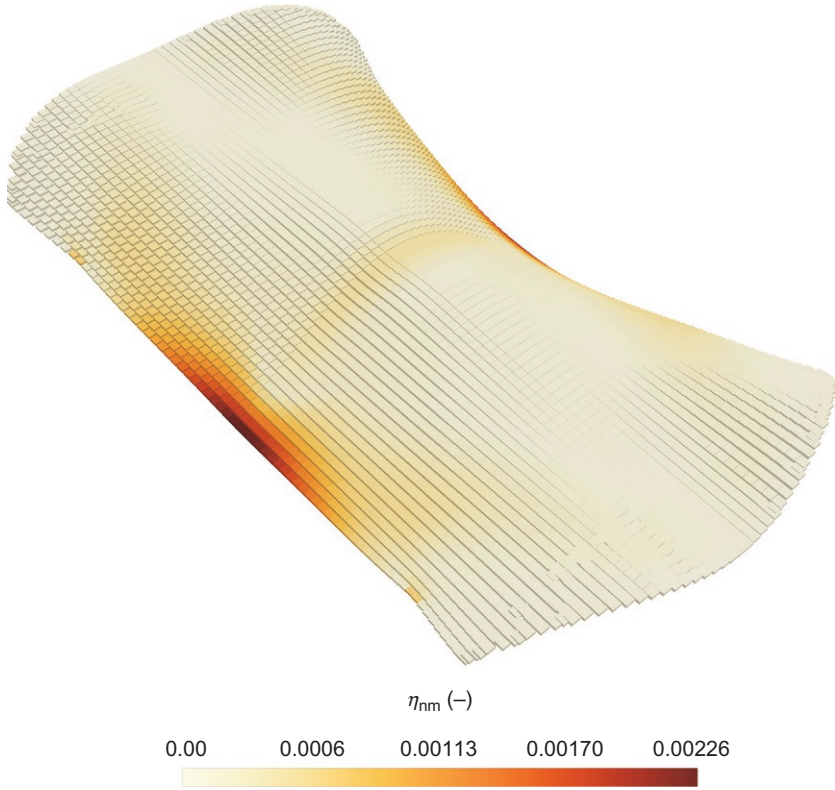
Figure 9.12 Full-sized test specimen, supports and loading equipment.

(a)   (b)
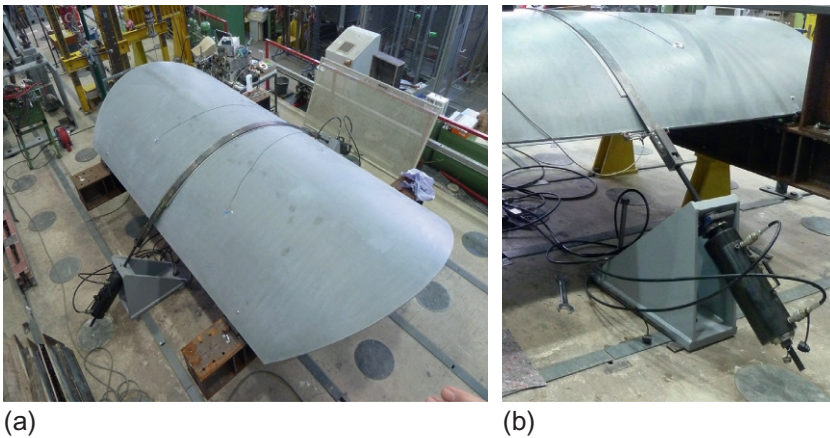
Figure 9.13 Prototype of the TRC shell tested in full-sized test (a) and detail of the load introduction via hydraulic cylinder (b).

During the test, information about the deformed shape was recorded by measuring the tensile strains in the region of the expected failure crack. As shown in Figure 9.12, the 300-mm long displacement gauges were placed along the shell edges in the middle section. Furthermore, the vertical displacements of seven points located along the top of the shell were measured. These gauges were mounted on the lower surface of the shell as shown in Figure 9.12.

9.4.2 Linear structural analysis

In order to validate the dimensioning approach introduced in Chapter 8 assuming linear material behavior, the test results are compared with the predicted ultimate load-bearing capacity using the assessment procedure. The starting point of the ULS assessment is the cross-sectional strength characteristics of the composite determined using tensile, bending and compression tests on specimens with thickness and fabric layout consistent with the cross-sectional layout of the shell (Figure 9.11). The mean values were evaluated to:

$n_{t,Rm} = 476 \, kN/m$ tensile strength corresponding to the mean composite and textile stresses, i.e., $\sigma_{comp} = 23.8 \, MPa$ and $\sigma_{tex} = 1483 \, MPa$, respectively;

$n_{c,Rm} = 1360 \, kN/m$ compressive strength corresponding to mean compressive stresses $f_{cm} = 68 \, MPa$;

$m_{Rm} = 3.3 \, kNm/m$ bending strength determined in three-point bending tests on strips with the dimensions: $b/L/t = 0.01 \, m / 0.50 \, m / 0.02 \, m$ and span of $l_0 = 0.46 \, m$.

With the described test setup and the mean strength characteristics of the material cross-section at hand, the ULS assessment was performed according to the procedure described in Chapter 8. For the considered load level $S_{ref} = 0.14 \, kN$, corresponding to the radial load $q_{ref} = 1 \, kN/m$, the distribution of the cross-sectional utilization factor was evaluated for the structure as shown in Figure 9.14. The critical cross-section at the middle of the longitudinal edge of the shell exhibited the maximum level of utilization $\eta_{nm,ref} = 0.00227$. This means that the ultimate load corresponding to full utilization $\eta_{nm,el} = 1.0$ would be attained for the load increased by the factor $1/0.00227$. Thus, the prediction of the ultimate failure of the considered structure based on the linear-elastic analysis should occur at the level of the load

$$S_{el} = S_{ref}/\eta_{nm,ref} = 0.14/0.00227 = 61.7 \, kN.$$

The real ultimate load-level measured in the test was $S_{test} = 94.4 \, kN$. Thus, the comparison between the measured ultimate load and the evaluation using the linear design model

$$S_{test}/S_{el} = 98.4 \, [kN]/61.7 \, [kN] = 1.59$$

reveals 59% of structural redundancy.
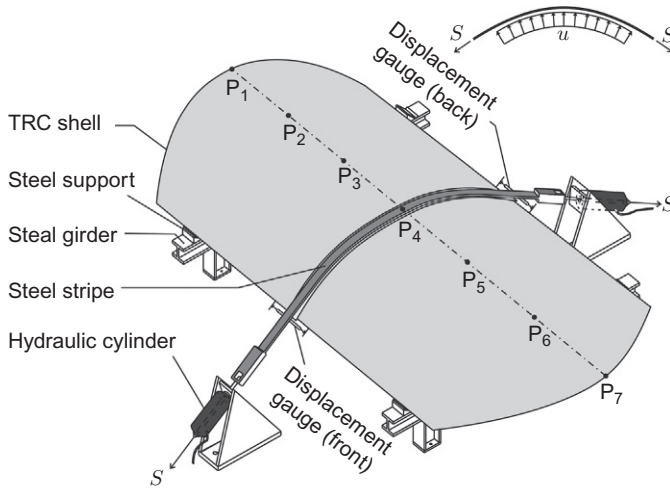
Figure 9.14 Utilization ratio of the TRC shell for the load imposed in the full-sized test based on the mean values of the strength characteristics.

9.4.3 Discussion

This structural redundancy measured in the test can again be explained by the positive effect of the interaction between the strain-hardening behavior and smooth profile of tensile strains leading to an activation of larger area of the structure during the load transmission.

This explanation is supported by the observed crack pattern depicted in Figure 9.15a at an intermediate stage of loading. The cracks covered large zones of the shell and, especially in the region where the ultimate crack localized, exhibited finely distributed cracks oriented perpendicularly to the shell edge. In contrast to this

(a)   (b)
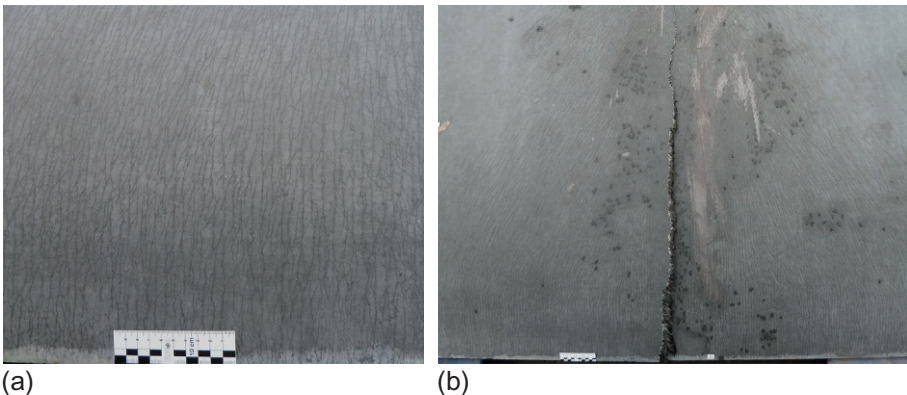
Figure 9.15 (a) Distributed fine crack pattern and (b) failure crack.

observation, the linear analysis shown in Figure 9.14 evaluates high utilization ratio only in a small short zone near the shell edge. This comparison documents the source of the measured structural redundancy with respect to the applied design model. Furthermore, it confirms the safety of the design approach. Figure 9.15b shows the ultimate crack developed at the middle section of the shell.

Besides the study of structural reserves, the full-sized test could also be indirectly used for an *in situ* verification of the cross-sectional tensile characteristics that were measured in the tensile test using small-scale strips of the composite. As mentioned above, the tensile strains were recorded during the loading process along the longitudinal edges of the barrel-vault shells in the locations where the ultimate failure crack appeared. In this region, the shell cross-section was primarily exposed to tension with almost no bending. The measured ultimate strain $\varepsilon_u = 8.5‰$ corresponded well with the value obtained in the tensile test's value of $\varepsilon_u = 7.6‰$. The slightly higher value obtained in the shell test can be explained by a smoother gradient of the tensile stress field along the shell edge as compared to the situation in the tensile test with inherently steep stress gradient in the clamped area of the specimen (Scholzen et al., 2015c).

The performed full-sized tests on the TRC barrel-vault shell prototypes provide valuable data for the verification of the dimensioning approach. The experimental data will be further exploited for the validation of the developed anisotropic strain-hardening damage model for TRC shells and further studies of structural effects like interaction of inelasticity and geometrical nonlinearity.

9.5 Further aspects of structural behavior

The discussed inelastic processes within the structure do not only affect the ultimate load. They certainly also strongly affect the deformation of TRC light-weight structures leading to larger deformations than predicted using linear-elastic analysis. Therefore, the question arises: is it always necessary to analyze the deformation of TRC structures using expensive nonlinear simulations? Such necessity would most probably have a dissuasive effect on the application of TRC in general engineering practice.

In our opinion, this is not necessarily the case for the load levels reached in the serviceability limit state, since the linear-elastic analysis predicts the real deformations relatively well. As documented in Figure 9.7, the deflection at the corner of the hypar-shell obtained using the nonlinear simulation remains almost linear in the range of service loads, and does not exhibit large deformation ratios until the high loading stages in the ULS are reached. Therefore, design models for serviceability might take the effect of inelasticity into account in a pragmatic way using a linear-elastic analysis in combination with a correction factor for the cracked state, at least for common structural configurations.

Concerning the serviceability limit state, creep effects also need to be considered for a realistic prediction of the deformations. Besides a pragmatic approach combining

linear-elastic analysis of deformations increased by a creep-coefficient for the applied fine-grained concrete matrix, advanced nonlinear modeling approaches including creep effect can also be employed to provide case studies on most common structural configurations.

Due to the slenderness of TRC shells, the effect of geometrical nonlinearity can become significant for certain geometries. Therefore, realistic predictions of the structural response need to account for both material and geometrical nonlinearity (Tysmans et al., 2009). Numerical and experimental studies of the response of a TRC dome shell charged with a uniform surface pressure were recently presented in Verwimp et al. (2015). Here, the sensitivity of the structure with respect to the imposed geometrical imperfections stemming, for example, from the manufacturing process is investigated. For shell structures exhibiting high normal forces, buckling of the thin-walled shell structure might also become decisive for the structural behavior.

Further important aspects of the structural behavior that need to be considered in the design of TRC structures are the required anchorage length (Lorenz et al., 2015), effecting the boundary zones of shell structures as well as joints between the fabrics. Here, overlapping joints or a butt joint in a multilayer cross-sectional layout (Scholzen et al., 2015a) can be distinguished. Additional phenomena such as high inplane shear stresses, longitudinal cracks inducing delamination and/or spalling, as well as complex 3D stress states arising in transition zones between smooth thin geometry and connections to other structural elements or to other reinforcement types, are to be mentioned. These aspects are still topics of ongoing research.

9.6   Conclusions

The main focus of this chapter was to study the structural redundancies due to interaction between the strain-hardening material behavior and the overall structural response. The intention was to provide additional insight into the effect of the inelastic material behavior on the stress redistribution process that is crucial for formulation and verification of design models developed for TRC structures.

The examples shown demonstrate that the degree of structural redundancy depends on the smoothness of the stress field induced by a particular load case. When, for example, a concentrated local load with highly localized stresses is considered, the effect of the inplane stress redistribution might be less pronounced or even negligible. Furthermore, no redundancy can be expected for pure uniaxial bending of the shell without any membrane stresses and, thus, no possibility for the damage to propagate to other zones of the shell. Nevertheless, the performed studies demonstrate that the linear-elastic design approach used provides a lower bound estimate of the ultimate load level. An important issue to mention is that structural reserves can be activated only for strain-hardening materials without significant slack of the textile fabrics as a delayed activation toward the redistribution effect in neighboring regions of the structure.

References

Barhum, R., Mechtcherine, V., 2012. Effect of short, dispersed glass and carbon fibres on the behaviour of textile reinforced concrete under tensile loading. Eng. Fract. Mech. 92, 56–71.

Carol, I., Jirásek, M., Bažant, Z., 2001. A thermodynamically consistent approach to microplane theory. Part I. Free energy and consistent microplane stresses. Int. J. Solids Struct. 38, 2921–2931.

Chudoba, R., Vořechovský, M., Konrad, M., 2006. Stochastic modeling of multi-filament yarns. I. Random properties within the cross-section and size effect. Int. J. Solids Struct. 43 (3-4), 413–434. ISSN 0020-7683, http://dx.doi.org/10.1016/j.ijsolstr.2005.06.063 (http://www.sciencedirect.com/science/article/pii/S0020768305004087).

Colombo, I.G., Magri, A., Zani, G., Colombo, M., di Prisco, M., 2013. Erratum to: textile reinforced concrete: experimental investigation on design parameters. Mater. Struct. 46, 1953–1971.

Contamine, R., Si Larbi, A., Hamelin, P., 2011. Contribution to direct tensile testing of textile reinforced concrete (TRC) composites. Mater. Sci. Eng. A 528, 8589–8598.

Cuypers, H., Wastiels, J., 2006. A stochastic cracking theory for the introduction of matrix multiple cracking in textile reinforced concrete under tensile loading. In: Hegger, J., Brameshuber, W., Will, N. (Eds.), 1st International Conference Textile Reinforced Concrete (ICTRC), 6–7 September 2006. RILEM Publications S.A.R.L., Aachen, Germany, pp. 192–202.

Hartig, J., Jesse, F., Schicktanz, K., Häußler-Combe, U., 2012. Influence of experimental setups on the apparent uniaxial tensile load-bearing capacity of textile reinforced concrete specimens. Mater. Struct. 45, 433–446.

Hinzen, M., Brameshuber, W., 2012. Load-bearing behaviour of textile reinforced concrete with short fibres. In: Barros, J.A.O. (Ed.), 8th RILEM International Symposium on Fiber Reinforced Concrete: Challenges and Opportunities (BEFIB 2012), 19–21 September 2012. RILEM Publications S.A.R.L., Guimaraes, Portugal, pp. 254–266.

Jirásek, M., 1999. Comments on microplane theory. In: Mechanics of Quasibrittle Materials and Structures. Hermes Science Publications, Paris, pp. 55–77.

Larrinaga, P., Chastre, C., San-Jose, J.T., Garmendia, L., 2013. Non-linear analytical model of composites based on basalt textile reinforced mortar under uniaxial tension. Compos. B 55, 518–527.

Li, Y., Chudoba, R., Sadílek, V., Rypl, R., Vořechovský, M., 2015. Analysis of the tensile response of textile reinforced concrete using digital image correlation technique combined with multi-scale stochastic modelling. In: Brameshuber, W. (Ed.), 11th International Symposium on Ferrocement (FERRO-11) and 3rd International Conference on Textile Reinforced Concrete (ICTRC-3), 7–10 June 2015. RILEM Publications S.A.R.L., Aachen, Germany, pp. 141–148.

Lorenz, E., Schütze, E., Weiland, S., 2015. Textile reinforced concrete: properties of the composite material (in German: Textilbeton—Eigenschaften des Verbundwerkstoffs). Beton-Stahlbetonbau, pp. 29–41. Special Publication.

Mobasher, B., Peled, A., Pahilajani, J., 2006. Distributed cracking and stiffness degradation in fabric-cement composites. Mater. Struct. 39, 317–331.

Möller, B., Graf, W., Hoffmann, A., Steiningen, F., 2005. Numerical simulation of RC structures with textile reinforcement. Comput. Struct. 83, 1659–1688.

Peled, A., Bentur, A., 2004. Mechanisms of fabric reinforcement of cement matrices: effect of fabric geometry and yarn properties. Beton Stahlbetonbau 99, 456–459.

Richter, M., Zastrau, B.W., 2006. On the nonlinear elastic properties of textile reinforced con-
crete under tensile loading including damage and cracking. Mater. Sci. Eng. A
422, 278–284.

Rypl, R., Chudoba, R., Scholzen, A., Vořechovský, M., 2013. Brittle matrix composites with
heterogeneous reinforcement: multi-scale model of a crack bridge with rigid matrix. Com-
pos. Sci. Technol. 89, 98–109.

Scholzen, A., Chudoba, R., Hegger, J., 2010. Damage based modeling of planar textile-
reinforced concrete structures. In: Brameshuber, W. (Ed.), Proceedings of the International
RILEM Conference on Material Science, 6–8 September 2010. RILEM Publications
S.A.R.L., Aachen, Germany, pp. 362–370.

Scholzen, A., Chudoba, R., Hegger, J., 2011. Calibration and validation of a microplane damage
model for cement-based composites applied to textile reinforced concrete. In: Barros, H.,
Faria, R., Pina, C., Ferreira, C. (Eds.), Proceedings of the International Conference on
Recent Advances in Nonlinear Models—Structural Concrete Applications, ECCOMAS
Thematic Conference, Coimbra, Portugal, 24–25 November 2011, pp. 417–427.

Scholzen, A., Chudoba, R., Hegger, J., 2015a. Thin-walled shell structure made of textile
reinforced concrete—part I: structural design and construction. Struct. Concr.
16, 106–114.

Scholzen, A., Chudoba, R., Hegger, J., 2015b. Thin-walled shell structure made of textile
reinforced concrete—part II: experimental characterization, ultimate limit state assess-
ment and numerical simulation. Struct. Concr. 16, 115–124.

Scholzen, A., Chudoba, R., Hegger, J., 2015c. Ultimate limit state assessment of TRC structures
with combined normal and bending loading. In: Brameshuber, W. (Ed.), 11th International
Symposium on Ferrocement (FERRO-11) and 3rd International Conference on Textile
Reinforced Concrete (ICTRC-3), 7–10 June 2015. RILEM Publications S.A.R.L.,
Aachen, Germany, pp. 159–166.

Sharei, E., Scholzen, A., Chudoba, R., Hegger, J., 2014. Anisotropic damage model for the
numerical simulation of textile reinforced concrete shell structures. In: Topping, B.H.V.,
Iványi, P. (Eds.),. The 12th International Conference on Computational Structures Tech-
nology, 2–5 September 2014. Civil-Comp Press, Naples, Italy. paper 9. http://dx.doi.org/
10.4203/ccp.106.9.

Sharei, E., Scholzen, A., Chudoba, R., 2015. Nonlinear analysis of TRC shells using an aniso-
tropic, damaged-based material model. In: Brameshuber, W. (Ed.), 11th International
Symposium on Ferrocement and 3rd ICTRC International Conference on Textile
Reinforced Concrete in Aachen, RILEM Proceedings PRO 98, 7–10 June 2015,
pp. 133–139.

Steinigen, F., Graf, W., Hoffmann, A., Kaliske, M., 2012. Retrofitted textile reinforced concrete
structures—structural analysis using fuzzy data (in German: Nachträglich textilverstärkte
Stahlbetontragwerke—Strukturanalyse mit unscharfen Daten). In: Curbach, M., Jesse, F.
(Eds.), 4th Colloquium on Textile Reinforced Structures (CTRS4), Dresden, Germany,
3–5 June 2009, pp. 301–312.

Tysmans, T., Adriaenssens, S., Cuypers, H., Wastiels, J., 2009. Structural analysis of small span
textile reinforced concrete shells with double curvature. Compos. Sci. Technol.
69, 1790–1796.

Verwimp, E., Tysmans, T., Mollaert, M., 2015. Experimental and numerical buckling analysis
of a thin TRC dome. Thin Walled Struct. 94, 89–97.

Applications of textile-reinforced concrete in the precast industry

10

C.G. Papanicolaou
University of Patras, Patras, Greece

10.1 Introduction

The vast majority of civil structures today use some form of prefabrication or offsite construction practice. Prefabrication offers a window to the application of new and innovative materials in combination with the development of nontraditional construction technologies for ready-made building components. With regard to the use of textile-reinforced concrete (TRC), a wide spectrum of prefabricated products exists, encompassing both architectural (nonloadbearing) and structural (loadbearing) elements. Exterior cladding panels, parapet walls and sound barriers comprise some of the most common architectural applications for TRC, whereas structural applications include (among others) posttensioned pedestrian bridge segments, loadbearing sandwich panels and stay-in-place formwork elements.

The increasing popularity of TRC-based prefabrication solutions is owed to the marked reduction of: (1) concrete consumption (by about 60–85%); (2) embodied energy of building components (entailing reduced production, transportation, erection and application costs) and (3) end-of-life waste (by about 60%). This chapter focuses on the most widespread precast applications of TRC technology, namely on exterior cladding systems and façades and on sandwich elements, while also providing brief information on various other innovative prefabricated TRC products. Future trends in TRC-based prefabrication are discussed in the last section of the chapter.

10.2 Exterior cladding systems and façades

Exterior cladding systems and façades are probably top in the TRC applications list. High-finished surface quality and aesthetics, good mechanical properties, freeform design possibilities, reduced product thicknesses (typically, in the range of 20–30 mm), enhanced durability characteristics, and low environmental impact are only a few of the advantages that TRC technology offers to the building envelopes industry.

The first thin-walled and lightweight, ventilated façade systems sprung from the extensive collaborative programs (e.g., the Collaborative Research Centre Project – CRC 532) that developed and promoted the TRC technology in Germany (Hegger et al., 2006). A ventilated façade system consists of a thin external-facing panel

separated from the primary wall structure by a naturally ventilated cavity (air gap). This cavity allows for drainage of moisture ingress from rain and condensation, which helps minimize the deterioration of the adjacent inner layers of the wall assembly (Williams Portal, 2013). Ventilated façade systems can either be used for new constructions as architectural concrete façades (or even as suspended ceilings) or for renovation of existing buildings as energy-saving façades. By changing the shape, texture and colour of the TRC panels, a multitude of architectural options may be available. Full reversibility and access to the supporting structure (if necessary) can be ensured through cladding systems that can be dismantled.

Two-dimensional (2D) textiles made of either alkali-resistant (AR) glass or carbon are predominantly used for the fabrication of TRC façades. Fibre rovings in textiles can be both in a dry condition or impregnated with an appropriate binding means (e.g., with a styrene-butadiene or epoxy resin). Resin impregnation ensures composite action of the fibre grid structure and, thus, better exploitation of fibres' mechanical characteristics; furthermore, the durability of the textile is enhanced. Matrix composition takes into account strength, durability and constructability requirements. Concrete grades with a compressive strength up to 90 N/mm^2 and a modulus of rupture up to 10 N/mm^2 are particularly suitable for the production of façade elements that are expected to remain crack-free under service conditions (Hegger et al., 2015). Maximum grain size has to be limited to 5 mm so the protrusion of the matrix through the small grid size of the reinforcement is facilitated and the workability of the finely grained concrete is improved. At the same time, the maximum grain size should be less than one-third of the minimum mesh opening so successful mesh incorporation can be achieved; otherwise, the mesh layer acts like a plane of discontinuity (a separation layer) for the concrete components (Hegger et al., 2010a).

Small-size TRC panels used as ventilated façade elements are of a surface area ranging between 0.5 and 3.0 m^2 with a thickness of 20–30 mm (Hegger et al., 2008a). Application examples of such systems include the extension of the Institute of Structural Concrete, RWTH Aachen University, Germany and the façade of the Community College in Leiden, Netherlands. For the first application, the panels (measuring 2685 mm × 325 mm × 25 mm) incorporated two near-surface layers of coated AR-glass fibre mesh (with a cover of approximately 3 mm) embedded in a self-compacting, finely grained concrete (with a maximum aggregate size 1–2 mm). The panels were designed at the CRC 532, Aachen and produced by Hering (Hegger et al., 2006). The fixing technique (a system of vertical and horizontal, light-gage steel profiles supporting the panels through a concealed 'agraffe' fixing device doweled into them) allowed for stress-free thermal deformations due to temperature changes. For the Leiden project (a community college in the Netherlands), the panels (each measuring 1.14 m^2 at a thickness of 30 mm) covered an area of approx. 10,000 m^2 and were also reinforced by a coated AR-glass fibre mesh. Both types of panels were designed for wind loads with no cracking under service loads.

Larger, ventilated façade elements (ranging from roughly 4–7 m^2 with a thickness of 22–25 mm) have been produced by the Fydro company from the Netherlands for a series of projects (early projects including the 'House Rheinlanddamm' office building in Dortmund, Germany, a school building in Düsseldorf, Germany and an office

building in Arnhem, the Netherlands with a coverage of 3000, 14,500 and 700 m^2, respectively). Their products comprise a combination of continuous AR-glass rovings and fibre meshes embedded in a self-compacting, fibre-reinforced microconcrete (Engberts, 2006). The fixing of panels is realized through concealed anchors, rivets or structural adhesive, whereas large panels are provided in combination with metal stud-frame systems.

The need for economy and fast assembly called for the reduction of transportation and installation costs (the latter requiring minimization of fixing points per m^2). This effort led to the development of even larger panels in the order of 12–18 m^2. For example, elements with a surface of 14.34 m^2 (developed at RWTH Aachen University together with experts from the prefabrication, fastening and textile industry) were used for partial cladding of the St. Leonhard secondary school in Aachen (Figure 10.1). Panel thickness was kept at 30 mm through the monolithic integration of concrete webs at the backside of the panel (acting as a bracing system that also accommodates the fixing devices) and the use of epoxy resin-impregnated carbon fibre meshes (Hegger et al., 2015). When concrete (or any other type of) braces are not an acceptable design choice, large TRC façade panels (in the order of 6 m^2) are also furnished with epoxy resin-impregnated carbon fibre meshes and comprise thicker cross-sections (50 mm).

A relatively limited number of proprietary TRC-ventilated façade products have been developed and commercialized such as the betoShell® family of TRC façades (by Hering Bau GmbH & Co. KG), the DinamiC CCC range of systems (by Fydro B.V.) and the panels developed by solidian GmbH. Henriksen (2012) also reports the development (by Rieder Smart Elements GmbH in collaboration with TUDelft) of AR-glass fibre-reinforced extruded concrete panels for cladding purposes incorporating two layers of textiles.

Design requirements for concrete façade elements stem from a variety of targeted performances, such as structural, functional (e.g., thermal performance, moisture and sound protection and fire resistance), aesthetical and long-term (durability-related).

Figure 10.1 Large façade panels covering part of the lateral envelope of the St. Leonhard school building.

The design solution must also take into account other aspects, such as constructability issues (e.g., dimension tolerances, transportation fixtures and inplace anchor assemblages, visible or concealed), cost efficiency, environmental impact, dismantlability/ maintenance requirements and recyclability potential. Most typically, concrete façade panels are treated as nonloadbearing elements and, hence, are designed against lateral loads (imparted by wind and earthquake), whereas the only vertical loads considered are those corresponding to the panels' self-weight. These loads must be transfered through the panels and secondary structural elements (if applicable) to the building's structure. Loads exerted on the panels during handling and erection, but also accidental loads (e.g., due to impact), must also be taken into account in the design. Panel-to-supporting structure load transfer and panel stability are ensured by anchorage systems that comprise an important component of the envelope system. Again, the design of such systems takes into consideration requirements for strength, deformation capacity, volume change accommodation, durability, fire resistance and constructability.

Currently, there are no design standards for TRC that specifically address precast applications. Up to present, the application of TRC façade elements in Germany requires either an individual test-driven approval for each project or a general approval for defined boundary conditions from the German building inspection body (Deutsches Institut für Bautechnik). The first national technical approval for TRC products in Germany was issued in 2014 for a system fitted for strengthening interventions of existing structures (TUDALIT®). Information regarding the design of TRC façade elements (as well as finite element (FE) analysis and experimental testing thereof) is given in Engberts (2006), Hegger et al. (2010a) and Pettersson and Thorsson (2014). According to Hegger et al. (2010a), typical load cases include wind pressure, wind suction, self-weight, thermal variations and shrinkage (the latter two generating stresses only when restraining and structurally indeterminate anchoring conditions are present). The bending capacity of the panels is calculated from cross-section analysis with knowledge of the tensile strength of the textile reinforcement (a fraction of the tensile strength of the individual filament) and the inner lever arm. Maximum allowable deflections are limited to L/250 (Pettersson and Thorsson, 2014) or to L/300 and L/200 for midspan and cantilever edge, respectively (Engberts, 2006). The bond-slip relationship between the textile reinforcement and the concrete (being an important parameter both for cracking and ultimate capacity) can be integrated in the FE analysis, provided that meaningful experimental data is available for the type of TRC in question. The lack of a homogenized or universally accepted textile-to-concrete bond test is noted.

Latest developments in fabrication processes of TRC cladding panels (or other) include the transition from lamination (alternate placement of concrete and textile layers) to casting (pouring of concrete in a mould that accommodates preinstalled textile layers). Casting aims to alleviate problems associated with the lamination technique which is a time-consuming, labour-intensive and anti-ergonomic procedure. Nevertheless, avoiding textile sagging (or misplacement) is a challenging task. Researchers from the Technical University of Dresden have developed a customized spacer system designed to secure individual textile layers in place without adversely

affecting a number of the panel's performance indicators such as strength, response under extreme thermal variations, fire resistance and durability (see Walther et al., 2014; Walther and Curbach, 2014). Casting processes will also allow for vertical mould arrangements and, thus, for double-sided fair-faced elements. On the other hand, lamination production processes create the opportunity for applying on the outer face of TRC panels a thin layer (approx. 3 mm in thickness) of a self-cleaning material, such as titanium dioxide. In parallel, such TRC panels (exposed to visible light irradiation) contribute to the improvement of ambient air quality through photocatalytic degradation of NO_x pollutants (see Brameshuber and Neunzig, 2012).

10.3   Sandwich elements

As derived from the previous section, ventilated AR-glass TRC façade elements with a surface area larger than 6–7 m^2 require some sort of bracing substructures to limit deformations and bowing effects. The elimination of such substructures and the production of larger, compact, yet lightweight, and stand-alone elements that retain (or even ameliorate) the heat protection and sound insulation properties of plain TRC façade panels result from a layer of insulating material sandwiched between two thin TRC faces. The concept is a variation of the conventionally reinforced precast concrete sandwich panels (PCSPs) that have been considered as an attractive system of prefabrication due to distinct advantages, such as structural, thermal and sound efficiency, enhanced durability characteristics, versatility by integrating the requirements of wall and roof elements into one unit and accommodation of architecturally acceptable finishes. These panels comprise two wythes (either one or both of them loadbearing) that typically consist of high-strength fibre-reinforced concrete (and rather rarely ferrocement); core materials are either plastic foams or lightweight concrete. A fully composite, a partially composite and a noncomposite action between the different layers of the component may be achieved depending on the type (strength and stiffness) of transverse reinforcement used and arrangement thereof. Minimum wythe thickness depends on its structural function, concrete cover, anchorage of connectors and stripping-, transportation- and handling-induced loads. For loadbearing wythes, minimum recommended thicknesses range between 50 and 75 mm (or 65 mm for prestressed wythes), whereas typical in-practice values range between 50 and 200 mm (PCI, 1997; CPCI, 1996). Nonloadbearing wythes (veneers) are at least 50 or 65 mm thick, for flat or profiled finishes, respectively. Based on the above, the savings from the replacement of conventionally reinforced concrete wythes with TRC result in obvious material, cost and space savings.

Fundamental work on sandwich panels with thin-walled TRC facings has been done by Hegger et al. (2008b). In this work different configurations of TRC sandwich panels were produced, tested and analytically assessed. Panels comprised a 150-mm thick insulating core made of polyurethane (PU) foam sandwiched between two AR-glass TRC skin layers with a thickness of 15 mm each (concrete having a

maximum aggregate size of 2 mm). Different core densities and methods for skin-to-core bonding were explored (glueing and pressing a notched core into the concrete of the TRC skin while the latter was still in a fresh state). Four-point bending tests were carried out on beam-type specimens of varying lengths in order to determine the flexural and shear capacity of the elements. As expected, the loadbearing and deformation capacity of the specimens were primarily dependent on the core stiffness. Beams with a high-density core exhibited partially to fully composite action and failed due to tensile rupture of the textile, whereas beams with a low-density core exhibited partially to noncomposite action failing either due to shear cracking of the core or due to skin-to-core bond failure. 'Wet' bonding of notched skins proved more efficient to glueing. Shear strengthening of the core by use of continuous textile connectors was also investigated. Moderate strength gains and a considerable residual flexural capacity following the shear core failure was achieved but at a high time and labour cost. Additionally, sound and heat insulation tests as well as reaction to fire (single burning item) tests were performed proving the suitability of the panels for use as façades for office buildings and factory floors.

The idea of using connectors in order to provide some degree of shear transfer between the wythes (without having to rely on weak glued skin-to-core interfaces or labour-intensive castellated TRC cross-sections) was further explored by Hegger and coworkers (see Hegger et al., 2010b; Shams et al., 2014a). Two different sandwich panel designs were proposed with the same 160-mm thick cellular polymeric core: the first design included two TRC wythes of equal thickness (30 mm); whereas the second comprised a thicker (70 mm) inner leaf made of either TRC or conventionally reinforced concrete. Both designs satisfied preset structural, architectural and building physics criteria. Foams of different strength and stiffness characteristics were investigated as core materials. Skin-to-core bonding relied solely on wet concrete-to-foam adhesion. AR-glass and carbon textiles (both epoxy-impregnated) were used for specimen production; textiles featured large grid openings favouring the use of a low-shrinkage concrete mix with a maximum aggregate size equal to 5 mm. Two types of connectors were investigated: a glass fibre-reinforced polymer pin-type connector (resulting from a modification of a commercial connector especially developed for PCSPs) and a continuous lattice-type carbon fibre-reinforced polymer (CFRP) connector (resulting from cutting strips from the biaxial carbon textile with an orthogonal rovings' arrangement at an angle of 45°). Figure 10.2 illustrates the different types of connectors used by Shams et al. (2014a). An extensive experimental campaign was
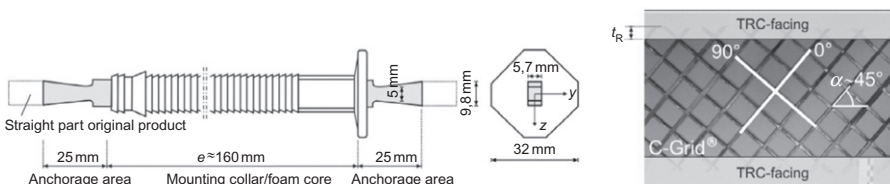
Figure 10.2 Connectors used by Shams et al. (2014a): pin-connector (left) and shear grid (right).

conducted aiming to shed light on the loadbearing behaviour and the required embedment length of the connectors through: (1) pullout, punch-through, shear and combined tensile/shear tests for pin-type connectors and (2) pullout tests for grid-type connectors with different anchorage conditions. In this case, single-roving configurations were tested involving either straight-end or hooked-end rovings, the latter accounting for a roving running to a joint with part of the transverse roving acting as a hook. Test results from this part of the program led to the design of small-scale component testing carried out in order to assess the panels' response under tensile loading perpendicular to the faces and the cores' (connectors + foam) response under direct shear loading. Finally, full-scale four-point bending tests were performed on beam-type specimens. Research outcomes include (but are not restricted to) the following:

- The pullout strength of pin-type connectors embedded in thin TRC plates (facings) increases with increasing tensile strength of the concrete and increasing embedment depth. For the specific connectors tested, embedment depths larger than 25 mm resulted in shearing of the connector. Inversely, punching shear strength of thin TRC facings bearing this type of connectors increases with decreasing embedment depth (i.e., with increasing concrete cover).
- Like in the case of pin-connectors (and as expected), the pullout strength of both straight-end and hooked-end CFRP rovings increases with increasing embedment depth. For the specific rovings tested, tensile failure (fibre rupture) occurred for an embedment depth of 30 and 40 mm for hooked-end and straight-end rovings, respectively. In order to accommodate these values a local increase of the TRC facings is necessary.
- Sandwich panels with unconnected TRC wythes fail under direct (out-of-plane) tension in a brittle manner at a load that is lower to the one corresponding to the cores' tensile strength. Pin-connectors (preinstalled in the core) disrupt the skin-to-core bond conditions leading to inferior bond quality and, hence, to negligible strength contributions. Grid-type connectors, on the other hand, increase the resistance of the panel under direct (out-of-plane) tension and provide postfailure strength uptake (one that follows the considerable loss in loadbearing capacity due to the complete detachment of the core from the wythe(s)) owing to further stressing of the grid. Both connection alternatives increase the stiffness of the panel.
- The in-plane shear strength of sandwich panels with unconnected TRC wythes (as derived from small-scale tests) is governed by the core's shear modulus and by the weakest skin-to-core adhesive joint. The detrimental effect of using pin-type connectors to the concrete-to-foam bond was reconfirmed. On the contrary, the use of continuous CFRP grid connectors in panels undergoing in-plane shear results in both stiffness and strength gains and imparts a postpeak pseudoductile response. These gains are larger for higher fibre volume fractions of the grid connector.
- The out-of-plane bending strength of full-scale sandwich panels with unconnected TRC wythes is also governed by the core's shear properties (shear modulus and shear strength); failure in this case is in the form of brittle shear cracking of the core. The introduction of pin-type connectors does not lead to any strength or stiffness gains but ensures the postpeak integrity of the panel at a constant residual bending strength. Remarkable strength gains (almost by a factor of 2) and appreciable stiffness increments are achieved when inserting a single layer of a continuous CFRP grid connector. Although flexural capacity does not increase with increasing grid layers, postpeak ductility is definitely improved by higher fibre volume fractions. Finally, thicker inner leaves (and, hence, larger overall section thickness and bending stiffness) do not entail higher flexural capacities (for reasons explained in the aforementioned publications).

A detailed analytical approach for the approximation of the load-deflection behaviour of sandwich panels undergoing out-of-plane bending is presented in Shams et al. (2014b). In this work, the idea of accounting for both axial and flexural rigidity reduction of cracked TRC facings (first introduced by Hegger et al., 2010b) was revised and further developed. The model assumes perfect skin-to-core bonding conditions and does not take account of the presence of any connectors. Good correlation between experimental (deriving from tests not included in previous companion papers) and theoretical load-deflection curves was achieved.

The driving force behind the heavy scientific work planned and carried out within the framework of the knowledge transfer phase of the CRC 532 'TRC – Development of a new technology' of the Deutsche Forschungsgemeinschaft was the development of an innovative and ecofriendly modular system for sandwich façades fit for large-scale building projects. This was accomplished through the EU cofunded Life06 INSU-SHELL project (environmentally friendly façade elements made of thermal insulated TRC), a collaboration between the Institut fuer Textiltechnik (ITA) and the Institute of Structural Concrete (IMB) of RWTH Aachen University as well as the industrial partners Durapact GmbH (manufacturing), Saint Gobain Technical Fabrics (consulting in textiles). Detailed information about the outcomes of this project, the prototypes developed and the first large-scale application thereof are given by Tomoscheit et al. (2011).

The design of the elements resulting from the INSU-SHELL project that comprised lightweight, insulated and self-supporting sandwich façades made of TRC wythes lies along the general lines described in the previous sections. The panels (with an overall thickness of 180 mm and two alternative surface areas roughly equal to either 3000 mm × 1000 mm or 3500 mm × 1000 mm) consisted of a PU foam core sandwiched between two 15 mm thick AR-glass TRC skins (mix containing discrete chopped glass fibres); TRC skins were enlarged to a thickness of 40 mm along the edges in order to accommodate two stainless steel ties used to transfer the self-weight of the outer wythe to the inner one and they were furnished with a combination of two textiles of different 2D structure (Figure 10.3). Out-of-plane deformation phenomena (e.g., due to wind suction or temperature differentials) were withstood by the introduction of ductile pin skin-to-skin connectors.

Apart from the already mentioned conclusive points deducted from experimental campaigns run in the framework of TRC sandwich façade development, Tomoscheit et al. (2011) also report that:

- cyclic loading has practically no influence on the shear capacity of the foam;
- even in the case of deficient skin-to-core bond (owing to poor workmanship or other construction flaws) the enlarged part of the wythes around the perimeter of the panel and the pin-connectors allow for secondary shear transfer mechanisms to develop and
- wythes' reinforcement (chopped fibres and textiles) ensures a crack-free response at the serviceability limit state and very limited cracking at the ultimate limit state.

By comparing of the INSU-SHELL façade element to a counterpart sandwich panel (of equal loadbearing capacity and insulation potential) made of conventionally
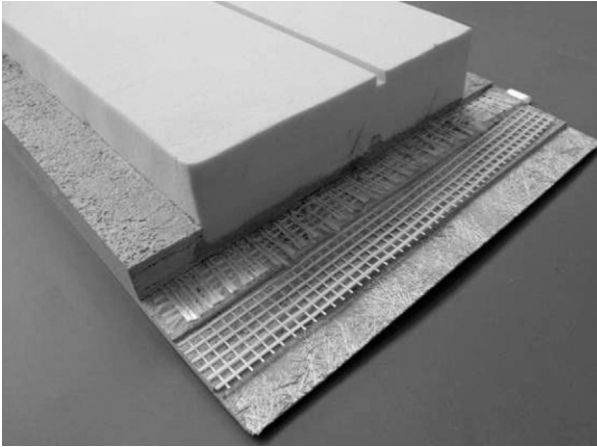
Figure 10.3 Different layers of the INSU-SHELL elements (Tomoscheit et al., 2011).

reinforced concrete wythes, the following points are highlighted (based on Tomoscheit et al., 2011):

- the weight of the TRC sandwich façade equals approximately 17% of the weight of the conventional one; a reduction of primary energy consumption associated with nonrenewable resources in the order of 45% is achieved when the façade comprises INSU-SHELL elements instead of conventional ones;
- the respective savings in global warming potential (expressed as kg CO_2-equivalent/m^2) amount to approximately 53%; the recycling potential of the TRC-based sandwich elements of this type remains to be explored;
- the cost breakdown of the INSU-SHELL element is as follows: insulating foam core (41%); finely grained concrete (27%); textile reinforcement (23%) and fixing the system to the existing substructure (9%) and
- when total material, production and transport costs are considered comparisons favour traditional façade solutions over innovative TRC-based solutions. More specifically, the total cost per unit area of the INSU-SHELL element (as previously defined) was estimated to be more than twice (134%) the respective cost of the conventional counterpart element. This is owed to the significantly higher production cost of the TRC-based façade, which (in the work of Tomoscheit et al., 2011 and as the authors point out) is inflated as it reflects the production cost of prototype elements instead of regular production lines. Scale economy is expected to reduce this cost.

The pilot production, modelling and full-scale testing of new lightweight sandwich elements incorporating AR-glass and carbon fibre TRC facings were the objective of another TRC-based research effort (Tekocrete project), this time in Sweden. Malaga et al. (2012) briefly report on selected results of this project including information on full-scale 'wind chamber' tests.

Cellular materials of foamed structure are not the only insulation means fit for use in TRC-based sandwich elements. Hülsmeier (2012) reports on the development of vacuum-insulated TRC sandwich façade elements (used as nonloadbearing curtain wall systems); these systems were the outcome of the research project 'vakutex'

undertaken by the Leipzig University of Applied Sciences. The curtain wall comprises two 55-mm thick vacuum insulation panels (VIPs) sandwiched between an inner (30-mm thick) and an outer (15-mm thick) TRC leaf. VIPs consist of a nearly gas-tight enclosure (in this case, a metalized high-barrier foil) surrounding an air-evacuated rigid core (in this case, a microporous silicic acid). Connection between inner and outer TRC leaves is achieved through a stud-frame system comprising glass fibre-reinforced polymer I-profiles. Compared to a conventional reinforced concrete sandwich panel (probably loadbearing, though unclear in the manuscript) the five-times-lighter vacuum-insulated TRC outperforms the former panel in terms of eco-performance indices (derived from a life cycle assessment (LCA)). Again, high-tech curtain wall products prove to be substantially more cost intensive in regards to 'traditional' solutions when initial investment costs are considered.

Research on TRC-based sandwich panels (in this case for possible use as impact-resistant structural members) has also been conducted by Schneider et al. (2009) and Finzel and Häußler-Combe (2010). In the latter work, the loadbearing capacity under three- or four-point out-of-plane bending and the associated failure modes were experimentally assessed through beam-type specimens of varying lengths; specimens consisted of 8 mm thick TRC facings with an 80-mm thick insulating core, comprised different textile materials (AR-glass and carbon) and reinforcement ratios and incorporated different core materials (PU of varying densities or aerated concrete). The TRC facing-to-core material bonding was achieved through an epoxy paste adhesive. In agreement to the findings of Hegger et al. (2008b), failure initiation was due to core shearing. Aerated concrete cores resulted in abrupt load reductions following their shear cracking; conversely, PU cores exhibited a postshear cracking strength uptake potential. The analytical assessment of the elements' mechanical response was realized by implementation of both 'classical' sandwich theory calculation models and FE analyses software programs. Both approaches resulted in reasonable prediction of the experimentally derived load-to-deflection ratios (up to the onset of the multiple cracking phase of the specimens' response).

In line with the idea of using loadbearing sandwich elements with TRC faces as impact mitigation means Cuypers et al. (2008) report on the potential of a special type of TRC (comprising E-glass fibre chopped strand mats embedded in an inorganic phosphate cement (IPC) matrix) to dissipate energy under low-velocity impact. Drop weight tests were carried out on filigree TRC plates. Visual crack interpretation, digital image correlation and postimpact tensile loading were used in order to identify damage mechanisms and determine the residual tensile strength of the specimens. It was concluded that for this type of TRC impact energy was dissipated without leading to considerable global loss of strength. Sandwich panels with textile (mat) reinforced IPC faces were both analytically and experimentally studied by Cuypers and Wastiels (2011). Testing involved beam-type specimens with PU cores undergoing four-point bending. Different combinations of face and core thicknesses were investigated. Face-to-core bonding was achieved by direct casting of the sandwich skins onto the foamed core material. Satisfactory capturing of the experimental load–displacement curves was achieved through FE modelling.

10.4   Other applications

The list of applications of TRC in prefabrication is extensive and limited only by the imaginative creativity of researchers and building sector players. Successful proof-of-concept and demonstration projects such as those for rhombic lattice structures (Schneider et al., 2006), integrated formwork elements (Brameshuber et al., 2004; Papantoniou and Papanicolaou, 2012; Verbruggen et al., 2013) and bridge components (Hegger et al., 2010c) have endowed TRC technology transfer with a strong momentum. This section provides brief information on the latest innovative applications of TRC.

Freeform structural members (or even whole structures) are one of the most noteworthy trends in contemporary architecture. TRC double-curved elements manufactured by various different novel methods serve this trend and boost further development. The concept has been proved through the construction of a demonstration pavilion building at RWTH Aachen University. The structure comprises four large (7 m × 7 m) 60-mm thick double-curved TRC shells centrally resting (through rigid connections) on precast reinforced concrete columns arranged in a 2 m × 2 m grid (Hegger et al., 2013; Scholzen et al., 2015a; see also Chapter 8 for more details). The shells were reinforced with 12 layers of dry carbon fibre textile spaced at 5 mm between alternated concrete layers. Shotcreting on conventional wooden formwork (reached by an overhang movable working platform) was the manufacturing method of choice. The design approach for such TRC shells is given by Scholzen et al. (2015b). An alternative production technique was successfully investigated by Kok (2013). In this work, reconfigurable flexible moulds (comprising an elastic layer supported by a system of actuators) in combination with a laminating process were used for the production of single- and double-curved laminated elements measuring 25 mm × 400 mm × 800 mm and comprising four layers of AR-glass textile reinforcement. In the same context, the potential of double-curved shell elements made of AR-glass TRC using fabric formwork has been explored by Cauberg et al. (2012). In this work, 36 and 16 mm thick double-curved shells with fibre volume fractions equal to 3% and 7%, respectively were produced by shotcreting and structurally tested. Substitution of the 2D AR-glass textile layers with a dense glass fibre mat and the use of an IPC micromortar (with max solid materials diameter of 100 μm) instead of an ordinary Portland cement mortar (with max aggregate size of 2 mm) result to 8 mm thick homologous shells with a fibre volume fraction equal to 13%.

The incorporation of TRC to hybrid precast products is yet another novelty. Along this line, hybrid pipes (Figure 10.4) have been developed comprising an inner polymer tube enveloped by an outer ring made of TRC (Lieboldt et al., 2005, 2006). Such pipes could potentially be used for water supply and sewage disposal (Butler et al., 2010). The polymer tube is kept as part of the composite pipe (serving as a lining material) due to its high chemical resistance, impermeability and smooth surface that facilitates flow. The TRC ring (furnishing textile reinforcement equivalent to 2–6% by volume embedded in a fibre-reinforced cement-based matrix) provides resistance against internal pressure and external loads. For the purpose of prototype manufacturing a

(a)   (b)
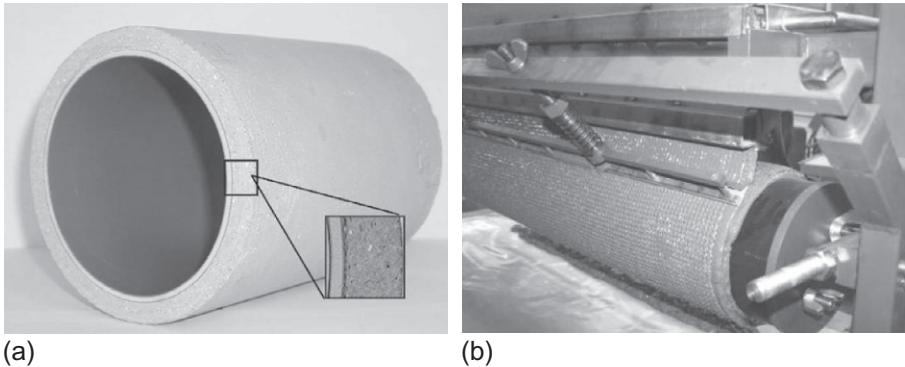
Figure 10.4 PVC/TRC composite pipe: (a) sample (Lieboldt et al., 2005) and (b) snapshot from the manufacturing process (Lieboldt et al., 2006).

custom-designed lab-scale production facility was set up at the Technical University of Dresden based on a technique combining pultrusion and multiple-turn coiling applicable to straight pipes. Another production technology applicable to elbow pipes was also developed and put into practice. From a series of three edge-bearing and internal pressure tests it is concluded that the loadbearing capacity of the hybrid pipe is greatly enhanced. The effect of chopped fibres volume fraction in the concrete and textile volume fraction in the TRC are also explored.

TRC has also found its way in the production of noise barrier parapets. These elements consist of a loadbearing TRC panel cast on top of a sound-absorbing profiled skin made of lightweight concrete. Prototype development and testing of such products was realized by Funke et al. (2015).

Other creative ways of exploiting TRC technology is the manufacture of handmade furniture (especially suited for outdoor use), ornaments, sculptures and small boats. TRC furniture has already been commercialized.

10.5 Summary and future trends

TRC has been characterized as a spearheading innovation. Prefabrication provides a fertile ground for the implementation of the TRC technology fostering high-quality-built outcomes in the sense of structural performance, energy efficiency and architectural/aesthetical value. Economic competitiveness of TRC-based solutions over conventional ones should be derived from LCAs and not on the basis of initial production cost estimates.

Although the knowledge curve on TRC technology is probably close to reaching a plateau there is still a lot of space for improving a large number of performance indices (e.g., strength-to-weight ratio or long-term behaviour and weathering resistance); most of these indices relate to the textile-to-matrix bond quality, to the durability characteristics of the composite and to their interrelation. Improvements can be achieved

through modifications of the TRC constituents on a nano, micro, meso and macro levels. Additional interesting research lines would be: (1) the development of light-weight finely grained concrete matrices – already suggested by Engler et al. (2003) – that fulfils all fresh- and hardened-state requirements set for normal weight matrices; (2) broader use of spatially arranged fibre structures (three-dimensional (3D) textiles; see Roye and Gries, 2007; Hegger et al., 2012) in an attempt to accommodate 3D loadbearing requirements and facilitate production processes; (3) the use of hybrid (bi- or multimaterial) textiles in order to optimize material usage (e.g., glass/ carbon textiles where the carbon rovings – corresponding to limited fibre volume fractions – are solely used for their electrothermal properties (see Xu et al., 2011) and not for structural purposes); (4) development of cementitious matrices of low alkalinity or even cement-free mixtures that would improve the durability of fibre nets prone to alkaline attack and (5) experimentation with textiles comprising natural fibres (Alves Fidelis et al., 2015) in order to refrain from resource-intensive production practices for man-made fibres.

Further to the above-stated considerations is a marked trend for enriching structural materials with capabilities other than structural rendering them multifunctional while in service. This trend is definitely applicable to TRC and has already been manifested through efforts aimed at furnishing the external surfaces of TRC façades with self-cleaning abilities. Extrapolating from this function, TRC may also be rendered with self-healing abilities or even self-sensing ones. On the latter issue, latest developments have led to the successful exploitation of the piezoresistive properties of carbon fibre textiles embedded in cementitious matrices in order to correlate changes in the electrical resistance (of either the composite as a whole or the textile alone) that are detected during tension and strain/damage evolution (see Goldfeld et al., 2015a,b; Plamantouras and Papanicolaou, 2015). Modification of the cementitious matrix by incorporation of carbon nanotubes enhances the aforementioned correlation (Plamantouras, 2015). Further development and full-scale implementation of this technology will allow for real-time strain and/or damage detection for TRC-based structural elements enabling timely rehabilitation interventions as part of structural health monitoring schemes of smart TRC structures.

Another groundbreaking achievement that paves the way for future innovations in the field of solar thermal energy exploitation is the development of a fluid-bearing thermally activated and structural TRC roof element (Herman-Czezuch et al., 2014). The element consists of a TRC sandwich panel comprising three layers: an upper (exposed) TRC face; an insulating (PU) core; and an expanded perlite composite inner face. The TRC face integrates a capillary tube mat (a thermal energy absorber) filled with water as a heat transfer fluid that ensures the transport of generated solar heat from the roof down to the heat supply system of the building. The energetic potential of the heat-supplying TRC roof element has been adequately modelled and successfully validated through bench tests simulating solar radiation.

Coming back to the imaginative creativity of designers and how this can be boosted by the adoption of TRC-based solutions one should make special reference to developments that result from out-of-the-box thinking. One such development is the origami-inspired design and production of precast TRC folded elements

(Koch et al., 2015) and spatial structures (Chudoba et al., 2014; van der Woerd et al., 2015). In both approaches, a textile layer provides the articulation means between adjacent TRC folding plates. In the work of Koch et al. (2015) a textile was developed with a special local configuration (different stitching pattern) that allowed problem-free textile adjustment to a supporting folded 3D formwork used for TRC casting. A different approach is followed by Chudoba and coworkers, eliminating the need for complex spatial formworks; their solution (oricrete) involves precasting a single continuously reinforced segmental TRC plate, with segments being separated by a crease pattern specifically designed to serve the final (targeted) 3D shape of the structure. The segmental plate is transported on site, folded into the final 3D shape and the creases are grouted in order to consolidate the structure (Figure 10.5). Although not an entirely new concept in architecture engineering, a new era in 'origamics' (standing for origami-like applications in engineering) is emerging with the development of deployable TRC structures. The construction process of the latter can only be realized through computer-aided design; computer-aided manufacturing or even robotic folding techniques could comprise prospect directions of applied research in the field.

(a)

(b)
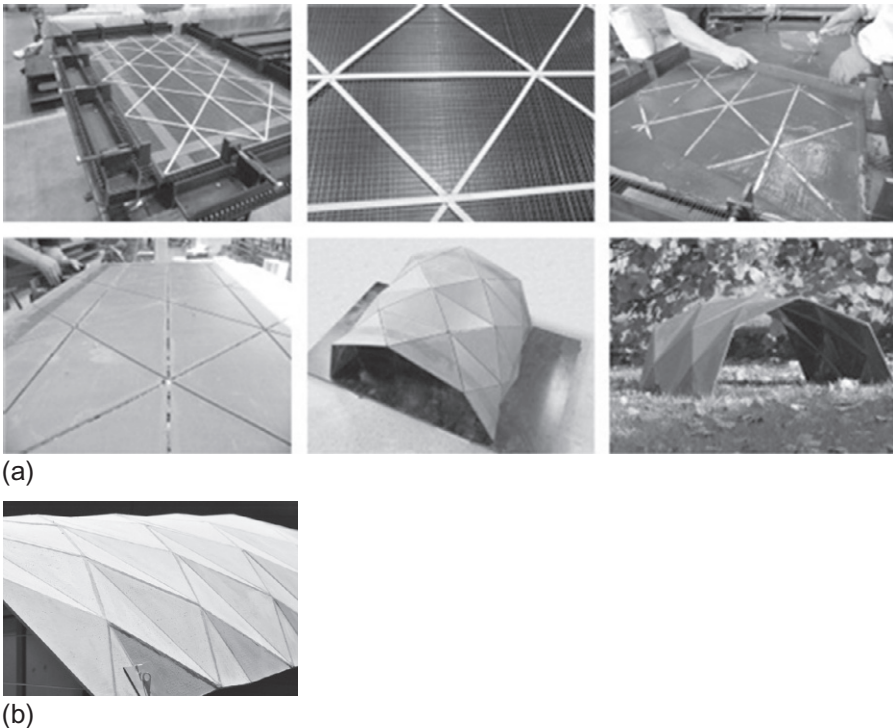
Figure 10.5 (a) Snapshots from the production of a prototype folded TRC vault (Chudoba et al., 2014) and (b) vault close-up (van der Woerd et al., 2015).

Based on the information presented in this chapter it can be postulated that the TRC technology is expected to be a catalyst for innovation in the prefabrication sector promoting its integration with automation and information technology.

References

Alves Fidelis, M.E., de Andrade Silva, F., Toledo Filho, R.D., Müller, S., Mechtcherine, V., 2015. The mechanics of natural jute TRC. In: Brameshuber, W. (Ed.), Proceedings of the 11th International Symposium on Ferrocement (FERRO-11) and 3rd ICTRC International Conference on Textile Reinforced Concrete. RILEM Publications S.A.R.L., Bagneux, pp. 255–265.

Brameshuber, W., Neunzig, C., 2012. Pollutant-reducing textile-reinforced concrete – for the sake of our environment – Schadstoffreduzierender textilbeton – der umwelt zuliebe. BFT Int. 78, 14–15.

Brameshuber, W., Koster, M., Hegger, J., Voss, S., Gries, T., Barle, M., Krüger, M., 2004. Textile Reinforced Concrete (TRC) for Integrated Formworks. In: American Concrete Institute (ACI) Special Publication, 224, pp. 45–53.

Butler, M., Lieboldt, M., Mechtcherine, V., 2010. Application of textile-reinforced concrete (TRC) for structural strengthening and in prefabrication. In: van Zijl, G.P.A.G., Boshoff, W.P. (Eds.), Advances in Cement-Based Materials. Taylor & Francis Group, London, pp. 127–136.

Cauberg, N., Tysmans, T., Adriaenssens, S., Wastiels, J., Mollaert, M., Belkassem, B., 2012. Shell elements of textile reinforced concrete using fabric formwork: a case study. Adv. Struct. Eng. 15, 677–690.

Chudoba, R., van der Woerd, J., Schmerl, M., Hegger, J., 2014. ORICRETE: modeling support for design and manufacturing of folded concrete structure. Adv. Eng. Softw. 72, 119–127.

CPCI (Canadian Prestressed Concrete Institute), 1996. Design Manual Precast and Prestressed Concrete. Canadian Prestressed Concrete Institute, Canada.

Cuypers, H., Wastiels, J., 2011. Analysis and verification of the performance of sandwich panels with textile reinforced concrete faces. J. Sandw. Struct. Mater. 13, 589–603.

Cuypers, H., Van Ackeren, J., Belkassem, B., Wastiels, J., 2008. Impact resistance of load bearing sandwich elements with textile reinforced concrete faces. In: Proceedings of the 13th European Conference on Composite Materials. KTH Royal Institute of Technology, Stockholm.

Engberts, E., 2006. Large-size facade elements of textile reinforced concrete. In: Hegger, J., Brameshuber, W., Will, N. (Eds.), Proceedings of the First International RILEM Symposium on Textile Reinforced Concrete. RILEM Publications S.A.R.L., Bagneux, pp. 297–307.

Engler, T., Franzke, G., Hempel, R., Kratz, M., Ortlepp, S., Schierz, M., 2003. Entwicklung einer großformatigen und dünnwandigen textilbewehrten brüstungsplatte (Development of large-size, thin-walled textile-reinforced balustrade panels). In: Proceedings of the Techtextil-Symposium 2003 (CD-Rom).

Finzel, J., Häußler-Combe, U., 2010. FEA bending analysis of TRC sandwich panels. In: Proceedings of the 18th European Conference on Fracture: Fracture of Materials and Structures from Micro to Macro Scale – ECF18 (CD-Rom).

Funke, H.L., Gelbrich, S., Kroll, L., 2015. Development of effective textile-reinforced concrete noise barrier. J. Mater. Sci. Res. 4, 33–39.

Goldfeld, Y., Rabinovitch, O., Fishbain, B., Quadflieg, T., Gries, T., 2015a. Sensory carbon fiber based textile-reinforced concrete for smart structures. J. Intell. Mater. Syst. Struct. http://dx.doi.org/10.1177/1045389X15571385.

Goldfeld, Y., Rabinovitch, O., Quadflieg, T., Gries, T., 2015b. Integrated monitoring of TRC using carbon fibers. In: Brameshuber, W. (Ed.), Proceedings of the 11th International Symposium on Ferrocement (FERRO-11) and 3rd ICTRC International Conference on Textile Reinforced Concrete. RILEM Publications S.A.R.L., Bagneux, pp. 327–334.

Hegger, J., Will, N., Aldea, C., Brameshuber, W., Brockmann, T., Curbach, M., Jesse, J., 2006. Applications of textile reinforced concrete. In: Brameshuber, W. (Ed.), State-of-the-Art Report of RILEM Technical Committee 201-TRC – RILEM Report 36. RILEM Publications S.A.R.L., Bagneux, pp. 237–270.

Hegger, J., Zell, M., Horstmann, M., 2008a. Textile reinforced concrete – realization in applications. In: Walraven, J., Stoelhorst, D. (Eds.), Proceedings of the International Fib Symposium Tailor Made Concrete Structures: New Solutions for Our Society. Taylor&Francis Group, London, pp. 357–362.

Hegger, J., Horstmann, M., Scholzen, A., 2008b. Sandwich panels with thin-walled textile-reinforced concrete facings. In: American Concrete Institute (ACI) Special Publication. 251.

Hegger, J., Schneider, M., Kulas, C., 2010a. Dimensioning of TRC with application to ventilated facade systems. In: Brameshuber, W. (Ed.), Proceedings of the International RILEM Conference on Material Science. RILEM Publications S.A.R.L, Bagneux, pp. 393–403.

Hegger, J., Horstmann, M., Feldmann, M., Pyschny, D., Raupach, M., Büttner, T., Feger, C., 2010b. Sandwich panels made of TRC and discrete and continuous connectors. In: Brameshuber, W. (Ed.), Proceedings of the International RILEM Conference on Material Science. RILEM Publications S.A.R.L, Bagneux, pp. 381–392.

Hegger, J., Kulas, C., Schneider, H.N., Brameshuber, W., Hinzen, M., Raupach, M., Büttner, T., 2010c. TRC pedestrian bridge-design, load-bearing behavior and production processes of a slender and light-weight construction. In: Brameshuber, W. (Ed.), Proceedings of the International RILEM Conference on Material Science. RILEM Publications S.A.R.L, Bagneux, pp. 353–364.

Hegger, J., Kulas, C., Horstmann, M., 2012. Spatial textile reinforcement structures for ventilated and sandwich façade elements. Adv. Struct. Eng. 15, 665–676.

Hegger, J., Bepple, S., Chudoba, R., Scholzen, A., 2013. Thin-walled shell structures made of textile-reinforced concrete. BFT Int. 2, 113–115.

Hegger, J., Rempel, S., Norbert, W., 2015. Slender façade elements made from textile-reinforced high-performance concrete – Schlanke fassadenelemente aus textilbewehrtem hochleistungsbeton. BFT Int. 81, 103–105.

Henriksen, T., 2012. Structural challenges of textile reinforced FRC panels. In: Müeller, H.S., Haist, M., Acosta, F. (Eds.), Proceedings of the 9th Fib International PhD Symposium in Civil Engineering. KIT Scientific Publishing, Karlsruhe, pp. 377–383.

Herman-Czezuch, A., Brüntjen, M.-A., Brunk, M., van Treeck, C., 2014. Modelling and validation of a textile reinforced concrete absorber roof for investigating its energetic potential. In: van Treec, C., Müller, D. (Eds.), Proceedings of BauSIM 2014, 5th German-Austrian Conference of the International Building Performance Simulation Association. International Building Performance Simulation Association, Aachen.

Hülsmeier, F., 2012. Vakutex – vacuum-insulated textile concrete facade elements. Concr. Plant Int. 6, 12–22.

Koch, A., Kerschl, C., Gries, T., Brameshuber, W., 2015. Locally adapted biaxial warp knitted textiles as reinforcement of folded concrete elements. In: Brameshuber, W. (Ed.), Proceedings of the 11th International Symposium on Ferrocement (FERRO-11) and 3rd ICTRC International Conference on Textile Reinforced Concrete. RILEM Publications S.A.R.L., Bagneux, pp. 419–426.

Kok, M.A.D., 2013. Textile Reinforced Double Curved Concrete Elements. Delft University of Technology, Delft.

Lieboldt, M., Hempel, R., Schorn, H., Franzke, G., Helbig, U., 2005. Development and testing of new innovative composite pipes (plastic – textile concrete – composite system) including their production technology. In: Balázs, G.L. (Ed.), Proceedings of the Fib Symposium: 'Keep Concrete Attractive', vol. 1. Publ. Company of the Budapest University of Technology and Economics, Budapest, pp. 339–344.

Lieboldt, M., Helbig, U., Engler, T., 2006. Textile reinforced concrete multi-layer composite pipes. In: Hegger, J., Brameshuber, W., Will, N. (Eds.), Proceedings of the First International RILEM Symposium on Textile Reinforced Concrete. RILEM Publications S.A.R.L., Bagneux, pp. 369–378.

Malaga, K., Tammo, K., Flansbjer, M., Blanksvärd, T., Peterson, Ö., 2012. Textile reinforced concrete sandwich panels. In: Bager, D.H., Silfwerbrand, J. (Eds.), Proceedings of the International Fib Symposium: Concrete Structures for Sustainable Community. Royal Institute of Technology, Stockholm, pp. 169–172.

Papantoniou, I.C., Papanicolaou, C.G., 2012. Flexural behavior of one-way textile reinforced concrete (TRC)/reinforced concrete (RC) composite slabs. In: Quaresimin, M., Kollar, L., Asp, L. (Eds.), Proceedings of the 15th European Conference on Composite Materials.European Conference on Composite Materials – ECCM, Venice.

PCI (Precast/Prestressed Concrete Institute) Committee on Precast Sandwich Wall Panels, 1997. State-of-the-art of precast/prestressed sandwich wall panels. PCI J. 42, 92–134.

Pettersson, M., Thorsson, P., 2014. FE-modelling of textile reinforced concrete façade elements. M.Sc. Thesis, Chalmers University, Gothenburg.

Plamantouras, V., 2015. Damage characterization of TRC elements through electrical resistivity measurements. M.Sc. Thesis, University of Patras, Patras (in Greek).

Plamantouras, V.D., Papanicolaou, C.G., 2015. Electrical resistivity measurements on TRC tensile coupons. In: Brameshuber, W. (Ed.), Proceedings of the 11th International Symposium on Ferrocement (FERRO-11) and 3rd ICTRC International Conference on Textile Reinforced Concrete. RILEM Publications S.A.R.L., Bagneux, pp. 319–325.

Roye, A., Gries, T., 2007. 3-D textiles for advanced cement based matrix reinforcement. J. Ind. Text. 37, 163–173.

Schneider, H., Schaetzke, C., Hegger, J., Voss, S., 2006. Structure construction/rhombic lattice structures. Bar nets of textile reinforced concrete – Tragwerkskonstruktion/rautenfoermige gitterstrukturen stabnetze aus textilbeton. BFT Int. 03, 34–40.

Schneider, H.N., Schätzke, C., Feger, C., Horstmann, M., Pak, D., 2009. Modulare bausysteme aus textilbetonsandwichelementen. In: Curbach, M., Jesse, F. (Eds.), 4th Colloquium on Textile Reinforced Structures (CTRS4), pp. 565–576.

Scholzen, A., Chudoba, R., Hegger, J., 2015a. Thin-walled shell structures made of textile-reinforced concrete – part I: structural design and construction. Struct. Concr. 16, 106–114.

Scholzen, A., Chudoba, R., Hegger, J., 2015b. Thin-walled shell structures made of textile-reinforced concrete – part II: experimental characterization, ultimate limit state assessment and numerical simulation. Struct. Concr. 16, 115–124.

Shams, A., Horstmann, M., Hegger, J., 2014a. Experimental investigations on textile-reinforced concrete (TRC) sandwich sections. Compos. Struct. 118, 643–653.

Shams, A., Hegger, J., Horstmann, M., 2014b. An analytical model for sandwich panels made of textile-reinforced concrete. Constr. Build. Mater. 64, 451–459.

Tomoscheit, S., Gries, T., Horstmann, M., Hegger, J., 2011. Project life INSUSHELL: reducing the carbon footprint in concrete construction. Int. J. Sustain. Build. Technol. Urban Dev. 2, 162–169.

van der Woerd, J.D., Chudoba, R., Hegger, J., 2015. Design and construction of a thin barrel vault by folding. In: Proceedings of the International Association for Shell and Spatial Structures (IASS) Symposium 2015, Amsterdam Future Visions, 17–20 August 2015, Amsterdam, The Netherlands.

Verbruggen, S., Remy, O., Wastiels, J., Tysmans, T., 2013. Stay-in-place formwork of TRC designed as shear reinforcement for concrete beams. Adv. Mater. Sci. Eng. 2013, 1–9.

Walther, T., Curbach, M., 2014. Mit DistTEX textilbeton gießend herstellen. In: Nguyen, V.T., Maydl, P., Freytag, B., Santner, G. (Eds.), Beton Graz '14 'Nachhaltig Bauen mit Beton: Werkstoff und Konstruktion'. Verlag der Technischen Universität Graz, Graz, pp. 197–204.

Walther, T., Schladitz, F., Curbach, M., 2014. Textilbetonherstellung im gießverfahren mit hilfe von abstandhaltern. Beton Stahlbetonbau 109, 216–222.

Williams Portal, N., 2013. Sustainability and flexural behaviour of textile reinforced concrete. Thesis for the Degree of Licentiate of Engineering, Chalmers University, Gothenburg.

Xu, S., Yu, W., Song, S., 2011. Numerical simulation and experimental study on electrothermal properties of carbon/glass fiber hybrid textile reinforced concrete. Sci. China Technol. Sci. 54, 2421–2428.

Optimum design of textile-reinforced concrete as integrated formwork in slabs

11

C.G. Papanicolaou, I.C. Papantoniou
University of Patras, Patras, Greece

11.1   Introduction

The continuously rising demands regarding the compliance of concrete structures with economic, environmental, and structural performance design criteria highlight the need for the integration of innovative materials in conventional prefabrication building techniques. Prefabrication and semi-prefabrication building techniques have proven to be a time- and cost-effective design solution, especially in large-scale construction projects.

A form of semi-prefabrication involves the use of permanent, integrated, or otherwise stay-in-place (SiP) formwork elements, which are produced in industrial plants. The SiP elements are transferred on site and placed in their final position, where the pouring of fresh concrete follows in order to form a composite structural element. The use of SiP formwork elements for the production of composite concrete slabs or beams satisfies a combination of favorable performance criteria, such as economy (e.g., reduced construction time, cut-backs on specialized technical personnel, and site ergonomy), aesthetics (ready-to-use finished surfaces), improved mechanical performance (through rigorous quality control), and relatively small environmental impact.

The main distinction of SiP formwork elements is between participating and non-participating ones. The former contribute to the bearing capacity of the structural member through composite action with the cast-in-situ parts, while the latter make no strength contributions. A wide range of materials has been utilized for the production of SiP formwork elements including steel, steel-reinforced or fiber-reinforced concrete, prestressed concrete, and fiber-reinforced polymers (FRP). These SiP formwork elements inherit drawbacks related to their production material, such as sensitivity against corrosion, performance reduction against high temperatures, and high self-weight for steel, FRP, and conventionally reinforced concrete (RC) elements, respectively. The use of textile-reinforced concrete (TRC) for the production of such formwork can be advantageous compared with SiP structural systems comprising other materials, due to the use of noncorroding reinforcement embedded in a thin-walled cementitious product of high loadbearing capacity. Also, compared to fiber-reinforced concrete elements, a higher exploitation of the tensile reinforcement is achieved.

This chapter is arranged in two parts. The first part introduces a design procedure for one-way composite slabs comprising a participating SiP textile-reinforced concrete formwork element monolithically connected to a concrete topping, reinforced with conventional steel reinforcement. Both the formwork and the composite slab are designed in fulfillment of serviceability limit state (SLS) and ultimate limit state (ULS) design criteria. In the second part of the chapter, the proposed design procedure is integrated into an optimum design methodology. The latter aims to determine critical design parameters that result in the minimum cost design solution for given spans and design loads.

11.2   Conceptual design

Some of the most crucial conceptual design considerations for the TRC SiP formwork elements and the deriving composite slabs are given schematically in Figure 11.1.
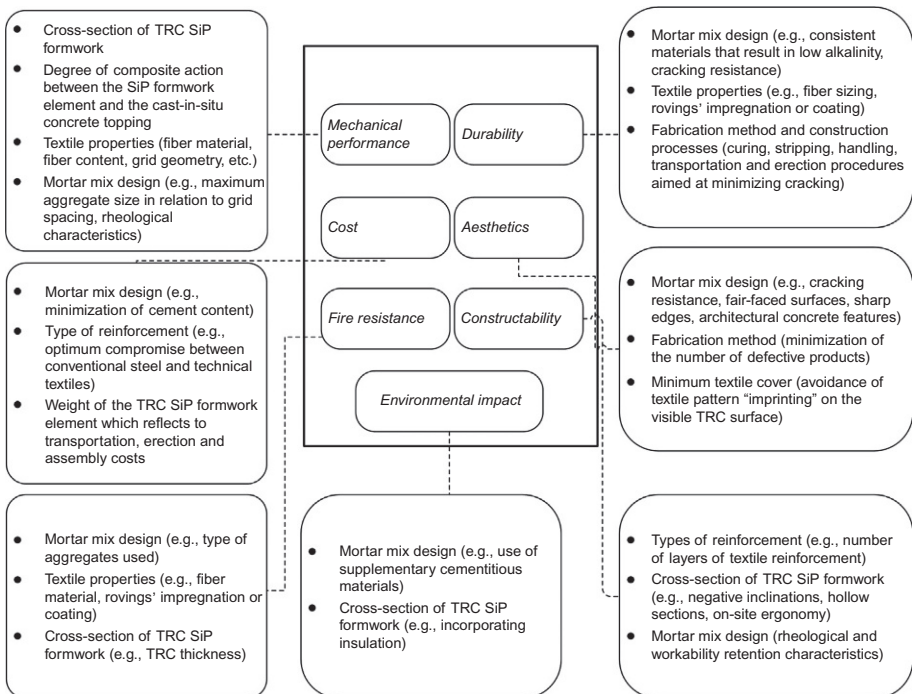
Figure 11.1 Crucial conceptual design considerations for the design of TRC SiP elements and RC/TRC composite slabs.

11.3   Design considerations and assumptions

This section outlines the design considerations and assumptions that are associated with the design of one-way composite TRC/RC slabs satisfying both SLS and ULS design criteria. The design procedure is composed of two design states: a temporary state (TS) and a permanent state (PS). The TS corresponds to the time period following the construction of the formwork and includes all possible loading conditions that might be imposed on it due to handling, storing, transportation, and on-site assembly. During this state, the formwork acts as a standalone element. The PS corresponds to the time period following the hardening of the cast-in-situ concrete; during this state, the formwork and the concrete topping act together as a composite member. Although the two states are examined independently, the design states cannot be decoupled. The shape, the geometric characteristics, and the reinforcement ratio of the SiP formwork element reflect the design of the composite slab. Figure 11.2 illustrates the morphology of probable TRC SiP formwork profiles and the respective TRC/RC composite slab cross sections.

For the TS, the critical design load is the uniform load corresponding to the sum of the self-weights of the TRC element, the steel reinforcement (if present), and the freshly poured concrete topping. According to Eurocode 1, Part 1-6 (CEN, 2004a), the recommended characteristic values of actions, due to construction loads, during the casting of concrete (e.g., working personnel with small site equipment) are given in Figure 11.3. Design loads for the composite slab are defined in Eurocode 1, Part 1-1 (CEN, 2002). Generally, all design formulas developed and presented herein are based on the Eurocode 2 (CEN, 2004b) norms and (where appropriate) on certain *fib* Model Code (2010a,b) (MC2010) clauses.
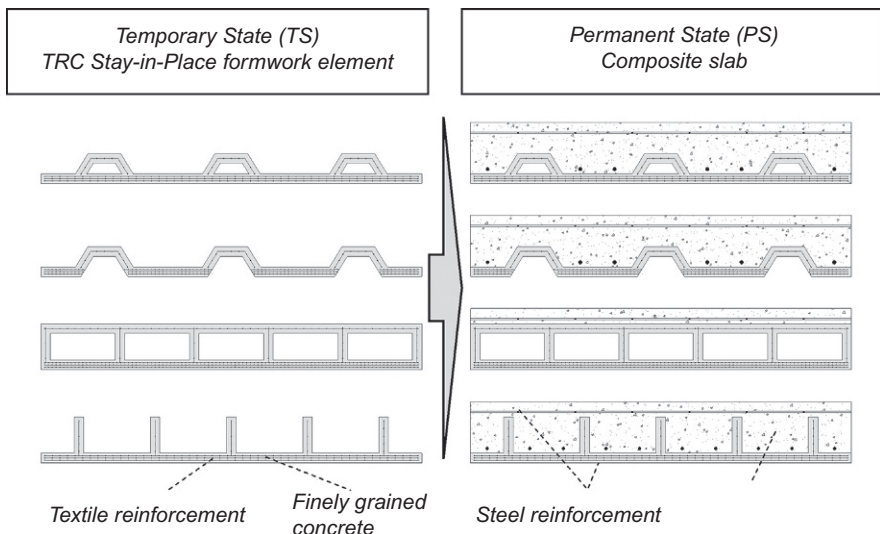
Figure 11.2 Probable TRC sections and the respective RC/TRC composite slabs.
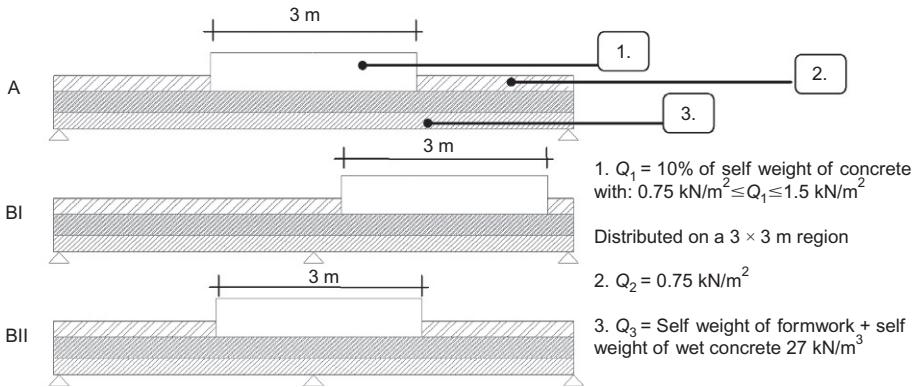
Figure 11.3 Loading schemes for the TRC SiP element.

1. Q_1 = 10% of self weight of concrete with: 0.75 kN/m$^2 \leq Q_1 \leq$ 1.5 kN/m^2

Distributed on a 3 × 3 m region

2. Q_2 = 0.75 kN/m^2

3. Q_3 = Self weight of formwork + self weight of wet concrete 27 kN/m^3

A fully composite action is assumed for the design of the slabs, even in cases where no transverse shear connectors are used. The validity of this assumption has been confirmed by Papantoniou and Papanicolaou (2012). Nevertheless, it should be noted that experimental studies in the field of composite structural members, incorporating participating SiP formwork elements of cementitious composition, are very scarce (Brameshuber et al., 2008; Papanicolaou and Papantoniou, 2010). Hence, more testing is needed in order to shed light onto areas of limited knowledge.

For large-support spacing (>3 m) of slender TRC elements, it is probable that the design bending may exceed the cracking bending moment. In this case, the designer has to decide if cracking formation is acceptable at this state of design (TS). If cracking is not acceptable, an intermediate support (propping) must be used (increasing the construction cost). Because of the integration of a propping system, the structural system is also changed (from a simply supported beam to a continuous beam), and tensile stresses in the upper part of the element are introduced. This calls for the addition of textile reinforcement (or other reinforcement) into new regions under tension. Regardless of the design solution adopted (i.e., allowing cracking during the TS or not), the amount of the embedded textile reinforcement should be adequate in order to undertake the tensile stresses, which are released from the cementitious matrix after cracking (accidental or not). This consideration determines the minimum textile reinforcement cross section area for the SiP formwork element and—in most cases— for the composite element when steel reinforcement is present.

In the case of unprompted SiP midspans, the total deflection of the composite element is given as the sum of calculated deflections at both the TS and the PS.

At this point, it has to be underlined that, although the high tensile loadbearing capacity of the textile reinforcement can lead to steel-free design solutions for the composite element, the authors suggest the utilization of tensile steel reinforcement in the conventional concrete topping for the following reasons:

- In cases where a deflection-dependent design is achieved, the designer (in order to increase the moment of inertia of the composite element) should also have steel reinforcement as a

design option (apart from the change of the element's dimensions). The optimum compromise between steel reinforcement content, textile reinforcement content, and geometric adjustment is detailed later in this chapter.

- For the same design loads, the absence of steel reinforcement leads to high textile reinforcement cross section area demands. Consequently, demands for advanced textile structures and cementitious matrix mixtures with high flowability are raised; this fact reflects directly on design solutions of high costs.
- The presence of steel reinforcement ensures that a sudden failure mode is avoided. This allows the designer to adopt as a desirable failure mode in flexure the rupture of textile reinforcement after the yielding of steel reinforcement. This leads to the maximum exploitation of the loadbearing capacity of steel reinforcement and, undoubtedly, of the textile reinforcement, which is the most expensive material. Also, the steel reinforcement acts as a crack arrester in the conventional concrete layer, when the crack propagates from the TRC bottom-up into the concrete topping.
- Steel corrosion issues are not raised, as the provided cementitious cover of the steel reinforcement is equal to at least 35 mm (minimum TRC thickness of 25 mm plus a 10 mm-high spacer); also, most of this cover consists of a cementitious matrix with a minimum cement dosage of 350 kg/m^3.

11.4 Design equations

11.4.1 Material laws

In order to deploy design equations and procedures, a stress–strain relationship for each material should be adopted. For textile reinforcement, a simple linear stress–strain relationship is adopted. The validity of the model is investigated in Papantoniou and Papanicolaou (2012) by the conduction of tensile and flexural tests on a wide range of TRC systems and TRC/RC composite elements.

The maximum tensile force in the composite results from the product of the failure stress of the textile reinforcement embedded in the composite and the textile's cross section area. The value of the aforementioned failure stress results from the product of an effectiveness coefficient (C_{eff}) and the tensile failure stress of the bare textile reinforcement (σ_{fu}) (almost in line with Hegger et al., 2006). The effectiveness coefficient (C_{eff}) yields from the ratio of the experimental ultimate tensile stress of the textile reinforcement in the composite element (σ_{TEX}) to the experimental ultimate tensile stress of the bare textile reinforcement (σ_{fu}). The experimental stress (σ_{TEX}) results from tensile characterization tests. Experimental results (Papantoniou, 2014) indicate that the value of C_{eff} is practically independent from the volumetric ratio of the textile reinforcement in the composite, and, as a consequence, it can be considered as a system-specific value. In some cases, such as in multilayered (e.g., four-layered) composites of a thickness in the order of 10–15 mm, a limited decrease of C_{eff} can be expected due to an insufficient matrix quantity between the textile layers. The C_{eff} coefficient accounts for all mechanisms that contribute to the decrease in the performance of textile reinforcement in the composite element. Design values for the coefficient (C_{effd}) yield from dividing the characteristic values of C_{eff} (C_{effk}) with a safety

factor (γ_{TEX}). A conservative value for γ_{TEX} equal to 1.50 is suggested. Characteristic values for C_{eff} derive from the following well-known equation.

$$x_k = \mu - k \times \sigma \tag{11.1}$$

where μ is the mean value of the experimentally derived C_{eff}; σ is the standard deviation of the experimentally derived C_{eff} values; and k is 1.64, if a 5% fractile for C_{eff} is considered.

Table 11.1 provides experimentally derived mean values of the effectiveness coefficient C_{eff} for different types of TRCs comprising different textile structures embedded in the same matrix material.

At this point, it has to be underlined that the performance of dry (i.e., uncoated or not impregnated) carbon fiber textile reinforcements is improved when the TRC composite element is subjected to flexure (Voss and Hegger, 2006; Bruckermann et al., 2007). Consequently, for this particular type of textile reinforcement, the value of C_{eff} is derived from either tensile tests (in which case the experimental value is multiplied by a conservative increasing factor) or directly from bending tests.

The tensile failure strain of TRC (ε_{cuc}) is derived from relevant characterization tests. To equate the TRC tensile failure strain with that of the bare textile reinforcement is not far from reality and has been proven both analytically (Aveston et al., 1971) and experimentally (Papantoniou, 2014).

In order to fulfill the demand for maintaining the long-term performance of the cementitious composite at a desired level, the effect of matrix alkalinity on the mechanical performance of the textile reinforcement (comprising glass fibers) should be considered. Experimental data on the issue are relatively limited (see: the work of Butler et al., 2009, 2010; Mechtcherine, 2012). Hegger and Kulas (2010) concluded that a 30% reduction in the loadbearing capacity of uncoated alkali-resistant (AR) glass textiles occurs after exposure to accelerating aging conditions, which simulate a 50-year period of real-time exposure. Hence, for the design procedure, the use of a reduction coefficient (C_{env}) for the loadbearing capacity of the textile reinforcement should be taken into account. The value of C_{env} is directly dependent upon the type of fibrous material used and the alkalinity of the cementitious matrix. In the absence of experimental data, the values proposed by ACI Committee 440 dealing with the utilization of FRP as internal reinforcement for concrete structural members, could be adopted. According to the ACI Committee 440, the C_{env} value for glass FRP bars and aggressive exposure conditions is 0.70, while the respective value for carbon FRP composites is 0.90. Figure 11.4 presents a simplified material law for the

Table 11.1 Experimentally derived mean values of the effectiveness coefficient C_{eff} for different textile structures (Papantoniou, 2014)

Type of rovings	Carbon (dry)	Carbon (coated)	AR glass (coated)
Grid spacing (mm)	10	10	10
C_{eff}	0.52	0.80	0.96
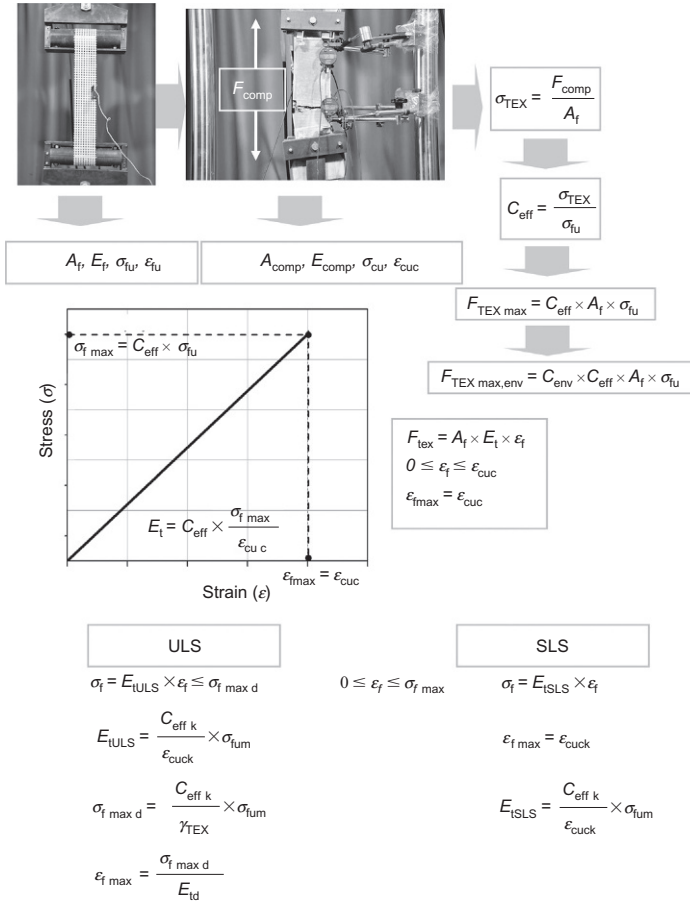
Figure 11.4 Material law for textile reinforcement.

TRC part of the composite slab, and all steps necessary for the calculation of the maximum attainable tensile force by the SiP element. It has to be underlined that, for design at ULS, the slope of the stress–strain curve is calculated by making use of C_{effd}, the σ_{fum} (mean value) and ε_{cuck} (characteristic value). For design at SLS, the value of γ_{TEX} is 1. Also, the mean value of σ_{fu} and the characteristic value of ε_{cu} are utilized.

Another consideration that is taken into account in the present design procedure is the effect of sustained loading on the loadbearing capacity of the TRC/RC composite element, an issue of limited knowledge up to now. The majority of relevant experimental results refer to FRP. The ACI Committee 440 design recommendations tackle the effect of sustained loading through the limitation of the working stress on the reinforcement. The same approach is followed herein. According to the aforementioned recommendations, the stress limit on the reinforcement (the TRC, or the textile, in this case) is equal to 20% and 55% for glass and carbon fiber textiles, respectively.

For the cementitious materials (concrete topping and cementitious matrix of the TRC), a parabolic stress–strain curve (Eurocode 2; CEN, 2004b) is considered; while, for steel reinforcement, a linear, elastic, and perfectly plastic stress–strain behavior is assumed.

11.4.2   Calculation of critical design values

- Determination of the formwork's cracking moment (M_{fcr})

The formwork's cracking moment is one of the most critical design criteria, especially when no cracking of the element is allowed at the TS, and no propping is previewed. If the contribution of the textile reinforcement to the cracking moment is not taken into account, the latter is overly underestimated. Indeed, experimental cracking moment values obtained from formwork elements—tested under four-point loading conditions—with identical cross sections but different textile reinforcement ratios (Papantoniou and Papanicolaou, 2012) varied significantly. This revealed the effect of the textile reinforcement ratio on the tensile strength of the cementitious matrix (i.e, the tensile strength of the matrix increases with increasing fiber volume fraction). This observation is in agreement with relevant findings from (homologous) tensile coupons testing. Both first crack load (in tensile TRC coupons), and cracking moment (in TRC formwork elements under bending) increase, if coated/impregnated textiles are used. Hence, not only the quantity, but also the type of utilized textiles influences the cracking moment of the formwork element. Very good correlation was observed between the experimental cracking moment and the analytical cracking moment, which was calculated by use of an experimental tensile stress obtained from characterization tests.

The equation for the analytical calculation of the formwork's cracking moment is given here:

$$M_{fcr} = \frac{\sigma_{fcr}}{y_t} \times I_{fgr} \qquad (11.2)$$

where σ_{fcr} is the stress of the extreme fiber under tension. The authors suggest the use of the experimental tensile stress corresponding to the first crack yielding from characterization tests of TRC coupon specimens furnished with the same textile reinforcement ratio as the formwork. This approach leads to a better exploitation of the textile reinforcement. I_{fgr} is the gross moment of inertia of the cross section of the TRC SiP formwork element. y_t is the distance of the extreme fiber under tension from the neutral axis of the formwork.

- Determination of the minimum textile reinforcement ratio at the TS and PS

In case of crack development, the cross section of the textile reinforcement should be adequate, in order to undertake the released tensile stresses which the cementitious matrix can no longer withstand. Consequently, the analytical expression for the determination of minimum textile reinforcement cross section area at TS is given from:

$$A_{f,min} \times \sigma_{fw} = k_c \times k \times \sigma_{fcr} \times A_{ct} \qquad (11.3)$$

where $A_{f,min}$ is the minimum cross section area of the textile reinforcement, σ_{fw} is the desirable working stress of textile reinforcement after cracking, and A_{ct} is the cross section area of the TRC SiP formwork element under tension.

Coefficients k and k_c are calculated from Eurocode 2 (CEN, 2004b) and account the effect of non-uniform self-equilibrating stresses, which lead to a reduction of restraint forces and for the stress distribution within the section prior to cracking, respectively.

The demand for an adequate quantity of tensile reinforcement (textile) in order to undertake tensile stresses after cracking is also active at the PS. In this design state the contribution of steel reinforcement in the total tensile load capacity is taken into account. Consequently, the relevant equation is:

$$F_{tex} + A_s \times \sigma_s \geq A_{ctc} \times k_c \times k \times f_{ctm} + \sigma_{fcr} \times b \times t \qquad (11.4)$$

where F_{tex} is the desirable level of developed tensile force after cracking, A_s is the cross section area of steel reinforcement, A_{ctc} is the cross section area of the part of the TRC/RC composite slab under tension, σ_s is the desirable stress level for steel after cracking, b is the width of the slab, t is the thickness of the TRC SiP formwork element's bottom flange, and f_{ctm} is the mean value of tensile strength of concrete.

11.4.3 Calculation of flexural loadbearing capacity

- Determination of flexural failure moment (M_{fu}) for the formwork element

Due to the complexity of the formwork's cross section, and for the sake of accuracy, a fiber model can be set up and used for the calculation of the failure moment of the TRC SiP formwork element. In this approach, all textile reinforcement layers located at the formwork's bottom flange are considered to be concentrated at the flange's mid-thickness. The use of a fiber model facilitates the integration of the contribution of the web textile reinforcement to the load-carrying capacity of the formwork (or the composite member at a later stage). This leads to more accurate estimations of the cross sections' moments of inertia. The failure bending moment is calculated through a simple cross section analysis. Based on the strain compatibility assumption, and depending on the failure mode considered, the strain profile across the height of the cross section is determined, and the stress of each fiber of the model is calculated from the respective material law. The contribution of the cementitious matrix of the TRC formwork element to the tensile load uptake is not ignored.

- Determination of yielding moment (M_{cy}) and failure moment (M_{cu}) for the composite element

It is advisable to also use a fiber model for the determination of the bending moment at steel yielding and at failure of the composite slab. Figure 11.5 depicts the respective fiber model and the nomenclature for a typical TRC/RC composite section. A full composite action between the formwork element and the cast-in-situ concrete topping is considered.

A_f: Cross section area of textile reinforcement

$x = \xi \times d_f$

$\xi = \dfrac{\varepsilon_c}{\varepsilon_c + \varepsilon_f}$

$\varepsilon_{s2} = \dfrac{x - d_1}{d_f - x} \times \varepsilon_f$

$\varepsilon_{s1} = \dfrac{d_s - x}{d_f - x} \times \varepsilon_f$

$b \qquad b_w = b_1 + b_2$

$F_{ci} = \sum A_{ci} \times \sigma_{ci}$

$\varphi = \dfrac{\varepsilon_c}{x} = \dfrac{\varepsilon_{s1}}{d_s - x} = \dfrac{\varepsilon_f}{d_f - x}$

$\sigma_c = f_{cm} \times \left[1 - \left(1 - \dfrac{\varepsilon_c}{\varepsilon_{c2}} \right)^n \right] \qquad 0 \leq \varepsilon_c \leq \varepsilon_{c2}$

$\sigma_c = f_{cm} \qquad \varepsilon_c \leq \varepsilon_{cu}$

$n = 2$

Figure 11.5 Fiber model and nomenclature for the composite slab.

- Closed-form equations for the determination of yielding moment M_{cy} and failure moment M_{cu} for the composite element

This part presents the closed-form equations for the calculation of the yielding moment and the ultimate failure moment of a composite TRC/RC composite slab. The equations presented are applicable to both solid- and hollow-core cross sections. The nomenclature is compatible with that given in Figure 11.5. The formulation of the equations is based on the one proposed in Fardis (2009). In order to obtain design values, design strengths are used. The following terms appear in the closed-form equations.

$$\rho_1 = \frac{A_{s1}}{b \times d_f}, \quad \rho_2 = \frac{A_{s2}}{b \times d_f}, \quad \rho_f = \frac{A_f}{b \times d_f} \tag{11.5}$$

$$\omega_1 = \frac{A_{s1}}{b \times d_f} \times \frac{f_{yd1}}{f_{cd}}, \quad \omega_2 = \frac{A_{s2}}{b \times d_f} \times \frac{f_{yd2}}{f_{cd}}, \quad \omega_f = \frac{A_f}{b \times d_f} \times \frac{f_{tu}}{f_{cd}} \tag{11.6}$$

$$a_s = \frac{E_s}{E_c}, \quad a_t = \frac{E_t}{E_c}, \quad a_{ts} = \frac{E_t}{E_s} \tag{11.7}$$

$$\delta_1 = \frac{d_1}{d_f}, \quad \delta_s = \frac{d_s}{d_f} \tag{11.8}$$

where E_c is the modulus of elasticity of in-situ concrete; E_t is the slope of the design tensile stress–strain curve of the textile reinforcement (design value); E_s is the modulus of elasticity of steel reinforcement; f_{yd1} is the design yield stress of tensile steel reinforcement; f_{yd2} is the design yield stress of compression steel reinforcement; ε_{fmax} is the design tensile strain of textile reinforcement at failure (equal to design tensile stress at failure stress divided by the design slope of stress–strain diagram); f_{tu} is the tensile failure stress of bare textile reinforcement; ε_{cu} is the ultimate compressive strain of in-situ concrete; ε_{c2} is the compressive strain at reaching the maximum stress in the parabola-rectangle stress–strain curve for in-situ concrete in compression and ε_{y2} is the strain of compressive steel at yielding.

For the calculation of the yielding moment, the depth of the neutral axis has to be calculated. A rational design goal at tensile steel yielding would be the restriction of the compressive strain of the in-situ concrete topping layer, so that it is kept less than or equal to the maximum strain corresponding to the end of the linear branch of the idealized stress–strain curve for concrete. The curvature of the composite TRC/RC cross section due to steel yielding is given by the equation:

$$\varphi_y = \frac{f_{yd1}}{E_s \times d_f \times (1 - \xi_y)} \tag{11.9}$$

From force equilibrium, the normalized over d_f depth of the neutral axis at steel yielding is given from the following equation.

$$\xi_y = \left(a_s^2 A^2 + 2 \times a_s \times B\right)^{1/2} - a_s \times A \tag{11.10}$$

where

$$A = \frac{b}{b_w} \times (\rho_1 + \rho_2 + a_{ts} \times \rho_f) + \frac{s}{d_f} \times \left(\frac{b}{b_w} - 1\right) \times \frac{1}{a_s} \tag{11.11}$$

$$B = \frac{b}{b_w} \times (\rho_1 \times \delta_s + \rho_2 \times \delta_1 + a_{ts} \times \rho_f) + \frac{1}{2a_s} \times \left(\frac{b}{b_w} - 1\right) \times \left(\frac{s}{d_f}\right)^2 \tag{11.12}$$

From moment equilibrium at the level of the textile reinforcement, the normalized yielding moment is given by:

$$\frac{My}{bd_f^3} = \varphi_y \times \left[\frac{1}{2} \times E_c \times \xi_y \times \left(1 - \frac{\xi_y}{3} \right) \times \frac{b_w}{b} + E_c \times \left(1 - \frac{b_w}{b} \right) \times \left(\xi_y - \frac{s}{2 \times d_f} \right) \right.$$

$$\left. \times \left(1 - \frac{s}{2 \times d_f} \right) \times \frac{s}{d_f} \right] + \cdots + \varphi_y \times \left[E_s \times (1 - \delta_1) \times (\xi_y - \delta_1) \times \rho_2 - E_s \right.$$

$$\left. \times (\delta_s - \xi_y) \times (1 - \delta_s) \times \rho_1 \right] \tag{11.13}$$

From equilibrium of moments at the level of the TRC reinforcement, the normalized value of ultimate failure moment is given as the sum of three terms that represent the contribution of concrete M_c, top steel reinforcement M_{Fs2}, and tensile steel reinforcement M_{Fs1}. Yielding of the tensile steel reinforcement is considered for all possible failure modes.

$$\frac{M_{cu}}{b \times d_f^2 \times f_{cd}} = \frac{M_c}{b \times d_f^2 \times f_{cd}} + \frac{M_{Fs2}}{b \times d_f^2 \times f_{cd}} + \frac{M_{Fs1}}{b \times d_f^2 \times f_{cd}} \tag{11.14}$$

The expression of each term differentiates depending on the failure mode considered and the yielding (or not) of the compression steel reinforcement. These expressions are the following:

a. Expressions for the concrete term:
    In the case of concrete crushing (prior to textile rupture), the expression is:

$$\frac{M_c}{b \times d_f^2 \times f_{cd}} = \xi_u \times \left[1 - \frac{\xi_u}{2} - \frac{1}{3} \times \frac{\varepsilon_{co}}{\varepsilon_{cu}} \times \left(1 - \xi_u + \frac{1}{4} \times \frac{\varepsilon_{co}}{\varepsilon_{cu}} \times \xi_u \right) \right] \tag{11.15}$$

    In the case of textile rupture (prior to concrete crushing), the expression is:

$$\frac{M_c}{b \times d_f^2 \times f_{cd}} = (1 - \xi_u) \times \left[\frac{\xi_u \times (2 - \xi_u)}{2 \times (1 - \xi_u)} - \frac{1}{3} \times \frac{\varepsilon_{co}}{\varepsilon_{fmax}} \times \left(1 - \xi_u + \frac{1}{4} \times \frac{\varepsilon_{co}}{\varepsilon_{fmax}} \times (1 - \xi_u) \right) \right] \tag{11.16}$$

b. Expression for the top steel reinforcement term:
    In the case of yielding of the top steel reinforcement, the expression is:

$$\frac{M_{Fs2}}{b \times d_f^2 \times f_{cd}} = (1 - \delta_1) \times \omega_2 \tag{11.17}$$

Else,

$$\frac{M_{Fs2}}{b \times d_f^2 \times f_{cd}} = (1 - \delta_1) \times \left(\frac{\xi_u - \delta_1}{\xi_u} \right) \times \frac{\varepsilon_{cu}}{\varepsilon_{y2}} \times \omega_2 \tag{11.18}$$

c. Expression for the tensile steel reinforcement term:

Yielding of the tensile steel reinforcement is considered for all possible failure modes. Hence:

$$\frac{M_{Fs1}}{b \times d_f^2 \times f_{cd}} = -(1 - \delta_s) \times \omega_1 \tag{11.19}$$

The depth of the neutral axis is calculated from force equilibrium at the cross section. The position of the neutral axis is determined by the following equations, depending on the failure mode considered and the strain of the top steel reinforcement. Different formulations are valid for the different failure modes achieved (hence, a relevant check is necessary):

i. For the case of concrete crushing (prior to textile rupture), the following two equations are valid.

For yielding of the top steel reinforcement:

$$\xi_u^2 \times \left(1 - \frac{\varepsilon_{c2}}{3\varepsilon_{cu}}\right) + \xi_u \times \left(\omega_2 - \omega_1 + \omega_f \times \frac{\varepsilon_{cu}}{\varepsilon_{f\,max}}\right) - \left(\frac{\varepsilon_{cu}}{\varepsilon_{f\,max}} \times \omega_f\right) = 0 \tag{11.20}$$

For linear elastic behavior of the top steel reinforcement:

$$\xi_u^2 \times \left(1 - \frac{\varepsilon_{c2}}{3\varepsilon_{cu}}\right) + \xi_u \times \left(\frac{\varepsilon_{cu}}{\varepsilon_{y2}} \times \omega_2 + \frac{\varepsilon_{cu}}{\varepsilon_{f\,max}} \times \omega_f - \omega_1\right) - \left(\delta_1 \times \frac{\varepsilon_{cu}}{\varepsilon_{y2}} \times \omega_2 + \frac{\varepsilon_{cu}}{\varepsilon_{f\,max}} \times \omega_f\right)$$
$$= 0 \tag{11.21}$$

ii. For the case of textile rupture (prior to concrete crushing), the following two equations apply:

For yielding of the top steel reinforcement:

$$\xi_u \times \left(1 + \frac{\varepsilon_{c2}}{3\varepsilon_{f\,max}}\right) + \omega_2 - \omega_1 - \omega_f - \frac{1}{3} \times \frac{\varepsilon_{c2}}{\varepsilon_{f\,max}} = 0 \tag{11.22}$$

For linear elastic behavior of the top steel reinforcement:

$$\xi_u^2 \times \left(1 + \frac{\varepsilon_{c2}}{3\varepsilon_{f\,max}}\right) - \xi_u \times \left(1 + \frac{2}{3} \times \frac{\varepsilon_{c2}}{\varepsilon_{f\,max}} + \omega_1 + \omega_f + \frac{\varepsilon_{f\,max}}{\varepsilon_{y2}} \times \omega_2\right) + \cdots$$
$$+ \left(\frac{1}{3} \times \frac{\varepsilon_{c2}}{\varepsilon_{f\,max}} + \omega_f + \delta_1 \times \omega_2 \times \frac{\varepsilon_{f\,max}}{\varepsilon_{y2}} + \omega_1\right) = 0 \tag{11.23}$$

11.4.4 Calculation of deflections

For uniform loading conditions of an uncracked, simply supported element (i.e., of either a standalone TRC formwork or a TRC/RC composite one-way slab), maximum deflection is calculated from the following equation:

$$\delta = \frac{5}{48} \times \varphi_\mathrm{I} \times l^2 \tag{11.24}$$

where φ_I is the element's curvature in the uncracked state (Stage I) at midspan and l is the span between supports.

The curvature φ_I is calculated from Equations (11.25) and (11.26) for the TS and the PS, respectively. At this point, it has to be noted that if formwork cracking (during the TS) occurs, then the contribution of the finely gained concrete matrix to the gross moment of inertia of the TRC/RC composite cross section (I_cgr) should be neglected, and only textile reinforcement should be taken into account.

$$\varphi_\mathrm{I} = \frac{M_\mathrm{fcr}}{E_\mathrm{m} I_\mathrm{fgr}} \tag{11.25}$$

$$\varphi_\mathrm{I} = \frac{M_\mathrm{ccr}}{E_\mathrm{com} I_\mathrm{cgr}} \tag{11.26}$$

where M_ccr is the cracking moment of the TRC/RC composite section. For the calculation of this moment, a cracking stress has to be determined. The mean tensile strength of the cast-in-situ concrete (f_ctm) would pose a conservative option. I_cgr is the gross moment of inertia of the TRC/RC composite section. E_com is the modulus of elasticity of the TRC/RC composite element, which can be calculated according to the rule of mixtures, namely the sum: $E_\mathrm{c} \times V_\mathrm{c} + E_\mathrm{m} \times V_\mathrm{m}$, where V_c and V_m are the volumetric ratios of the cast-in-situ concrete and cementitious matrix, respectively. The steel reinforcement and textile reinforcement can be neglected.

In most cases, the calculations for deflections at the PS are performed in the cracked state (Stage II). Similar calculations in the uncracked state are also performed at the TS, if development of cracking occurs.

As MC2010 proposes, instantaneous deflections should be calculated through double integration of curvatures along the member length. The member is divided into segments, and at each integration point (i) with an acting moment (M_i), the respective curvature (φ_i) is calculated for both an uncracked $\left(\dfrac{M_i}{E \times I_\mathrm{gr}}\right)$ and a fully cracked $\left(\dfrac{M_i}{E \times I_\mathrm{u}}\right)$ stage. For the calculation of the moment of inertia at a fully cracked stage, the neutral axis position has to be determined. For the TS (i.e., for the TRC SiP formwork element), the depth of the neutral axis corresponds to the textile rupture. For the PS (i.e., for the TRC/RC composite element), the depth of the neutral axis corresponds to the tensile steel yielding, even though the element exhibits significant post-yield load-carrying capacity. Finally, Equation (11.27) provides the values of φ_i, taking into account tension stiffening.

$$\varphi_i = \left(1 - \beta \times \left(\frac{M_{\mathrm{cr}}}{M_{i\mathrm{sd}}}\right)^2\right) \times \varphi_{\mathrm{II}i} + \beta \times \left(\frac{M_{\mathrm{cr}}}{M_{i\mathrm{sd}}}\right)^2 \times \varphi_{\mathrm{I}i} \tag{11.27}$$

where $\varphi_{\mathrm{I}i}$ is the curvature at integration point i, calculated assuming an uncracked stage (linear elastic response). $\varphi_{\mathrm{II}i}$ is the curvature at integration point i, calculated assuming a fully cracked stage. β is the coefficient accounting for the influence of the duration of loading or repeated loading. M_{cr} is the cracking moment. $M_{i\mathrm{sd}}$ is the design moment at integration point i.

It should be noted that, generally, curvatures resulting from the differential shrinkage of the TRC and cast-in-situ components of the composite slab should be taken into consideration. Nevertheless, the issue is not dealt with herein.

11.4.5 Calculations for crack widths

The crack width calculations, as proposed by the MC2010, for conventionally reinforced concrete members can also be implemented in the case of TRC/RC hybrid members. If cracking at the TS is (from a design point of view) acceptable, then calculations for crack widths should also be carried out for this state. Neglecting shrinkage-induced strains, the design crack width is given from the following equation.

$$w_{\mathrm{d}} = 2 \times \ell_{\mathrm{fmax}} \times (\varepsilon_{\mathrm{fm}} - \varepsilon_{\mathrm{mm}}) \tag{11.28}$$

Where

$$\varepsilon_{\mathrm{fm}} - \varepsilon_{\mathrm{mm}} = \frac{\sigma_{\mathrm{f}} - k_{\mathrm{t}} \times \dfrac{f_{\mathrm{mt}}}{\rho_{\rho,\,\mathrm{eff}}} \times \left(1 + a_{\mathrm{tm}} \times \rho_{\rho,\,\mathrm{eff}}\right)}{E_{\mathrm{t}}} \tag{11.29}$$

$$\rho_{\rho,\,\mathrm{eff}} = \frac{A_{\mathrm{f}}}{A_{\mathrm{m,\,eff}}} \tag{11.30}$$

where $\varepsilon_{\mathrm{fm}}$ is the mean tensile strain of the textile reinforcement over ℓ_{fmax}. $\varepsilon_{\mathrm{mm}}$ is the mean tensile strain of the cementitious matrix over ℓ_{fmax}. ℓ_{fmax} is the length along which slippage between the textile reinforcement and the surrounding the cementitious matrix occurs. $A_{\mathrm{m,eff}}$ is the effective area of the cementitious matrix in tension (details given in MC2010). f_{mt} is the mean tensile strength of the cementitious matrix. k_{t} is the coefficient dependent on the duration of the loading. σ_{f} is the stress in the textile reinforcement for the given magnitude of the load. α_{tm} is the modular ratio $E_{\mathrm{t}}/E_{\mathrm{m}}$.

From force equilibrium, it yields that:

$$\ell_{f\,max} = \frac{\sigma_{fcr} \times A_{m,\,eff}}{\tau_f \times U_{TEX}} \tag{11.31}$$

where τ_f is the mean bond stress of the textile reinforcement, and U_{TEX} is the contact area between the cementitious matrix and the textile reinforcement.

The product $\tau_f \times U_{TEX}$ is a characteristic value for a given textile/matrix combination (i.e., for a specific TRC composite) and can be derived from characterization tests on tensile coupon tests with equivalent textile reinforcement ratios. Assuming that the measured experimental crack spacing X is equal to $1.337 \times \ell_{f\,max}$ (Cuypers and Wastiels, 2006), force equilibrium yields:

$$\tau_f \times U_{TEX} = 1.337 \times \frac{\sigma_{fcr} \times A_{spe}}{X} \tag{11.32}$$

where A_{spe} is the cross section area of the tensile test coupon.

Regarding crack width calculations at the PS, the designer has to bear in mind that the stress is carried by both the fibrous and the steel reinforcement. Literature related to the textile/steel interaction is limited (Weiland et al., 2010). Nevertheless, this issue can be dealt with following the MC2010 approach, referring to mixed, prestressed, and conventionally reinforced concrete members. The basic assumption for the adoption of the formulations to follow is that both the textile and the steel reinforcement share the same crack width. From force equilibrium, the stress of the textile reinforcement can be expressed in terms of the steel reinforcement ratio.

$$\sigma_f = \frac{\ell_{s,\,max}}{\ell_{f,\,max}} \times \frac{E_t}{E_s} \times \sigma_s \tag{11.33}$$

With

$$\frac{\ell_{f,\,max}}{\ell_{s,\,max}} = \sqrt{\frac{E_t \times A_f}{E_s \times A_s} \times \frac{\tau_s}{\tau_f} \times \frac{U_s}{U_{TEX}}} \tag{11.34}$$

Resulting to

$$\sigma_f = \sqrt{\frac{E_t \times A_s}{E_s \times A_f} \times \frac{\tau_f}{\tau_s} \times \frac{U_{TEX}}{U_s}} \times \sigma_s \Rightarrow \sigma_f = \sqrt{\xi_1} \times \sigma_s \tag{11.35}$$

where $\ell_{s,max}$ is the length along which slippage between steel reinforcement and surrounding cast-in-situ concrete occurs. τ_s and τ_f are the mean bond stress of steel and textile reinforcement, respectively. U_s is the perimeter of steel rebar.

and

$$\xi_1 = \frac{E_t \times A_s}{E_s \times A_f} \times \frac{\tau_f}{\tau_s} \times \frac{U_{TEX}}{U_s} \tag{11.36}$$

The crack width can be determined by the equation:

$$w_d = 2 \times \ell_{s\,max} \times (\varepsilon_{sm} - \varepsilon_{sm}) \tag{11.37}$$

where

$$\varepsilon_{sm} - \varepsilon_{cm} = \frac{\sigma_s - k_t \times \dfrac{f_{ctm}}{\rho_{\rho,\,eff}} \times (1 + a_s \times \rho_{\rho,\,eff})}{E_s} \tag{11.38}$$

$$\rho_{\rho,\,eff} = \frac{A_s + \xi_1^2 \times A_f}{A_{c,\,eff}} \tag{11.39}$$

where f_{ctm} is the tensile strength of cast-in-situ concrete.

11.4.6 Calculations for sustained loading

Considering that the position of the neutral axis of the composite section remains unchanged at Stage II, a cross section analysis is performed for $\xi = \xi_y$ and σ_f equal to the limiting sustained stress in order to calculate the sustained moment in the section for the given strain distribution. The derived limiting moment is compared with the respective acting design moment.

11.4.7 Calculations for shear

Calculations for shear should be conducted at both design states. Regarding the calculations at the TS, the equations proposed by Voss and Hegger (2006) could be adopted. Regarding the PS, checks for vertical and longitudinal shear should be conducted at the interfaces of the critical sections, as those presented in MC2010. Also, checks in the uncracked areas from bending near the supports of the composite should be conducted.

11.5 Formulation of optimum (minimum cost) design

A structural optimization process aims to determine the values of critical design parameters that fulfill the objective of extremizing an overall target property (e.g., minimizing cost), while satisfying a set of performance requirements under given constraints.

11.5.1   Mathematical expression

The mathematical expression of a typical optimization problem is given below.

Let X be the set of design variables within S.

$$X = [x_1, x_2, \ldots, x_n] \in S \tag{11.40}$$

where $x_i \in S_i$ and $S = S_1 \times S_2 \times \cdots \times S_n$, $S \subseteq R$, $i = 1, 2, \ldots, n$.

X minimizes (or maximizes) the function $f(X)$, while simultaneously satisfying the constraints:

$$g_j(X) \leq 0, \quad j = 0, 1, 2, \ldots, m \tag{11.41}$$

$$I_k(X) = 0, \quad k = 0, 1, 2, \ldots, p \tag{11.42}$$

11.5.2   Design variables and objective function

The majority of structural optimization problems aim to minimize the structural element's weight. In many cases, the element's weight also reflects the minimization of the total production cost (this is especially true for FRP and/or structural steel elements). The optimum design formulation presented herein aims to minimize the production cost of TRC/RC composite one-way slabs, excluding cost factors such as the SiP formwork element's transportation and erection expenditures, costs associated to the production facilities (which are perceived as fixed production plant investment costs), or any other labor-related costs. Hence, only material costs are taken into account.

In order to achieve realistic optimum design solutions—and to save in computational time—a careful selection of the design variables is imperative, as they must have a direct impact on the target property under optimization (in this case, on the cost). Under this scope, the main criterion for the selection of a design variable is the degree of participation in the total cost of the composite element. As will be discussed in the following paragraphs in more detail, the production cost of the TRC SiP formwork element amounts to approximately 70% of the TRC/RC composite production cost. Consequently, the design variables of the formwork element (e.g., the textile reinforcement ratio and the shape-forming geometric parameters) are of major importance to the procedure.

The global design variables of the problem presented herein can be classified into two categories. The first one includes the parameters that define the cross section geometry for both elements (i.e., for both the TRC SiP formwork element and the resulting composite one). Different formwork cross sections may be considered, such as hollow tapered (or else "capped" or "delta") or "channel" shaped ones (see Figures 11.6 and 11.7, respectively). Although different production set-up costs may be (and in reality are) associated with different cross sections (depending on the degree of manufacturing difficulty of each cross section), no such considerations are taken into account in the procedure. Geometric parameters include the ratio of the
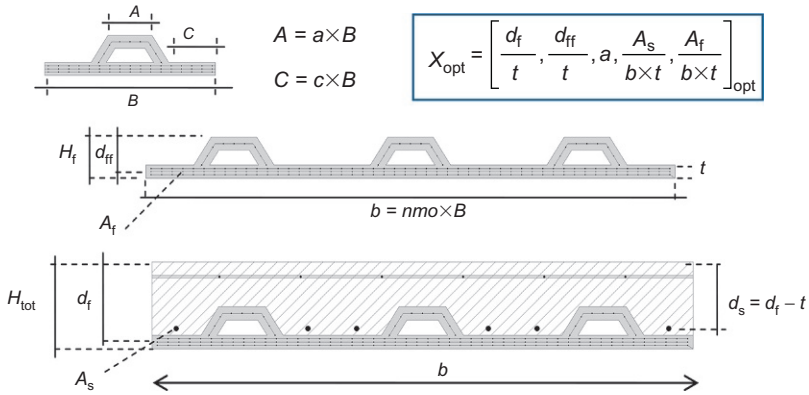
Figure 11.6 Cap-shaped section and the respective design variables for optimization.
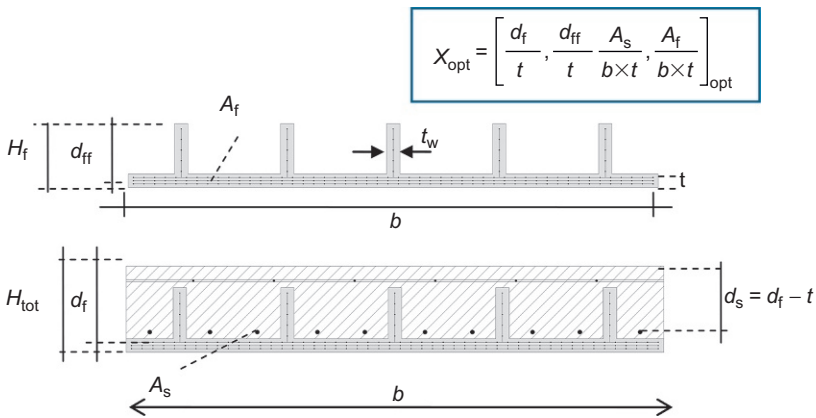
Figure 11.7 Channel shaped section and the respective design variables for optimization.

effective depth of the textile reinforcement in the composite member (measuring from the reinforcement middle layer level to the full height of the composite member) to the thickness of the TRC element (d_f/t). The ratio of the effective depth of the textile reinforcement in the TRC element (measuring from the reinforcement middle layer level to the height of the TRC element) to the thickness of the TRC element (d_{ff}/t) is also included. Cross section-specific (local geometric) design parameters are also assigned for each type of cross section considered. For example, coefficients α and c in Figure 11.6 control the formwork's "cap" shape and correspond to the ratios of dimensions A and C, respectively, to the width of the formwork's basic module, B. The second category of design variables includes the textile and steel reinforcement ratios ($A_f/b \times t$ and $A_s/b \times t$, respectively). For the sake of generality, it should be noted that, as in the case of structural performances, the design variables are introduced to the problem in a normalized form. Here, they are normalized over the SiP formwork

element's thickness and, where appropriate, the composite element's width. The design variables' vector is also presented in Figures 11.6 and 11.7. Another design variable that is probably quite decisive for the overall cost of the TRC/RC composite element is the tensile strength of the cementitious matrix that comprises the TRC formwork. Taking into account that the cost of a high-performance cementitious mixture is generally a nonlinear function of its compressive strength, and expressing the tensile strength of such a material in terms of its compressive strength, one could expand the design variables vector to include the compressive strength of the cementitious matrix in the TRC formwork. Nevertheless, what is even more important is to identify those design parameters that maximize the matrix-to-textile bond capacity. This is a complex task involving many difficult-to-quantify parameters, such as the type of rovings' coatings (if any), the degree of mortar penetrability through the grid's openings, the effect of multiple textile layers, etc. Hence, in the procedure described in this chapter, the characteristic compressive strength of the mortar and the associate cost per unit volume are considered as input. Other individual material costs are given in the worked example section. The total cost objective function of the problem is given by the following equation.

$$C = C_c \times \frac{A_c}{bd_s} + C_m \times \frac{A_m}{bd_f} + C_s \times \gamma_s \times \rho_s + C_{tex} \times \gamma_f \rho_f \qquad (11.43)$$

where C is the total cost of the composite slab per unit of reference volume (€/m³). (As reference volume is taken, the product is ℓbd_f, where ℓ and b are the length and the width of the element respectively, and d_f is the effective depth of the slab.) C_m is the cost of cementitious matrix of TRC (€/m³). C_s is the cost of steel reinforcement per weight unit (€/g). C_{tex} is the cost of textile reinforcement per weight unit (€/g). C_c is the cost of normal concrete per volume unit (€/m³). A_c and A_m are the cross section area of normal and fine concrete, respectively. γ_s and γ_f are the density of steel and fibrous material, respectively. ρ_s and ρ_f are the steel and textile volumetric reinforcement ratio, respectively. The volumetric reinforcement ratio is defined as the ratio of the cross section area of the reinforcing material to the product bd_f.

11.5.3   Constraints

The mathematical constraints are posed by the demand that all calculated performance (i.e., structural response) values derived from the serviceability and ultimate limit states are less than or equal to the ones that cause failure, or are unacceptable in terms of user' comfort. Geometric-specific constraints are also imposed on individual cross sections, dictated by both geometric compatibility conditions between the TRC formwork elements, and the resulting composite elements. Anthropometric restrictions that take into account the on-site constructability and site safety are also considered. Additionally, the design variables vector is set to vary between a lower and an upper bound; these bounds are selected based, mainly, on practical considerations, as code-imposed

values are nonexistent. All inequality and equality constraints applicable to the problem at hand are given in Tables 11.2–11.4.

11.5.4   Optimization procedure using genetic algorithms

The optimum design procedure presented in this chapter can be programmed and solved using a multitude of different algorithms. Among these, genetic algorithms pose an interesting alternative, especially for highly nonlinear problems. A genetic algorithm (GA) is a method for solving both constrained and unconstrained optimization problems based on a natural selection process that mimics biological evolution.

Table 11.2 Inequality constraints for the TRC SiP formwork element

TRC SiP in TS			
Limit state	**Expression**	**Description**	**Comment**
Serviceability	$\mu_{sd} - \mu_{cr} \leq 0$	No cracking	Midspan–bottom flange
Serviceability	$\mu_{sdrev} - \mu_{crrev} \leq 0$	No cracking	Upper flange-on support
Ultimate	$\mu_{sd} - \mu_{rd} \leq 0$	Failure moment	–
Ultimate	$v_{vsd} - v_{vrd} \leq 0$	Vertical shear	–
Serviceability	$\delta_f - \delta_{flim} \leq 0$	Deflection after casting	$\delta_{flim} = l/400$
Serviceability	$w_f - w_{flim} \leq 0$	Crack width	–
Serviceability	$\rho_{ffmin} - \rho_{ff}^1 \leq 0$	Minimum textile reinforcement ratio	See Equation (11.3)

Table 11.3 Inequality constraints for the composite element

Composite slab in PS			
Limit state	**Expression**	**Description**	**Comment**
Ultimate	$\mu_{sd} - \mu_{rd} \leq 0$	Failure moment	–
Ultimate	$v_{Ed} - v_{Rd,c} \leq 0$	Vertical shear	Cracked areas
Ultimate	$v_{Ed} - v_{Rd,unc} \leq 0$	Vertical shear	Uncracked areas
Ultimate	$v_{Ed,i} - v_{Rd,i} \leq 0$	Longitudinal shear	–
Serviceability	$\delta_{tot} - \delta_{lim} \leq 0$	Deflection	$\delta_{lim} = l/250$, $\delta_{tot} = \delta_{TS} + \delta_{PS}$
Serviceability	$w_{tot} - w_{lim} \leq 0$	Crack width	–
Serviceability	$\sigma_f - k_f \times \sigma_{fukmax} \leq 0$	Stress limitation	$k_f = 0.20$ for glass textiles
Serviceability	$F_{tex} + A_s \times \sigma_s \geq A_{ct} \times k_c \times k \times f_{ctm} + \sigma_{cr} \times b \times t$		See Equation (11.4)

Table 11.4 Geometric and special constraints

Composite slab in PS		
Limit state	**Expression**	**Description**
Ultimate	$\varepsilon_f - \varepsilon_{fu} = 0$	Desirable failure mode
Ultimate	$\varepsilon_{sy} - \varepsilon_{suls} \leq 0$	Failure after steel yielding (tensile steel strain level at the fracture of textile reinforcement should be higher from yield stress)
Serviceability	$\varepsilon_{csy} - \varepsilon_{c2} \leq 0$	Linear behavior of concrete at steel yielding
–	$50 - H_{tot} + H_f \leq 0$	Minimum concrete depth between the top surface of the concrete slab and the upper flange of the SiP element
–	$d_f = d_s + t$	Geometric constraints

The algorithm repeatedly modifies a population of individual solutions. At each step, the GA selects (either randomly or according to user-specified rules) individuals from the current population and uses them as parents to produce the children for the next generation. Over successive generations, the population "evolves" toward an optimal solution (Matlab®). The results shown in the worked example section of this chapter are derived from solving the optimum design problem using the GA functions provided in the Global Optimization Toolbox of the Matlab® platform.

The specifics of the solving procedure are briefly presented next. Algorithm convergence is facilitated by the use of a population of at least 180 individuals. The structure of the next generation is advised not to be entirely random, but to consist of the two best performing individuals (i.e., those with the lower cost) from the previous generation, as well as 107 and 71 individuals resulting from crossover and mutation, respectively, of randomly selected individuals from the previous generation. The tolerance criterion for the constraints was 1×10^{-5}, and the convergence-stop criterion for the objective function was 0.10€.

11.5.5 Worked example

The following example illustrates the design solutions attained for a TRC/RC composite slab that yield the minimum production cost of the finished product. More specifically, the design basis is a TRC SiP formwork element of a "cap shaped" cross section comprising three modules (three "caps" per unitary width). In order to minimize the computational time and to simplify the presentation of the results, coefficient c was 0.25. This assumption is not far from reality, as preliminary runs (which included coefficient c as a design variable) revealed that this coefficient remains fairly unaffected by other variables' fluctuations. It has a mean value of 0.25. Additionally, this value satisfies the anthropometric constraint related to the available step area for workers.

Analyses were carried out for propped formwork elements, with propping placed at midspan; the resulting composite members were simply supported, one-way slabs with a width equal to 1.0 m. The investigated span lengths ranged between 2.0 and 6.0 m, with an incremental step equal to 250 mm. The permanent load (G) was taken equal to 3.0 kN/m^2, whereas three levels of live load (Q) were explored, namely 3.0, 5.0, and 7.5 kN/m^2. Runs were performed in a batch mode, and the available design resources (lower and upper bounds for each design variable) were the same for all spans and design loads. Flexural loadbearing capacities and cross-sectional characteristics were calculated using a fiber model.

A polymer-coated 2D E-glass textile was selected as reinforcement for the cementitious composite. Steel reinforcement of class B500C was used as conventional reinforcement for the cast-in-situ concrete topping (placed adjacent to the TRC/RC interface); a welded wire mesh (Ø4.2/150, not subjected to optimization) was also included close to the composite element's top surface in order to minimize shrinkage- and/or handling-induced cracking. A cementitious mortar with a maximum grain size equal to 4 mm and a conventional C20/25 concrete mix were assumed for constructing the TRC formwork element and the cast-in-situ topping, respectively. Finally, a full composite behavior between concrete topping and SiP element was considered. Consequently the constraint for longitudinal shear was inactive. Tables 11.5–11.7 list key mechanical properties (characteristic values), safety factors, and costs. For the cost derivation of the cementitious matrix, the mix design depicted in Table 11.8 was considered.

For the specific worked example, a conservative σ_{fcr} value equal to 2.75 MPa was taken into account, regardless of the sensitivity of the value to textile reinforcement volumetric ratio. This value yields from experimental investigation on tensile coupon tests carrying the textile reinforcement, which is utilized in this example.

Table 11.5 Key mechanical properties for the analyses

Steel reinforcement	Coated E-glass textile reinforcement				Cementitious mortar	Conventional concrete
f_{yk}	C_{effk}	σ_{fum}	ε_{cuk}	C_{env}	f_{mk}	f_{ck}
500 MPa	0.45	1111 MPa	9.35‰	0.70	45 MPa	20 MPa

Table 11.6 Adopted safety factors for the materials

	Steel	Coated E-glass textile reinforcement	Cementitious mortar	Conventional concrete
Safety factor	1.15	1.50	1.50	1.50

Table 11.7 Cost of materials

	Steel	Coated E-glass textile reinforcement	Cementitious matrix	Conventional concrete
	C_s	C_{tex}	C_m	C_c
	€/kg	€/g	€/m³	€/m³
Cost	0.80	0.02	147.3	77.0

Table 11.8 Mix design for the derivation of cost of cementitious matrix

Material	Density (kg/m³)	Unit	Mass per m³
Cement CEM II 42.5N (C)	2900	kg	450
Polymers (3% per weight of cement)	500	kg	13.5
Antifoam powder (0.3% per weight of total mix weight)	350	kg	0.255
Calcium carbonate powder	2700	kg	260
Sand 0/2	2620	kg	–
Sand 0/4	2420	kg	1185
Super-plasticizer	1010	lt	5.8
Water (W)	1000	kg	224
Water to cement ratio ($w = W/C$)	–	–	0.43
Total weight		kg	2138.9

The lower and upper bounds for each design variable are given in Table 11.9. For the textile reinforcement, the minimum and maximum cross section area reflects three layers of textile reinforcement with a nominal thickness of 0.054 mm each. Four layers of textile reinforcement have a nominal thickness of 0.125 mm.

Figures 11.8–11.13 depict the results for the optimum (minimum cost) design problem. More specifically, Figure 11.8 depicts the optimum effective depth of the textile reinforcement in the composite slab and in the formwork element. Also, the bottom

Table 11.9 Upper and lower bound for design variables

	x_1	x_2	x_3	x_4	x_5
	d_f	d_{ff}	α	A_s	A_f
	mm	mm	–	mm²	mm²
$X_{i\min}$	100	65	0.25	200	162.5
$X_{i\max}$	400	325	0.60	550	500
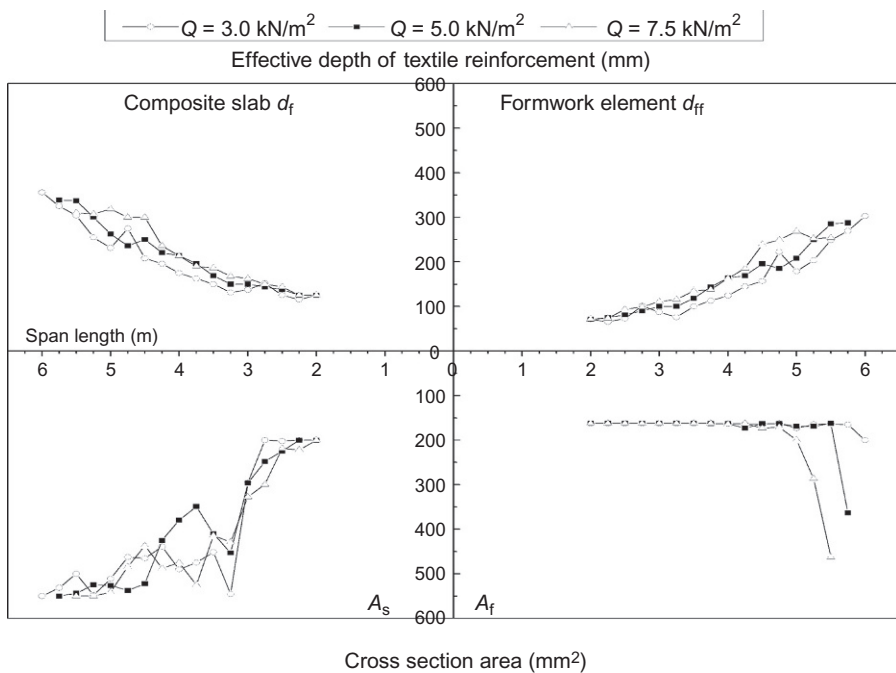
Figure 11.8 Effective depth (SiP & slab) and cross section reinforcement (steel & textile).
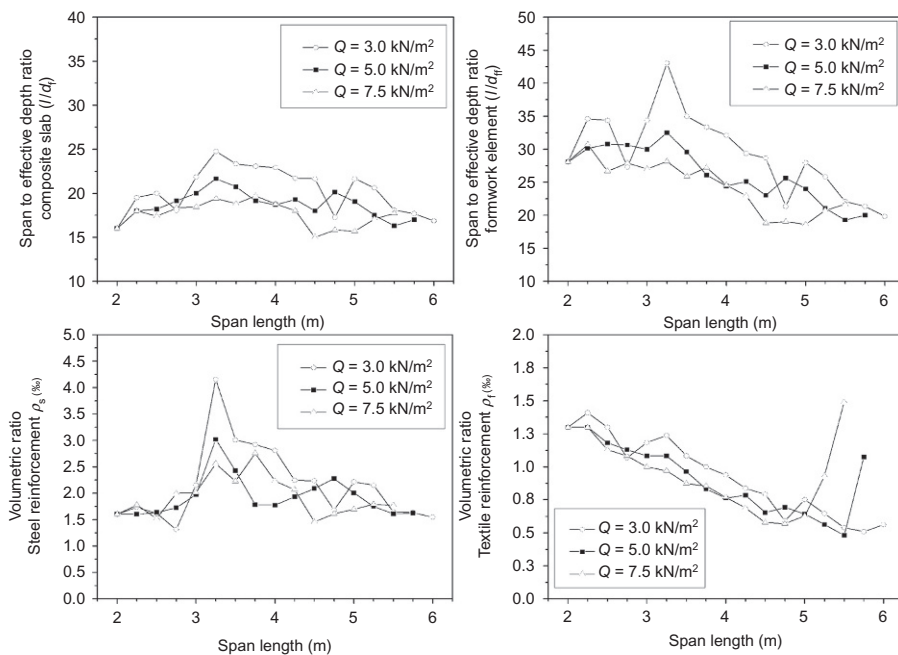
Figure 11.9 Normalized values of design parameters.
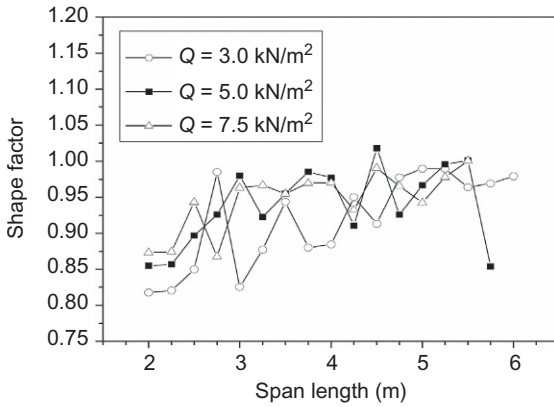
Figure 11.10 Shape factor of SiP's cross section.
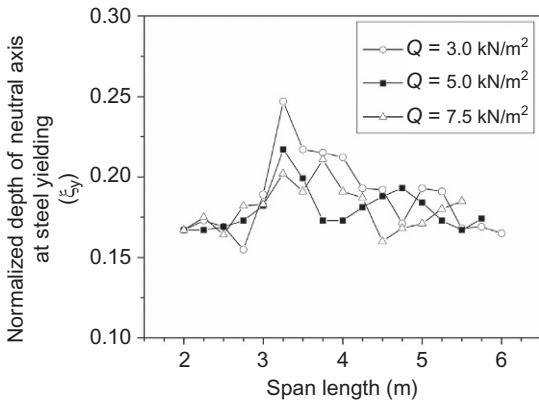
Figure 11.11 Normalized depth of neutral axis at steel yielding.
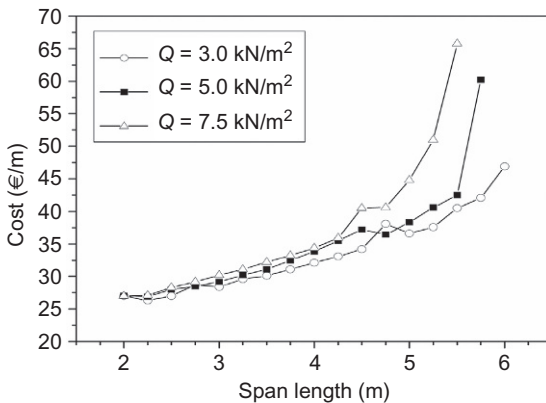
Figure 11.12 Cost per running meter for each design solution.
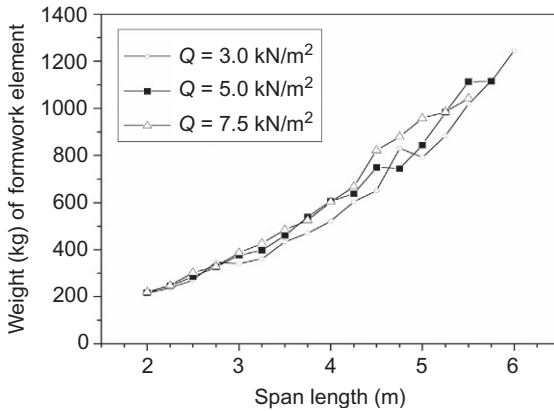
Figure 11.13 Weight of the formwork for each design solution.

subgraphs of the same figure present the optimum cross section areas for both textile and steel reinforcements. Figure 11.9 presents the results in a normalized form. More specifically, the composite's and SiP formwork element's slenderness ratios $\left(\frac{l}{d_f \text{ or } d_{ff}}\right)$ are given. Also, the volumetric ratio of the textile $\left(\frac{A_f}{b \times d_f}\right)$ and steel reinforcement $\left(\frac{A_s}{b \times d_f}\right)$ in the composite slab are presented. Figure 11.14 depicts the ratios (r) of certain design values of performance requirements (i.e., certain "$_{Sd}$" values) to the respective maximum allowable ones at failure (i.e., the respective "$_{Rd}$" values). Specifically, the figure depicts values corresponding to: (1) the cracking moment for the TRC SiP formwork element $r_{M_{cr} @ SiP}$, (2) the bending moment for the composite element $r_{M_{cu}}$, (3) the deflection for the composite element at the SLS $r_{\delta_c @ SLS}$, and (4) the sustained tensile stress in the textile reinforcement to avoid creep rupture, $r_{\sigma_{fum \, sustained}}$. Values of ratio r close to unity denote the activation of the respective design constraint. For each feasible combination of span length and live load level, more than one constraint may be active.

The fifth parameter for optimization is presented indirectly through the shape factor coefficient in Figure 11.10. Also, for each design solution, the neutral axis (normalized by effective depth of textile reinforcement d_f) at steel yielding is given in Figure 11.11. Finally, the achieved minimized production cost per running meter and the total weight of each formwork are presented in Figures 11.12 and 11.13, respectively. As can be inferred by the aforementioned figures, the convergence of the algorithm to a feasible solution was not possible in three cases: for (span length, live load) = (6.0 m, 5.0 kN/m^2), (7.5 m, 5.75 kN/m^2), and (7.5 m, 7.5 kN/m^2). The available design sources were not adequate for these design combinations. The spikes-free minimum cost curve is indicative of the effectiveness of the optimum design procedure that was followed and of the algorithm that was implemented.

As depicted in Figure 11.8, the algorithm results in optimum design solutions that favor the gradual increase of the effective depth (both that of the TRC SiP formwork element and of the composite slab), while keeping the textile reinforcement area at

minimum for as long as possible. It also adjusts the amount of steel reinforcement accordingly. This trend applies roughly until the span reaches 5 m in length. For longer spans, the textile reinforcement must increase; this need arises at shorter spans as the live load increases. Comparing the shape of the resulting curve of Figure 11.12 with that of the optimum cross section area for the textile reinforcement, a direct relation is observed. Cost increases abruptly with an increase of the textile content for spans longer than approximately 5 m.

From the above, it becomes clear that the algorithm yields the minimum cost solution by giving priority to low-cost design alternatives (an increase of steel reinforcement ratio and a decrease of the member's slenderness). Textile reinforcement is only increased in cases where all the other resources are fully exploited under the given constraints.

Another interesting observation is that the increase in the composite slab's effective depth is always linked to a respective increase in the effective depth of the formwork itself; the latter leads to the increase of the formwork's moment of inertia and to the minimization of the cast-in-situ concrete volume. The need for achieving the maximum moment of inertia for the formwork is also indicated by the increase of the shape factor value; values close or equal to unity indicate a perpendicular arrangement of TRC webs in regards to the TRC bottom flange.

Regarding the activation of design constraints, refer to Figure 11.14. From here, it can be argued that for nearly all feasible span and live load combinations, at least one constraint is activated (none of which is the one corresponding to the cracking moment
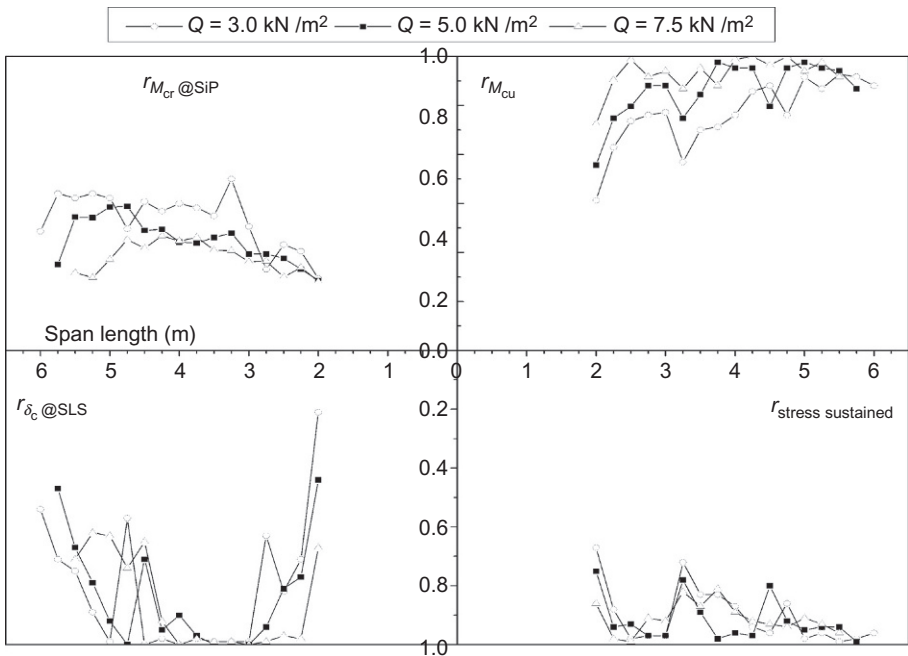
Figure 11.14 Adequacy ratios (demand value to performance of element).

of the TRC SiP formwork element, as propping has been previewed). The simultaneous activation of different design constraints denotes the efficiency of the algorithm in terms of solving for global minimum costs.

11.6 Summary and future trends

In the first part of this chapter, a design procedure was introduced for one-way composite slabs comprising a participating SiP textile-reinforced concrete formwork element monolithically connected to a concrete topping reinforced with conventional steel reinforcement. Closed-form equations for the determination of critical design performances were also presented. In the second part of the chapter, the proposed design procedure was integrated into an optimum design methodology. The aim was to determine key design parameters that result in the minimum cost design solution for given spans and design loads. A worked example was used to demonstrate the effectiveness of the methodology. Input data for the example was limited to a single type of TRC, whereas propping had been previewed for the on-site production phase.

From the results, the authors deduced that the dominating design criteria, which are pointed out from the value of design constraints, are the deflection of the composite slab in SLS, the stress limitation in textile reinforcement for permanent loading, and the design failure moment in ULS for the composite. For moderate span lengths ranging from 3 to 4 m, the defection constraint is the dominating design constraint, where the most slender solutions are achieved. Depending on the live load level, a shift in this area, just as in all the design curves, is observed. For spans greater than 5 m, the critical design constraint is the stress limitation criterion accompanied by the loadbearing capacity criterion. Also, the presence of support under the midspan of the formwork element deteriorated the severity of the SiP's cracking moment constraint.

The analytical results highlight the directions for future research. Specifically, the flexural behavior of RC/TRC composite slabs under permanent loading should be investigated. Regarding the exhibited deformation of these elements, experimental results should be obtained in order to verify and improve the adopted material law (e.g., a bilinear model could be adopted).

Regarding the optimum design procedure, the possible improvements involve the integration of the weight of the SiP element into the optimum design procedure. Also, it would be of great interest to integrate to the group of objective functions that concern the carbon footprints of the respective elements.

References

ACI 440 (IR-03). Guide for the design and construction of concrete reinforced with FRP bars.

Aveston, J., Cooper, G.A., Kelly, A., 1971. The properties of fiber composites. In: Conference Proceedings, National Physical Laboratory (IPC Science and Technology Press Ltd), Paper 1, p. 15.

Brameshuber, W., Koster, J., Hegger, J., Voss, S., 2008. Integrated formwork elements made of textile reinforced concrete. ACI SP 250 104 (5), 35–48.

Bruckermann, O., Hegger, J., Sherif, A., 2007. Modeling of textile reinforced concrete with inclined textile orientation. ACI Mater. J. 104, 511–519.

Butler, M., Mechtcherine, V., Hempel, S., 2009. Experimental investigations on the durability of fibre–matrix interfaces in textile-reinforced concrete. Cem. Concr. Compos. 31 (4), 221–231.

Butler, M., Mechtcherine, V., Hempel, S., 2010. Durability of textile reinforced concrete made with AR glass fibre: effect of the matrix composition. Mater. Struct. 43 (10), 1351–1368.

CEN, 2002. European Standard EN 1991-1-1:2002 Eurocode 1: Actions on Structures Part 1-1: Densities, Self-Weight, Imposed Loads for Buildings. Comité Européen de Normalisation, Brusells.

CEN, 2004a. European Standard EN 1991-1-6:2004 Eurocode 1: Actions on Structures Part 1-6: Actions During Execution. Comité Européen de Normalisation, Brusells.

CEN, 2004b. European Standard EN 1992-1-1:2004 Eurocode 2: Design of Concrete Structures Part 1-1: General Rules and Rules for Buildings. Comité Européen de Normalisation, Brusells.

Cuypers, H., Wastiels, J., 2006. A stochastic cracking theory for the introduction of matrix multiple cracking. In: Hegger, J., Brameshuber, W., Will, N. (Eds.), Proceedings of the 1st International RILEM Symposium Textile Reinforced Concrete, Aachen, Germany, pp. 193–202.

Fardis, M., 2009. Seismic Design Assessment and Retrofitting of Concrete Buildings. Springer, Dordrecht.

fib (2012), fib Model Code for Concrete Structures, 2010a. Final draft, Bulletin No. 65, Berlin, Ernst & Sohn.

fib (2012), fib Model Code for Concrete Structures, 2010b. Final draft, Bulletin No. 66, Berlin.

Hegger, J., Will, N., Bruckermann, O., Voss, S., 2006. Load-bearing behaviour and simulation of textile reinforced concrete. Mater. Struct. 39 (8), 765–776.

Hegger, J., Kulas, C., 2010. TRC pedestrian bridge-design load-bearing behavior and production processes of a slender and light weight construction. In: Brameshuber, W. (Ed.), Proceedings of the 2nd International RILEM Symposium Textile Reinforced Concrete, Aachen, Germany, pp. 353–364.

Matlab®, e-manual for genetic algorithms. http://www.mathworks.com/discovery/genetic-algorithm.html.

Mechtcherine, V., 2012. Towards a durability framework for structural elements and structures made of or strengthened with high-performance fibre-reinforced composites. Constr. Build. Mater. 31, 94–104.

Papantoniou, I.C., Papanicolaou, C.G., 2012. Flexural behavior of one-way textile reinforced concrete (TRC)/reinforced concrete (RC) composite slabs. In: Proceedings of the 15th European Conference on Composite Materials—ECCM15, Venice, Italy, 24–28 June 2012 (in CD Proceedings).

Papantoniou, I., 2014. Reinforced concrete composite slabs cast over stay-in-place textile reinforced concrete formwork elements: experimental investigation and optimum design. Ph.D. Thesis, University of Patras (in Greek).

Papanicolaou, C., Papantoniou, I., 2010. Mechanical behavior of textile reinforced concrete (TRC)/concrete composite elements. Adv. Concr. Technol. 8, 35–48.

Voss, S., Hegger, J., 2006. Dimensioning of textile reinforced concrete structures. In: Hegger, J., Brameshuber, W., Will, N. (Eds.), Proceedings of the 1st International RILEM Symposium Textile Reinforced Concrete, Aachen, Germany, pp. 151–160.

Weiland, S., Lorenz, E., Curbach, M., 2010. Interaction of mixed reinforcements at the strengthening of reinforced concrete with textile reinforced concrete. In: Aldea, C.-M. (Ed.), Proceedings of the ACI 2010 Fall Convention, Pittsburgh, 24–28 October, 2010.

Textile-reinforced concrete: Selected case studies

M. Raupach, C. Morales Cruz
RWTH Aachen University, Aachen, Germany

12.1 Loadbearing and self-supporting new building structures with prefabricated textile-reinforced concrete

One area for the application of new constructions with textile-reinforced concrete (TRC) is the building of new prefabricated pedestrian bridges. Old bridges often do not have a sufficient concrete cover thickness to protect their steel reinforcement, leading to corrosion and spalling. The use of salt for de-icing also acerbates the process. This does not only leave visual defects but can also reduce the loadbearing capacity and thereby the safety of the bridges. If a repair or strengthening is too expensive or not worth it, then these existing bridges will be replaced by new ones. One advantage of TRC is its high adaptability to its surroundings, due to the slim cross-sections compared to concrete, reinforced concrete with steel or even fiber-reinforced polymers. This enhances the freedom of design of the architect and engineer. In addition, transportation costs of the unit-segments are lower compared to steel–concrete, as a result of the lower weight.

The very first TRC bridge was built and opened to the public in Oschatz, Germany (see Figure 12.1a). For the state horticultural show in 2006, a bridge was needed for pedestrians and cyclists to cross a stream. To minimize the required material and weight, the concrete was reinforced with technical textiles and steel tendons, allowing for a mere thickness of 30 mm and a weight of 6 t (Ehlig et al., 2012).

The bridge spans 8.60 m and consists of U-shaped segments. These segments are haunched at the frame corners and reinforced segment edges. Additionally, all other edges are rounded in order to minimize the stress-concentrations. Both the railing and the superstructure cross-section area, which has a width of 3.1 m and a total walking width of 2.5 m, are loadbearing. To accommodate this, the 1.31 m-high segments were prestressed with six steel-tendons, and the superstructure cross-section area was strengthened with ribs on the lower surface (see Figure 12.1b) (Ehlig et al., 2012; Fußgängerbrücke Oschatz, 2006).

The fine concrete was reinforced with alkali-resistant (AR) glass rovings, which were woven into mats and then inserted in four layers on the segments. The textile reinforcement served as minimum reinforcement and also reduced the crack widths and spacing in the serviceability state (Ehlig et al., 2012).

(a)   (b)
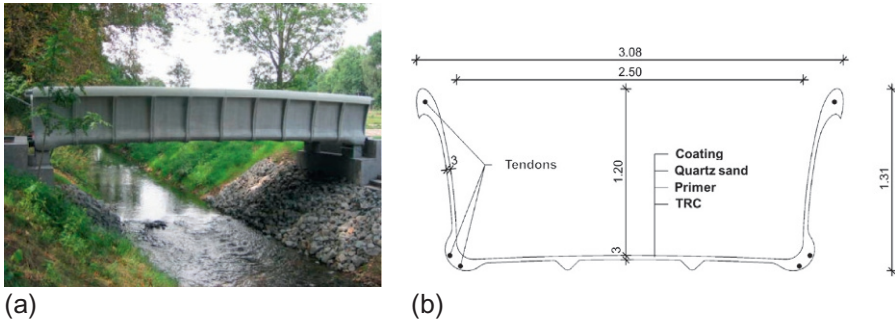
Figure 12.1 First segmental TRC Bridge in Oschatz, Germany. (a) Overview (Fußgängerbrücke Oschatz, 2006) and (b) U-shaped cross-section of the TRC (Ehlig et al., 2012).

Before construction, the segments and a prototype of this bridge were tested for safety and loadbearing capacity in a laboratory. Due to the novelty of this composite material at this time, a partial safety factor ($\gamma = 2.5$) compared to the service load was required. This, however, was easily proven (Ehlig et al., 2012).

Adapted from this U-shaped structural system, a 17-m long TRC bridge was built in Kempten, Germany. While the height of the segments was maintained, the total walking width was reduced to 2.0 m. This bridge is innovative, in so far that clearance vehicles with a weight of up to 3.5 t are allowed to briefly pass through it. Due to the axle loads, additional crossbeams were added to the superstructure cross-section. As a result of the greater spans, higher pretension loads had to be safely introduced into the structure via cross-sectional reinforcements (Ehlig et al., 2012).

A more recent construction is the pedestrian bridge in Albstadt, Germany (see Figure 12.2a). In 2010, the original pedestrian bridge across a motorway in Albstadt had to be replaced because of serious damage by steel-corrosion. To avoid high costs of restoration, and to enable a slender and durable bridge, TRC was chosen as building material. Compared to conventional construction material, a reduced weight and a longer service life were achieved (Ehlig et al., 2012; Hegger et al., 2010).

With a length of 97 m, the resulting slim TRC bridge is the longest in the world (Kulas and Goralski, 2014).

AR glass was also used as reinforcement in this case. However, the mesh (laid scrim) with a maximal intercept of 15 mm was coated with a warm hardening epoxy, namely a PrePreg System (Pre impregnated) (Raupach et al., 2006). Thus nearly the full tensile strength of the AR glass was activated and the shapes needed for the crosslines and caps of the bridge could be formed freely (see Figure 12.2b). Additionally, the strength loss during the accelerated aging laboratory tests was compared to the non-impregnated AR-glass significantly reduced (Hegger et al., 2010).

The fine concrete used here, strength class C55/65, was chosen for its frost resistance, surface quality and high workability. The maximum grain diameter was set at 4 mm to allow for adequate adhesion of the fine concrete to the textile and cohesion through the mesh (Hegger et al., 2010).

(a)   (b)
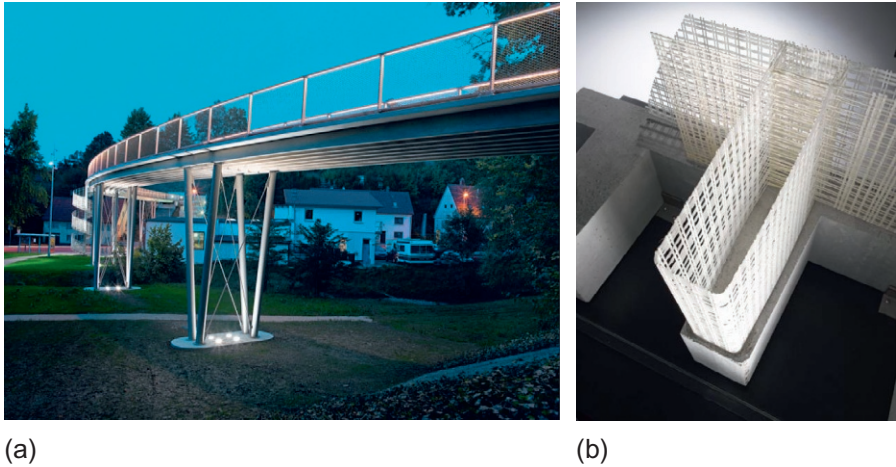
Figure 12.2 Pedestrian Bridge in Albstadt, Germany. (a) Overview (Kulas and Goralski, 2014) and (b) cross-section of the T-beam superstructure (solidian GmbH).

The bridge is 97-m long and consists of six elements with lengths between 11.8 m and 17.2 m (border fields) with a maximum span of 15.1 m. The superstructure consists of 435-mm high and 3.21-m wide concrete T-beams with seven webs each. They were prestressed by four single-strand cables and reinforced with three glass fibre reinforced plastic (GFRP)-bars, in addition to the textile reinforcement. With a slenderness ratio of only H:L = 1:35, a slender bridge construction was achieved. Using TRC, the minimum concrete cover was 15 mm, enabling the application of the textile (warp-knit frayed structure) with a width of 120 mm. Near the ends of the bridge, the height of the plate is reduced to only 90 mm. These elements were prefabricated to be assembled at the construction site (Kulas and Goralski, 2014).

Before the bridge was built, a large-scale test was carried out on a 17.2 m × 3.21 m element. The bridge cross-section remained intact throughout the entire test. At 80% of the maximum load, cracks of 0.3 mm were observed; at the maximum load of 100 t, cracks of 0.7 mm appeared, and the element showed a deflection of 500 mm. This low crack diameter can be attributed to the finely woven textile reinforcement with its fine rovings (Kulas and Goralski, 2014).

Besides bridges, there are other architecturally sophisticated building structures, which reflect the slimming and the elegance of face concrete, that can be achieved with prefabricated TRC. Due to its minimal concrete cover, very thin plates, which can be used for façades, can be fabricated. The use of fine concrete with a maximum grain size of 8 mm allows for thin, sharp-edged components and high-quality surfaces.

To improve the appearance of buildings, reduce carbon dioxide emissions, and the costs of material and transport, façade elements made of TRC can be used. To add an element of insulation to these façades, sandwich elements are built. These offer not only ecological, but also economic advantages. Therefore, many sandwich façades and elements can be found in recent constructions. They consist of two textile

elements embedded in concrete enclosing light material such as foam. Sandwich elements are very light, thus they can support their own weight.

In the context of façades, the concept of "betoShell©" is relevant. The company Hering Bau developed betoShell© in collaboration with RWTH Aachen University and TU Dresden. betoShell© is a TRC plate that can be used to clad a façade. They are available in various sizes, colors, and surface structures. Furthermore, they excel in their low thickness and fine edge shaping.

The betoShell© CLASSIC of 1200 mm × 600 mm × 20 mm was the first general construction approval for such components. The betoShell© BIG is also widespread, with dimensions of 2400 mm × 1200 mm × 30 mm (see Figure 12.3). Both systems can be used to build rear-ventilated façades and suspended ceilings up to a characteristic wind load of 2.2 kN/m^2 (Ehlig et al., 2012).

One example of the application of betoShell© is the façade of an auditorium of the Faculty of civil engineering at RWTH Aachen University (see Figure 12.4). The existing façade had to be renewed because of its age and lack of sufficient anchorage. Due to the lower weight and the overall climate and environmental balance, betoShell© was preferred over conventional materials. It was then furnished with thermal insulation and clad in betoShell© XXL plates with dimensions of 3 m × 3 m. The plates are fixed and anchored through two vertical back-mounted reinforcing ribs (Grebe, 2011).

Another example for the application of TRC façade elements is the expansion of a testing hall of the Institute of Structural Concrete of RWTH Aachen University. The façade of the laboratory hall was clad in small-format textile-reinforced façade panels. A total of 226 plates with the size of 2.685 m × 0.325 m and a thickness of 25 mm were used to cover a surface of 200 m^2. Also in this case, the lower weight, the associated cost savings for transport and mounting as well as the architectural design options played a decisive role in the choice of construction materials. A fine concrete
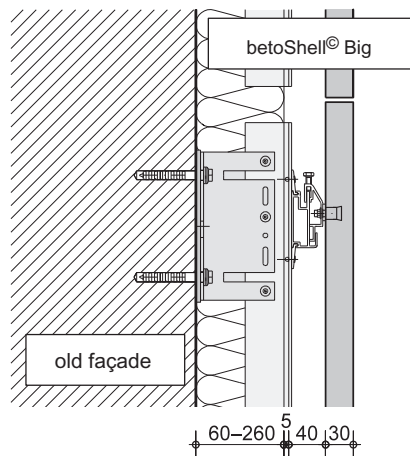
Figure 12.3 Technical drawing of the betoShell© BIG with dimensions of 2400 mm × 1200 mm × 30 mm as part of a rear-ventilated façade (Hering Bau).

Figure 12.4 View of the auditorium of the Civil Engineering Faculty, RWTH Aachen University (Grebe, 2011).

with a maximum grain size of 2 mm was applied using the lamination method. The textile reinforcement consists of 2200/320 tex (warp/fill direction) AR glass fibers and has a distance of 8 mm between the rovings (Kulas et al., 2011). Further projects include the façade panels of the community college in Leiden, Netherlands, the TRC façade of the Alfred-Hütter Laboratory Hall in Dresden, the façade of the city library of Almere, Netherlands and the façade of the educational department of the Hogeschool van Arnhem and Nijmegen (HAN) in Nimwegen (Rempel et al., 2015).

In order to reduce the quantity of anchorage per square meter, thus reducing the mounting costs, large façade panels with dimensions of 2.51 m × 4.88 m and thicknesses of only 30 mm were developed by Hering Bau and institutes of RWTH Aachen University. Additionally, the number of gaps between the elements was reduced, resulting in the enhancement of the appearance (Rempel and Hegger, 2015). Further projects include the pilot application on the large façade panel of the laboratory hall of the Institute of Structural Concrete of the RWTH Aachen University (Rempel and Hegger, 2015), the large façade with TRC elements on the cafeteria of the St. Leonard School in Aachen (Rempel and Hegger, 2015) and the façade of "SchieferErlebnis" in Dormettingen (Rempel et al., 2015).

Currently, top layers of sandwich panels are made of steel-reinforced concrete or metal. However, the transportation, the mounting, and coupling agent costs can be reduced by using TRC top layers. An example of a sandwich element construction is the institute building INNOTEX of RWTH Aachen University (see Figure 12.5a). 590 m^2 of its façade are clad in sandwich elements with dimensions of 3.45 m × 1.0 m × 0.18 m (see Figure 12.5b). The glass fiber concrete panels were reinforced with AR glass textiles. They enclose 150 mm of rigid polyurethane foam

(a)   (b)
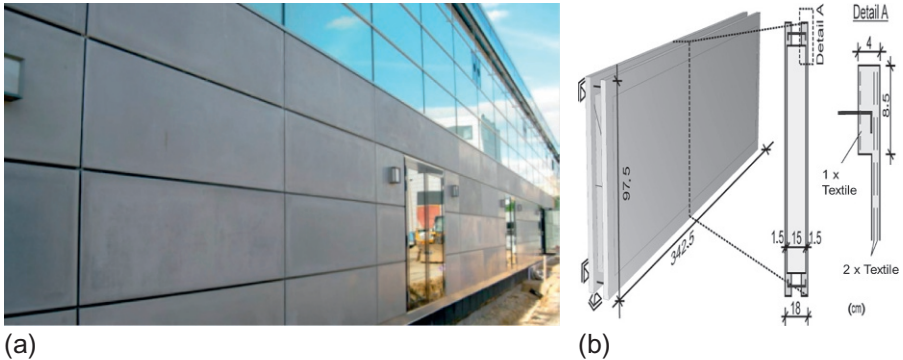
Figure 12.5 Façade of the INNOTEX building, RWTH Aachen University. (a) Overview
(Rempel et al., 2015) and (b) cross-section (Horstmann et al., 2009).

and are kept in place by eight nails and two transverse anchors of stainless steel.
This ensures stability under strain through wind, temperature, and shrinkage
(Rempel et al., 2015).

A further demonstration of the novel composite material, TRC, is the T3-Pavilion
in Aachen, Germany (see Figure 12.6a). The cost-intensive production of the shell
structures and later occurring corrosion of the steel reinforcement are arguments
against a construction with steel-reinforced concrete, which, at the same time, speak
in favor for TRC.

Four large-format TRC shells with dimensions of 7 m × 7 m form the roof of the
glassed pavilion. The dimensions of the building exterior are 14 m × 14 m × 4 m
(Scholzen et al., 2012). The textile concrete shells were produced by the company
GQ Quadflieg Bau GmbH from Aachen in cooperation with engineers of RWTH
Aachen University. A total of twelve layers of carbon textile were used within the only
60-mm thick shells. Each shell rests in the midst of the filigree arches on a single
steel-reinforced concrete column (Rempel et al., 2015).

(a)   (b)
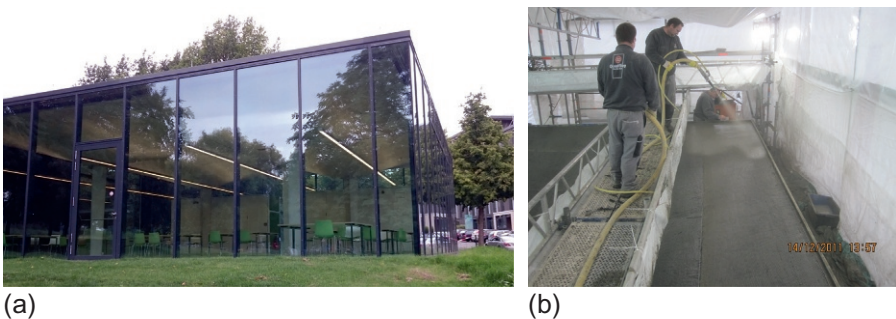
Figure 12.6 T3-Pavilion of RWTH Aachen University. (a) Overview and (b) spraying of the
mortar on the carbon textiles from the moveable working platform (GQ Quadflieg Bau GmbH).

In order to secure the positional accuracy of the textile reinforcement, to reach every point of the shell and to prevent damage caused during the construction, a precast concept was developed. Part of the concept was a temporary manufacturing tent in which a formwork was built for the textile concrete shells (see Figure 12.6b). Another part of the concept is a moveable working platform, from which any point of the shell could be reached without entering and damaging the shell during its manufacture (Scholzen et al., 2012).

Another useful application for new TRC structures are precast garages. Nowadays, many garages are built using prefabricated parts. These heavy elements need to be transported to the construction site. Usually, two garages are transported on a single trailer truck. For this purpose, there is currently a special permission which is being reevaluated, possibly limiting the allowed weight to 40 t. To avoid high transport costs, the much lighter TRC can be used to create prefabricated garages weighing only 15 t. An example are the prefabricated garages made by the company solidian GmbH (see Figure 12.7) (Kulas, 2014).

The dimensions of these garages are 6000–8000 mm × 2980 mm × 2590 mm and are composed of a base plate of steel-reinforced concrete, four wall panels and a ceiling of TRC. The concrete used has a maximum grain size of 8 mm and is in accordance with class C40/50, while the concrete cover of the textile reinforcement is merely 10 mm (Kulas, 2014).

The textile reinforcement consists of AR glass fibers that are impregnated with a warm hardening epoxy resin. This allows for a light, sturdy and dimensionally stable construction. Additionally, the beams of the garage openings are reinforced with GFRP-bars with vinyl-ester-resin-coated AR glass filaments and a diameter of 10 mm (Kulas, 2014).

With a thickness of just 60 mm for the ceiling and 40–50 mm for the walls, the weight can be reduced to such an extent that two garages can be transported by the same truck even under the impending new restrictions (Kulas, 2014).

In 2014, TRC was used by Hering Bau to restore a run-down platform in Walleshausen, Germany (see Figure 12.8a). This had to be done with a minimal
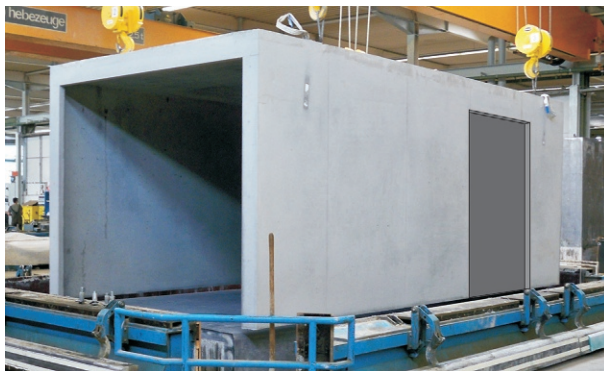
Figure 12.7 Precast garage from the company solidian GmbH (solidian GmbH).

(a)   (b)
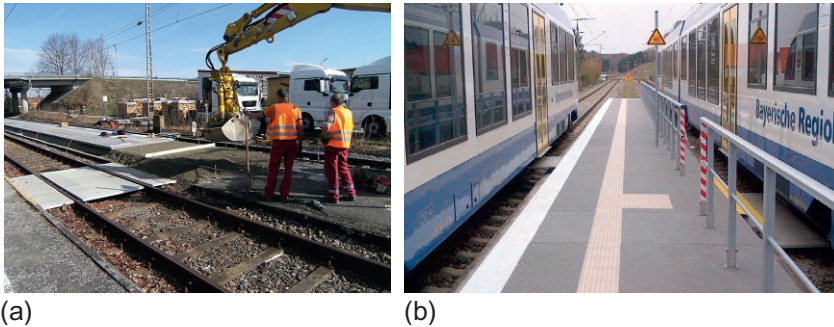
Figure 12.8 (a) Platform under construction (Hering Bau) and (b) the completed platform (Hering Bau).

impact on rail traffic, as several tracks had to be closed for the maintenance. In this context, the platform level had to be raised to a new level of 0.38 m above the tracks (Grebe, 2014).

A composite material to compensate for different platform levels was found in the thin and flexible TRC. To minimize work on the construction site and the impact on rail traffic, prefabricated plates were used. These already included the textured platform edge, a slip-resistant surface coating and a guide strip for people with visual disabilities (Grebe, 2014).

Because of the high flexural strength required by the platform, two layers of carbon fiber textiles were imbedded into the concrete. The concrete panels with a dimension of 2.5 m $\times$ 1.35 m were put on a frost-proof concrete layer and fixed there with two stainless steel mandrels. During the process, the components did not need to be grounded because of the absence of steel reinforcement (Grebe, 2014).

The company Hering Bau was awarded the "Qualitätspreis Gleisbau 2014" ("Prize for Quality in Track Construction") for their work restoring the platform of Walleshausen with TRC (see Figure 12.8b).

12.2 Strengthening of steel-reinforced concrete structures

TRC can be used to strengthen existing steel-reinforced concrete, masonry or even wood structures. So far, TRC is mostly used for the strengthening of steel-reinforced concrete. By combining the advantages of sprayed concrete, such as productivity and high concrete compaction, with the advantages of light, non-corrosive reinforcement, a high-performance composite material can be achieved through TRC. Since 2014, a general type approval for the strengthening of steel-reinforced concrete (TUDALIT®) has been given. Various construction structures such as columns, roofs, floor slabs, a monument, a sugar silo and balconies have already been strengthen with TUDALIT® (Scheerer et al., 2015). However, this approval only covers the strengthening

(a)   (b)

Figure 12.9 The hypar-shell structure in Schweinfurt. (a) Overview (TORKRET GmbH) and (b) application of TRC through spraying with final laminating process (TORKRET GmbH).

of interior structures with mainly stationary loads. Before that, an approval for each individual case had to be gained, as for all of the following sprayed fine concrete constructions. Some applications are presented next, whereas others are given in Chapter 17.

In 2006, the existing steel-reinforced hypar-shell structure of the FH Schweinfurt had to be strengthened to prevent further damage through wind and snow loads because of an unacceptable amount of stress and deformation (see Figure 12.9a). Due to its form, a hyperbolic parabolic, and the need for as little additional weight as possible, a TRC was chosen as the reinforcement (see Figure 12.9b) (Ehlig et al., 2012; Curbach et al., 2007).

The hypar-shell has a span width of 38 m × 39 m and consists of steel-reinforced concrete. The thickness of the structure varies: it is 80 mm in the middle, 367 mm at the edges and up to 772 mm where it rests on the massive pylons. In the area over these pylons, defects in the structure were discovered. 800 tex carbon rovings, combined to structural elements, were used for the textile reinforcement. These had a spacing of 10.8 mm in warp and 18 mm in fill direction and were not impregnated. The fine concrete had to have a good adhesion even on vertical surfaces, combine well with the textile reinforcement, be compatible to the existing structure and be optimized for shrinking. As no manufacturer for such a concrete could be found, it was mixed at the construction site. Further information on the concrete mixture is given in Ehlig et al. (2012) and Curbach et al. (2007).

Prior to the application of TRC, the old concrete was roughened through sand blasting and moistened to ensure good adhesion. The concrete was sprayed on in layers of approximately 3–5 mm, alternating with the textile reinforcement. Thus a strengthening layer of only 15 mm in thickness was created and, using TRC in contrast to steel-reinforced concrete, the additional weight could be reduced by over 80%. Before construction started, the adhesive bonding and the anchoring of the textile reinforcement were tested using samples of the components described above. This resulted in an average bonding of 3.71 N/mm^2, which is far above the bonding of the existing structure, and is therefore sufficient. Furthermore, the transverse

(a)   (b)

Figure 12.10 The tax office in Zwickau, Germany. (a) The completed reinforced barrel vaulting (Erhard et al., 2015) and (b) the sprayed TRC layer (TORKRET GmbH).

reinforcement and the breaking load of the strengthening layer were examined through tensile tests. They also proved to be sufficient (Curbach et al., 2007).

From 2007 to 2009, the former building of the School of Engineering, Zwickau, was reconstructed into a tax office. During a reevaluation of structural properties, the loadbearing capacity of the barrel vaulting (see Figure 12.10a) could no longer be guaranteed. Because the building is protected as a historical monument, the original filigree structure had to be preserved. Different solutions for strengthening were proposed but only TRC could meet the requirements of a flexible, thin and stable reinforcement for a fire-safe building (see Figure 12.10b) (Ehlig et al., 2012; Erhard et al., 2015; Schladitz et al., 2009).

The barrel vaulting covers a room of approximately 16 m × 7 m without supports, rising to a height of 2.2 m. Eleven beams of 200 mm × 250 mm are connected to the steel-reinforced concrete plate, enclosing the ten roof panels, nine of which have a skylight of 1 m × 3 m (Erhard et al., 2015).

For the reinforcement, an orthogonal structure of 800 tex uncoated carbon rovings with a spacing of 7.2 mm in warp and 14.4 mm in fill directions was created. Three layers were applied both on the outside and inside of the building. Additionally, seven layers were applied on the arch ribs, five of which were applied in the longitudinal direction and two embracing the arch (Schladitz et al., 2009).

The fine, wet-sprayed concrete was mixed on-site. Before the concrete was added in sprayed layers of 3 mm, the surface was moistened to ensure good adhesion. Alternating between concrete and textile components, while still wet, the textile reinforcement was incorporated through light impressing and the renovation was completed with a final layer of concrete. To reduce shrinking, the finished TRC layer of 20-mm thickness, on average, was instantly covered by wet fleece and foils. Thereby, the filigree structure of the original building could be conserved; the applied layer of TRC was only about the size of the plaster removed beforehand. Also, the

(a)   (b)

Figure 12.11 Strengthening of the ceilings of a business building in Prague, Czech Republic. (a) Overview (TORKRET GmbH) and (b) spraying of the mortar (TORKRET GmbH).

nature of the textile structure enabled a flexible application to the rounded barrel vaulting (Ehlig et al., 2012; Erhard et al., 2015; Schladitz et al., 2009).

In the context of a strengthening application in 2009 on a residential and business building in Prague, Czech Republic, the company TORKRET carried out work with TRC (see Figure 12.11a). For the ceilings, only TRC could be used because other measures would have limited the room heights and increased the load considerably.

The six-story building is 30 m × 70 m in size and its ceilings are point-supported flat slabs with non-prestressed steel reinforcement. The supports had a diameter of 0.8 m and were arranged in a grid of 12.8 m × 13.1 m. Carbon fiber textiles and 3 mm of sprayed concrete were applied in up to four alternating layers (see Figure 12.11b). Because of the extensive size of this ceiling, these layers could be attached simultaneously for each cycle. One person sprayed the concrete, a second rolled out the textile mats and another embedded the reinforcement into the concrete. This reduced the costs and necessary time, even though the personnel expenditure was higher. The resulting TRC layer was 20 mm in thickness at maximum (Erhard et al., 2015).

In a similar application, the ceiling of a production hall in Koblenz, Germany, was reinforced (see Figure 12.12). It showed severe deflection of up to 90 mm, leading to damage of the walls and the floors above due to mechanical stress (Erhard et al., 2015). The reason for this was two flange straps of 1.5 m × 10.2 m, which were insufficiently reinforced with steel (Erhard et al., 2015).

To fulfill these conditions TRC was chosen, in part because of its own low weight. To ensure the stability and loadbearing capacity, the flange straps were reinforced with carbon. Before renovations began, the effectiveness and quality were tested using samples and verified through the material parameters. Three layers of fine concrete and carbon reinforcement were applied through spraying; the last layer of concrete

(a)   (b)
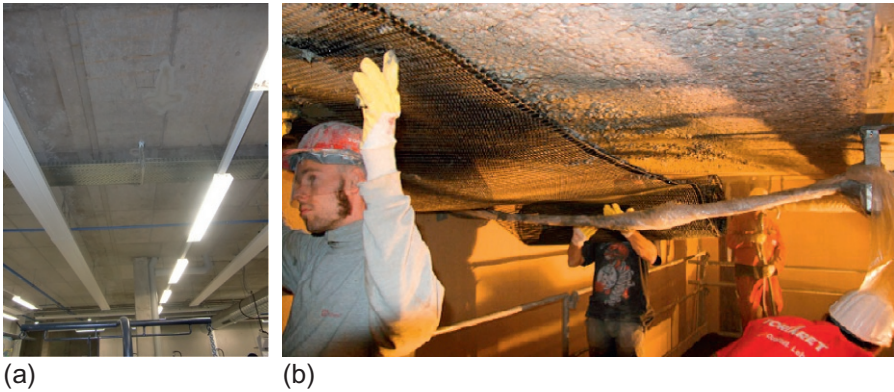
Figure 12.12 Strengthening of the ceilings of a production hall in Koblenz, Germany. (a) Overview (TORKRET GmbH) and (b) application of the textile reinforcement on the sprayed mortar (Erhard et al., 2015).

was rubbed down. Finally, the last layer was painted using acrylate-based paint. The resulting TRC layer was only 15 mm in thickness, and reinforced the ceiling to the full satisfaction of all involved partners (Scheerer et al., 2015).

12.3   Repair and restoration with TRC

TRC is especially suited for the surface repair of cracked building structures and it additionally works well for the reinforcement of round structures. The flexible styrene–butadiene–rubber (SBR)-impregnated textiles show excellent draping properties and can be shaped to fit exactly to the individual structure. One such example is the sugar silo in Uelzen, Germany (see Figure 12.13). The silo, built in 1962, had to undergo crack repair in 2012. Although it still proved to be sufficiently stable, cracks of up to 1.6 mm could be observed. These were due to the thick concrete cover and the resulting sensitivity to flexural stress. The dual compartment silo consists of prestressed steel-reinforced concrete, has a diameter of 30 m and a height of 45 m. The outer wall has a thickness of 200 mm, and the inner wall has a thickness of 180 mm. It can hold up to 20,000 t of sugar. The crack repair on the inside of the silo was necessary to ensure the purity of the sugar and maintain the use of the silo (Erhard et al., 2015; Weiland et al., 2013).

The textile mats can have diameters of a few millimeters and are thus ideal for a fine crack distribution and bridging. This also leads to a very thin layer of necessary reinforcement and reduces the capacity of the silo by a minimum. Using concrete, the approved special coating suitable for food can still be applied, as it is only suitable for mineral surfaces. Another factor was the difficult transport of the building materials into the silo. Less TRC was needed than any other suitable materials and was therefore favored (Weiland et al., 2013).

(a)   (b)
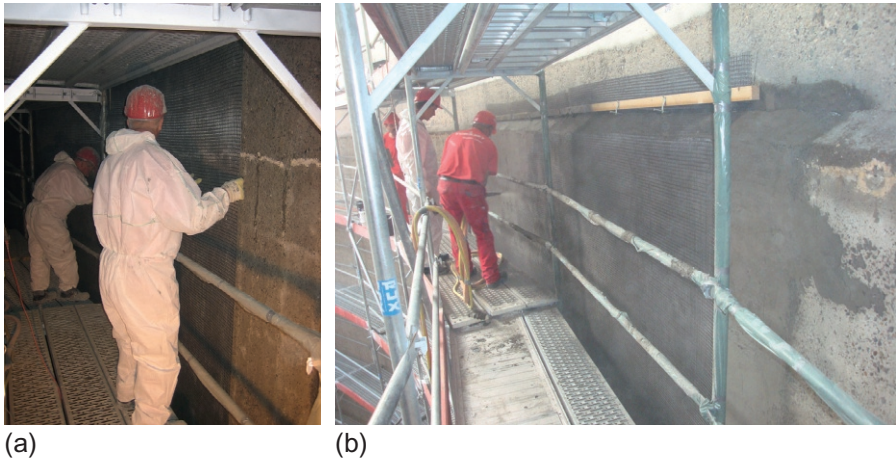
Figure 12.13 Sugar Silo in Uelzen. (a) Application of the carbon textile (TORKRET GmbH) and (b) application of the spayed "fine" concrete (TORKRET GmbH).

The fine concrete used for this project was developed from the company Pagel. The textile reinforcement consisted of 600 tex carbon textiles. TRC was then applied in four layers by alternately spraying on the concrete and applying the textile reinforcement. The layers of the latter were overlapped gradually to ensure a homogenous TRC layer. The textile reinforcement had been cut to size beforehand, enabling a faster working speed. To reduce shrinking, the new layer underwent post-treatment for a week (Weiland et al., 2013).

The draping properties of TRC were also important while renovating an oval-shaped sewer in Dresden, Germany (see Figure 12.14).

According to a survey from 2009, 17% of the 541,000 km sewage system in Germany required restoration (Walther and Curbach, 2015). The quality and stability of the existing concrete was not only too poor from the start, but also further weakened by the corrosive fluids passing through.

Figure 12.14 Sewer restoration with TRC in Dresden (Walther and Curbach, 2015).

Of the many possible methods for restoration, few are applicable to the given conditions. TRC can be applied in layers flexible in shape and low in thickness. Resulting in a finer crack distribution, its application lowers the permeability for liquids, for example, water. The high compressive strength of the dense concrete matrix also limits the penetration of pollutants. One approach is the external preparation of concrete and materials and the subsequent transport into the sewer. The limited space and accessibility, however, only allowed for the hand-laminating process (Walther and Curbach, 2015).

This solution has already been applied to a sewage system in Dresden, Germany, where a 68 m segment of the public sewer system was restored using TRC. This pilot project covered a section of an oval-shaped canal with a straight horizontal crown, which had a length of 70 m and a clearance height of 1.7 m. The canal is used for rain- and wastewater and its steel reinforcement showed signs of corrosion (Walther and Curbach, 2015).

A conventional mortar for the restoration of sewers was used. The textile reinforcement consists of 800 tex biaxial SBR-impregnated carbon rovings with a mesh size of 7.2 mm. The advantage to a comparable 3300 tex roving is a finer crack distribution and better processing in points of detail, like corners. Two layers of TRC were applied using the hand-lamination process. The resulting layer has a thickness of 9 mm and forms a good surface (Walther and Curbach, 2015).

Before installation, uniaxial tension tests and pullout tests of the material were carried out to determine bonding behavior and loadbearing capacity under different storage conditions; they gave favorable results. The TRC was also tested for endurance under sulfate solution, comparable in corrosiveness to the fluids passing through sewers, except for biogene sulfuric acid corrosion (Walther and Curbach, 2015).

TRC has also proven to be a very efficient solution for the restoration of historical buildings, such as the Aachen Cathedral and the Aachen Town Hall. The protection of the Aachen Cathedral is an example of the application of TRC on masonry made of natural stone.

The Aachen Cathedral was built around the year 800, and has since been a landmark of the city. The Aachen Cathedral is not only the most striking building in Aachen, but also the first German monument that was added to the list of the UNESCO World Heritage Sites (see Figure 12.15a). During the repair of historically important mosaics, a crack through the major structure of the "octagon vault" was discovered (see Figure 12.15b). The crack movement damages the mosaics; therefore it has to be constrained (Raupach et al., 2010).

The crack was under a lead roof, so the restoration was not needed for waterproofing, but as a fail-safe protection in case the roof above should leak. The existing crack had to be bridged and the crack displacements reduced, so the mosaics on the other side of the wall would be protected from damage. Because of the importance of Aachen Cathedral, all retrofitting work had to be done in accordance to the guidelines of preserving such an important structure, as well as allowing for a very limited invasion of the structure. Also, the added thickness could not exceed 30 mm and intrusions into the existing structure had to be minimal (Raupach et al., 2010).

(a)   (b)
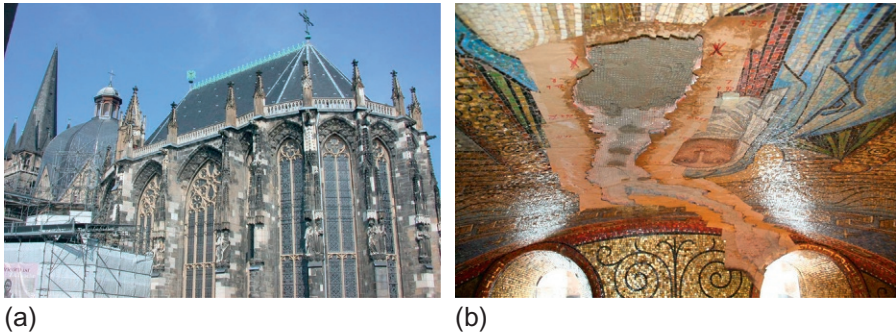
Figure 12.15 Aachen Cathedral. (a) Overview (Büttner and Raupach, 2012) and (b) crack through the mosaics on the "octagon vault" (Büttner, 2012).

The mortar used there is based on the grouting mortar developed specifically for the cathedral taking the requirements of the preservation of the historic materials into account. The reinforcement consists of two layers of a 2D carbon textile and has a mesh size of 7 mm and 1600 tex rovings in both warp and fill directions. The surface of the cathedral is irregular. To ensure the necessary high system rigidity, the textile structure was impregnated with a warm curing epoxy, which hardened at 120 °C for 2 h (Raupach et al., 2010).

Before application, the surface was prepared by cleaning and smoothing. It was then roughened with a toothed trowel in order to improve the adherence and bonding behavior. The leveling grout was post-treated with water for 18 days before application. Then it was applied manually with a trowel in layers of 5–10 mm while still wet, along with the textile reinforcement (see Figure 12.16a). The entire protection layer has a maximum thickness of 30 mm (see Figure 12.16b) (Raupach et al., 2010).

(a)   (b)
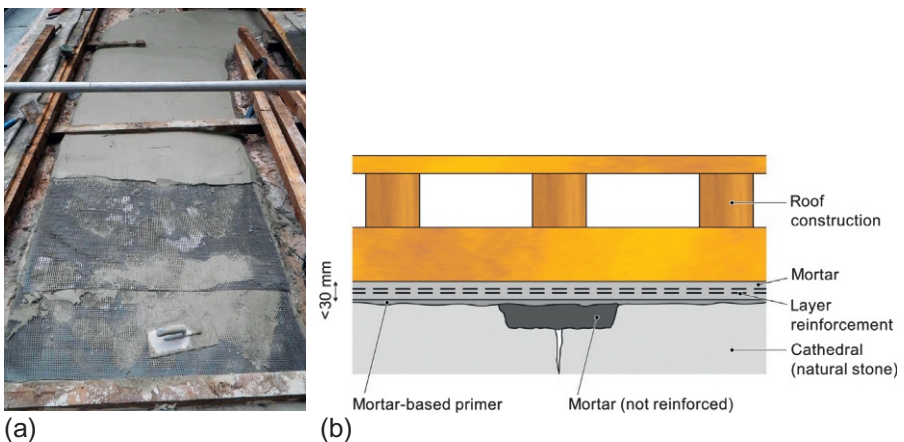
Figure 12.16 TRC layer structure. (a) Overview during application (Büttner and Raupach, 2012) and (b) schematic drawing of the protective layer (Büttner and Raupach, 2012).

(a)   (b)
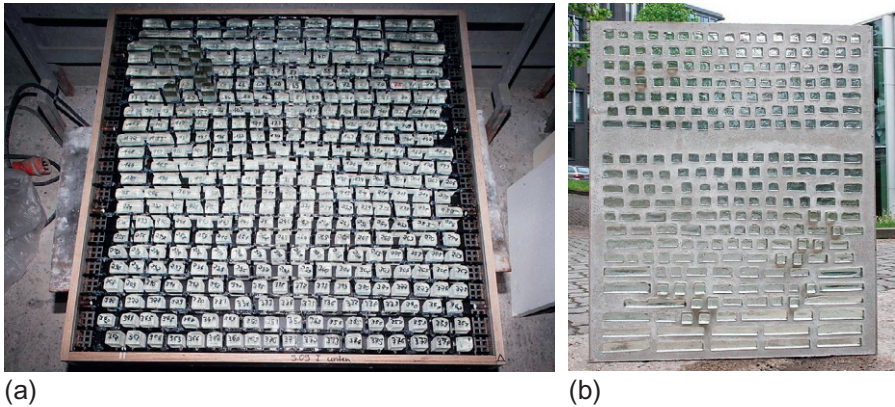
Figure 12.17 Restauration of the glass windows of the Marien Tower. (a) Production process of the concrete–glass window (Rempel and Geßner, 2015) and (b) finished construction before installation (S. Rempel, Institute of Structural Concrete of RWTH Aachen University).

As one of the most important medieval buildings in Germany, the Aachen Town Hall was erected on the foundation of the King's Hall that was used for the coronation of Charlemagne in the eighth century. Since then, it has undergone many restorations and changes. One of its towers, the Marien Tower, was destroyed in World War II. For the reconstruction, 19 concrete glass windows were installed, designed to remind the viewer of quarry stone walls (Rempel and Geßner, 2015).

After 60 years, these historic concrete–glass windows suffered from corrosion and spalling of the thin layer of steel-reinforced concrete (see Figure 12.17a). The thickness of the layer could not be changed, nor could the size and position of the glass stones. To repair the windows, the steel-reinforced concrete was exchanged for non-corrosive TRC (see Figure 12.17b). This has the advantage of fulfilling the guidelines of preserving historic structures and eliminating the risk of further corrosion (Rempel and Geßner, 2015).

The windows are 2-m high and consist of different-sized glass stones embedded in a 35-mm layer of concrete. The glass stones are arranged in rows with a distance of 25 mm and separated by reinforcing horizontal steel bars with a diameter of 5 mm. They are anchored in a steel frame, through which the load of the windows is transferred uniaxial into the masonry with the help of a perforated plate. Originally, the frame was used as lost formwork. This original frame was replaced by one made of stainless steel, onto which the restored windows were attached with welded screws. These are screwed halfway into the sleeves and halfway into modified bearing rails anchored in the masonry, so the original mechanism for the force transmission is maintained (Rempel and Geßner, 2015).

A concrete mixture developed by the company Hering Bau, commonly used for TRC, was applied. It is a concrete composition with a maximum grain size of 5 mm, which has a compressive strength of 87 N/mm^2 and a flexural strength of 10.6 N/mm^2. The textile reinforcement consists of carbon filaments arranged in a

mesh with a cross-sectional area of 110 mm^2/m. Additionally, the textile was coated with epoxy, resulting in a high tensile strength of over 3000 N/mm^2. Comparable to the original reinforcement, the textile reinforcement was only added horizontally between the rows of glass stones; the warp direction was not reinforced (Rempel and Geßner, 2015).

After their documentation in great detail, the original windows were disassembled. Because TRC allows for the creation for sharp-edged components, the frame was not needed for stability, so the large windows could be restored in more manageable parts. Firstly, the glass stones were fixed to a formwork of custom-fit anchoring rails with acrylic in the exact positions they had held in the original window. Then, the carbon reinforcement was installed and fixed to the perforated plates. In a casting process, the concrete was added, first compacted on site with a table shaker. After removing the formwork, the remaining traces of acrylic were wiped off, and the surfaces of the concrete were acidified. The windows were then reinstalled in the town hall with the use of bearing rails, which were afterwards plastered with a similar colored mortar (Rempel and Geßner, 2015).

Not only historic buildings, but also many existing concrete or steel–concrete structures are currently in need of surface maintenance and repair. At the Institute of Building Materials Research (ibac) of RWTH Aachen, "DURTEX" was developed for the repair of concrete and steel–concrete structures (see Figure 12.18). DURTEX is a textile-reinforced protective layer. It distinguishes itself by its durable, water-impermeable and crack-bridging characteristics. "DURTEX" is an acronym for German words meaning "durable," "water-impermeable," "crack-bridging," and "TRC." It consists of several components: the (sprayed on) concrete, textile reinforcement, a delamination area and, if necessary, an anchorage (Morales Cruz and Raupach, 2014a).

The debonding area is necessary to ensure a fine crack distribution, while still maintaining the sealing effect. In comparison to the total area, the debonding area is relatively small. There, the protective layer does not adhere, or only slightly adheres, to the surface, and so it can elongate freely. The effect has been confirmed through crack-bridging tests (Morales Cruz and Raupach, 2014a).
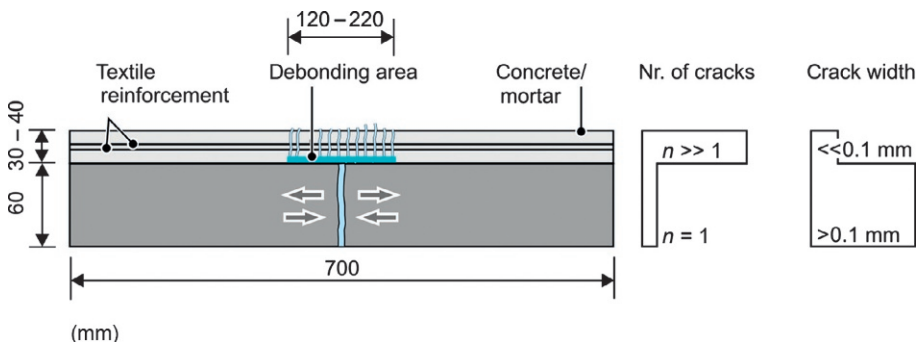
Figure 12.18 Scheme of the DURTEX protective layer (Morales Cruz and Raupach, 2014a).

Depending on the type of structures, different compositions of concrete or mortar and different textile reinforcements can be used. Generally, concrete with a maximum grain size of up to 6 mm is used for layers of 30–35 mm. The reinforcement consists of polymer-coated or noncoated carbon or AR glass fibers. DURTEX is then applied in its layers directly to the part of the structure in need of repair (Büttner and Morales Cruz, 2013).

To test the composite system, its loadbearing and crack-bridging abilities, uniaxial tension tests were carried out. The temporal evolution of the cracks and their widths were observed with the optical 3D deformation measurement system ARAMIS®, because cracks with widths of <0.1 mm are not clearly visible with the naked eye (Morales Cruz and Raupach, 2014b).

Many existing waterway structures are currently in need of maintenance and repair. The choices of material and application method are limited to anchored, steel-reinforced or sprayed concrete systems over 90 mm thick. For the old concrete classes, A2–A4 (with low concrete strengths between 10 and 40 N/mm²), thinner (20–60 mm), nonreinforced and nonanchored layers can also be utilized. These do not eliminate the risk of snap-through of cracks, or increase the diameter of the structures significantly. DURTEX was first applied at a weir in Horkheim, Germany in 2010 (see Figure 12.19a) (Rempel and Geßner, 2015).

The work at the weir was a pilot project to test the application of TRC for the repair and maintenance of hydraulic structures. The weir was completed in 1929 and has since been in use. It was built with steel-reinforced concrete which has low strength and many cracks ranging from 0.1 to 3.0 mm in width, in addition to the open construction joints. The weir pier is directly exposed to natural weather, has wet and

(a)   (b)
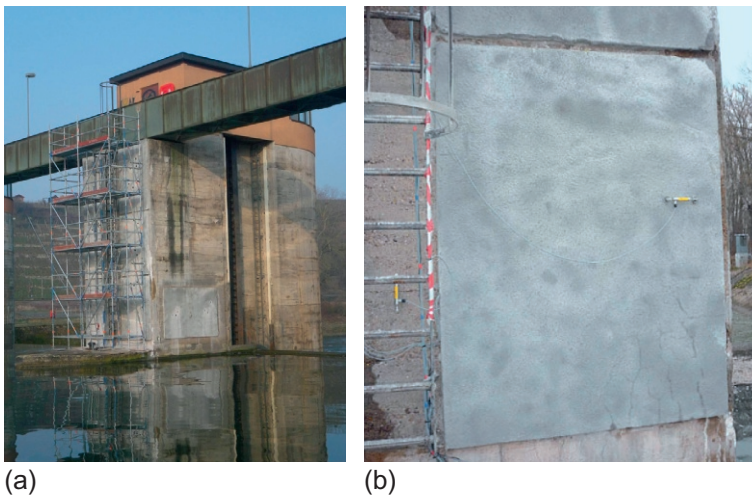
Figure 12.19 Weir structure at Horkheim, Germany. (a) Overview of the sample areas 1–7 (Büttner and Morales Cruz, 2013) and (b) close-up of sample area Nr. 1 (Büttner and Morales Cruz, 2013).

dry cycles and, depending on low or high the water levels are, is affected by bed-load material and ice. Unreinforced mortars for restoration cannot be relied on to prevent the propagation of cracks and, considering the risk of water ingress, this could lead to detachment or failures in adhesion. Therefore, the DURTEX-Concept was suggested. The testing of the DURTEX-Concept was carried out in September 2010 on two pillars of the Horkheim weir. A total of eight sample areas with textile-reinforced sprayed concrete were created. The aim of the project was to both seal the cracks and to protect the surface of the weir pier, on which the sample restoration was carried out (Büttner and Morales Cruz, 2013).

The commercial mortar used for the restoration is StoCrete TS 118 from the company StoCretec. After the surface had been prepared with a pressure washer, the mortar was applied using the dry shotcreting procedure. Different 2D textiles of both AR glass and carbon fibers were used in two layers. They were partly impregnated with epoxy and partly in SBR. The delamination area was realized using a self-adhesive plastic film applied to both sides of the cracks (Büttner and Morales Cruz, 2013).

In order to observe the deformation arising while in use, internal strain gages and temperature sensors were installed in the DURTEX layer (see Figure 12.19b). A maximal movement of 0.28 mm was observed in the underlying concrete. The application can distribute the cracks in a manner so fine that they cannot be detected with the naked eye. This demonstrates the desired reversible deformation of the protection layer (Morales Cruz et al., 2014).

Two years after the installation, there were no significant cracks in the protection layer and no defects, even in the cycle areas. The results of the examination after almost 4 years of production present no significant cracks in the textile-reinforced protective layers, whereas a snap-through of the cracks in the unreinforced area was identified. The findings also show that sufficient adhesion between the textile-reinforced protective layer and the concrete is provided. Even the underwater sample area presented no damage whatsoever (Morales Cruz et al., 2014).

12.4   Future applications of TRC

The list of TRC applications introduced previously in this chapter is in no way exhaustive. The new, innovative building material can and will be used for more structures, renovations and projects in the future. In the context of investigations of the research project C3—carbon, concrete, composite, various applications will be either newly developed or further researched (Scheerer et al., 2015). A few of these future applications and new methods of textile reinforcement are presented in this chapter.

The loadbearing capacity potential of TRC can be used to great effect, where 3D dissolved cross-sections are realized. However, it is very difficult to create such 3D TRC components, and different methods are currently being investigated. Because of the high costs of molds for extruded TRC, the presently used methods are mostly practical for single applications. One of the most economic and efficient methods
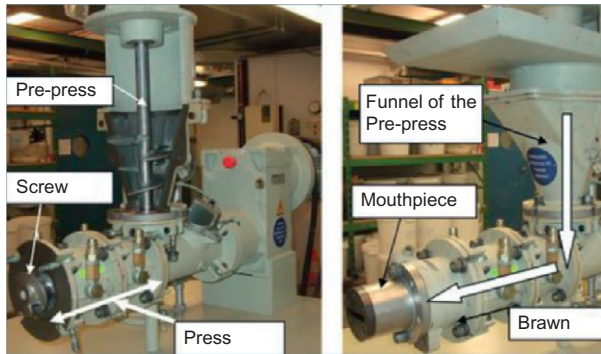
Figure 12.20 TRC extruder. (a) Opened (Brameshuber, 2015), (b) fully mounted (Brameshuber, 2015), and (c) extruded specimen (Mott and Brameshuber, 2012).

to continuously create TRC is an extrusion of the material, which is currently being tested at the Institute of Building Materials Research (see Figure 12.20a and b).

First, concretes with and without addition of short fibers were developed. They had to be extrudable, have a good green strength and form a good bonding behavior with the textile reinforcement (see Figure 12.20c). All concretes had a maximum grain diameter of 5 mm, a high content of binding agents and a very low water content. To ensure the workability of such a mixture, extruding improvers, based on methyl-cellulosis, have to be added (Brameshuber, 2015).

Both impregnated and nonimpregnated textiles were tested in pilot projects. The flexibility of the uncoated textiles proved to be disadvantageous, because they were stretched and corrugated when inserted into the concrete. Their exact placing and good bonding behavior with the concrete must be guaranteed to form an applicable component. This was the main difficulty and focus of the tests. While extruding, the mixture is constantly stirred and then, following a funnel, extruded with a constant volume flow through a mouthpiece. To combine concrete and textile reinforcement, the textile is guided with a rail from outside through the mouthpiece to the outlet. There, it must be embedded into the concrete, which is pressed onto the textile from all sides with the same velocity. The resulting TRC has a high loadbearing capacity and a compressive concrete strength of actually up to 70 N/mm^2 (Brameshuber, 2015).

(a)   (b)
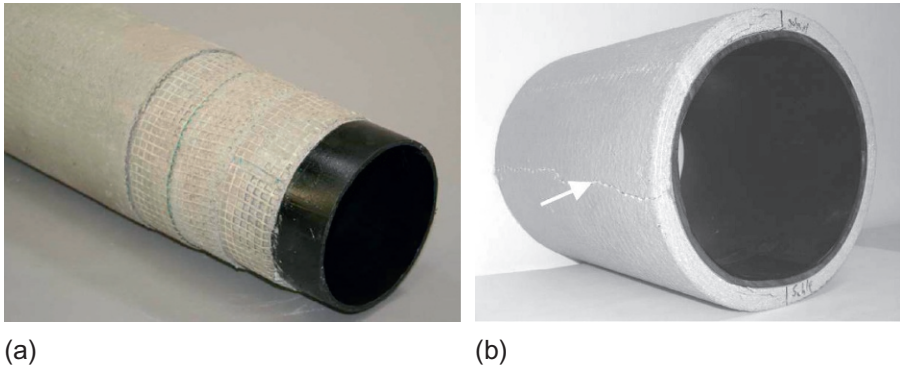
Figure 12.21 Multilayer composite pipes composed of Polyethylene (interior tube) and TRC (exterior tube). (a) Layer structure (V. Mechtcherine, Institut of Construction Materials, TU Dresden) and (b) tube after stress test (Lieboldt et al., 2006).

The method of extruding for the production of TRC components is very promising. However, to apply this method in future projects, further studies to optimize extrusion have to be conducted.

Another future application for TRC is the construction of multilayer composite pipes (see Figure 12.21). These pipes can either be pressure pipes or pressure-free pipes, tunneling pipes or used for corrosion protection of steel pipes. As seen in the previous section, the flexibility of TRC allows for rounded structures like sewer channels, silos, or pipes.

Pressure pipes used in sewage disposal and water supply have to withstand high internal and external pressures. To better distribute the load and increase the pipe's strength, a layer of textile-reinforced, fine-grained concrete was added to the outer side of the conventional plastic pipe. Also, the material of the plastic pipes is more expensive than cement-based mortar, and, by using concrete, the plastic pipe thickness can be reduced (Lieboldt et al., 2006).

The concrete is designed in order to ensure stability and to avoid deformations, due to the loads during and after application. The fine concrete used to cover the pipes consisted of three mass parts of sand with a maximum grain size of 2 mm, three mass parts of binding agent and one mass part of water. The binding agent consisted of two mass parts of cement (CEM III/B 32.5N-NWH/HS/NA) and one mass part of pozzolanic additive (90% fly ash and 10% microsilica). To increase stability, short glass fibers (9 mm, >1% by volume) were added. Thus, the spreading and crack behavior was improved. The concrete was reinforced with warp-knitted AR glass yarns. Experiments showed that biaxial-reinforced structures consisting of 2400 tex yarns in the circumferential direction and 1280 tex in longitudinal direction were the most suitable, so these structures were applied here (Lieboldt et al., 2006).

The TRC is added to the plastic pipe through a winding technology to achieve a minimum layer thickness. For that, the bare textile structure is first conducted through a funnel filled with the concrete and is then wound around the plastic pipe. The plastic pipe is spun, and a predetermined tension is applied to the fabric. The layer thickness is
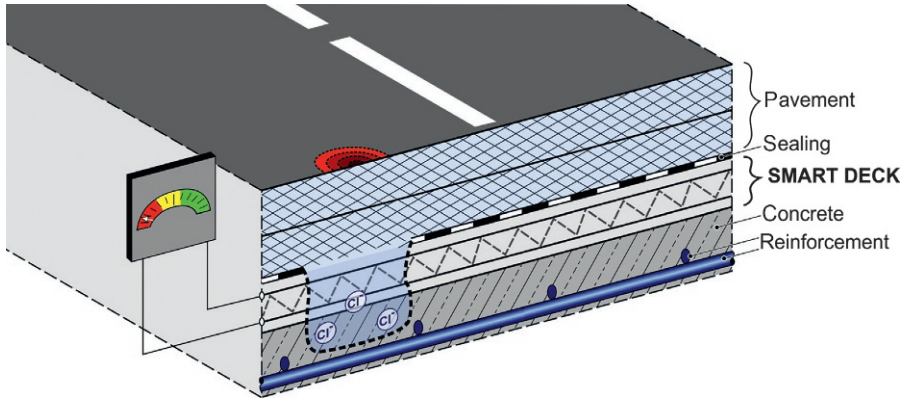
Figure 12.22 Operation method of the multifunctional layer "SMART DECK" for road bridges (C. Driessen, Institute of Building Materials Research, RWTH Aachen University).

controlled through the funnel opening and the compacting device, taking into account both the thickness of the textile structure and the maximum size of the concrete mixture (Lieboldt et al., 2006).

As of today, the applications have only been in the laboratory, and further studies will be necessary to determine the applicability in public sewer systems.

Earlier in the chapter, the issues regarding the durability of steel-reinforced concrete were introduced. Protective measures can be carried out to prevent the corrosion of this material. One such method, namely cathodic protection (CP), is currently being researched in order to increase the service life of road bridges and parking structures using TRC (see Figure 12.22).

The durability and use of road bridges is often limited significantly by both leakage of a sealing layer above the concrete structure as well as by an insufficient shear resistance for existing buildings. In particular, corrosion damage due to chloride-induced corrosion cannot be detected accurately or early enough with the currently used locally limited measuring sensors (Driessen and Raupach, 2015).

As part of the currently running project SMART DECK, an innovative, multifunctional bridge deck will be developed for new constructions, as well as for the repair and strengthening of road bridges to increase their service life significantly. At the same time, SMART DECK aims to reduce economic losses due to traffic delays because of the extensive repair work (Driessen and Raupach, 2015).

To avoid these costly and time-intensive works, SMART DECK will fully observe the condition of the sealing during operation and offer preventive protection of reinforcement. This is performed without any disruption of the traffic flow, even if leaks develop. Additionally, the system offers the possibility to increase the flexural and shear force resistance. This high-tech system thus combines durability and construction-relevant functions in an approximately 30-mm thick interlayer, without making a significant contribution to the weight of the structure (Driessen and Raupach, 2015).

This new future application is based on preliminary research on CP with TRC. Currently, the impressed current anode system is state-of-the-art technology. In this

(a)　　　　　　　　　　　　　　(b)
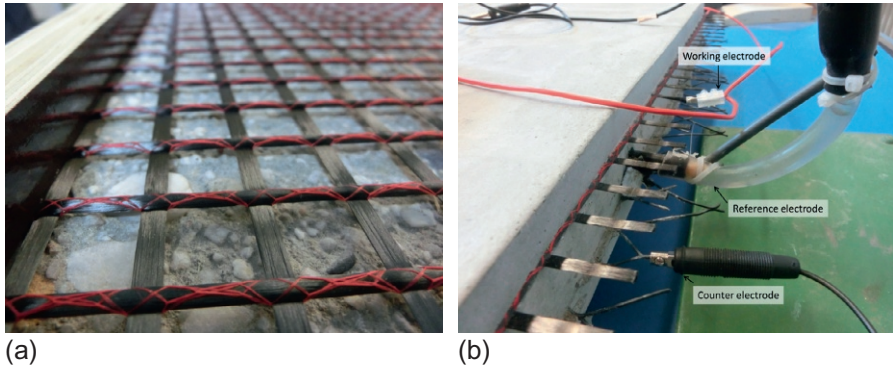
Figure 12.23 (a) One of the investigated carbon textiles—SBR impregnated (A. Asghar Zadeh, Institute of Building Materials Research, RWTH Aachen University). (b) Laboratory specimen to simulate the polarization of carbon textiles in order to determine their suitability for Cathodic Protection (A. Asghar Zadeh, Institute of Building Materials Research, RWTH Aachen University).

system, the CP anodes are embedded in mortar, applied as coating or as a distinct anode on the repair structure surface. They are then exposed to an external current, which causes an excess of electrons and shifts the potential of the carbon steel reinforcement in the cathodic direction. The corrosion process is composed of two electrochemical partial reactions and this change of potential inhibits one of the two. Thus (e.g., chloride-induced) corrosion can no longer take place and the reinforcement will not be dissoluted anodically (Asgharzadeh et al., 2015).

The CP anodes normally consist of mixed metal oxide (MMO)-coated titanium, but the conductive carbon fibers used in carbon textile reinforcement also show promise. They are therefore currently being studied for their suitability for CP (see Figure 12.23) (Asgharzadeh et al., 2015).

In preliminary tests, several different carbon textiles were investigated (see Figure 12.23a). The tests were carried out on specimens simulating corrosion-damaged steel-reinforced concrete. These specimens consisted of a layer of steel-reinforced concrete (MMO for its chemical inertness and reticular structure, leading to a homogenous electric field). This was topped by a concrete cover without reinforcement. Finally, carbon textiles were attached using three types of specially developed mortar in a 15-mm thick layer. The textiles varied in their mesh-width and coating. The four different textiles were: single mesh carbon-coated in SBR (14 mm in warp/8 mm in fill direction), single mesh carbon-coated in epoxy (20/20), double mesh carbon-coated in SBR (15/15) and single mesh carbon-coated also in SBR (14/13) (Asgharzadeh et al., 2015).

On those, galvanostatic tests with stepwise-increased applied electrical currents and instant-off potential measurements were carried out, and the depolarization was determined (see Figure 12.23b). After that, it can be stated that carbon textiles, and therefore TRC, are a suitable material for CP. The best results were found with the single mesh SBR-coated textiles. More research is needed to apply this method under different conditions for longer periods (Asgharzadeh et al., 2015).

12.5 Conclusion

The goal of this chapter was to give an overview of selected case studies and future applications of TRC. A complete overview cannot be given, as the number of applications is continuously increasing.

In this chapter, it has been shown that TRC is a suitable composite material for the repair and strengthening of existing structures, as well as for the design of new constructions due to the lower layer thicknesses, the associated weight reduction and the high filigree quality and flexibility. Additionally, TRC has a good cracking behavior, with which smaller crack widths and crack spacings are visible on the building surface. DURTEX uses this property and increases the crack-bridging ability of TRC, resulting in production of durable protective layers. Due to these and many other advantages that TRC has to offer compared to conventional materials, a further increase in the areas of application is conceivably possible.

References

Asgharzadeh, A., Raupach, M., Koch, D., 2015. Investigations on the suitability of technical textiles for cathodic corrosion protection. In: International Conference on Concrete Repair, Rehabilitation and Retrofitting (ICCRRR).

Brameshuber, W., 2015. Extrusion of textile reinforced concrete. In: Ferro-11, pp. 427–434.

Büttner, T., Raupach, M., 2012. Denkmalgerechte Verstärkung des Aachener Doms mit einer dauerhaften textilbewehrten Rissbandage. TUDALIT Leichter Bauen—Zukunft formen, p. 8.

Büttner, T., Morales Cruz, C., Raupach, M., 2013. Dauerhafte Schutzschichten aus Textilbeton für Bauwerksoberflächen im Wasserbau. Bautechnik 90 (8), 485–490.

Büttner, T., Raupach, M., 2012. Des Bauwerks neue Kleider. Bauen im Bestand 35 (6), 70–75.

Curbach, M., Hauptenbuchner, B., Ortlepp, R., Weiland, S., 2007. Textilbewehrter Beton zur Verstärkung eines Hyparschalentragwerks in Schweinfurt. Beton-und Stahlbetonbau 102, 353–361.

Driessen, C., Raupach, M., 2015. Intelligent, multifunctional textile reinforced concrete interlayer for bridges. In: International Conference on Concrete Repair, Rehabilitation and Retrofitting (ICCRRR).

Ehlig, D., Schladith, F., Frenzel, M., Curbach, M., 2012. Textilbeton—Ausgeführte Projekte im Überblick. Beton-und Stahlbetonbau 107 (11), 777–785.

Erhard, E., Weiland, S., Lorenz, E., Schladitz, F., Beckmann, B., Curbach, M., 2015. Anwendungsbeispiele für Textilbetonverstärkung—Instandsetzung und Verstärkung bestehender Tragwerke mit Textilbeton. Beton-und Stahlbetonbau 110, 74–82.

Fußgängerbrücke Oschatz, 2006. Baunetzwissen. http://www.baunetzwissen.de/objektartikel/Beton_Fussgaengerbruecke-in-Oschatz_69960.html (retrieved 05.13.15).

Grebe, R., 2011. betoShell—Architekturfassaden aus Textilbeton. TUDALIT Leichter Bauen—Zukunft formen, p. 10.

Grebe, R., 2014. Sanierung eines maroden Bahnsteiges mit textilbewehrtem Betonplatten. TUDALIT Leichter Bauen—Zukunft formen, p. 4.

Hegger, J., Kulas, C., Schneider, H.N., Brameshuber, W., Hinzen, M., Raupach, M., Büttner, T., 2010. TRC pedestrian bridge—design, load-bearing behavior and production processes of a slender and light-weight construction. In: International RILEM Conference on Material Science, pp. 353–364.

Horstmann, M., Hegger, J., Büttner, T., Tomoscheit, S., Pachow, U., 2009. Neue Entwicklungen Berechnung und Anwendung von Sandwichfassaden aus Textilbeton. 4. Kolloquium zu Textilbewehrten Tragwerken (CTRS4), pp. 503–514.

Kulas, C., 2014. Fertigteilgaragen aus Textilbeton. TUDALIT Leichter Bauen—Zukunft formen, p. 3.

Kulas, C., Goralski, K., 2014. Die weltweit längste Textilbrücke—Technische Details und Praxiserfahrungen. Beton-und Stahlbetonbau 109, 812–817.

Kulas, C., Schneider, M., Will, N., Grebe, R., 2011. Hinterlüftete Vorhangfassaden aus Textilbeton. Bautechnik 88, 271–280.

Lieboldt, M., Helbig, U., Engler, T., 2006. Textile reinforced concrete multilayer composite pipes. In: 1st International Conference Textile Reinforced Concrete (ICTRC), pp. 369–378.

Morales Cruz, C., Raupach, M., 2014a. Textile reinforced concrete layers for a durable protection of building surfaces. Structural faults and repair. In: 15th International Conference and Exhibition—London.

Morales Cruz, C., Raupach, M., 2014b. Untersuchungen zur kontrollierten Rissverteilung textilbewehrter Schutzschichten mit optischer 3D-Verformungsanalyse. Restor. Build. Monuments 8, 325–336.

Morales Cruz, C., Raupach, M., Westendarp, A., Bruder, S., 2014. Untersuchungen an einer vier Jahre alten Schutzschicht aus textilbewehrtem Spritzbeton am Wehr Horkheim. Beton 64 (10), 390–395.

Mott, R., Brameshuber, W., 2012. Erste Erkenntnisse zum Extrudieren von Textilbeton. TUDALIT Leichter Bauen—Zukunft formen, p. 23.

Raupach, M., Orlowsky, O., Büttner, T., Dilthey, U., Schleser, M., 2006. Epoxy-impregnated textiles in concrete—load bearing capacity and durability. In: International RILEM Conference on Material Science, pp. 77–78.

Raupach, M., Büttner, T., Maintz, H., 2010. Retrofitting AACHEN cathedral with a flexible textile reinforced mortar bandage. In: Conservation of Heritage Structures. Proceedings of the Third International Workshop on Civil Structural Health Monitoring: Conservation of Heritage Structures Using FRM and SHM, pp. 47–60.

Rempel, S., Geßner, S., 2015. Restoration of the historical concrete-glass windows of the town-hall in aachen. In: Ferro-11, pp. 559–564.

Rempel, S., Hegger, J., 2015. Slender facade structures made of textile-reinforced high performance concrete. In: Ferro-11, pp. 337–345.

Rempel, S., Will, N., Hegger, J., Beul, P., 2015. Filigrane Bauwerke aus Textilbeton—Leistungsfähigkeit und Anwendungspotenzial des innovioven Verbundwerkstoffs. Beton-und Stahlbetonbau Spezial 110, 83–93.

Scheerer, S., Schladitz, F., Curbach, M., 2015. Textile reinforced concrete—from the idea to a high performance material. In: Ferro-11, pp. 15–33.

Schladitz, F., Lorenz, E., Jesse, F., Curbach, M., 2009. Verstärkung einer denkmalgeschützten Tonnenschale mit Textilbeton. Beton-und Stahlbetonbau 7, 432–437.

Scholzen, A., Chudoba, R., Hegger, J., 2012. Dünnwandiges Schalentragwerk aus textilbewehrtem Beton. Entwurf, Bemessung und baupraktische Umsetzung. Beton-und Stahlbetonbau 107, 767–776. Heft 11.

Walther, T., Curbach, M., 2015. Textile reinforced concrete for sewer, rehabilitation. In: Ferro-11, pp. 277–285.

Weiland, S., Schladitz, F., Schütze, E., Timmers, R., Curbach, M., 2013. Rissinstandsetzung eines Zuckersilos. Bautechnik 90, 498–504.

This page intentionally left blank

Part Four

Strengthening and seismic retrofitting of existing structures: Structural behaviour, design and case studies

This page intentionally left blank

Strengthening of existing concrete structures: Concepts and structural behavior

13

T. Triantafillou
University of Patras, Patras, Greece

13.1 Introduction

A number of techniques have been developed that aim at increasing the strength and/or deformation capacity of existing reinforced concrete (RC) structures. These include the use of shotcrete overlays, steel jacketing, externally bonded fiber-reinforced polymers (FRP, such as epoxy-bonded strips or *in situ* impregnated fabrics) and near-surface mounted FRP reinforcement. FRP-based strengthening and/or seismic retrofitting techniques have been well-established in the civil engineering community due to favorable properties offered by these materials. These include high strength and stiffness to weight ratio, corrosion resistance, ease and speed of application and minimal change in the geometry. Despite these advantages over other methods, the FRP strengthening technique entails a few drawbacks, which are mainly attributed to the organic resins used to bind and impregnate the fibers.

The replacement of organic binders with inorganic ones, cement-based polymer-modified mortars, for example, would seem to be the logical course of action. This would target the alleviation of all resin-related problems. Nevertheless, the substitution of FRP with fiber-reinforced mortars would be inhibited by the relatively poor bond conditions in the resulting cementitious composite; due to the granularity of the mortar, penetration and impregnation of fiber sheets is very difficult to achieve. Enhanced fiber–matrix interactions could be achieved when continuous fiber sheets are replaced by textiles. This results in a new generation of materials, which may be thought of as an alternative to FRP in the field of strengthening and seismic retrofitting. These materials have been given the name "textile-reinforced mortar" (TRM) by Triantafillou et al. (2006), "textile-reinforced concrete" (TRC) by German researchers (e.g. Curbach and Jesse, 1999; Brameshuber et al., 2001) and "fabric-reinforced cementitious matrix systems" by ACI (2013). Strictly speaking, the inorganic matrix of textile-based composites is not classified as "concrete," due to the very small size of the aggregates, and does not necessarily contain cement. Hence, the term TRM might be more appropriate.

Textiles comprise fabric meshes made of long-woven, knitted or even unwoven fiber rovings in at least two (typically orthogonal) directions (Figure 13.1). The quantity and spacing of rovings in each direction can be independently controlled, thus affecting the mechanical characteristics of the textile and the degree of penetration
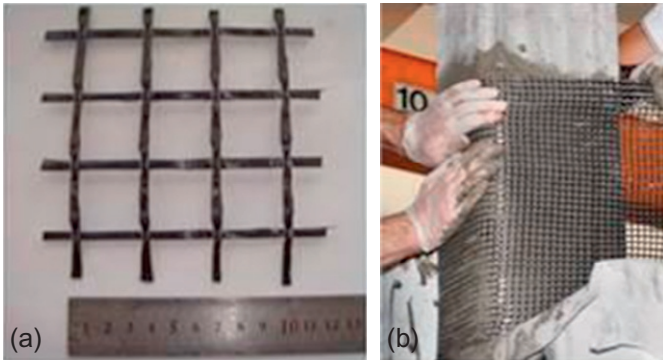
Figure 13.1 (a) Bidirectional textile and (b) application on concrete column.

of the mortar matrix through the mesh openings. The latter is a measure of the composite action achieved for the mortar-grid structure through mechanical interlock. For the inorganic (typically cementitious) matrix (mortar) of externally applied TRM overlays used for strengthening purposes, the following requirements should be met: no shrinkage; high workability (application should be possible using a trowel); high viscosity (application should not be problematic on vertical or overhead surfaces); low rate of workability loss (application of each mortar layer should be possible while the previous one is still in a fresh state) and sufficient shear (hence, tensile) strength in order to avoid premature debonding. Moreover, in cases where E-glass fiber textiles are used, the cement-based matrix should be of low alkalinity.

The TRM system is applied in a way similar to FRP. The concrete is first ground or brushed clean. Then dust and any loose particles are removed (e.g. with air pressure). Finally, a standard wet lay-up procedure is followed to bond the textile layers on the surface of the concrete members. The procedure involves application of the mortar on the (dampened) concrete surface and subsequent application of the textile by hand (Figure 13.1b) and roller pressure. The mortar is also applied in between layers and on top of the last fabric layer. Application of the mortar is made in a few-millimeter (e.g. 3–4 mm) thick layers using a smooth metal trowel. The textile is pressed slightly into the mortar, which protrudes through the perforations between fiber rovings.

This chapter covers basic principles and aspects of the mechanical behavior of RC strengthening with TRM. A number of relevant studies which have provided basic knowledge on the use of TRM as strengthening and seismic retrofitting materials of RC structures are reviewed. In a number of cases, the effectiveness of TRM systems is compared with the one of equivalent FRP systems. The following topics are covered:

- flexural strengthening,
- shear strengthening,
- confinement of axially loaded concrete,
- seismic retrofitting by improving plastic hinge behavior and
- seismic retrofitting of masonry infilled reinforced concrete frames.

13.2 Flexural strengthening

Reinforced concrete elements, such as beams or slabs, may be strengthened in flexure through the use of TRM applied to their tension zones (Figure 13.2). Such reinforcement is not fully effective in the case of beams, as only fibers parallel to the member axis will be activated. Typical load–deflection curves for unstrengthened and strengthened RC beams are compared in Figure 13.3. An increase in the stiffness of the cracked beam can be noted, depending on the amount of axial stiffness added to the beam through the TRM. The increased stiffness limits deflections at the service load level. In terms of cracking, typically more, yet smaller cracks will be observed for the strengthened beam. The yield moment is slightly increased. A considerable increase in the loadbearing capacity is obtained through the additional TRM reinforcement at the expense of a reduction of the ultimate deflection at which the strengthened beam fails. The failure mode often tends to be of a brittle nature, and may typically correspond to debonding between the TRM and the concrete.

A concrete beam strengthened in flexure with externally applied TRM may fail according to the following failure modes: steel yielding followed by concrete
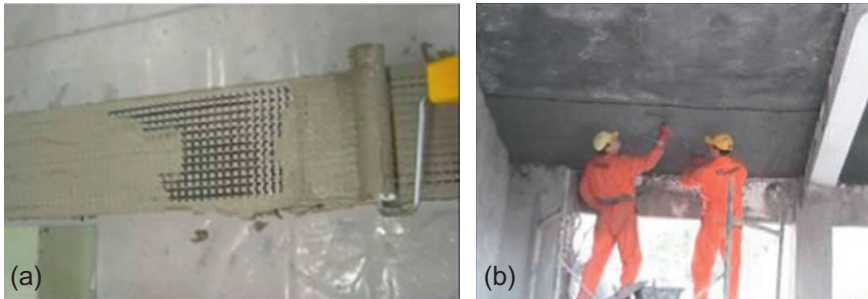
Figure 13.2 Flexural strengthening of (a) beam and (b) two-way slab with TRM.
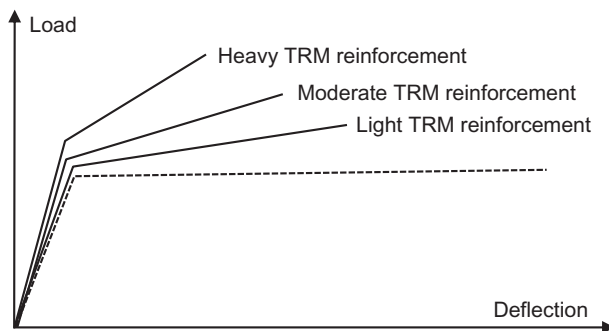
Figure 13.3 Load–deflection curves for different degrees of flexural strengthening.

crushing; steel yielding followed by TRM rupture; concrete crushing (this brittle fail-
ure mode is not permitted) and loss of composite action due to debonding, typically
after steel yielding (this is the most prevalent failure mode).

In cases where the TRM will reach its design tensile strain before the concrete
crushes, failure normally occurs due to debonding rather than rupture. If the mortar
in the TRM has shear strength higher than that of concrete, debonding occurs through
the concrete, which is the "weak link" in terms of bond capacity. This happens
according to one of the following three failure modes: intermediate crack debonding,
that is, debonding starting at intermediate cracks; end debonding, that is, failure of end
anchorage or concrete cover separation (rip-off). However, if the mortar has relatively
low shear strength, debonding will develop due to cracking through the mortar, either
between layers of the textile (interlaminar shear failure) or between the first layer of
textile and the concrete.

The effectiveness of TRM versus FRP as externally applied flexural strengthening
reinforcement of RC *beams* was examined in Triantafillou (2007). The results
reported in this study refer to the testing of three under-reinforced beams in four-point
bending at a span length of 2.0 m and a shear span of 0.75 m. The beams had a cross
section of 150×250 mm and were reinforced with 2Ø12 longitudinal rebars on each
side (top and bottom) at a cover of 25 mm. The shear reinforcement comprised Ø8 stir-
rups at a small spacing of 100 mm to ensure that failure would be controlled by flex-
ural yielding. Self-compacting concrete was used for the casting of the beams with a
mean 28-day compressive strength of 34.5 MPa. The steel reinforcement had an aver-
age yield stress equal to 530 MPa. The textile comprised equal quantities of carbon
fiber rovings in two orthogonal directions with a mass of 168 g/m^2 and a nominal
thickness of each layer (corresponding to the equivalent smeared distribution of
fibers) equal to 0.047 mm. The mortar had a 28-day compressive and flexural strength
of 30.6 and 4.2 MPa, respectively.

One of the three beams was tested without strengthening, as a control specimen
(C_fl); a second one was strengthened with four layers of textile bonded with
cement-based mortar (M4_fl); and the third beam was identical to the second but with
an epoxy resin-based matrix material for the textile reinforcement (R4_fl). The exter-
nally bonded reinforcement had a width and a length of 120 mm and 1.90 m, respec-
tively, so that its distance from each support was 50 mm.

The load versus midspan displacement curves for all beams are given in
Figure 13.4, which shows that the TRM-strengthened beam (M4-fl) displayed similar
characteristics to its FRP counterpart, with some distinct differences: its response was
a little more ductile, yielding initiated at a lower load, and the ultimate load was lower.
It is believed that these differences are attributed to the lower stiffness of the bond
between the external reinforcement and the concrete, which may result in reduced
composite action.

The effectiveness of TRM as a measure of increasing the strength and deformation
capacity of centrally loaded *two-way slabs* was investigated in Papanicolaou et al.
(2009a). To examine this, four slabs cast with perimeter beams (Figure 13.5) were
tested under monotonic flexure.
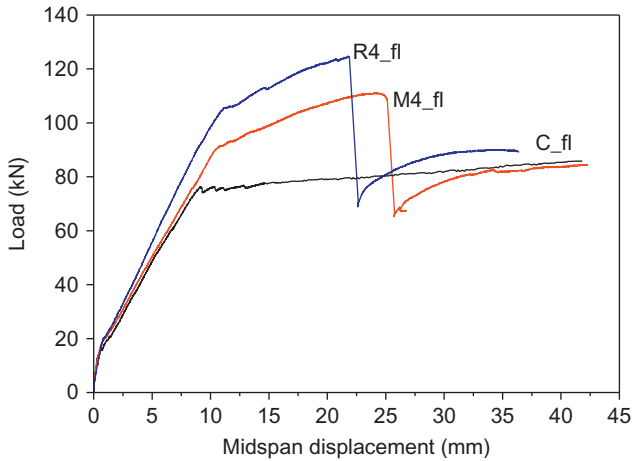
Figure 13.4 Load–displacement response of three simply supported beams strengthened in flexure (Triantafillou, 2007).
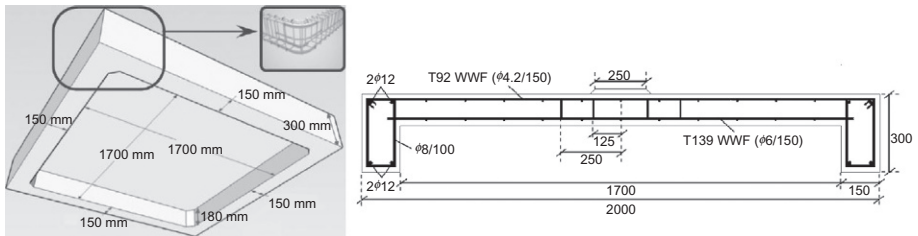
Figure 13.5 Geometry of centrally loaded two-way slabs.

All slabs were fabricated with identical structural steel reinforcement simulating lightly reinforced or, alternatively, moderately corroded slabs. Two welded wire fabrics (WWF) were used: the first comprised a T139 WWF (i.e. 100×100-W13.8 $\times$ W13.8 [mm $\times$ mm-mm$^2 \times$ mm^2]) and was placed at the bottom (tension) surface of the slabs. (The resulting reinforcement ratio was equal to 0.14%.) Whereas the second one was a T92 WWF (i.e. 150×150-W13.8 $\times$ W13.8 [mm $\times$ mm-mm$^2 \times$ mm^2]) and was placed at their top (compression) surface. The slabs were cast using concrete of mean 28-day compressive strength of 25.6 MPa (31.2 MPa at the day of testing). The steel had a conventional yield stress of 645 MPa (at plastic strain 0.2%).

For the specimens receiving TRM overlays, commercial textiles with either carbon or E-glass fiber rovings arranged in two orthogonal directions were used. Both types of textiles shared the same geometry and comprised equal (but different between textiles) quantities of fibers in each direction. The weight of fibers in the textiles was 350 and 500 g/m^2 for the carbon fiber and the E-glass fiber textile, respectively. The nominal thickness of each layer (based on the equivalent smeared distribution

of fibers) was 0.18 mm for both types of textile. The inorganic binder had a 28-day flexural and compressive strength of 6.5 and 24.6 MPa, respectively.

Three specimens were strengthened in total, whereas one served as the control specimen (designated as CON). One specimen received one layer of carbon fiber textile (specimen 1C), another one received two (specimen 2C), whereas the third specimen was strengthened with three layers of E-glass fiber textile (specimen 3G) that had the same axial rigidity (i.e. equal product of fibers' modulus of elasticity and textile thickness) as the single-layered carbon fiber textile (in both directions). These strengthening schemes were selected in this study, so that they would provide useful insight into the effects of the fiber reinforcement ratio and the number of TRM layers (of equivalent axial rigidity).

All specimens were simply supported at their corners on ball-bearing hinges (thus, they were free to rotate at these points) and were subjected to monotonic compressive loading at midspan in a displacement-control mode. The load versus center-point deflection for all specimens is shown in Figure 13.6. All specimens responded in a similar manner in terms of crack development and failure mode. In the uncracked stage, the initial stiffness of all strengthened specimens was higher than that of the control specimen. For all slabs, first cracking due to flexure occurred—as expected—directly below the load application area and at approximately the same load value. With increasing imposed displacement, more flexural cracks formed in both directions along the bars of the tensile steel reinforcement grid (this being more visible in the control specimen). Diagonal cracks were generated propagating from the centers of the specimens to the corners. As recorded by strain gauges, yielding of tensile reinforcement in both directions was delayed in all strengthened specimens.

The failure mechanism involved the sudden punching out of a pyramoid concrete plug at the center of the slabs, accompanied by an immediate and significant drop in
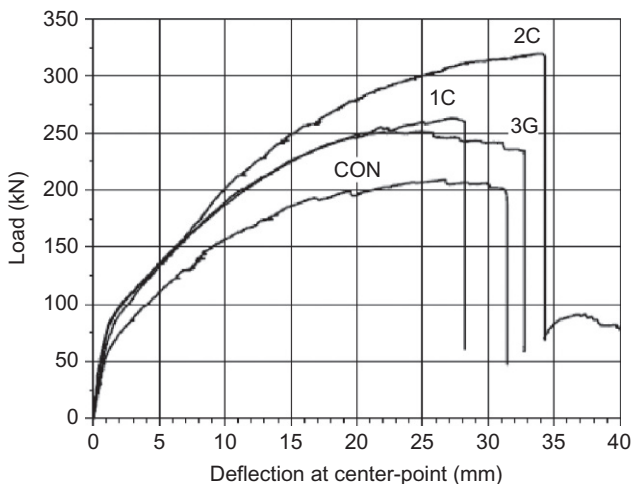
Figure 13.6 Load–center-point deflection curves.

load. Failure was characterized as "flexural punching," as punching occurred shortly after the yielding of the flexural reinforcement (in both directions) near the load application point.

It was concluded in this study that TRM overlays are successful in increasing the load-carrying capacity of flexure-critical RC two-way slabs. Load-carrying capacity increases with increasing fiber reinforcement ratio. Overlays of equal axial rigidity per direction result in a comparable increase of ultimate strength, and interlayer-relative slippage in multilayered systems seems to enhance the deformation capacity of the slabs. Although all strengthened specimens in this study failed due to flexural punching, the failure mode is likely to change to a brittle shear punching should TRM overlays of higher axial rigidity be used. Further details on these test results as well as a comparison with analytical predictions, in good agreement with test results, are given in Papanicolaou et al. (2009b).

13.3   Shear strengthening

The shear capacity of RC members can be enhanced by using TRM jackets, which are activated by bridging shear cracks. Such enhancement is maximized if the TRM forms a closed-force system, for example, by fully wrapping the cross section (Figure 13.7a). Open TRM systems (Figure 13.7b) may also be used for shear strengthening, as long as the reduced effectiveness of the TRM due to debonding is taken into account. Open systems are much more effective when combined with anchorages, as illustrated in Figure 13.7c.

The shear strengthening of beams with rectangular cross sections and *closed jackets* has been investigated by Triantafillou and Papanicolaou (2006). The investigation was carried out on six beams deficient in shear (i.e. with a large spacing of stirrups in the shear span) in four-point bending. The beams measured 2.60 m in length and had a cross section of 150×300 mm. The geometry of the beams, the reinforcement details and the general set-up of the test are shown in Figure 13.8a and b.

The beams were cast using a concrete of mean 28-day compressive strength equal to 30.5 MPa. The steel used for transverse and longitudinal reinforcement had an average yield stress of 275 and 575 MPa, respectively. Textile, mortar, and resin matrices
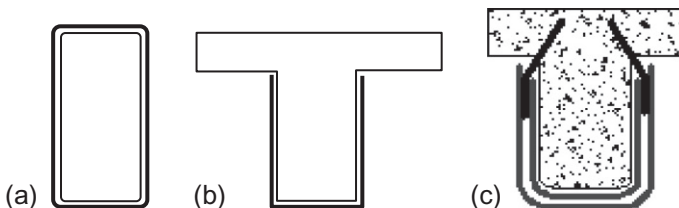
Figure 13.7 Shear strengthening with (a) closed jacket, (b) three-sided jacket, and (c) anchored three-sided jacket.
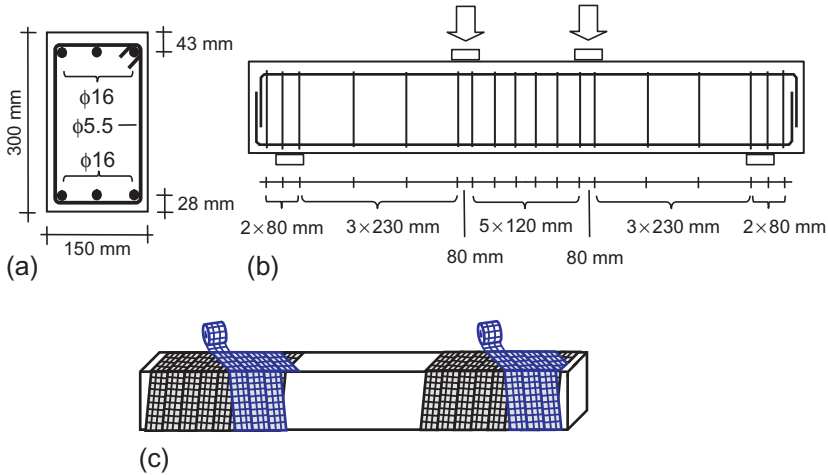
Figure 13.8 (a, b) Geometry of beams and (c) spiral application of strips at the shear spans.

were the same materials as those in the experimental study on flexural strengthening presented in Section 13.2. The influence of three parameters was considered in the experimental investigation: the use of inorganic mortar versus resin-based matrix material for the textile reinforcement, the number of layers (one versus two) and the use of conventional wrapping versus "spirally applied" textiles. Here, "conventional wrapping" corresponds to a single textile sheet being wrapped around the shear span until the desired number of layers is achieved. "Spirally applied" jacketing (Figure 13.8c) was also implemented in one beam and involved the formation of each layer through the use of a single strip, approximately 150-mm wide. The first strip was wrapped around the member in a spiral configuration, starting from one end of the shear span and stopping at the other; the next strip was wrapped in the same configuration but in a direction opposite to that of the first strip. Both strips formed a 10° angle with respect to the transverse to the member axis.

Four of the beams were tested monotonically, and two of them were subjected to cyclic loading. One of the four monotonically tested beams served as a control specimen (C); a second one was wrapped with two layers of mortar-based jacket in the shear span (M2); a third beam was identical to the second, but with a resin-based matrix material for the textile reinforcement (R2); and a fourth beam was strengthened with jackets formed by spirally applied strips (M2-s). The next two specimens were identical to the second and third, but with one layer (instead of two) of textile in a mortar-based (M1) and a resin-based (R1) matrix, respectively. Specimens C, M2, R2, and M2-s were tested monotonically, whereas the remaining two were subjected to quasistatic cyclic loading, all in displacement control. The load versus midspan displacement curves for all specimens are given in Figure 13.9.

The control beam (C) failed in shear, as expected, through the formation of diagonal cracks in the shear spans; the ultimate load was 116.5 kN. No sudden drop in the
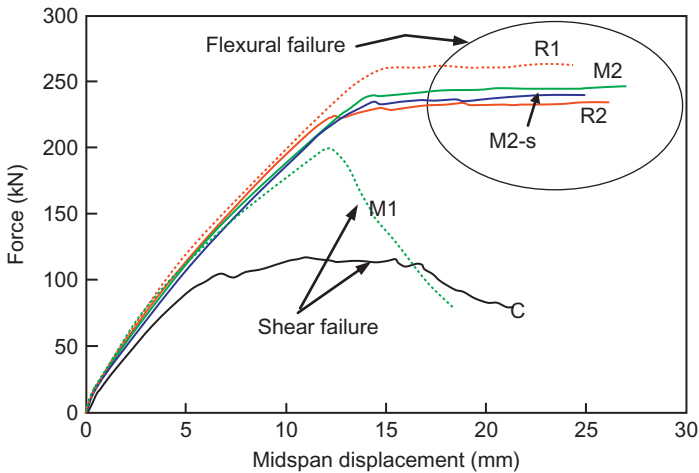
Figure 13.9 Force–midspan displacement curves for all beams tested (for beams M1 and R1 subjected to cyclic loading, the envelope curves in the push direction are given).

load was recorded after diagonal cracking, as considerable contribution to shear resistance was provided by both the stirrups crossing the crack and the strong dowel action (activated by the three Ø16 mm longitudinal rebars).

The behavior of beams R2, M2, M2-s, and R1 indicated that shear failure was suppressed, and that failure was controlled by flexure. Cracks in the constant moment region became wide, and yielding of the tension reinforcement resulted in a nearly horizontal branch of the force versus displacement curve. The maximum loads in specimens R2, M2, and M2-s were 233.4, 243.8, and 237.7 kN, respectively, in other words, nearly the same. This confirms the fact that the shear strengthening scheme selected in this study did not affect the flexural resistance. But the increase in shear resistance was dramatic (more than 100%), regardless of the strengthening scheme. Two layers of textile reinforcement (either in the form of continuous sheets or spirally applied strips) with the cementitious binder performed equally well to the epoxy-bonded (FRP) jacket (with two layers of textile reinforcement). Specimen R1 experienced a flexural yielding failure mode with unequal capacities in the push and pull directions (261.9 and 201.4 kN, respectively). This was possibly due to the unintentionally larger concrete cover at the top of each beam compared to the bottom. Specimen M1 failed in shear (at a peak load of 200.1 kN); this was evident by diagonal cracking in the shear span as well as by the rather sudden strength and stiffness degradation. In this case, the application of a single-layer TRM jacket resulted in a substantial increase in the specimen's shear capacity, with respect to the control specimen, in the order of 70%. It should be noted that for specimen M1: (1) the fracture of the fibers in the cement-based jacket was gradual, starting from a few fiber bundles and propagating slowly in the neighboring fibers and (2) contrary to conventional FRP jackets, beam cracking was clearly visible on the TRM jacket, a feature that facilitates damage assessment.

Overall, it may be concluded that the closed-type TRM jackets employed in this study were quite effective in increasing the shear resistance of RC members. Two layers of textile reinforcement (with a nominal thickness per layer of only 0.047 mm in each of the principal fiber directions) were sufficient to prevent sudden shear failure. Whereas one layer proved less effective compared to its resin-bonded (FRP) counterpart, but still sufficient to provide a substantially increased shear resistance. More details, including modeling aspects, are given in Triantafillou and Papanicolaou (2006).

Shear strengthening of T-beams with *three-sided TRM jackets* has been studied by Brueckner et al. (2006, 2008). A more comprehensive study was carried out by Tzoura and Triantafillou (2014), who investigated experimentally the following parameters not studied before: cyclic loading; fixed support conditions; different types of textiles; different numbers of layers; anchors; the relative performance of TRM versus equivalent FRP systems and different displacement amplitudes of the loading cycles. Tzoura and Triantafillou (2014) tested 13 T-beams as cantilevers (Figure 13.10a) in order to simulate realistic boundary conditions of continuous beams near their supports (columns). All beams were intentionally designed so that their flexural resistance exceeded the shear resistance not only before strengthening but also after, hence only shear failure could develop. Details of beam geometry and reinforcement are given in Figure 13.10b.

For the specimens receiving jacketing (Figure 13.11a), two different textiles ("light" and "heavy") with equal quantities of carbon rovings in two orthogonal directions were used. Each roving was approximately 3-mm wide, and the spacing between rovings (axis-to-axis) was 10 mm. The mass per unit area was 174 g/m^2 for the light textile and 348 g/m^2 for the heavy textile, resulting in a nominal thickness of each layer (based on the equivalent smeared distribution of fibers) of 0.048 and 0.096 mm for the light and the heavy textile, respectively. For the specimens receiving mortar as a binding material, a cementitious dry binder mixed with redispersible polymers was used. The mean compressive and flexural strength of the mortar on the day of testing were 21.8 and 5 MPa, respectively.
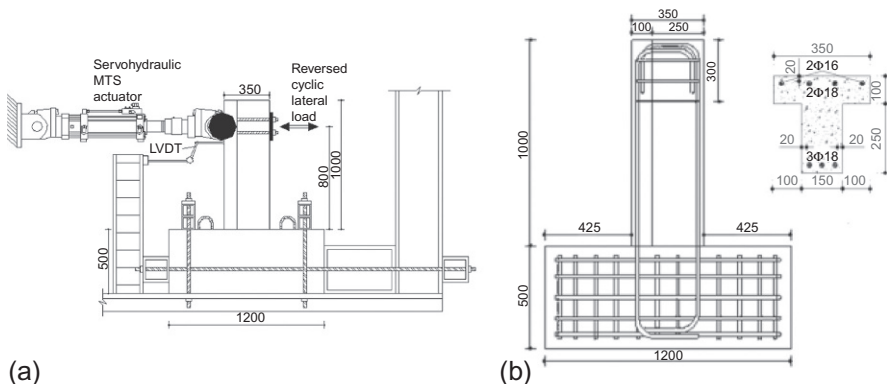
Figure 13.10 (a) Test set-up and (b) beam geometry and reinforcement (dimensions in mm).
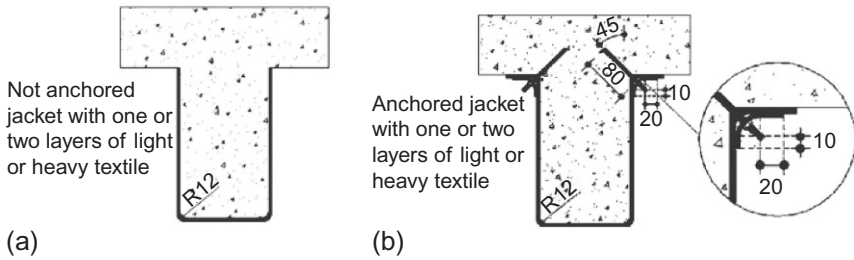
Figure 13.11 Strengthening configuration of the beams tested: (a) U-jackets without anchors and (b) use of anchors.

The anchorage system comprised 3-mm thick curved steel sections fixed at the slab with steel anchors (Figure 13.11b). The steel sections were placed at the corners between the slab and the web, on top of the ends of the jacket, at a radius of 20 mm, while the mortar was still wet. The anchors were made of threaded rods that were 6 mm in diameter; the rods were placed inside 45° holes drilled at a fixed spacing (150 or 100 mm). Holes were drilled into the slab with dimensions of 80 mm in depth and 9 mm in diameter. The holes were filled with a two-part epoxy adhesive to half of their depths, and the anchors were inserted into the holes. Excessive resin was removed, and the steel sections were fixed by tightening the bolts through the use of nuts after hardening of the epoxy adhesive. This method of anchoring was selected on the basis of transferring the tension forces from the jacket into the slab.

All beams were subjected to lateral cyclic loading with a shear span of 0.8 m. Loading comprised successive cycles that progressively increased by fixed amplitudes. The main conclusions from this study are summarized as follows: (a) The effectiveness of TRM jackets without anchorage increases nonproportionally to the number of textile layers. Moreover, for the same total volume fraction of fibers in the jacket, one layer is more effective than two. (b) The anchorage system developed and tested dramatically increases the effectiveness of TRM (and FRP) jackets. (c) Nonanchored FRP jackets are nearly twice as effective as their TRM counterparts. However, if the jackets are anchored, the TRM system is marginally inferior to the FRP system. (d) Modeling of the TRM jacket contribution to the shear resistance of T-beams may be based on the well-known truss analogy, with the stress in the jacket (effective strength) in the range 0.002–0.008, depending on the presence of anchors and their spacing.

13.4 Confinement of axially loaded concrete

In applications where the loading is predominantly static, TRM wrapping may be used in columns to activate a multiaxial state of stress so as to benefit from the commensurate increase in confined concrete strength and deformation capacity. Hence, the axial load capacity will be increased through confinement. The fibers in the hoop direction resist lateral expansion due to compressive stresses in the concrete. This

results in a confining stress to the core, delaying fracture of the concrete and thereby enhancing the compressive strength and the ultimate compressive strain of concrete. This process is significantly more efficient with circular columns than with square or rectangular columns. This is because, with the latter, the confining action is mostly concentrated at the corners, whereas the local strain demand of the TRM jackets increases the risk of localized premature rupture at the corners. Furthermore, similar to FRP, TRM deforms elastically up to very high stresses, and therefore exerts an increasing confining action on concrete until the fibers rupture in the hoop direction.

The effectiveness of TRM versus FRP as a measure of confining axially loaded plain concrete cylinders (150×300 mm, Series A) and short column-type reinforced concrete prisms with a rectangular cross section (200×200 mm, Series B) was reported in Triantafillou et al. (2006) and Bournas et al. (2007), respectively. Each specimen series was cast using the same ready-mix concrete batch (but slightly different from series to series, in terms of water to cement ratio). The steel used for both longitudinal and transverse reinforcement in Series B specimens (Figure 13.12) had an average yield stress of 560 MPa. The four corners of all rectangular prisms were rounded at a radius of 25 mm.

All specimens received textiles as externally bonded reinforcement, except for some of the Series B specimens, in which the epoxy resin-impregnated jackets consisted of fabrics (unidirectional fiber sheets). Specimens are given the notation Y_XN, where Y denotes the series designation (A, B); X denotes the type of jacket—C for the unjacketed/control specimens, M_A for Series A cylinders with mortar jackets, M_B for Series B prisms with mortar jackets (mortar quality in this case being different from mortar M_A) and R for resin-based jackets (FRP); and N denotes the number of layers. Two different commercial unwoven textiles with equal quantities of high-strength carbon fiber rovings in two orthogonal directions were used in these tests. The mass of
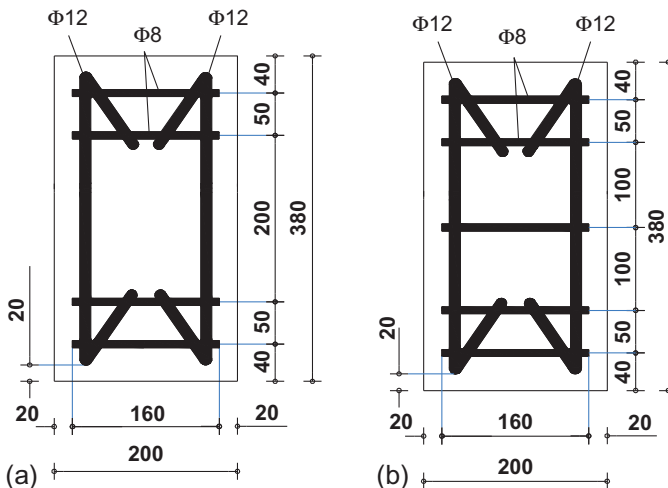
Figure 13.12 Reinforcement configurations for axially loaded RC prisms with stirrups every (a) 200 mm and (b) 100 mm.
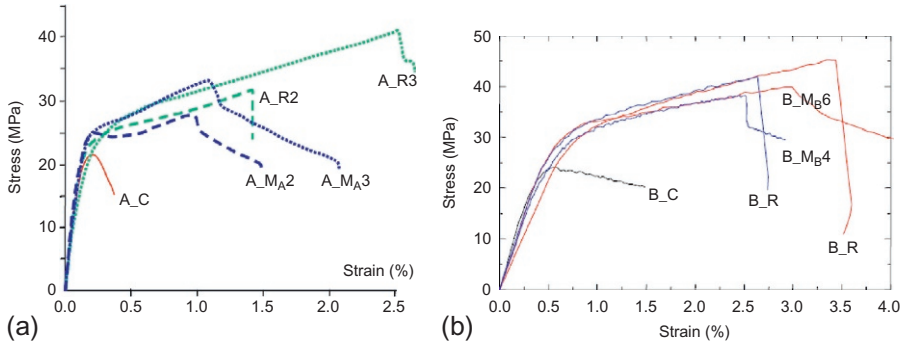
Figure 13.13 Typical stress–strain curves for (a) plain concrete cylinders and (b) RC prisms with stirrups every 100 mm.

fibers in the textile used for all specimens of Series A was 168 g/m^2, and the nominal thickness of each layer (corresponding to the equivalent smeared distribution of fibers) was 0.047 mm. The corresponding values in the textile used in Series B receiving mortar were double (in this case, the rovings were also impregnated with a low-strength polymer). The fabric used for specimens of Series B that were receiving epoxy resin had a unit mass of 300 g/m^2 and a nominal thickness of 0.17 mm. Mortars M_A and M_B were commercial dry polymer-modified, cement-based binders with a 28-day compressive and flexural strength of 30.6 and 4.2 MPa, respectively, for M_A and 22.1 and 6.8 MPa, respectively, for M_B.

Based on the response of all specimens (selected plots are given in Figure 13.13), it is concluded that: (a) TRM confining jackets provide substantial gain in compressive strength and deformation capacity. This gain is higher as the number of confining layers increases. It also depends on the shear strength of the mortar, which determines whether failure of the jacket will occur due to fiber fracture or debonding. (b) Compared with their resin-impregnated counterparts (FRP), TRM jackets may result in a slightly reduced effectiveness, depending on the type of mortar. (c) TRM jackets experienced gradual fracture and a post-peak behavior that was distinctively more compliant than their FRP counterparts, due to the slowly progressing fracture of individual fiber bundles. A more detailed analysis of the results, as well as some modeling aspects of TRM-confined concrete, may be found in Triantafillou et al. (2006) and Bournas et al. (2007).

13.5 Seismic retrofitting by improving plastic hinge behavior

TRM jackets may also be used in plastic hinge confinement (Figure 13.14) of old-type RC columns designed with poorly detailed reinforcement. What matters for earthquake resistance in columns is the compression zone at the ends and, notably, the flexure-controlled ultimate deformation of the member. This ultimate deformation

Figure 13.14 Application of TRM to confine plastic hinge in RC column.

is conveniently expressed by the ultimate curvature (φ_u) of the cross section, which depends heavily on the ultimate strain of the confined concrete ε_{ccu}.

Selected results from the study of Bournas et al. (2007) are presented next. They illustrate a comparison between the increase in ductility provided by TRM jackets and equivalent (i.e. with the same amount of fibers in the circumferential direction) FRP jackets. In this study, three full-scale, identical RC columns were cast using ready-mix concrete with a mean 28-day compressive strength of 25 MPa. The columns measured 1.80 m in height and had a cross section of 250×250 mm. Testing was done in a cantilever configuration, with a shear span of 1.60 m. The geometry of the columns, the reinforcement details and the general set-up of the test are shown in Figure 13.15. Details are provided in Bournas et al. (2007). An in-depth experimental investigation for columns with lap-splices is given in Bournas et al. (2011), and the problem of bar buckling is analyzed in Bournas and Triantafillou (2011).

One column was unstrengthened (control specimen); another one received a four-layer TRM jacket in the plastic hinge region (jacket height was equal to 430 mm, accounting for the calculated height of the plastic hinge, Figure 13.14); and a third column was jacketed with two layers of resin-impregnated carbon fiber fabric (FRP). The materials used for jacketing were identical to the ones used for strengthening specimens of Series B in the previously described experimental investigation on confinement of RC prisms. The columns were subjected to lateral cyclic loading under a constant axial load of 460 kN corresponding to 30% of the member's compressive strength. The load versus piston displacement curves for all specimens are given in Figure 13.16.
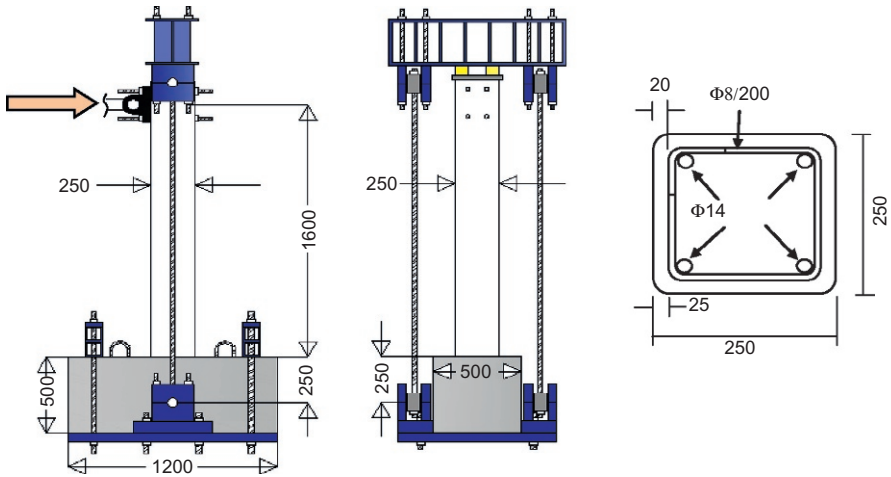
Figure 13.15 Geometry of columns (tested as vertical cantilever) and details of cross section (dimensions in mm).
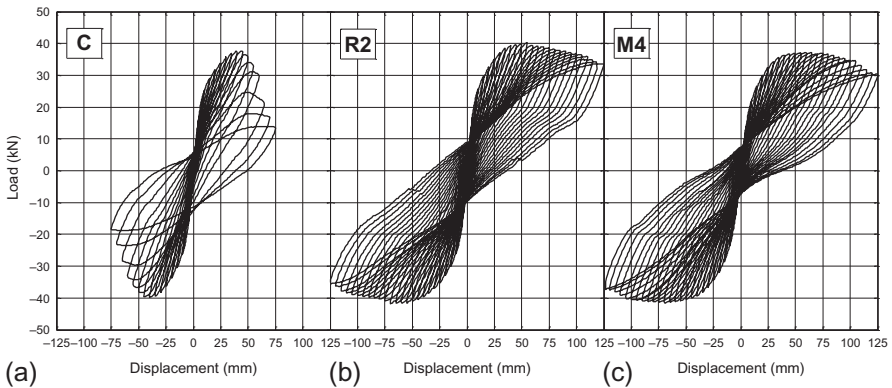
Figure 13.16 Load–displacement curves for (a) the control specimen, (b) the FRP-confined specimen (R2), and (c) the TRM-confined specimen (M4).

The performance and failure mode of all tested columns was controlled by flexure. The concrete cover and part of the core over the lower 200 mm of the unretrofitted column (Figure 13.16a) disintegrated, and bar buckling initiated after the concrete cover spalled off. The behavior of the two retrofitted columns was very similar (Figure 13.16b and c for columns R2 and M4, respectively), but quite different from and far better than their unretrofitted counterpart. Member deformation capacity increased by a factor of more than two; peak resistance was practically the same as in the unretrofitted column; and the post-peak response was quite stable, displaying gradual strength degradation. Although the FRP jacket in column R2 exhibited limited rupture over the lower 50 mm, the TRM jacket remained intact until the test was

Figure 13.17 Pseudodynamic testing of two-story RC building retrofitted at column ends with TRM jacketing.

terminated. When the jackets were removed in both retrofitted columns after the end of the tests, a completely disintegrated concrete core was exposed. It had been kept in place by the heavy confinement provided by the jackets (both FRP and TRM). These tests show that TRM jackets are very effective as a means of increasing the cyclic deformation capacity and the energy dissipation of old-type RC columns with poor detailing, by delaying bar buckling. Compared with equal stiffness and strength FRPs, TRM jacketing has practically the same effectiveness. The high effectiveness of TRM jacketing as a measure of improving plastic hinge behavior was also demonstrated through nearly full-scale testing of a two-story RC building (Figure 13.17), as reported in Bousias et al. (2007).

13.6 Seismic retrofitting of infilled reinforced concrete frames

The contribution of masonry infills to the seismic resistance of existing RC structures is significant, both before separation of the infill from the surrounding frame occurs and during large cycles of imposed deformations near collapse. Strengthening of this type of structure usually aims at increasing the resistance and deformation capacity of the frame itself, setting aside the contribution of infills as a source of strength reserve. An alternative route at improving the performance of existing building structures,

while avoiding the drawbacks of the approach above, is to convert masonry infilling to a more reliable source of resistance by guaranteeing its contribution over the whole spectrum of structural response. This has been examined experimentally and analytically by Koutas et al. (2014a,b). They employed the very promising technique of TRMs on nearly full-scale, as-built and retrofitted three-story masonry infilled frames (Figure 13.18). The frames were subjected to cyclic loading.

Their test results, presented in detail in Koutas et al. (2014a), concluded that: (a) The TRM retrofitting scheme resulted in an enhanced global response of the infilled frame, both in terms of lateral strength and deformation capacity (Figure 13.19). More than a 50% increase in the lateral strength was observed,
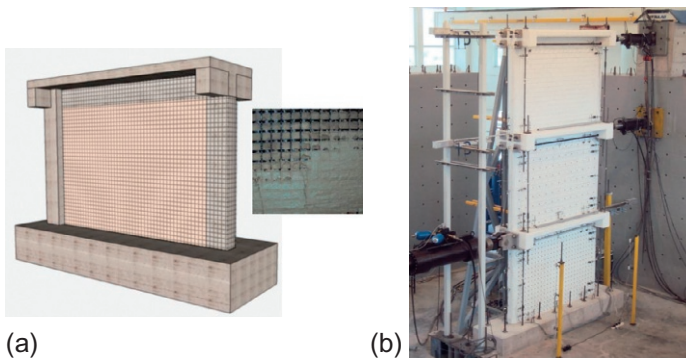
Figure 13.18 Seismic retrofitting of masonry infilled RC frame with TRM: (a) the concept and (b) in-plane testing of three-story frame.
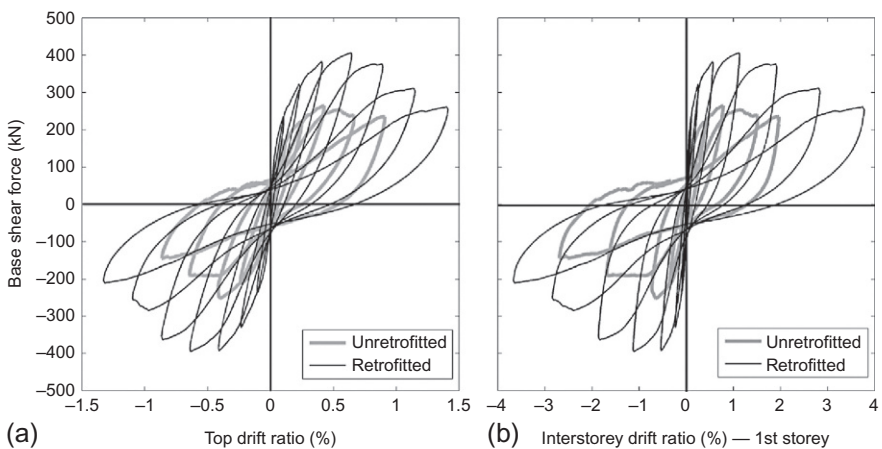
Figure 13.19 Comparative response curves for the two specimens (Sp.#1—unretrofittited and Sp.#2—retrofitted with TRM) in terms of base shear versus (a) top drift ratio and (b) first story drift ratio.

accompanied with more than a 50% higher deformation capacity at the top of the structure at the ultimate strength state. (b) The retrofitted specimen dissipated about 25% more energy than the unretrofitted control for the same loading history. The effect of retrofitting on the lateral stiffness of the first story was an almost twofold increase for low drift levels (up to 0.5%); this became less pronounced at higher drift levels. (c) The height-wise distribution of the lateral story displacements was drastically modified in the retrofitted specimen. Column shear capacity enhancement by TRM wrapping suppressed preemptive column shear failure. This was caused in the control specimen by the lack of adequate transverse reinforcement and the concentration of high shear demands at column end regions, induced by the so-called "diagonal strut." (d) The application of TRM over the entire surface of infills should be supplemented with an adequate infill-frame connection, if a reliable resisting system is to be obtained. For example, this can be done through the use of custom-fabricated, textile-based anchors, which were proved to be particularly effective in delaying or even precluding the debonding of TRM. (e) TRM jacketing proved to be effective in withstanding large shear deformations through the development of a multi-crack pattern and by introducing an efficient load transferring mechanism at the local level. This mechanism is enabled by the capability of the textile itself to distort in shear, while retaining, at the same time, its structural integrity.

An analytical model for describing the behavior of TRM-strengthened masonry-infilled RC frames is introduced in Koutas et al. (2014b), based on the use of a pair of elements per infill diagonal. This simple "macro-modeling" approach was implemented in the *OpenSees* (McKenna et al., 2000) open-source software. It was employed to simulate the response of the three-story masonry infilled RC frame strengthened with TRM and tested under cyclic loading by Koutas et al. (2014a). Model predictions are shown to compare satisfactorily with the experimentally observed response results in terms of the lateral force–displacement response and other response characteristics, such as stiffness and energy dissipation.

13.7   Summary

Fundamental aspects of RC strengthening and seismic retrofitting were presented in this chapter, with a view, in most cases, of comparing the effectiveness of TRM systems with equivalent—in terms of strength and stiffness—FRP ones. The chapter covered: flexural strengthening of RC beams and two-way slabs; shear strengthening of RC beams with rectangular or T-sections, using closed or three-sided jackets, respectively; confinement of axially loaded concrete subjected to concentric compression; seismic retrofitting of columns by improving plastic hinge behavior and seismic retrofitting of masonry infilled reinforced concrete frames. The author demonstrated that, in all cases, TRM jacketing was quite effective—and nearly as effective as FRPs—in improving mechanical performance. This was quantified through strength and/or ductility calculations.

References

ACI 549.4R-13, 2013. Guide to Design and Construction of Externally Bonded Fabric-Reinforced Cementitious Matrix (FRCM) Systems for Repair and Strengthening Concrete and Masonry structures. American Concrete Institute, Farmington Hills, USA.

Bournas, D.A., Triantafillou, T.C., 2011. Bar buckling in RC columns confined with composite materials. J. Compos. Constr. 15 (3), 393–403.

Bournas, D., Lontou, P., Papanicolaou, C.G., Triantafillou, T.C., 2007. Textile-reinforced mortar (TRM) versus FRP confinement in reinforced concrete columns. ACI Struct. J. 104 (6), 740–748.

Bournas, D.A., Triantafillou, T.C., Zygouris, K., Stavropoulos, F., 2011. Bond strength of lap spliced bars in concrete confined with composite jackets. J. Compos. Constr. 15 (2), 156–167.

Bousias, S.N., Spathis, A.-L., Fardis, M.N., Triantafillou, T.C., Papanicolaou, T.C., 2007. Pseudodynamic tests of non-seismically designed RC structures retrofitted with textile-reinforced mortar. In: 8th International Symposium on Fiber-Reinforced Polymer Reinforcement for Concrete Structures—FRPRCS8, Patras, Greece, July 16–18.

Brameshuber, W., Brockmann, J., Roessler, G., 2001. Textile reinforced concrete for formwork elements—investigations of structural behaviour. In: Burgoyne, C.J. (Ed.), FRPRCS-5 Fiber Reinforced Plastics for Reinforced Concrete Structures, vol. 2. Thomas Telford, London, pp. 1019–1026.

Brueckner, A., Ortlepp, R., Curbach, M., 2006. Textile reinforced concrete for strengthening in bending and shear. Mater. Struct. 39 (8), 741–748.

Brueckner, A., Ortlepp, R., Curbach, M., 2008. Anchoring of shear strengthening for T-beams made of textile reinforced concrete (TRC). Mater. Struct. 41 (2), 407–418.

Curbach, M., Jesse, F., 1999. High-performance textile-reinforced concrete. Struct. Eng. Int. 4, 289–291.

Koutas, L., Bousias, S.N., Triantafillou, T.C., 2014a. Seismic strengthening of masonry infilled RC frames with TRM: experimental study. J. Compos. Constr. http://dx.doi.org/10.1061/(ASCE)CC.1943-5614.0000507.

Koutas, L., Triantafillou, T.C., Bousias, S.N., 2014b. Analytical modeling of masonry-infilled RC frames retrofitted with textile reinforced mortar. J. Compos. Constr. http://dx.doi.org/10.1061/(ASCE)CC.1943-5614.0000553.

McKenna, F., Fenves, G.L., Scott, M.H., Jeremic, B., 2000. Open System for Earthquake Engineering Simulation (OpenSees). Pacific Earthquake Engineering Research Center, University of California, Berkeley, CA.

Papanicolaou, C., Triantafillou, T.C., Papantoniou, I., Balioukos, C., 2009a. Strengthening of two-way slabs with textile-reinforced mortars (TRM). In: 11th International fib Symposium, London, June 22–24.

Papanicolaou, C., Triantafillou, T.C., Papantoniou, I., Balioukos, C., 2009b. Strengthening of two-way reinforced concrete slabs with textile reinforced mortars (TRM). In: 4th Colloquium on Textile Reinforced Structures (CTRS4), Dresden, June 3–5.

Triantafillou, T.C., 2007. Textile-reinforced mortars (TRM) versus fibre-reinforced polymers (FRP) as strengthening and seismic retrofitting materials for reinforced concrete and masonry structures. In: International Conference on Advanced Composites in Construction (ACIC07), University of Bath, April 2–4.

Triantafillou, T.C., Papanicolaou, C.G., 2006. Shear strengthening of RC members with textile reinforced mortar (TRM) jackets. Mater. Struct. RILEM 39 (1), 85–93.

Triantafillou, T.C., Papanicolaou, C.G., Zisimopoulos, P., Laourdekis, T., 2006. Concrete con-
    finement with textile reinforced mortar (TRM) jackets. ACI Struct. J. 103 (1), 28–37.
Tzoura, E.A., Triantafillou, T.C., 2014. Shear strengthening of reinforced concrete T-beams
    under cyclic loading with TRM or FRP jackets. Mater. Struct. http://dx.doi.org/
    10.1617/s11527-014-0470-9.

Strengthening of existing concrete structures: Design models

<div style="text-align:right">**14**</div>

E. Müller, S. Scheerer, M. Curbach
Technische Universität Dresden, Dresden, Germany

14.1 Preliminary note

The models presented in this chapter were developed primarily in different subprojects of the Collaborative Research Center SFB 528 (SFB 528; Curbach and Ortlepp, 2012). The SFB 528 was funded from 1999 to 2011 by the German Research Foundation DFG. Some of the models were refined later on. Thus, the authors would like to point out that the results are a product of an intensive, collaborative research of many participants. Significant developments in the various aspects related to this technology are as follows:

- Fundamental material investigations (e.g., Jesse, 2004; Ortlepp, 2007; Lorenz, 2014).
- Flexural strengthening. First, basic models were developed by Bösche (2007) and Weiland (2009). Schladitz et al. (2012) extended the approaches to the newly available textile reinforcement. An engineering-based treatment, including design charts and diagrams, was developed by Frenzel and Curbach (2011) and Frenzel (2015).
- Shear strengthening. The research was conducted by Brückner (2011). A confirmation of the results and an extension for beams with dynamic loading was carried out by Brückner et al. (2013).
- Torsional strengthening. The scientific findings are taken from Schladitz (2011).
- Axial strengthening. The fundamental research was done by Ortlepp and Curbach (2009) and Ortlepp et al. (2011a).

The models are based on extensive experimental and theoretical studies (Curbach and Scheerer, 2011). Nevertheless, in some cases, the textile materials presented differ from those that have been intensively investigated, especially if they show a peculiar failure or bond behavior. Therefore, in every part of the chapter, there is a short characterization of the textile reinforcement used. The issue of end-anchoring and overlapping is not considered, because research on this field is still underway. The constitutive laws and partial safety factors for concrete and steel are taken from the standards as indicated.

The determination of the material properties for a TRC-strengthening layer is usually carried out by using the following specimens:

- Prism ($40 \times 40 \times 160$ mm) for the compressive strength of the fine-grained concrete.
- Uniaxial tension specimens for the tensile strength of the textile.

More information about the recommended test procedures are given in (RILEM TC 232-TDT, 2015) and in Schütze et al. (2015). The design value of the compressive strength of fine-grained concrete can be calculated according to DIN EN 1992-1-1 (2011). The concrete is treated like a normal-weight concrete of the appropriate strength class.

To determine the design value of the tensile strength of the composite material, statistical analysis of results obtained from previous research is required; see Section 14.2 or DIBt (2014). Among them, Just (2015) calculated the partial safety factor for a carbon textile, considering the following values:

- Partial safety factor: $\beta = 3.8$ according to DIN EN 1990 (2010).
- Average value of a sample of the tensile strength: $\mu = 1872$ N/mm^2.
- Standard deviation: $\sigma = 148.5$ N/mm^2.
- Characteristic value $= 1.5‰$ value: $f_{tk,tex} = 1550$ N/mm^2.
- Partial factor of the textile reinforcement: $\gamma_{t,tex} = 1.20$.
- Additional reduction factor due to:
  - temperature influence: $\alpha_{T,tex} = 0.85$,
  - creep resistance (static): $\alpha_{t\infty,tex} = 0.7$,
  - durability: $\alpha_{D,tex} = 0.7$ (in general); $\alpha_{D,tex} = 1$ (indoor, dry site conditions).

An overall safety γ_{tex} factor is often specified, which has already taken into account all reduction factors α:

$$\overline{\gamma}_{tex} = \frac{\gamma_{t,tex}}{\alpha_{T,t} \cdot \alpha_{t\infty,t} \cdot \alpha_{D,t}} = \begin{cases} 2.02 & \text{indoor, dry site conditions} \\ 2.88 & \text{in general} \end{cases} \tag{14.1}$$

The design value $f_{td,tex}$ for textile reinforcements is calculated according to the approval (DIBt, 2014) as follows:

$$f_{td,tex} = \alpha_{T,tex} \cdot \alpha_{t\infty,tex} \cdot \alpha_{D,tex} \cdot \frac{f_{tk,tex}}{\gamma_{t,tex}} = 0.85 \cdot 0.7 \cdot \alpha_{D,tex} \cdot \frac{1550}{1.2}$$
$$= \alpha_{D,tex} \cdot 769 \text{ N/mm}^2 \tag{14.2}$$

The safety factor for other textile reinforcements can be determined in an analogous manner.

14.2 Bending strengthening

14.2.1 General

Floor and ceiling slabs under flexural bending represent the majority of the components to be strengthened. Therefore, the application of TRC for members under bending was intensively investigated under a comparative study conducted within the Collaborative Research Center SFB 528. On the basis of small-scale slab tests, Bösche conducted an iterative calculation model for the strengthening of RC-members in

bending (Bösche, 2007). The developed model is based on the standard design model proposed by DIN 1045-1 (2001). This model has been further modified by the addition of a tensile force representing the textile-reinforced concrete (TRC) layer. Weiland's research was of significant importance, as he expanded the experimental basis significantly, while verifying the design model (Weiland, 2009; Weiland et al., 2010). Towards the end of the SFB 528, in 2011, full-scale slab tests were carried out with spans up to 7 m. At this time, improved carbon textiles, with heavy tow yarns, and a density of yarns of 3300 tex were used. Later on, a simplified model version was used by Schladitz et al. (2012). The researchers showed, on the basis of the full-scale tests, that the developed analytical formulae allow a very good prediction of the ultimate load for the flexural loadbearing capacity of TRC-strengthened members. Frenzel and Curbach (2011) validated the model by Bösche by recalculating slab tests with numerous different geometric and material parameters. Additionally, Frenzel and Curbach (2011) and Frenzel (2015) included into the calculation procedure stresses and strains of the reinforced concrete member prior to strengthening, and they developed design tables and charts for a practice-oriented application.

14.2.2   Material constitutive laws

The constitutive laws, in terms of a stress–strain relationship, as defined in EN 1992-1-1 (EC2) for concrete and steel reinforcement, are used for the calculation (DIN EN 1992-1-1, 2011; DIN EN 1992-1-1/NA, 2013). The constitutive law for the textile reinforcement is determined by uniaxial tension tests. In general, the stress–strain relation for TRC can be characterized in condition I (non-cracked concrete), condition IIa (cracking) and condition IIb (cracked concrete); see, for example, Jesse (2004) and Schütze et al. (2015). At this time, uniaxial tensile test results, used for the approved textile reinforcements, showed a deviant stress–strain behavior of two conditions instead of three. Condition I and condition IIa could not clearly be identified (DIBt, 2014), because the cracked condition was reached rather fast under loading. Figure 14.1 shows the idealized stress–strain relation for a textile reinforcement, neglecting the tension-stiffening effect caused by the concrete (Frenzel and Curbach, 2011; Curbach et al., 2014). The bilinear curve in Figure 14.1 represents the constitutive law of the textile reinforcement in general, and it is used for the design model.

Currently, there are no standard material specifications for textile reinforcements. Therefore, the stress–strain relationship must be determined separately for each textile fabric. Figure 14.2 shows the main material properties for the carbon reinforcement, which is currently approved in Germany (DIBt, 2014), and is applicable for indoor strengthening measures. The characteristic value of the ultimate tensile strength corresponds to the 1.5‰, from which the general design value was determined, see Chapter 1.

14.2.3   Derivation of the analysis method

The following assumptions for the design model were made in compliance with (DIN EN1992-1-1, 2011):
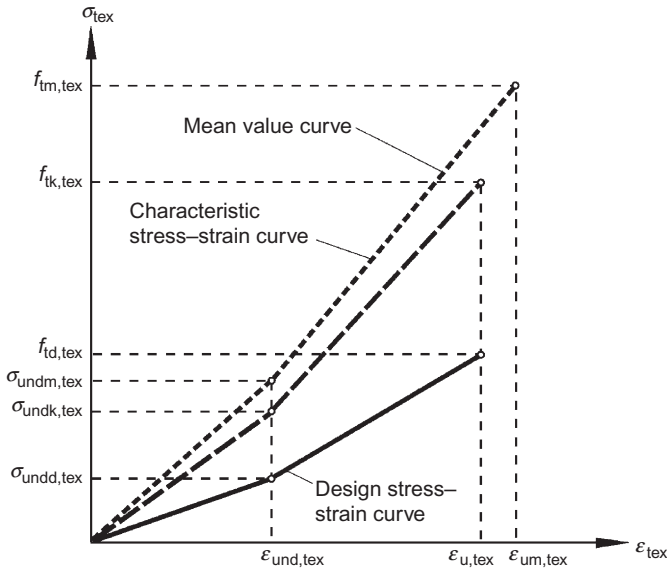
Figure 14.1 Bilinear stress–strain-relationship of the textile reinforcement for the limit state design, according to Curbach et al. (2014).
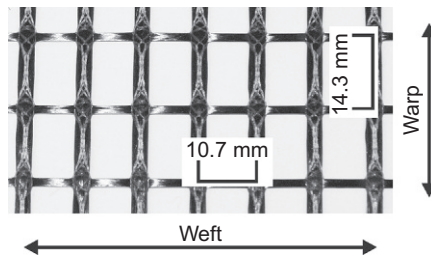
Figure 14.2 Approved textile reinforcement (DIBt, 2014) and material properties that belong to it in the warp direction for indoor applications (Curbach et al., 2014).

– Plane sections remain plane.
– The strain in bonded reinforcement, whether in tension or in compression, is the same as that in the surrounding concrete.
– The tensile strength of the concrete is ignored.
– The concrete stresses in compression are derived from the design stress–strain relationship.
– The steel stresses are derived from the given bilinear design curve.
– Failure is not governed by debonding.

The required parameters for the calculation of a strengthened, reinforced rectangular cross section are summarized in Figure 14.3.

| Cross section | Longitudinal section | Strains | Stresses | Inner forces | External forces |
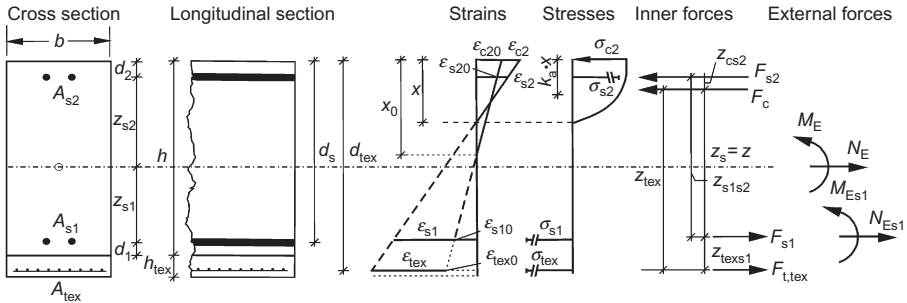
Figure 14.3 Strains, stresses, internal and external forces of a strengthened section, according to Frenzel (2015).

The parameters are:

A_{s1}; A_{s2}	Area of reinforcement for reinforcement under tension and compression
b; h; h_{tex}	Width, depth of cross-section; depth of the TRC layer
z_{s1}, z_{s2}; d_1, d_2	Inner lever arm and edge distances
d_s; d_{tex}	Effective depth of the steel and textile reinforcements
x_0	Depth of neutral axis
F_c, F_{tex}, F_{s2}, F_{s1}	Resulting inner forces of the concrete, the textile and steel reinforcement
N_E, M_E; N_{Es1}, M_{Es1}	Outer forces in the center of gravity of the uncracked section and A_{s1}
z	Inner lever arm of steel reinforcement A_{s1}
σ_{c2}, σ_{s2}, σ_{s1}, σ_{tex}	Compressive and tensile stresses in the concrete, steel and textile reinforcement
ε_{c2}, ε_{s2}, ε_{s1}, ε_{tex}	Compressive and tensile strains in the concrete, steel and textile reinforcement
ε_{c20}, ε_{s20}, ε_{s10}	Strains at initial time $t=0$, before the strengthening measure
ε_{tex0}	Fictitious strain (explanation follows)
z_{texs1}	Inner lever arm between steel and textile reinforcement

In order to exclude a component failure, equilibrium between internal and external forces must exist (see Equations 14.3 and 14.4). When designing for bending, the moment equilibrium is formed around the center of the reinforcing steel (outer forces M_{Es1} and N_{Es1} marked with index s1).

$$N_{Es1} = F_{tex} + F_{s1} - F_c - F_{s2} \tag{14.3}$$

$$M_{Es1} = F_{tex} \cdot z_{tex1} + F_c \cdot z_s + F_{s2} \cdot z_{s1s2} \tag{14.4}$$

The two Equations (14.3) and (14.4), show five unknown values F_{tex}, F_{s1}, F_{s2}, F_c, and z_s. In order to solve the system of equations simultaneously, three other equations must be introduced. Based on the assumption of a linear strain distribution in the cross section, the strains ε_{s1} and ε_{s2} can be determined as follows:

$$\varepsilon_{s1} = \varepsilon_{c2} + (\varepsilon_{tex} + \varepsilon_{tex0} - \varepsilon_{c2}) \cdot \frac{d_s}{d_{tex}} \tag{14.5}$$

$$\varepsilon_{s2} = \varepsilon_{c2} + (\varepsilon_{s1} - \varepsilon_{c2}) \cdot \frac{d_2}{d_s} \tag{14.6}$$

Furthermore, in the ultimate limit state, it can be assumed that either the ultimate compressive strain ε_{c2u} of the concrete in the compression zone, or the ultimate strain of the steel ε_{su} or textile reinforcement or $\varepsilon_{u,tex}$ is achieved. Based on this assumption, the system of equations has a unique solution.

The term ε_{tex0}, in Equation (14.5) describes a fictitious strain of the textile reinforcement to be applied in the imaginary location of the tensile force F_{tex} of the unstrengthened cross section (see Figure 14.3). Thus, the known strain distribution, which is defined by the concrete and steel strains ε_{c20} and ε_{s10}, can be taken into account for the strain distribution of the strengthened cross-section. ε_{tex0} is calculated with Equation (14.7):

$$\varepsilon_{tex0} = \varepsilon_{s10} + (\varepsilon_{s10} - \varepsilon_{c20}) \cdot \frac{z_{texs1}}{d_s} \tag{14.7}$$

Based on the presented formula, it is now possible to determine the textile reinforcement area by iteration. At first, an initial strain distribution is assumed. The next step includes the calculation of the resisting inner forces and moments followed by a comparison of the initial values (acting forces/moment). The stresses and strains are varied, as long as the inner and outer forces are in equilibrium. The general procedure is given in Bösche (2007); examples are shown in Frenzel (2015).

14.2.4 Design tables

14.2.4.1 Initial value

In order to provide a practical solution for the bending design and an easy determination of the required area of textile reinforcement, design tables have been established. In general, a safety concept, as described in current standards, is integrated (e.g., the EC2: verification by the partial factor method). Based on economic considerations, the efficiency of a cross section in the ultimate limited state is given, if at least one of the materials (concrete, steel, or textile) reaches its ultimate strain.

While the safety factors for concrete and steel reinforcement are given by EC2, Just (2015) determined the required safety factor for the textile reinforcement approved by the DIBt (2014). Table 14.1 gives the design values that are needed for the design calculation and form the basis for design tables.

14.2.4.2 Derivation of the initial equation

In addition to the already presented equations in Section 14.2.3 and the design values of Figure 14.3 and Table 14.1, all other required parameters are referenced with a more detailed description in the relevant literature, for example, for the

Table 14.1 **Parameters (Frenzel, 2015)**

Material (standard, publications, etc.)	Specification	Value	Unit
Concrete	Characteristic strength f_{ck}	12–50	N/mm^2
DIN EN 1992-1-1 (2011)	Reduction factor α_{cc}	0.85	
DIN EN 1992-1-1/NA (2013)	Partial safety factor γ_c	1.5[a]	
	Design strength f_{cd}	7–28	N/mm^2
Steel reinforcement B500	Modulus of elasticity E_s	200,000	N/mm^2
DIN EN 1992-1-1 (2011)	Partial safety factor γ_s	1.15	
DIN EN 1992-1-1/NA (2013)	Yield strength $f_{yk}|f_{yd}$	500|435	N/mm^2
	Yield strain $\varepsilon_{yk}|\varepsilon_{yd}$	2.50|2.18	‰
	Tensile strength $f_{tk,cal}|f_{td,cal}$	525|457	N/mm^2
	Ultimate strain $\varepsilon_{su,cal}$	25	‰
Textile[b]	Tensile strength $f_{tk,tex}|f_{td,tex}$	1550|769	N/mm^2
Just (2015)	Partial safety factor $\bar{\gamma}_{tex}$	2.02[c]	
Lorenz et al. (2015)	Ultimate strain $\varepsilon_{u,tex}$	7.5	‰
DIBt (2014)	Strength $\sigma_{undk,tex}|\sigma_{undd,tex}$	620|307	N/mm^2
	Strain $\varepsilon_{und,tex}$	3.0	‰

[a]Depending on the combination of the loading condition; for example: unfavorable.
[b]In warp direction.
[c]See (1.1) and (1.2) in Chapter 1 (indoor application) and DIBt (2014).

German-speaking countries (Löser et al., 1986; Zilch and Zehetmaier, 2009). Besides, the following parameters according to Equations (14.8) and (14.9) are needed:

μ_{tex}, ω_{tex}	Normalized moment, mechanical reinforcement ratio
ξ_{tex}, ζ_{tex}	Normalized depth of the neutral axis and normalized inner lever arm

Such terms can be expressed as follows:

$$\xi_{tex} = \frac{x}{d_{tex}} \tag{14.8}$$

$$\zeta_{tex} = \frac{z_s}{d_{tex}} \tag{14.9}$$

Equations (14.3) and (14.4) (equilibrium of horizontal forces and moments) can be further manipulated and equated to the textile tensile force F_{tex}:

$$M_{Ed1} + F_{s1d} \cdot z_{texs1} - F_{s2d} \cdot z_{s1s2} = F_{cd} \cdot z_{texs1} + F_{cd} \cdot z_s + (N_{Es1} + F_{s2}) \cdot z_{texs1} \tag{14.10}$$

Considering Equations (14.8) and (14.9), the term $F_{cd} \cdot z_s$ from Equation (14.10) is composed by the respective values:

$$F_{cd} \cdot z_s = \alpha_R \cdot d_{tex}{}^2 \cdot b \cdot f_{cd} \cdot \xi_{tex} \cdot \zeta_{tex} \qquad (14.11)$$

If Equation (14.11) is substituted into Equation (14.10), and the term $F_{cd} \cdot z_{texs1}$ is modified by the ratio $\frac{z_s}{z_s}$, the design depth of the section ζ_{tex} can be determined from Equation (14.9); it results in:

$$M_{Ed1} + F_{s1d} \cdot z_{texs1} - F_{s2d} \cdot z_{s1s2} = \alpha_R \cdot d_{tex}{}^2 \cdot b \cdot f_c \cdot \xi_{tex} \cdot \frac{z_{texs1}}{d_{tex}}$$
$$+ \alpha_R \cdot d_{tex}{}^2 \cdot b \cdot f_c \cdot \xi_{tex} \cdot \zeta_{tex} + (N_{Es1} + F_{s2}) \cdot z_{texs1} \qquad (14.12)$$

At this stage, the design bending moment μ_{tex} can be calculated. Equation (14.12) can be expressed as follows:

$$\mu_{tex} = \frac{M_{Ed1} - F_{s2d} \cdot z_{s1s2} + F_{s1d} \cdot z_{texs1}}{b \cdot d_{tex}{}^2 \cdot f_{cd}}$$
$$= \alpha_R \cdot \xi_{tex} \cdot \zeta_{tex} + \alpha_R \cdot \xi_{tex} \cdot \frac{z_{texs1}}{d_{tex}} + \frac{(N_{Ed1} + F_{s2d}) \cdot z_{texs1}}{b \cdot d_{tex}{}^2 \cdot f_{cd}} \qquad (14.13)$$

Equation (14.4) can be formulated by recalling that $F_{td,tex} = A_{tex} \cdot \sigma_{td,tex}$, as follows:

$$A_{tex} = \frac{1}{\sigma_{td,tex}} \cdot \frac{M_{Ed1} - F_{s2d} \cdot z_{s1s2} - F_{cd} \cdot z_s}{z_{texs1}} \qquad (14.14)$$

By rearranging the expression and substituting relevant terms, for example, the normalized moment μ_{tex} and the reinforcement ratio ω_{tex}, Equations (14.15) and (14.16) can be formulated as follows:

$$\omega_{tex} = \alpha_R \cdot \xi_{tex} \qquad (14.15)$$

$$A_{tex} = \frac{1}{\sigma_{td,tex}} (\omega_{tex} \cdot d_{tex} \cdot f_{cd} \cdot b + N_{Ed} + F_{s2d} - F_{s1d}) \qquad (14.16)$$

With this formula, it is now possible to calculate the required amount of textile reinforcement and to prepare easy-to-use design tables for the different strain states as a function of the parameters μ_{tex} and ω_{tex}. However, it should be taken into account that μ_{tex} and ω_{tex} depend on the ratios of z_{tex1}/d_{tex}, d_2/d_{tex} (under the assumptions of steel reinforcement requirements in the compressive zone) and the strain ε_{tex0} in the nonstrengthened cross section (Frenzel and Curbach, 2011). However, the necessary values can be clearly identified from the existing cross section and the estimated geometry of the strengthening layer.

14.2.5   Application of a design table

In addition to the equations presented in Sections 14.2.3 and 14.2.4, at this point, an illustrative example of a design table for a strengthened rectangular cross section without acting axial force, without compression steel reinforcement and without predeformation ($\varepsilon_{\text{tex},0}=0$) is presented. In the first step, the normalized moment μ_{tex} is determined as a function of the moment M_E, the known cross section values, and the concrete compressive strength f_{cd}:

$$\mu_{\text{tex}} = \frac{M_{\text{Ed}} + \sigma_{\text{s1d}} \cdot A_{\text{s1}} \cdot (d_{\text{tex}} - d_{\text{s}})}{b \cdot d_{\text{tex}}^{2} \cdot f_{\text{cd}}} \tag{14.17}$$

For each μ_{tex} ratio, a strain state and a mechanical reinforcement ratio ω_{tex} are assigned. All possible combinations are prepared in a tabular form, provided that the ratio $z_{\text{texs}}/d_{\text{tex}}$, the preloading $\varepsilon_{\text{tex0}}$ and the concrete, steel and textile design strengths and ultimate strains are known. The amount of the required textile reinforcement A_{tex} can be calculated, using the equation:

$$A_{\text{tex}} = \frac{(\omega_{\text{tex}} \cdot b \cdot d_{\text{tex}} \cdot f_{\text{cd}} - \sigma_{\text{s1d}} \cdot A_{\text{s1}})}{\sigma_{\text{td,tex}}} \tag{14.18}$$

The design table has been created for a ratio of z_{texs1} to d_{tex} of 0.15, a normal concrete $\leq$C50/60 with a parabolic-rectangular-diagram, according to EC2 and typical steel bar B500 (DIN EN 1992-1-1, 2011) (Chart 14.1).

Based on the previous discussion, a design chart was developed, see Figure 14.4. Here the value of $\varepsilon_{\text{tex0}}$ is not fixed. The concrete, steel and textile strains $\varepsilon_{\text{c2}}, \varepsilon_{\text{s1}}, \varepsilon_{\text{tex}}$ in the strengthened state, the mode of failure and the depending mechanical reinforcement ratio ω_{tex} can be determined as a function of μ_{tex}. Figure 14.4 shows the relations for a ratio $z_{\text{texs1}}/d_{\text{tex}}$ of 0.15, reinforcing steel bars B500 and for normal concrete $\leq$C50/60. In addition, the following information is relevant, as indicated in the design diagram:

- The green area represents a failure range of the textile reinforcement ($\varepsilon_{\text{tex}}=7.5\text{‰}$). The concrete stress ε_{c2}, the steel strain ε_{s1} and the mechanical reinforcement ratio ω_{tex} can be determined subjected to a pre-strain ε_{tex} and the design bending moment μ_{tex}.
- The red area describes the range due to failure of the compressive zone of the existing concrete $\varepsilon_{\text{c2}}=-3.5\text{‰}$ (uneconomical application for textile reinforcement). The strain of the textile reinforcement varies in a range between 2.5% and 7.5‰, and the reinforcing steel varies from 2% to 25‰.
- In the brown area, a failure of the steel reinforcement occurs ($\varepsilon_{\text{su}} \geq 25\text{‰}$). In such case, the limiting values of the concrete stress and the textile reinforcement strain are not reached.
- The green dashed lines, indicating the mechanical reinforcement ratio ω_{tex}, show that the strain state in the un-strengthened cross section does not have a major impact on the required amount of the textile reinforcement A_{tex}.

Intermediate values, not directly specified, can be interpolated from the table.

$$\mu_{tex} = \frac{M_{Ed} + \sigma_{s1d} \cdot A_{s1} \cdot (d_{tex} - d_s)}{b \cdot d_{tex}^2 \cdot f_{cd}} \qquad A_{tex} = \frac{(\omega_{tex} \cdot b \cdot d_{tex} \cdot f_{cd} - \sigma_{s1d} \cdot A_{s1})}{\sigma_{td,tex}}$$

μ_{tex}	ω_{tex}	$\xi_{tex} = \dfrac{x}{d_{tex}}$	$\zeta_{tex} = \dfrac{z_s}{d_{tex}}$	ε_{c2}	ε_{s1}	σ_{s1d}**	σ_{s1d}***	ε_{tex}	$\sigma_{td,tex}$	
(–)	(–)	(–)	(–)	(‰)	(‰)	(N/mm²)	(N/mm²)	(‰)	(N/mm²)	
0.01	0.010	0.05	0.83	−0.42	6.31	435	439	7.50	769	
0.02	0.021	0.08	0.82	−0.61	6.28	435	439	7.50	769	
0.03	0.031	0.09	0.82	−0.77	6.26	435	439	7.50	769	
0.04	0.042	0.11	0.81	−0.91	6.24	435	439	7.50	769	
0.05	0.052	0.12	0.81	−1.04	6.22	435	439	7.50	769	
0.06	0.063	0.13	0.80	−1.16	6.20	435	439	7.50	769	
0.07	0.074	0.15	0.80	−1.28	6.18	435	439	7.50	769	Failure of textile reinforcement (economical application)
0.08	0.085	0.16	0.79	−1.40	6.16	435	439	7.50	769	
0.09	0.096	0.17	0.79	−1.52	6.15	435	439	7.50	769	
0.10	0.107	0.18	0.78	−1.64	6.13	435	439	7.50	769	
0.11	0.118	0.19	0.78	−1.76	6.11	435	439	7.50	769	
0.12	0.130	0.20	0.78	−1.88	6.09	435	439	7.50	769	
0.13	0.141	0.21	0.77	−2.01	6.07	435	438	7.50	769	
0.14	0.153	0.22	0.77	−2.14	6.05	435	438	7.50	769	
0.15	0.165	0.23	0.76	−2.28	6.03	435	438	7.50	769	
0.16	0.177	0.24	0.76	−2.42	6.01	435	438	7.50	769	
0.17	0.189	0.26	0.75	−2.57	5.99	435	438	7.50	769	
0.18	0.201	0.27	0.74	−2.73	5.97	435	438	7.50	769	
0.19	0.214	0.28	0.74	−2.89	5.94	435	438	7.50	769	
0.20	0.227	0.29	0.73	−3.06	5.92	435	438	7.50	769	
0.21	0.240	0.30	0.73	−3.24	5.89	435	438	7.50	769	
0.22	0.253	0.31	0.72	−3.43	5.86	435	438	7.50	769	
0.2235	0.258	0.32	0.72	−3.50	5.85	435	438	7.50	769	
0.23	0.266	0.33	0.71	−3.50	5.54	435	438	7.13	731	
0.24	0.280	0.35	0.71	−3.50	5.09	435	438	6.60	677	
0.25	0.295	0.36	0.70	−3.50	4.68	435	437	6.12	627	
0.26	0.309	0.38	0.69	−3.50	4.29	435	437	5.67	581	
0.27	0.324	0.40	0.68	−3.50	3.94	435	436	5.25	538	Failure of concrete (uneconomical application)
0.28	0.339	0.42	0.68	−3.50	3.60	435	436	4.86	498	
0.29	0.355	0.44	0.67	−3.50	3.29	435	436	4.49	460	
0.30	0.371	0.46	0.66	−3.50	3.00	435	436	4.15	425	
0.31	0.387	0.48	0.65	−3.50	2.72	435	435	3.82	392	
0.32	0.404	0.50	0.64	−3.50	2.46	435	435	3.52	361	
0.33	0.421	0.52	0.63	−3.50	2.22	435	435	3.23	331	
0.3319	0.424	0.52	0.63	−3.50	2.17*	435	435	3.18	326	
0.34	0.439	0.54	0.62	−3.50	1.99	397	397	2.95	303	
0.35	0.458	0.57	0.61	−3.50	1.76	353	353	2.69	276	

* yield strain of steel reinforcement B500, **σ–ε—diagram without hardening, *** σ–ε—diagram with hardening.

Chart 14.1 Design table with dimensionless values for rectangular cross sections, without compressive reinforcement and without preloading ($\varepsilon_{tex0} = 0$) for bending without axial forces; normal concrete $\leq$ C50/60, $(d_{tex} - d_s)/d_{tex} = 0.15$ and B500, according to Frenzel (2015).
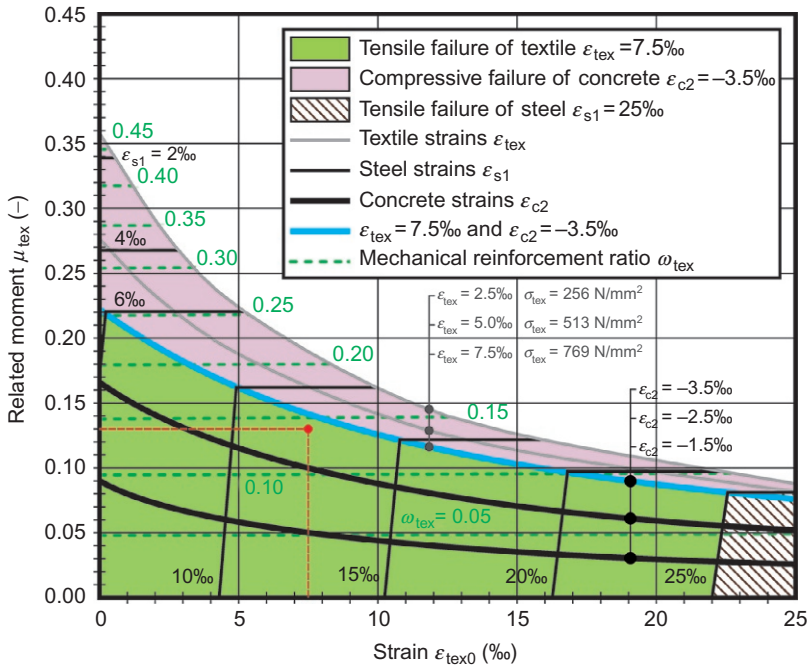
Figure 14.4 Design chart, the concrete strains ε_{c2}, the steel and the textile strains ε_{s1}, ε_{tex} and the mechanical reinforcement ratio ω_{tex}, depending on the related moment μ_{tex} and the fictitious strain ε_{tex0} due to preloading for $(d_{tex} - d_s)/d_{tex} = 0.15$ and B500 (Frenzel, 2015).

The following example illustrates the procedure. Before strengthening, the calculation of the strain state provides a fictitious strain ε_{tex0} of 7.5‰ and a related moment μ_{tex} of 0.13. From this, the reinforcement ratio ω_{tex} is determined to be 0.145. Based on these parameters, the required reinforcement area can be determined. Furthermore, the steel strain ε_{s1} is determined to be 12‰ and the concrete stress ε_{c2} is determined to be -3.3‰. The textile strain ε_{tex} is 7.5‰. Accordingly, the full load capacity of the textile reinforcement is used and an economical application of the cross section can be guaranteed by a failure of the textile layer.

14.3   Shear strengthening

14.3.1   General

Today, the general shear design procedure for reinforced concrete structures is still based on empirically derived formulas. The design criteria basis was provided by Mörsch (1950). Mörsch analyzed the crack pattern of a beam in flexural tests and

validated the truss model developed by Hennesbique and Ritter (Mörsch, 1950). Proceeding from this, Mörsch developed a truss model for state II (cracked state), where the forces in the tension and compression chord require the equilibrium of moments of the bending design. Based on new findings, the design models have been further developed and refined. Nevertheless, the accurate prediction of shear resistance is still an unsolved problem today.

In order to predict the shear resistance of strengthened components, there are different approaches. For example, the ACI (2008) and Fib (2001) proposed design models that have also been empirically derived from known reinforced concrete models. One possibility is to design a shear strengthening with TRC, as presented in the following sections.

14.3.2   Design model for shear strengthening according to Brückner (2011)

14.3.2.1   Basic research

As part of the Collaborative Research Center SFB 528 (SFB, 2015), experimental and theoretical investigations of plates and T-shaped beams that were strengthened with TRC were carried out (Weiland et al., 2007; Brückner et al., 2008; Brückner, 2011). In the experiments, AR glass textile reinforcements were used, in which the warp and weft were inclined at 45° (see Figure 14.5).

Based on these experiments, Brückner (2011) concluded that the previous approach by Khalifa et al. (1998) and Triantafillou (1998), developed for FRP-strengthened concrete, does not describe the material behavior accurately. These researchers assumed that the increase of the load-carrying capacity is only subjected to the TRC strengthening. In the opinion of Brückner, the ultimate load difference between a component with and without strengthening is not equal to load-carrying capacity of the TRC strengthening. Strengthening with textile reinforcement limits the strain of the steel reinforcement at the ultimate limit state and affects the inclination of the strut. Thus, the load transfer of the steel stirrups is reduced.
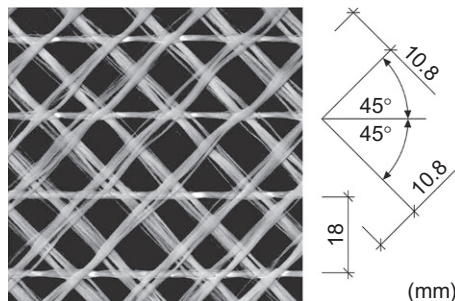
Figure 14.5 AR glass fabric for shear strengthening, from Ortlepp et al. (2010).

This should be taken into account in the design model. That means that the strengthened TRC layer increases the stiffness of the tension strut and results in a steeper strut inclination. This effect is independent of the predamage state of the component.

Based on the tests conducted as part of the SFB 528, static and dynamic load tests were carried out on T-beams that had been strengthened with a 45° carbon textile reinforcement (Brückner et al., 2013). Based on these tests, the model of Brückner was verified.

14.3.2.2 Truss model for shear (Brückner, 2011)

Based on the existing analysis models (ACI, 2008; Fib, 2001), Brückner introduced a new analysis model for the ultimate load, which included the steel stirrups and the textile reinforcement. Figure 14.6a–c shows the underlying truss model of a strengthened T-beam with a centrally placed point load $V_{R,t}$.

The parameters are:

a_R	Vertical distance between the change of the inclination of the strut and the edge of the plate of the T-shaped beam
a_1	Width of the support
a_2	Width of the load distribution
b_w	Web width of the T-shaped beam (without TRC layer)
d_1	Distance between the resultant force of the steel reinforcement and the lower edge of the T-shaped beam
d_2	Distance between the resultant force of the bending compression zone and the upper edge of the T-beam
D_{at}	Compressive force due to adhesive tensile force
$D_{A,t}, D_{bi}, D_{w,t}, D_{LE}$	Strut
F_{at}	Adhesive tensile force
γ	Inclination of the upper strut
Ψ	Inclination of the concrete arch
t_m	Average thickness of the strengthened layer
$V_{R,t}$	Concentrated point load
z	Lever arm of force
z_1	Vertical distance between the resultant force of the steel reinforcement and the point of the change of the inclination of the strut; height of the lower strut
z_2	Vertical distance between the resultant force of the bending compression zone and the point of the change of the inclination of the strut; height of the upper strut
$Z_{w,t}$	Ultimate load of the tie
ϑ	Inclination of the lower strut

Based on the assumption that the TRC reinforcement can be anchored only in the bending zone, Brückner has added the upper strut D_{b1} diagonal to the concentrated load V_{Rt} (see Figure 14.6). As a result, the newly developed truss model depends on the geometry. This condition has also an impact on the strain at the tie. Due to
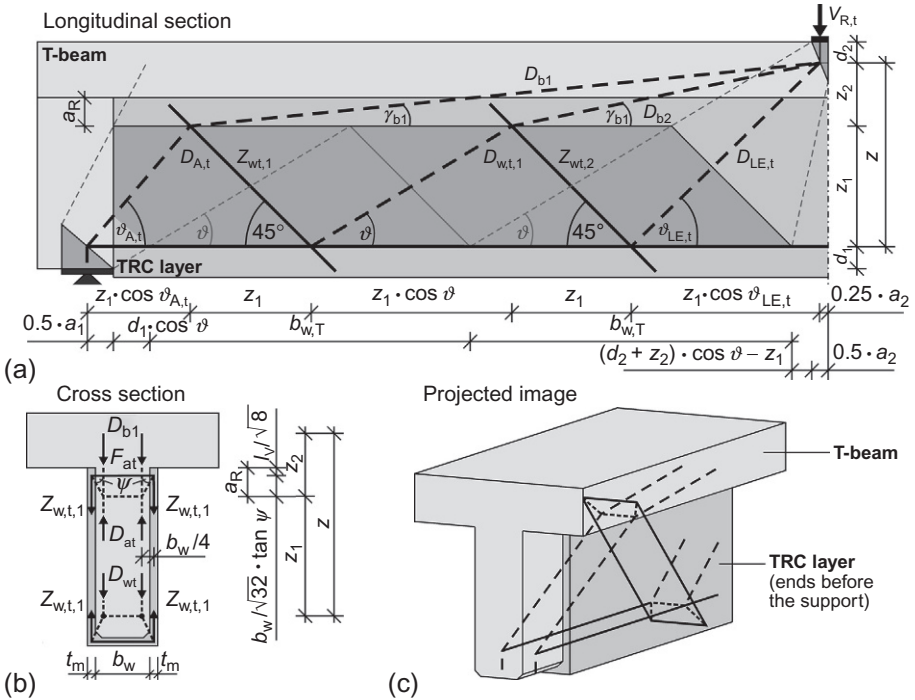
Figure 14.6 Truss model for strengthening with TRC of T-shaped beams, from Brückner (2011).

the inclination of the upper strut D_{b1}, the load carried by the tie will be reduced. In the event that the distance between the concentrated point load and the support area is increased, the inclination γ_{b1} decreases, and the effect it produces in the tie is reduced. Therefore, the effect of the strut can be ignored and the truss model can be simplified (see Figure 14.7). For more information on the simplified truss model, refer to the work of Brückner (2011).

14.3.3 Analysis of the ultimate shear load of a strengthened component (Brückner, 2011)

14.3.3.1 Inclination ϑ of the strut

In truss models for the shear design, an inclination ϑ of the strut is implemented. According to DIN EN 1992-1-1 (2011) and DIN EN 1992-1-1/NA (2013), the inclination of reinforced concrete components under bending without axial force can be determined as follows:

$$0.58 \le \cot \vartheta \le \frac{1.2}{1 - V_{\mathrm{Rd,cc}}/V_{\mathrm{Ed}}} \le 3.0 \tag{14.19}$$
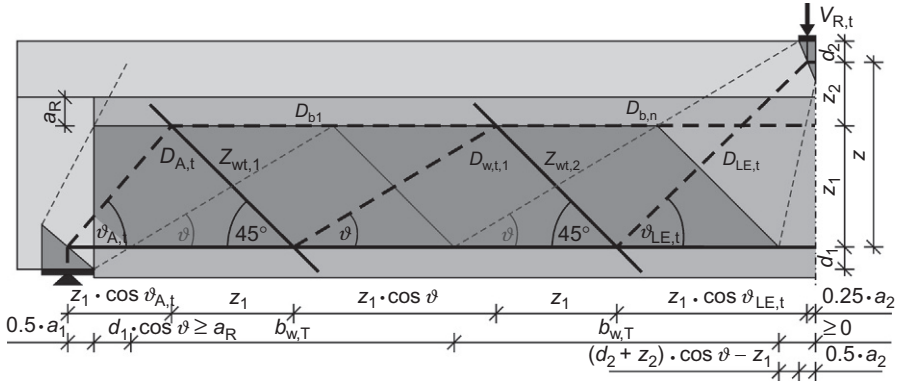
Figure 14.7 Simplified truss model for strengthening with TRC of T-shaped beams, from Brückner (2011).

with:

ϑ	Inclination of the strut
$V_{Rd,cc}$	Load component of the strut with $V_{Rd,cc} = 0.24 \cdot f_{ck}^{1/3} \cdot b_w \cdot z$
f_{ck}	Characteristic compressive strength of concrete
b_w	Web width of the T-shaped beam (without TRC layer)
z	Lever arm of internal forces, primarily of bending design, simplified with $z \approx 0.9 \cdot d$
V_{Ed}	Design value of the applied shear force

14.3.3.2 Load component of the steel stirrups and the TRC layer (tie)

According to DIN EN 1992-1-1 (2011), the load component of a vertical steel stirrup with only bending load and without axial forces subjected to the inclination of the strut (see Equation 14.19) can be calculated as follows:

$$V_{Rd,s} = \frac{A_{w,s}}{s_{w,s}} \cdot f_{ywd} \cdot z \cdot \cot \vartheta \tag{14.20}$$

$V_{Rd,s}$	Design value of the shear force reinforcement
$A_{w,s}/s_{w,s}$	The cross-sectional area of the shear reinforcement per meter
f_{ywd}	Design value of yield strength of the shear reinforcement (for the calculation, the stress value at the strain limit of 0.2% is used to reflect the limited extensibility of the textile reinforcement)

The tensile force of the textile reinforcement can be determined in a similar way:

$$V_{\mathrm{Rd,tex}} = \frac{A_{\mathrm{w,s}}}{s_{\mathrm{w,s}}} \cdot f_{\mathrm{t}} \cdot b_{\mathrm{w,t}} \cdot \sin\alpha \tag{14.21}$$

with

$V_{\mathrm{Rd,tex}}$	Design value of the shear force component in the textile reinforcement
$A_{\mathrm{w,t}}/s_{\mathrm{w,t}}$	Cross-sectional area of the textile reinforcement per meter component length
f_{t}	Tensile strength of TRC (determined on an uniaxial strain specimen)
$b_{\mathrm{w,T}}$	Width of the tie
α	Angle between textile reinforcement and the T-beam axis

Based on the angle of inclination between the textile reinforcement and the T-beam axis, the width of the tie of the TRC layer $b_{\mathrm{w,T}}$ (see Figure 14.6) depends of the following two conditions, according to Brückner (2011):

1. The tensile forces in the TRC layer have to be anchored nearby the support area, as well as in the crossing section between the web and plate section. Furthermore, these loads must be introduced in the struts. This only happens when the resultant force of the steel reinforcement layer crosses the compression field at the support area with a distance of at least V_{R}.
2. The line of action of the force $V_{\mathrm{R,t}}$ in a directly loaded area may not be crossed from the tie (see Figure 14.7).

After considering these two conditions the width of the strengthened web of the tie $b_{\mathrm{w,T}}$ as well as the inclination of $\vartheta_{\mathrm{A,t}}$ and $\vartheta_{\mathrm{E,t}}$, for textile reinforcements with warp and weft inclined by 45°, can be determined according to the following process (see Figure 14.8 and Table 14.2).

Based on the formulas presented, it is now possible to calculate the additional shear load capacity of a tie in a strengthened cross section (with the implementation of a truss model).

14.3.3.3 Load capacity of the strut in the TRC layer

An additional TRC layer not only increases the resistance to diagonal tensile stresses, but it also has an effect in regards to the inclined compressive stresses, which are usually shown by struts in the models. This additional load capacity has not been the
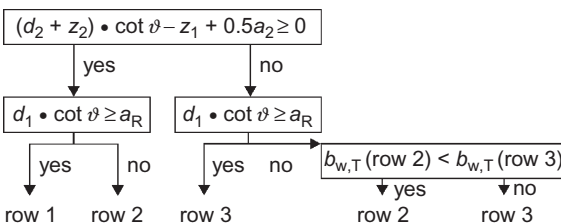
Figure 14.8 Process for the equations of calculation in Table 14.2 (Brückner, 2011).

Table 14.2 Equations of calculation for the TRC truss model (Brückner, 2011)

	$b_{w,T}$	$\cot \vartheta_A$	$\cot \vartheta_{LE}$
1	$z_1 \cdot (\cot \vartheta + 1)$	$\dfrac{2d_1 \cot \vartheta + z_1(\cot \vartheta - 1) + \alpha_1}{2z_1}$	$\dfrac{2d \cot \vartheta - z_1(\cot \vartheta + 1) + 0.5\alpha_1}{z}$
2	$z_1 \cdot (\cot \vartheta + 1)$ $+ d_1 \cdot \cot \vartheta - \alpha_R$	$\dfrac{d_1 \cot \vartheta + z_1(\cot \vartheta - 1) + \alpha_1 + \alpha_R}{2z_1}$	$\dfrac{(2d - d_1)\cot \vartheta - z_1(\cot \vartheta + 1) + 0.5\alpha_2 + \alpha_R}{2z}$
3	$d \cdot \cot \vartheta + 0.5 \cdot \alpha_2$	$\dfrac{(2d_1 + d)\cot \vartheta - 2z_1 + \alpha_1 + 0.5\alpha_2}{2z_1}$	$\dfrac{d \cot \vartheta}{2z}$

subject of any research yet. However, a failure of the strut has not been observed in any of the experiments. Looking at standard components, in which the shear resistance is not sufficient, the loadbearing resistance of the steel reinforcement cannot be proven. This means that the strut is not crucial for the design.

If this is the case, the compressive strength of the TRC layer must be realistically evaluated. Indications can be found in Molter (2005) and Voss (2008). Both researchers studied compressive stresses parallel to the TRC layer and discovered some significant losses in the compressive strength. The reason for this is that the TRC layer can act divisive, and therefore, they decrease the compressive strength compared to that of unreinforced fine concrete samples. The size of the strength reduction depends on many factors, for example, the thickness of yarn, mesh size or coating. Probably, it also depends on the application: whether the application consists on an existing section strengthened with a TRC layer, or whether a new cross section is built with TRC. A recent research project at TU Dresden contributes to close the knowledge gap by related studies (Jesse, 2012).

14.3.3.4 Load capacity interface

Basically, in the anchored area of a TRC layer, which is marked in Figure 14.9a, there are a various failure scenarios in the interface (Ortlepp, 2007):

1. Failure in the layer of the old concrete (Figure 14.9b).
2. Failure of the interface between old concrete and TRC layer (Figure 14.9c).
3. Delamination in the TRC layer (Figure 14.9d).

In the experimental tests, Brückner observed a delamination of the TRC layer from the old concrete surface. She concluded that the adhesive tensile stress of the textile reinforcement in the anchorage area was too high, according to the basic research on the bond behavior of the TRC layer by Ortlepp (2007). In the opinion of Brückner, the shear stresses in the interface were too small to be the only responsible cause for a failure of the bond.

The adhesive tensile force F_{at}, which is drawn in Figure 14.6b, can be converted in an adhesive tensile stress f_{at}. The adhesive tensile stress f_{at} can be calculated as:
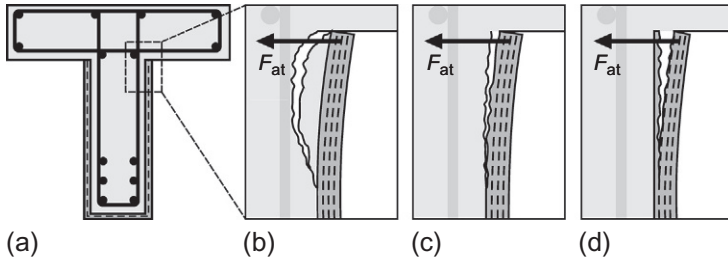
Figure 14.9 Failure modes of strengthened components with TRC, according to Brückner (2011). (a) Strengthened T-beam, (b) interface old concrete, (c) interface joint, and (d) interface first layer.

$$f_{at} = \frac{A_{w,t}}{s_{w,t} \cdot l_V \cdot \sin 45°} \cdot f_t \cdot \cot \Psi \leq f_{c,at} \tag{14.22}$$

with:

$l_V \cdot \sin 45°$	Vertical projection of the anchorage length
$f_{c,at}$	Adhesive tensile strength of the old concrete

A selected inclination Ψ of the concrete arch of 45° showed a good correlation to the tested adhesive tensile strength of the old concrete during the analysis of the test results. If the existing adhesive tensile stress would be greater than the adhesive tensile strength, additional anchorage material would have to be used (e.g., Brückner et al., 2008). Further information to various parameters of the shear strengthening can be found in the literature (Brückner, 2011). Ortlepp discussed more extensive and general considerations on the different failures (Ortlepp, 2007).

14.3.3.5 Limitations of the presented model

The design model that has been presented was developed on the basis of experimental results on beams with rectangular or T-sections. This fact has to be considered for components with a different geometry. Brückner compared the test results with those results obtained from the design model, and she determined that the load capacity of the tie in the experiments was consistently greater than the calculated values. This was independent of components with or without a TRC layer. Therefore, the shear design model of the EC2 (DIN EN 1992-1-1, 2011) does not take into account a percentage of the load capacity. Conversely, this means that Brückner can predict the additional load capacity of the tie very well (Brückner, 2011). Hence, the calculated loads of the strengthened cross section should be regarded as conservative and on the safe side. These observations were also confirmed in experiments with dynamic loads on T-beams that have been strengthened (Brückner et al., 2013).

An explicit model to calculate the load capacity of the strut has not been created yet. A reliable estimation of the load capacity in a strengthened cross section is not possible, because this problem is still not solved for the shear design model in general. Also there are no results available to determine the compressive strength reduction for TRC under uniaxial pressure in the parallel direction. More research is needed in this area.

A practical approach to determine the anchorage of the TRC layer at the web of a T-beam is proved in Brückner (2011), including an increase in load capacity of the cross-section. However, there is also still room for improvement (Brückner et al., 2008).

14.4 Torsional strengthening

14.4.1 Experimental analysis

14.4.1.1 Preliminary consideration

The following formulas for the material behavior of strengthened cross-sections are based on experiments and the analysis of their results presented in Chapter 3 (Schladitz, 2011; Schladitz and Curbach, 2012). Accordingly, Table 14.3 shows the material properties of textile reinforcement used in such studies. For other types of material, the models presented in this section should be modified. Of particular interest are the reduction factors, especially if the TRC layer exhibits a different failure behavior.

14.4.1.2 Verification procedure

Basically, with more TRC layers the cracking moment, the load capacity and the stiffness of torsional rotation resistance increase. In addition, the textile reinforcement causes spreading of the cracks, while simultaneously reducing the crack spacing and, consequently, the crack width. Schladitz also noticed that only one layer of fine-grained concrete increases the cracking moment, and sometimes, this load capacity was greater than the limit of the ultimate load of the old concrete cross-section. Thus, a minimum textile reinforcement in the strengthened layer is necessary to ensure a ductile material behavior.
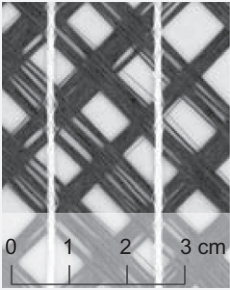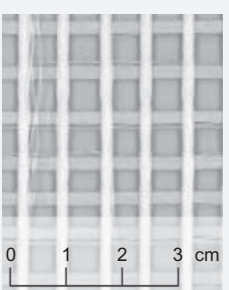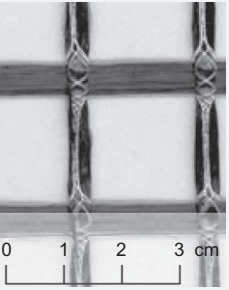
Based on the torsional strut-and-tie model with an inclination of 45° (e.g., Leonhardt and Mönnig, 1984; Zilch and Zehetmaier, 2009) and on the observation during the experiments, the following checks should be done (Schladitz, 2011):

- Verification procedure of ductile material behavior (Section 14.4.2.2),
- Ultimate limited load (strut and tie; Section 14.4.3),
- Verification procedure of the steel reinforcement (Section 14.4.4).

The following models are presented in detail in Schladitz (2011).

Table 14.3 Material properties of textile reinforcement, from Schladitz (2011)

Geometry	0 1 2 3 cm	0 1 2 3 cm	0 1 2 3 cm
Material	Carbon	AR glass	Carbon
Fineness[a] (tex)	803	2356	3300
Cross section (mm²/m)	41.5	120.0	84.9
Tensile strength (N/mm²)	2125	615[b]/810[c]	1300[b]/1670[c]
Tensile strain (‰)	10.5	11[b]/12.5[c]	10[b]/9[c]

[a]In yarn's direction.
[b]In warp direction.
[c]In weft direction.

14.4.2 Minimum reinforcement

In order to prevent that the cracking moment exceeds the ultimate load limit of the old concrete cross-section, minimum textile reinforcement is necessary.

14.4.2.1 Theoretical analysis of the calculation of the shear strength and the cracking moment in the first state (uncracked)

The shear stress distribution in reinforced concrete cross-sections in the first state (uncracked) is presented in Figure 14.10. Applying the elastic theory, a homogeneous, isotropic and linear elastic material behavior is assumed.

The torsional resistance $T_{I,max}$ of the reinforced concrete cross section can be determined as follows:

$$T_{I,max} = \tau_{c,max} \cdot W_{T,c} \tag{14.23}$$
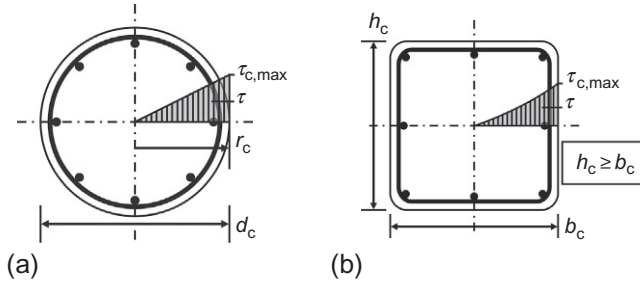
Figure 14.10 Shear stress distribution of the reinforced concrete cross section (uncracked), from Schladitz (2011). (a) Circular cross section and (b) rectangular-shaped cross section.

(a) round cross-section:

$$T_{\mathrm{I,max}} = \tau_{\mathrm{c,max}} \cdot \frac{\pi}{2} \cdot r_{\mathrm{c}}^{3} \tag{14.24}$$

(b) for approximately rectangular-shaped reinforced cross-sections (for more information see Schladitz (2011)):

$$T_{\mathrm{I,max}} = \tau_{\mathrm{c,max}} \cdot \beta \cdot b_{\mathrm{c}}^{2} \cdot h_{\mathrm{c}} \tag{14.25}$$

The parameters are:

$T_{\mathrm{I,max}}$	Maximum torsional resistance/torsional moment
$\tau_{\mathrm{c,max}}$	Maximum shear stress in concrete, corresponding to the tensile strength as first approximate value
$W_{\mathrm{T,c}}$	Moment of torsional resistance of the unstrengthened, reinforced concrete cross-section
r_{c}	Outer radius of the reinforced concrete cross-section
β	Coefficient for a simplified calculation of the moment of the torsional resistance $W_{\mathrm{T,c}}$ for a square-shaped cross section (Table 14.4)
$b_{\mathrm{c}}, h_{\mathrm{c}}$	Geometry parameter of the cross-section; $h_{\mathrm{c}} \geq b_{\mathrm{c}}$

Several models of the shear stress distribution in a twisted, TRC-strengthened and reinforced concrete cross section exist. Based on the model shown in Figure 14.11, Schladitz was able to estimate the cracking moment that corresponds to the test results. Just before reaching the second state (cracked), the plastic stage of the reinforcement in the strengthened concrete cross section is almost achieved. At this stage, the crack width of the reinforced concrete cross section is expected to be very small.

In the basic model, the partly plasticized areas are neglected. The design torsional resistance moment $T_{\mathrm{I,max}}$ is determined as follows:

(a) strengthened, circular cross-sections:

$$T_{\mathrm{I,max}} = 2 \cdot \pi \cdot \int_{0}^{r_{\mathrm{v}}} \tau(r) \cdot r^{2}\,\mathrm{d}r \tag{14.26}$$

Table 14.4 **Coefficient β for determination of W_T (Albert, 2014)**

h/b	1	1.24	1.5	2	3	4	6	10	∞
β	0.208	0.211	0.231	0.246	0.267	0.282	0.299	0.313	0.333
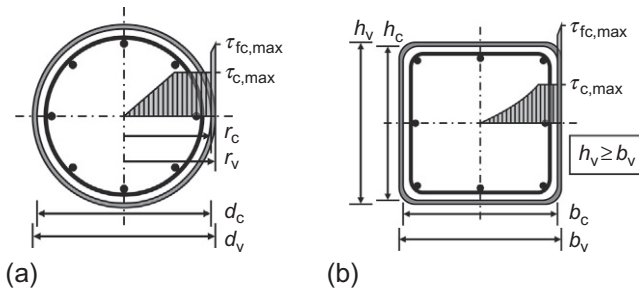
Figure 14.11 Shear stress distribution of the strengthened, reinforced concrete cross section (uncracked), from Schladitz (2011). (a) Circular cross section and (b) rectangular-shaped cross-section.

with:

$$\tau(r) = \frac{\tau_{fc,max}}{r_v} \cdot r \tag{14.27}$$

$\tau_{c,max}$	Maximum shear stress of the (old) concrete; corresponding approximately to the tensile strength
$\tau_{fc,max}$	Maximum shear stress in the TRC layer
$\tau_{fc,max} = f_{fct,flm}$	Application of the flexural tensile strength of the fine-grained concrete provides realistic results (Schladitz, 2011)

(b) for rectangular, reinforced concrete cross-sections:

$$T_{I,max} = \int_A \left(\tau_{xz}(y,z) \cdot y - \tau_{xy}(y,z) \cdot z \right) dA \tag{14.28}$$

with:

$$\tau_{xy}(y,z) = -8 \cdot G \cdot \vartheta \cdot b_v \cdot$$
$$\sum_{n=0}^{\infty} \frac{(-1)^n}{(2n+1)^2 \pi^2 \cosh \dfrac{(2n+1)\pi h_v}{2b_v}} \cos \frac{(2n+1)\pi y}{b_v} \sinh \frac{(2n+1)\pi z}{b_v} \tag{14.29}$$

$$\tau_{xz}(y, z) = 8 \cdot G \cdot \vartheta \cdot b_{\mathrm{v}} \cdot$$

$$\left[\frac{y}{4} - \sum_{n=0}^{\infty} \frac{b_{\mathrm{v}}(-1)^n}{(2n+1)^2 \pi^2 \cosh \dfrac{(2n+1)\pi h_{\mathrm{v}}}{2b_{\mathrm{v}}}} \cos \frac{(2n+1)\pi y}{b_{\mathrm{v}}} \sinh \frac{(2n+1)\pi z}{b_{\mathrm{v}}} \right]$$

(14.30)

$$G \cdot \vartheta = \frac{\tau_{\mathrm{fc,max}}}{-8 \cdot b_{\mathrm{v}} \left[\dfrac{1}{8} - \displaystyle\sum_{n=0}^{\infty} \dfrac{1}{(2n+1)^2 \pi^2 \cosh \dfrac{(2n+1)\pi h_{\mathrm{v}}}{2b_{\mathrm{v}}}} \right]}$$

(14.31)

with:

G	Shear modulus
ϑ	Twisting axis of the cross-section
A	Cross section area
n	Running index

After that the shear stress $\tau(y,z)$ of the rectangular, reinforced concrete cross section can be determined:

$$\tau(y, z) = \sqrt{\tau_{xy}(y, z)^2 + \tau_{xz}(y, z)^2}$$

(14.32)

Then, the shear stresses $\tau(r)$ or $\tau(y,z)$ of the old concrete cross section are limited to the maximum flexural strength $\tau_{\mathrm{c,max}}$ of the old concrete to show the plastificated areas:

$$\tau_{\mathrm{c,max}} \geq \begin{cases} \tau(r) \\ \tau(y, z) \end{cases} \text{for} \begin{cases} r \leq r_{\mathrm{c}} \\ |y| < b_{\mathrm{c}}/2 \text{ and } |z| < h_{\mathrm{c}}/2 \end{cases}$$

(14.33)

The calculation of the presented model requires a computer aid. Therefore, a simplified model is introduced in the next chapter.

14.4.2.2 Engineering model for the determination of the load for the first crack

In the simplified engineering model, it is assumed that the strengthened cross section consists of a material that has a homogeneous, isotropic and linear elastic behavior. The maximum design shear stress $\tau_{\mathrm{fc,max}}$ of the TRC layer is defined as the flexural tensile strength of the fine-grained concrete (see Figure 14.12).

Considering this, the cracking moment can be estimated with a good approximation. Analysis of the test results by Schladitz show that the average torsional moment $T_{\mathrm{I,max}}$ for rectangular cross-sections was overestimated by 10%. For circular cross-sections,
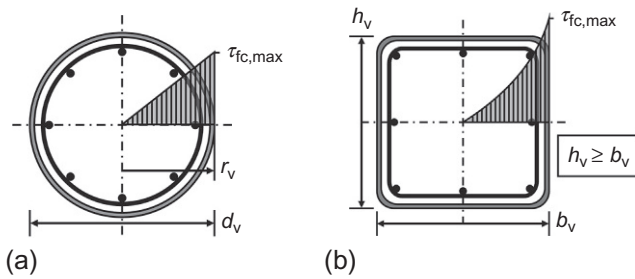
Figure 14.12 Shear stress distribution of the engineering model, according to Schladitz (2011). (a) Circular cross section and (b) rectangular-shaped cross section.

the cracking moment was overestimated by 30–50%. This could cause that the minimum textile reinforcement to be larger than necessary. The actual flexural tensile strength of the fine-grained concrete in the TRC layer is known; therefore, Schladitz suggests to reduce the torsional moment $T_{\mathrm{I,max}}$ for circular cross-sections by a factor of 0.7. Based on this, the minimum textile reinforcement for the cracking moment to ensure a ductile material behavior is estimated as follows:

(a) for circular cross-sections:

$$T_{\mathrm{I,max}} = 0.7 \cdot \tau_{\mathrm{fc,max}} \cdot \frac{\pi}{2} \cdot r_{\mathrm{v}}^{3} \tag{14.34}$$

(b) for rectangular cross-sections:

$$T_{\mathrm{I,max}} = \tau_{\mathrm{fc,max}} \cdot \beta \cdot b_{\mathrm{v}}^{2} \cdot h_{\mathrm{v}} \tag{14.35}$$

To ensure a ductile material behavior, the design value is to be checked:

$$\mathrm{Design\,crucial} = \max \begin{cases} T_{\mathrm{I,max}} \\ T_{\mathrm{II,max}} \end{cases} \tag{14.36}$$

with:

| $T_{\mathrm{II,max}}$ | Torsional moment in the ultimate limited load |

14.4.3 Ultimate limited load of the torsional moment

14.4.3.1 Strut-and-tie model for a strengthened cross section

The derivation of the strut-and-tie model for a strengthened, reinforced concrete cross section with TRC layers is based on the standard strut-and-tie-model of reinforced concrete. The following parameters are used for the calculation:

b_c, h_c, d_c	Geometrical dimensions of old concrete (see Figure 14.10)
n_t	Number of TRC layers used
s_t	Distance of textile reinforcement to one another
$c_{nom,t}$	Concrete cover of textile reinforcement
Index w	Transverse reinforcement
Index f	Longitudinal reinforcement
$A_{f,w}, A_{f,l}$	Cross section area of the roving
$s_{f,w}, s_{f,l}$	Distance of the rovings in the textile reinforcement
$\alpha_{f,w}, \alpha_{f,l}$	Textile reinforcement cross-sectional area per roving per meter
$f_{f,\alpha,l}, f_{f,\alpha,w}$	Tensile strength of the textile reinforcement, depending on the inclination of the rovings
$k_{\Delta lf}$	Factor to reduce the excess quantity of the textile reinforcement overlap

Schladitz (2011) suggested the following strut-and-tie models be used to chara-cterize the effect of a strengthening with TRC (see Figures 14.13 and 14.14). The parameters are:

$A_{k,tcl}$	Core cross-section of the TRC layer
θ	Angle of compression struts

Textile reinforcements with a different geometry of the roving arrangement can be used for strengthening. As a general rule, textile reinforcements with 0°/90° rovings are common. Both the strut-and-tie models in Figures 14.13a and14.14a show textile reinforcement with an angle of 0°/90° in the longitudinal axis. This is a typical way to integrate the steel reinforcement in reinforced concrete cross-sections. Rovings in both directions transfer some parts of the tensile strength. The textile reinforcement of the models shown in Figures 14.13b and 14.14b work like a spiral reinforcement. Hence, only the rovings located along the tensile forces can be taken into consider-ation during calculations (Schladitz, 2011).
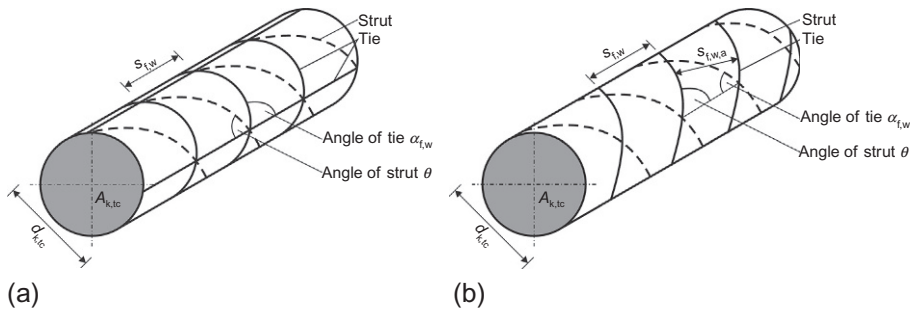
Figure 14.13 Strut-and-tie model for circular cross sections, from Schladitz (2011). (a) Angle 0°/90° of the rovings and (b) angle ±45° of the rovings.
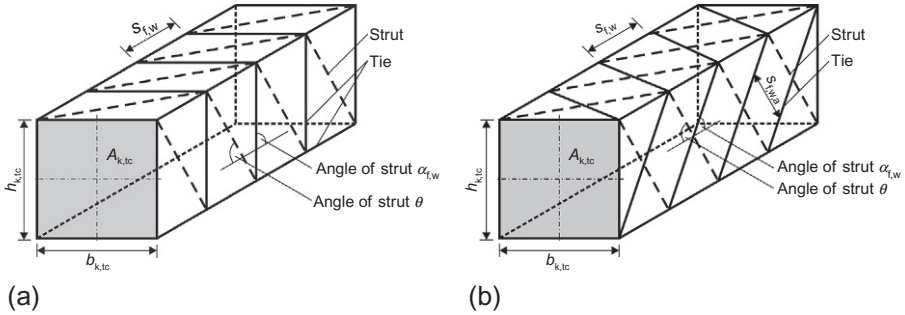
Figure 14.14 Strut-and-tie model for rectangular cross sections, from Schladitz (2011). (a) Angle 0°/90° of the rovings and (b) angle ±45° of the rovings.

14.4.3.2   Maximum design torsional moment

The equations to determine the load capacity of the TRC layers are based on the standard torsional design, according to DIN EN 1992-1-1 (2011). With the following formulas, the ultimate limited load of the torsional moment, in the transverse direction $T_{\text{II,max,f,w}}$, the longitudinal direction $T_{\text{II,max,f,l}}$ and the capacity of the concrete strut $T_{\text{II,max,f,tc}}$, can be determined (Schladitz, 2011), see Section 14.4.3.3.

$$T_{\text{II,max,f,w}} = f_{\text{f},\alpha,\text{w}} \cdot 2 \cdot A_{\text{k,tc}} \cdot a_{\text{f,w}} \cdot \left(\cot\theta + \cot\alpha_{\text{f,w}}\right) \cdot \sin^2\alpha_{\text{f,w}} \tag{14.37}$$

$$T_{\text{II,max,f,l}} = \frac{f_{\text{f},\alpha,1} \cdot 2 \cdot A_{\text{k,tc}} \cdot a_{\text{f,l}}}{\cot\theta - \cos\alpha_{\text{f,w}}} \tag{14.38}$$

$$T_{\text{II,max,f,tc}} = \frac{f_{\text{c}} \cdot 2 \cdot A_{\text{k,tc}} \cdot t_{\text{eff,tc}} \cdot \left(\cot\theta + \cot\alpha_{\text{f,w}}\right)}{(1 + \cot^2\theta)} \tag{14.39}$$

width:

$f_{\text{f},\alpha}$	Textile tensile strength (see Section 14.4.3.3)
$u_{\text{k,tc}}$	Perimeter of the core cross section (see Section 14.4.3.3)
$t_{\text{eff,tc}}$	Effective thickness of the TRC layer (see Section 14.4.3.3)

Because the angle of the strut θ depends on the steel and textile reinforcement, both parts have to be considered in the analysis models.

0°/90° textile reinforcement

Both parts of the textile reinforcement transfer some loads in a similar manner as the longitudinal steel and stirrup reinforcement do. This means that the equations of the ultimate load limits for transverse and longitudinal torsional moments of the old concrete and the TRC layer can be solved to determine the angle of the strut θ. The derivation is shown in Schladitz (2011). The angle of the strut can be calculated as follows:

$$\cot\theta = \sqrt{\frac{f_{s,1}\cdot A_{k,c}\cdot a_{s,1}+f_{f,\alpha,1}\cdot A_{k,tc}\cdot a_{f,1}}{f_{s,w}\cdot A_{k,c}\cdot a_{s,w}+f_{f,\alpha,w}\cdot A_{k,tc}\cdot a_{f,w}}} \tag{14.40}$$

with:

$f_{s,1}, f_{s,w}$	Permitted stress in steel reinforcement, generally yield strength
$A_{k,c}, A_{k,tc}$	Core cross section (see Section 14.4.3.3)

The torsional resistance $T_{II,max}$ is the minimum of:

- Load capacity in longitudinal reinforcement $T_{II,max,l}$
- Load capacity in transverse reinforcement $T_{II,max,w}$
- Load capacity of the strut $T_{II,max,c,tc}$:

$$T_{II,max} = \min \begin{cases} T_{II,max,l} \\ T_{II,max,w} \\ T_{II,max,c,tc} \end{cases} \tag{14.41}$$

$$\begin{aligned} T_{II,max,l} &= T_{II,max,s,1}+T_{II,max,f,1} \\ &= \frac{f_{s,1}\cdot 2\cdot A_{k,c}\cdot a_{s,1}}{\cot\theta}+\frac{f_{f,\alpha,1}\cdot 2\cdot A_{k,tc}\cdot a_{f,1}}{\cot\theta} \end{aligned} \tag{14.42}$$

$$\begin{aligned} T_{II,max,w} &= T_{II,max,s,w}+T_{II,max,f,w} \\ &= f_{s,w}\cdot 2\cdot A_{k,c}\cdot a_{s,w}\cdot \cot\theta + f_{f,\alpha,w}\cdot 2\cdot A_{k,tc}\cdot a_{f,w}\cdot \cot\theta \end{aligned} \tag{14.43}$$

$$T_{II,max,c,tc} = T_{II,max,c}+T_{II,max,tc} = \frac{f_c\cdot 2\cdot A_{k,c}\cdot t_{eff}}{(\cot\theta+\tan\theta)}+\frac{f_{fc}\cdot 2\cdot A_{k,tc}\cdot t_{eff,tc}}{(\cot\theta+\tan\theta)} \tag{14.44}$$

$\pm 45°$ textile reinforcement

If the textile reinforcement is made of diagonal rovings only one part of the roving can carry some tensile stresses. By solving the equations of transverse and longitudinal torsional moments, the angle of the strut θ can be calculated, but the angle of the textile reinforcement has to be considered (see Figure 14.13b). The angle of the strut can be calculated as follows:

$$\cot\theta = \sqrt{\frac{f_{s,1}\cdot 2\cdot A_{k,c}\cdot a_{s,1}+f_{f,\alpha,w}\cdot A_{k,tc}\cdot a_{f,w}}{f_{s,w}\cdot 2\cdot A_{k,c}\cdot a_{s,w}+f_{f,\alpha,w}\cdot A_{k,tc}\cdot a_{f,w}}} \tag{14.45}$$

Again, the torsional resistance can be calculated with Equation (14.41), as follows:

$$\begin{aligned} T_{II,max,l} &= T_{II,max,s,1}+T_{II,max,f,1} \\ &= \frac{f_{s,1}\cdot 2\cdot A_{k,c}\cdot a_{s,1}}{\cot\theta}+\frac{f_{f,\alpha,w}\cdot 2\cdot A_{k,tc}\cdot a_{f,1}\cdot (\cot\theta+1)\cdot 0.5}{\cot\theta} \end{aligned} \tag{14.46}$$

$$T_{\mathrm{II,max,w}} = T_{\mathrm{II,max,s,w}} + T_{\mathrm{II,max,f,w}}$$
$$= f_{\mathrm{s,w}} \cdot 2 \cdot A_{\mathrm{k,c}} \cdot a_{\mathrm{s,w}} \cdot \cot\theta + f_{\mathrm{f},\alpha,\mathrm{w}} \cdot 2 \cdot A_{\mathrm{k,tc}} \cdot a_{\mathrm{f,w}} \cdot (\cot\theta + 1) \cdot 0.5$$

$$(14.47)$$

$$T_{\mathrm{II,max,c,tc}} = T_{\mathrm{II,max,c}} + T_{\mathrm{II,max,tc}}$$
$$= \frac{f_{\mathrm{c}} \cdot 2 \cdot A_{\mathrm{k,c}} \cdot t_{\mathrm{eff}}}{(\cot\theta + \tan\theta)} + \frac{f_{\mathrm{fc}} \cdot 2 \cdot A_{\mathrm{k,tc}} \cdot t_{\mathrm{eff,tc}} \cdot (\cot\theta + 1)}{(1 + \cot^2\theta)}$$

$$(14.48)$$

14.4.3.3 Determination of the required parameters

Core cross section $A_{\mathrm{k,tc}}$ and effective thickness $t_{\mathrm{eff,tc}}$ of the TRC layer

The torsional load case can be idealized with a strut-and-tie model (see Figures 14.8 and 14.9). The struts and ties create a box girder around the core cross section A_{k}. For reinforced concrete structures, the standard (DIN EN 1992-1-1, 2011) is valid. For strengthened cross-sections, both the cross section area $A_{\mathrm{k,tc}}$ and the thickness of the TRC layer $t_{\mathrm{eff,tc}}$ values are defined. In Figures 14.15 and 14.16, two possibilities are shown (Schladitz, 2011). The core cross section is defined by the inner line of the TRC layer (on the left) or the centerline of the TRC layer (on the right).

Considering the observation during the experiments and the analysis of the test results, Schladitz suggested to use the centerline as the boundary of the core section $A_{\mathrm{k,tc}}$. This means that the strain distribution in each TRC layer is equal. If a much larger number of TRC layers is used in the strengthening, the inner line should be considered as the boundary to ensure the ultimate limited load.

The core cross section $A_{\mathrm{k,tc}}$ or the perimeter $u_{\mathrm{k,tc}}$ can be determined as follows:

(a) for a rectangular cross-section:

$$A_{\mathrm{k,tc}} = b_{\mathrm{k,tc}} \cdot h_{\mathrm{k,tc}}$$

$$(14.49)$$
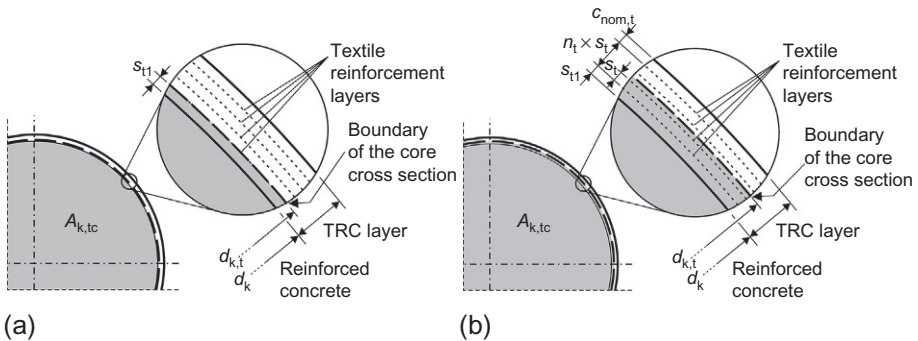
Figure 14.15 Circular core cross sections $A_{\mathrm{k,tc}}$ of TRC layer (Schladitz, 2011). (a) Inner line as boundary and (b) centerline as boundary.
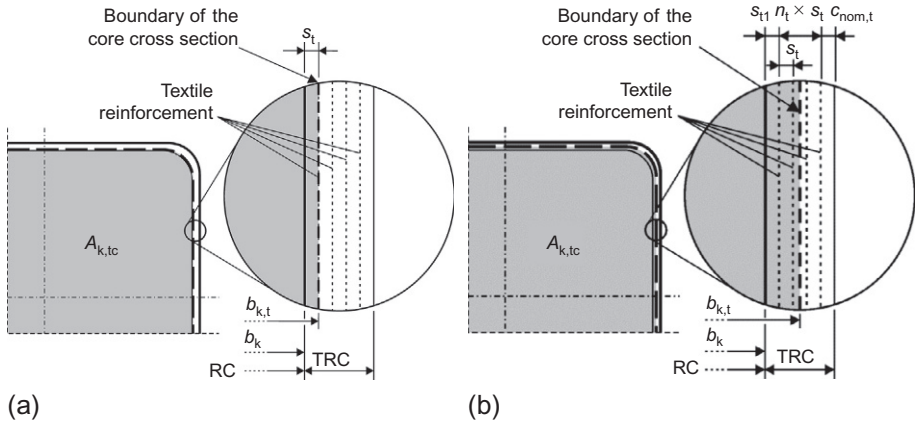
Figure 14.16 Rectangular core cross sections $A_{k,tc}$ of TRC layer (Schladitz, 2011). (a) Inner line as boundary and (b) centerline as boundary.

$$u_{k,tc} = 2 \cdot \left(b_{k,tc} + h_{k,tc} \right) \tag{14.50}$$

$$b_{k,tc} = b_c + t_{eff,tc} \quad \text{and} \quad h_{k,tc} = h_c + t_{eff,tc} \tag{14.51}$$

(b) for a circular cross section:

$$A_{k,tc} = \frac{d_{k,tc}^2 \cdot \pi}{4} \tag{14.52}$$

$$u_{k,tc} = d_{k,tc} \cdot \pi \tag{14.53}$$

$$d_{k,tc} = d_c + t_{eff,tc} \tag{14.54}$$

The effective thickness $t_{eff,tc}$ can be calculated as follows (Figures 14.15 and 14.16):

$$b_{k,tc} = b_c + 2 \cdot \min \left\{ s_{t,1} \,|\, c_{nom,t} \right\} + (n_t - 1) \cdot s_t \tag{14.55}$$

$$h_{k,tc} = h_c + 2 \cdot \min \left\{ s_{t,1} \,|\, c_{nom,t} \right\} + (n_t - 1) \cdot s_t \tag{14.56}$$

with:

$s_{t,1}$	Distance between the surface of an old concrete and the first textile reinforcement
s_t	Distance to the next textile reinforcement
n_t	Number of the TRC layers
$c_{nom,t}$	Concrete cover between the last layer of the textile reinforcement and the surface of the strengthening

For simplification purposes, all geometric values refer to the centroid of the textile reinforcement. Because the textile reinforcement is embedded in the fine-grained concrete, this assumption is acceptable. By using the minimum values of $s_{t,1}$ and $c_{nom,t}$, the core cross section is calculated in a conservative manner.

Design textile tensile strength $f_{f,\alpha}$

The tensile strength of the TRC is usually determined by uniaxial tensile tests. In case of a noncentric load to the rovings, the tensile strength $f_{f,\alpha}$ has to be reduced (Jesse, 2011; Schladitz, 2011):

$$f_{f,\alpha} = k_{0,\alpha} \cdot f_f \tag{14.57}$$

Schladitz found a correlation between the reduction factor and the angle of the rovings in the textile reinforcement (see Figure 14.17). For circular and rectangular cross sections, the following is recommended:

(a) $\pm45°$-textile reinforcement with the same reinforcement area in bars and stirrups for transverse and longitudinal direction $a_{s,w} \approx a_{s,l}$: $k_{0,\alpha} = 1$ ($\alpha = 0°$)
(b) $\pm45°$-textile reinforcement with a different reinforcement area in bars and stirrups for transverse and longitudinal direction $a_{s,w} \neq a_{s,l}$: $k_{0,\alpha}$ is subjected to the angle of the strut θ (see Figure 14.17).
(c) $0°/90°$-textile reinforcement: $k_{0,\alpha} = k_{0,\alpha}(\alpha = 45°)$ according to Figure 14.17.

It is important to notice that the reduction factors are valid only for the textile reinforcements used by Schladitz. For the other textile reinforcements, the reduction factors should be determined again.

Cross-sectional area of the textile reinforcement a_f per unit of length

The cross-sectional area of the textile reinforcement per unit of length for both longitudinal and transverse directions can be calculated as follows:
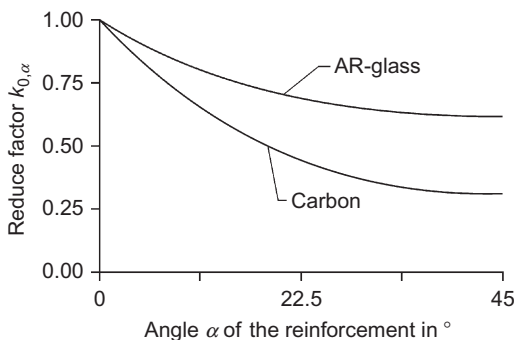
Figure 14.17 Reduction coefficient of the tensile strength subjected to the angle of the strut (Schladitz, 2011).

$$a_{\mathrm{f,w}} = n_{\mathrm{t}} \cdot \frac{A_{\mathrm{f,w}}}{s_{\mathrm{f,w}}} \quad \text{and} \quad a_{\mathrm{f,l}} = n_{\mathrm{t}} \cdot \frac{A_{\mathrm{f,l}}}{s_{\mathrm{f,l}}} \tag{14.58}$$

with:

$A_{\mathrm{f,w}}, A_{\mathrm{f,l}}$	Cross-sectional area of the rovings in transverse and longitudinal direction

According to Schladitz (2011) the increase in the amount of the textile reinforcement provided in the overlapping areas has a positive effect for the ultimate limited load of the torsional resistance. However, no detailed research considering this effect was conducted. Therefore this effect should be neglected to ensure the ultimate limited load.

Material resistance for the calculation of the load capacity of the strut

As already mentioned in Sections 14.3.3.3 and 14.3.3.5, the behavior of the TRC material under the pure compression has not been investigated in detail. Schladitz did not determine any failure of the compressive strut in the experiments (Schladitz, 2011). Upcoming research will investigate whether the implementation of the reduction factor is necessary.

14.4.4 Utilization of the bars and stirrups

According to Schladitz (2011), the torsional resistance of strengthened structures with a rare textile reinforcement might be smaller than the torsional resistance of the old concrete structure. In this case, it was not absolutely clear if the bars and stirrups reached their yield strength, although this was assumed in the calculations, as shown in Section 14.4.3.2. Therefore, the minimum textile reinforcement requirement is necessary. Based on the experiments, Schladitz suggests the following delimitations:

- Tensile force in the strengthening shall be greater than the tensile strength of concrete (in old concrete and fine-grained concrete),
- Maximum crack spacing in TRC layers shall be smaller than the anchorage length of textile reinforcement.

14.5 Column strengthening

14.5.1 General

Columns are an important part of the static systems in buildings. Due to the ever-changing use requirements and load demands for existing buildings, as well as the expected damage due to aging or randomly occurring fires, columns need to be strengthened. In addition to the classic reinforced shotcrete or CFRP sheet strengthening measures, TRC is a feasible alternative. The confinement provided by an additional layer of TRC results in an increased axial loadbearing capacity in the column.

Compared to a shotcrete reinforced layer, the increase in the structural member geometry is minimal, and the usage of space in the building is not affected.

14.5.2   Design model

The design model for strengthening columns with TRC is based on studies by Ortlepp et al. (Ortlepp and Curbach, 2009; Ortlepp et al., 2011a). Two mechanisms must be taken into account: the load increase due to the confinement provided by both the textile reinforcement and the additional fine-grained concrete layer. For further information, reference is made to previous research (Triantafillou et al., 2006; Ortlepp and Curbach, 2009). The applicability of the model on large columns is described as well, and it has been validated for circular columns (Ortlepp et al., 2011a).

14.5.2.1   Basic model

Based on small, unreinforced test specimens, (Ortlepp et al., 2011a) developed a basic model for describing the axial capacity N_u of a TRC element under normal force, where N_u is determined as the larger of two axial capacity values, N_{u1} or N_{u2}, as follows:

$$N_u = \max\left(N_{u1}, N_{u2}\right) \tag{14.59}$$

The parameter N_{u1} (axial force resistance) is calculated as follows:

$$N_{u1} = N_c + N_{fc} = f_{cm} \cdot A_c + 0.27 \cdot f_{fcm} \cdot A_{fc,\,eff} \tag{14.60}$$

with:

N_c	Axial load capacity of the old concrete
N_{fc}	Axial load capacity of the fine-grained concrete layer
f_{cm}	Mean value of concrete cylinder compressive strength
f_{fcm}	Mean value of fine-grained concrete cylinder compressive strength
A_c	Core cross section of old concrete
$A_{fc,eff}$	effective cross-sectional area of fine-grained concrete according to Equation (14.61)

$$A_{fc,\,eff} = A_{fc} - A_t \tag{14.61}$$

with:

A_{fc}	Cross-sectional area of TRC layer
A_t	Textile reinforcement cross-sectional area

The factor 0.27, used as a strength reduction factor for fine-grained concrete, was determined empirically based on small-scale experiments (Ortlepp et al., 2011a). Only 60% of fine-grained concrete matrix strength was utilized. This is because, at that stress level, failure in the cross section of the old concrete started. Spalling of the reinforcement layer at the concrete, which occurred as the load was increased, was detected in the vicinity around the area, where the load was applied. This was due to load transfer and distribution mechanisms, which further justifies the use of a reduction factor of 0.6. Furthermore, a 0.75 factor to account for the use of carbon reinforcement has been recommended. The second term N_{u2} of Equation (14.59) is determined as follows:

$$N_{u2} = A_c \cdot f_{cm} \cdot \left[1 + 0.27 \cdot \frac{\sigma_{lu}}{f_{cm}} + 5.55 \cdot \left(\frac{\sigma_{lu}}{f_{cm}}\right)^2 - \left(\frac{\sigma_{lu}}{f_{cm}}\right)^2\right],$$

$$\text{valid for} \quad \sigma_{lu}/f_{cc} < 0.8$$

(14.62)

The stress σ_{lu} resulting from the confinement of the reinforcing layer can be calculated with the help of Equation (14.63):

$$\sigma_{lu} = k_e \cdot \frac{b+d}{b \cdot d} \cdot a_f \cdot n_{t,\,eff} \cdot f_f$$

(14.63)

with:

f_{cc}	Triaxial compressive strength of the old concrete, in Hampel et al. (2009)
a_f	Cross-sectional area of the textile reinforcement per meter of the column height
$n_{t,eff}$	Effective number of textile layers (without anchorage areas)
f_f	Tensile strength of the textile reinforcement
b, d	Length of the edge (square) or diameter (circular) of cross-sectional area of the old concrete
k_e	Coefficient for consideration of the cross section geometry used in Equation (14.64)

$$k_e = 1 - \frac{b_n^2 \cdot d_n^2}{3 \cdot A_c}$$

(14.64)

with:

b_n, d_n	Free length of the edge between the fillet radius (square columns); $b=d=0$ for round columns

For circular columns, $k_e = 1$ can be taken as a maximum value.

14.5.2.2 Extension of the basic model

Based on the small-sized specimen tests and the basic model assumptions discussed in Section 14.5.2.1, a refined model to account for a large-scale effect was subsequently developed. The concrete strength used was determined from 150 mm cube specimen tests. In reality, considering real column geometries, the size effect must be taken into account in the formulas. For further information on the size effect in reinforced concrete, see Löser et al. (1986). Therefore, for the design of the strengthening, at the column head, Equations (14.60) and (14.62) are modified by a factor k_m to account for the size effect in the unreinforced old concrete cross section at the top of the column.

$$N_{u1} = N_c + N_{fc} = k_m \cdot f_{cm} \cdot A_c + 0.27 \cdot f_{fcm} \cdot A_{fc,\,eff} \tag{14.65}$$

$$N_{u2} = k_m \cdot f_{cm} \cdot A_c \cdot f_{cm} \cdot \left[1 + 0.27 \cdot \frac{\sigma_{lu}}{k_m \cdot f_{cm}} + 5.55 \cdot \left(\frac{\sigma_{lu}}{k_m \cdot f_{cm}} \right)^2 - \left(\frac{\sigma_{lu}}{k_m \cdot f_{cm}} \right)^2 \right] \tag{14.66}$$

Similarly, for design at the middle of the column, Equation (14.65) can be further manipulated into Equation (14.67):

$$N_{u1} = N_c + N_{fc} = k_m \cdot f_{cm} \cdot A_c + 0.45 \cdot f_{fcm} \cdot A_{fc,\,eff} \tag{14.67}$$

The load capacity is greater, as the previous reduction by the factor 0.6, which was taken into account due to spalling of the textile reinforcement layer, may be omitted. If the cross section of the old concrete is reinforced, the contribution of the longitudinal steel reinforcement to the axial capacity N_{u1} is added to Equation (14.67); this considers the ultimate strain level of the cross section of the old concrete ε_{cu}:

$$N_{u1} = N_c + N_{fc} + N_s = k_m \cdot f_{cm} \cdot A_{c,\,netto} + 0.45 \cdot f_{fcm} \cdot A_{fc,\,eff} + \sigma_s(\varepsilon_{cu}) \cdot A_s \tag{14.68}$$

Therefore, the equation for the design of the column head is as follows:

$$N_{u1} = N_c + N_{fc} + N_s = k_m \cdot f_{cm} \cdot A_{c,\,netto} + 0.27 \cdot f_{fcm} \cdot A_{fc,\,eff} + \sigma_s(\varepsilon_{cu}) \cdot A_s \tag{14.69}$$

By comparison, the contribution to the axial capacity of the column, resulting from the confinement due to the steel stirrups, is lower than that provided by the confining effect due to the outer TRC layer. Therefore, it is not taken into consideration in the equations (Ortlepp et al., 2011b). However, the contribution of longitudinal steel reinforcement of reinforced cross-sections must not be underestimated; accordingly, such a contribution is added to Equations (14.66) and (14.70):

$$N_{u2} = k_m \cdot f_{cm} \cdot A_c \cdot f_{cm} \cdot \left[1 + 0.27 \cdot \frac{\sigma_{lu}}{k_m \cdot f_{cm}} + 5.55 \cdot \left(\frac{\sigma_{lu}}{k_m \cdot f_{cm}} \right)^2 - \left(\frac{\sigma_{lu}}{k_m \cdot f_{cm}} \right)^3 \right]$$
$$+ \sigma_s(\varepsilon_{cu}) \cdot A_s \tag{14.70}$$

In large-scale tests, the model presented here was validated (Ortlepp et al., 2011b). It should be noted that the model, so far, has only been verified on circular columns with satisfactory results. Validation of the model for columns with square cross-sections is still pending.

14.6   Conclusion

In this section, four analysis models (bending, shear on T-beams, torsional and axial force) to increase the load capacity were introduced. These analysis models were developed and verified on experimental research. With the analysis models, it was possible to predict the results of the experiments successfully. In today's research, even more structural components are tested to develop analysis models for their additional load capacity, when they are strengthened with TRC.

It is important to note that the analysis models introduced in this chapter were developed with the existing textile reinforcement and fine-grained concrete at this time. Both components will be refined with time, and maybe material properties will change. One result could be that the developed analysis models have to be modified.

Acknowledgments

References

American Concrete Institute (ACI), 2008. Guide for the Design and Construction of Externally Bonded FRP Systems for Strengthening Concrete Structures. American Concrete Institute, Farmington Hills, MI.

Albert, A., 2014. Schneider Bautabellen für Ingenieure. Bundesanzeiger Verlag, Köln.

Bösche, A., 2007. Möglichkeiten zur Steigerung der Biegetragfähigkeit von Beton- und Stahlbetonbauteilen durch den Einsatz textiler Bewehrungen – Ansatz für ein Bemessungsmodell. Technische Universität Dresden, Dresden.

Brückner, A., 2011. Querkraftverstärkung von Bauteilen mit textilbewehrtem Beton. Technische Universität Dresden, Dresden.

Brückner, A., Ortlepp, R., Curbach, M., 2008. Anchoring of shear strengthening for T-beams made of TRC. Mater. Struct. 41, 407–418.

Brückner, A., Wellner, S., Ortlepp, R., Scheerer, S., Curbach, M., 2013. Plattenbalken mit Querkraftverstärkung aus Textilbeton unter nicht vorwiegend ruhender Belastung. Beton- und Stahlbetonbau 108 (3), 169–178. Heft.

Curbach, M., Lorenz, E., Schladitz, F., Schütze, E., Weiland, S., 2014. Gesamtbericht der experimentellen Untersuchungen zur allgemeinen bauaufsichtlichen Zulassung für ein

Verfahren zur Verstärkung von Stahlbeton mit TUDALIT® (Textilbewehrter Beton). Deutsches Institut für Bautechnik (DIBt), Berlin.

Curbach, M., Ortlepp, R., 2012. Sonderforschungsbereich 528 – Textile Bewehrungen zur bautechnischen Verstärkung und Instandsetzung. Abschlussbericht (gekürzte Fassung). Technische Universität Dresden, Dresden.

Curbach, M., Scheerer, S., 2011. Concrete light – possibilities and visions. In: Šrůma, V. (Ed.), Proceedings fib Symposium Prague 2011: Concrete Engineering for Excellence Efficiency, Prague, pp. 29–44.

Deutsches Institut für Bautechnik (DIBt), 2014. Verfahren zur Verstärkung von Stahlbeton mit TUDALIT (Textilbewehrter Beton), Zulassungsnummer Z-31.10-182.

DIN 1045, 2001. Tragwerke aus Beton, Stahlbeton und Spannbeton – Teil 1: Bemessung und Konstruktion. Beuth Verlag, Berlin.

DIN EN 1990, 2010. Grundlagen der Tragwerksplanung; Deutsche Fassung EN 1990:2002 + A1:2005 + A1:2005/AC:2010. Beuth Verlag, Berlin.

DIN EN 1992-1-1 (Eurocode 2), 2011. Bemessung und Konstruktion von Stahlbeton- und Spannbetontragwerken – Teil 1-1: Allgemeine Bemessungsregeln und Regeln für den Hochbau; Deutsche Fassung EN 1992-1-1:2004 + AC:2010. Beuth Verlag, Berlin.

DIN EN 1992-1-1/NA (Eurocode 2), 2013. Nationaler Anhang – National festgelegte Parameter – Eurocode 2: Bemessung und Konstruktion von Stahlbeton- und Spannbetontragwerken – Teil 1-1: Allgemeine Bemessungsregeln und Regeln für den Hochbau. Beuth Verlag, Berlin.

Fib Task Group 9.3, 2001. Externally bonded FRP reinforcement for RC structures. International Federation for Structural Concrete (fib), Bulletin 14. Stuttgart: Sprint-Digital-Druck.

Frenzel, M., 2015. Bemessung texilbetonverstärkter Stahlbetonbauteile unter Biegebeanspruchung. Beton- und Stahlbetonbau 110 (S1), 54–68.

Frenzel, M., Curbach, M., 2011. Bemessungsmodell zur Berechnung der Tragfähigkeit von biegeverstärkten Stahlbetonplatten. In: Curbach, M., Ortlepp, R. (Eds.), Textilbeton Theorie und Praxis – 6. Kolloquium zu textilbewehrten Tragwerken (CTRS6). Eigenverlag, Institut für Massivbau der TU Dresden, pp. 381–399.

Hampel, T., Speck, K., Scheerer, S., Ritter, R., Curbach, M., 2009. High performance concrete under biaxial and triaxial loads. ASCE J. Eng. Mech. 135, 1274–1280.

Jesse, D., 2011. Tragverhalten von textilbewehrtem Beton unter zweiaxialer Zugbeanspruchung. Technische Universität Dresden, Dresden.

Jesse, F., 2012. Experimentelle Untersuchungen des Tragverhaltens von Textilbeton unter einaxialer Druckbeanspruchung. DFG-Forschungsantrag (unveröffentlicht).

Jesse, F., 2004. Tragverhalten von Filamentgarnen in zementgebundener Matrix. Technische Universität Dresden, Dresden.

Just, M., 2015. Sicherheitskonzept für Textilbeton. Beton- und Stahlbetonbau, Spezial 110 (S1), 42–46.

Khalifa, A., Gold, W.J., Nanni, A., Abdel Aziz, M.I., 1998. Contribution of externally bonded FRP to shear capacity of RC flexural members. ASCE J. Compos. Constr. 2 (4), 195–202.

Leonhardt, F., Mönnig, E., 1984. Vorlesung über Massivbau – Teil 1 Grundlagen zur Bemessung im Stahlbetonbau. Springer-Verlag, Berlin.

Lorenz, E., 2014. Endverankerung und Übergreifung textiler Bewehrungen in Betonmatrices. Technische Universität Dresden, Dresden.

Lorenz, E., Schütze, E., Weiland, S., 2015. Textilbeton – Eigenschaften des Verbundwerkstoffes. Beton- und Stahlbetonbau, Spezial 110, 29–41.

Löser, B., Löser, H., Wiese, H., Stritzke, J., 1986. Bemessungsverfahren für Beton- und Stahlbetonbauteile. Ernst & Sohn, Berlin.

Molter, M., 2005. Zum Tragverhalten von textilbewehrtem Beton. RWTH Aachen, Aachen.

Mörsch, E., 1950. Die Schubsicherung der Eisenbetonbalken. Verlag Konrad Wittwer, Stuttgart.

Ortlepp, R., 2007. Untersuchungen zur Verbundverankerung textilbewehrter Feinbetonverstärkungsschichten. Technische Universität Dresden, Dresden.

Ortlepp, R., Brückner, A., Curbach, M., 2010. Influence of textile reinforcement on the principle stress condition of strengthened RC beams. In: 3rd International Fib Congress, Washington, DC.

Ortlepp, R., Curbach, M., 2009. Verstärken von Stahlbetonstützen mit textilbewehrtem Beton. Beton- und Stahlbetonbau 104 (10), 681–689.

Ortlepp, R., Lorenz, A., Curbach, M., 2011a. Umschnürungswirkung textilbewehrter Verstärkungen im Lasteinleitungsbereich von Stützen in Abhängigkeit von der Geometrie. Beton- und Stahlbetonbau 103 (7), 490–500.

Ortlepp, R., Schladitz, F., Curbach, M., 2011b. Textilbetonverstärkte Stahlbetonstützen. Beton- und Stahlbetonbau 106 (9), 640–648.

Schladitz, F., 2011. Torsionstragverhalten von textilbetonverstärkten Stahlbetonbauteilen. Technische Universität Dresden, Dresden.

Schladitz, F., Curbach, M., 2012. Torsion tests on textile-reinforced concrete strengthened specimens. Mater. Struct. 45 (1–2), 31–40.

Schladitz, F., Frenzel, M., Ehlig, D., Curbach, M., 2012. Bending load capacity of reinforced concrete slabs strengthened with textile reinforced concrete. Eng. Struct. 40, 317–326.

Schütze, E., Lorenz, E., Curbach, M., 2015. Test methods for textile reinforced concrete. In: Brameshuber, W. (Ed.), Proceedings FERRO-11 3rd ICTRC (PRO98), S.A.R.L. Rilem Publications, pp. 307–318.

Triantafillou, T.C., 1998. Shear strengthening of reinforced concrete beams using epoxy-bonded FRP composites. ACI Struct. J. 95 (2), 107–115.

Triantafillou, T.C., Papanicolaou, C.G., Zissimopoulos, P., Laourdekis, T., 2006. Concrete confinement with textile-reinforced mortar jackets. ACI Struct. J. 103 (1), 28–37.

Voss, S., 2008. Ingenieurmodelle zum Tragverhalten von Textilbewehrtem Beton. RWTH Aachen, Aachen.

Weiland, S., 2009. Interaktion von Betonstahl und textiler Bewehrung bei der Biegeverstärkung mit textilbewehrtem Beton. Technische Universität Dresden, Dresden.

Weiland, S., Ortlepp, R., Brückner, A., Curbach, M., 2007. Strengthening of RC-structures with textile reinforced concrete (TRC). In: *ACI SP-244* "*Thin fiber and textile reinforced cementitious systems*".

Weiland, S., Lorenz, E., Curbach, M., 2010. Interaction of mixed reinforcements at the strengthening of reinforced concrete with textile reinforced concrete. In: Aldea, C.-M. (Hrsg.), Proceedings of the ACI 2010 Fall Convention. Pittsburgh.

Zilch, K., Zehetmaier, G., 2009. Bemessung im konstruktiven Betonbau. Springer-Verlag, Berlin.

This page intentionally left blank

Strengthening of existing masonry structures: Concepts and structural behavior

15

T. Triantafillou
University of Patras, Patras, Greece

15.1 Introduction

Unreinforced masonry bearing wall construction, commonly termed URM, is one of the oldest construction types found worldwide. URM walls have been proven to be prone to failure during high or even moderate intensity earthquakes or high wind pressure; therefore, they represent a significant safety hazard. A causal breakdown of earthquake fatalities for the second half of the last century revealed that almost 60% of the lives lost were attributed to URM failures (Coburn and Spence, 2002). Moreover, structural decay due to aging or cumulative seismic-induced damage poses a direct threat to the preservation and safeguarding of historical structures that comprise an important part of many countries' cultural heritage. Thereby, there is a tremendous and urgent need for upgrading existing URM structures. In seismic areas, structures designed according to old seismic codes must meet upgraded performance levels demanded by current seismic design standards. In non-seismic areas, URM structures must be updated due to change of usage and/or the introduction of more stringent design requirements.

Numerous techniques have been developed aiming at increasing the strength and/ or ductility of URM walls. These include the use of metallic or polymeric grid-reinforced surface coatings, shotcrete overlays, internal or external prestressing with steel ties, externally bonded fiber-reinforced polymers (FRP, such as epoxy-bonded strips or *in situ* impregnated fabrics) and near-surface mounted FRP reinforcement. FRP-based strengthening and/or seismic retrofitting techniques have been well-established in the civil engineering community due to the favorable properties offered by these materials. These include high strength and stiffness to weight ratio, corrosion resistance, ease and speed of application and minimal change in the geometry. Despite the many advantages associated with the use of FRP, the relevant strengthening techniques are not entirely problem-free. There are some drawbacks associated with the organic resins used to bind or impregnate the fibers. In addition, certain restrictions related to intervention strategies for historic masonry buildings (e.g., requirements for reversibility) may possibly inhibit FRP application.

One interesting solution to the above problems would be the replacement of organic binders with inorganic ones, for example, cement-based or hydraulic lime

mortars. Bond conditions in mortar-based composites could be improved, and fiber–matrix interactions could be made tighter through the use of open-weaved fabrics instead of continuous fiber sheets. The resulting textile-based system, termed herein as textile-reinforced mortar (TRM) system, may be thought of as an alternative to the FRP-based system (Papanicolaou et al., 2007, 2008).

In this chapter, we aim to present (a) concepts for the strengthening of masonry structures with TRM and (b) key aspects of structural behavior. The following topics, also presented in Fyfe Europe SA and Triantafillou (2012), are covered:

- Brief description of materials and their properties.
- Intervention requirements and strengthening rationale.
- Aspects of structural modeling and retrofitting for seismic applications.
- Strengthening of masonry walls for out-of-plane or in-plane loads.
- Strengthening of curved masonry elements.
- Confinement of masonry columns.

15.2   Textile-reinforced mortar system

The TRM system may be considered as an alternative to FRP, which have already found their way into the field of strengthening and seismic retrofitting. With the aim of alleviating specific problems associated with the use of organic resins in FRP systems, the TRM system comprises an open weaved fabric made of long woven, knitted or even unwoven fiber rovings (e.g., glass, basalt, or carbon) in at least two (typically orthogonal) directions (Figure 15.1a), along with an inorganic mortar matrix (Triantafillou et al., 2006). The density, that is, the quantity of the spacing of rovings in

(a)   (b)
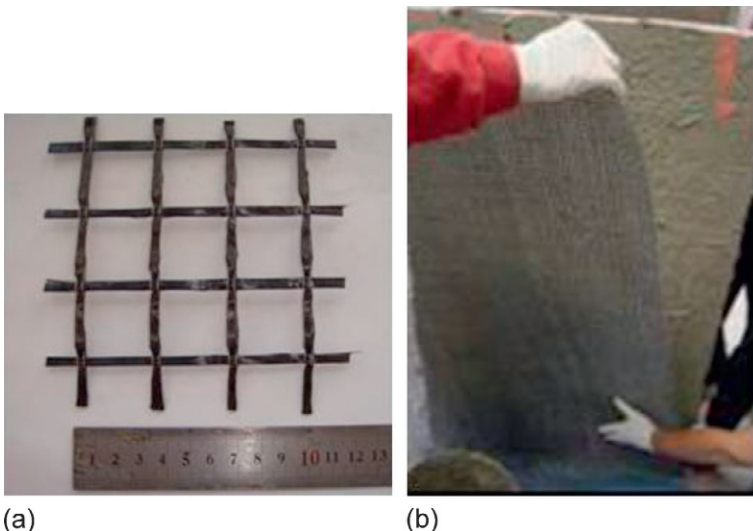
Figure 15.1 (a) Bidirectional textile and (b) application on masonry specimen.

each direction can be controlled independently. Thus, this affects the mechanical characteristics of the open weaved fabric and the degree of penetration of the mortar matrix through the woven mesh.

The TRM system is applied similarly to FRP. The walls are first ground at locations where materials are protruding (e.g., irregular blocks or mortar at joints) and brushed clean. Then, dust and any loose particles are removed (e.g., with air pressure). Finally, a standard wet lay-up procedure follows to bond the textile layers on the surface of the masonry wall. The procedure involves application of the mortar on the (dampened) wall surface, subsequent application of the textile by hand (Figure 15.1b) and roller pressure. The mortar is also applied in between layers and on top of the last textile layer. Application of the mortar is made in a few millimeter (e.g., 3–4 mm) thick layers using a smooth metal trowel. The textile is pressed slightly into the mortar, which protrudes through the perforations between fiber rovings.

15.3 Mechanical properties

In the TRM system, fibers provide tensile load capacity and stiffness, while the matrix ensures sharing of the load among fibers and protects the fibers from the environment. The composite action between the open weaved fabrics and mortars is achieved through a mechanical interlock of mortar at fabric perforations. This is also achieved through some impregnation of fibers near the surface of the rovings, in case the fabrics are not coated (dry fibers). As a consequence, bond conditions between fibers and matrix are not perfect and the development of relative slip is possible.

The result of debonding at the fiber–matrix interface is that TRM, unlike FRP, does not behave as a linear elastic material. Its response in uniaxial tension parallel to a principal fiber direction (illustrated in Figure 15.2) is characterized by an initial linear elastic part (uncracked matrix), followed by a branch associated with extensive cracking in the mortar (stage IIa). When this cracking is stabilized, the fibers are tensioned and carry the load until they debond, pullout and eventually rupture.
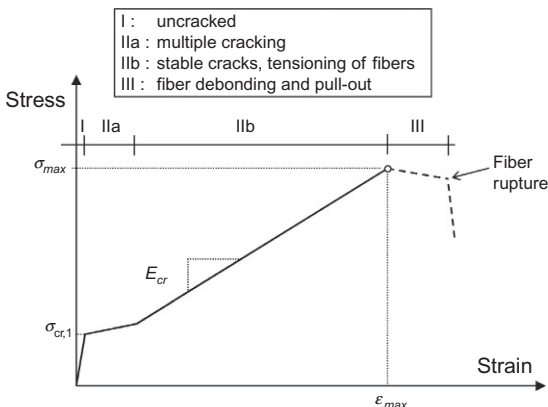
Figure 15.2 Idealized stress–strain curve in uniaxial tension parallel to a principal fiber direction.

I : uncracked specimen
IIa : multiple cracking
IIb : stable cracks, tensioning of fibers
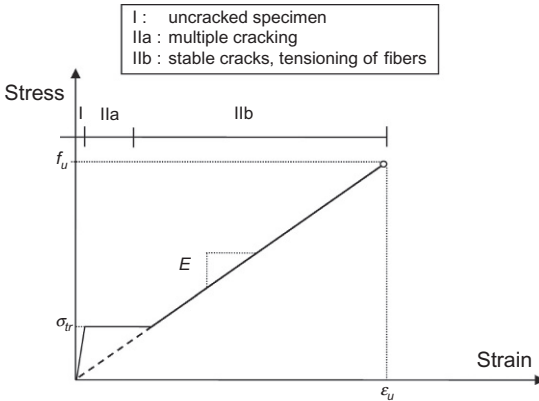
Figure 15.3 Simplified stress–strain curve.

It can be assumed that the "multiple cracking" branch (IIa) can be represented by a horizontal line, because of its small slope (even zero in some cases). Thereby, the stress–strain behavior can be further simplified, as shown in Figure 15.3.

Values of practical interest on the simplified stress–strain curve are the ultimate tensile strength (f_u), the maximum elongation at ultimate (ε_u), the transition zone tensile stress (σ_{tr}) and the tensile modulus (E). Such values are obtained on the basis of experimental investigations.

15.4 Intervention requirements and strengthening rationale

The primary objective of strengthening with TRM is to increase the strength of masonry elements, as well as the overall capacity of a masonry structure. TRM in the form of externally applied jackets should be located primarily in areas where tensile stresses are to be carried and should not be relied upon to carry compressive stresses, due to possible local instability.

If TRM strengthening concerns historical structures, a critical evaluation and proper selection of the system should be made with respect to standards for preservation and evaluation. The adopted solution, then, shall guarantee compatibility, durability, and reversibility.

For the appropriateness of the TRM system for a specific application, the engineer should evaluate the existing structure to establish its existing capacity, identify deficiencies and their causes, and determine the condition of the masonry substrate. The evaluation should include a field inspection, review of relevant documents, and a structural analysis. The TRM system application can be employed for the following reasons: flexural and shear strengthening to resist tensile stresses within a structural member or between adjoining members; connection between members (e.g., connections between orthogonal walls or vault and wall ties); floor stiffening; crack width limitation;

confinement; and axial capacity enhancement of columns. Hence, the TRM system application may be aimed at increasing the capacity of walls, arches, or vaults; wrapping of columns to increase compressive strength and ductility; reducing thrust forces in thrusting structures; transforming non-structural members into structural members by increasing their stiffness and strength; strengthening and stiffening horizontal non-thrusting structures; and wrapping buildings at floor and roof locations.

TRM can be applied to structural members that have suitable mechanical properties. If the masonry is damaged, cracked, etc., it should first be repaired with appropriate techniques (e.g., grout injection) to ensure a proper sharing of loads between TRM and masonry.

For masonry structures subjected to cyclic loads (e.g., seismic or thermal variations), the bond between masonry and TRM may degrade during the structure's lifetime. In such cases, it is advisable to properly anchor the TRM to the masonry using anchors.

15.5   Structural modeling

The performance of a TRM system can be assessed on the basis of a structural idealization representing the behavior of the structure for the expected future use. Internal forces in the masonry can be determined using methods of structural analysis (e.g., frame models and finite element analysis). In particular, the structure can be modeled as either linear elastic, or through proven nonlinear models capable of simulating the inelastic behavior and the negligible tensile strength of masonry.

Simplified methods can also be used to describe the behavior of the structure. For instance, assuming that tensile stresses are directly carried by the TRM, stresses may be determined by adopting a simplified stress field that satisfies the equilibrium conditions, but not necessarily strain compatibility. This method may be realized for in-plane loaded masonry structures through the well-known strut-and-tie modeling (e.g., Krevaikas and Triantafillou, 2005). According to this procedure, the engineer calls upon experience and intuition to draw load paths through the structure in the form of a truss. The truss is analyzed for the design loads and proportioned according to the applicable code and/or to other rules of practice. Truss elements in tension (ties) indicate regions where TRM strips should be placed; masonry itself constitutes the struts. The dimensioning of the TRM is achieved based on the calculated tensile force in each tie and the design value of the force in the strengthening system. In this exercise, the engineer may be aided by knowledge of the magnitude and directions of principal stresses, obtained by a linear elastic plane stress finite element analysis of the structural element under the design loads. The struts and ties of the model may then be drawn collinear to the principal stress resultants.

The use of simplified stress fields should be carefully chosen, because a statically admissible stress field could have already caused structural collapse due to the brittle nature of the masonry system. In the case of structures with regular or repetitive parts, substructures may be identified that allow for a rapid evaluation of the global behavior

of the strengthened structure. Similarly, simplified models may be adopted for verifications of local failure mechanisms, provided that their use is properly justified.

As described in Chapter 16 safety verifications at the ultimate limit state are done easily at the member level, implying that internal forces and moments are compared to the respective resistances. Such forces and moments may be obtained directly through proper analysis methods, or indirectly by integrating stresses obtained by finite element analysis.

15.6   Design of retrofitting for seismic applications

Seismic retrofitting with the TRM system is typically aimed at total or partial strengthening, replacing or rebuilding of structural members and modifying the overall structural behavior by connecting different structural members. The type and size of selected TRM systems shall take into account the following:

- Poor connections between floors/roof and vertical walls shall be improved.
- Connections in walls ending on masonry T-junctions or masonry edges may need improvement.
- Floors effectively connected to vertical walls may have to be properly stiffened in their plane to be able to transfer horizontal forces to the vertical walls parallel to the earthquake direction. They also shall provide restraint to the movement of vertical walls perpendicular to the earthquake direction.
- TRM strengthened members where local ductility is enhanced are always recommended. Moreover, local TRM strengthening shall not reduce the overall ductility of the structure.
- Weak members, for which strengthening is not appropriate or possible, shall be eliminated.
- In the case of strongly irregular buildings, it may not be possible to improve structural behavior substantially by TRM strengthening. In such cases, TRM may be used for few structural members, to ensure a minimum regularity to the structure.

The TRM-based retrofitting strategy follows the principle of increasing the capacity of under-designed members. It does this with the aim of achieving, at the same time, a greater structural regularity and the elimination of possible local collapse of masonry walls or structural components. To avoid seismic vulnerability, care should be taken to ensure that the TRM will not decrease the overall ductility of the structure. Particular care should be taken to interventions aiming at joining vertical columns to avoid the formation of hinges in arches and vaults. The increase of hinge ductility of both columns and vaults is of crucial importance.

15.7   Strengthening of masonry walls
for out-of-plane loads

Out-of-plane collapse of masonry walls is one of the most frequent failure mechanisms. Such a mechanism is primarily the result of seismic actions (inertia forces) and secondarily of horizontal forces originated by the presence of arches and vaults.

Out-of-plane collapse can develop as *overturning*, *vertical flexural failure* or *horizontal flexural failure*.

Collapse by overturning (Figure 15.4a) may occur by the formation of a hinge at the bottom of walls neither connected to the orthogonal walls, nor restrained at their top. This mechanism depends on several factors, including the boundary conditions and the slenderness of the wall.

A possible retrofitting solution may involve the use of TRM applied to the top part of the masonry and properly anchored into the orthogonal walls, e.g., in the form of an embracing "belt" (Figure 15.4b). In this case, resistance to overturning is provided by the horizontal fibers of the TRM System. Particular care should be taken in the rounding of masonry corners to avoid stress concentrations in the fibers.

Masonry walls restrained at both top and bottom regions and subjected to horizontal loading may fail due to flexure with formation of three hinges at the top, bottom and in between (Figure 15.5a). Vertical flexural failure may occur in high masonry walls and/or walls restrained far apart from orthogonal walls. In the case of seismic loads, masonry walls loaded from opposite sides by floors located at different heights are
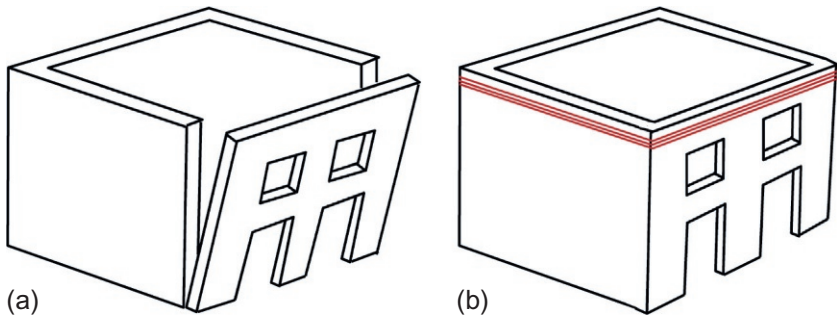
Figure 15.4 (a) Collapse by overturning and (b) application of embracing belt.
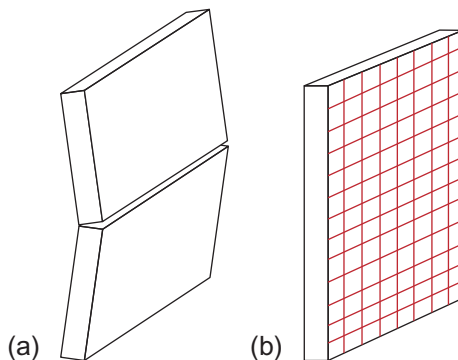
Figure 15.5 (a) Vertical flexural failure and (b) strengthening by TRM.
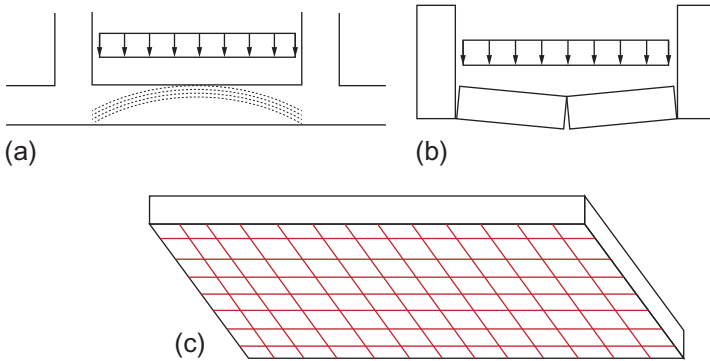
Figure 15.6 (a) Arching effect, (b) collapse due to horizontal flexure, and (c) strengthening by TRM.

particularly sensitive to vertical flexural collapse mechanisms. Such walls may be strengthened with TRM on the tension side, with effective fibers being those running in the vertical direction (Figure 15.5b).

Masonry walls restrained at the bottom, as well as firmly connected with (vertical) transverse walls, behave in a way analogous to three-side supported "slabs." They resist horizontal forces by an arching effect of the top strip (Figure 15.6a). Masonry walls restrained at the bottom, but not firmly connected with transverse walls, may collapse as illustrated in Figure 15.6b. Such walls may be strengthened with TRM on the tension side. The effective fibers are those running in the horizontal direction (Figure 15.6c).

TRM-based strengthening of masonry walls subjected to out-of-plane cyclic loads has been studied experimentally by Papanicolaou et al. (2008). In this study, it was shown that TRM overlays provide an extremely high gain in strength and deformation capacity, comparable—if not higher—to that provided by equivalent FRP systems.

15.8   Strengthening of masonry walls for in-plane loads

In-plane failure of masonry walls is also a frequent failure mechanism, as a result of seismic actions parallel to the walls. Typical actions include *combined bending and axial load* and *shear force*. Special attention in this regard should be given to *lintels and tie areas.*

Masonry walls subjected to combined bending and axial load are column-type members, which can be strengthened with TRM containing vertical fibers as close as practically possible to the most highly stressed areas (see Figure 15.7a for cyclic in-plane bending). Quite often, strengthening for in-plane bending may be combined with that for other cases, hence full coverage of the wall may be selected (Figure 15.7b). The strengthening system should be adequately anchored to the end parts (top and bottom) of the masonry wall.
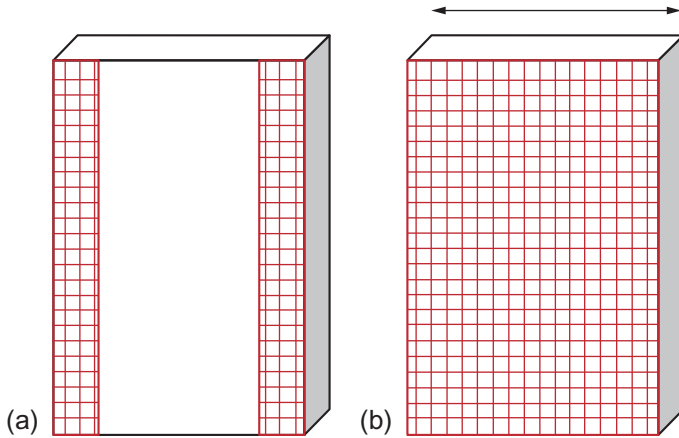
Figure 15.7 TRM strengthening of masonry walls subjected to in-plane combined bending and axial load: (a) placement of fibers in the highly stressed areas and (b) full coverage of the wall.

In-plane shear failure in masonry is typical in shear wall—type elements. Strengthening can be provided by applying TRM jackets on the wall sides (as shown in Figure 15.7b) so that a "truss" mechanism may be activated (analogous to the way a shear is carried by reinforced concrete members). Jacketing may be two-sided (preferably), or even one-sided, if interventions on both sides are not permitted, or if they are not practically possible.

The areas connecting different wall bays within a masonry panel are named tie areas (Figure 15.8). Their role is (a) to restrain the adjoining (vertical) walls to assume deformed shapes compatible with the applied horizontal load and (b) to support the masonry wall above openings. The former generates shear and flexural stresses and is significant in the case of seismic loading; whereas the latter is played by lintels located above openings (Figure 15.8).

As a result of vertical loads, the following effects in the areas above openings are displayed: (a) the part of the masonry wall above the opening cannot carry its own
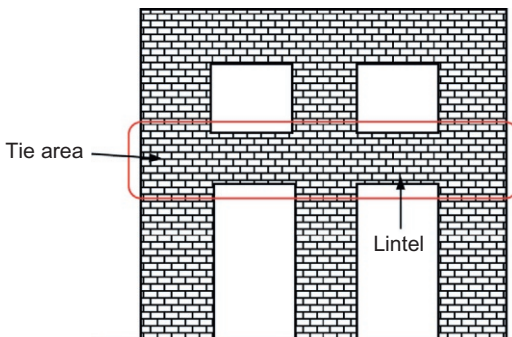
Figure 15.8 Lintels and tie areas.

Tie area

Lintel

weight and is supported by a lintel functioning as a beam; (b) when the wall bays surrounding the openings are slender, so as not to withstand horizontal loads due to the presence of the opening itself, the lintel provides adequate strength to carry the tensile stresses and ensure the overall equilibrium of the wall.

Lintels may be realized using structural elements having both axial and flexural capacity; alternatively, they may have only axial capacity. In the former case lintels function as beams and carry tension to ensure the overall equilibrium of the wall. In the latter, support to the wall above the opening is ensured by formation of a reinforced masonry member located just above the opening. Tensile stresses in this member are carried by the TRM strengthening system, which is applied preferably on the bottom face of the lintel. In this case, equilibrium conditions are probably reached after the masonry wall above the strengthened member has developed substantial deformations. To ensure proper functioning of lintels formed through strengthening, the TRM should be properly anchored into the adjacent masonry walls (as in Figure 15.9a).

Tie areas strengthened with TRM should be verified for bending moment, shear force and axial force (if any) acting at the connection with vertical masonry walls. Strengthening may be carried out by installing externally or internally (ideally both) horizontal TRM tapes. Flexural strengthening requires horizontal fibers and is better achieved by placing TRM at upper and lower regions of the ties. Shear strengthening, on the other hand, requires mainly vertical fibers covering the full height of the ties. Hence, a TRM jacket with full coverage of the tie (Figure 15.9b) would serve all functions. Moreover, if the jacket is external and continuous, it also may function as external wrapping of the masonry structure.

TRM-based strengthening of masonry walls subjected to in-plane cyclic loads has been studied experimentally by Papanicolaou et al. (2007). In this study, it was shown that TRM overlays provide an extremely high gain in strength and deformation capacity, comparable—if not higher—to that provided by equivalent FRP systems.
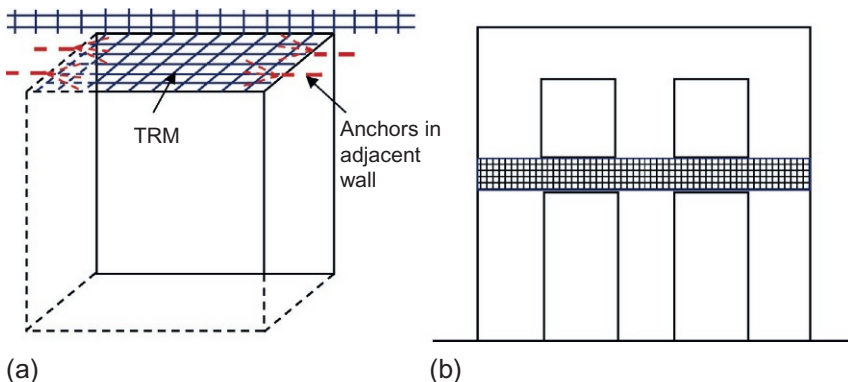
Figure 15.9 Strengthening of (a) lintel above an opening and (b) tie area.

15.9   Strengthening of curved masonry elements

Masonry elements with single curvature (arches, barrel vaults) or double curvature (domes) may fail due to the formation of "hinges" that correspond to a mechanism of collapse. Hinges form as a result of practically zero tensile strength and are located in the intrados or extrados, with eccentricity to the mid-plane of the structure (Figure 15.10a). As a result, the hinged section can only carry an axial force, which acts at an eccentricity equal to half the thickness of the masonry element.

TRM reinforcement delays the opening of cracks and formation of hinges on the opposite side with respect to the one where the TRM system is installed (Figure 15.10b). However, it should be remembered that this reinforcement is not effective in controlling crushing of the masonry or shear failure.

15.9.1   Arches

Arches may be of two types: (a) arch schemes, that is, arches resting on fixed or hinged supports; or (b) arch-pier schemes, which are frame-type structures, comprising arches resting on piers. Both schemes generally tend to collapse due to the formation of at least four hinges.

The collapse mechanism associated with the formation of four hinges may be prevented by bonding TRM to the extrados (Figure 15.10b) or the intrados (Figure 15.10c) of the masonry arch. If practically possible (this is rare), TRM should be applied to both the extrados and the intrados. However, access to the intrados is typically not possible, hence TRM should be applied to the extrados. This configuration also has the advantage that compressive stresses developing at the TRM-masonry interface (Figure 15.10b) improve bond conditions.

For arch–pier structures, the application of TRM to the extrados or intrados may not be sufficient to prevent relative displacement of the pier-arch connections. In such a case, it is preferable to act on the piers or set a tie rod between the pier–arch connections.

15.9.2   Barrel vaults

Barrel vaults have a single curvature; hence, their behavior is similar to that of arches. Strengthening with TRM may be applied to the extrados and/or the intrados. An advantage of the TRM system here is that fibers may also be activated in the
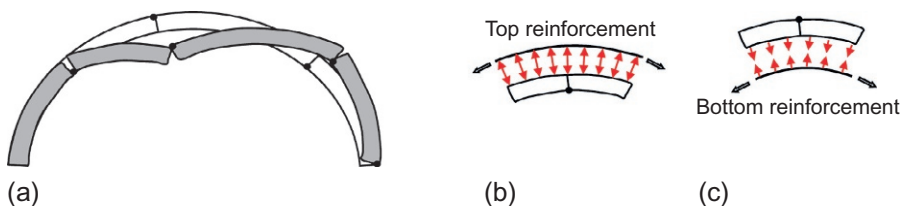
Figure 15.10 (a) Collapse mechanism in curved masonry element. Activation of fibers in (b) the extrados and (c) the intrados prevents the formation of hinges.

longitudinal direction (perpendicular to the plane of curvature), bridging the ideal arches forming the barrel vault. Such a mechanism is of particular importance in cases of horizontal loading. It is recommended to use bidirectional TRM with fibers in the longitudinal direction amounting to approximately 25% of those installed in the transverse direction.

15.9.3   Domes

Domes are double curvature vaults and exhibit both membrane-type and flexural-type stresses. In a dome subjected to vertical loads, membrane-type tension stresses develop along the dome parallels and may cause cracking along the meridians, especially near the connection with the supporting structure. In this case, application of TRM in a circular configuration around the lower part of the dome's perimeter (Figure 15.11) may help prevent the opening of cracks, as well as reduce the magnitude of the horizontal force acting on the supporting structure.

Flexural-type stresses are typically localized where the dome meets the supporting structure or at the edge of a skylight, if present. Such stresses may cause collapse of parts of the dome between meridian cracks. If the load carrying capacity of such parts is controlled by failure of the region connecting the dome to the supporting structure, then the dome may be strengthened by applying the TRM system in a circle around the lower part of the dome perimeter, as shown in Figure 15.11. This is done so that horizontal fibers may be activated. However, if the dome supporting structure does not develop any displacement, then the horizontal fibers are inactive; TRM should be applied along the dome meridians, implying that the vertical fibers of TRM will become effective. Special attention in TRM strengthening for flexural-type stresses should be given to debonding near the supporting structure, which may be controlled through the application of anchors.

15.10   Confinement of masonry columns

TRM confinement of masonry columns subjected to compression increases both ultimate load capacity and failure strain. It also may improve the column performance under the serviceability limit state. Confinement with TRM jacketing is typically achieved by wrapping the member along the perimeter (Figure 15.12).
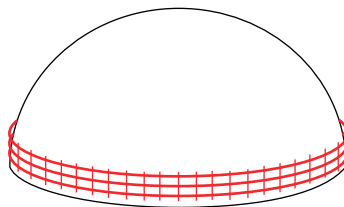
Figure 15.11 Strengthening at the lower part of a dome.
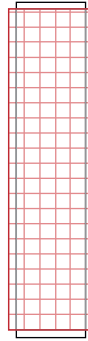
Figure 15.12 Masonry column wrapping.

(a)   (b)
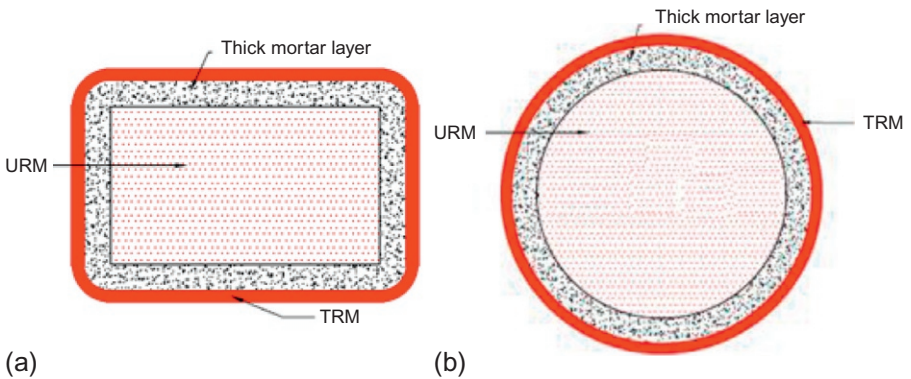
Figure 15.13 Confinement of (a) a rectangular masonry column and (b) a circular masonry column.

Finally, a possible configuration is the confined enlargement of the section by application of a thick mortar layer on the masonry. This should be done prior to the application of the TRM (Figure 15.13a and b).

15.11   Summary

In this chapter, the author presented concepts for strengthening of masonry structures with TRM, as well as key aspects of structural behavior. The following topics were covered: brief description of TRMs and their properties, with an emphasis on tensile behavior; intervention requirements and strengthening rationale; aspects of structural modeling and retrofitting for seismic applications; strengthening of masonry walls for out-of-plane or in-plane loads; strengthening of curved masonry elements, such as arches, barrel domes and vaults and confinement. It was shown that TRM is an effective and convenient solution in a variety of applications involving the retrofitting of unreinforced masonry walls.

References

Coburn, A.W., Spence, R.J.S., 2002. Earthquake Protection, second ed. Wiley, Chichester.

Fyfe Europe SA and Triantafillou, 2012. Strengthening of Unreinforced Masonry with Tyfo RM (Reinforced Mortars) System: A Simplified Design Approach. Fyfe Europe Design Report, Athens, Greece.

Krevaikas, T.D., Triantafillou, T.C., 2005. Computer-aided strengthening of masonry walls using fibre-reinforced polymer strips. Mater. Struct. RILEM 38, 93–98.

Papanicolaou, C.G., Triantafillou, T.C., Karlos, K., Papathanasiou, M., 2007. Textile reinforced mortar (TRM) versus FRP as strengthening material of URM walls: in-plane cyclic loading. Mater. Struct. RILEM 40 (10), 1081–1097.

Papanicolaou, C.G., Triantafillou, T.C., Papathanasiou, M., Karlos, K., 2008. Textile reinforced mortar (TRM) versus FRP as strengthening material of URM walls: out-of-plane cyclic loading. Mater. Struct. RILEM 41 (1), 143–157.

Triantafillou, T.C., Papanicolaou, C.G., Zisimopoulos, P., Laourdekis, T., 2006. Concrete confinement with textile reinforced mortar (TRM) jackets. ACI Struct. J. 103 (1), 28–37.

Strengthening of existing masonry structures: Design models

16

T. Triantafillou
University of Patras, Patras, Greece

16.1 Introduction

Building on the concepts presented in Chapter 15, this chapter aims to present simplified design procedures and models for unreinforced masonry structures (URM) strengthened with fiber composites comprising textiles in inorganic matrices. This strengthening system is given the term textile-reinforced mortar (TRM). The following topics, also presented in Fyfe Europe SA and Triantafillou (2012), are covered herein:

- General safety principles and safety verifications
- Strengthening of masonry walls for out-of-plane or in-plane loads
- Strengthening of curved masonry elements
- Confinement of masonry columns

16.2 General safety principles

Masonry elements and structures strengthened with TRM should have design strength (R_d) at all sections that is at least equal to the required strength (E_d) calculated for the factored loads and forces in combinations as stipulated by the relevant building code:

$$E_d \leq R_d. \tag{16.1}$$

The design values are obtained from the characteristic values through appropriate partial factors for each limit state. For instance, in Eurocode format (EN 1996-1-1, 2005), for the generic property X of a TRM material, the design value (X_d) is expressed as:

$$X_d = \frac{X_k}{\gamma_m}, \tag{16.2}$$

where X_k is the characteristic value of the property being considered, and γ_m is the partial factor of the material. Values for X_k should be provided by the material supplier, and, until more experimental data become available, $\gamma_m = 1.5 \ (=\gamma_t)$.

According to the aforementioned format, the design strength (R_d) is expressed as follows:

$$R_d = \frac{1}{\gamma_{Rd}} R\left(X_{d,i}; a_{d,i}\right). \tag{16.3}$$

In Equation (16.3), $R()$ is a suitable function for the specific mechanical model being considered, and γ_{Rd} is a partial factor covering model uncertainties (1.0 for bending or combined bending and axial load, 1.2 for shear, and 1.1 for confinement). The arguments of the function $R()$ are typically the design values ($X_{d,i}$) of the materials used for strengthening or the existing materials, and the nominal values ($a_{d,i}$), of the geometrical parameters involved in the model.

16.3 Safety verifications

Failure modes of masonry structures strengthened with TRM may involve excessive cracking due to tensile stresses, shear slip of masonry, crushing of masonry, TRM rupture, and TRM debonding.

Masonry exhibits a brittle behavior when subjected to tensile loading; the corresponding tensile strength is quite low and, for design purposes, can be neglected. The shear strength of masonry depends on the level of applied axial load, as it relies upon cohesion and friction of the material. The design stress–strain relationship of masonry in compression may be idealized as parabolic-rectangular (Figure 16.1), linear-rectangular, or even just rectangular for the sake of cross section analysis. Unless experimental data are available, the masonry ultimate strain (ε_{mu}) may be assumed to be 0.35% and $\varepsilon_{m1} = 0.2\%$.

The characteristic values for masonry strength are f_{mk} for vertical compression, f_{mk}^{h} for horizontal compression, and f_{vk} for shear. In the absence of specific information or experimental data, f_{mk}^{h} may be taken as 50% of f_{mk}.

TRM materials stressed parallel to a principal fiber direction may be approximately idealized through the adoption of a trilinear stress–strain curve. In this curve, the slope
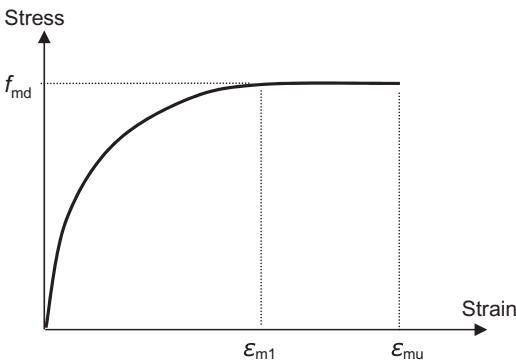
Figure 16.1 Idealized stress–strain curve for masonry in uniaxial compression.
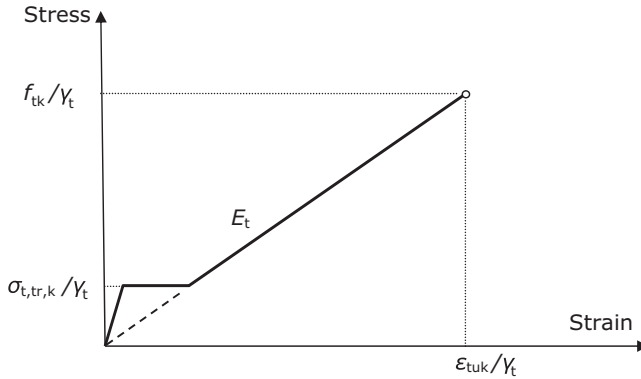
Figure 16.2 Idealized stress–strain curve for TRM system in uniaxial tension.

of the second branch corresponding to multiple cracking may be taken as zero (horizontal branch). The elastic modulus of the cracked material is $E_t = f_{tk}/\varepsilon_{tuk}$ (Figure 16.2), where f_{tk} = characteristic strength and ε_{tuk} = characteristic strain at failure. $\sigma_{t,tr,k}$, in Figure 16.2, is the characteristic stress at the transition zone.

The maximum design stress allowed to the TRM is expressed as follows:

$$f_{td} = \min\left(\frac{f_{tk}}{\gamma_t}, f_{tbd}\right) \tag{16.4}$$

where f_{tbd} is the TRM (design) stress once debonding takes place. Reliable models for the evaluation of the debonding stress of TRM are not available yet. Unless reliable experimental data are provided for a specific TRM system (with possible anchorage), it is suggested to assume that debonding initiates with the TRM at a strain $\varepsilon_{tb} = 0.003$ (which usually is in the transition zone, stage IIa in Figure 15.3). The deboning stress (f_{tbd}) is equal to $0.003E$, where E is the tensile modulus of the TRM that, depending on whether it corresponds to stage IIa or IIb, is defined by the following equation:

$$E = \max\left(\frac{\sigma_{t,tr,d}}{\varepsilon_t}, E_t\right) \tag{16.5}$$

For ultimate limit state analysis, two possible approaches may be followed, depending on the type of structural analysis performed. If nonlinear models are used, the member's carrying capacity shall be larger than the factored applied load. Care shall be taken to ensure that the proposed solution is not affected by the particular discretization adopted in the analysis. If linear elastic models or simplified methods adopting an admissible distribution of stresses (that satisfy equilibrium but not necessarily strain compatibility) are used, the resulting stresses on each structural member shall be verified. In particular, for bi-dimensional members (slabs, shells), the unit stress shall be considered (i.e., the per unit length of the member shall be evaluated). Assuming that a plane section, before loading, remains a plane after loading, the safety

is verified when factored shear forces and bending moments (calculated as a function of the applied axial force), due to the applied loads, are smaller than the corresponding design factored shear and flexural capacities. Note that forces and moments may be calculated through the integration of stresses.

16.4 Strengthening of masonry walls for out-of-plane loads

As discussed in Chapter 15, out-of-plane collapse can develop as *overturning*, *vertical flexural failure*, or *horizontal flexural failure*. Design equations for each case are presented next.

16.4.1 Overturning

Consider the masonry wall shown in Figure 16.3, subjected to the following forces (design values): P_d=wall self-weight; N_d=axial force acting on top of the wall; Q_d=horizontal force due to seismic effects; and T_d=force exerted on the top part of the wall by the TRM system. The wall has a height (h) and a thickness (t).

Assuming that floors and walls perpendicular to the wall provide negligible restraint, T_d can be calculated via moment equilibrium as follows:

$$T_d = \frac{1}{2d}(Q_d h - N_d t - P_d t),\tag{16.6}$$

where d=distance from center of TRM to the bottom of the wall.

To design against overturning, it shall be verified that

$$T_d \leq 2T_{Rd} = 2A_t f_{td},\tag{16.7}$$
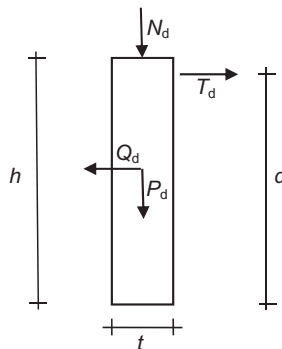
Figure 16.3 Overturning: forces acting on wall.

where A_t is the TRM cross section area and f_{td} is the maximum design stress. Note that in the case of a fully wrapped structure, TRM will fail by tensile rupture. Hence, f_{td} is the design tensile strength, possibly reduced, for example, due to stress concentrations. But in case of open TRM systems involving anchorage on the orthogonal walls, failure may be governed by TRM debonding, hence $f_{td} = f_{tbd}$.

16.4.2 Vertical flexural failure

Consider a unit width masonry wall (Figure 16.4), subjected to the following external forces (design values): $P_{u,d}$ = weight of the wall upper part; $P_{l,d}$ = weight of the wall lower part; N_d = axial force acting on the wall; $Q_{u,d}$ = seismic force related to the upper part of the wall; $Q_{l,d}$ = seismic force related to the lower part of the wall; and Q_d = force related to additional horizontal loading.

The masonry wall at cross section B, where the TRM is applied to prevent formation of the hinge, is subjected to axial force (N_{Ed}) and bending moment (M_{Ed}) equal to:

$$N_{Ed} = N_d + P_{u,d}, \tag{16.8a}$$

$$M_{Ed} = H_{C,d} h_u - Q_{u,d} \frac{h_u}{2}, \tag{16.8b}$$

where $H_{C,d}$ is the horizontal reaction at C, equal to:

$$H_{C,d} = \frac{(2Q_d + Q_{l,d})h_l + Q_{u,d}(2h - h_u) - (N_d + P_{u,d} + P_{l,d})t}{2h}. \tag{16.9}$$

The masonry wall flexural capacity is verified when the following condition is met:

$$M_{Ed} \leq M_{Rd}. \tag{16.10}$$
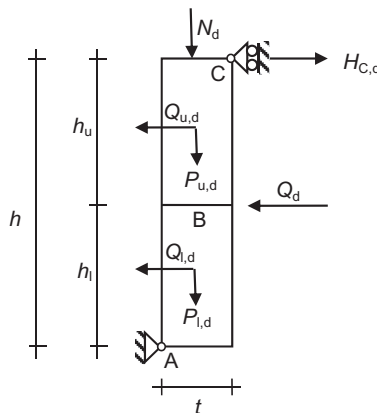
Figure 16.4 Vertical flexural failure: forces acting on wall.

The flexural capacity M_{Rd} of the strengthened masonry wall may be calculated on the basis of cross section analysis (Figure 16.5). The calculation may be done as a function of the mechanical properties of the masonry and TRM, the thickness (t), the width (l) and the value of the applied axial force (N_{Ed}). Failure is defined when either the masonry fails in compression (ε_{mu} is reached) or the TRM fails in tension [$\varepsilon_{t,lim} = \min(\varepsilon_{tu}, \varepsilon_{tb})$ is reached, where $\varepsilon_{tu} = \varepsilon_{tuk}/\gamma_t$], whichever comes first.

For the case of the parabolic-rectangular stress–strain relationship shown in Figure 16.1 (with $\varepsilon_{m1} = 0.2\%$ and $\varepsilon_{mu} = 0.35\%$), the resulting expressions for M_{Rd} are obtained as follows (assuming that the TRM is cracked, i.e., in stage IIa or IIb):

$$\text{Force equilibrium: } k_1 f_{md} lx - A_t \sigma_{td} = N_{Ed} \tag{16.11}$$

with

$$\sigma_{td} = E\varepsilon_t.$$

$$\text{Strain compatibility: } \varepsilon_t = \varepsilon_m \frac{t-x}{x} \le \varepsilon_{t,lim} = \min(\varepsilon_{tu}, \varepsilon_{tb}). \tag{16.12}$$

1. Compression failure of masonry ($\varepsilon_m = \varepsilon_{mu}$, $\varepsilon_t < \varepsilon_{t,lim}$):

$$\frac{M_{Rd}}{lt^2 f_{md}} = \frac{1}{\gamma_{Rd}} \left[\frac{1}{2} \frac{\left(1 - \frac{x}{t}\right)}{\frac{x}{t}} \omega_t + \frac{1}{2} k_1 \frac{x}{t} \left(1 - 2k_2 \frac{x}{t}\right) \right], \tag{16.13}$$

where x/t, the normalized neutral axis depth, is
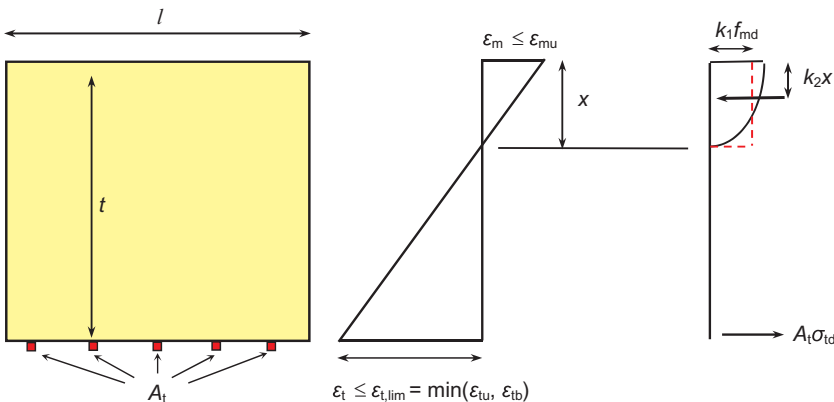
Figure 16.5 Cross-section analysis at the ultimate limit state.

$$\frac{x}{t} = \frac{1}{2k_1}\left[-\omega_t + \frac{N_{Ed}}{ltf_{md}} + \sqrt{\left(\omega_t - \frac{N_{Ed}}{ltf_{md}}\right)^2 + 4k_1\omega_t}\right]$$ (16.14)

and ω_t is defined as

$$\omega_t = \frac{A_t\,\varepsilon_{mu}E}{lt\;f_{md}}.$$ (16.15)

Finally, $k_1 = 0.8$, $k_2 = 0.4$, and γ_{Rd} = partial factor for flexure (=1.0).

2. Failure of TRM by rupture or debonding ($\varepsilon_m < \varepsilon_{mu}$, $\varepsilon_t = \varepsilon_{t,lim}$):

$$\frac{M_{Rd}}{lt^2f_{md}} = \frac{1}{\gamma_{Rd}}\left[\frac{1}{2}\frac{\varepsilon_{t,lim}}{\varepsilon_{mu}}\omega_t + \frac{1}{2}k_1\frac{x}{t}\left(1 - 2k_2\frac{x}{t}\right)\right],$$ (16.16)

where

$$\frac{x}{t} = \frac{1}{k_1}\left(\omega_t\frac{\varepsilon_{t,lim}}{\varepsilon_{mu}} + \frac{N_{Ed}}{ltf_{md}}\right)$$ (16.17)

and

$$k_1 = \begin{cases} 1000\varepsilon_m\left(0.5 - \dfrac{1000}{12}\varepsilon_m\right) & \text{if } \varepsilon_m \leq 0.002 \\[3mm] 1 - \dfrac{2}{3000\varepsilon_m} & \text{if } 0.002 \leq \varepsilon_m \leq 0.0035 \end{cases}$$ (16.18)

$$k_2 = \begin{cases} \dfrac{8 - 1000\varepsilon_m}{4(6 - 1000\varepsilon_m)} & \text{if } \varepsilon_m \leq 0.002 \\[3mm] \dfrac{1000\varepsilon_m(3000\varepsilon_m - 4) + 2}{2000\varepsilon_m(3000\varepsilon_m - 2)} & \text{if } 0.002 \leq \varepsilon_m \leq 0.0035 \end{cases}$$ (16.19)

$$\varepsilon_m = \varepsilon_{t,lim}\frac{\dfrac{x}{t}}{1 - \dfrac{x}{t}} \leq 0.0035.$$ (16.20)

16.4.3 Horizontal flexural failure

In the case of horizontal flexural failure, the applied bending moment M_{Ed} is due to earthquake loads, wind pressure and other possible horizontal loads that are due to the presence of other structural members. The masonry wall flexural capacity is verified when the condition (16.10) is met. The flexural capacity (M_{Rd}) of the strengthened masonry wall corresponding to a strip of unit width may be calculated on the basis of cross section analysis (Figure 16.5) as a function of the mechanical properties of masonry and TRM, the thickness (t) and the width (l) of the wall. Note that unless a more detailed analysis is available, the horizontal force due to the presence of

transverse walls (axial force in the horizontal direction) may be assumed to be zero. Failure is defined when either the masonry fails in compression (ε_{mu} is reached) or the TRM fails in tension ($\varepsilon_{t,lim}$ is reached), whichever comes first.

For the case of the parabolic-rectangular stress–strain relationship shown in Figure 16.1 (with $\varepsilon_{m1} = 0.2\%$ and $\varepsilon_{mu} = 0.35\%$), the resulting expressions for M_{Rd} are as given in Section 16.4.2. $N_{Ed} = 0$, f_{md} is replaced by the design value of the masonry strength in the horizontal direction (f_{md}^h) and length of the wall (l) replaced by the height of the wall (h).

16.5   Strengthening of masonry walls for in-plane loads

The following verifications shall be carried out for masonry *walls subjected to in-plane loads: combined bending and axial load* or *shear* force. Furthermore, *lintels and tie areas* should be given special attention.

16.5.1   Combined bending and axial load

The flexural capacity (M_{Rd}) of a strengthened masonry wall may be calculated on the basis of cross section analysis (Figure 16.6). The calculation may be performed as a function of the mechanical properties of the masonry and TRM, the wall dimensions (length l, thickness t) and the value of the applied axial force (N_{Ed}). Again, failure is defined when either the masonry fails in compression (ε_{mu} is reached) or the TRM fails in tension ($\varepsilon_{t,lim}$ is reached), whichever comes first.

For the case of two-sided full coverage by TRM (Figure 16.6), and considering the parabolic-rectangular stress–strain relationship shown in Figure 16.1 (with $\varepsilon_{m1} = 0.2\%$ and $\varepsilon_{mu} = 0.35\%$), the resulting expressions for M_{Rd} are as follows (assuming that the TRM is cracked, i.e., in stage IIa or IIb):
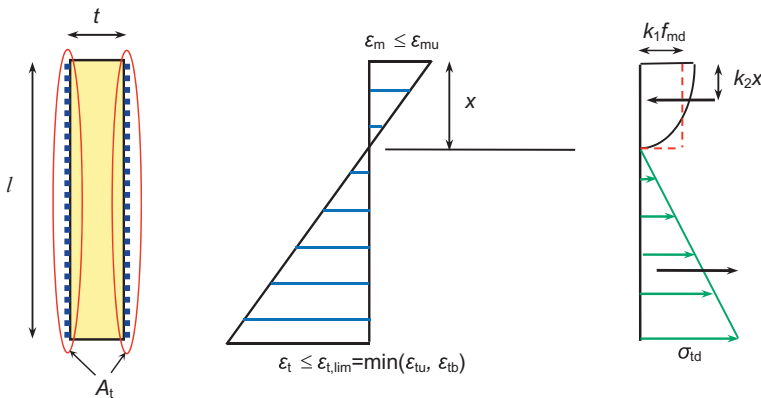
Figure 16.6 Cross-section analysis at the ultimate limit state.

Force equilibrium: $k_1 f_{md} t x - \dfrac{1}{2} A_t \sigma_{td} \dfrac{l-x}{l} = N_{Ed}$ (16.21)

with

$\sigma_{td} = E \varepsilon_t.$

Strain compatibility: $\varepsilon_t = \varepsilon_m \dfrac{l-x}{x} \le \varepsilon_{t,lim} = \min(\varepsilon_{tu}, \varepsilon_{tb})$ (16.22)

1. **Compression failure of masonry** ($\varepsilon_m = \varepsilon_{mu}$, $\varepsilon_t < \varepsilon_{t,lim}$):

$$\frac{M_{Rd}}{tl^2 f_{md}} = \frac{1}{\gamma_{Rd}} \left[\frac{1}{12} \frac{\left(1-\frac{x}{l}\right)^2 \left(1+2\frac{x}{l}\right)}{\frac{x}{l}} \omega_t + \frac{1}{2} k_1 \frac{x}{l} \left(1 - 2k_2 \frac{x}{l}\right) \right]$$ (16.23)

where x/l, the normalized neutral axis depth, is

$$\frac{x}{l} = \frac{1}{2\left(k_1 - \frac{\omega_t}{2}\right)} \left[-\omega_t + \frac{N_{Ed}}{ltf_{md}} + \sqrt{\left(\omega_t - \frac{N_{Ed}}{ltf_{md}}\right)^2 + 2\left(k_1 - \frac{\omega_t}{2}\right)\omega_t} \right]$$ (16.24)

ω_t is defined as before,

$$\omega_t = \frac{A_t}{lt} \frac{\varepsilon_{mu} E}{f_{md}}$$ (16.15)

and $k_1 = 0.8$, $k_2 = 0.4$.

2. **Failure of TRM by rupture or debonding** ($\varepsilon_m < \varepsilon_{mu}$, $\varepsilon_t = \varepsilon_{t,lim}$):

$$\frac{M_{Rd}}{tl^2 f_{md}} = \frac{1}{\gamma_{Rd}} \left[\frac{1}{2} \frac{\varepsilon_{t,lim}}{\varepsilon_{mu}} \omega_t \frac{\left(1-\frac{x}{l}\right)\left(1+2\frac{x}{l}\right)}{6} + \frac{1}{2} k_1 \frac{x}{l} \left(1 - 2k_2 \frac{x}{l}\right) \right],$$ (16.25)

where

$$\frac{x}{l} = \frac{\frac{1}{2} \omega_t \frac{\varepsilon_{t,lim}}{\varepsilon_{mu}} + \frac{N_{Ed}}{ltf_{md}}}{k_1 + \frac{1}{2} \omega_t \frac{\varepsilon_{t,lim}}{\varepsilon_{mu}}}$$ (16.26)

k_1 and k_2 are as given by Equations (16.18) and (16.19) and

$$\varepsilon_m = \varepsilon_{t,lim} \frac{\frac{x}{l}}{1-\frac{x}{l}} \le 0.0035.$$ (16.27)

16.5.2 Shear force

The shear resistance (V_{Rd}) of masonry walls strengthened with TRM (e.g., Figure 15.7b) is computed as the sum of the masonry contribution ($V_{Rd,m}$) and TRM contribution ($V_{Rd,t}$) up to the maximum value ($V_{Rd,max}$) corresponding to compression failure of the struts in the truss:

$$V_{Rd} = \min\left(\frac{V_{Rd,m} + V_{Rd,t}}{\gamma_{Rd}}, \frac{V_{Rd,max}}{\gamma_{Rd}}\right) \tag{16.28}$$

The above contributions may be evaluated as follows:

$$V_{Rd,m} = f_{vd}tl \tag{16.29}$$

$$V_{Rd,t} = 0.9l(nt_f)f_{td} \tag{16.30}$$

$$\frac{V_{Rd,max}}{tl} = 2 \quad (\text{MPa}) \tag{16.31}$$

where γ_{Rd} = partial factor for shear (=1.2), t = thickness of masonry wall, l = length of wall, f_{vd} = design shear strength of masonry, f_{td} = design strength of TRM, defined in Equation (16.4), and n = number of sides strengthened with a jacket of thickness t_f each ($n=2$ for two-sided jacketing, $n=1$ for one-sided jacketing).

16.5.3 Lintels and tie areas

As an approximation, a TRM-strengthened lintel may be idealized as a beam fixed at both ends, under the action of factored dead loads. The flexural capacity M_{Rd} of this beam, calculated on the basis of cross section analysis as described above, shall exceed the applied moment M_{Ed}:

$$M_{Ed} = \gamma_G \frac{1}{24} gtL^3 \tag{16.32}$$

where g = masonry weight/m^3, t = thickness of masonry wall, L = clear span of the opening, and γ_G = partial factor for self-weight at the ultimate limit state.

Moreover, by considering the TRM-strengthened lintel as an axially loaded element, the TRM shall be designed to resist the following axial force (Figure 16.7):

$$N_{Ed} = \frac{q_d L^2}{8h'} \tag{16.33}$$

where q_d is the design vertical load acting on the lintel (the sum of factored dead and live loads) and h' is the internal lever arm. This is not to be taken larger than the span (L) of the opening, nor the height (h) of the tie area.
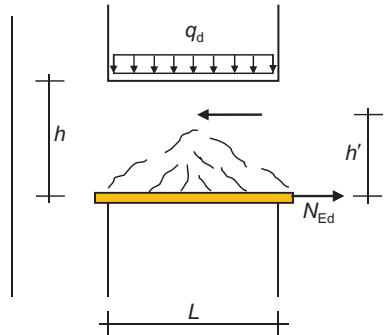
Figure 16.7 Tensile force in lintel.

Tie areas strengthened with TRM shall be verified for the bending moment, shear force and axial force (if any) acting at the connection with vertical masonry walls. The flexural and shear capacity shall be calculated on the basis of the procedures described in previous sections (Sections 16.5.1 and 16.5.2), with proper modifications.

16.6 Strengthening of curved masonry elements: Arches, barrel vaults, domes

When computing internal forces in an arch strengthened with TRM, the formation of hinges at supports shall always be considered (unless such formation is prevented). Moreover, the formation of hinges located on the opposite side of the TRM installation shall be taken into account. Arches strengthened with TRM can be designed by checking their overall stability and by applying the procedures described above for masonry subjected to combined out-of-plane bending and axial force. Special attention should be given to debonding, which may be controlled through the application of anchors.

Barrel vaults have a single curvature; hence, the design of their strengthening is similar to that of arches.

Domes are double curvature vaults and exhibit both membrane-type and flexural-type stresses. In a dome subjected to vertical loads, membrane-type tension stresses develop along the dome parallels and may cause cracking along the meridians. This is especially true near the connection with the supporting structure. In this case, the required cross section of TRM in a circular configuration around the lower part of the dome's perimeter shall be calculated for the full magnitude of tensile stresses. TRM strengthening for flexural-type stresses can be designed by applying the procedures described above for masonry that has been subjected to combined bending and axial force to unit dome elements.

16.7   Confinement of masonry columns

The axial capacity (N_{Rd}) of a strengthened column shall exceed the design axial force due to applied loads (N_{Ed}):

$$N_{Rd} \geq N_{Ed} \tag{16.34}$$

$$N_{Rd} = \frac{1}{\gamma_{Rd}} A_m f_{mcd} \geq \frac{1}{\gamma_{Rd}} A_m f_{md} \tag{16.35}$$

where A_m = cross sectional area of confined column, f_{md} = design compressive strength of unconfined masonry, f_{mcd} = design compressive strength of confined masonry and γ_{Rd}, the partial factor, is 1.1.

The design compressive strength (f_{mcd}) for confined masonry may be related to f_{md} through the use of an appropriate confinement model that has the following general form:

$$\frac{f_{mcd}}{f_{md}} = 1 + k \left(\frac{\sigma_{lud}}{f_{md}} \right)^m \tag{16.36}$$

where σ_{lud} is the design effective confining pressure and k, m are nondimensional empirical constants obtained from calibration with test results for the masonry material under consideration. Because of the lack of adequate test data, these parameters are not calibrated yet. Nevertheless, an estimate for the values could equate m to 1 and k to 1.5. However, those values should be used with circumspection until verification by experimental data becomes available.

To restrict axial deformation and prevent damage at the serviceability limit state, the increased axial capacity due to TRM shall be limited to 50% of f_{md}.

In columns with *circular* cross section, the confining stress σ_l is given in terms of the TRM jacket tensile stress σ_t as follows (Figure 16.8):

$$\sigma_l = \frac{2t_t}{D} \sigma_t \tag{16.37}$$

where D = cross section diameter and t_t thickness of TRM jacket. σ_{lud} is obtained from Equation (16.37), with σ_t equals the design value of the stress in the jacket at failure
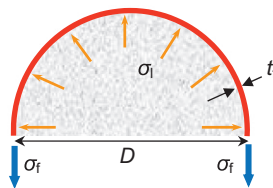
Figure 16.8 Confining stress.
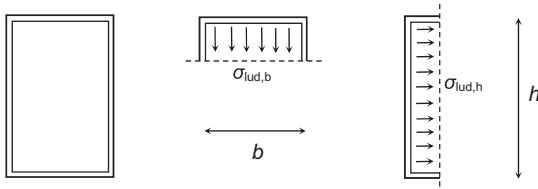
Figure 16.9 Approximate confining stresses in a rectangular cross-section.

$f_{\text{ted}} = \eta_e f_{\text{tk}}/\gamma_t$. η_e is a strength reduction factor to account for the multi-axial state of stress in the jacket, stress concentrations etc. Unless experimental support is available, η_e is 0.8.

In columns with a *rectangular* cross section, the confining stress is not uniform, especially near the corners. As an average for σ_{lud}, one may write (Krevaikas and Triantafillou, 2005; Bournas et al., 2007; Figure 16.9):

$$\sigma_{\text{lud}} = \frac{\sigma_{\text{lud,h}} + \sigma_{\text{lud,b}}}{2} = \frac{1}{2}\left(k_e \frac{2t_t}{h} f_{\text{ted}} + k_e \frac{2t_t}{b} f_{\text{ted}}\right) = \frac{1}{2} k_e \frac{(b+h)}{bh} t_t f_{\text{ted}}, \tag{16.38}$$

where k_e is the effectiveness coefficient, which, for continuous jackets with fibers in the direction perpendicular to the column axis (in addition to those parallel to the column), is defined as the ratio of the effectively confined area (A_e in Figure 16.10) to the total cross sectional area A_g:

$$k_e = 1 - \frac{b'^2 + h'^2}{3A_g}. \tag{16.39}$$

In columns with *section enlargement* (Figure 15.13), by application of a thick mortar layer on the masonry prior to the application of the TRM, the total axial load capacity of the composite section is calculated as follows:

$$N_{\text{Rd}} = \frac{1}{\gamma_{\text{Rd}}}(A_m f_{\text{mcd}} + A_l f_{\text{ld}}), \tag{16.40}$$

where A_m = cross sectional area of confined masonry, A_l = cross sectional area of thick mortar layer, f_{mcd} = design compressive strength of confined masonry, and f_{ld} = design compressive strength of thick mortar layer.
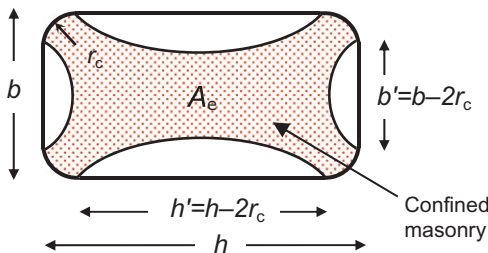
Figure 16.10 Effectively confined area in columns with a rectangular cross-section.

16.8   Summary

Building on the concepts presented in the previous chapter, this chapter aimed to present simplified design procedures and models for URMs strengthened with TRM. The following topics were covered: general safety principles and safety verifications; strengthening of masonry walls for out-of-plane loading (overturning, vertical flexural failure and horizontal flexural failure) or in-plane loading (combined bending and axial loading, shear forces, lintels and tie areas); strengthening of curved masonry elements and confinement of masonry columns with circular or rectangular cross sections. Design equations were given for most of the cases listed above, within the framework of Eurocode format.

References

Bournas, D., Lontou, P., Papanicolaou, C.G., Triantafillou, T.C., 2007. Textile-reinforced mortar (TRM) versus FRP confinement in reinforced concrete columns. ACI Struct. J. 104 (6), 740–748.

EN 1996-1-1, 2005. Eurocode 6—Design of Masonry Structures—Part 1-1: General Rules for Reinforced and Unreinforced Masonry Structures. European Committee for Standardization, Brussels.

Fyfe Europe SA, Triantafillou, T.C., 2012. Strengthening of Unreinforced Masonry with Tyfo RM (Reinforced Mortars) System: A Simplified Design Approach. Fyfe Europe Design Report, Athens, Greece.

Krevaikas, T.D., Triantafillou, T.C., 2005. Masonry confinement with fiber reinforced polymers. J. Compos. Constr. 9 (2), 128–135.

Strengthening of existing structures: Selected case studies

17

D. Bournas
University of Nottingham, Nottingham, UK[1]

17.1 Introduction

This chapter presents selected case studies of existing structures strengthened with externally bonded textile-reinforced mortar (TRM). During the last decade or so, a number of commercial projects in Europe (Italy, Greece, The Netherlands, France, Germany, Spain, and Turkey), Russia, the United States, and Latin America have demonstrated the great potential of TRM as a strengthening material for both concrete and masonry structures. The following case studies involve composites made from carbon and polyparaphenylene benzobisoxazole (PBO) textile fibers applied in combination with inorganic cement-based matrices.

17.2 Concrete strengthening case studies

17.2.1 Strengthening of the Stadium San Siro (Italy 2003)

The Stadium "San Siro" or "Meazza" in Milan was constructed in 1925 and renovated in 2002. The bearing structure of the lower ring of the Stadium is a reinforced concrete (RC) frame, as illustrated in Figure 17.1a (Trimboli and Mantegazza, 2004). The renovation included new steel structures that remained disconnected from the existing RC structures; a new foundation system transferred the new loads to the ground. However, on the occasion of these works, the structural state of the RC frame was inspected and significant deterioration in the beams was revealed. The deterioration was mainly due to the corrosion of the steel reinforcement (Figure 17.1b). Subsequently, the client requested the contractors to strengthen the existing RC beams.

To increase the flexural and shear capacity of the beams, a number of conventional strengthening techniques were initially considered. These included (a) bonding of steel plates to the faces of the beams and (b) insertion of new steel stirrups followed by shotcreting. These interventions were rejected for different reasons. To ensure the transfer of forces at the contact interfaces, the steel plates are required to be smooth, but the epoxy resins that are typically used for this purpose cannot be applied directly on the deteriorated concrete surface (Figure 17.1b). The insertion of stirrups would have required drilling the beams; this was avoided, because the concrete was of low strength.

---

[1] Current address: European Laboratory for Structural Assessment, Institute for the Protection and Security of the Citizen, Joint Research Centre, European Commission, T.P. 480, I-21020 Ispra (VA), Italy

Figure 17.1 (a) Existing RC frame supporting the tier of seats; (b) typical damage found in RC beams; (c) application of a U-shaped TRM jacket for shear strengthening of the beam; and (d) strengthened beam at the end.
Kind permission of Ruredil SPA.

The strengthening system that was finally selected involved the use of a carbon fiber textile in an inorganic cementitious matrix. TRM turned out to be the ideal solution, as it required operating directly by applying the bonding agent, namely without preparation of the damaged concrete surface. Moreover, the pozzolanic cementitious matrix used was fully compatible with the substrate (concrete). The actual time available to execute the works was limited. The special bonding matrix enabled the application of the reinforcement on the surfaces of the beams and the reshaping of them with a thixotropic fiber-reinforced cementitious mortar, without waiting for the cure of the thixotropic mortar. If the bonding matrix was polymeric, which must be laid exclusively on completely dry surfaces, this advantage would had been lost. Photographs of the application method of textiles combined with mortar binder are illustrated in Figure 17.1c and d.

A commercial textile with an equal quantity of high-strength carbon fibers in two orthogonal directions was used. The nominal thickness (based on the equivalent smeared distribution of fibers) was 0.017 mm. According to the manufacturer datasheets, the tensile strength and the modulus of elasticity of the carbon fibers were 3400 and 227,000 N/mm^2, respectively.

It should be noted that this is the first case study ever reported where TRM was used as a strengthening material for an existing structure. The total area of carbon fibers used was around 700 m^2.

17.2.2 Strengthening of a barrel-shaped roof (Germany 2007)

The school of engineering in Dresden, which was built in 1903, was reconstructed from 2007 to 2009 and now houses the IRS office of Zwickau. The monument conservation authority required the barrel-shaped roof construction, which is located on the west wing of the building, to be preserved as part of the terms for reconstruction. This RC barrel-shaped roof spans a column-free hall measuring approximately 16 m × 7 m. In total, 11 beams are aligned by an 80-mm thick monolithic RC slab. Nine out of ten roof zones have a light opening in their mid-section measuring about 1 m × 3 m (Figure 17.2). The roof construction itself lies partially on brickwork and partially on steel beams. It is a curved and textured shell structure.

A re-evaluation of the roof's static bearing capacity indicated that the structure did not meet the code requirements currently enforced by DIN 1045-1:2008. Monument preservation concerns precluded the construction of a new structure, truss-support of the existing roof structure, as well as the use of traditional strengthening methods. All were deemed to be inappropriate. Strengthening using concrete jacketing would lead to a large deadweight increase. The required concrete cover of about 60–80 mm would result in additional loading to the structure and its subordinated support links. Furthermore, the now filigree T-beam-construction would become a rough, irreconcilable structure, with regard to the demands of the monument preservation. Externally bonded fiber-reinforced polymers (FRP) strips were considered as a retrofitting solution as well; however, the load distribution within the slab would require a high material effort due to the necessarily small spacing of the strips. In addition, measures for securing the compound of the negative curvature on the underside of the beam would also be significant. The application of TRM to the substructure enabled the preservation of the original geometry, and thus the original filigree character of the historical roof construction. TRM strengthening was selected as the method of rehabilitation to
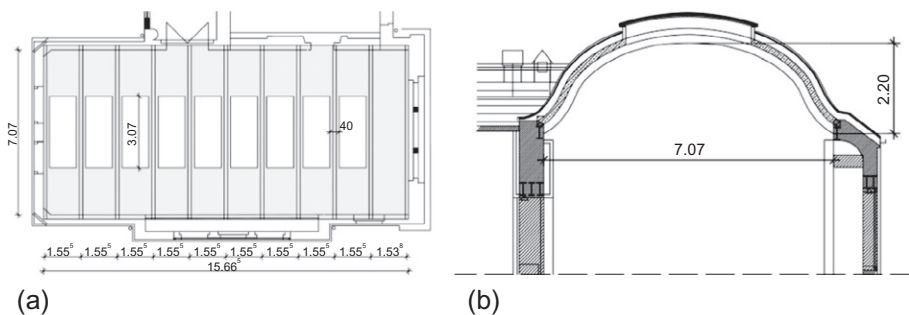
Figure 17.2 (a) Plan view of the barrel-shaped roof and (b) section of the barrel-shaped roof (Schladitz et al., 2008).

be used, as it takes monument preservation, fire protection and static-constructive deliberations into consideration.

A bidirectional textile reinforcement was manufactured at the TU Dresden. The carbon rovings possess a fineness of 800 tex (tex expresses linear density and is the weight in grams of 1 km of textile yarn) and a cross-sectional area of 0.45 mm^2. The modular dimension is 7.2 mm in the warp and 14.4 mm in the weft direction. The modulus of elasticity, ultimate compression and tensile strength of the inorganic matrix were measured to be 28,500, 76.3, and 7.11 N/mm^2, respectively. Based on uniaxial strain specimen tests, the tensile strength of TRM was assumed to be $f_{tu} = 1600$ N/mm^2 and the ultimate strain $\varepsilon_u = 8$‰. The global safety factor was conservatively established at $\gamma = 3.2$.

To improve the bond between of TRM and concrete surface, the existing concrete was uncovered by sandblasting after first removing the existent plaster layers to expose the granular structure of the concrete. After prewetting the subsurface, the first layer of fine-grained concrete was applied using a wet-spray coating method, as shown in Figure 17.3a. A mortar pump delivered the concrete mixture to the work area about 8-m high. There, it was eventually sprayed onto the subsurface one layer at a time until a thickness of 3 mm was achieved. The textile reinforcement was worked into the existing concrete by slightly pressing and smoothing it with a trowel (Figure 17.3b). This procedure was repeated until reaching the required number of layers to obtain the predetermined strength levels. The final result was the provision of a strong TRM strengthening cover layer with a thickness of approximately 3 mm. All reinforcing layers were applied fresh-in-fresh in order to ensure the presence of a good bond between each individual fine-grained concrete layer. This process was assured through accurate construction work and supervision.

17.2.3 Strengthening of a school building (Greece 2007)

TRM was selected to strengthen a school building in Karystos, Greece (Triantafillou, 2007). This involved both flexural strengthening of RC slabs (Figure 17.4a) with heavily corroded reinforcement and shear strengthening of unreinforced stone
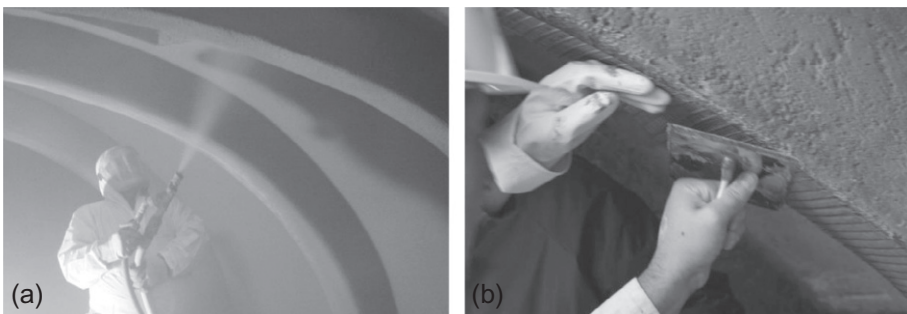
Figure 17.3 (a) Application of mortar by shotcreting and (b) insertion of the textile reinforcement (Schladitz et al., 2008).

Figure 17.4 Strengthening of (a) concrete slabs and (b) stone masonry walls in a mixed concrete–masonry school building.
Kind permission of Triantafillou (2007).

masonry walls (Figure 17.4b). Strengthening was carried out using carbon fiber meshes combined with cementitious mortar. A commercial textile was used with equal quantities of high-strength carbon fibers in two orthogonal directions. The weight of the textile was 348 g/m^2; whereas its nominal thickness (based on the equivalent smeared distribution of fibers) was 0.095 mm. According to the manufacturer datasheets, the tensile strength and the modulus of elasticity of the carbon fibers were 3800 and 225,000 N/mm^2, respectively.

Application of the mortar was made in approximately 2-mm thick layers with a smooth metal trowel. After application of the first mortar layer on the (dampened) concrete surface, the textile was applied and pressed slightly into the mortar, which protruded through all the perforations between fiber rovings. The next mortar layer covered the textile completely, and the operation was repeated until all textile layers were covered by the mortar. Of crucial importance in this method, as in the case of epoxy resins, was the application of each mortar layer while the previous one was still in a fresh state. Photographs of the application method of textiles combined with mortar binder in this case study are shown in Figure 17.4.

17.2.4 Strengthening of RC bridge piers (Russia 2007)

In this case study, TRM was chosen for the strengthening of RC bridge piers in Novosibirsk, Russia. The bridge had been reconstructed in 1958, and since then significant temperature and shrinkage stresses had caused the formation of cracks on construction joints. Those cracks were epoxy-injected in 1991; however, inspections in 1997 indicated that the cracks had reopened, with widths ranging from 2 to 5 mm, as shown in Figure 17.5a.

Then in 2007, a decision was made to repair and strengthen the bridge using TRM. The strengthening procedure comprised the following steps: (1) preparation of the concrete surface by sandblasting; (2) pointing out the cracks and filling them with
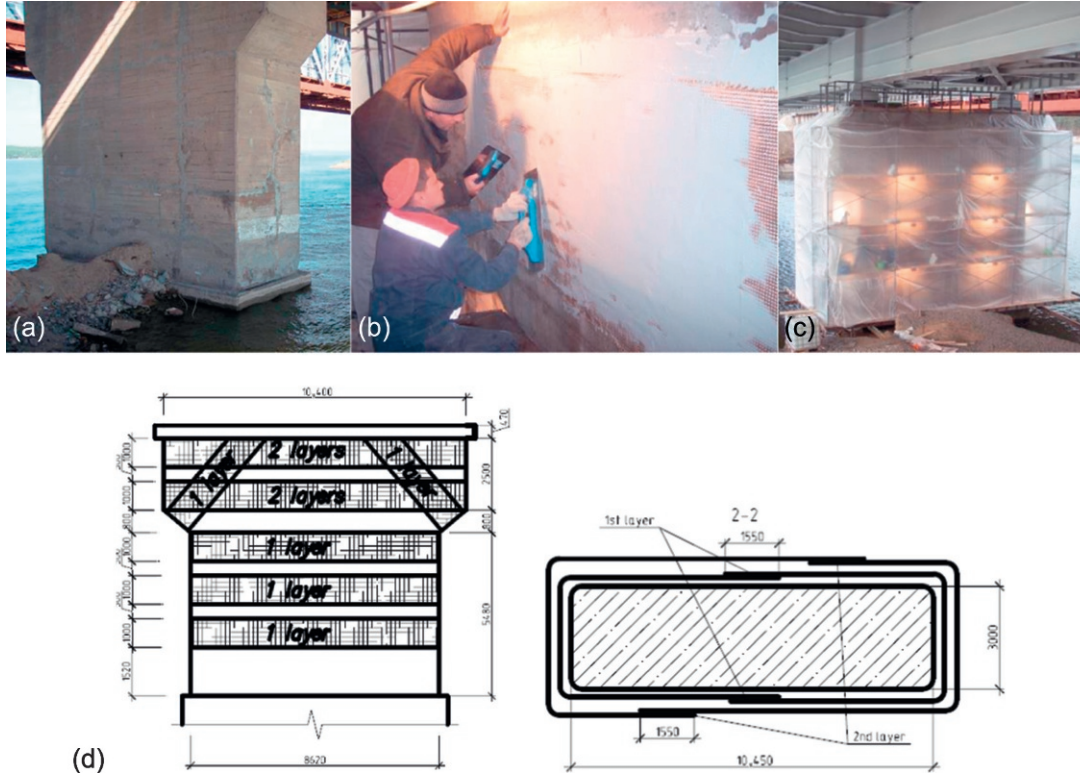
Figure 17.5 (a) Reopened cracks were repaired using epoxy injection; (b) application of the inorganic matrix and the PBO textile reinforcement; (c) overall view of the heating tent constructed to allow curing of the cementitious mortar; and (d) strengthening reinforcement configuration and cross section of the bridge pier.

Kind permission of Ruredil SPA.

a repair mortar; (3) rounding of the corners to a radius of 30 mm; (4) application of the PBO reinforcement of the TRM jacket on the bridge pier (Figure 17.5b); and (5) covering the external surface with waterproof mortar. As shown in Figure 17.5c, heating tents were used to maintain an air temperature of around 16 °C for 7 days after completion of the strengthening application to allow for the curing of the cementitious mortar. The strengthening configuration and the bridge pier's cross section and dimensions are illustrated in Figure 17.5d. The total area of PBO fibers used was 600 m^2.

17.2.5   Strengthening of a highway RC tunnel lining (Greece 2008)

Egnatia Odos A2 is the Greek part of the European route E90. It is a motorway in Greece that extends from the western port of Igoumenitsa to the eastern Greek–Turkish border. It runs a total of 670 km. In 2008, the RC lining of a vehicular tunnel along the Egnatia Odos was strengthened with TRM to correct a structural deficiency (Nanni, 2012). The original lining was 650 mm thick with a clear cover of 50 mm and was reinforced with top and bottom steel bar mats. During inspections, some flexural cracks on the concrete lining were observed. Also, finite element analyses confirmed that there was a need to increase the RC lining moment of resistance in both the circumferential and longitudinal directions.

A PBO fiber-unbalanced textile with rovings spaced at 10 and 20 mm, respectively, was used (Fyfe, 2009). The equivalent nominal fiber thickness of the textile in two directions was equal to 0.046 and 0.011 mm, respectively, whereas the weight of the PBO fibers in the textile was 88 g/m^2. The ultimate strength, ultimate strain, and elastic modulus of the PBO fibers provided by the composite manufacturer were 5800, 0.025, and 270,000 N/mm^2, respectively. The matrix comprised high-fineness cement, an adhesion promoter, inorganic nanoparticles, microaggregates and a polycarboxylate water-reducing admixture. This matrix was designed to achieve a chemical bond with the PBO fibers. The ultimate compressive and tensile strength of the inorganic matrix were, according to the manufacture, greater than 30 and 4 N/mm^2, respectively.

Calculations indicated that the addition of a single layer of PBO fiber textile increased the circumferential flexural strength of the lining by 14% and 4% at the top and side portions of the tunnel, respectively. The addition of two PBO–TRM layers increased the flexural strength by 100% in the longitudinal direction on the top portion of the tunnel lining. The concrete surface was prepared using hydrojetting prior to the installation of the PBO fibers and the application of a finishing coat of the matrix as summarized in Figure 17.6.

The cost of the project (in 2008) was around €800,000, which was less than any other retrofit measure considered. The total area of PBO fibers used was 12,000 m^2.

17.2.6   Strengthening of unreinforced concrete vaults (Italy 2010)

The Rome–Formia–Naples railway is part of the main north–south trunk line of the Italian railway network. It was opened in 1927 as an alternative link to the existing Rome–Naples route (via the Cassino line), and reduced journey times significantly.

Figure 17.6 (a) Surface preparation by hydrojetting; (b) application of the inorganic matrix; and (c) application of the PBO textile reinforcement.
Kind permission of Ruredil SPA.

A railway bridge along the Rome–Formia–Naples was strengthened using TRM. The 10.5-m wide bridge deck is supported by six semicircular, plain concrete vaults supported by masonry abutments made of blocks of tuff. The thickness of each vault varies from 0.7 m at the crown to 1.0 m at the skewback (Berardi et al., 2011). An overview of the bridge is shown in Figure 17.7a.

A field inspection to capture the bridge geometry and to assess the mechanical properties of the materials was initially conducted. This was followed by limit state
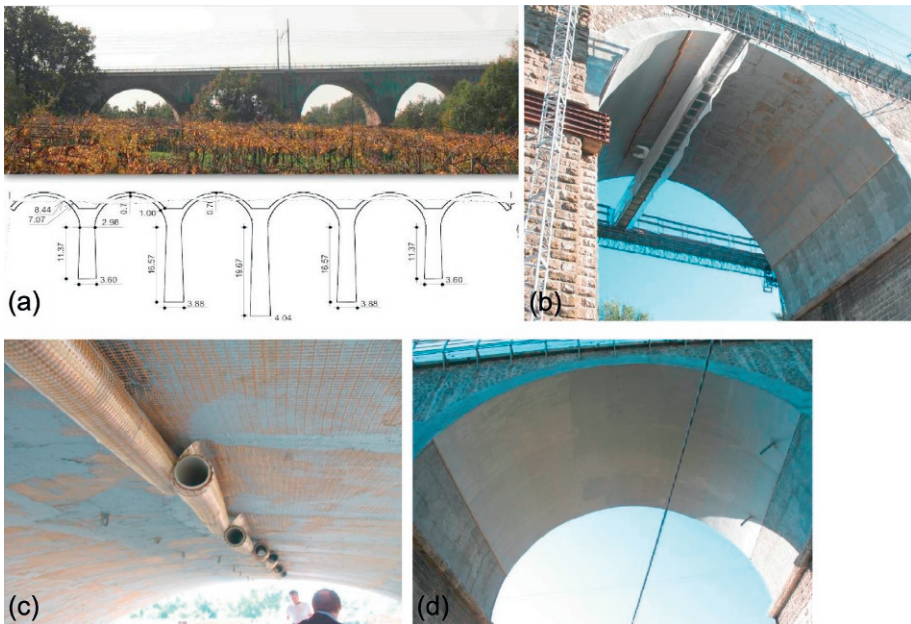
Figure 17.7 Strengthening of a bridge on the Rome–Formia–Naples railway: (a) overview of the bridge; (b) application of the first PBO–TRM layer on the soffit of a concrete arch; (c) the second layer of PBO fiber is installed over the first layer; and (d) strengthened vault.
Kind permission of Ruredil SPA.

analyses of the bridge, which identified possible collapse mechanisms with formation of hinges under factored loads. Therefore the strengthening design was aimed at increasing the safety against collapse. To this end, TRM was bonded to the soffit of each vault to prevent the formation of hinges at the exterior surface.

The design of the intervention required the strengthening of the soffit of each vault. This was achieved by an application of two layers of PBO–TRM to the intrados. Strengthening the intrados did not interrupt the use of the bridge, which would have been necessary if strengthening of the extrados had been done.

Prior to the application of the TRM the concrete surface was prepared by removing and reconstructing the deteriorated concrete. Then an approximately 5-mm thick mortar layer was applied on the concrete surface. The first layer was applied by pressing the textile slightly into the mortar, which protruded through all the perforations between fiber rovings to ensure good impregnation (Figure 17.7b and c). Then additional mortar was placed and the second layer of textile was pressed into the second matrix layer. The final step of the strengthening procedure comprised the application of a final top mortar layer as illustrated in Figure 17.7d. It is worth noting that the project was completed very fast, without interruption of the train traffic.

17.2.7 Strengthening of cooling towers (Germany 2012)

The Niederaussem Power Station is a lignite-fired power station in the Bergheim Niederaussem. It consists of nine units, which were built between 1963 and 2003. It has a total output capacity of 3864 MW and a net capacity of 3627 MW.

From the moment of their construction, the cooling towers were exposed to weather conditions and multiple loading, and therefore have been constantly deteriorating. A natural draft cooling tower built in 1968 (cooling tower E) was damaged as a result of the operation of a subsequently built flue gas discharge unit, high wind pressures and temperatures stresses. The cooling tower shell E has a height of about 96 m, a diameter of 70 m at the bottom and a minimum wall thickness of 0.14 m, as illustrated in Figure 17.8a. A detailed view of damaged cross section of the tower is given in Figure 17.8b. More details about the damage mechanisms of the cooling tower are presented by Altmeyer et al. (2012).

Following the inspections that detected the damage, a detailed assessment of the tower's ultimate capacity was conducted. The new and more rational methods of calculation employed and the better understanding of the exact loading conditions revealed that the tower that was designed based on old codes did not fulfill all actual demands. This was applied in particular to the serviceability limit state of the DIN 1045-1:2008. Therefore, a rehabilitation measure to guarantee safe operation during the remaining lifetime of the tower was deemed necessary.

The TRM system was selected to strengthen the cooling tower for a number of reasons. First, application of TRM allowed operation with mobile platforms, without interrupting the operation of the cooling tower. In addition, given the exposure of the strengthening system to the weather conditions and the high temperatures of the fumes at the concrete surface, the use of textiles in inorganic matrices guaranteed the long-term durability of the retrofitting system.
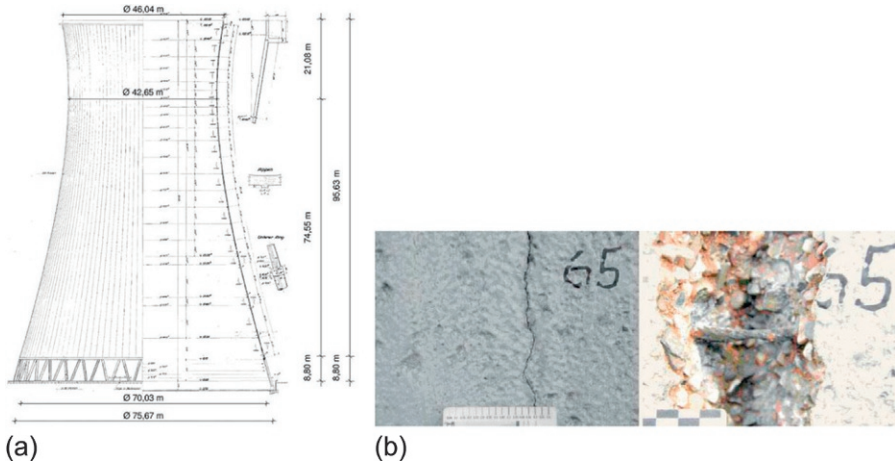
Figure 17.8 Cooling Tower E: (a) main dimensions and (b) detail view of a damaged section (Altmeyer et al., 2012).

The PBO–TRM composite material (described in Section 17.2.6) was selected for this intervention as well. Figure 17.9 summarizes the procedure of the strengthening application.

17.2.8   Trestle bridge base confinement (United States 2012)

The Metro North Railroad, a suburban commuter rail service, is the busiest commuter railroad in the United States in terms of monthly ridership. In the Metro North Railway trestle, located in northern New York, the concrete pedestals supporting the structural steel trestle were heavily deteriorated (as illustrated in Figure 17.10a). Therefore, in this case study, it was necessary to provide confinement and protection to the concrete pedestals. The solution of using FRP was rejected due to the lack of vapor permeability of epoxy-bonded systems. TRM composites were eventually selected, because a breathable strengthening material was required.

The pedestals have a truncated pyramid shape and vary in size depending on the configuration of the ground. The pedestal measured about 2.4 m × 2.4 m at the base and was 2.4 m in height (Nanni, 2012). As shown in Figure 17.10a, over the years, the environment-induced degradation had led to severe cracking and concrete spalling. Despite this structural deterioration, it was assessed that the pedestals were still adequate to carry the loads for which they were designed. Nevertheless, to recover the initial strength and, most importantly, to ensure reliable long-term performance, it was decided to repair and strengthen the pedestals. Confinement and protection of the concrete called for encapsulation of the entire pedestal. A PBO–TRM system was chosen, because its cementitious matrix ensures vapor permeability.

Figure 17.9 (a) Screeding of the inorganic matrix on the tower shells; (b) application of two layers of PBO textile reinforcement; and (c) overview of the strengthening application. Kind permission of Ruredil SPA.
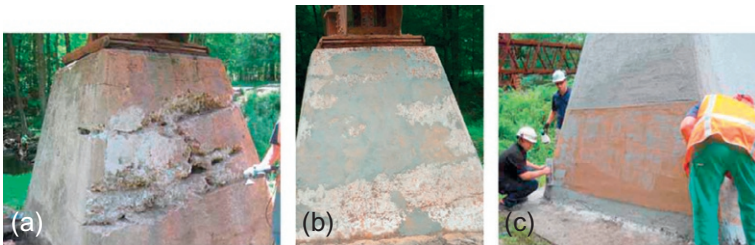
Figure 17.10 Metro North Railway trestle in northern New York: (a) removal of deteriorated concrete from pedestal; (b) filling of cavities with mortar; and (c) application of the PBO grid over a layer of cementitious mortar. Kind permission of Ruredil SPA.

The repair was conducted according to the International Concrete Repair Institute (ICRI) guideline ICRI 310.1R (ICRI 310, 2008), starting with the removal and replacement of deteriorated concrete (Nanni, 2012). After all deteriorated concrete was removed, the cavities were filled with an engineered mortar compatible with the TRM system (Figure 17.10b). The substrate surface was then prepared by grinding

and rounding the corners to a desirable radius. Then, a layer of the cementitious matrix was troweled onto the substrate, and sheets of cut-to-size textile were pressed into the matrix, such that the mortar pushed out through the grid openings to encapsulate the fibers (Figure 17.10c). A second layer of the cementitious matrix completed the repair.

17.2.9   Maracanã Stadium (Brazil 2012)

The TRM material was successfully applied for the strengthening of the Maracanã Stadium in Rio de Janeiro. With the challenge of delivering the stadium on time for the 2013 FIFA Confederations championship test for the 2014 World Cup in Brazil, the concern about the delivery schedule dominated the decisions on the intervention project.

With the insertion of a new roof on the stadium, the axial load of the existing columns increased considerably. Therefore, it was deemed necessary to increase the axial capacity in 60 RC columns. Although technically feasible, the use of steel jacketing was rejected due to the increase of column sections. In addition, steel jacketing required more time to be realized and a high consumption of material for coverings. Therefore the application of TRM jacketing was chosen. The choice of using a carbon fiber grid allowed the column strengthening to be completed in about 30 days—four columns per day on average. Two layers of the S&P Clever Reinforcement "ARMO-system" were used.

This retrofitting system comprises a grid of carbon fiber reinforcement, two layers of which were initially wrapped around the columns and fastened with a few headed clasps (Figure 17.11a). The effectiveness of confinement with composite jackets in wall-like columns is improved by the use of FRP anchors (Triantafillou et al., 2015; Bournas et al., 2015); this concept was adopted for the stadium columns, as shown in Figure 17.11b. Then the strengthening procedure involved applying a 10 mm layer of shotcrete, as shown in Figure 17.11c. Finally the mortar was leveled using a metal trowel (Figure 17.11d). Such a system did not require additional protection, so there was no need for coverings.

In addition to the columns, 14,000 m^2 of the old stadium tiers also had to be reinforced. It was estimated that, by using steel mesh reinforcement, the work would have required 32 people working for around 75 days. Following several consultations with the engineers, the contractor once again decided to use carbon fiber TRM, and the strengthening intervention was completed in 22 days by only two employees (Figure 17.12).

17.2.10   Strengthening of supermarket slabs
(The Netherlands 2013)

During a renovation project of a busy supermarket in Hilversum, the load-carrying capacity of the ground floor appeared to be less than the standard load requirements (minimum 4 KN/m^2). Because the space beneath the floor was used as an underground

Figure 17.11 (a) Fastening of the carbon textile reinforcement; (b) FRP anchors in wall-like columns; (c) a building worker is spraying shotcrete on the fastened carbon reinforcement; and (d) strengthened column at the end.
Kind permission of S&P Clever Reinforcement.

Figure 17.12 Strengthening the stadium tiers using carbon fiber TRM.
Kind permission of S&P Clever Reinforcement.
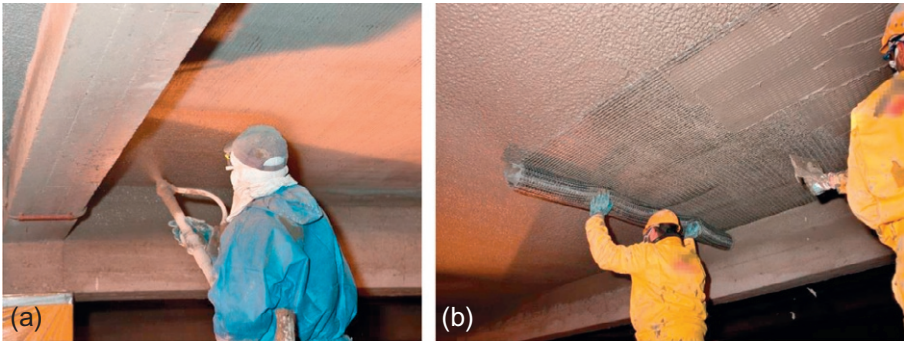
Figure 17.13 Strengthening of RC slab: (a) shotcreting and (b) application of the reinforcement.
Kind permission of S&P Clever Reinforcement.

parking lot, the fire resistance of the floor also had to be considered. The solution was found using the TRM system, which was implemented in the Netherlands for the first time in this case study.

The first proposal for reinforcing the ground floor was the fairly common carbon fiber strips (carbon-fiber-reinforced polymer), glued to the bottom of the floor. Because of the fire resistance requirements, it was necessary to protect the carbon fiber strips with flame retardant coating or plating. This could significantly increase the project's cost, and therefore a new technique was introduced by S&P Clever Reinforcement, the "ARMO-system." This retrofitting system comprises a grid of carbon fiber reinforcement that is applied to wet shotcrete without adding epoxy or organic adhesive. The total layer thickness is approximately 25 mm. Such a system did not require additional protection or heat shielding, and the extra shotcrete layer on top of the original reinforcement made the entire construction even more fire resistant.

The strengthening procedure involved applying a 10-mm thick layer of shotcrete beneath the concrete floor after the surface was pretreated (Figure 17.13a). The first carbon textile layer was embedded in this layer (Figure 17.13b), which was then covered by a second layer of shotcrete. The second layer of reinforcement was applied to the second layer of shotcrete, which was finally covered up by shotcreting.

17.3　Masonry strengthening case studies

17.3.1　Repair and seismic retrofitting of Tuna Plant (Italy 2005)

The project for the restoration of the former Florio tuna processing plant was funded by the region of Sicily. The tuna processing plant was restored to be used as a museum, providing in this way an opportunity to preserve the island's tradition and anthropological heritage. The work involved the adaptation of various buildings standing in the area (which measures about $45,000 \text{ m}^2$) and reorganization of the outdoor areas for

public use. The restoration and reuse of the industrial complex involved three stages: structural repair, restoration of the architecture and finishes on the buildings and recovery of the local anthropological heritage. The degree of decay and collapse necessitated substantial structural work. Workers employed traditional techniques and local materials side by side with specialized, innovative forms of intervention. The innovative aspect of the project was its ability to combine the methods and techniques of modern scientific restoration with recovery and reuse of traditional techniques.

The vaulted structures on the intermediate levels in various buildings (measuring about 3000 m^2, i.e., Figure 17.14) were strengthened with application of TRM consisting of a carbon fiber grid and a cement matrix (Ruredil X Mesh C10).

The structure of the two-level buildings of the former Florio tuna processing plant consists of pillars of tuff masonry with 0.75 m square sections laid out to form a square grid measuring about 4.5 m per side. At the level of the intermediate floors, the pillars are linked in both directions by full arches consisting of blocks of tuff stone measuring 0.35 m $\times$ 0.35 m $\times$ 0.50 m. The vaults making up the first floor of these buildings are characterized by a very low rise and a structure made of white, tuff, hollow, and flat blocks with an average thickness of 0.15 m. Having identified the sections of maximum stresses in the structures and vaults, the application of a structural reinforcement was planned. The tuff vaults were connected with the application of TRM mesh by means of the following operations:

1. The supporting filler from the extrados was emptied out. The crushed material from joints was removed, and the vault extrados were successively wedged and dampened.
2. A clinging rough coat made with premixed mortar that contained hydraulic binders with a low-soluble mineral content was applied. This was followed by the application of 3-mm thick mortar, over which a carbon mesh was applied (Figure 17.15a). This exerted a certain amount of pressure to allow the mortar below to penetrate through the mesh. Joints were
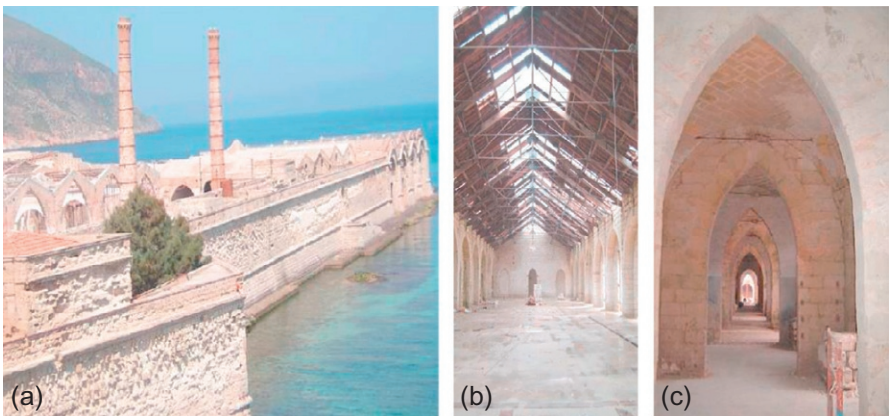
Figure 17.14 The tuna factory.
Kind permission of Ruredil SPA.
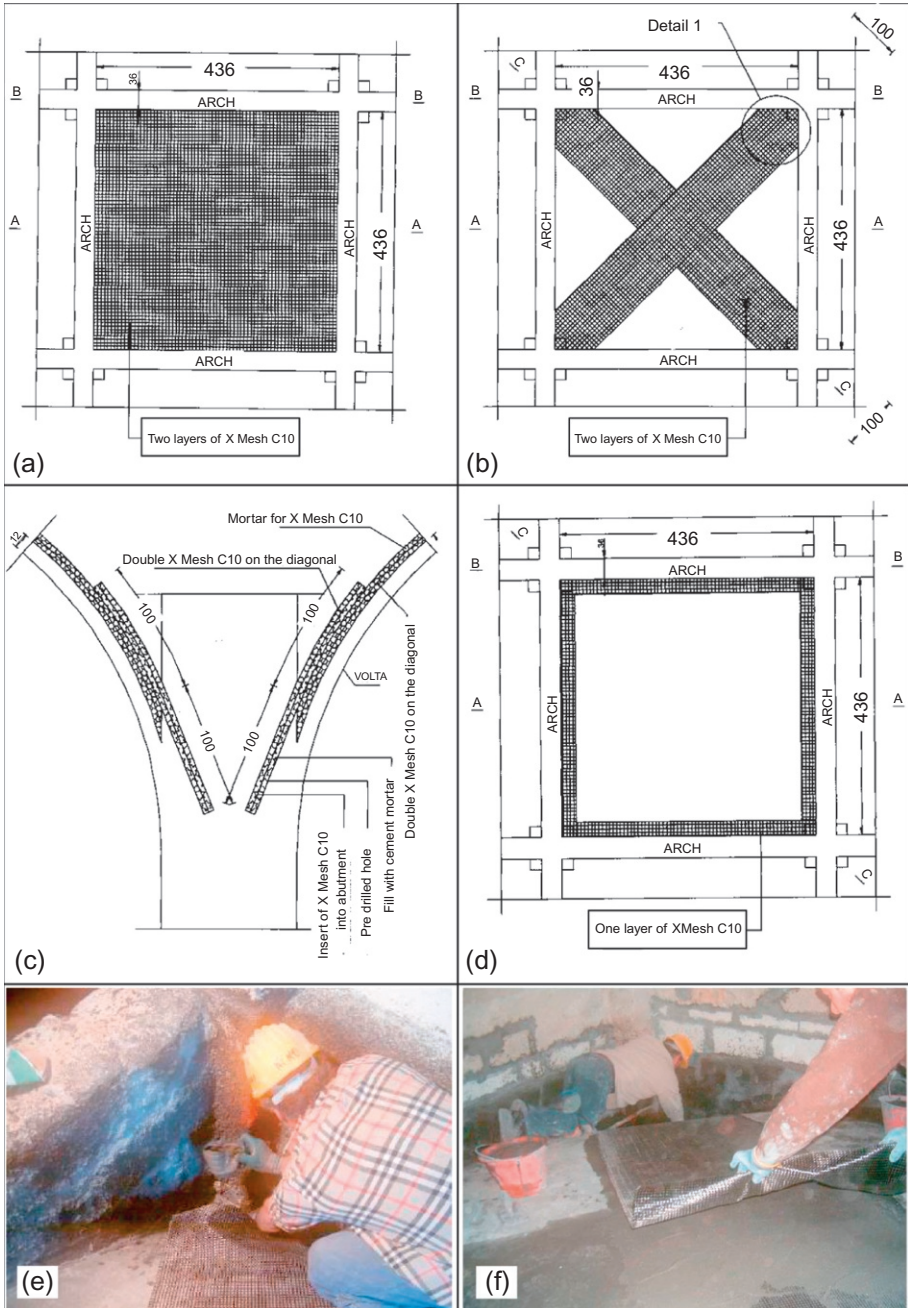
Figure 17.15 Strengthening of the vaults.
Kind permission of Ruredil SPA.

overlapped by at least 0.10 m, and a second layer of pozzolanic hydraulic mortar that was identical to the first (at least 3 mm thick) was applied over this.

3. The same procedure was used to apply two overlapping 1-meter-long strips of carbon mesh in the two diagonal directions over the fresh mortar layer (Figure 17.15b). They were applied in two stages, following the same initial procedure. These diagonal pieces were linked to the pillars supporting the vault by a piece of carbon mesh that was 0.50 m wide and 2 m long (1 m was in a 36 mm hole made in the pillars and sealed with injections of special hydraulic binder with compensation for shrinkage, and 1 m overlapped and sealed on the diagonals— Figure 17.15c).

4. An additional 0.25-m wide carbon mesh strip was applied, by means of the method described above, to the outer perimeter of the vault extrados (Figure 17.15d).

Photographs of the application method of textiles combined with mortar binder are shown in Figure 17.15e and f.

Further information on this project can be obtained in Biondo et al. (2007).

17.3.2 Strengthening of the Romanesque Church of San Roque (Spain 2008)

The historic San Roque church is located in Renedo de la Inera, which belongs to the ancient medieval area known as Campoo. It is made of masonry, stonework and timber elements. Due to earthquakes, the church was experiencing problems concerning the outer walls out-of-plane separation (Figure 17.16a). This caused serious cracks on the main vault (Figure 17.16b), and therefore strengthening was deemed necessary.

This case study, the EU project OPERHA, focused on the sacristy of the church. At that time, the church was stable; however, previous movement had left some cracks, which had increased the damage in localized areas of the church. The vault of the sacristy presented a map of cracks; the most important crack was the longitudinal one (Figure 17.16b). The TRM system was applied on the extrados of the vault. This was done firstly to prevent further development of the existing cracks, and secondly to prevent the opening of new cracks. The intervention consisted of the following steps:
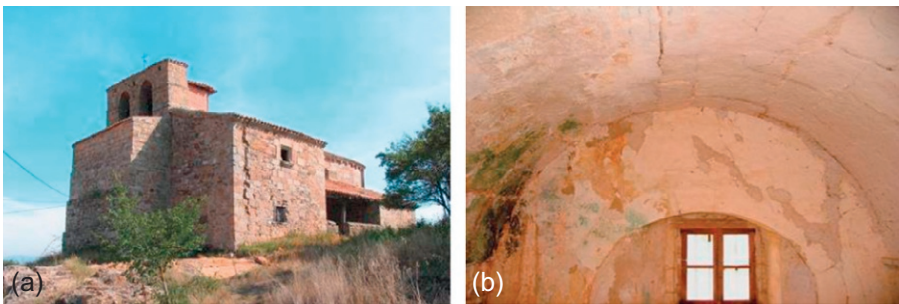
Figure 17.16 San Roque church earthquake damage: (a) wall out-of-plane separation and (b) critical cracks on the main vault.
Kind permission of Fyfe Europe SA.
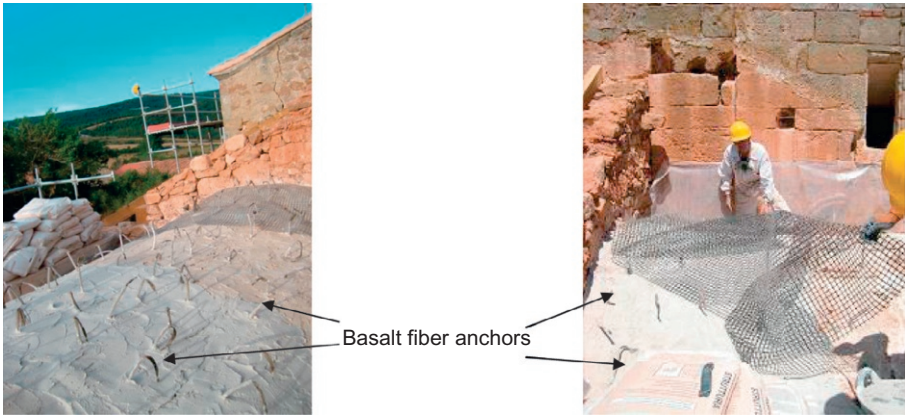
Figure 17.17 Installation of basalt fiber anchors and basalt fabric on the extrados of the vault. Kind permission of Fyfe Europe SA.

1. shoring up the vault during restoration;
2. protecting the thirteenth century windows, which were discovered during this intervention, by plastic canvas;
3. cleaning dirt and debris from the roof and convex surfaces;
4. filling the seam and reinforcing the wall cornice;
5. drilling the ashlars for repositioning the Tyfo® Basalt Fiber Anchors;
6. installing the Tyfo® Basalt Fiber Anchors in the holes filled with mortar (Figure 17.17);
7. applying mortar at all surfaces;
8. installing the Tyfo® EP-B Basalt fabric with appropriate overlapping; and
9. covering the fabric with mortar.

17.3.3 Strengthening of unreinforced masonry chimney (France)

TRM was used to strengthen an unreinforced masonry chimney of a historic sawmill in the municipality of Gerardmer, France (ACI, 2013). This chimney, which is now closed, comprises a symbol of industrial heritage and had to be preserved and restored using a strengthening system that was not only compatible with the existing materials but also reversible. The height of the chimney is about 38 m, and its diameter ranges from 3.60 to 1.70 m from the base to the top (Figure 17.18a). Today, the structure is used to support several telephone antennas and their cabling.

The high capillary absorption of the clay bricks, sand and lime joints (Figure 17.18b) was addressed by using a cementitious repair mortar to rectify the existing surface without any surface pretreatment, such as sandblasting.

The chimney was modeled as a cantilever beam, and wind was found to be the most critical loading case. The structural analysis results indicated that strengthening of the structure was required in both the hoop and vertical directions. Therefore, a commercial textile (Ruredil X Mesh C10) with equal quantity of high-strength carbon rovings in two orthogonal directions was used (Figure 17.18c). The weight of
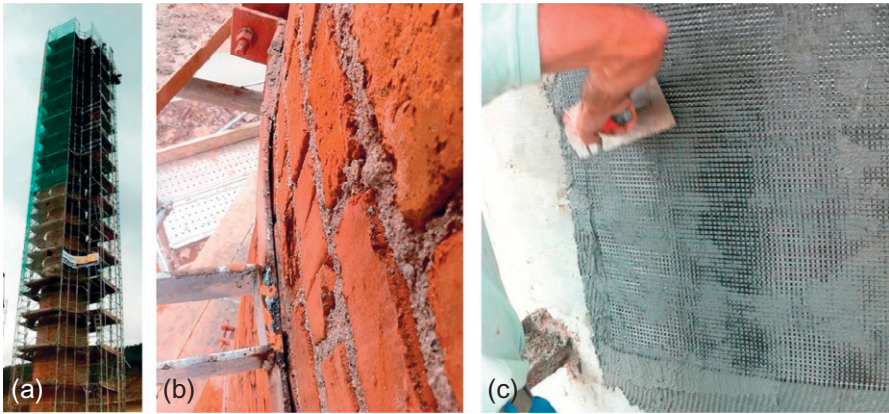
Figure 17.18 The unreinforced masonry chimney: (a) with scaffolding during repair; (b) before strengthening; and (c) during strengthening with carbon fiber textile bonded in a cementitious matrix.
Kind permission of Ruredil SPA.

the textile was 168 g/m^2, whereas its nominal thickness (based on the equivalent smeared distribution of fibers) was 0.047 mm. According to the manufacturer data sheets, the tensile strength and the modulus of elasticity of the carbon fibers were 3800 and 240,000 N/mm^2, respectively.

The analysis indicated that it was necessary to strengthen the structure with 10-mm thick TRM reinforced by a single layer of carbon fiber textile. According to Nanni (2012), this composite thickness scheme provided strength equivalent to an application of welded wire reinforcement with steel bars with a 6-mm diameter and spacing of 0.50 m in both the hoop and vertical directions.

17.3.4 Strengthening the masonry dome of Molla Çelebi Mosque (Turkey 2013)

The Molla Çelebi Mosque (Figure 17.19a) was built by architect Mimar Sinan in the Fındıklı neighborhood of the Beyoğlu district in Istanbul. Although the exact construction date is unknown, it is believed that the mosque was completed around 1584. The Turkish state directorate that is responsible for the mosque decided to renovate the historical monument. During the renovation, due to the presence of minor cracking, it was clear that the main dome needed strengthening at the support level. Because of the historic character of the mosque, the strengthening system had to be compatible with the existing materials of the dome, as well as reversible. Therefore, the use of epoxy-based systems was rejected, and the TRM strengthening technique was selected (Fyfe Europe SA, 2013).

"Horasan" mortar (pink colored, weak mortar with lime and brick pieces) was applied on the outside of the dome (Figure 17.19b). Afterwards, four layers of open-weaved basalt fabric, in combination with the cementitious mortar matrix of

Figure 17.19 Strengthening the masonry dome of Molla Çelebi Mosque: (a) the mosque; (b) application of "Horasan" mortar on the outside of the dome; and (c) application of the textile basalt grid over a layer of cementitious mortar.
Kind permission of Fyfe Europe SA.

the system (Tyfo® EP-B RM System), were applied around the drum of the dome in the hoop direction to confine the dome externally and maintain the structural integrity (Figure 17.19c). The principal tensile stresses, as well as the displacements that are going to be developed along the hoop direction of the dome due to future loading, are expected to be reduced significantly.

The Tyfo® EP-B RM System was developed by Fyfe Europe to cover the needs of the heritage and monument structures, where the strengthening system should be compatible with the existing materials of the structure. The mortar matrix used was totally compatible with the substrate and the materials of the structure. The texture and the color of the system were consistent with the original masonry. Moreover, this is a fully reversible technique, and thus compliant with international historic monument preservation directives. It also has excellent resistance to fire.

17.3.5 Strengthening of a masonry wall in historical building (Turkey 2014)

Constructed in 1884, the building was designed by French-Ottoman architect Alexander Vallaury, and is one of İstiklal Avenue's unique structures in Istanbul. Recently, the building was lent to a private firm for the duration of 25 years. The firm performed an assessment of the existing structure and found out that the in-plane shear capacity of some of the masonry walls was insufficient to carry the required action due to earthquake loading. Thus, they decided to increase the in-plane shear capacity of the masonry walls by an appropriate strengthening technique. As the building is a historical structure, traditional strengthening techniques, such as adding RC shear walls, could not be implemented. TEKSTAR—a certified applicator trained by FYFE Europe SA—proposed a solution combining the TRM Basalt System and steel anchors (Fyfe Europe, 2014).

The strengthening procedure (Figure 17.20) included the following steps: (1) the wall surfaces were prepared, and loose mortar and unsound material was removed; (2) the basalt fabric-reinforced hydraulic mortar system was applied on the wall to

Figure 17.20 (a–c) Strengthening of a masonry wall in the historical building.
Kind permission of Fyfe Europe SA.

be strengthened; (3) masonry anchors were installed at an angle of around 30° to the horizontal side, and at a distance of 0.35 m vertically and 0.50 m horizontally; (4) galvanized steel plates were fastened onto the wall using nuts, so that a uniform pressure was applied across the Tyfo® RM Basalt System to delay debonding during a possible seismic event; and (5) finally, the wall was covered with "Horasan" mortar (pink colored, weak mortar with lime and brick pieces).

The total area of basal fibers used was around 1500 m^2.

17.4 Future trends

As soon as more experimental results and design guidelines on TRM systems are available and designers become aware of this technology, the number of strengthening projects using textile reinforcement in inorganic matrices will increase considerably. This will be particularly true in the case of projects where special design requirements need to be met (i.e., high temperatures, reversibility of the intervention, etc.). Following the trend of the FRP, TRM is expected to become a very popular composite material for the strengthening of existing concrete and masonry structures within the next decade.

17.5 Source of further information and advice: Design codes

Recently, design guidelines and specifications have been published by technical organizations that provide guidance for design with TRM materials in strengthening and seismic retrofitting applications. The key publications are listed below.

ACI, 2013. Guide to Design and Construction of Externally Bonded Fabric-Reinforced Cementitious Matrix (FRCM) Systems for Repair and Strengthening Concrete and Masonry Structures, 549.4R-13, American Concrete Institute, Farmington Hills, MI, USA.

Brameshuber, W. (Ed.), 2006. Textile Reinforced Concrete, State-of-the-Art Report of RILEM Technical Committee 201-TRC. RILEM Report 36. RILEM Publications, Bagneux, France.

Federation International du Beton—fib, 2001. Externally Bonded FRP Reinforcement for RC Structures, Bulletin 14, Lausanne.

Valluzzi. M. (Ed.), 2015. Masonry Strengthening with Composite Materials, State-of-the-Art Report of RILEM Technical Committee 223-MSC. RILEM Report XX. RILEM Publications, Bagneux, France.

Acknowledgments

References

ACI, 2013. Guide to Design and Construction of Externally Bonded Fabric-Reinforced Cementitious Matrix (FRCM) Systems for Repair and Strengthening Concrete and Masonry Structures, 549.4R-13. American Concrete Institute, Farmington Hills, MI, USA.

Altmeyer, F., Weigl, J., Scharf, A., 2012. Safety analysis and rehabilitation of the natural draft cooling tower Block E at the power plant of Niederaußem. Beton Stahlbetonbau 107 (5), 318–327 (in German).

Berardi, F., Focacci, F., Mantegazza, G., Miceli, G., 2011. Rinforzo di un viadotto ferroviario con PBO-FRCM. In: 22. Proceedings, 1°Convegno Nazionale Assocompositi, Milan, Italy, May 2011 (in Italian).

Biondo, S., Cusenza, A.M., Mantegazza, G., 2007. Restoration of the Florio tuna plant on the island of Favignana (Trapani). In: Proceedings of the 8th International Conference on FRP for Reinforced Concrete Structures (FRPRCS-8), Patras, Greece, July 16–18. Paper ID 18-15.

Bournas, D.A., Pavese, A., Tizani, W., 2015. Tensile capacity of FRP anchors in connecting FRP and TRM sheets to concrete. Elsevier Eng. Struct. 82 (1), 72–81.

DIN 1045-1 08/2008, 2008. Concrete, Reinforced and Prestressed Concrete Structures—Part 1: Design and Construction. Beuth Verlag, Berlin.

Fyfe Europe SA, 2013. Masonry Dome of Molla Çelebi Mosque Strengthened with Tyfo® RM Reinforced Mortar Systems [Online]. Available at: http://fyfeeurope.com/en/data/projects/historic/01.Masonry%20Dome%20of%20Molla.pdf (accessed 10.03.15).

Fyfe Europe SA, 2014. 19th Century Historical Building Masonry Wall Strengthening [Online]. Available at: http://fyfeeurope.com/en/data/projects/historic/03.Strengthening%20of%20a%2019th%20century%20historical%20building.pdf (accessed 10.03.15).

ICRI Committee 310, 2008. Guide for Surface Preparation for the Repair of Deteriorated Concrete Resulting from Corrosion (ICRI 310.1R, Formerly No. 03730). International Concrete Repair Institute, Rosemont, IL, 12 pp.

Nanni, A., 2012. A new tool in the concrete and masonry repair. Concr. Int. 34 (4), 43–49.

Schladitz, F., Lorenz, E., Jesse, F., Curbach, M., 2008. Strengthening of a barrel-shaped roof using textile reinforced concrete. IABSE Symposium Report 12/2008, http://dx.doi.org/10.2749/222137809796088567.

Triantafillou, T.C., 2007. Personal communication.

Triantafillou, T.C., Choutopoulou, E., Fotaki, E., Skorda, M., Stathopoulou, M., Karlos, K., 2015. FRP confinement of wall-like reinforced concrete columns. RILEM Mater. Struct. http://dx.doi.org/10.1617/s11527-015-0526-5.

Trimboli, A., Mantegazza, G., 2004. Special Fiber Reinforced Cementitious Matrix (FRCM) for the Shear Strengthening of Reinforced Concrete Beams Technical Report [Online]. Available at: http://www.ruredil.com.do/contentManager/productos/files/%5B19%5Darticolosansiro.pdf (accessed 10.03.15).

This page intentionally left blank

Thin TRC products: Status, outlook, and future directions

A.E. Naaman
University of Michigan, Ann Arbor, MI, USA

18.1 Introduction: Summary

While textile-reinforced concrete (TRC) encompasses, in principle, all structural concrete applications using nonmetallic textile reinforcements, this chapter focuses on thin TRC products and suggests that their success is more likely to be achieved in the near future than thicker products. Thin TRC products are compared to conventional ferrocement and other laminate cement composites, and a possible working definition is suggested for their characterization and identification. In order to achieve a functioning composite, some practical guidelines for mechanical compatibility between textile reinforcements and cement matrices are proposed in this chapter. A simplified heuristic rule for textile selection is proposed. A framework for evaluating any product for mechanical performance, comparative cost effectiveness, and willingness-to-pay price is described and applied to real examples. A strong case is made for the development and use of pre-engineered 3D textiles in thin products particularly in order to minimize labor cost and improve composite reliability; the use of ultra high performance concrete matrices is discussed. The author further suggests that composite performance and cost can be improved by using discontinuous fibers in the matrix and possibly introducing self-stressing. Numerous areas of research for the near future are listed to ensure the success of thin TRC products.

18.2 Status report

During the 2003 symposium on fiber-reinforced polymer (FRP) reinforcement in concrete structures in Singapore, an assessment survey of the state of progress and future outlook for FRP reinforcements was carried out (Naaman, 2003a). It was pointed out then that some key drawbacks of FRP reinforcements in conventional reinforced concrete (RC) structures include poor resistance to shear and lack of ductility. It was also pointed out that, while solutions to such drawbacks are available (such as by adding proper fiber reinforcement to the matrix or confining the concrete compression zone), the additional cost made their use cost-ineffective in most applications at the time. However, the drawbacks mentioned above diminish significantly when thin products (cement boards, sheets, shells, etc.) are used. This is true either in standalone applications or in repair and rehabilitation projects where the cost of labor is high in proportion to the cost of materials. Indeed, extensive experimental testing on thin

reinforced sheets using FRP meshes indicated sufficient ductility and a good shear resistance (Balaguru, 1994; Daniel and Shah, 1990; Dubey, 2004; Guerrero and Naaman, 1998; Lopez and Naaman, 1998; Mobasher et al., 2000; Naaman and Al-Shannag, 1994; Naaman and Guerrero, 1996; Naaman and Chandrangsu, 2000; Naaman, 2000, 2002, 2012; Parra-Montesinos and Naaman, 2001; Peled et al., 1999). The improved ductility issue was explained by the slow progressive failures of the many fibers, threads, or yarn of the mesh or fabric or textile used, which provided sufficient deflection and warning. Additionally, the shear resistance, while always less critical in thin structural elements than in thick ones (ferrocement vs. reinforced concrete) is helped by the high reinforcement content, and its layered configuration in the loading direction. Experimental tests have shown that the addition of discontinuous fibers to thin elements reinforced with steel or FRP textiles can improve both vertical and interlaminar shear resistance when needed (Guerrero and Naaman, 1998; Naaman and Guerrero, 1996; Naaman and Chandrangsu, 2000; Naaman, 2000, 2003a,b).

It is thus necessary to first distinguish between thick structural elements (such as RC reinforced with steel reinforcing bars or FRP reinforcements) and thin reinforced cement products, such as ferrocement (ACI Committee 549, 1988, 1997; ACI Committee, 2004; Balaguru, 1994; Daniel and Shah, 1990; Dubey, 2004). In 2003 the terminology used for such products included ferrocement, thin cement product, or laminate cementitious composite reinforced with FRP meshes or fabrics or textiles. The term TRC was first used in the late 1990s and was not yet universally known (Curbach, 2003; Hegger, 2001; Scheerer et al., 2015).

Today, TRC encompasses thin cement products reinforced with FRP meshes or textiles or fabrics. The focus of this discussion will be on such thin products only. For such applications, the term textile implies a properly designed fabric or mesh for use as reinforcement. Here the term "properly" implies compatible material characteristics and textile architecture or topography.

Typical textile reinforcing materials used in cement composites include Kevlar (aramid fibers), Spectra (high molecular weight polyethylene fibers), carbon, PVA (poly-vinyl-alcohol), glass (alkali-resistant or resin-coated), and PP (polypropylene). Sometimes a particular textile may contain two different materials, such as carbon as the primary fiber in the warp direction and glass in the weft direction. Hybrid combinations of reinforcement imply a combination of continuous textiles, such as glass and PP textiles, or a combination including a continuous textile with discontinuous fibers, such as a carbon textile with PVA fibers added. The discontinuous fibers are generally premixed with the mortar matrix or could be assembled in a fiber mat. 2D and 3D textile configurations are thus considered.

18.2.1 Definition of thin textile reinforced concrete—TRC

In a 2010 paper, the author discussed a possible definition for TRC (Naaman, 2010); it is repeated below to help narrow the scope of this discussion.

Assume, hypothetically, that a new structural composite called TRC is to be defined, in which "true concrete" is implied, such as in conventional, large-scale structural concrete applications. The definition, then, of TRC would be the same as that of conventional RC, except that the reinforcement is made out of nonmetallic or polymer-based bars or textiles instead of reinforcing steel bars or welded wire fabrics. This is same as what is considered today as RC with FRP reinforcements.

However, for thin TRC products, the author suggested the following definition, using the definition of ferrocement by the ACI Committee 549 (1997) as a basis, with some relevant modifications:

> *Textile reinforced concrete is a type of reinforced concrete commonly constructed of hydraulic-cement matrix reinforced with several layers of closely spaced continuous 2D textiles, or one or several layers of 3D textiles. At least one textile layer should be placed near each of the two extreme surfaces of the resulting structure. The textiles may be made of polymer, synthetic, metallic, organic or other suitable materials. The fineness of the cementitious matrix and its composition should be compatible with the textile armature system it is meant to encapsulate. The matrix may contain discontinuous fibers or microfibers of appropriate dimensions.*

Figure 18.1 illustrates typical sections of thin TRC products satisfying the suggested definition. Depending on the application, typical thickness ranges from 5 to 50 mm. A 3D textile could be made of two layers of 2D textiles connected along the third dimension. In all cases, the cover of cement matrix to the reinforcement is small and can be as little as zero. Codes, such as the Ferrocement Model Code (Ferrocement Model Code, 2001), but specifically dedicated to TRC, will eventually provide guidance for the recommended cover.

To support the above definition, it is first essential to define a textile in general terms, such as a 2D textile or a 3D textile, without reference to any process of fabrication or material. The compatibility of a particular textile (plain, tricot, jersey, leno, braided, etc.) for use in concrete products will need to be assessed for physical, chemical, and mechanical properties.

By stating that the textile could be "metallic," TRC would allow the use of conventional steel wire meshes (woven or welded), and thus TRC could also cover conventional ferrocement. In a similar manner, because the ACI definition of ferrocement allows the use of nonmetallic meshes, it can be argued that ferrocement encompasses TRC. The only issue we would have to explain is whether a TRC with a single layer of 2D reinforcement, such as in conventional stucco applications, is acceptable. Conversely, we could insist on at least two layers, such as in a sandwich construction, where each layer is placed close to one extreme surface of the composite to optimize bending resistance. On the other hand, a TRC could use a single layer of 3D textile, fulfilling the same function of a reinforcing system as several 2D textiles. In such a case, one layer of a 3D textile would be acceptable, as stated in the proposed definition and shown in Figure 18.1d and e.
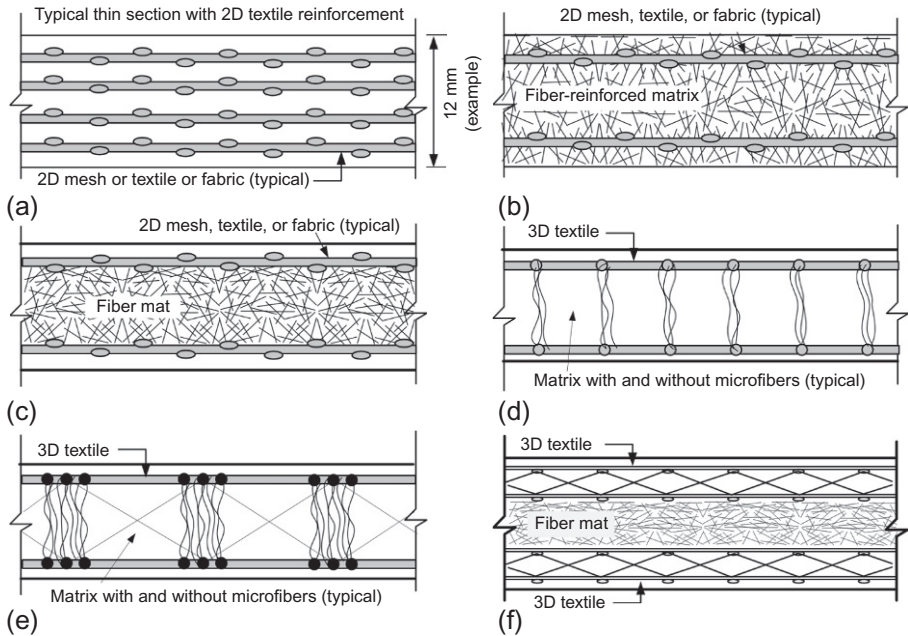
Figure 18.1 Typical sections of thin TRC products satisfying the suggested definition. (a) Several layers of 2D textile: minimum of two layers, one near each face, (b) most efficient for bending: two extreme layers of 2D textile with fiber reinforced matrix, (c) two layers of 2D textile sandwiching a fiber mat, (d) one layer of 3D textile covering entire depth, (e) one layer of 3D textile covering entire depth, and (f) two layers of 3D textile sandwiching a fiber mat.

18.2.2   *Relevant differences between ferrocement and thin TRC*

Clearly ferrocement and thin TRC are part of the same family when viewed at the structural level; that is, they could be classified as part of thin RC products, thin cement composite products, or cementitious composite laminates. Both ferrocement and TRC allow the use of a variety of reinforcing materials, including hybrid combinations, such as steel and aramid or PP. Both allow the use of fibers or microfibers in the matrix, leading to hybrid combinations of continuous and discontinuous reinforcements (ACI Committee 549, 1997; ACI Committee, 2004; Balaguru, 1994; Daniel and Shah, 1990; Dubey, 2004; Naaman, 2005, 2006, 2008; Naaman et al., 2005).

What fundamental differences can then exist between ferrocement and TRC? It can be certainly argued that the primary reinforcement in ferrocement, as used so far in practice and for which design guidelines have been developed, is made out of steel; "primary" implies resisting a significant portion of the load-carrying capacity. Not only is the primary reinforcement in TRC not steel, but it generally exhibits properties significantly different from the properties of steel, particularly in terms of ductility,

post-elastic response, and thermal properties. Ferrocement is a mature technology with documented characteristics, verified long-term properties, and a proven service life spanning several decades. TRC is a relatively young technology, still in the making, still in need of time. It can be therefore argued that, although there are many similarities between ferrocement and TRC, there are also sufficiently important differences between them; thus, it is beneficial to consider them separately for purposes of research and applications. For instance, the bond characteristics at the reinforcement–matrix interface in TRC are totally different from those encountered in ferrocement with steel wire meshes. Durability issues, when related to the corrosion of steel, are nonexistent in TRC; while durability issues related to the alkalinity of the matrix could be significant in some TRC applications. The coefficient of thermal expansion of steel is of the same order as that of a typical cement matrix, while that of most polymeric fibers is significantly different. This difference warrants particular considerations for design under long-term conditions and where significant cyclic differences in temperature occur. Textiles can be made easily drapable to allow forms with particular curvature in one or two directions, while steel wire meshes would require significantly more labor to achieve the same effect.

In summary, in order to allow TRC to develop its greatest potential and its own personality, it is best to consider it, for the time being, as a new cementitious composite—a sort of sibling of ferrocement. From here, we can proceed accordingly in developing it to its full potential in applications where it can be most competitive. This is what technical committees can address best. Figure 18.2 offers a perspective on where TRC falls within the general family of structural concrete composites that have developed since the mid-nineteenth century. These include the most widely used structural materials, namely reinforced and prestressed concrete. While Figure 18.2 seems to confine TRC to passive reinforcement, such as in RC, active reinforcement, such as in prestressing or self-stressing, also applies to TRC. So far, however, the latter has been very limited.

18.2.3 Main focus of this chapter

As is clear from the above discussion, the author believes that the outlook for TRC is much brighter in the near future when confined to thin products. Figure 18.3 illustrates the classification of thin RC products that are the main focus of this chapter. In the figure, the term "hybrid" is used very generally and implies the combined use of continuous and discontinuous reinforcements, as well as reinforcements made from different materials. Applications include not only standalone products (such as wall panels, pipes, and unit shell shelters) but also support for new or existing structures (such as permanent molds for RC beams, and column confinement) and repair and rehabilitation of all structural concrete, including masonry (such as seismic retrofitting of masonry walls) (ACI Committee, 2004; Balaguru, 1994; Daniel and Shah, 1990; Dubey, 2004; Koustas et al., 2014; Si Larbi et al., 2010; Triantafilou and Papanicolaou, 2006).
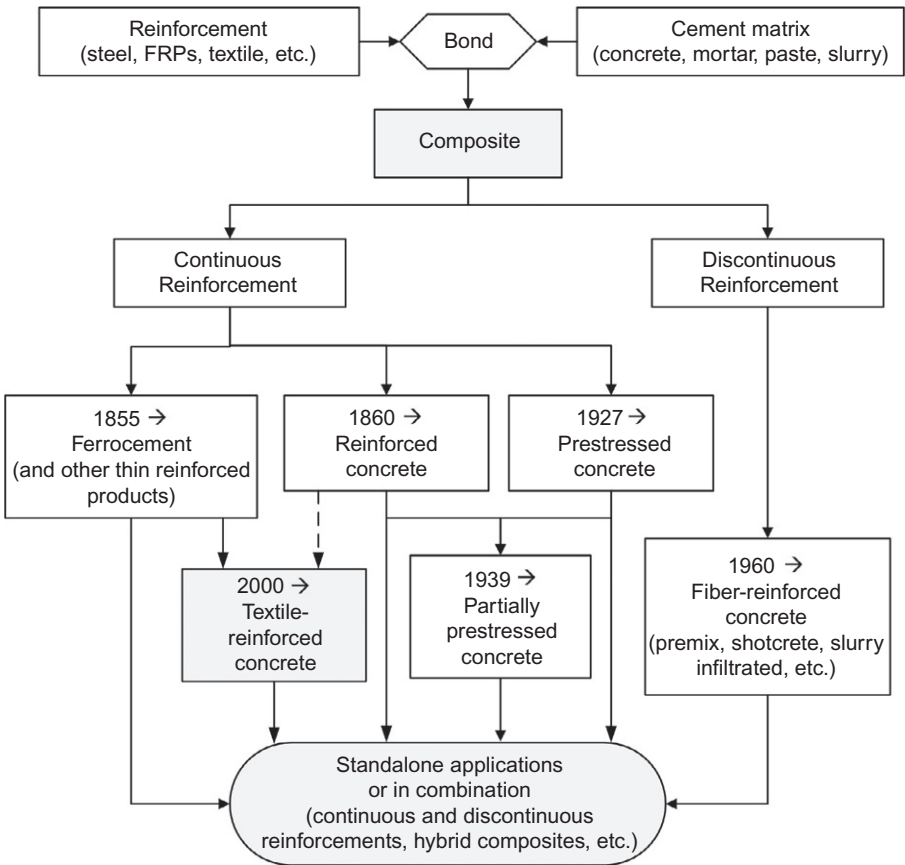
Figure 18.2 Classification of common cement-based composites and possible hybrid combinations.
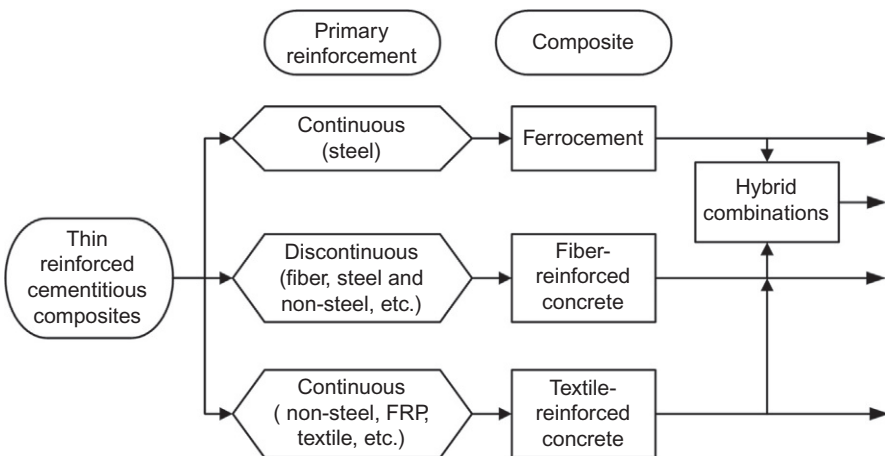
Figure 18.3 Classification of thin RC products.

18.3 Matrix and reinforcement: Compatibility for a successful composite

18.3.1 Intrinsic and effective properties

It is important to distinguish first between the fiber material used to produce a textile and the textile itself. Some properties may change considerably. Consider, for instance, a carbon fiber with a tensile strength exceeding 4000 MPa and an elastic modulus of 230 GPa. When such a fiber is used to produce a yarn for a textile, the effective tensile strength of the yarn can be about 3000 MPa, if it is impregnated with an epoxy resin; 2000 MPa, if the yarn is coated with, for instance, styrol-butadiene; and 1500 MPa, if the yarn left without coating (Hegger et al., 2015). The effective tensile strength of a textile comprising many yarns will be even smaller than that of a single yarn. Similarly starting with a glass fiber that has a tensile strength of 3000 MPa and an elastic modulus of 70 GPa, one can get an epoxy impregnated yarn (about 200 filaments) with an effective tensile strength of 1300–1400 MPa, a virgin uncoated yarn with an effective tensile strength of 700 MPa, and a coated yarn with an effective tensile strength somewhere in between. Moreover, the effective elastic modulus of the yarn will be generally smaller than that of the fiber material, but close. If the yarn is used to produce a textile for reinforcing a cement matrix, the tensile strength of the textile itself may be close to that of the yarn. However, the effective elastic modulus of the textile (whether taken by itself or embedded in the matrix) could be significantly smaller based on the textile architecture. For steel meshes used in ferrocement, the term "apparent modulus" or "equivalent modulus" was used in the past, and there is a test to help determine its value (ACI Committee 549, 1988; Ferrocement Model Code, 2001; Naaman, 2000). Thus, "leno" or "tricot" weaves are likely to produce a textile with a smaller effective elastic modulus than a "plain woven" textile.

18.3.2 Mechanical compatibility guidelines for textile selection

Assuming effective tensile strength and effective modulus are based on the textile itself, not the fiber or the yarn, a number of key measures can be taken to increase the likelihood of developing a successful composite. Based on a similar study related to fiber-reinforced cement and concrete composites, a number of qualitative measures are recommended by the author, as shown in Figure 18.4. In the figure, both the tensile strength and elastic modulus should be interpreted as the effective values.

By its very definition, a reinforcement (i.e., the textile or fiber) is supposed to induce an increase in the tensile strength of the material to be reinforced (i.e., the matrix). Both analysis and experimental test results suggest that, in order to be effective in concrete matrices, reinforcements or textiles must preferably have the following qualitative properties (Figure 18.4): (1) an effective tensile strength significantly higher than that of concrete (two to three orders of magnitude); (2) a bond strength
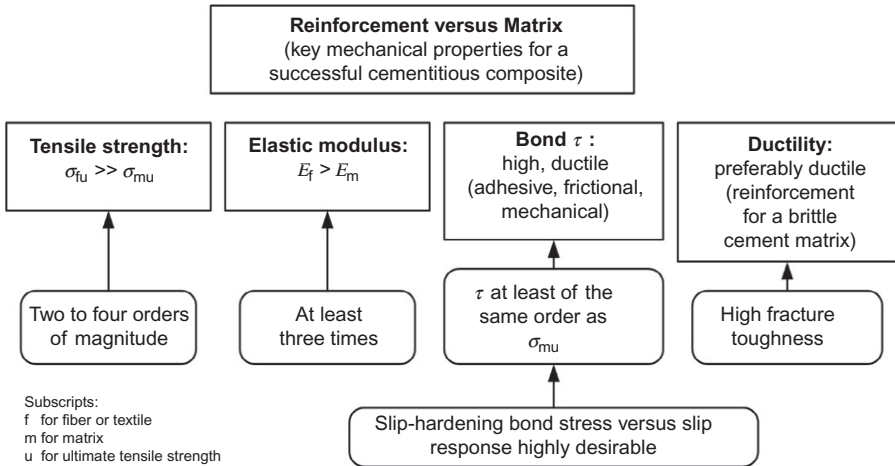
Figure 18.4 Desirable fiber (textile) versus matrix properties for a successful cementitious composite.

with the concrete matrix preferably of the same order as, or higher than, the tensile strength of matrix; and (3) unless self-stressing is used through fiber reinforcement, an effective elastic modulus in tension significantly higher than that of the concrete matrix.

Moreover, everything else being equal, a ductile fiber under tension is preferred to a brittle fiber; a ductile or slip-hardening bond-stress versus slip response is preferred to a brittle or slip-softening one. The Poisson's ratio of the fiber material or yarn and its coefficient of thermal expansion should preferably be of the same order for both the fiber and the matrix. Indeed, if the Poisson's ratio of the fiber is significantly larger than that of the matrix, detrimental debonding will occur under tensile load. However, these drawbacks can be overcome by various methods, such as inducing surface deformation to create mechanical anchorage.

In all non-prestressed applications, the bond between the reinforcement and the matrix is paramount for the success of the composite (see the top of Figure 18.2). The bond is a very complex property and includes adhesion, friction, and mechanical anchorage to the matrix, as well as fiber-to-fiber interaction. It is generally assumed that the textile material and the cement matrix are chemically compatible, and that good bond exists at the interface between the reinforcement and the matrix. More specifically, it is desirable to have a bond stress versus slip relationship with a high initial stiffness that undergoes little or no deterioration during cyclic service loads, and for normal fluctuations in service temperature. The bond is so complex that it would require a extensive treatment on its own (Brameshuber, 2006, 2010, 2015; Curbach, 2003; Curbach and Jesse, 2009; Hegger, 2001; Hegger et al., 2006; Jesse and Curbach, 2003; Parra-Montesinos et al., 2012; Reinhardt and Naaman, 2007). It suffices here to say that a good bond is necessary.
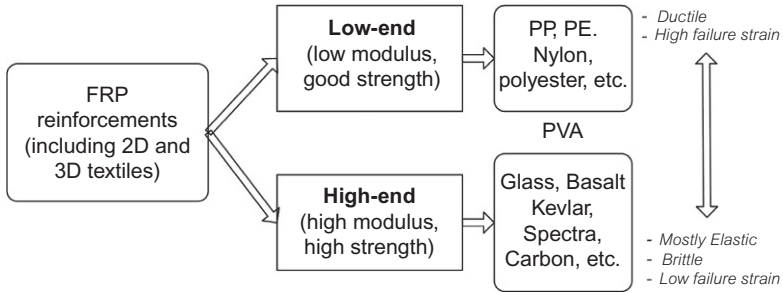
Figure 18.5 Useful classification of nonmetallic polymer and mineral fibers.

A normal-weight concrete matrix has an elastic modulus in the range of 15–50 GPa, depending on its compressive strength and numerous other parameters. Given this fact, it is clear from Figure 18.4 that fiber materials used in textiles that are intended to act as reinforcement for concrete should have not only a high strength (effective), but also a relatively high elastic modulus (effective). As many fibers can satisfy the strength requirement, nonmetallic mineral and polymer fibers can then be classified according to their elastic modulus. This is shown qualitatively in Figure 18.5. It is clear from Figure 18.5 that high-end fibers are more suitable for use in normal-weight cement and concrete matrices. However, low-end fibers, with a relatively low elastic modulus, are likely to be effective in lightweight and very lightweight cement matrices. which are characterized by very low values of elastic modulus. Note that PVA fibers have an elastic modulus somewhat at the limit between the low-end and high-end fibers, essentially suggesting that the scale between the two extreme cases is really continuous.

18.3.3 Simplified heuristic rule for textile selection

Assuming that a good bond (adhesive, frictional, mechanical, or a combination of them) can be achieved for a particular reinforcement or textile, the author suggests the following simple two-part rule. The rule is based on mechanics for the initial design of TRC composites with improved performance:

> *Increase both the ratio of effective tensile strength of the textile reinforcement to the compressive strength of the matrix, and the ratio of effective tensile elastic modulus of the textile to that of the matrix.*

The above rule assumes that cementitious composites will crack under tension (or bending tension), leaving the reinforcement in the cracked zone to contribute to both stiffness and strength, while the matrix is cracked and thus contributes little in tension. The requirement related to the moduli ratio may explain why low-end polymer meshes or textiles made of PP, for instance, were not widely or successfully used in normal-weight cementitious matrices, although their tensile strength was

comparable to that of conventional steel-wire meshes. However, based on the above simple rule, it can also be predicted that PP-based textiles may be compatible mechanically with very lightweight cementitious matrices, which show both low compressive strengths and low elastic moduli. For example, aerated concrete with a dry density in the range of 0.4–0.88 shows elastic modulus values ranging from about 0.250 to 1.8 GPa. PP- and particularly PVA-based textiles may prove suitable for such matrices.

On the other hand, for ultra-high strength concrete (UHPC), which has very small particles sizes (generally less than 1 mm), the matrix modulus is in the range of 45–55 GPa (Fehling et al., 2004, 2008; Richard and Cheyrezy, 1995; Rossi, 2008; Russell and Graybeal, 2013; Schmidt et al., 2004, 2012; Ulm and Acker, 2008). Thus only high-end fiber materials are likely to succeed, with carbon and steel being most suitable at this time.

18.4   Cost considerations: Fiber volume fraction versus weight fraction

18.4.1   Background

Conventional steel RC structures use volume fractions of reinforcement commonly ranging from about 0.8% to 3%. In ferrocement composites, the range is mostly between 2% and 7%. When short discontinuous fibers are added to the matrix, fiber content can add up to an additional 3%, and significantly more for SIFCON (Slurry Infiltrated Fiber Concrete) and similar products. The volume fraction of the reinforcement is defined as the volume of the reinforcement per unit volume of the composite. Due to the fact that in a given composite, every 1% of textile reinforcement generally costs more than the entire concrete matrix, cost efficiency is of paramount importance for the widespread success of TRC products.

18.4.2   Examples: Volume fraction versus weight fraction

The cost of a given reinforcement is based on unit weight (i.e., dollar per kg), while its mechanical efficiency is based on its volume fraction in the composite. Because the unit weight of steel ranges from 3 to 8 times that of most synthetic fiber materials, and because the composite properties are based on a volume fraction (or volume) of reinforcement, cost comparison should be based on equal performance. Cost comparison may favor, in some instances, synthetic textile reinforcement over steel reinforcement. It is likely that future developments and applications will make textile reinforcement increasingly cost competitive, especially when life-cycle cost analysis is considered.

Table 18.1 provides some information on the density of some common reinforcing materials. Kevlar is an aramid-based fiber, while Spectra is a high-density or high-molecular-weight polyethylene fiber. The last column shows the density ratio of steel

Table 18.1 Typical fiber characteristics and density ratios

Mesh, textile, or fiber material	Density (=1 for water)	Ratio density of fiber material to steel	Ratio density of steel to fiber material
Steel	7.85	1	1
Glass	2.60	0.3265	3.02
Carbon	1.8	0.2286	4.36
Kevlar	1.44	0.1835	5.45
PVA	1.3	0.1602	6.03
Spectra (HDPE)	0.97	0.1236	8.09
PP	0.91	0.1159	8.63

to other fiber materials. In view of the above observation on weight and volume fraction, the following conclusion could be made in looking at the last column of Table 18.1:

> *Assuming the same level of performance can be obtained in a composite with the same volume fraction of either steel reinforcement or carbon-fiber textile, one should be willing to pay for the carbon textile 4.36 times the price of steel per unit weight. It would be 8.09 times if Spectra fibers are used for the textile reinforcement.*

Clearly in some cases, synthetic fibers may offer advantages in spite of their initial high cost, particularly when steel wires are used as in wire meshes for ferrocement. This is because, unlike steel wires, synthetic fibers can be tailored to finer diameters (or denier) at little extra cost, and they are lightweight. Because the unit price ($/kilo) of synthetic fibers is significantly higher than the unit price of steel wires, there is need to provide a rational cost comparison of these reinforcement systems based on equal performance of composite.

18.4.3 Examples of comparative willingness-to-pay price

An example of a cost versus performance study using continuous reinforcement in thin cement products can be found in Naaman (2005). An extensive number of bending tests were carried out on thin cement-based composite plates that were reinforced with either steel wire meshes (ferrocement) or synthetic textiles or fabrics. The performance measure for comparison was the modulus of rupture (MOR) observed, that is, the maximum equivalent elastic flexural stress.

Column 5 of Table 18.2 shows the calculated willingness-to-pay price for a typical mesh reinforcement, based on its performance compared to that of conventional steel wire mesh. Note that the willingness-to-pay price of a given mesh reinforcement represents the maximum price one should be willing to pay for using such a mesh, assuming equal performance is achieved. Details of the study are given in Naaman (2005), where prices are given in US dollars reflecting prices in 2004. The willingness-to-pay price takes into consideration the fact that composite performance is based on the

Table 18.2 **Comparative performance of thin cement composites reinforced with various polymeric meshes based on MOR and willingness to pay price compared to conventional steel wire meshes**

Reinforcement type (1)	MOR per 1% total reinf., Vr, (MPa) (2)	Assumed density (3)	Reinforcement density ratio used (steel to fiber material) (4)	Willingness-to-pay price per unit weight assuming steel unit price is 1 unit/kg (5)
Conventional steel wire mesh	7	7.9	1	1
Very high strength steel mat (with microfibers)	21–24	7.9	1	3–3.4
PP	3.6	0.93	8.5	4.37
PVA	6.2	1.3	6.03	5.38
Carbon 1 (manual construction)	13–18.3	1.8	4.36	8.1–11.4
Carbon 1 (machine pultruded)	26.7	1.8	4.36	16.6
Carbon 2	11–17.9	1.8	4.36	6.9–11.1
Kevlar	16.7–18.1	1.44	5.45	13–14.1
Spectra	13.9–15.6	0.97	8.2	17.1–19.2
3D glass	5.28–10.4	2.6	3.02	2.28–4.48

volume fraction of the reinforcement, while the reinforcement cost is based on the per unit weight, not volume. To make the table more useful with time and geographic location, a unit price of 1 unit is taken here for 1 kg of conventional steel-galvanized wire mesh of the type used in typical ferrocement applications; it is considered as a reference base. Such a value may correspond, for instance, to 3 Euros per kilo in Germany or 4 US dollars per kilo in the United States. Other prices are relative to the 1 unit price of conventional galvanized steel wire mesh.

Table 18.2 illustrates relative values of willingness-to-pay price for various reinforcements based on equal MOR (or bending resistance). In Columns 2 and 5 of Table 18.2, when a range is shown, the lower value reflects the use of 1% PVA short microfibers in the cement matrix. Microfibers improve the vertical and interlaminar shear resistance of the composite. The total reinforcement considered in the analysis includes the amount of microfibers when used. In that case, the corresponding willingness-to-pay price may be slightly biased, because it assumes that the cost of fiber and mesh are equal. Because the cost per unit weight of PVA fibers is, at the time of this writing, smaller than that of carbon, Kevlar, or Spectra meshes, the

corresponding willingness-to-pay price calculated is slightly on the low side. Should there be need for a more precise evaluation, it is possible to separate the price of the fiber and mesh materials and provide an adjusted willingness-to-pay price for the mesh. Nevertheless, the values given in Table 18.2 are very useful in providing a rough initial estimate.

Thus, the last column of Table 18.2 suggests that one should be willing to pay 3–3.4 times more for a steel mesh or mat made with very high strength steel wires than for a conventional galvanized steel wire mesh, such as the ones typically used in ferrocement. Similarly, one should be willing to pay up to 14.1 times more for a Kevlar (aramid) mesh.

Table 18.3, also adapted from Naaman (2005), provides a comparison between actual price ratios (Column 2) in Germany in 2004 for some FRP meshes (or textiles or fabrics), compared to conventional steel wire meshes. The corresponding willingness-to-pay price ratio calculated from Column 5 of Table 18.2, assuming equal performance, is also presented. The unit prices taken for the glass, carbon, and aramid fabrics were initially taken from *Kruger* (Kruger, 2004) and were for the year 2004 in Germany. Table 18.3 is meant for illustration purposes, using only bending resistance and prices at a given time and location. It can be observed, for instance, that while carbon and glass are cost competitive, aramid is not. However,

Table 18.3 **Price ratios for 2004 compared to willingness-to-pay prices (assuming the price of conventional galvanized steel wire mesh is 1 unit/kg)[b]**

Material (1)	Unit price ratio, 2004, unit/kg (2)	Willingness-to-pay price ratio (3)	Remark (4)
Conventional galvanized steel wire mesh	1	1	Reference base for comparison
Very high strength steel mats	2.25	3–3.4	Competitive
AR-Glass, 2500 tex, 500 g/m^2	2.25	2.25–4.5	Competitive
Carbon, 1700 tex, 320 g/m^2	7.8	6.75–11.5	Competitive
Aramid, 1288 tex, 260 g/m^2	17.25	13–14	Not competitive
AR-Glass, 2500 tex, 500 g/m^2, Epoxy[a]	5	2.25–4.5	Almost competitive
Carbon, 1700 tex, 333/m^2, Epoxy[a]	11.6	6.75–11.5	Almost competitive
Aramid, 1288 tex, 260 g/m^2, Epoxy[a]	22.5	13–14	Not competitive

[a]Epoxy: means yarns impregnated with epoxy.
[b]The base unit prices for glass, carbon and aramid textiles in Euro/kilo were taken from Kruger (2004) before being normalized to the price of steel.

note that the performance characteristics, other than bending resistance, should be eventually included and weighed in the willingness-to-pay price in order to provide a fair overall comparison.

Beyond the results of this preliminary analysis, FRP reinforcement in the form of meshes, textiles, or fabrics may offer advantages in spite of their initial high cost. This is because, unlike steel reinforcements, they can be tailored to exact requirements (i.e., fiber denier or diameter, mesh opening, etc.) at little extra cost. They can also be delivered in virtually any length; they are lightweight; and they can be easily shaped to requirements. The resulting textile can be relatively stiff or highly drapable. Moreover, they offer a corrosion-free service, which is particularly important in thin products where the cover to the reinforcement can be almost zero. Their nonmagnetic property could be critical in some applications. It is thus likely that future developments and applications will make FRP-based textiles increasingly cost competitive, especially when labor cost and life-cycle cost analysis are considered.

18.5   The case for 3D textiles

18.5.1   Why 3D reinforcements?

The above performance comparison and willingness-to-pay price (Tables 18.2 and 18.3) was based on comparing only the different reinforcing materials. Other factors may have a sufficiently high influence to change the rankings observed for a final product. One of them is labor or manufacturing cost, and that brings the subject of 3D reinforcements into the discussion.

Three-dimensional reinforcement systems for ferrocement applications have been thought of by many users of ferrocement wishing to simplify the construction process and reduce the construction labor cost (Naaman, 2000, 2006, 2008, 2010). The proper placement of several layers of mesh reinforcement requires significant labor commitment. For instance, in ferrocement where steel meshes are used, the cost of labor can be as high as 50% of the total cost of the composite (Naaman, 2000). Using a pre-engineered 3D reinforcing system can thus have enormous impact on final cost.

2D textiles or fabrics using high-performance fibers (carbon, Kevlar, Spectra, etc.) have been evaluated for ferrocement applications since the early 1990s (Balaguru, 1994; Daniel and Shah, 1990; Dubey, 2004; Naaman and Al-Shannag, 1994; Naaman and Guerrero, 1996). However, it was only in the late 1990s and early 2000s that 3D meshes (or textiles or fabrics), derived from the technology of textiles and fabrics, became available for research studies in thin cement composite products. In particular, the Institute of Textiles in Aachen (ITA), Germany, in collaboration with the Technical University in Dresden, Germany, has pioneered a number of 3D textiles for applications in thin cement and concrete composites. The term TRC was used in Germany and most of Europe for such applications (Brameshuber, 2006, 2010, 2015; Curbach, 2003; Curbach and Jesse, 2009; Hegger, 2001; Hegger et al., 2006, 2015; Scheerer et al., 2015). Textile technology offers the advantage of placing as much reinforcement as needed by design (generally less than 4% by volume of composite)

exactly where it is needed, and tailoring the fabric properties and shell volume for particular applications. They also offer a tremendous advantage in simplifying the construction process and saving on labor cost. Essentially, the 3D textile (now acting as an armature system) is placed into a mold and infiltrated or encapsulated by a cement-based matrix. Thus, with an open box-shaped mold, a thin, flat reinforced-cement sheet can be easily produced. 3D textiles can be readily manufactured in thicknesses from about 5 to 50 mm, a range perfectly suitable for thin RC products, including ferrocement. Today's research and technology also allow for a 3D textile with variable thickness and with curvatures in two directions; textiles can be made more or less drapable, and could incorporated in special sections to allow sharp changes in direction, such as at a joint (Brameshuber, 2015).

Three-dimensional textiles can be designed to fulfill more than one function. They can be used as primary reinforcement, secondary reinforcement (such as for shear strength), or simply as a supporting structure for the main reinforcement, which could be made from high-performance materials, such as carbon yarns or steel strands. For this last function, that is, a supporting structure for the primary reinforcement, the textile material may use low-end and cost-effective materials, such as PP.

Examples of 3D textiles produced at the ITA in Aachen for thin TRC products are shown in Figure 18.6. Their thickness is about 15–18 mm. The textile shown in Figure 18.6b incorporates steel strands, which significantly enhance the bending resistance of the composite.

Figure 18.7 shows an example of a 3D textile with double curvature developed by a research group at ETH in Zurich (Hack et al., 2015). Some other 3D textiles that are
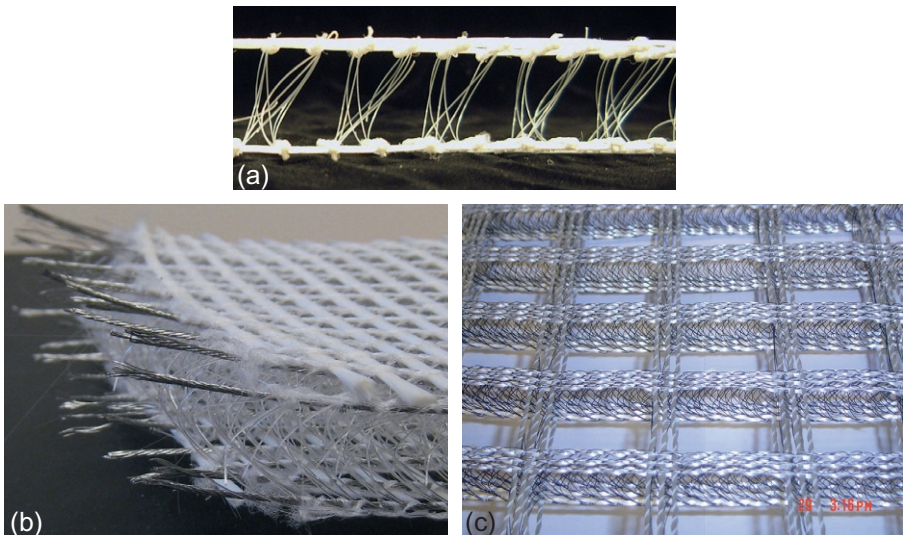
Figure 18.6 Examples of 3D textile reinforcements produced at the ITA in Aachen Germany: (a) spacer textile; (b) hybrid spacer textile acting as a support structure for incorporated steel strands; and (c) grid textile.
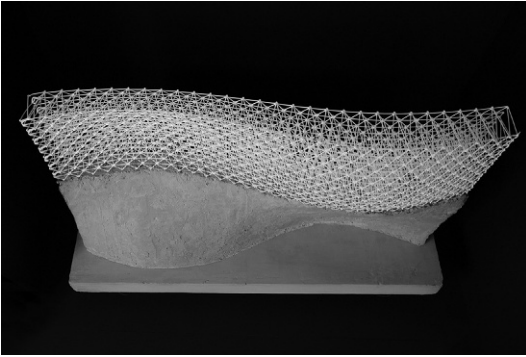
Figure 18.7 3D textile with double curvature half filled with concrete developed at ETH in Zurich (Chair of Architecture and Digital Fabrication) (Hack et al., 2015).
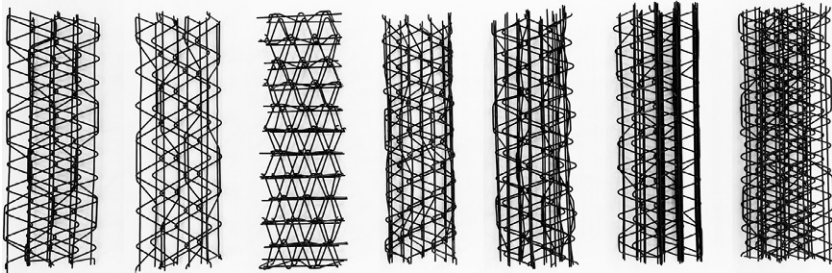
Figure 18.8 Examples of 3D robotically fabricated meshes under developments at ETH in Zurich (Chair of Architecture and Digital Fabrication) (Hack et al., 2015).

being developed by the same group with different geometric topography are shown in Figure 18.8. They suggest that the possibilities for the future are enormous.

18.5.2   Status of applicability to 2D and 3D textiles to thin reinforced cementitious products

Ferrocement, laminate cementitious composites, and TRC comply with the same principles of mechanics as RC. However, the cement matrix is made out of much finer components (such as those containing fine sand vs. coarse aggregates) and the reinforcement has much smaller diameter or denier (such as that of a steel wire vs. a reinforcing bar). These composites offer all the inherent benefits of using a concrete matrix, namely high compressive strength, stiffness, durability, fire resistance, abrasion resistance, unlimited availability, and safety (when properly designed).

Thin TRC, ferrocement, and laminate cementitious composites can fulfill the dual role of light-manufactured structural elements (wall panels for housing, corrugated roofing panels, etc.), and protective skin (cladding) for other structures. They can also be used for entire structures, such as a house or a shell-type roof, and for retrofitting existing structures, such as in seismic retrofitting of masonry walls. Both analytical

and experimental research has indicated that they can achieve a high level of performance (strength and ductility) at a competitive cost (Section 18.5 and Table 18.3). In particular, it was observed that a hybrid combination using textiles or meshes in sandwich construction, combined with short discontinuous fibers, reduces the need for multiple layers of reinforcement. It does this while providing competitive bending and sufficient shear resistance (vertical shear and interlaminar or horizontal shear), and significantly reducing material and labor costs (Figure 18.1b and c). Note that fibers or microfibers added to the matrix also serve other functions, such as improving first cracking strength, impact resistance, ductility, the bond of the main reinforcement, energy absorption, and, in many cases, contribute to bending resistance, as well.

18.5.3   Steel versus fiber reinforced polymer reinforcements and textiles

Looking ahead, when comparing high-performance textile reinforcements (made with high-performance fibers) with steel reinforcements, it is likely that the advantage of one over the other will depend on criteria other than strength or MOR. These criteria may include weight, ease of handling, and life-cycle cost. Moreover, the ease of producing 3D textile architectures (or topographies) and the possibility of using hybrid compositions of reinforcement (steel and FRP, with or without fibers or microfibers in the matrix) may provide the best solution (Naaman, 2008). Clearly the ability to manufacture a particular 3D textile at a reasonable cost will provide a key advantage.

Note that pre-engineered 3D textile reinforcement (say in the form of flat panels, corrugated sheets, or shells) can serve as light reinforcement for several applications. For instance, the weight of a 3D carbon or Kevlar reinforcement in a cement composite panel can be as little as 2% of the weight of the composite. The matrix, essentially made of cement, sand, and water, can be cast in place where the structure or element is needed or in a nearby facility. Special cementitious matrices can harden sufficiently in less than 24 h. This approach will offer enormous cost savings, for instance, for emergency shelters following natural disasters, in comparison to airlifting entire shelter systems. The final product can be eventually turned into permanent, durable, and reliable housing.

18.5.4   The case for prestressing, including self-stressing

Cement and ceramic matrices are brittle in nature. They generally have a compressive strength much higher than their tensile strength, and thus tend to crack under tensile stresses induced by service loads. Prestressing these matrices, such as in the case of prestressed concrete, leads to a better composite, in which higher tensile stresses can be applied to the structure and cracking can be avoided or delayed under service load conditions. The structure becomes more impervious to penetration by liquids and gases, thus providing significantly higher durability.

Prestressing cementitious composite products such as thin sheets, boards, cladding, pipes, and the like should bring an enormous impetus to their use and development.

However, prestressing using conventional methods such as pre-tensioning or post-tensioning (by mechanical stretching and releasing of the reinforcement) requires relatively high technical skill, is labor intensive, and necessitates very special care when thin polymer fibers are used (Reinhardt et al., 2002). Thus, conventional prestressing methods are not cost-effective at this time for thin cementitious products. Nevertheless, prestressing can be accomplished using the principles of internal prestressing or self-stressing.

In the self-stressing technique, the reinforcement is first placed in the mold and then encapsulated by a cement matrix similarly to conventional RC. Self-stressing of cement composites can be achieved (after the matrix has hardened) by one of three possible methods: expansion of the matrix, contraction of the reinforcement, and a combination of both.

Prestressing (by contraction of the reinforcement) is self-induced when needed by simple heating or radiation or another treatment of special reinforcing materials, such as shape memory alloys (SMA). Self-stressing by expansion of the cement matrix occurs automatically with time. No labor is involved in stressing the reinforcement. Self-stressing incurs significant savings in labor cost and reduces the need for a highly technical labor force. Moreover, the method of self-stressing allows the reinforcement to be formed in any shape in a two- or three-dimensional space without special devices.

For self-stressing by the reinforcement, there are today "smart" materials that allow us to envision self-stressing, which produces sufficient prestress levels. SMA (Krstulovic-Opara and Naaman, 2000; Naaman, 2000) and some special polymeric fibers, such as liquid crystal polymers, possess the unique property of being able to be frozen temporarily in a particular state (imagine a stretched state). Then, with proper heat or radiation treatment, they can go back to their previous equilibrium state (thus shortening elastically). This deformation-controlled recovery property of a material is a property that produces a shortening of the material when it passes from one state to the other. In attempting to shrink back to its previous state, the reinforcement provides, through bond and/or anchorage, the necessary prestressing. The treatment (heat or radiation or other exposure) to trigger shortening of the reinforcement can be applied any time after hardening of the cement matrix. The special reinforcement needed, a 2D or, better, a 3D textile or fabric or armature system, can be machine manufactured, stored, shelved, placed in the composite, and triggered to recover its deformation (inducing prestressing) at any appropriate time. Prestressing could help make textiles with low-end fibers more competitive for thin TRC products.

18.6   Ultra-high performance cement matrices in thin cement composites

Cementitious materials with compressive strengths over 150 MPa can be qualified as UHPC or ultra-high performance concrete. In order to achieve the high strength in UHPC, particle packing is optimized within the matrix. Dense particle packing implies high durability, improved freeze–thaw resistance, increased resistance against various chemicals, and higher penetration resistance. Thus the potential of UHPC in

various applications, including blast- and impact-resistant structures, has attracted high interest by both the research and professional communities (ACI Committee 239, 2015; Fehling et al., 2004, 2008; Graybeal and Davis, 2008; Naaman and Wille, 2012; Richard and Cheyrezy, 1995; Rossi, 2008; Russell and Graybeal, 2013; Schmidt et al., 2004, 2012; Ulm and Acker, 2008).

The most common UHPC mixtures developed so far should be called "mortar," and not "concrete," because they do not use large aggregates. Instead they utilize very fine particles including cement, glass powder (or silica powder), silica fume, fly ash, and sand, with a maximum particle size generally less than 1 mm. The finest particles in the mixture come from silica fume, and are, on average, about 0.5 μm in diameter; generally, they are less than 1 μm in diameter ($1 \mu m = 10^{-3}$ mm). Moreover, even with a low water-to-binder ratio, given the help of superplasticizers (HWRA) and viscous agents, these mixtures are commonly self-consolidating or self-compacting. This means that they can easily flow on their own inside a mold and entirely encapsulate existing reinforcement without any vibration. Such self-consolidating UHPC mixtures are particularly compatible with and suitable for thin TRC products and ferrocement constructed using molds, because the armature systems (multiple layers of mesh, 3D textile, etc.) in these composites have very small openings. Thus, they require a matrix with very fine particles to pass through such openings.

Referring to the simple mechanical compatibility between the reinforcement and the matrix (Figure 18.4), note that the modulus of UHPC matrices is of the order of 50 GPa. Thus, compatible reinforcements should preferably have as high an elastic modulus as possible, unless prestressing is considered. Besides steel, a potential reinforcement among high-end FRP meshes or textiles or fabrics, is carbon.

Looking ahead, it is conceivable today to envision the combination of ultra-high performance, fiber-reinforced cement matrices with self-stressing to produce truly outstanding TRC composites that could resist cracking under service loads and have a service life that could be measured in decades and centuries.

18.7 Summing up: Mechanical performance

1. *Compressive performance*. The compressive strength of cement composites including ferrocement, fiber RC, and TRC is predominantly dictated by the strength of the cementitious matrix. Thus any advances in the matrix can be translated to the composite, such as the use of high performance or ultra-high performance matrices of strength exceeding 150–200 MPa, and where durability is expected to be significantly improved.
2. *Bending resistance*. According to several investigations of ferrocement and thin cement composite plates reinforced with either conventional steel wire meshes or high performance FRP meshes (or textiles or fabrics of Carbon, Kevlar, Spectra), a limit of about 50 MPa for the MOR or equivalent elastic bending strength was observed (Naaman and Al-Shannag, 1994; Naaman and Guerrero, 1996; Naaman and Chandrangsu, 2000; Naaman, 2000, 2003b, 2005; Naaman et al., 2005). With FRP or textile reinforcements, this limit was obtained when microfibers were used in the matrix to improve both vertical and interlaminar shear resistance. Analytical studies suggest optimum values would reach 60–70 MPa in multilayered bending elements (Parra-Montesinos and Naaman, 2001). In prior studies

involving low-end polymeric meshes (or textiles or fabrics), such as PP and nylon, a MOR limit of 25 MPa was obtained, even when the volume fraction of the reinforcement was as high as practicable (Naaman, 2000). Moreover, with low-end polymeric textiles and normal-weight cement matrices, large crack width and large permanent (not recoverable) creep deformations were observed (Naaman, 2000). This represents a significant drawback.

3. *Potential bending resistance*. Using a UHPC matrix and hybrid steel reinforcements comprised of continuous strands and discontinuous fibers in about 10% of the total volume fraction of the reinforcement, Wille and Naaman reported a MOR value close to 230 MPa (Wille and Naaman, 2012). Such a value will remain a target to be achieved by TRC, although much lower values are sufficient for numerous applications.

4. *Tensile resistance*. The tensile resistance of most cement composites with continuous reinforcement can be predicted directly by using the following simple relation (Naaman, 2000): $\sigma_{tu-composite} = \eta_o \times V_r \times \sigma_{ru}$, where η_o is the efficiency factor of reinforcement in the direction considered, V_r is the total volume fraction of reinforcement, and σ_{ru} is the ultimate tensile resistance of the reinforcement. It is assumed that the matrix is cracked and does not contribute any resistance. Note, however, that a high tensile resistance does not always imply good performance, as deformations and crack widths could be too large for a given application.

5. *Cost*. The cost of the matrix in typical thin reinforced cement composites is very small (5%) compared to that of the reinforcement and labor, which, in most developing countries, are of the same order (Naaman, 2000, 2005). Thus, cost reduction should focus not only on material cost, but on labor cost. The use of 3D textiles will have a significant impact on reducing labor cost.

6. *Lightweight matrices*. As suggested in the simple mechanical rule stated in Section 18.3, textiles or fabrics made with low-end polymeric fibers may be compatible with lightweight cement matrices. Lightweight implies, here, a density ranging between 0.5 and 1. The author is not aware of any systematic study involving such matrices. One can simply predict that their MOR will be less than 25 MPa (as observed with polymeric meshes and normal-weight cement matrices).

7. *Self-stressing composites*. Very little has been done so far in that field. Prestress levels close to 7 MPa were reported in (Krstulovic-Opara and Naaman, 2000; Naaman, 2000) for thin cement specimens.

18.8   Summing up: Functions and applications

For their use in thin cementitious composites, textiles can play several roles or functions that extend the scope of their applicability: (1) as primary reinforcement throughout (bending, shear, torsion, etc.); (2) as secondary reinforcement (shear, crack control, transverse reinforcement, etc.); and/or (3) as supporting structure for the primary reinforcement, including conventional steel wires, bars, and strands. Figure 18.9 illustrates these functions. Note also that textiles can be used in combination with steel wire meshes and with the possible addition of discontinuous fibers to the matrix.

Applications of thin TRC composites include: (1) standalone structures or structural elements (wall panel, housing unit, pipe, water tank, etc.); (2) applications in
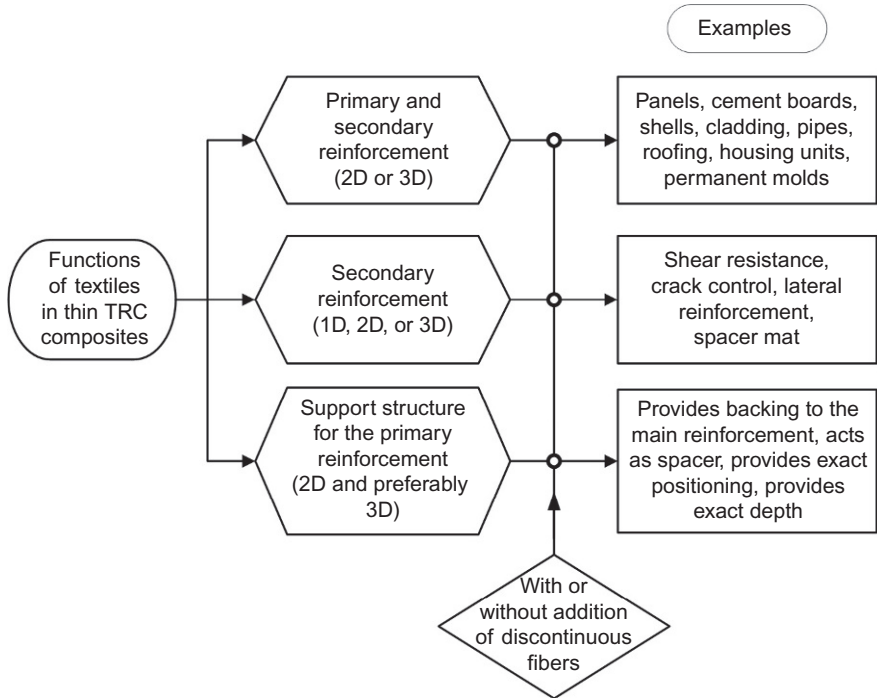
Figure 18.9 Typical functions of textiles in thin TRC products.

combination with conventional reinforced or prestressed concrete structures (such as the shell roof of an RC building, the wall or dome of PC water tank and permanent mold for an RC slab); and (3) use in repair, strengthening or seismic retrofit of existing structures (such as confinement of an RC column, seismic retrofit of a masonry wall, replacement of the damaged cover of an RC beam, and lining of a water tank).

18.9 Suggested research needs and directions for successful thin TRC products

As expected, researchers will keep exploring new grounds, breaking existing barriers, and exceeding existing limits. Looking ahead, some areas of potential research to improve composite performance and guarantee the success of thin TRC products are listed in the following:

1. Identify high-strength high-modulus reinforcements to produce textiles or fabrics for TRC applications; most promising at this time are carbon-based fibers or yarns based on carbon fibers. The general rule is to find a material with combined high-strength, high-elastic modulus, and, preferably, good bond with the cement matrix.

2. While carbon fibers are extremely attractive for use in TRC structures, it is necessary to ascertain that high electric charges, such as from lightning, do not reach such structures. Indeed, carbon can burn, decompose, and disintegrate under a high electrical charge. On the other hand, such a characteristic can be advantageous for demolition purposes.

3. Develop textile architecture(s) or topographies that favor achieving an equivalent elastic modulus as close as possible to the elastic modulus of the fiber material.

4. Develop 3D textiles tailored for optimum performance in specific applications, such as for thin plates or corrugated sheets or pipes or columns. This is an area that is potentially cost-competitive today, and thus should be given some priority.

5. Develop 3D textiles using low-end polymer fibers to act as the supporting structure for high-end carbon yarns or steel wires or strands or wire meshes; these can function similarly to a fiber mat in a sandwich-type construction.

6. Develop 2D or 3D textiles with hybrid reinforcement, such as carbon and PP (carbon for strength and modulus, and PP as armature support).

7. Develop 3D textiles with built-in curvature in one or two directions, such as is needed for a pipe or a shell.

8. Develop 3D textiles that can accommodate a joint with a sharp change in curvature.

9. Develop drapable 2D and 3D textiles for use in curved structures (shells).

10. Develop optimized 2D textiles designed for use in combination with fibers or fiber mats to produce sandwich-type construction.

11. Develop optimized 2D or 3D textiles for thin TRC sheets that are similarly suitable for structural strengthening as externally bonded FRP sheets are.

12. Explore self-stressing composites using fibers or textiles with useful deformation recovery property. Self-stressing can be achieved by a possible combination of controlled matrix expansion and fiber or textile deformation recovery.

13. Explore the use of high-performance and ultra-high performance cement matrices of compressive strengths exceeding 150–200 MPa, with and without the addition of microfibers, with 2D and 3D textile topographies that they can encapsulate.

14. Research in-depth and extensively the durability of TRC using various types of reinforcements and under different environmental exposures, short- and long-term. Although corrosion, as with the use of steel reinforcements, is not a problem, other issues related to deterioration with time and under various environmental conditions (including extreme temperature cycling) need to be clearly ascertained and included in the performance and cost evaluation of the final product.

15. Develop compatible lightweight cementitious matrices and low-end fibers and textiles (2D or 3D) designed for optimizing composite performance and minimizing cost.

16. Assuming a TRC composite is optimized (textile, matrix, bond) for a particular structural application, it is necessary to provide a framework for optimizing its overall performance (i.e., structural, mechanical, environmental, esthetic, etc.) to minimize the overall life-cycle cost.

17. Modify existing construction processes or develop new ones that are more suitable for TRC applications.

18. Develop standard operating procedures for field implementation and develop standards for TRC products.

19. Exploit specialized products such as floating concrete, transparent concrete, and composites with nonmagnetic characteristics. These use special textile reinforcements and are likely to provide a solid niche for TRC.

20. Develop large-scale 3D textiles for possible applications in conventional RC structures, starting with slabs, shells, and small beams (say up to 150 mm in thickness).

It can be said, at time of this writing, that TRC is at a very promising junction of its development. While advanced technology is allowing extensive research on the material properties and topographies of a variety of textile reinforcements, recent advances in the cementitious matrix, such as self-compacting, self-leveling, ultra-high performance, density control, particle packing, etc., are sufficient to allow TRC to succeed and flourish in the near future and beyond.

While it is always healthy to dream of what seems like the impossible at a given time, the author believes that the following dream is possible in the near future. That dream is the common availability of thin TRC products, using normal-weight and/or lightweight cementitious matrices, with compressive strengths from very low to very high (2–200 MPa). These products will use pre-engineered 3D textiles, possibly in combination with fibers, and possibly self-stressed. The 3D textile could act as primary reinforcement, secondary reinforcement, or simply a support structure for conventional steel reinforcements.

Acknowledgments

References

ACI Committee 549, 1988, and later. Guide for the Design, Construction and Repair of Ferrocement. ACI 549.1R-88, ACI Structural Journal, May–June, 1988, pp. 325–351. Also reinstated as 549.1R-93 and published in ACI Manual of Concrete Practice, American Concrete Institute, Farmington Hills, MI, 27 pp.

ACI Committee 549, 1997. State-of-the-art report on ferrocement. Concr. Int. 4 (8), 13–38 (August 1982). Reinstated as ACI 549-R97. In: Manual of Concrete Practice, American Concrete Institute, Farmington Hills, MI, 26 pp.

ACI Committee 549, 2004. Report on Thin Reinforced Cementitious Products. 549.2R-04. American Concrete Institute, Farmington Hills, MI.

ACI Committee 239, 2015. Report on Ultra High Performance Concrete (UHPC). Document Under Development.

Balaguru, P. (Ed.), 1994. Thin Reinforced Concrete Products and Systems. SP-146. American Concrete Institute, Farmington Hills, MI. 106 pp.

Brameshuber, W. (Ed.), 2006. Textile Reinforced Concrete. State-of the-Art Report of RILEM Technical Committee 201-TRC, Report 36. Rilem Publications, Bagneux, France. 273 pp.

Brameshuber, W. (Ed.), 2010. Proceedings of Rilem 2nd International Conference on Textile Reinforced Concrete. Aachen, Germany, September 2010, Rilem Pro. 75. 420 pp.

Brameshuber, W. (Ed.), 2015. Ferro-11: Proceedings of the 11th International Symposium on Ferrocement and 3rd International Conference on Textile Reinforced Concrete. Aachen, Germany, Rilem Publication PRO 98. 540 pp.

Curbach, M. (Ed.), 2003. Proceedings of Second "Colloquium on Textile Reinforced Structures—CTRC2," Dresden, SFB 528. Technische Universitat Dresden, Germany. 550 pp.

Curbach, M., Jesse, F. (Eds.), 2009. Proceedings of the 4th Colloquium on Textile Reinforced Structures (CTRS4). Dresden, SFB 528. Technische Universitat Dresden.

Daniel, J.I., Shah, S.P. (Eds.), 1990. Thin-Section Fiber Reinforced Concrete and Ferrocement (SP-124). American Concrete Institute, Detroit, MI. 448 pp.

Dubey, A. (Ed.), 2004. Thin Reinforced Cement-Based Products and Construction Systems. American Concrete Institute, Farmington Hills, MI. Special Publication SP-224.

Fehling, E., Bunje, K., Leutbecher, T., 2004. Design relevant properties of hardened ultra high performance concrete. In: Schmidt, M., Fehling, E., Geisenhanslüke, C. (Eds.), Proceedings of the International Symposium on Ultra High Performance Concrete. Kassel University Press, Kassel, Germany, pp. 327–338.

Fehling, E., Schmidt, M., Sturwald, S. (Eds.), 2008. Ultra high performance concrete (UHPC).Proceedings of Second International Symposium on Ultra High Performance Concrete, Kassel University Press (Schriftenreihe Baustoffe und Massivbau 10), GmbH, Germany. 902 pp.

Ferrocement Model Code, 2001. By IFS Committee 10-01. International Ferrocement Society. Asian Institute of Technology, Bangkok, Thailand. 95 pp.

Graybeal, B.A., Davis, M., 2008. Cylinder or cube: strength testing of 80 to 200 MPa (11.6 to 29 ksi) ultra-high-performance fiber-reinforced concrete. ACI Mater. J. 105 (6), 603–609.

Guerrero, P., Naaman, A.E., 1998. Bending behavior of hybrid ferrocement composites reinforced with PVA meshes and PVA fibers. In: Naaman, A.E. (Ed.), Ferrocement 6—Lambot Symposium, Proceedings of Sixth International Symposium on Ferrocement, University of Michigan, CEE Department, pp. 361–374.

Hack, N., Lauer, W., Gramazio, F., Kohler, M., 2015. Mesh mould: robotically fabricated metal meshes as concrete formwork and reinforcement. In: Brameshuber, W. (Ed.), Proceedings of the 11th International Symposium on Ferrocement and 3rd International Conference on Textile Reinforced Concrete. Rilem Publication PRO 98, Aachen, Germany, pp. 347–358.

Hegger, J. (Ed.), 2001. Fachkolloquium der Sonderforschungsbereiche 528 und 532. RWTH, Aachen (in German).

Hegger, J., Brameshuber, W., Will, N. (Eds.), 2006. Textile reinforced concrete.Proceedings of 1st International RILEM Symposium, PRO 50, Rilem Publications, Bagneux, France.

Hegger, J., Will, N., Chudoba, R., Scholzen, A., 2015. Classification of approaches to dimensioning and assessment of lightweight TRC structures. In: Brameshuber, W. (Ed.), Ferro-11: Proceedings of the 11th International Symposium on Ferrocement and 3rd International Conference on Textile Reinforced Concrete, Aachen, Germany, Rilem Publication PRO 98, pp. 45–50.

Jesse, F., Curbach, M., 2003. Strength of continuous AR-glass fiber reinforcement of cementitious composites. In: Naaman, A.E., Reinhardt, H.W. (Eds.), Proceedings of High Performance Fiber Reinforced Cement Composites—HPFRCC4, Rilem Pro 30, Rilem Publications, pp. 337–348.

Koustas, L., Bousias, S.N., Triantafillou, T.C., 2014. Seismic strengthening of in-filled RC frames with TRM: experimental study. J. Compos. Construct. http://dx.doi.org/10.1061/(ASCE)CC.1943-5614.0000507. ASCE, 94014048.

Krstulovic-Opara, N., Naaman, A.E., 2000. Self-stressing fiber composites. ACI Struct. J. 97 (2), 335–344.

Kruger, M., 2004. Vorgespannter Textilebewhehrter Beton (Prestressed Textile Reinforced Concrete), in German. Doctoral Dissertation, University of Stuttgart, Institut fur Werkstoffe im Bauwesen, Stuttgart, Germany, 201 pp., http://elib.uni-stuttgart.de/opus/volltexte/2004/1985/.

Lopez, M.M., Naaman, A.E., 1998. Study of shear joints in fiber reinforced plastic (FRP) ferrocement bolted connections. J. Ferrocement 28 (4), 249–337. Also in Ferrocement 6—Lambot Symposium, Proceedings of Sixth International Symposium on Ferrocement, A.E. Naaman, Editor, University of Michigan, CEE Department, June 1998.

Mobasher, B., Pahilajani, J., Peled, A., 2000. Analytical simulation of tensile response of fabric reinforced cement based composites. Cem. Concr. Compos. 28, 77–89.

Naaman, A.E., 2000. Ferrocement and laminated cementitious composites. Techno Press 3000, Ann Arbor, MI, USA. ISBN: 0-9674939-0-0. 370 pp. www.technopress3000.com

Naaman, A.E., 2002. Ferrocement: international revival. In: Balaguru, P., Naaman, A.E., Weiss, W. (Eds.), Proceedings of ACI Symposium on Concrete: Material Science to Applications, a Tribute to S.P. Shah, ACI SP-206, pp. 323–340.

Naaman, A.E., 2003a. FRP reinforcements in structural concrete: assessment, progress and prospects. In: Tan, K.H. (Ed.), Proceedings of International Conference on FRP Reinforcements in Concrete Structures, FRPRCS6, Singapore, World Scientific, vol. 1, pp. 3–24.

Naaman, A.E., 2003b. Progress in ferrocement and hybrid textile composites. In: Curbach, M. (Ed.), Proceeding of Colloquium on Textile Reinforced Concrete—CTRC2, Dresden University, Germany.

Naaman, A.E., 2005. Thin cement composites: performance comparison between steel and textile reinforcements. In: Hamelin, P., Bigaud, D., Ferrier, E., Jacquelin, E. (Eds.), In: Composites in Construction, vol. 2. University of Lyon, France, pp. 1155–1164.

Naaman, A.E., 2006. Ferrocement: four decades of progress. J. Ferrocement 36 (1), 741–756. Also in Proceedings of International Symposium on Ferrocement and Thin Cement Products, Bangkok, Thailand, February 2006.

Naaman, A.E., 2008. From wire mesh to 3D textiles: progress in reinforcement for ferrocement and thin cement products. In: Bell, M., Buckley, C. (Eds.), Proceedings of Conference on Solid States: Changing Times for Concrete, Columbia University, US, October, 2008, pp. 147–157. Printed in "Solid States in Transition" Princeton Architectural Press, 2010.

Naaman, A.E., 2010. Thin textile reinforced cement composites: competitive status and research directions. In: Brameshuber, W. (Ed.), Proceedings of Rilem 2nd International Conference on Textile Reinforced Concrete, Aachen, Germany, Rilem Pro. 75, pp. 3–22.

Naaman, A.E., 2012. Evolution in ferrocement and thin cementitious composites. Arabian Journal of Science and Engineering. King Saud University of Petroleum and Minerals, KFUPM, Dhahran, Saudi Arabia, pp. 1–19. ISSN 1319-8025. http://dx.doi.org/10.1007/s13369-01200187-4.

Naaman, A.E., Al-Shannag, J., 1994. Ferrocement with fiber reinforced plastic meshes: preliminary investigation. In: Nedwell, P., Swamy, N.R. (Eds.), Proceedings of the Fifth International Symposium on Ferrocement, Manchester, England, E. and FN Spon, London, pp. 435–445.

Naaman, A.E., Chandrangsu, K., 2000. Bending behavior of laminated cementitious composites reinforced with FRP meshes. In: Peled, A., Shah, S.P., Banthia, N. (Eds.), ACI Symposium

on High Performance Fiber-Reinforced Concrete Thin Sheet Product. American Concrete Institute, Farmington Hills, pp. 97–116. ACI SP 190.

Naaman, A.E., Guerrero, P., 1996. Bending behavior of thin cement composites reinforced with FRP meshes. In: Saadatmanesh, H., Ehsani, M. (Eds.), Proceedings of First International Conference on Fiber Composites in Infrastructures ICCI 96, University of Arizona, Tucson, pp. 178–189.

Naaman, A.E., Wille, K., 2012. The path to ultra-high performance fiber reinforced concrete (UHP-FRC): five decades of progress. In: Schmidt, M., Fehling, E., Giotzbach, C., Frohlish, S., Piotrovski, S. (Eds.), Proceedings of Hipermat 2012, 3rd International Symposium on Ultra High Performance Concrete and Nanotechnology in Construction. Kassel University, Germany, pp. 3–15.

Naaman, A.E., Wongtanakitcharoen, T., Likhitruangsilp, V., 2005. High performance hybrid composites for thin cementitious products: the next generation. In: Biernacki, J.J., Shah, S.P., Lakshmanan, N., Gopalakrishnan, S. (Eds.), High-Performance Cement-Based Concrete Composites. In: Materials Science of Concrete—Special Volume, The American Ceramic Society, pp. 55–72.

Parra-Montesinos, G., Naaman, A.E., 2001. Parametric evaluation of the bending response of ferrocement and hybrid composites with FRP reinforcements. In: Mansur, M.A., Ong, K.C.G. (Eds.), Proceedings of Seventh International Symposium on Ferrocement and Thin Reinforced Cement Composites, Singapore, pp. 227–238.

Parra-Montesinos, G., Reinhardt, H.W., Naaman, A.E. (Eds.), 2012. High Performance Fiber Reinforced Cement Composites 6—HPFRCC6. Rilem Publications, Springer. ISBN: 978-94-007-2435-8, 559 pp.

Peled, A., Bentur, A., Yankelevsky, D., 1999. Flexural performance of cementitious composites reinforced with woven fabrics. J. Mater. Civ. Eng. ASCE 325–330.

Reinhardt, H.W., Naaman, A.E. (Eds.), 2007. High Performance Fiber Reinforced Cement Composites—HPFRCC 5. RILEM Proceedings, Pro. 53, S.A.R.L., Cachan, France. 518 pp.

Reinhardt, H.W., Kruger, M., Grosse, C.U., 2002. Thin plates prestressed with textile reinforcements. In: Balaguru, P., Naaman, A.E., Weis, J. (Eds.), Concrete: Materials Science to Applications: A Tribute to Surendra P. Shah. American Concrete Institute, Farmington Hills, MI, USA, pp. 355–372. SP 206.

Richard, P., Cheyrezy, M., 1995. Composition of reactive powder concretes. Cem. Concr. Res. 25 (7), 1501–1511.

Rossi, P., 2008. Ultra high performance concretes—a summary of the current knowledge. Concr. Int. 31–34.

Russell, H.G., Graybeal, B.A., 2013. Ultra high performance concrete: a state-of-the-art report for the bridge community. FHWA, Report No. FHWA-HRT-13-060, US Department of Transportation, Federal Highway Administration, USA, 163 pp.

Scheerer, S., Schladitz, F., Curbach, M., 2015. Textile reinforced concrete: from the idea to a high performance material. In: Brameshuber, W. (Ed.), Ferro-11: Proceedings of the 11th International Symposium on Ferrocement and 3rd International Conference on Textile Reinforced Concrete, Aachen, Germany, Rilem Publication PRO 98, pp. 15–33.

Schmidt, M., Fehling, E., Geisenhanslüke, C. (Eds.), 2004. Ultra high performance concrete (UHPC). Proceedings of the International Symposium on UHPC. Kassel University Press GmbH, Germany. 868 pp.

Schmidt, M., Fehling, E., Giotzbach, C., Frohlish, S., Piotrovski, S. (Eds.), 2012. Proceedings of Hipermat 2012, "3rd International Symposium on Ultra High Performance Concrete and Nanotechnology in Construction". Kassel University, Germany. 1036 pp.

Si Larbi, A., Ferrier, E., Hamelin, P., 2010. Study of reinforced concrete beams strengthened with textile reinforced concrete. In: Brameshuber, W. (Ed.), Proceedings of Rilem 2nd International Conference on Textile Reinforced Concrete, Aachen, Germany, September 2010, Rilem Pro. 75, pp. 227–234.

Triantafilou, T., Papanicolaou, C.G., 2006. Shear strengthening of reinforced concrete members with textile reinforced mortar (TRM) jackets. Mater. Struct. 39 (1), 93–103.

Ulm, F.-J., Acker, P., 2008. Nanoengineering UHPC materials and structures. In: Fehling, E. et al., (Ed.), Ultra High Performance Concrete (UHPC), Proceedings of Second International Symposium on Ultra High Performance Concrete. Kassel University Press (Schriftenreihe Baustoffe und Massivbau 10), GmbH, Germany, pp. 3–9.

Wille, K., Naaman, A.E., 2012. Preliminary investigation on ultra-high performance ferrocement. In: Wainstock Rivas, H., Prada Seoane, L., Randa Castro, I. (Eds.), Proceedings of 10th International Symposium on Ferrocement and Thin Reinforced Cement Composites, La Havana, Cuba. ISBN: 978-959-247-098-9, pp. 251–260.

This page intentionally left blank

Index

Note: Page numbers followed by *f* indicate figures and *t* indicate tables.

Textile Fibre Composites in Civil Engineering provides a state-of-the-art review from leading experts in the field on those developments which have appeared over the last decade or so, on the use of textile fibre composites in civil engineering, with a focus on both new and existing structures. Textile-based composites are new materials for civil engineers. Recent developments have demonstrated their potential in the prefabrication of concrete structures as well as in strengthening and seismic retrofitting of existing concrete and masonry structures, including those of a historical value. The book will review materials, production technologies, fundamental properties, testing, design aspects, applications, and directions for future research and developments.

Following the opening introductory chapter, Part One covers materials, production technologies and manufacturing of textile fibre composites for structural and civil engineering. Part Two moves on to review testing, mechanical behaviour and durability aspects of textile fibre composites used in structural and civil engineering. Chapters here cover topics such as the durability of structural elements and bond aspects in textile fibre composites. Part Three analyses the structural behaviour and design of textile reinforced concrete. This section includes a number of case studies providing thorough coverage of the topic. The final section of the volume details the strengthening and seismic retrofitting of existing structures. Chapters investigate concrete and masonry structures, in addition to providing information on case studies and insight into future directions in the field.

Textile Fibre Composites in Civil Engineering is a key volume for researchers, academics, practitioners and students working in civil and structural engineering and advanced construction materials. The book provides broad coverage of a wide range of topics and includes contributions from leading experts in the field.

Thanasis C. Triantafillou is Professor in the Department of Civil Engineering, University of Patras, Greece.